

FEBRUARY 2019

AJNR

VOLUME 40 • PP 205-385

AJNR

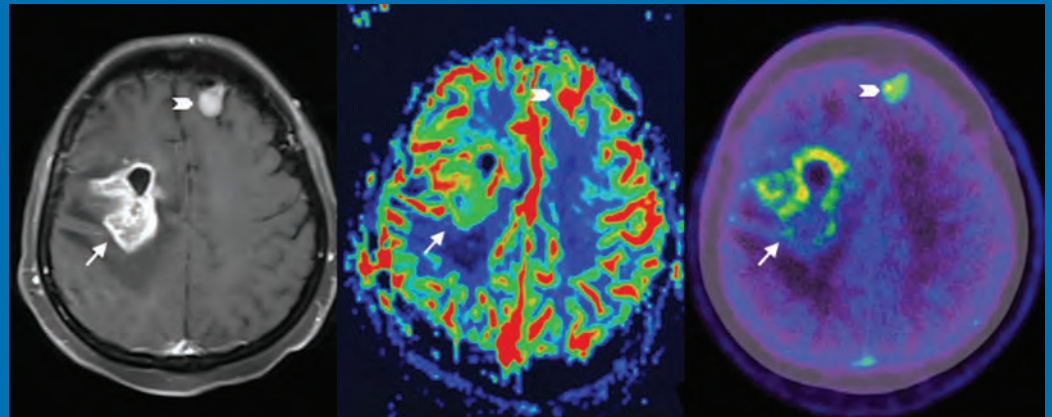
AMERICAN JOURNAL OF NEURORADIOLOGY

FEBRUARY 2019
VOLUME 40
NUMBER 2
WWW.AJNR.ORG

THE JOURNAL OF DIAGNOSTIC AND
INTERVENTIONAL NEURORADIOLOGY

DSC PWI and methionine PET/CT in tumor vs radiation injury
Improving the quality of synthetic FLAIR images with deep learning
Acute toxic leukoencephalopathy

Official Journal ASNR • ASFNR • ASHNR • ASPNR • ASSR



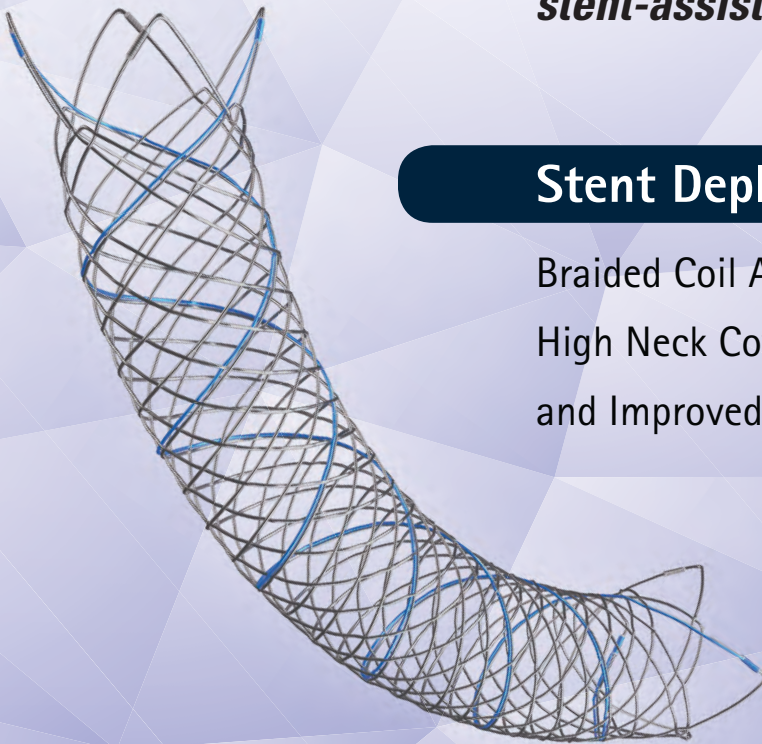


Aneurysm
Therapy
Solutions

LVIS[®]

Intraluminal Support Device

*The first and only stent with
Premarket Approval (PMA) for use in
stent-assisted coil embolization*



Stent Deployment. Refined.

Braided Coil Assist Stents with
High Neck Coverage, Excellent Visibility
and Improved Conformability*

Low-profile Visualized Intraluminal Support



INDICATIONS FOR USE:

The LVIS[®] and LVIS[®] Jr. devices are indicated for use with neurovascular embolization coils in patients ≥ 18 years of age for the treatment of wide-neck (neck width ≥ 4 mm or dome to neck ratio < 2) saccular intracranial aneurysms arising from a parent vessel with a diameter ≥ 2.0 mm and ≤ 4.5 mm.

Rx Only: Federal (USA) law restricts this device to sale by or on the order of a physician.

The HydroCoil[®] Embolic System (HES) and MicroPlex[®] Coil System (MCS) are intended for the endovascular embolization of intracranial aneurysms and other neurovascular abnormalities such as arteriovenous malformations and arteriovenous fistulae. The HES and MCS are also intended for vascular occlusion of blood vessels within the neurovascular system to permanently obstruct blood flow to an aneurysm or other vascular malformation and for arterial and venous embolizations in the peripheral vasculature.

The device should only be used by physicians who have undergone pre-clinical training in all aspects of HES/MCS procedures as prescribed by MicroVention.

CE
0297

A Complete Coil Portfolio

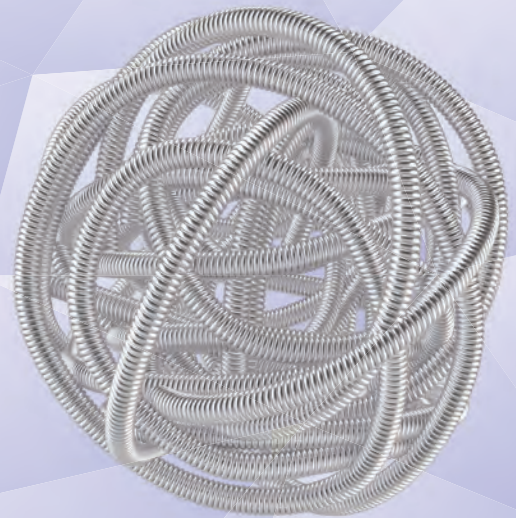
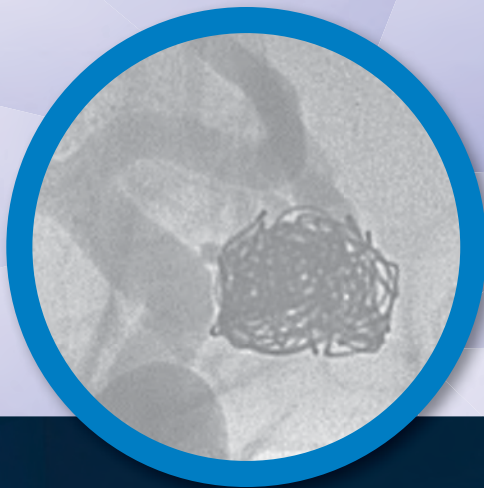
Hydrogel Embolic Coils & Platinum Coils

MicroVention's comprehensive portfolio features clinically proven Hydrogel coils, which can be used exclusively or in combination with our trusted Platinum coils to treat a wide range of aneurysms and neurovascular lesions.

Breakthrough Hydrogel Technology

- Less Recurrence
- Less Retreatment
- More Progressive Occlusion

Compared to platinum coils with comparable safety¹



REFERENCES:

1. Taschner et al. Second-Generation Hydrogel Coils for the Endovascular Treatment of Intracranial Aneurysm; A Randomized Controlled Trial. 2018;49:00-00. DOI:10.1161/STROKEAHA.117.018707

For more information or a product demonstration,
contact your local MicroVention representative:



**MicroVention Worldwide
Innovation Center**
35 Enterprise
Aliso Viejo, CA 92656 USA
MicroVention UK Limited
MicroVention Europe, S.A.R.L.
MicroVention Deutschland GmbH
microvention.com

PH +1.714.247.8000

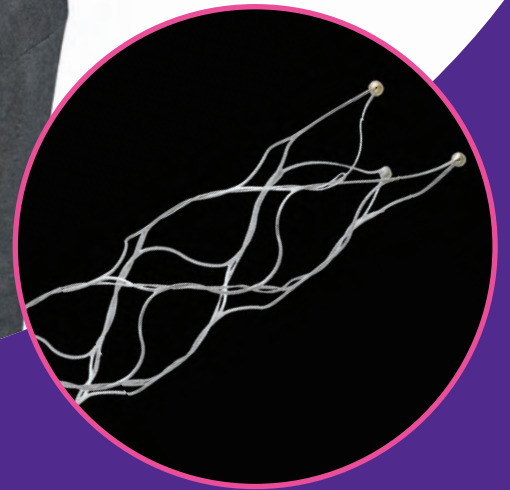
PH +44 (0) 191 258 6777

PH +33 (1) 39 21 77 46

PH +49 211 210 798-0

stryker

Now you have **24 hours** to make a lifetime of difference in stroke patients like Nora



The Trevo Retriever is the only device cleared to **reduce disability in stroke patients up to 24 hours** from time last seen well.

For more information, visit strykerneurovascular.com/trevo24hours

Trevo[®] XP
PROVUE RETRIEVER

Copyright © 2018 Stryker
AP002078 v1.0

Official Journal:

American Society of Neuroradiology
American Society of Functional Neuroradiology
American Society of Head and Neck Radiology
American Society of Pediatric Neuroradiology
American Society of Spine Radiology

EDITOR-IN-CHIEF

Jeffrey S. Ross, MD

Professor of Radiology, Department of Radiology,
Mayo Clinic College of Medicine, Phoenix, AZ

SENIOR EDITORS

Harry J. Cloft, MD, PhD

Professor of Radiology and Neurosurgery,
Department of Radiology, Mayo Clinic College of
Medicine, Rochester, MN

Thierry A.G.M. Huisman, MD

Radiologist-in-Chief, Texas Children's Hospital,
Houston, TX

Yvonne W. Lui, MD

Associate Professor of Radiology,
Chief of Neuroradiology,
New York University School of Medicine,
New York, NY

C.D. Phillips, MD, FACR

Professor of Radiology, Weill Cornell Medical
College, Director of Head and Neck Imaging,
New York-Presbyterian Hospital, New York, NY

Pamela W. Schaefer, MD

Clinical Director of MRI and Associate Director of
Neuroradiology, Massachusetts General Hospital,
Boston, Massachusetts, Associate Professor,
Radiology, Harvard Medical School, Cambridge, MA

Charles M. Strother, MD

Professor of Radiology, Emeritus, University of
Wisconsin, Madison, WI

STATISTICAL SENIOR EDITOR

Bryan A. Comstock, MS

Senior Biostatistician,
Department of Biostatistics,
University of Washington, Seattle, WA

ARTIFICIAL INTELLIGENCE DEPUTY EDITOR

Christopher G. Filippi, MD

Professor and Vice Chair of Biomedical and
Translational Science,
Donald and Barbara Zucker School of Medicine at
Hofstra/Northwell,
Lenox Hill Hospital and Greenwich Village
Healthplex, New York, NY

EDITORIAL BOARD

Ashley H. Aiken, Atlanta, GA
Lea M. Alhilali, Phoenix, AZ
Kubilay Aydin, Istanbul, Turkey
John D. Barr, Dallas, TX
Ari Blitz, Baltimore, MD
Barton F. Branstetter IV, Pittsburgh, PA
Jonathan L. Brisman, Lake Success, NY
Keith Cauley, Danville, PA
James Y. Chen, San Diego, CA
Asim F. Choudhri, Memphis, TN
Daniel Chow, Irvine, CA
J. Matthew Debnam, Houston, TX
Seena Dehkharghani, New York, NY
Yonghong Ding, Rochester, MN
Clifford J. Eskey, Hanover, NH
Saeed Fakhran, Phoenix, AZ
Massimo Filippi, Milan, Italy
Reza Forghani, Montreal, Quebec, Canada
Nils D. Forkert, Calgary, Alberta, Canada
Wende N. Gibbs, Los Angeles, CA
Christine M. Glastonbury, San Francisco, CA
John L. Go, Los Angeles, CA
Philipp Göllitz, Erlangen, Germany
Allison Grayev, Madison, WI
Brent Griffith, Detroit, MI
Ajay Gupta, New York, NY
Rakesh Kumar Gupta, Haryana, India
Lotfi Hacein-Bey, Sacramento, CA
Christopher P. Hess, San Francisco, CA
Andrei Holodny, New York, NY
Benjamin Huang, Chapel Hill, NC
Mahesh V. Jayaraman, Providence, RI
Valerie Jewells, Chapel Hill, NC
Christof Karmonik, Houston, TX
Timothy J. Kaufmann, Rochester, MN
Hillary R. Kelly, Boston, MA
Toshibumi Kinoshita, Akita, Japan
Kenneth F. Layton, Dallas, TX
Alexander Lerner, Los Angeles, CA
Michael Lev, Boston, MA
Karl-Olof Lovblad, Geneva, Switzerland
Franklin A. Marden, Chicago, IL
Joseph C. McGowan, Merion Station, PA
Stephan Meckel, Freiburg, Germany
Christopher J. Moran, St. Louis, MO
Takahisa Mori, Kamakura City, Japan
Suresh Mukherji, Ann Arbor, MI
Alexander J. Nemeth, Chicago, IL
Renato Hoffmann Nunes, Sao Paulo, Brazil
Sasan Partovi, Cleveland, OH
Laurent Pierot, Reims, France
Jay J. Pillai, Baltimore, MD
Whitney B. Pope, Los Angeles, CA
Joana Ramalho, Lisbon, Portugal
Otto Rapalino, Boston, MA

Álex Rovira-Cañellas, Barcelona, Spain
Paul M. Ruggieri, Cleveland, OH
Amit M. Saindane, Atlanta, GA
Erin Simon Schwartz, Philadelphia, PA
Lubdha M. Shah, Salt Lake City, UT
Maksim Shapiro, New York, NY
Timothy Shepherd, New York, NY
Mark S. Shiroishi, Los Angeles, CA
Bruno P. Soares, Baltimore, MD
Maria Vittoria Spampinato, Charleston, SC
Khin Khin Tha, Sapporo, Hokkaido, Japan
Krishnamoorthy Thamburaj, Hershey, PA
Cheng Hong Toh, Taipei, Taiwan
Aquilla S. Turk, Charleston, SC
Anja G. van der Kolk, Madison, WI
Willem Jan van Rooij, Tilburg, Netherlands
Arastoo Vossough, Philadelphia, PA
Elysa Widjaja, Toronto, Ontario, Canada
Max Wintermark, Stanford, CA
Ronald L. Wolf, Philadelphia, PA
Kei Yamada, Kyoto, Japan
Carlos Zamora, Chapel Hill, NC
Vahe M. Zohrabian, New Haven, CT

EDITORIAL FELLOW

Alireza Radmanesh, New York, NY

SPECIAL CONSULTANTS TO THE EDITOR

AJNR Blog Editor

Neil Lall, Denver, CO

Case of the Month Editor

Nicholas Stence, Aurora, CO

Case of the Week Editors

Juan Pablo Cruz, Santiago, Chile

Sapna Rawal, Toronto, Ontario, Canada

Classic Case Editor

Sandy Cheng-Yu Chen, Taipei, Taiwan

Health Care and Socioeconomics Editor

Pina C. Sanelli, New York, NY

Physics Editor

Greg Zaharchuk, Stanford, CA

Podcast Editor

Wende N. Gibbs, Los Angeles, CA

Twitter Editor

Jennifer McCarty, Houston, TX

Founding Editor
Juan M. Taveras

Editors Emeriti

Mauricio Castillo, Robert I. Grossman,
Michael S. Huckman, Robert M. Quencer

Managing Editor
Karen Halm

Assistant Managing Editor

Laura Wilhelm

Communications Coordinator

Rebecca Artz

Executive Director, ASNR

Mary Beth Hepp

CALL FOR AJNR EDITORIAL FELLOWSHIP CANDIDATES

2019 Candidate Information and Requirements

ASNR and AJNR are pleased once again to join efforts with other imaging-related journals that have training programs on editorial aspects of publishing for trainees or junior staff (3–5 years after training), including Radiology (Olmsted fellowship), AJR (Figley and Rogers fellowships), JACR (Bruce J. Hillman fellowship), and Radiologia.

GOALS

- Increase interest in editorial and publication-related activities in younger individuals.
- Increase understanding and participation in the AJNR review process.
- Incorporate into AJNR's Editorial Board younger individuals who have previous experience in the review and publication process.
- Fill a specific need in neuroradiology not offered by other similar fellowships.
- Increase the relationship between “new” generation of neuroradiologists and more established individuals.
- Increase visibility of AJNR among younger neuroradiologists.

ACTIVITIES OF THE FELLOWSHIP

- Serve as Editorial Fellow for one year. This individual will be listed on the masthead as such.
- Review at least one manuscript per month for 12 months. Evaluate all review articles submitted to AJNR.
- Learn how electronic manuscript review systems work.
- Be involved in the final decision of selected manuscripts together with the Editor-in-Chief.
- Participate in all monthly Senior Editor telephone conference calls.
- Participate in all meetings of the Editors during the annual meetings of ASNR and RSNA and the Radiology Editors Forum as per candidate's availability. The Foundation of the ASNR will provide \$2000 funding for this activity.
- Evaluate progress and adjust program to specific needs in annual meeting or telephone conference with the Editor-in-Chief.
- Embark on an editorial scientific or bibliometric project that will lead to the submission of an article to AJNR or another appropriate journal as determined by the Editor-in-Chief. This project will be presented by the Editorial Fellow at the ASNR annual meeting.
- Serve as liaison between AJNR and ASNR's Young Professionals Network. Participate in meetings and telephone calls with this group. Design one electronic survey/year, polling the group regarding readership attitudes and wishes.
- Recruit trainees as reviewers as determined by the Editor-in-Chief.
- Organize and host a Fellows' Journal Club podcast.
- Serve as Guest Editor for an issue of AJNR's News Digest with a timely topic.

QUALIFICATIONS

- Be a fellow in neuroradiology from North America, including Canada (this may be extended to include other countries).
- Be a junior faculty neuroradiology member (< 3 years) in either an academic or private environment.
- Be an “in-training” or member of ASNR in any other category.

APPLICATION

- Include a short letter of intent with statement of goals and desired research project. CV must be included.
- Include a letter of recommendation from the Division Chief or fellowship program director. A statement of protected time to perform the functions outlined is desirable.
- Applications will be evaluated by AJNR's Senior Editors prior to the ASNR meeting. The name of the selected individual will be announced at the meeting.
- Applications should be received by March 1, 2019 and sent to Ms. Karen Halm, AJNR Managing Editor, electronically at khalm@asnr.org.

AXS Infinity LS™ Plus Long Sheath

See package insert for complete indications, contraindications, warnings and instructions for use.

INDICATIONS FOR USE

The AXS Infinity LS Plus Long Sheath is indicated for the introduction of interventional devices into the peripheral, coronary, and neuro vasculature.

RX ONLY

CONTRAINDICATIONS

There are no known contraindications.

POTENTIAL ADVERSE EVENTS

- Acute vessel occlusion
- Air embolism
- Death
- Distal embolization
- Emboli
- False aneurysm formation
- Hematoma or hemorrhage at the puncture site
- Infection
- Intracranial hemorrhage
- Ischemia
- Neurological deficit including stroke
- Vessel spasm, thrombosis, dissection or perforation

WARNINGS

Contents supplied STERILE using an ethylene oxide (EO) process. Do not use if sterile barrier is damaged. If damage is found, call your Stryker Neurovascular representative.

For single use only. Do not reuse, reprocess or resterilize. Reuse, reprocessing or resterilization may compromise the structural integrity of the device and/or lead to device failure which, in turn, may result in patient injury, illness or death. Reuse, reprocessing or resterilization may also create a risk of contamination of the device and/or cause patient infection or cross-infection, including, but not limited to, the transmission of infectious disease(s) from one patient to another. Contamination of the device may lead to injury, illness or death of the patient.

After use, dispose of product and packaging in accordance with hospital, administrative and/or local government policy.

1. Do not re-sterilize or reuse, intended for single use only. Re-sterilization and/or reuse may result in cross contamination and/or reduced performance.
2. When the long sheath is exposed to the vascular system, it should be manipulated while under high-quality fluoroscopic observation. Do not advance or retract the long sheath if resistance is met during manipulation; determine the cause of the resistance before proceeding.

PRECAUTIONS

1. Store in a cool, dry, dark place.
2. Do not use kinked, damaged, or opened devices.
3. Use the device prior to the "Use By" date specified on the package.
4. Exposure to temperatures above 54°C (130°F) may damage device. Do not autoclave.
5. Torquing or moving the device against resistance may result in damage to the vessel or device.
6. Maintain a constant infusion of appropriate flush solution.
7. If flow through the device becomes restricted, do not attempt to clear the lumen by infusion. Remove and replace the device.
8. Examine the device to verify functionality and to ensure that its size and shape are suitable for the specific procedure for which it is to be used.
9. The AXS Infinity LS Plus Long Sheath should be used only by physicians trained in percutaneous procedures and/or interventional techniques.
10. Do not use if labeling is incomplete or illegible.

AXS Vecta™ 71 Aspiration Catheter

See package insert for complete indications, contraindications, warnings and instructions for use.

INDICATIONS FOR USE

The AXS Vecta™ Aspiration System, including the AXS Vecta 71 Aspiration Catheter, Aspiration Tubing Set, and VC-701 Cliq Aspirator Pump, is indicated in the revascularization of patients with acute ischemic stroke secondary to intracranial large vessel occlusive disease (within the internal carotid, middle cerebral – M1 and M2 segments, basilar, and vertebral arteries) within 8 hours of symptom onset. Patients who are ineligible for intravenous tissue plasminogen activator (IV t-PA) or who failed IV t-PA therapy are candidates for treatment.

Stryker Corporation or its divisions or other corporate affiliated entities own, use or have applied for the following trademarks or service marks: AXS Infinity LS, AXS Vecta, Stryker. All other trademarks are trademarks of their respective owners or holders.

Scout is a trademark of InNeuroCo, Inc.

Copyright © 2018 Stryker

AP002264 v1.0 | Page 2 of 2

Trevo® XP ProVue Retrievers

See package insert for complete indications, complications, warnings, and instructions for use.

INDICATIONS FOR USE

1. The Trevo Retriever is indicated for use to restore blood flow in the neurovasculature by removing thrombus for the treatment of acute ischemic stroke to reduce disability in patients with a persistent, proximal anterior circulation, large vessel occlusion, and smaller core infarcts who have first received intravenous tissue plasminogen activator (IV t-PA). Endovascular therapy with the device should start within 6 hours of symptom onset.
2. The Trevo Retriever is intended to restore blood flow in the neurovasculature by removing thrombus in patients experiencing ischemic stroke within 8 hours of symptom onset. Patients who are ineligible for intravenous tissue plasminogen activator (IV t-PA) or who fail IV t-PA therapy are candidates for treatment.
3. The Trevo Retriever is indicated for use to restore blood flow in the neurovasculature by removing thrombus for the treatment of acute ischemic stroke to reduce disability in patients with a persistent, proximal anterior circulation, large vessel occlusion of the internal carotid artery (ICA) or middle cerebral artery (MCA)-M1 segments with smaller core infarcts (0-50cc; for age < 80 years, 0-20cc; for age ≥ 80 years). Endovascular therapy with the device should start within 6-24 hours of time last seen well in patients who are ineligible for intravenous tissue plasminogen activator (IV t-PA) or who fail IV t-PA therapy.

COMPLICATIONS

Procedures requiring percutaneous catheter introduction should not be attempted by physicians unfamiliar with possible complications which may occur during or after the procedure. Possible complications include, but are not limited to, the following: air embolism; hematoma or hemorrhage at puncture site; infection; distal embolization; pain/headache; vessel spasm, thrombosis, dissection, or perforation; emboli; acute occlusion; ischemia; intracranial hemorrhage; false aneurysm formation; neurological deficits including stroke; and death.

COMPATIBILITY

3x20mm retrievers are compatible with Trevo® Pro 14 Microcatheters (REF 90231) and Trevo® Pro 18 Microcatheters (REF 90238). 4x20mm retrievers are compatible with Trevo® Pro 18 Microcatheters (REF 90238). 4x30mm retrievers are compatible with Excelsior® XT-27™ Microcatheters (150cm x 6cm straight REF 275081) and Trevo® Pro 18 Microcatheters (REF 90238). 6x5mm Retrievers are compatible with Excelsior® XT-27™ Microcatheters (115cm x 6cm straight REF 275081). Recommended minimum vessel ID for all Retriever sizes is 2.5mm. Compatibility of the Retriever with other microcatheters has not been established. Performance of the Retriever device may be impacted if a different microcatheter is used.

Balloon Guide Catheters (such as Mercor® Balloon Guide Catheter and FlowGate® Balloon Guide Catheter) are recommended for use during thrombus removal procedures.

Copyright © 2018 Stryker

AP002078 v1.0 | Page 2 of 2

RX ONLY

DEVICE DESCRIPTION

The AXS Vecta Aspiration System consists of the AXS Vecta 71 Aspiration Catheter, the Aspiration Tubing Set, and the VC 701 Cliq Aspirator Pump. The AXS Vecta 71 Aspiration Catheter is a single lumen, flexible, variable stiffness catheter. It has a radiopaque marker band on the distal end and a Luer hub at the proximal end. The AXS Vecta 71 Aspiration Catheter shaft has a lubricious coating at the distal end to reduce friction during use. The Scout Introducer may be used in conjunction with the AXS Vecta 71 Aspiration Catheter to facilitate in the introduction of the AXS Vecta 71 Aspiration Catheter into distal vasculature and aid in navigation to distal anatomy. The Scout Introducer has a lubricious coating at the distal end to reduce friction during use. The inner lumen of the AXS Vecta 71 Aspiration Catheters is compatible with the Scout Introducing, guide wires and micro catheters. The inner lumen of the Scout Introducer is compatible with guide wires and micro catheters of an outer diameter of less than 0.044in. Each package includes one AXS Vecta 71 Aspiration Catheter, one Scout Introducer, one hemostasis valve, and two peel-away introducers. Dimensions of the AXS Vecta 71 Aspiration Catheter and Scout Introducer are included on the individual device label. The AXS Vecta 71 Aspiration Catheters are available in 3 different lengths, the device configurations including the length of the Scout packaged with each catheter and the recommended microcatheter length is presented in the table below.

Catheter part number	INC-11129-115	INC-11129-125	INC-11129-132
Catheter inner diameter (in)	0.071	0.071	0.071
Distal catheter outer diameter (in)	0.082	0.082	0.082
Catheter working length (cm)	115	125	132
Scout Introducer length (cm)	133	143	150
Recommended compatible microcatheter length (cm)	150	160	160
Recommended compatible microcatheter outer diameter (in)	0.044 max	0.044 max	0.044 max
Recommended compatible guidewire outer diameter (in)	0.038 max	0.038 max	0.038 max

The AXS Vecta Aspiration System is recommended for use in the following vessel size ranges based on non-clinical testing:

AXS Vecta 71 Aspiration Catheter	Vessel size (mm)
INC-11129-115	2-4
INC-11129-125	2-4
INC-11129-132	2-4

CONTRAINDICATIONS

The AXS Vecta 71 Aspiration Catheter has not been evaluated for use in the coronary vasculature. Do not use automated high-pressure contrast injection equipment with the AXS Vecta 71 Aspiration Catheter because it may damage the device.

POTENTIAL ADVERSE EVENTS

- Acute vessel occlusion
- Air embolism
- Allergic reaction and anaphylaxis from contrast media
- Arteriovenous fistula
- Death
- Device malfunction
- Distal embolization
- Emboli
- False aneurysm formation
- Hematoma or hemorrhage at the puncture site
- Inability to completely remove thrombus
- Infection
- Intracranial hemorrhage
- Ischemia
- Kidney damage from contrast media
- Neurological deficit including stroke
- Risks associated with angiographic and fluoroscopic radiation including but not limited to: alopecia, burns ranging in severity from skin reddening to ulcers, cataracts, and delayed neoplasia
- Vessel spasm, thrombosis, dissection or perforation

WARNINGS

Contents supplied STERILE using an ethylene oxide (EO) process. Do not use if sterile barrier is damaged. If damage is found, call your Stryker representative. For single use only. Do not reuse, reprocess or resterilize. Reuse, reprocessing or resterilization may compromise the structural integrity of the device and/or lead to device failure which, in turn, may result in patient injury, illness or death. Reuse, reprocessing or resterilization may also create a risk of contamination of the device and/or cause patient infection or cross-infection, including, but not limited to, the transmission of infectious disease(s) from one patient to another. Contamination of the device may lead to injury, illness or death of the patient.

After use, dispose of product and packaging in accordance with hospital, administrative and/or local government policy.

1. The AXS Vecta 71 Aspiration Catheter has not been evaluated for more than one (1) clot retrieval attempt.
2. The AXS Vecta 71 Aspiration Catheter was evaluated for an average duration of direct aspiration of 4 minutes.
3. This product is intended for single use only, do not re-sterilize or reuse. Re-sterilization and/or reuse may result in cross contamination and/or reduced performance.
4. When the catheter is exposed to the vascular system, it should be manipulated while under high-quality fluoroscopic observation. Do not advance or retract the catheter if resistance is met during manipulation; determine the cause of the resistance before proceeding.
5. Operators should take all necessary precautions to limit x-radiation doses to patients and themselves by using sufficient shielding, reducing fluoroscopy times, and modifying x-ray technical factors where possible.

PRECAUTIONS

1. Store in a cool, dry, dark place.
2. Do not use kinked, damaged, or opened devices.
3. Use the device prior to the "Use By" date specified on the package.
4. Exposure to temperatures above 54°C (130°F) may damage device. Do not autoclave.
5. Torquing or moving the device against resistance may result in damage to the vessel or device.
6. Maintain a constant infusion of appropriate flush solution.
7. If flow through the device becomes restricted, do not attempt to clear the lumen by infusion. Remove and replace the device.
8. Examine the device to verify functionality and to ensure that its size and shape are suitable for the specific procedure for which it is to be used.
9. The AXS Vecta Aspiration System should be used only by physicians trained in percutaneous procedures and/or interventional techniques.
10. The Scout Introducer should be used with a guidewire and microcatheter inserted when in vasculature.
11. If using the AXS Vecta Aspiration System for thrombectomy, monitor the canister fluid level and replace the canister if the fill level reaches 75% of the canister volume.
12. Administration of anticoagulants and antiplatelets should be suspended until 24 hours post-treatment. Medical management and acute post stroke care should follow the American Stroke Association (ASA) guidelines.
13. Any neurological determination should be evaluated by urgent CT scan and other evaluations as indicated according to investigator/hospital best practice.
14. As in all surgical interventions, monitoring of intra-procedural blood loss is recommended so that appropriate management may be instituted.
15. Limit the usage of the AXS Vecta 71 Aspiration Catheter to arteries greater than the catheter's outer diameter.
16. Excessive aspiration with the distal tip of the AXS Vecta 71 Aspiration Catheter covered by the vessel wall may cause vessel injury. Carefully investigate location of the distal tip under fluoroscopy prior to aspiration.
17. There is an inherent risk with the use of angiography and fluoroscopy.
18. When transporting the VC-701 Cliq pump, utilize the pump handle.
19. Do not use if labeling is incomplete or illegible.



Stryker Neurovascular
47900 Bayside Parkway
Fremont, CA 94538

strykerneurovascular.com

Date of Release: SEP/2018

EX_EN_US

Retrievers are compatible with the Abbott Vascular DOC® Guide Wire Extension (REF 22260).

Retrievers are compatible with Boston Scientific Retriever Hemostatic Valve (REF 421242).

SPECIFIC WARNINGS FOR INDICATION 1

- The safety and effectiveness of the Trevo Retrievers in reducing disability has not been established in patients with large core infarcts (i.e., ASPECTS ≤ 7). There may be increased risks, such as intracerebral hemorrhage, in these patients.
- The safety and effectiveness of the Trevo Retrievers in reducing disability has not been established or evaluated in patients with occlusions in the posterior circulation (e.g., basilar or vertebral arteries) or for more distal occlusions in the anterior circulation.

SPECIFIC WARNINGS FOR INDICATION 2

- To reduce risk of vessel damage, take care to appropriately size Retriever to vessel diameter at intended site of deployment.

SPECIFIC WARNINGS FOR INDICATION 3

- The safety and effectiveness of the Trevo Retrievers in reducing disability has not been established in patients with large core infarcts (i.e., ASPECTS ≤ 7). There may be increased risks, such as intracerebral hemorrhage, in these patients.
- The safety and effectiveness of the Trevo Retrievers in reducing disability has not been established or evaluated in patients with occlusions in the posterior circulation (e.g., basilar or vertebral arteries) or for more distal occlusions in the anterior circulation.
- Users should validate their imaging software analysis techniques to ensure robust and consistent results for assessing core infarct size.

WARNINGS APPLIED TO ALL INDICATIONS

- Administration of IV t-PA should be within the FDA approved window (within 3 hours of stroke symptom onset).
 - To reduce risk of vessel damage, adhere to the following recommendations:
 - Do not perform more than six (6) retrieval attempts in same vessel using Retriever devices.
 - Maintain Retriever position in vessel when removing or exchanging Microcatheter.
 - To reduce risk of kinking/fracture, adhere to the following recommendations:
 - Immediately after unsheathing Retriever, position Microcatheter tip marker just proximal to shaped section. Maintain Microcatheter tip marker just proximal to shaped section of Retriever during manipulation and withdrawal.
 - Do not rotate or torque Retriever.
 - Use caution when passing Retriever through stented arteries.
 - The Retriever is a delicate instrument and should be handled carefully. Before use and when possible during procedure, inspect device carefully for damage. Do not use a device that shows signs of damage. Damage may prevent device from functioning and may cause complications.
 - Do not advance or withdraw Retriever against resistance or significant vasospasm. Moving or torquing device against resistance or significant vasospasm may result in damage to vessel or device. Assess cause of resistance using fluoroscopy and if needed resheath the device to withdraw.

- If Retriever is difficult to withdraw from the vessel, do not torque Retriever. Advance Microcatheter distally, gently pull Retriever back into Microcatheter, and remove Retriever and Microcatheter as a unit. If undue resistance is met when withdrawing the Retriever into the Microcatheter, consider extending the Retriever using the Abbott Vascular DOC guidewire extension (REF 22260) so that the Microcatheter can be exchanged for a larger diameter catheter such as a DAC® Catheter. Gently withdraw the Retriever into the larger diameter catheter.
- Administer anti-coagulation and anti-platelet medications per standard institutional guidelines.
- Users should take all necessary precautions to limit X-radiation doses to patients and themselves by using sufficient shielding, reducing fluoroscopy times, and modifying X-ray technical factors where possible.

PRECAUTIONS

- Prescription only – device restricted to use by or on order of a physician.
- Store in cool, dry, dark place.
- Do not use open or damaged packages.
- Use by "Use By" date.
- Exposure to temperatures above 54°C (130°F) may damage device and accessories. Do not autoclave.
- Do not expose Retriever to solvents.
- Use Retriever in conjunction with fluoroscopic visualization and proper anti-coagulation agents.
- To prevent thrombus formation and contrast media crystal formation, maintain a constant infusion of appropriate flush solution between guide catheter and Microcatheter and between Microcatheter and Retriever or guidewire.
- Do not attach a torque device to the shaped proximal end of DOC® Compatible Retriever. Damage may occur, preventing ability to attach DOC® Guide Wire Extension.

DOC is a trademark of Abbott Laboratories.



Stryker Neurovascular
47900 Bayside Parkway
Fremont, CA 94538

strykerneurovascular.com

Date of Release: APR/2018

EX_EN_US

Redefine aspiration.

AXS Vecta 71 Aspiration Catheter

Big 0.071in ID aspiration lumen
to ingest more clot

Deliver through a 0.088in ID
long sheath or **the new**
0.091in AXS Infinity LS™
Plus Long Sheath

**Packaged with
the Scout Introducer,**
a 0.044in lumen nitinol
cross coil catheter that
replaces the need for
a 3MAX or other
delivery catheter

AXS Vecta™ 71
ASPIRATION CATHETER

AJNR

AMERICAN JOURNAL OF NEURORADIOLOGY

FEBRUARY 2019
VOLUME 40
NUMBER 2
WWW.AJNR.ORG

Publication Preview at www.ajnr.org features articles released in advance of print. Visit www.ajnrblog.org to comment on AJNR content and chat with colleagues and AJNR's News Digest at <http://ajnrdigest.org> to read the stories behind the latest research in neuroimaging.

205 **PERSPECTIVES** *S.M. Schonfeld*

REVIEW ARTICLE

   206 **A Review of Magnetic Particle Imaging and Perspectives on Neuroimaging** *L.C. Wu, et al.*

PRACTICE PERSPECTIVES

 213 **A Call to Improve the Visibility and Access of the American College of Radiology Practice Parameters in Neuroradiology: A Powerful Value Stream Enhancer for Both Neuroradiologists and Patients** *J.E. Jordan, et al.*

GENERAL CONTENTS

  217 **A Deep Learning–Based Approach to Reduce Rescan and Recall Rates in Clinical MRI Examinations** *A. Sreekumari, et al.* **ADULT BRAIN**

  224 **Improving the Quality of Synthetic FLAIR Images with Deep Learning Using a Conditional Generative Adversarial Network for Pixel-by-Pixel Image Translation** *A. Hagiwara, et al.* **ADULT BRAIN**

  231 **Effect of Gadolinium on the Estimation of Myelin and Brain Tissue Volumes Based on Quantitative Synthetic MRI** *T. Maekawa, et al.* **ADULT BRAIN**

 238 **FDG-PET and MRI in the Evolution of New-Onset Refractory Status Epilepticus** *T. Strohm, et al.* **ADULT BRAIN**

245 **Alterations in Brain Metabolites in Patients with Epilepsy with Impaired Consciousness: A Case-Control Study of Interictal Multivoxel ¹H-MRS Findings** *Z. Tan, et al.* **ADULT BRAIN**

   253 **Utility of Dynamic Susceptibility Contrast Perfusion-Weighted MR Imaging and ¹¹C-Methionine PET/CT for Differentiation of Tumor Recurrence from Radiation Injury in Patients with High-Grade Gliomas** *Z. Qiao, et al.* **ADULT BRAIN FUNCTIONAL**

 260 **Standardized MR Perfusion Scoring System for Evaluation of Sequential Perfusion Changes and Surgical Outcome of Moyamoya Disease** *Y.-H. Lin, et al.* **ADULT BRAIN FUNCTIONAL**

   267 **Acute Toxic Leukoencephalopathy: Etiologies, Imaging Findings, and Outcomes in 101 Patients** *C. Özütemiz, et al.* **ADULT BRAIN**

276 **Sexual Dimorphism and Hemispheric Asymmetry of Hippocampal Volumetric Integrity in Normal Aging and Alzheimer Disease** *B.A. Ardekani, et al.* **ADULT BRAIN**

AJNR (Am J Neuroradiol ISSN 0195–6108) is a journal published monthly, owned and published by the American Society of Neuroradiology (ASNR), 800 Enterprise Drive, Suite 205, Oak Brook, IL 60523. Annual dues for the ASNR include \$170.00 for journal subscription. The journal is printed by Cadmus Journal Services, 5457 Twin Knolls Road, Suite 200, Columbia, MD 21045; Periodicals postage paid at Oak Brook, IL and additional mailing offices. Printed in the U.S.A. POSTMASTER: Please send address changes to American Journal of Neuroradiology, P.O. Box 3000, Denville, NJ 07834, U.S.A. Subscription rates: nonmember \$410 (\$480 foreign) print and online, \$320 online only; institutions \$470 (\$540 foreign) print and basic online, \$935 (\$1000 foreign) print and extended online, \$380 online only (basic), extended online \$825; single copies are \$35 each (\$40 foreign). Indexed by PubMed/Medline, BIOSIS Previews, Current Contents (Clinical Medicine and Life Sciences), EMBASE, Google Scholar, HighWire Press, Q-Sensei, RefSeek, Science Citation Index, SCI Expanded, Meta/CZI and ReadCube. Copyright © American Society of Neuroradiology.

	283	Clinical Outcome after Thrombectomy in Patients with Stroke with Premorbid Modified Rankin Scale Scores of 3 and 4: A Cohort Study with 136 Patients <i>F. Seker, et al.</i>	INTERVENTIONAL
	287	Commentary Selection of Patients with Stroke for Thrombectomy Must Be Judicious and Should Not Be Offered to Any Patient with Large-Vessel Occlusion with a Femoral Pulse <i>B. Yan</i>	INTERVENTIONAL
  	288	Ostium Ratio and Neck Ratio Could Predict the Outcome of Sidewall Intracranial Aneurysms Treated with Flow Diverters <i>N. Paliwal, et al.</i>	INTERVENTIONAL
	295	Endothelialization following Flow Diversion for Intracranial Aneurysms: A Systematic Review <i>K. Ravindran, et al.</i>	INTERVENTIONAL
   	302	High-Definition Zoom Mode, a High-Resolution X-Ray Microscope for Neurointerventional Treatment Procedures: A Blinded-Rater Clinical-Utility Study <i>S.V. Setlur Nagesh, et al.</i>	INTERVENTIONAL
	309	Percutaneous CT-Guided Skull Biopsy: Feasibility, Safety, and Diagnostic Yield <i>A. Tomasian, et al.</i>	INTERVENTIONAL
	313	Transient Ischemic Attack and Carotid Web <i>H. Hu, et al.</i>	EXTRACRANIAL VASCULAR
	319	Resting-State Functional Connectivity of the Middle Frontal Gyrus Can Predict Language Lateralization in Patients with Brain Tumors <i>S. Gohel, et al.</i>	FUNCTIONAL
  	326	Treatment Response Prediction of Nasopharyngeal Carcinoma Based on Histogram Analysis of Diffusional Kurtosis Imaging <i>N. Tu, et al.</i>	HEAD & NECK
	334	Contrast-Enhanced 3D-FLAIR Imaging of the Optic Nerve and Optic Nerve Head: Novel Neuroimaging Findings of Idiopathic Intracranial Hypertension <i>E. Golden, et al.</i>	HEAD & NECK
  	340	Cavum Septum Pellucidum in the General Pediatric Population and Its Relation to Surrounding Brain Structure Volumes, Cognitive Function, and Emotional or Behavioral Problems <i>M.H.G. Dremmen, et al.</i>	PEDIATRICS
	347	MR Imaging Scoring System for White Matter Injury after Deep Medullary Vein Thrombosis and Infarction in Neonates <i>K.L. Benninger, et al.</i>	PEDIATRICS
	353	Volumetric MRI Study of the Brain in Fetuses with Intrauterine Cytomegalovirus Infection and Its Correlation to Neurodevelopmental Outcome <i>A. Grinberg, et al.</i>	PEDIATRICS
	359	Brain DSC MR Perfusion in Children: A Clinical Feasibility Study Using Different Technical Standards of Contrast Administration <i>S. Gaudino, et al.</i>	PEDIATRICS FUNCTIONAL
	366	High-Grade Gliomas in Children with Neurofibromatosis Type 1: Literature Review and Illustrative Cases <i>C.D. Spyris, et al.</i>	PEDIATRICS
	370	A 3T Phase-Sensitive Inversion Recovery MRI Sequence Improves Detection of Cervical Spinal Cord Lesions and Shows Active Lesions in Patients with Multiple Sclerosis <i>A. Fechner, et al.</i>	SPINE
	376	Renal Contrast on CT Myelography: Diagnostic Value in Patients with Spontaneous Intracranial Hypotension <i>K.A. Kinsman, et al.</i>	SPINE
	382	Single-Needle Lateral Sacroplasty Technique <i>P.J. Nicholson, et al.</i>	SPINE

ONLINE FEATURES

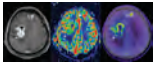
LETTERS

- E6 **Maternal-Fetal Medicine Specialists Should Manage Patients Requiring Fetal MRI of the Central Nervous System** *C.M. Pfeifer*
- E7 **The “Bovine Aortic Arch”: Time to Rethink the True Origin of the Term?**
L.J. Ridley, et al.
- E9 **Reply** *R. Rajagopal, et al.*
- E10 **Is Delayed Speech Development a Long-Term Sequela of Birth-Related Subdural Hematoma?** *N. Lynøe, et al.*
- E11 **Reply** *V.J. Rooks, et al.*

BOOK REVIEWS

R.M. Quencer, Section Editor

Please visit www.ajnrblog.org to read and comment on Book Reviews.



Contrast-enhanced T1-weighted MR image (left), a relative CBV map (center), and MET PET/CT image (right) for a 41-year-old woman with recurrent glioblastoma. The lesion in the right frontal lobe shows enhancement and positive findings on both the rCBV map and MET PET/CT image. The small lesion localized in the anterior left frontal lobe is a presumed meningioma, stable for several years.



Indicates Editor's Choices selection



Indicates Fellows' Journal Club selection



Indicates open access to non-subscribers at www.ajnr.org



Indicates article with supplemental on-line table



Indicates article with supplemental on-line photo



Indicates article with supplemental on-line video



Evidence-Based Medicine Level 1



Evidence-Based Medicine Level 2



Title: Wildebeests after the Rain, Serengeti, Tanzania. As the clouds rolled out, after a much needed rain, the wildebeests came out of the forest and started to graze.
Steven M. Schonfeld, MD, FACR, University Radiology Group, PA, East Brunswick, New Jersey

A Review of Magnetic Particle Imaging and Perspectives on Neuroimaging

L.C. Wu, Y. Zhang, G. Steinberg, H. Qu, S. Huang, M. Cheng, T. Bliss, F. Du, J. Rao, G. Song, L. Pisani, T. Doyle, S. Conolly, K. Krishnan, G. Grant, and M. Wintermark



ABSTRACT

SUMMARY: Magnetic particle imaging is an emerging tomographic technique with the potential for simultaneous high-resolution, high-sensitivity, and real-time imaging. Magnetic particle imaging is based on the unique behavior of superparamagnetic iron oxide nanoparticles modeled by the Langevin theory, with the ability to track and quantify nanoparticle concentrations without tissue background noise. It is a promising new imaging technique for multiple applications, including vascular and perfusion imaging, oncology imaging, cell tracking, inflammation imaging, and trauma imaging. In particular, many neuroimaging applications may be enabled and enhanced with magnetic particle imaging. In this review, we will provide an overview of magnetic particle imaging principles and implementation, current applications, promising neuroimaging applications, and practical considerations.

ABBREVIATIONS: FFL = field-free line; FFP = field-free point; FFR = field-free region; MPI = magnetic particle imaging; SPIO = superparamagnetic iron oxide; SPION = superparamagnetic iron oxide nanoparticle

Magnetic particle imaging (MPI) is a new tomographic technique developed in the early 2000s.¹ In contrast to traditional imaging modalities such as MR imaging, sonography, x-ray, and CT, MPI is not a structural imaging technique. Instead, it is a tracer imaging technique similar to PET and SPECT. MPI allows tracking and quantification of tracer materials, specifically magnetic nanoparticles. It is a quantitative 3D imaging technique with high spatial and high temporal resolution, which may allow real-time high-resolution *in vivo* imaging. Prototype scanners and, more recently, commercial animal scanners have yielded the first *in vivo* MPI studies demonstrating applications in vascular imaging,²⁻⁴ oncology,⁵⁻⁷ and cell-tracking.^{8,9} Human scanners are being developed and will become available in a few years. As an

emerging imaging technique, MPI may open up new possibilities in 3D *in vivo* real-time imaging.

In this review, we will introduce the principles and applications of MPI for researchers and clinicians in the neuroimaging field. We will start with a basic description of the physics and construction of MPI, then talk more in depth about the current applications and discuss promising neuroimaging applications. We will also include practical considerations and comparisons with other imaging modalities for reference.

Magnetic Particle Imaging Principles

MPI Physics. MPI uses a magnetic gradient field, known as a selection field, to saturate all superparamagnetic iron oxide (SPIO) magnetization outside a central field-free region, known as a field-free point (FFP) or field-free line (FFL). The FFL is rapidly shifted over an imaging volume via a rapidly varying excitation/drive field to produce an image. Large fields of view are traversed using slower shift fields and mechanical translation. To produce a signal, as the FFL traverses a SPION's location, the SPION's magnetization changes nonlinearly in response. This time-varying magnetization induces a voltage in the receiver coil, which can be assigned to the instantaneous FFL location to produce a magnetic particle image. The voltages induced are linearly proportional to the number of SPIONs at the instantaneous FFL location, enabling quantification of SPIONs. Most importantly, biologic tissue does not generate or attenuate the low-frequency magnetic fields used in MPI, giving the technique ideal contrast

Received April 23, 2018; accepted after revision July 6.

From the Departments of Bioengineering (L.C.W.), Neurosurgery (G.S., M.C., T.B., F.D., G.G.), Radiology (Y.Z., H.Q., S.H., M.W.), Neuroradiology Section, Radiology (J.R., G.S., L.P.), and Pediatrics (T.D.), Stanford University, Stanford, California; Department of Electrical Engineering and Computer Sciences (S.C.), University of California Berkeley, Berkeley, California; Departments of Materials Sciences and Engineering and Physics (K.K.), University of Washington, Seattle, Washington; and Chongqing Medical University (S.H.), Traditional Chinese Medicine College, Chongqing, China.

Please address correspondence to Max Wintermark, MD, Stanford University School of Medicine, Department of Radiology, Neuroradiology Section, 300 Pasteur Dr, Grant 5047, Stanford, CA 94305; e-mail: max.wintermark@gmail.com

Indicates open access to non-subscribers at www.ajnr.org

Indicates article with supplemental on-line appendix.

Indicates article with supplemental on-line photos.

<http://dx.doi.org/10.3174/ajnr.A5896>

Comparison of MPI with common clinical imaging modalities^{21–25}

Modality	Ultrasound	CT	MRI	PET	SPECT	MPI
Main clinical applications	Structural imaging	Structural imaging	Structural imaging	Tracer imaging	Tracer imaging	Tracer imaging
Spatial resolution	1 mm	<1 mm	1 mm	4 mm	3–10 mm	1 mm
Temporal resolution	<1 second	Seconds	Seconds to hours	Minutes	Minutes	<1 second to minutes
Contrast agents/tracers	Microbubbles	Iodine	Gadolinium, iron oxide particles	Radioactive tracers	Radioactive tracers	Iron oxide particles
Sensitivity	Low	Low	Low	High	High	High
Patient risk	Heating and cavitation	Radiation	Heating and peripheral nerve stimulation	Radiation	Radiation	Heating and peripheral nerve stimulation
Cost	Low	Medium	High	High	Medium	Medium

independent of the source depth. These fields are further described in the On-line Appendix.

Scanner Construction

The magnetic fields required for MPI are very different from those used in MR imaging, so MPI scans cannot be acquired on a standard MR imaging scanner. A magnetic particle imager has 3 major components: The main magnet subsystem generates the main magnetic field gradient and shifts the field-free region (FFR) to cover the full FOV, the transmit/receive subsystem generates the drive field and receives the signal produced by the nanoparticles, and the control console coordinates operation of the major subsystems and processes the received signal to produce an image.¹⁰ Typically, the main magnet produces both the selection field and the slow-shift fields, driving the native resolution of the system. The drive coils in the transmit/receive subsystem generate the excitation signals in the nanoparticles, and this subsystem is designed for decoupling much lower nanoparticle signals from the excitation/drive signal. These MPI scanner components are further described in the On-line Appendix.

Resolution, Contrast, and Sensitivity

The Table provides a comparison of MPI with common clinical imaging modalities. The resolution of the technique is driven by the interaction of the nanoparticle and the gradient.^{11–13} This drives the native resolution of the system, which can be expressed as full width at half maximum.¹³ For stronger gradient strengths such as 6.1 T/m used in a MOMENTUM system (Magnetic Insight, Alameda, California), tailored nanoparticles have been demonstrated to have ~700- μ m full width at half maximum resolution, and point sources remain distinguishable at a 600- μ m separation.¹⁴ While the native resolution of a system derives only from interaction of the gradient and nanoparticle, there are numerous techniques for improving the visual quality of the images by trading the SNR of the technique for image resolution.¹⁵ These techniques are frequently used in MPI to good effect and can appreciably improve resolution for lower systems with lower gradient strengths.¹⁵ The resolution compares well with clinical nuclear medicine. For example, clinical PET cameras have a fundamental resolution limit of ~2 mm, with a practical resolution limit of ~2.5 mm,¹⁶ and typically SPECT has a resolution of ~10 mm,¹⁷ though some systems have a resolution as fine as 3 mm (eg, G-SPECT; MILabs, Utrecht, the Netherlands).

The contrast and signal to noise ratio is excellent with MPI because MPI sees only a tracer and does not see tissue. More specifically, MPI is not affected by the endogenous iron present in the body: It can see only injected SPIONs. This is similar to PET and SPECT, which also have no background signal from tissue. However, PET and SPECT, with imaging times on the order of minutes, are not suited for dynamic imaging applications. PET and SPECT tracers also have half-lives on the order of minutes to hours, while MPI tracers can last for days to weeks.¹⁸ MPI contrast shows the greatest benefits in techniques in which the high contrast can lead to higher accuracy, such as perfusion imaging and cell tracking. This benefit compares favorably with traditional structural imaging techniques such as MR imaging and CT, which can struggle to produce reliable perfusion imaging.¹⁹

The sensitivity of the technique is because MPI directly detects the electronic magnetization of iron oxide nanoparticles, a magnetization that is large compared with the nuclear magnetization detected in MR imaging.²⁰ This feature gives MPI a low detection limit, meaning that minute amounts of tracer material can be detected. For example, the iron detection limit was 1.1 ng (SNR = 3.9) in a voxel of tailored MPI tracers using a high-sensitivity FFL scanner with a 5.7-T/m gradient with a native resolution of 800- μ m full width at half maximum.¹⁴ The system was also used to detect dilute tracer (550 pg Fe/ μ L), which could be seen with SNR = 4.9.¹⁴ As MPI systems begin to mature, their sensitivity should continue to improve. Current systems have limits as low as ~200 cells in a voxel,^{9,18} and theoretically, the MPI detection limit may be as little as 1–10 iron oxide cells in a voxel.¹⁸

Applications of MPI and Perspectives on Neuroimaging

Vascular Imaging. Currently the standard of care for cerebral blood perfusion imaging is CT perfusion, which poses ionizing radiation risks. MPI is well-suited for measuring perfusion. A study demonstrated imaging of cerebral blood flow in living mice using MPI.² This was followed by a demonstration of MPI perfusion in mice for imaging stroke.³ In our work, we recently measured CBV and CBF in a rat.⁴ In addition, we performed in vivo cerebral blood perfusion in stroke mice with MPI (Fig 1), in which an intravenous bolus of iron nanoparticles was administered to mice. Tomographic 3D-MPI was performed using a MOMENTUM MPI system (Magnetic Insight). We

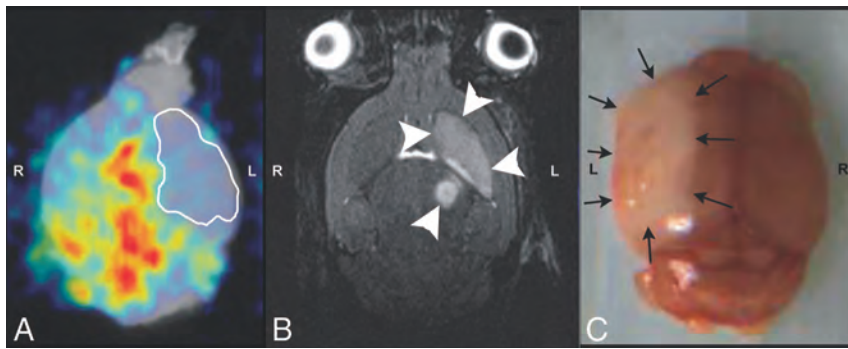


FIG 1. Perfusion, structural, and histology images from a mouse injected with the nanoparticles. The parameters were the following: FOV = 4 cm, 35 projections, best image quality, Lodespin scan mode. A 70- to 100- L intravenous bolus of iron nanoparticles (0.949 mg Fe/mL; core diameter, 27.6 nm) donated by Dr Kannan Krishnan, University of Washington, was administered to C57Bl/6 stroke mice through tail veins. The mice were sacrificed within 30 minutes postinjection, and 3D-MPI was performed using a MOMENTUM MPI system. Anatomic images were collected on the eXplore CT-120 microCT (GE Healthcare, Milwaukee, Wisconsin) and a 7T MR imaging scanner (BioSpec; Bruker Instruments, Billerica, Massachusetts). Data analysis and image registration were performed using the Horos (<https://sourceforge.net/projects/horos/>) and VivoQuant software (Invivo, Boston, Massachusetts). In vivo iron oxide quantification was performed by imaging fiducials containing a known concentration of tracer positioned beside the animal. A, In the 2D coregistered image from CT and MPI, the MPI signal (red if high, yellow if intermediate, blue if low) from the left hemisphere is less than that from the contralateral side (*red spots* indicate vascular structures with high blood volume). B, The high T2 signal (stroke lesion, *arrowheads*) in the left basal ganglia and thalamus. C, The histology image of a perfusion-fixed whole brain shows the stroke lesion on the left (L). R indicates right.

showed that lower MPI signal (a measure of CBV) is observed on the side of the brain with the stroke lesion.

Another promising application of MPI is to image vasculature. MPI provides 3D information, and the signal is directly related to blood volume in a vessel. This is an improvement over 2D techniques such as x-ray or DSA. CT or MR angiography, while providing 3D images, has background noise from the surrounding tissue and calcium, which is not a concern for MPI. In MPI, 3D angiography can be performed using bolus tracking or blood pool agents. An MPI-specific long circulating nanoparticle can repeatedly measure the blood pool with 1 single injection, enabling tracking of changes from minutes to hours.²⁶ For example, we recently demonstrated use of a long circulating tracer to detect gut bleed,²⁷ in which a transgenic mouse model with bleeding induced in the gut using heparin was imaged with 21 repeat MPI scans for 80 minutes. In another study in a rat model of traumatic brain injury, animals were monitored longitudinally to study cerebral bleeding caused by the impact. We showed differences in the nanoparticle clearance rate in different regions of the brain in the impacted animals compared with the controls over a 2-week period.²⁸

MPI is also capable of very fast imaging, similar to x-ray and DSA, enabling tracking of fast blood flow dynamics. Previously, 1 study demonstrated 3D in vivo imaging of a beating mouse heart using a clinically approved concentration ($<40 \mu\text{mol} [\text{Fe}] \text{L}^{-1}$) of Resovist (ferucarbotran; Bayer Schering Pharma, Berlin, Germany), with a temporal resolution of 21.5 ms, FOV of 1–2 cm, and resolution sufficient to resolve heart chambers.²⁹ In addition, it has been shown that catheters and guidewires can be tracked with MPI, enabling image-guided interventions.^{30,31}

Oncology. A promising application for MPI is in oncology. MPI could be used to image tumor vascularization, which may be im-

portant in indicating tumor stage and treatment efficacy. We recently demonstrated MPI visualization in a breast cancer xenograft model and showed that MPI can see both the early dynamic contrast-enhanced effect of nanoparticles flowing into a tumor, followed by the enhanced permeability and retention effect during the following 48 hours.³²

In neuro-oncology, conventional MR imaging and CT lack reliability in assessing the size and location of brain tumors, and they are often not specific enough to differentiate tumor progression from other treatment-related changes.^{33,34} While traditional PET for glucose metabolism is often used in peripheral tumor imaging, it cannot provide good contrast for brain tumors due to the high levels of glucose metabolism inherent in the brain, and novel tracers such as radio-labeled amino acids are required for better contrast.³⁵ MPI may provide a promising alternative, especially as brain-specific MPI tracers are

developed to improve specificity, enhance retention times, and reduce potential harm to the patient.

In brain tumor studies, SPION size can be optimized to passively target and accumulate in a brain tumor because the tumor is hypervascularized with leaky vessels while the blood-brain barrier blocks access to healthy brain tissue.^{36–38} Active tumor targeting can also be achieved via surface chemistry modifications or the use of magnetic fields. For example, it was shown that lactoferrin-conjugated nanoparticles can be used to target brain glioma cells in MPI.⁵ By means of a human glioblastoma mouse model, fluorescent magnetic nanoparticles could be magnetically retained in the neovasculature as well as tissue of the tumor, using a magnetic micromesh.⁶

MPI can also be used for sentinel lymph node imaging and hyperthermia treatment. The current state of the art is to use radioactive colloid tracers, which could be replaced with MPI tracers. This was demonstrated in a mouse cancer model,⁷ in which magnetic tracer material was seen depositing in tumor tissue and/or sentinel lymph nodes near tumors. In hyperthermia treatment, magnetic particles injected into tumors can locally heat the tissue around the FFR. It was demonstrated that the MPI-measured magnetic particle concentration correlated well with tumor volume decrease after magnetic hyperthermia.³⁹ In another study, it was shown that magnetic nanofibers loaded with magnetic nanoparticles could be visualized using MPI and used for magnetic hyperthermia.⁴⁰

Cell Labeling and Tracking. MPI is promising for cell tracking because the technique is independent of depth in tissue with millimeter-scale resolution, robust linear quantification, and high sensitivity. We evaluated MPI for tracking of systemically administered mesenchymal stem cells.⁸ Mesenchymal stem cells are of

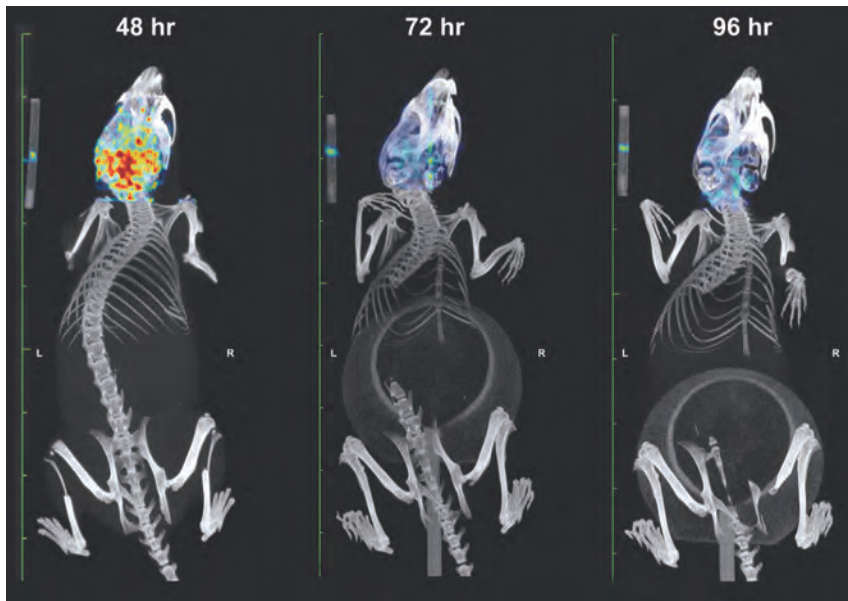


FIG 2. SPION-labeled macrophages have long retention times in the brain of a stroke mouse. We administered $1\text{--}2 \times 10^6$ nanoparticle (VivoTrax; Magnetic Insight)-labeled mouse macrophages (Raw 264.7; American Type Culture Collection, Manassas, Virginia) to BALB/c mice through tail veins 24 hours after stroke. At 48, 72, and 96 hours poststroke, 2D-MPI was performed using a MOMENTUM MPI system. The MPI protocol used the parameters of FOV = 4 cm, 55 projections, best image quality, and default scan mode. Anatomic images were collected on the eXplore CT-120 microCT. Data analysis and image registration were performed using the Horos and VivoQuant software. In vivo iron oxide quantification was performed by imaging a fiducial containing a known concentration of tracer positioned beside the animal. The MPI signal was detected in the brain at 48, 72, and 96 hours poststroke; the accumulation of iron-labeled cells was the highest at 48 hours and reduced with time.

particular therapeutic interest because they can control inflammation and modify the proliferation and cytokine production of immune cells.⁴¹ Intravenous injections are sometimes used to deliver mesenchymal stem cells in both animal models and clinical trials.^{42,43} Our proof-of-concept study confirmed that >80% of mesenchymal stem cells are entrapped in pulmonary vasculature following intravenous injection.⁸ In a different study, it was shown that rat and human adult stem cells can uptake SPIONS and they localize in the cytoplasm.⁴⁴ Blood cell tracking is another application for MPI as a method for increasing circulation time.⁴⁵ Using red blood cells as the carriers also has the advantage of being able to increase circulation time from minutes to hours.^{2,46,47} Additionally, there is ongoing work on the development of MPI-tailored nanoparticles, which can be functionalized for efficient targeting and cell labeling. We recently demonstrated that Janus nanoparticles made by encapsulating iron oxide nanoparticles in semiconducting polymers allowed efficient cell labeling and were sensitive enough to track 250 labeled HeLa cells after implantation in mice.⁹

These cell-labeling and tracking methods may also be applied to neuroimaging. In one study, it was shown that neural grafts could be monitored in rats. This study implanted neural progenitor cells into the forebrain of rats and measured nonsignificant signal decay during 87 days.¹⁸ The authors demonstrated a detection sensitivity of <1000 cells in a voxel. As commercial development continues, we estimate that the theoretic detection limit may approach as little as 1–10 cells in a voxel. For comparison, these numbers compare favorably with MR imaging, in which the

first clinical cell-tracking detection limit was 15,000 cells.⁴⁸ In a preliminary experiment, we administered SPION-labeled mouse macrophages to stroke mice to test the localization and retention of signals for stroke monitoring (Fig 2). We showed that while the accumulation of iron-labeled cells was highest at 48 hours, there was still detectable MPI signal at 96 hours postinjection.

Inflammation Tracking. Inflammation is involved in many disease processes, including immune disorders, neurologic/neuropsychological disorders, and cancer. Detection and tracking of inflammation could help with diagnosis and monitor treatment outcomes. Unfortunately, current practices in tracking inflammation often involve biopsies or imaging methods that have low specificity and quantifiability. MPI may be a promising quantitative imaging alternative. Previous studies have already shown the use of SPIO tracers to target inflammation. SPIOs may be injected intravenously and may be taken up at inflammation sites, such as by macrophages at active phagocytic sites^{49,50} or by atherosclerotic plaques.^{51,52} Previous studies have used MR imaging to detect

the SPIONs for inflammation tracking.^{49,50,53,54} However, with high magnetic susceptibility, SPIOs cause a decrease in signal intensity, which could often be confused with signal voids from bone, air bubbles, susceptibility blowouts, and imaging artifacts. With the use of MPI, SPIONs can be more specifically detected with a higher signal-to-noise ratio.

Contrast Agent. SPIO contrast agents have previously been developed for MR imaging contrast enhancement. SPIOs are relatively safe for the patient and are biodegradable through the reticuloendothelial system.⁵⁵ As mentioned previously, SPIO agents can achieve long retention times in the body up to hours or days when loaded into cells. In PET or SPECT, the radioactive tracers have shorter half-lives in the body, especially for the high-energy probes required in PET. In addition, due to the short half-life of PET tracers, PET requires a cyclotron on site. In comparison, the SPIOs used in MPI are much more stable and have longer shelf lives with lower production cost.⁵⁶ There are a number of commercial SPIO agents that have either received FDA approval or are in a clinical trial phase⁵⁷ to serve as potential contrast agents for MPI.^{58–61} SPIONs have historically been used in humans as MR imaging contrast agents, and 2 tracers, ferucarbotran (Resovist) and ferumoxytol, remain on the market in the European Union/Asia Pacific and the United States/European Union/Asia Pacific, respectively. These agents have been approved for contrast-enhanced MR imaging of the liver/spleen.^{62,63} MR imaging contrast agents can also be used for MPI. Additionally,

development and synthesis of MPI-tailored contrast agents are an emerging and important field of research.

MPI performance is affected by particle size, size distribution, relaxation properties, surface chemistry, and the environment.^{61,64-66} MPI tracer development has so far been dominated by optimizing for particle core size and size distribution. This is especially important for MPI because particle size directly affects image resolution. We have shown that single-core tracers with core diameters of 26–27 nm provide excellent performance for MPI, and modeling studies predict 25–30 nm as the optimal diameter for iron oxide magnetic nanoparticles, with improved performance for uniform size and optimized magnetic properties.^{67,68} Early research also shows that there is an optimal core size for each operating frequency that is driven by transition of the dominant relaxation effect from Néel to Brownian.^{67,68} Additionally, for in vivo applications, further considerations need to be made for circulation time, biodistribution, and cellular uptake. Thus, new contrast agents more specifically targeted for MPI applications are being actively developed. These new particles are optimized for size and size distributions,^{68,69} quality of crystal structure,⁹ mass sensitivity,⁶⁷ high stability,⁷⁰ rich harmonic spectrum,⁷¹ and surface chemistry.⁷²⁻⁷⁴

Safety Considerations. The current consensus is that MPI is safe to scale to human sizes. The primary concerns for MPI are the safety of the SPIONs and the safety of the time-varying magnetic fields. SPIONs are considered a low risk to patients and are well-tolerated, with some exceptions. First, large concentrations can lead to decreased cell proliferation.⁷⁵ Second, there have been some cases of moderate-to-severe allergic reactions to injections of SPIONs.⁷⁶⁻⁷⁸

There is comparatively less risk in the magnetic fields used by MPI, which is governed by the same limits to peripheral nerve stimulation and specific absorption rate that are seen in MR imaging. In a human subject study, it was found that the safe limit for peripheral nerve stimulation and the specific absorption rate in the chest is about 7 mT, between 25 and 50 kHz.⁷⁹ Cardiac stimulation and peripheral nerve stimulation will not be a limitation for clinical MPI systems.⁷⁹⁻⁸¹ In addition, for applications in which guidewires and catheters are used, heating of the equipment is also a potential concern.⁸²

Practical Considerations. The hardware complexity of MPI is comparable with that of MR imaging. One of the difficult engineering tasks is while MR imaging requires a parts-per-million accurate main magnetic field, MPI requires a parts-per-million accurate sinusoidal drive field.⁸³ Both techniques require real-time control of magnetic fields and involve pulse sequences and reconstruction algorithms. In contrast to MR imaging, however, MPI scanning and imaging are straightforward, and we have not found that specialized training is required to acquire or interpret MPI. MPI contrast agents are widely available, easy to handle, and less expensive than commonly used radioactive probes. Like nuclear medicine, it can be helpful to have structural information with which to overlay MPI, and we frequently coregister MPI with CT and MR imaging. Thus, construction of hybrid systems to ease coregistration with anatomic images may be desirable in the future.

CONCLUSIONS

MPI is a novel, promising imaging technique for sensitive, quantitative, and high-resolution in vivo imaging. Preliminary animal studies have shown promising applications, including vascular imaging, oncology imaging, cell tracking, and inflammation imaging. Much development work is being done to further improve imager design, tracer design, and imaging protocols. With these improvements and the upcoming development of human-sized scanners, MPI has the potential to become a widely adopted clinical tool for neuroimaging.

ACKNOWLEDGMENTS

We would like to thank Anna Christensen, Patrick Goodwill, Jeff Gaudet, and Prachi Pandit from Magnetic Insight (<https://www.magneticinsight.com/>) and Daniel Smerin for their support in conducting our experiments.

Disclosures: Gary Steinberg—UNRELATED: Royalties: Peter Lasic US; Stock/Stock Options: Qool Therapeutics, NeuroSave, Comments: stock options only from both companies. Tim Doyle—UNRELATED: Payment for Lectures Including Service on Speakers Bureaus: Magnetic Insight, Comments: talk presented at a magnetic particle imaging workshop at the 2017 World Molecular Imaging Congress (Philadelphia). Honorarium was paid. Steven Conolly—UNRELATED: Grants/Grants Pending: National Institutes of Health, University of California, Office of the President.* Max Wintermark—UNRELATED: Board Membership: GE NFL Advisory Board; Stock/Stock Options: MORE Health, Icometrix; Other: Equity, Comments: Magnetic Insight. Kannan Krishnan—UNRELATED: Grant: University of Washington.* *Money paid to the institution.

REFERENCES

1. Gleich B, Weizenecker J. **Tomographic imaging using the nonlinear response of magnetic particles.** *Nature* 2005;435:1214–17 CrossRef Medline
2. Rahmer J, Gleich B, Weizenecker J, et al. **3D real-time magnetic particle imaging of cerebral blood flow in living mice.** In: *Proceedings of the International Society for Magnetic Resonance in Medicine*, 18, 2010
3. Ludewig P, Gdaniec N, Sedlacik J, et al. **Magnetic particle imaging for real-time perfusion imaging in acute stroke.** *ACS Nano* 2017;11:10480–88 CrossRef Medline
4. Orendorff R, Keselman K, Conolly S. **Quantitative cerebral blood flow and volume measurements by magnetic particle imaging.** In: *13th European Molecular Imaging Meeting*, March 20–23, 2018. San Sebastián, Spain
5. Tomitaka A, Arami H, Gandhi S, et al. **Lactoferrin conjugated iron oxide nanoparticles for targeting brain glioma cells in magnetic particle imaging.** *Nanoscale* 2015;7:16890–98 CrossRef Medline
6. Fu A, Wilson RJ, Smith BR, et al. **Fluorescent magnetic nanoparticles for magnetically enhanced cancer imaging and targeting in living subjects.** *ACS Nano* 2012;6:6862–69 CrossRef Medline
7. Finas D, Baumann K, Sydow L, et al. **Lymphatic tissue and superparamagnetic nanoparticles: magnetic particle imaging for detection and distribution in a breast cancer model.** *Biomed Tech* 2013 Sep 7. [Epub ahead of print] CrossRef Medline
8. Zheng B, von See MP, Yu E, et al. **Quantitative magnetic particle imaging monitors the transplantation, biodistribution, and clearance of stem cells in vivo.** *Theranostic* 2016;6:291–301 CrossRef Medline
9. Song G, Chen M, Zhang Y, et al. **Janus iron oxides @ semiconducting polymer nanoparticle tracer for cell tracking by magnetic particle imaging.** *Nano Lett* 2018;18:182–89 CrossRef Medline
10. Goodwill PW, Lu K, Zheng B, et al. **An x-space magnetic particle imaging scanner.** *Rev Sci Instrum* 2012;83 CrossRef Medline
11. Rahmer J, Weizenecker J, Gleich B, et al. **Signal encoding in magnetic particle imaging: properties of the system function.** *BMC Med Imaging* 2009;9:4 CrossRef Medline

12. Goodwill PW, Conolly SM. **The X-space formulation of the magnetic particle imaging process: 1-D signal, resolution, bandwidth, SNR, SAR, and magnetostimulation.** *IEEE Trans Med Imaging* 2010; 29:1851–59 CrossRef Medline
13. Goodwill PW, Conolly SM. **Multidimensional X-space magnetic particle imaging.** *IEEE Trans Med* 2011;30:1581–90 CrossRef
14. Arami H, Teeman E, Troksa A, et al. **Tomographic magnetic particle imaging of cancer targeted nanoparticles.** *Nanoscale* 2017;9: 18723–30 CrossRef Medline
15. Knopp T, Biederer S, Sattel TF, et al. **Prediction of the spatial resolution of magnetic particle imaging using the modulation transfer function of the imaging process.** *IEEE Trans Med Imaging* 2011;30: 1284–92 CrossRef Medline
16. Moses WW. **Fundamental limits of spatial resolution in PET.** *Nucl Instrum Methods Phys Res A* 2011;648(Supplement 1):S236–40 CrossRef Medline
17. Bailey DL, Willowson KP. **An evidence-based review of quantitative SPECT imaging and potential clinical applications.** *J Nucl Med* 2013;54:83–89 CrossRef Medline
18. Zheng B, Vazin T, Goodwill PW, et al. **Magnetic particle imaging tracks the long-term fate of in vivo neural cell implants with high image contrast.** *Sci Rep* 2015;5:14055 CrossRef Medline
19. Wintermark M, Sesay M, Barbier E, et al. **Comparative overview of brain perfusion imaging techniques.** *Stroke* 2005;36:83–99 CrossRef Medline
20. Saritas EU, Goodwill PW, Croft LR, et al. **Magnetic particle imaging (MPI) for NMR and MRI researchers.** *J Magn Reson* 2013;229: 116–26 CrossRef Medline
21. Knopp T, Buzug TM. *Magnetic Particle Imaging: An Introduction to Imaging Principles and Scanner Instrumentation.* Heidelberg: Springer-Verlag; 2012
22. Kherlopian AR, Song T, Duan Q, et al. **A review of imaging techniques for systems biology.** *BMC Syst Biol* 2008;2:74 CrossRef Medline
23. Weissleder R. **Scaling down imaging: molecular mapping of cancer in mice.** *Nat Rev Cancer* 2002;2:11–18 CrossRef Medline
24. Cox B, Beard P. **Imaging techniques: super-resolution ultrasound.** *Nature* 2015;527:451–52 CrossRef Medline
25. Goodwill PW, Saritas EU, Croft LR, et al. **X-space MPI: magnetic nanoparticles for safe medical imaging.** *Adv Mater* 2012;24:3870–77 CrossRef Medline
26. Khandhar AP, Keselman P, Kemp SJ, et al. **Evaluation of PEG-coated iron oxide nanoparticles as blood pool tracers for preclinical magnetic particle imaging.** *Nanoscale* 2017;9:1299–306 CrossRef Medline
27. Yu EY, Chandrasekharan P, Berzon R, et al. **Magnetic particle imaging for highly sensitive, quantitative, and safe in vivo gut bleed detection in a murine model.** *ACS Nano* 2017;11:12067–76 CrossRef Medline
28. Orendorff R, Peck AJ, Zheng B. **First in vivo traumatic brain injury imaging via magnetic particle imaging.** *Phys Med Biol* 2017;62: 3501–09 CrossRef Medline
29. Weizenecker J, Gleich B, Rahmer J, et al. **Three-dimensional real-time in vivo magnetic particle imaging.** *Phys Med Biol* 2009;54: L1–10 CrossRef Medline
30. Haegele J, Biederer S, Wojtczyk H, et al. **Toward cardiovascular interventions guided by magnetic particle imaging: first instrument characterization.** *Magn Reson Med* 2013;69:1761–67 CrossRef Medline
31. Haegele J, Rahmer J, Gleich B, et al. **Magnetic particle imaging: visualization of instruments for cardiovascular intervention.** *Radiology* 2012;265:933–38 CrossRef
32. Yu EY, Bishop M, Zheng B, et al. **Magnetic particle imaging: a novel in vivo imaging platform for cancer detection.** *Nano Lett* 2017;17: 1648–54 CrossRef Medline
33. Ryken TC, Aygun N, Morris J, et al. **The role of imaging in the management of progressive glioblastoma: a systematic review and evidence-based clinical practice guideline.** *J Neurooncol* 2014;118: 435–60 CrossRef Medline
34. Verma N, Cowperthwaite MC, Burnett MG, et al. **Differentiating tumor recurrence from treatment necrosis: a review of neuro-oncologic imaging strategies.** *Neuro Oncol* 2013;15:515–34 CrossRef Medline
35. Langen KJ, Watts C. **Neuro-oncology: amino acid PET for brain tumours—ready for the clinic?** *Nat Rev Neurol* 2016;12:375–76 CrossRef Medline
36. Maeda H, Wu J, Sawa T, et al. **Tumor vascular permeability and the EPR effect in macromolecular therapeutics: a review.** *J Control Release* 2000;65:271–84 CrossRef Medline
37. Béduneau A, Saulnier P, Benoit JP. **Active targeting of brain tumors using nanocarriers.** *Biomaterials* 2007;28:4947–67 CrossRef Medline
38. Cheng Y, Morshed RA, Auffinger B, et al. **Multifunctional nanoparticles for brain tumor imaging and therapy.** *Adv Drug Deliv Rev* 2014;66:42–57 CrossRef Medline
39. Murase K, Aoki M, Banura N, et al. **Usefulness of magnetic particle imaging for predicting the therapeutic effect of magnetic hyperthermia.** *Open Journal of Medical Imaging* 2015;5:85–99 CrossRef
40. Murase K, Mimura A, Banura N, et al. **Visualization of magnetic nanofibers using magnetic particle imaging.** *Open Journal of Medical Imaging* 2015;05:56–65 CrossRef
41. Eggenhofer E, Luk F, Dahlke MH, et al. **The life and fate of mesenchymal stem cells.** *Front Immunol* 2014;5:148 CrossRef Medline
42. Wu Y, Zhao RC. **The role of chemokines in mesenchymal stem cell homing to myocardium.** *Stem Cell Rev* 2012;8:243–50 CrossRef Medline
43. Harting MT, Jimenez F, Xue H, et al. **Intravenous mesenchymal stem cell therapy for traumatic brain injury.** *J Neurosurg* 2009;110: 1189–97 CrossRef Medline
44. Lütke-Buzug K, Rapoport D. **Characterization of iron-oxide loaded adult stem cells for magnetic particle imaging in targeted cancer therapy.** *AIP Conf Proc* 2010;1311:244–48
45. Antonelli A, Sfara C, Rahmer J, et al. **Red blood cells as carriers in magnetic particle imaging.** *Biomed Tech (Berl)* 2013;58:517–25 CrossRef Medline
46. Markov DE, Boeve H, Gleich B, et al. **Human erythrocytes as nanoparticle carriers for magnetic particle imaging.** *Phys Med Biol* 2010; 55:6461–73 CrossRef Medline
47. Haegele J, Duschka R, Graeser M, et al. **Magnetic particle imaging: kinetics of the intravascular signal in vivo.** *Int J Nanomedicine* 2014; 9:4203–09 CrossRef Medline
48. de Vries IJ, Lesterhuis WJ, Barentsz JO, et al. **Magnetic resonance tracking of dendritic cells in melanoma patients for monitoring of cellular therapy.** *Nat Biotechnol* 2005;23:1407–13 CrossRef Medline
49. Lefevre S, Ruimy D, Jehl F, et al. **Septic arthritis: monitoring with USPIO-enhanced macrophage MR imaging.** *Radiology* 2011;258: 722–28 CrossRef Medline
50. Lutz AM, Weishaupt D, Persohn E, et al. **Imaging of macrophages in soft-tissue infection in rats: relationship between ultrasmall superparamagnetic iron oxide dose and MR signal characteristics.** *Radiology* 2005;234:765–75 CrossRef Medline
51. Ruehm SG, Corot C, Vogt P, et al. **Magnetic resonance imaging of atherosclerotic plaque with ultrasmall superparamagnetic particles of iron oxide in hyperlipidemic rabbits.** *Circulation* 2001;103: 415–22 CrossRef Medline
52. Sigovan M, Boussel L, Sulaiman A, et al. **Rapid-clearance iron nanoparticles for inflammation imaging of atherosclerotic plaque: initial experience in animal model.** *Radiology* 2009;252:401–09 CrossRef Medline
53. Metz S, Beer AJ, Settles M, et al. **Characterization of carotid artery plaques with USPIO-enhanced MRI: assessment of inflammation and vascularity as in vivo imaging biomarkers for plaque vulnerability.** *Int J Cardiovasc Imaging* 2011;27:901–12 CrossRef Medline
54. McAteer MA, Sibson NR, von Zur Muhlen C, et al. **In vivo magnetic resonance imaging of acute brain inflammation using microparticles of iron oxide.** *Nat Med* 2007;13:1253–58 CrossRef Medline
55. Wang YX. **Superparamagnetic iron oxide based MRI contrast agents: current status of clinical application.** *Quant Imaging Med Surg* 2011;1:35–40 CrossRef Medline
56. Panagiotopoulos N, Duschka RL, Ahlborg M, et al. **Magnetic particle**

- imaging: current developments and future directions.** *Int J Nano-medicine* 2015;10:3097–114 CrossRef Medline
57. Wang YX, Hussain SM, Krestin GP. **Superparamagnetic iron oxide contrast agents: physicochemical characteristics and applications in MR imaging.** *Eur Radiol* 2001;11:2319–31 CrossRef Medline
 58. Bonnemain B. **Superparamagnetic agents in magnetic resonance imaging: physicochemical characteristics and clinical applications—a review.** *J Drug Target* 1998;6:167–74 CrossRef Medline
 59. Sun C, Lee JS, Zhang M. **Magnetic nanoparticles in MR imaging and drug delivery.** *Adv Drug Deliv Rev* 2008;60:1252–65 CrossRef Medline
 60. Publico-Lansigan MH, Situ SF, Samia AC. **Magnetic particle imaging: advancements and perspectives for real-time in vivo monitoring and image-guided therapy.** *Nanoscale* 2013;5:4040–55 CrossRef Medline
 61. Bauer LM, Situ SF, Griswold MA, et al. **Magnetic particle imaging tracers: state-of-the-art and future directions.** *J Phys Chem Lett* 2015;6:2509–17 CrossRef Medline
 62. Reimer P, Tombach B. **Hepatic MRI with SPIO: detection and characterization of focal liver lesions.** *Eur Radiol* 1998;1204:1198–204 CrossRef Medline
 63. Reimer P, Balzer T. **Ferucarbotran (Resovist): a new clinically approved RES-specific contrast agent for contrast-enhanced MRI of the liver—properties, clinical development, and applications.** *Eur Radiol* 2003;13:1266–76 CrossRef Medline
 64. Eberbeck D, Wiekhorst F, Wagner S, et al. **How the size distribution of magnetic nanoparticles determines their magnetic particle imaging performance.** *Appl Phys Lett* 2011;98:182502 CrossRef
 65. Khandhar AP, Ferguson RM, Arami H, et al. **Tuning surface coatings of optimized magnetite nanoparticle tracers for in vivo magnetic particle imaging.** *IEEE Trans Magn* 2015;51:395–401 CrossRef
 66. Arami H, Ferguson RM, Khandhar AP, et al. **Size-dependent ferrohydrodynamic relaxometry of magnetic particle imaging tracers in different environments.** *Med Phys* 2013;40:071904 CrossRef Medline
 67. Ferguson RM, Minard KR, Khandhar AP, et al. **Optimizing magnetite nanoparticles for mass sensitivity in magnetic particle imaging.** *Med Phys* 2011;38:1619–26 CrossRef Medline
 68. Ferguson RM, Minard KR, Krishnan KM. **Optimization of nanoparticle core size for magnetic particle imaging.** *J Magn Magn Mater* 2009;321:1548–51 CrossRef Medline
 69. Ferguson RM, Khandhar AP, Krishnan KM. **Tracer design for magnetic particle imaging (invited).** *J Appl Phys* 2012;07B318 CrossRef
 70. Arami H, Krishnan KM. **Highly stable amine functionalized iron oxide nanoparticles designed for magnetic particle imaging (MPI).** *IEEE Trans Magn* 2013;49:3500–03 CrossRef
 71. Ludwig F, Wawrzik T, Yoshida T, et al. **Optimization of magnetic nanoparticles for magnetic particle imaging.** *IEEE Trans Magn* 2012;48:3780–83 CrossRef
 72. Starmans LW, Burdinski D, Haex NP, et al. **Iron oxide nanoparticle-micelles (ION-micelles) for sensitive (molecular) magnetic particle imaging and magnetic resonance imaging.** *PLoS One* 2013;8:e57335 CrossRef Medline
 73. Starmans LW, Moonen RP, Aussems-Custers E, et al. **Evaluation of iron oxide nanoparticle micelles for magnetic particle imaging (MPI) of thrombosis.** *PLoS One* 2015;10:e0119257 CrossRef Medline
 74. Ishihara Y, Honma T, Nohara S, et al. **Evaluation of magnetic nanoparticle samples made from biocompatible ferucarbotran by time-correlation magnetic particle imaging reconstruction method.** *BMC Med Imaging* 2013;13:15 CrossRef Medline
 75. Lindemann A, Lüdtkke-Buzug K, Fräderich BM, et al. **Biological impact of superparamagnetic iron oxide nanoparticles for magnetic particle imaging of head and neck cancer cells.** *Int J Nanomedicine* 2014;9:5025–40 CrossRef Medline
 76. Kehagias DT, Gouliamos AD, Smyrniotis V, et al. **Diagnostic efficacy and safety of MRI of the liver with superparamagnetic iron oxide particles (SH U 555 A).** *J Magn Reson Imaging* 2001;14:595–601 CrossRef Medline
 77. Bernd H, De Kerviler E, Gaillard S, et al. **Safety and tolerability of ultrasmall superparamagnetic iron oxide contrast agent: comprehensive analysis of a clinical development program.** *Invest Radiol* 2009;44:336–42 CrossRef Medline
 78. Singh A, Patel T, Hertel J, et al. **Safety of ferumoxytol in patients with anemia and CKD.** *Am J Kidney Dis* 2008;52:907–15 CrossRef Medline
 79. Saritas EU, Goodwill PW, Zhang GZ, et al. **Magnetostimulation limits in magnetic particle imaging.** *IEEE Trans Med Imaging* 2013;32:1600–10 CrossRef Medline
 80. Saritas EU, Goodwill PW, Zhang GZ, et al. **Safety limits for human-size magnetic particle imaging systems.** In: Buzug TM, Knopp T, eds. *Magnetic Particle Imaging*. Berlin: Springer-Verlag; 2011:325–30
 81. Schmale I, Gleich B, Rahmer J, et al. **MPI safety in the view of MRI safety standards.** *IEEE Trans Mag* 2015;51:1–4 CrossRef
 82. Duschka RL, Wojtczyk H, Panagiotopoulos N, et al. **Safety measurements for heating of instruments for cardiovascular interventions in magnetic particle imaging (MPI): first experiences.** *J Healthc Eng* 2014;5:79–93 CrossRef Medline
 83. Croft LR, Goodwill PW, Konkle JJ, et al. **Low drive field amplitude for improved image resolution in magnetic particle imaging.** *Med Phys* 2016;43:424 CrossRef Medline

A Call to Improve the Visibility and Access of the American College of Radiology Practice Parameters in Neuroradiology: A Powerful Value Stream Enhancer for Both Neuroradiologists and Patients

J.E. Jordan and A. Norbash



SUMMARY: Clinical practice guidelines and clinical practice parameters are among the tools that clinicians and radiologists use to inform decision making in the diagnosis and treatment of patients. Radiologists have been urged to objectively establish their value and measurable contributions to patient care. Radiology's contribution to the health care value stream can be established in the development of sound clinical practice guidelines. Neuroradiologists have been quite active in developing clinical guidelines, particularly in collaboration with the American College of Radiology, but there is a need to increase the visibility and accessibility of such documents. Increasing access and visibility can contribute to improved patient outcomes and an improved overall quality of care.

ABBREVIATIONS: ACR = American College of Radiology; AHCPR = Agency for Health Care Policy and Research; CPG = Clinical Practice Guideline; GIN = Guidelines International Network; IOM = Institute of Medicine; PP = Practice Parameter

Clinical Practice Guidelines (CPGs), clinical standards, consensus statements, and Practice Parameters are among the tools that clinicians use to inform clinical decision-making in the diagnosis and treatment of patients.¹⁻³ When guidelines are rigorously developed using an evidence-based approach derived from scientific knowledge, clinical trials, expert opinion, and expert consensus, the result is advanced and improved patient outcomes and an improved overall quality of care. Clinical Practice Guidelines have become increasingly visible within medical specialties. There are currently over 3700 guidelines contained within the Guidelines International Network (GIN; <https://www.g-i-n.net/>) data base from 39 countries.¹ Such guidelines are intended to help with routine and complex patient management decisions while reducing the variability of practice. Evidence-based guidelines inform health and public policy decisions and also guide appropriate allocations of resources. Concerning radiology, the terminology referring to this effort to minimize unnecessary practice variability has evolved from “standards,” to “guidelines,” to the currently favored terminology “Practice Parameters” (PPs). We will therefore refer to CPGs when the larger house of medicine is concerned, and when possible, we will refer

to these Practice Guidelines as PPs when contemporary radiology is concerned.³

Neuroradiologists have actively collaborated with the American College of Radiology (ACR) in developing clinical Practice Parameters with the assistance of the ACR Commission on Neuroradiology; the ACR Committee on Practice Parameters, Neuro-radiology; and the American Society of Neuroradiology Standards and Guidelines Committee. Neuroradiology subspecialty input and representation have also been voluntarily provided by additional national neuroradiology and subspecialty societies, including the American Society of Pediatric Neuroradiology, the American Society of Spine Radiology, the American Society of Functional Neuroradiology, the Society of Neurointerventional Surgery, and the ACR Committee on Practice Parameters and Technical Standards—Nuclear Medicine and Molecular Imaging.

Background of CPG Development in the United States

The Institute of Medicine (IOM) is a nonprofit organization within the National Academies of Sciences, Engineering, and Medicine. The IOM has defined Clinical Practice Guidelines, initially as a result of the Omnibus Budget Reconciliation Act of 1989.^{1,4} The Omnibus Act sought to address concerns regarding variability in medical practice, in addition to addressing uncontained health care costs. Among the principal objectives of The Omnibus Act was the creation of the Agency for Health Care Policy and Research (AHCPR). The AHCPR contracted with the IOM in 1990 to create the Committee to Advise the Public Health Service on Clinical Practice Guidelines. This committee then issued its report, *Clinical Practice Guidelines: Directions for a New Program* in 1990, and defined CPGs as “systematically developed

Received August 18, 2018; accepted after revision October 29.

From the Department of Radiology (J.E.J.), Providence Little Company of Mary Medical Center, Torrance, California; Department of Radiology (J.E.J.), Stanford University School of Medicine, Stanford, California; and Department of Radiology (A.N.), University of California, San Diego School of Medicine, La Jolla, California.

Please address correspondence to John E. Jordan, MD, MPP, PO Box 6481, San Pedro, CA 90734; e-mail: jjordan_us@yahoo.com

<http://dx.doi.org/10.3174/ajnr.A5923>

Recommended Attributes of CPGs^a

Attributes
Validity: Practice guidelines are valid if, when followed, they lead to the health and cost outcomes projected for them, with other things being equal. A prospective assessment of validity will consider the projected health outcomes and costs of alternative courses of action, the relationship between the evidence and recommendations, the substance and quality of the scientific and clinical evidence cited, and the means used to evaluate the evidence.
Reliability/Reproducibility: Practice guidelines are reliable and reproducible. 1) if—given the same evidence and methods for guidelines development—another set of experts would produce essentially the same statements; and 2) if—given the same circumstances—the guidelines are interpreted and applied consistently by practitioners or other appropriate parties. A prospective assessment of reliability may consider the results of independent external reviews and pretests of guidelines.
Clinical Applicability: Practice guidelines should be as inclusive of appropriately defined patient populations as scientific and clinical evidence and expert judgment permit, and they should explicitly state the populations to which statements apply.
Clinical Flexibility: Practice guidelines should identify the specifically known or generally expected exceptions to their recommendations.
Clarity: Practice guidelines should use unambiguous language, define terms precisely, and use logical, easy-to-follow modes of presentation.
Multidisciplinary Process: Practice guidelines should be developed by a process that includes participation by representatives of key affected groups. Participation may include serving on panels that develop guidelines, providing evidence and viewpoints to the panels, and reviewing draft guidelines.
Scheduled Review: Practice guidelines should include statements about when they should be reviewed to determine whether revisions are warranted, given new clinical evidence or changing professional consensus.
Documentation: The procedures followed in developing guidelines, the participants involved, the evidence used, the assumptions and rationales accepted, and the analytic methods employed should be meticulously documented and described.

^a Reproduced with permission from Graham et al.¹

statements to assist practitioner and patient decisions about appropriate health care for specific clinical circumstances.”¹ The reputation of the AHCPR later was questioned as it undertook development and implementation of Clinical Practice Guidelines, ultimately resulting in changes in the name and charge of the AHCPR. Following congressional lobbying by physician groups under the Healthcare Research and Quality Act of 1999, the AHCPR became the Agency for Healthcare Research and Quality. The Agency for Healthcare Research and Quality focuses on outcomes and effectiveness research.⁵

There was considerable dissatisfaction and questionable quality concerning CPGs despite these developments. This dissatisfaction led Congress to authorize the United States Department of Health and Human Services to contract with the IOM to develop standards for Clinical Practice Guidelines. It was determined that these standards could be realized through the Medicare Improvements for Patients and Providers Act of 2008.⁶ The IOM then created the Committee on Standards for Developing Trustworthy Clinical Practice Guidelines to undertake this effort. This committee reconfigured both the definitions and recommendations of the IOM concerning CPGs. In its report, *Clinical Practice Guidelines We Can Trust*,¹ the IOM defined CPGs in the following manner: “Clinical Practice Guidelines are statements that include recommendations intended to optimize patient care that are informed by a systematic review of evidence and an assessment of the benefits and harms of alternative care options.” The IOM CPG report recommended 8 attributes that CPGs should have, including validity, reproducibility, clinical relevance, clinical flexibility, clarity, multidisciplinary process, scheduled review, and meticulous documentation (Table).¹ The IOM also recognized the added value of expert consensus documents, clinical standards, white papers, and practice parameters, though it did not specifically assess them due to the limited scope of its mandate. Radiologists have collaborated with other specialties in developing CPGs and these other types of documents, though more collaboration is needed between radiologists and multidisciplinary groups to enhance the impact and visibility of radiology-related CPGs.⁷

Historical Practice Parameter Development in Radiology

As a result of the revised IOM definition of Clinical Practice Guidelines published in 2011, the ACR soon after renamed its CPGs—formerly known as the ACR Practice Guidelines and Technical Standards—the ACR Practice Parameters and Technical Standards. This specific change in verbiage from practice guidelines to Practice Parameters recognized that radiology differs from other clinical specialties, with an understanding that patient outcomes from radiology are challenging to assess. The change in verbiage was intended to convey the reality that PPs are collaborative documents and that collaboration in generating the PPs by necessity principally took place among radiology or imaging subspecialties, whereas cross-specialty nonimaging multidisciplinary collaboration was more limited. To better understand the nuances of deliberations that led to these changes, some background information of how the ACR PPs evolved may be helpful.

The 1980s witnessed accelerating medical costs and increasing calls by medical specialties, payers, and policy makers for the development of clinical guidelines. The variability of practice in health care and escalating costs alarmed many, and ultimately culminated in legislation to facilitate clinical guideline development.⁴ During this same period, the ACR took the initiative to develop clinical guidelines for radiologists, resulting in approval of its first 9 guidelines in 1990, referred to at the time as “standards.” These standards proliferated to include subspecialties such as neuroradiology, and by 2003, about 121 ACR standards had been developed.⁸ In May 2003, at the ACR Council Annual Meeting, the term “practice guidelines” was adopted as a preferred replacement for the term “standards,” which would later be replaced by the term “Practice Parameters.” The reason the term “practice guidelines” replaced standards in 2003 was the perception of greater flexibility for the practicing radiologist. The word “standards” was believed to confer less flexibility, requiring radiologists to practice in accordance with the standard or be judged as practicing substandard care. For a small number of the documents, the term “technical standard” was chosen when addressing subjects requiring strict adherence such as the development of

equipment specifications, radiation safety issues, and instrument monitoring, and deviations would be considered contributing to substandard practice.⁸ Many of the technical standards were crafted and sponsored by the American Association of Physicists in Medicine.

ACR Practice Parameters are developed and refined through a lengthy process of gathering evidence and generating expert consensus.⁹ The PPs undergo additional scrutiny during committee member reviews, then subspecialty society review, and next general member review and commentary. Finally, PPs are debated, amended, revised, and approved or rejected by the ACR Council at its annual meeting. Once adopted by the Council, the proffered PP is finally considered a policy statement of the ACR. Rather than representing rigid guidelines, the PPs are designed to provide guidance and principles to improve the practice of radiology and health care outcomes. The technical standards, in contrast, serve the radiologists' needs while also providing guidance for physicians and medical physicists working in radiology and imaging. Other PPs are developed for the practice of radiation oncology.

As stated in the ACR Practice Parameters handbook, the Practice Parameters, "describe a range of acceptable approaches for the diagnosis and/or treatment of disease for most patients in most circumstances. Given differences in training, experience, and local conditions, the ACR Practice Parameters and technical standards acknowledge the need for health care providers to exercise their independent medical judgment in making decisions regarding the use and specific details of any procedure.... Used in conjunction with the ACR Appropriateness Criteria, it is expected that the ACR Practice Parameters and technical standards will increase the likelihood that appropriate procedures will be performed in a safe and acceptable manner and will help reduce unnecessary ones. ACR Practice Parameters and technical standards are intended to be living documents that are regularly reviewed and revised to reflect changes in radiologic and radiation oncology practice."⁹

There are currently 175 ACR PPs and technical standards. Of these, 19 or nearly 11% have been primarily and individually developed by neuroradiologists, though 53 are relevant to the practice of neuroradiology, even though not developed by neuroradiologists. These relevant PPs range from such subjects as communication standards to PPs addressing approaches in the interpretation of various specific imaging modalities, with particular relevant PPs relating to interventional techniques. Other PPs relevant to the practice of neuroradiology include sonographic evaluation of the head/neck/brain/spine, vascular imaging, biopsy/drainage procedures, nuclear medicine of the CNS (eg, PET, dementia), and radiography.¹⁰ A number of collaborative societies have participated in generating neuroradiology documents pertaining to the development of the PPs; these collaborating societies include the Society of Interventional Radiology, Society of Nuclear Medicine and Molecular Imaging, Society of Pediatric Radiology, American Association of Physicists in Medicine, ACR Committee on Body Imaging (Musculoskeletal), and the aforementioned neuroradiology subspecialty societies. Regarding technical standards, approximately 18 exist and are primarily established for equipment quality control for the principal use of medical physicists.¹⁰ Many of these PPs and standards documents

are not readily familiar to the American Society of Neuroradiology or neuroradiology community members because they may be categorized under various modalities, specialties, or organ systems. Nevertheless, these relevant PPs and technical standards are meaningful and relevant for the house of neuroradiology.

Challenges to Quality Practice Parameter Development

High-quality evidence may be lacking in some disciplines, including radiology, challenging the development of bona fide evidence-based clinical guidelines.⁷ Much of the radiology literature deals with observational and anecdotal evidence, limiting the ability of radiology to establish the impact and effectiveness of radiologic services—especially diagnostic procedures—on downstream patient outcomes. Neuroradiology has a significant impact on social consequences, including costs of care and quality of life when considering such varied and ubiquitous neurologic diseases as stroke, dementia, and movement disorders, with the potential to guide patient management decisions and thereby improve outcomes.¹¹

Most medical specialties have succeeded in producing CPGs. Not all CPGs are based on appropriately high-quality evidence. The limited number of studies demonstrating the positive contribution of radiology to patient outcomes is problematic for all radiologists because patient outcomes are one of the few principal determinants of value in health care. Value in health care, as in other disciplines, should ideally be defined in reference to the customer who also happens to be the patient. Patient outcomes are therefore a central measure of value in health care from a population health and societal perspective, underlining the need for radiologists to understand and appreciate the actual outcomes of our patients.¹²

Incentives and payments are continuously evolving to include value-based credit, as payment gradually shifts from fee for service to value-based care. With this new calculus, the metrics that permit accurate measurement of both quality of delivered care and patient outcomes become increasingly important. An inherent limitation of radiology is that most of our published quality metrics are related more to structure and process than outcomes. For example, Narayan et al¹³ reported that a systematic review of the literature for quality metrics in radiology found measures related to outcomes in only 27%, whereas the inverse, 73% of metrics, was related to structure and process. As outcomes are progressively studied with increasing sophistication in all health care domains, it is apparent that relatively few studies in other areas of health care have consistently and convincingly shown that adherence to CPGs improves patient outcomes.^{14,15} While it is reasonable to expect a positive correlation between these 2, more investigation in establishing this connection may be necessary if clinicians are to be fully convinced of the value of CPGs and if they are expected to incorporate them into their everyday practice.

Why This Matters to the House of Neuroradiology

Despite a limited number of high-quality studies, there is a growing body of evidence that CPGs enhance the value of care delivery by enhancing quality, improving clinical outcomes, and reducing costs. As 1 example, a report by the Agency for Healthcare Research and Quality found that an estimated 87,000 fewer deaths

were associated with advances in addressing hospital-acquired conditions when comparing 2010 and 2014, with an estimated cost savings of \$19.8 billion. While the exact causes of the reductions were difficult to pinpoint, greater adoption and use of CPGs was thought to be a major contributing factor to this change.^{3,16}

Radiologists have been advised—both within and outside the house of neuroradiology—to objectively establish their value and measurable contributions to patient care. The contribution of radiology to the health care value stream can be established in the development of sound clinical Practice Parameters. The PPs generally are not published in medical journals and, despite their high quality, are not readily accessed or used by potential users when one assesses the distribution of this knowledge by examining MEDLINE or PubMed searches. As disclosed by the National Library of Medicine, “Approximately 30,000 records are included in the PubMed journal list which is updated daily and includes all MEDLINE titles as well as other non-MEDLINE titles in PubMed.... The non-MEDLINE journals include those whose content is deposited in PubMed Central. PubMed Central is also the repository for author manuscripts that are required under the National Institutes of Health Public Access Policy to be deposited when the research is funded by National Institutes of Health.... National Library of Medicine creates a cataloging record for every journal with a full text article in PubMed Central. Therefore, while most MEDLINE journals over the years have citations for all substantive content published, some of the non-MEDLINE journals may contribute far fewer citations over the years.”¹⁷ In this context, the ACR PPs continue to miss salient opportunities for vast exposure and visibility.

Radiologists Accessing Practice Parameters

Society will likely expect that radiologists establish and substantiate our contributions to improved patient outcomes. Neuroradiologists should be leaders in developing high-quality evidence-based clinical Practice Parameters to advance the progress of the specialty and improve patient care.

New Practice Parameters will continue to be developed in neuroradiology and radiology, and it is essential that these documents be more accessible to all clinicians through MEDLINE and PubMed and that radiologists be familiar with accessing and implementing these Practice Parameters. The PPs are high-quality documents reflecting the vast expertise of imaging specialists, and both clinicians and patients will benefit from these documents being readily available and identifiable when undertaking medical literature searches.

We suggest that practitioners gain a high degree of familiarity with accessing Practice Parameters. Doing so will provide additional reference and access to the PPs when medical literature searches are undertaken or when questions arise regarding best practices. Such an approach will ensure that future neuroradiology clinical guidelines or technical standards documents are provided as broad an exposure as possible. This effort could enhance the visibility and accessibility of the quality of practice for neuro-radiologists, provide needed clinical guidance to practice state-of-

the-art neuroradiology/radiology, and ensure the visibility of our valuable contributions to both individual patient care and collective patient outcomes.

Disclosures: John E. Jordan—*OTHER RELATIONSHIPS*: Past Chair, Committee on Practice Parameters, Neuroradiology, American College of Radiology. Alexander Norbash—*UNRELATED: Board Membership*: Stryker, GE Healthcare, GE Data, Penumbra, *Comments*: scientific advisory boards; *Stock/Stock Options*: Boston Imaging Core Laboratories, *Comments*: Cofounder.

REFERENCES

1. Graham R, Mancher M, Miller Wolman D, et al, eds. Institute of Medicine (US) Committee on Standards for Developing Trustworthy Clinical Practice Guidelines. *Clinical Practice Guidelines We Can Trust*. Washington, DC: National Academies Press; 2011
2. National Institutes of Health: National Center for Complementary and Integrative Health. Clinical Practice Guidelines. <http://nccih.nih.gov/health/providers/clinicalpractice.htm>. Accessed July 20, 2018
3. Hoensing, H. Joint Commission International. Clinical Practice Guidelines. **Closing the gap between theory and practice**. Elsevier, 2016 https://www.elsevier.com/_data/assets/pdf_file/0007/190177/JCI-Whitepaper_cpigs-closing-the-gap.pdf. Accessed July 23, 2018
4. Omnibus Budget Reconciliation Act of 1989, 42 U.S.C. S 901, Public Law 101–239. (1989)
5. Healthcare Research and Quality Act of 1999, Title IX, 42 U.S.C. S 901
6. Medicare Improvements for Patients and Providers Act, 42 U.S.C. S 304, Public Law 110–275 (2008)
7. Manchikanti, L, Falco, Singh V, et al. **An update of comprehensive evidence-based guidelines for interventional techniques in chronic spinal pain, Part I: introduction and general considerations**. *Pain Physician* 2013;16:S1–48 Medline
8. Guiberteau MJ, Wilcox PA, Bjork S. **Practice guidelines: the radiology perspective**. *J Am Coll Radiol* 2004;1:92–97 Medline
9. American College of Radiology. *Practice Parameters and Technical Standards: Development and Revision Handbook*. <http://www.acr.org/-/media/ACR/Files/Practice-Parameters/DevelopmentHandbook.pdf>. Accessed July 16, 2018
10. American College of Radiology. Practice Parameters and Technical Standards. <https://www.acr.org/Clinical-Resources/Practice-Parameters-and-Technical-Standards>. Accessed July 12, 2018
11. Wintermark M, Colen R, Whitlow CT, et al. **The vast potential and bright future of neuroimaging**. *Br J Radiol* 2018;91:20170505 CrossRef Medline
12. Porter ME. **What is value in health care?** *N Engl J Med* 2010;363:2477–81 CrossRef Medline
13. Narayan A, Cinelli C, Carrino JA, et al. **Quality measurements in radiology: a systematic review of the literature and survey of radiology benefit management groups**. *J Am College Radiol* 2015;12:1173–81 CrossRef Medline
14. Hubbard IJ, Harris D, Kilkenny MF, et al. **Adherence to clinical guidelines improves patient outcomes in Australian audit of stroke rehabilitation practice**. *Arch Phys Med Rehabil* 2012;93:965–71 CrossRef Medline
15. Gagliardi AR, Brouwers MC. **Integrating guideline development and implementation: analysis of guideline development manual instructions for generating implementation advice**. *Implement Sci* 2012;7:67 CrossRef Medline
16. AHRQ (Agency for Healthcare Research and Quality). Saving Lives and Saving Money: Hospital-Acquired Conditions Update. Washington, DC, 2015. <https://www.ahrq.gov/professionals/quality-patient-safety/pfp/interimhacrate2014.html>. Accessed July 20, 2018
17. List of All Journals Cited in PubMed. NIH: National Library of Medicine. http://www.nlm.nih.gov/bsd/serfile_addedinfo.html. Accessed July 20, 2018

A Deep Learning–Based Approach to Reduce Rescan and Recall Rates in Clinical MRI Examinations

 A. Sreekumari,  D. Shanbhag,  D. Yeo,  T. Foo,  J. Pilitsis,  J. Polzin,  U. Patil,  A. Coblenz,  A. Kapadia,  J. Khinda,  A. Boutet,  J. Port, and  I. Hancu



ABSTRACT

BACKGROUND AND PURPOSE: MR imaging rescans and recalls can create large hospital revenue loss. The purpose of this study was to develop a fast, automated method for assessing rescan need in motion-corrupted brain series.

MATERIALS AND METHODS: A deep learning–based approach was developed, outputting a probability for a series to be clinically useful. Comparison of this per-series probability with a threshold, which can depend on scan indication and reading radiologist, determines whether a series needs to be rescanned. The deep learning classification performance was compared with that of 4 technologists and 5 radiologists in 49 test series with low and moderate motion artifacts. These series were assumed to be scanned for 2 scan indications: screening for multiple sclerosis and stroke.

RESULTS: The image-quality rating was found to be scan indication– and reading radiologist–dependent. Of the 49 test datasets, technologists created a mean ratio of rescans/recalls of $(4.7 \pm 5.1)/(9.5 \pm 6.8)$ for MS and $(8.6 \pm 7.7)/(1.6 \pm 1.9)$ for stroke. With thresholds adapted for scan indication and reading radiologist, deep learning created a rescan/recall ratio of $(7.3 \pm 2.2)/(3.2 \pm 2.5)$ for MS, and $(3.6 \pm 1.5)/(2.8 \pm 1.6)$ for stroke. Due to the large variability in the technologists' assessments, it was only the decrease in the recall rate for MS, for which the deep learning algorithm was trained, that was statistically significant ($P = .03$).

CONCLUSIONS: Fast, automated deep learning–based image-quality rating can decrease rescan and recall rates, while rendering them technologist-independent. It was estimated that decreasing rescans and recalls from the technologists' values to the values of deep learning could save hospitals \$24,000/scanner/year.

ABBREVIATIONS: CB = clinically bad; CG = clinically good; CNN = convolutional neural network; DL = deep learning; D0–D5 = radiologists; IQ = image quality; R0 = radiologist; ROC = receiver operating characteristic; T1–T4 = MR imaging technologists

MR imaging is the preferred approach for diagnosing neurologic disorders due to its versatile contrast. Its high cost, however, limits its use. It was recently discovered that repeat acquisitions can significantly extend MR imaging examination time and increase hospital costs. Up to 20% of MR imaging examina-

tions have at least a repeat series, leading to the loss to a hospital of ~\$115,000/scanner/year.¹

Series are repeated when the scanning technologist decides that image quality (IQ) is inadequate for diagnosis. A related problem, wherein a patient is sent home with the technologist assessing that the IQ is sufficient and then recalled due to a radiologist's inability to diagnose, also exists. Reducing rescans and recalls is important for optimizing the efficiency of the health care system. This problem, however, is not easy to solve, as it is the radiologist who decides if IQ is sufficient, and the technologist who makes the rescan decision. In addition, reports document different radiologists' opinions regarding IQ² or diagnosing disease.³ It is likely that a given IQ level may be sufficient for a given physician and insufficient for another.

A few publications exist, documenting means for automated IQ assessments in MR imaging.^{2,4–8} In most reports, the IQ of specific imaging sequences (such DWI,^{5,6} or of particular acquisitions scanned for a cohort study^{2,7}) is assessed. Time-intensive preprocessing, such as brain tissue classification or registration,²

Received August 15, 2018; accepted after revision November 2.

From the GE Global Research Center (A.S., D.S., U.P.), Bangalore, India; GE Global Research Center (D.Y., T.F., I.H.), Niskayuna, New York; Albany Medical College (J.Pilitsis), Albany, New York; GE Healthcare (J.Polzin), Milwaukee, Wisconsin; University Hospital Network (A.C., A.K., J.K., A.B.), Toronto, Ontario, Canada; and Mayo Clinic (J.Port), Rochester, Minnesota.

This work was prepared while Ileana Hancu was employed at GE Global Research Center Niskayuna, NY 12309. The opinions expressed in this article are the author's own and do not reflect the view of the National Institutes of Health, the Department of Health and Human Services, or the United States government.

Please address correspondence to Ileana Hancu, PhD, GE Global Research Center, 1 Research Circle, K-1 NMR 138, Niskayuna, NY 12309; e-mail: ihancu1@gmail.com

 Indicates article with supplemental on-line photos.

<http://dx.doi.org/10.3174/ajnr.A5926>

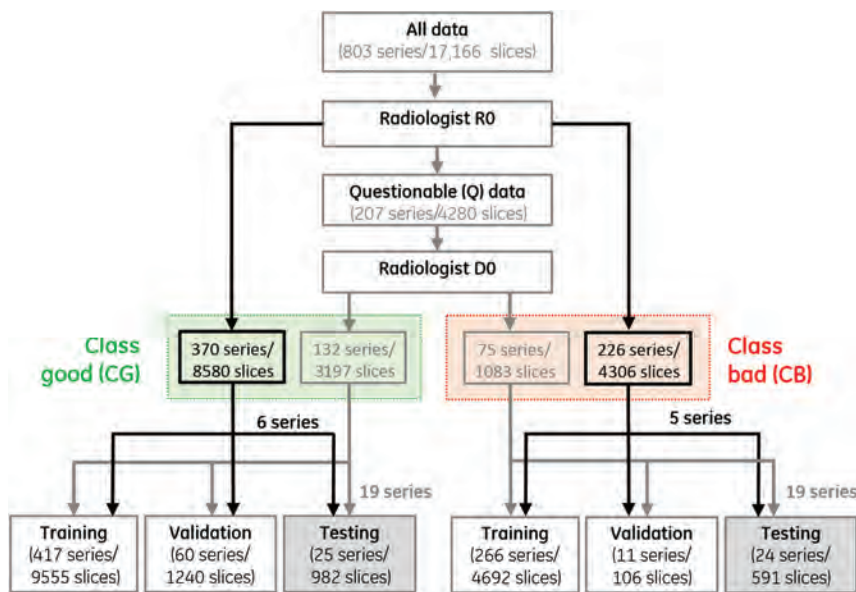


FIG 1. Workflow for image rating and usage.

or the extraction of many image features,⁴ precludes real-time IQ determination. Faster machine and deep learning (DL)–based methods for artifact detection in MR images have also been reported, generally resulting in per-patch or per-slice classification.^{2,4,9–14} While artifact detection on a per-patch or per-slice basis is helpful, it does not inform the technologist about whether a series needs to be rescanned. In many instances, artifacts present in select slices do not require a series rescan.

The fundamental goal of this article was to develop a real-time approach for helping technologists decide whether a series needs to be rescanned. Image quality of individual brain slices of any contrast, pathology, or orientation is first assessed by a DL architecture. Individual slice ratings are subsequently used to compute a per-series score, which is compared against a threshold to decide whether the series requires a rescan. This threshold can be adjusted to accommodate different clinical scan indications and reading radiologists. The performance of this algorithm is validated against assessments from multiple MR imaging technologists and radiologists and for multiple scan indications.

MATERIALS AND METHODS

Training, Validation, and Testing Data

This retrospective study was approved by the institutional review board of Albany Medical College. Brain examinations from patients scanned on three HDx 1.5T scanners (GE Healthcare, Milwaukee, Wisconsin) were used for training the DL-based approach. Data were intentionally enriched in questionable/poor IQ series. While series with any type of artifact were initially accepted in the study, it was found that motion was the dominant cause of artifacts (~95%). Due to the lack of data, only motion-corrupted datasets were included in training/validation/testing. Anatomic images of all orientations, all contrast types, and all pathologies (strokes/mass occupying lesions/multiple sclerosis, etc) for cartesian *k*-space sampling schemes were included. Due to the lack of sufficient training sets, DWI datasets were excluded. A good algorithm to identify motion in DWI, based on the phase-stripping pattern of moving subjects, has already been published.⁵

Data were initially rated by a single radiologist (R0) with 20 years of experience and partitioned into clinically good (CG), clinically bad (CB), and questionable (Q). The questionable series were then passed to a second radiologist, D0, with 36 years of experience, who, by using the clinical indication of MS, classified them as CG and CB. This 2-tiered rating (exemplified in Fig 1) was undertaken to enable testing in predominantly questionable datasets. Making the right rescan decisions in such cases is truly relevant because very good/bad datasets can be easily classified. Figure 1 also summarizes the data partitioning into training/validation/testing sets; 30%/23%/24%/23% of the (original) datasets used for training belonged to the T1/T2/FLAIR/T2* categories, respectively. To better balance the number of

training images in the CB and CG classes, hence classification accuracy, zooms and translations of the initial 4692 images existent in the 266 CB training series were also performed, generating a total of 7783 CB training slices.

On-line Fig 1 presents image examples that were initially rated by R0 as CG/CB (upper/lower rows). The middle rows of this figure represent images that were initially rated as questionable by R0 and ultimately moved by D0 to CG (second row)/CB (third row), respectively.

Deep Learning–Based Classification

A 2D classification model, implemented in Chollet¹⁵ with a Tensorflow backend was trained to classify individual MR imaging slices into CG or CB. The architecture of the convolutional neural network (CNN), with 7 convolutional layers, 4 max pooling layers, and 3 batch normalization layers (Fig 2), was inspired by ResNet (<https://its.unc.edu/resource/resnet/>).¹⁶ The number of filters for convolution layers 1 through 7 are 32/64/32/64/32/128/256, while the filter sizes are (3 × 3)/(5 × 5)/(3 × 3)/(5 × 5)/(3 × 3)/(5 × 5)/(5 × 5), respectively. The activation function, a nonlinear exponential linear unit, helps learn complex patterns from data. To enhance dominant features, 2 merge layers were introduced using the multiplication operation. At the end of all the convolutional layers, a “flatten” layer was used, which converts the feature tensor from convolutional layers to a 1D tensor. A “tanh” activation was followed by a fully connected layer and “softmax” output.¹⁷ The fully connected layer further helps learn the nonlinear combinations of features provided by CNN layers. The softmax function provides probabilities for each class, with the sum of the probabilities equaling 1. Categorical cross-entropy was used as a loss function, and the optimizer was set to “RMSprop”.¹⁵ All images used for training and testing were converted to a 128 × 128 size. Pixel values were transformed into *z* score maps, defined as $(Pixel_{\text{value}} - Mean[Series])/Standard_Deviation(Series)$. Training and testing of the model were performed on a 7910 workstation (Dell, Austin, Texas; 48 CPU cores

with an NVIDIA P5000 GPU card). The size of the trained Keras model (h5 format) was ~8 MB.

The DL model outputs the probability for each slice belonging to the CG class. Because rescan decisions are made on a per-series, not per-slice, basis, individual slice ratings were pooled to compute a per-series score, expressed as the geometric mean of the per-slice probabilities ($P [Series] = \sqrt{P_1 \times P_2 \times \dots \times P_n}$, where P_1, P_2, \dots, P_n are predictions for slices 1, 2, . . . n). Finally, a series is rated as CG if $P (Series) \geq t$, and as CB if $P (Series) < t$, where t is a threshold that can vary as a function of scan indication and reading radiologist.

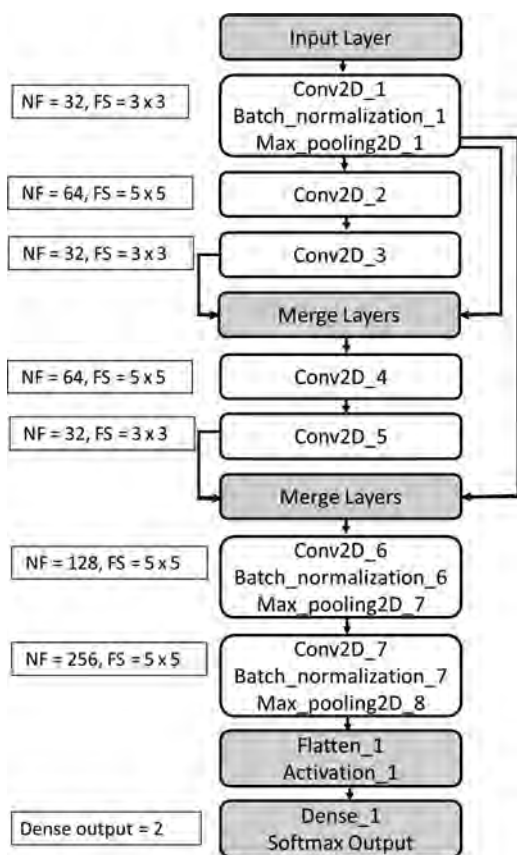


FIG 2. CNN architecture used in the experiment. Here NF represents number of filters and FS represents filter size.

Classification Algorithm Testing and Technologist and Radiologist Survey

Forty-nine series not included in training (grayed-out cells of Fig 1) were set aside for DL classification testing. This dataset (of all orientations, contrast types, and pathologies) consisted predominantly of images with low/moderate levels of artifacts. Of these 49 series, 5 were initially rated by R0 as CB, 6 as CG and 38 as questionable. The same test series were also evaluated by 5 radiologists (D1–D5), with 3–18 years of experience in reading MR images, and 4 MR imaging technologists (T1–T4), with 5–26 years of experience in performing MR imaging. All 9 survey participants were asked to rate series as CG or CB, assuming that patients were scanned to rule out stroke and MS. Lower/higher IQ is typically required for stroke and MS, respectively. When rating, radiologists were not considering sequence appropriateness for diagnosis.

Data Analysis

“Rescan” was defined as a series rated CG by the physician and CB by the technologist/DL. “Recall” was defined as a series rated CB by the physician and CG by technologist/DL. They represent false-positives and false-negatives, respectively. The true-positives and true-negatives (series called good/bad by both the radiologists and technologists) were not considered because they cause no additional burden to the health care system and require no corrective action. Differences between recall and rescan rates among different raters were analyzed using ANOVA in Minitab 12 (<http://www.minitab.com/en-us/>). Receiver operating characteristic (ROC) curves were computed in the Scikit-learn package (Python 2.7; <https://scikit-learn.org/stable/index.html>).

RESULTS

Rater Survey

Tables 1 and 2 summarize the number of series (of 49) rated as insufficient quality by each rater and the unneeded rescans and recalls of different raters. It was assumed that patients were scanned to rule out MS (Table 1) and stroke (Table 2). The data in these tables highlight the fact that physicians differ in their tolerance for artifacts. For example, D1 can render a diagnosis when presented with a lower IQ than D2, D4, and D5. Additionally, radiologists’ IQ ratings differed, depending on scan indication, in 36% of the cases surveyed, while technologists’ IQ ratings only changed in 11% of the cases. Depending on who scans the patient and who reads the scan, there can be a large number of unneeded

Table 1: Results of the survey—rule out MS clinical scan indication^a

Doctor ID	No. Series of Insufficient Quality	Technician ID							
		T1 (n = 26)		T2 (n = 31)		T3 (n = 12)		T4 (n = 13)	
		Unneeded Rescans	Unneeded Recalls						
D0	24	7	5	7	0	2	14	0	11
D1	13	14	1	19	1	4	5	2	2
D2	35	4	13	4	8	0	23	0	22
D3	24	11	8	13	5	2	13	0	10
D4	28	7	8	6	2	1	16	0	14
D5	30	4	8	4	3	1	19	0	17
Mean ± SD	25.7 ± 7.4	7.8 ± 4	7.2 ± 4	8.8 ± 6	3.2 ± 2.9	1.7 ± 1.4	15 ± 6.1	0.3 ± 0.8	12.7 ± 6.8

Note:—ID indicates identification. The numbers in parenthesis next to the technician identification numbers represent the total numbers of insufficient quality series identified by each rater.

^a All numbers reported are from the 49 series of the survey. Each series was evaluated twice, assuming that the scan indication was MS and stroke.

Table 2: Results of the survey—rule out stroke clinical scan indication^a

Doctor ID	No. Series of Insufficient Quality	Technician ID							
		T1 (n = 12)		T2 (n = 28)		T3 (n = 7)		T4 (n = 13)	
		Unneeded Rescans	Unneeded Recalls						
D1	2	10	0	26	0	5	0	11	0
D2	13	2	3	15	0	0	6	2	2
D3	8	6	1	22	1	3	3	7	1
D4	11	4	3	18	1	2	6	0	4
D5	7	5	0	21	0	3	3	6	0
Mean ± SD	8.2 ± 4.2	5.4 ± 3	1.4 ± 0.7	20.4 ± 4.2	0.4 ± 0.2	2.6 ± 0.8	3.6 ± 1.1	6 ± 3.4	1 ± 0.4

Note:—ID indicates identification. The numbers in parenthesis next to the technician identification numbers represent the total numbers of insufficient quality series identified by each rater.

^a All numbers reported are from the 49 series of the survey. Each series was evaluated twice, assuming that the scan indication was multiple sclerosis and stroke.

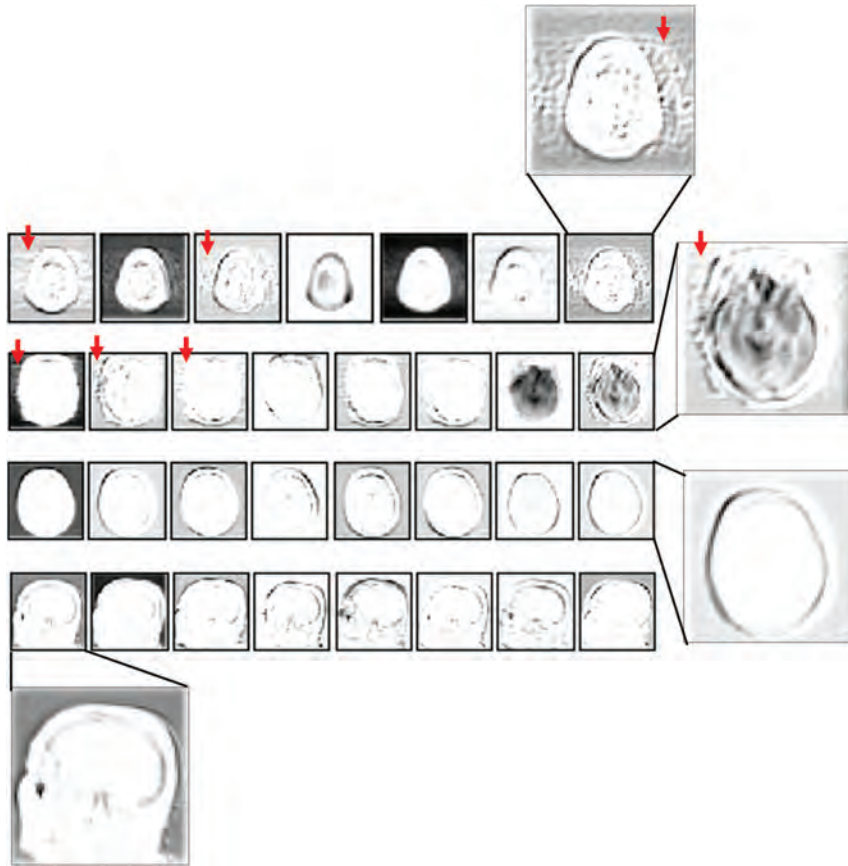


FIG 3. Representative filter responses from the fourth convolution layer of the CNN (Conv2D_4). Rows 1 and 2, Filter responses for motion-corrupted axial FLAIR/T2* input images, respectively. Rows 3 and 4, Filter responses from axial/sagittal T1 input images without motion, respectively. Filter responses are independent of image contrast and highlight the recognizable motion artifacts in the motion-corrupted images (arrows).

rescans or recalls. On average, technologists generated $(4.7 \pm 5.1)/(9.5 \pm 6.8)$ rescans/recalls for the MS scan indications and $(8.6 \pm 7.7)/(1.6 \pm 1.9)$ rescans/recalls for the stroke scan indication. Their IQ estimation for MS was generally underestimated (more recalls), and their IQ estimation for stroke was generally underestimated (more rescans).

DL Classification: General Results

Representative convolutional filter responses from one of the intermediate steps of the CNN (Conv2D_4 layer of Fig 2) for different imaging contrasts (T1, FLAIR, and T2*) and in cases with/without motion are presented in Fig 3. In cases with motion (rows 1 and 2 of

Fig 3), the filter responses show distinct patterns highlighting motion-related ghosting in the foreground and background of the response images (arrows). Filter responses are insensitive to image contrast, ensuring that a slightly different contrast, not seen during training, will likely not influence classification accuracy.

Three examples of DL classification results (using physician D0 as ground truth) are presented in Fig 4. While probabilities for individual slices can be variable, a few poor-quality slices do not necessarily imply that a rescans is needed. The rescans decision depends on the clinical scan indication and reading radiologist (Tables 1 and 2). Score prediction for a 25-slice volume took ~0.9 seconds. The ROC curve for the DL-based classification of the 49 test series (shown in On-line Fig 2) resulted in an area under the curve of 92%, comparable with the best classification results published elsewhere.⁴

DL Classification: MS

Given the rating variability of Tables 1 and 2, it became clear that physicians tolerate different artifact levels. Consequently, the per-series score was checked against 3 different thresholds ($P[\text{series}] = [0.1, 0.5, 0.8]$) to decide the IQ rating of a given series. Table 3 summarizes the number of rescans and recalls of the DL with different thresholds, assuming that patients were scanned to rule out MS. Varying DL classification thresholds effectively change the rescans/recall ratio; lowering the threshold increases recalls, while increasing the threshold increases rescans. A single common threshold of 0.5 for all physicians results in $(7 \pm 4.7)/(5.3 \pm 3.4)$ rescans/recalls, which represent a lower misclassification rate than that of the average technologist of $(4.7 \pm 5.1)/(9.5 \pm 6.8)$, but without reaching statistical significance. Because of reading radiologists' varying artifact tolerances, a single threshold for highlighting series that need rescans is inefficient. Selecting an average threshold (eg, 0.5) results in too many rescans if an

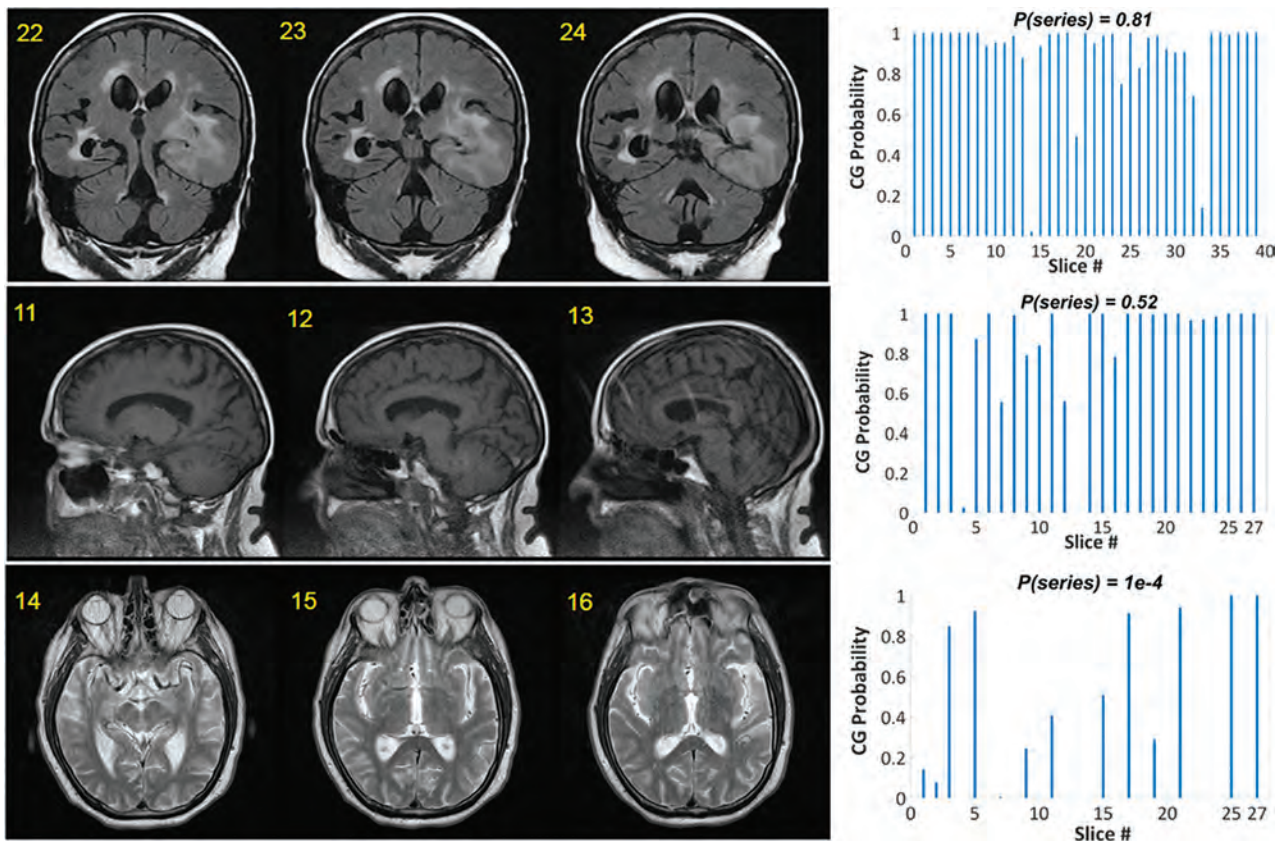


FIG 4. Examples of classification performance for 3 series. A few slices are displayed from each series (*left*), together with the slice ratings for the entire series (*right*). The numbers at the top left corner of each image represent the slice number.

Table 3: Matrix documenting the number of unneeded rescans and recalls created by the DL approach with different thresholds, assuming that series were scanned to rule out MS^a

	DL (T = 0.1)		DL (T = 0.5)		DL (T = 0.8)	
	Rescans	Recalls	Rescans	Recalls	Rescans	Recalls
D0	2	8	6	3	9	0
D1	8	3	15	1	21	1
D2	1	18	3	11	4	6
D3	5	10	10	6	14	4
D4	2	11	5	5	7	1
D5	1	13	3	6	6	3
Mean ± SD	3.2 ± 2.8	10.5 ± 2.1	7 ± 4.7	5.3 ± 1.4	10.2 ± 2.6	2.5 ± 0.9

^a All numbers are from the 49 test series. Here D0–D5 represent the same individuals as in Tables 1 and 2.

artifact-tolerant physician reads the scans (eg, D1), and in too many recalls, if an artifact-intolerant physician reads them (eg, D2).

Additionally, absolute minimization of the sum of rescans and recalls should not be the final goal of an automated rating approach. For example, a threshold of 0.1 for D3 results in the smallest sum of rescans and recalls. This, however, comes at the expense of generating 5/10 rescans/recalls, which may not be better than creating 10/6 rescans/recalls (which is what a threshold of 0.5 generates). One should aim for a constrained minimization of the sum of rescans and recalls, while maintaining an economically optimal rescan/recall ratio.

With automated rating tools, hospitals can enable per-radiologist thresholds resulting in optimal rescan/recall ratios. Such individualized thresholds could be easily implemented. For example, each radiologist can rate a single batch of datasets for a few

clinical scan indications. For each indication, the concordance between the DL algorithm and the individual physician can be ascertained for a range of thresholds. The threshold resulting in the best DL-radiologist concordance will then be preserved for that physician for all ensuing scans. Assuming that a hospital aims for a rescan/recall ratio of 1.5 (equivalent to weighting rescan/recall classification errors by 0.4/0.6, respectively), the optimal thresholds for our 6 reading radiologists become 0.8/0.1/0.8/0.5/0.8/0.8, respectively. This results in 7.3 ± 2.2 rescans (statistically equivalent to the 4.7 ± 5.1 rescans caused by the technologists, $P = .22$) and 3.2 ± 2.5 recalls, which are statistically lower than the 9.5 ± 6.8 recalls caused by the technologists ($P = .03$).

DL Classification: Stroke

The same DL network, without further training, was used to classify the same 49 series, assuming that patients were scanned to rule out stroke. While the probabilities output by the DL algorithm are independent of scan indication, it was hypothesized that adapting thresholds could compensate for the lower IQ needed from a scan obtained to rule out stroke. Lower thresholds of $P(\text{Series}) = (0.5, 0.1, 5e-4, 1e-6)$ were now explored. Table 4 summarizes the number of rescans and recalls of different raters, assuming that patients were scanned to rule out stroke. Significantly lower

Table 4: Matrix documenting the number of unneeded rescans and recalls created by the DL approach with different thresholds, assuming that the series were scanned to rule out stroke^a

	DL (T = 0.5)		DL (T = 0.1)		DL (T = 5e-4)		DL (T = 1e-6)	
	Rescans	Recalls	Rescans	Recalls	Rescans	Recalls	Rescans	Recalls
D1	25	0	16	0	11	0	4	0
D2	15	1	8	3	3	3	0	7
D3	20	0	13	2	8	2	3	4
D4	17	1	10	3	6	4	2	7
D5	20	1	12	1	7	1	2	3
Mean ± SD	19.4 ± 3.8	0.4 ± 0.2	11.8 ± 1.4	1.8 ± 1.3	7 ± 2.9	2 ± 1.6	2.2 ± 1.5	4.2 ± 3

^a All numbers are from the 49 test series. Here D1–D5 represent the same individuals as in Tables 1 and 2. Physician D0, whose ratings were used to train the DL algorithm, is now absent (as in Table 2) because no “stroke” ratings were available for this reader.

thresholds are now needed to separate CG from CB series in our DL-based approach. In fact, using the same average single classification threshold of 0.5, which was optimal for MS screening, would result in a generally higher misclassification rate than that of the average technologist ($P = .06$).

Assuming that the hospital aims for the same rescan-to-recall ratio of 1.5, the optimal thresholds for our 5 reading radiologists to rule out stroke become $1e-6/5e-4/1e-6/5e-4/1e-6$, respectively. These result in $(3.6 \pm 1.5)/(2.8 \pm 1.6)$ rescans/recalls, which are equivalent to the technologists’ $(8.6 \pm 7.7)/(1.6 \pm 1.9)$ rescans/recalls ($P > .05$).

DISCUSSION

In this work, a fast, automated methodology to determine the diagnostic utility of a MRI series was demonstrated. A ResNet-inspired CNN architecture outputs a probability for each slice as belonging to CG or CB. A per-series score, computed as the geometric mean of the individual slice probabilities, is then compared to a threshold based on scan indication, or scan indication and reading radiologist, to decide whether a rescan is needed.

This approach was trained and tested on anatomic brain images of all orientations, contrasts, and pathologies for Cartesian sampling schemes. It was found that testing the architecture for the clinical scan indication on which it was trained (ie, MS) while using a single, cross-radiologist threshold of 0.5, results in fewer rescans/recalls ($7 \pm 4.7)/(5.3 \pm 3.4)$ than the technologists’ rescans/recalls of $(4.7 \pm 5.1)/(9.5 \pm 6.8)$, without reaching statistical significance. With personalized thresholds, accounting for physicians’ different artifact tolerances, this improvement became statistically significant, maintaining rescans to an equivalent (7.3 ± 2.2), but reducing recalls to (3.2 ± 2.5) . The use of such an algorithm would closely match the radiologist assessing IQ in real-time.

When the same algorithm, without different training, was tested in rating the same image sets (now presumed to be acquired to rule out stroke), a significant lowering of the threshold was needed to render the algorithm’s prediction similar to the physicians’ rating. This finding is consistent with clinicians themselves requiring lower IQ images to diagnose stroke. Even with personalized thresholds, the rescans/recalls of $(3.6 \pm 1.5)/(2.8 \pm 1.6)$ of the DL remained statistically equivalent to technologists’ rescans/recalls of $(8.6 \pm 7.7)/(1.6 \pm 1.9)$. This result is largely caused by the variability in the technologists’ performances; a larger pooled technologist population may have altered the results.

This work is one of the first presenting evidence that MR imaging IQ is not an absolute measure, but a function of scan indication and reading radiologist. This information needs to be available for rating

purposes to reduce rescans; otherwise, a single DL network with a single threshold could, in fact, increase the number of rescans or recalls. To maximize classification accuracy, a hospital can implement indication- and reading radiologist-level thresholds. Alternatively, considering that second-opinion radiologists and referring physicians may also read images, an indication-dependent threshold may be implemented that would work for the average physician, at the expense of decreasing classification accuracy.

While MRI examination indications span a broad range, grouping scan indications into 3–4 categories requiring similar IQ would likely suffice. For example, if 3 categories are chosen, the lowest acceptable IQ category could encompass scan indications such as screening for stroke, hemorrhage, or large masses. The second, midlevel IQ category could encompass screening for multiple sclerosis or spread of known tumor, while the third, highest IQ category could cover scan indications such as screening for epilepsy foci or small brain metastases.

Caution is advised when comparing our rescan/recall numbers with those in other studies. To test the performance of our classification algorithm in situations in which nonprofessional readers could not easily decide the clinical utility of a given series, our test data were purposely enriched in difficult cases; 78% of our test datasets were initially rated as questionable, which is higher than the occurrence of such cases in daily scanning. Consequently, our classification accuracy may appear artificially low.

Our per-slice rating approach is somewhat similar to one recently documented, in which the IQ of individual image patches was assessed using a 3-layer DL-based architecture.¹³ Our full image classification, however, avoids false-positives in air-dominated patches. In addition to the architecture documented here containing residual in-network connections (Fig 2), a 5-convolutional-layer (no residual in-network connection) architecture was also tested. Our final implementation had a smaller size due to the reduced number of filters (8 versus 34 MB for the 5 convolutional layers) and a shorter prediction time (0.9 versus 1 second for the 5 convolutional layers in the same 25 slices). With identical, full training, the 2 implementations had comparable classification accuracy. While only using one-third of the data for training, our final implementation outperformed the 5-convolutional-layer architecture (area under the curve for D0 of 86% versus 92% in our 49 test datasets).

To understand the potential economic impact of automated IQ rating, we used the assumptions of Andre et al.¹ Without published recall rates or institutional costs, recall rates at 1 of the authors’ outpatient imaging facilities, Albany Medical College, were first surveyed. Among the recalled examinations (0.6%),

most were due to lack of contrast uptake, incorrect protocol, or scanner failure. Only 6 examinations in 1 calendar year (0.05%) were due to patient motion. At \$600/brain examination,¹ the 6 recalls caused \$3600 in revenue loss. Scaling this number up to the outpatient/inpatient proportion of Andre et al¹ and considering that inpatients/outpatients cause rates of 7.5%/29.4% of moderate and severe artifacts,¹ a recall-induced revenue loss of \$7700 results. Assuming that our test series are reflective of the examinations performed at a given site in 1 year, technologists generated 4.7/9.5 rescans/recalls (MS) and 8.6/1.6 rescans/recalls (stroke), for a total of 13.3 rescans, costing \$115,000,¹ and 11.1 recalls, costing \$7700 (as per the calculation above). Our test series enrichment in questionable datasets has no impact on this economic calculation because everything is scaled by the documented loss/site. By using individualized thresholds for clinical scan indications and reading radiologist, DL generated 7.3/3.2 rescans/recalls (MS), and 3.6/2.8 rescans/recalls for stroke, for a total of 10.9 rescans and 6 recalls. Scaling these numbers by the cost of rescans/recalls per site results in a revenue loss of \$98,400 with DL versus \$122,700 without DL. More than \$24,000 savings per site are obtained without negatively affecting patient care.

Interestingly, it was found that, although technologists generate comparable rates of rescans and recalls, the rate of motion-induced examination recalls was remarkably low (0.05%). Recalls are aggressively avoided because they are costly and are not covered by insurance. Patients who moved during MR imaging examinations are sometimes directed to follow-up contrast CT. Such examinations are shorter and hence have higher compliance rates. They are also generally reimbursed by insurance, hence not affecting the profits of the imaging center. Second, there is some redundancy in the prescribed series, and radiologists can often perform a diagnosis with only a few series of diagnostic quality. While this fact suggests that an examination-level (as opposed to a series-level) automated rating may be more appropriate, such examination-level ratings would not be actionable, as they would not be able to highlight the series that needs to be rescanned.

This study has a few limitations. Only single-site, 1.5T data were used for training and testing, while DWI was excluded. Further performance validation will need to include 3T data. In addition, only brain data were used for both training and testing; while no brain-specific features were extracted, it remains to be tested how well this automated method works with other anatomies and multiple *k*-space sampling schemes.

CONCLUSIONS

A fast, deep learning based approach similar to the one described here could soon aid technologists in deciding whether a MRI series needs to be rescanned, thereby reducing rescan and recall rates. For optimal performance, scan indication or scan indication and reading radiologist information will need to be provided to the algorithm.

Disclosures: Arathi Sreekumari—UNRELATED: Employment: GE Healthcare. Dattesh Shanbhag—UNRELATED: Employment: GE Healthcare. Desmond Yeo—UNRELATED: Employment: GE Healthcare; Grants/Grants Pending: National Institutes of Health, Comments: National Institutes of Health notice of award pending for an R01 for which I am a site Principal Investigator*; Stock/Stock Options: GE Healthcare; Other: University of Michigan, Comments: I am an external advisory board (EAB) member of the University of Michigan Biomedical Engineering Department. Aside from receiving lodging from the University of Michigan for annual EAB meetings, no financial remuneration is provided for this role.

Thomas Foo—UNRELATED: Employment: GE Global Research. Uday Patil—UNRELATED: Consultancy: GE India Industrial Private Limited (Division: John F Welch Technology Centre, formerly GE India Technology Centre Pvt Ltd). John Port—UNRELATED: Consultancy: Biomedical Systems, Neuro-netics Inc, Comments: I serve as an image-reading service for both of these companies. Money paid to Mayo Clinic*; Patents (Planned, Pending or Issued): Mayo Clinic, Comments: I have a provisional patent under consideration.* Ileana Hancu—UNRELATED: Employment: GE Healthcare. Julie Pilitsis—UNRELATED: Grant: GE Global Research.* *Money paid to the institution.

REFERENCES

- Andre JB, Bresnahan BW, Mossa-Basha M, et al. **Toward quantifying the prevalence, severity, and cost associated with patient motion during clinical MR examinations.** *J Am Coll Radiol* 2015;12:689–95 CrossRef Medline
- Pizarro RA, Cheng X, Barnett A, et al. **Automated quality assessment of structural magnetic resonance brain images based on a supervised machine learning 28066227 algorithm.** *Front Neuroinform* 2016;10:52 95 CrossRef Medline
- Hagens MH, Burggraaff J, Kilsdonk ID, et al. **Impact of 3 Tesla MRI on interobserver agreement in clinically isolated syndrome: a MAGNIMS multicentre study.** *Mult Scler* 2018 Jan 1. [Epub ahead of print] CrossRef Medline
- Gatidis S, Liebgott A, Schwartz M, et al. **Automated reference-free assessment of MR image quality using an active learning approach: comparison of support vector machine versus deep neural network classification.** In: *Proceedings of the Annual Meeting of the International Society for Magnetic Resonance in Medicine*, Honolulu, Hawaii. April 22–27, 2017; 3979
- Elsaid N, Roys S, Stone M, et al. **Phase-based motion detection for diffusion magnetic resonance imaging.** In: *Proceedings of the Annual Meeting of the International Society for Magnetic Resonance in Medicine*, Honolulu, Hawaii. April 22–27, 2017; 1288
- Kelly C, Pietsch M, Counsell S, et al. **Transfer learning and convolutional neural net fusion for motion artefact detection.** In: *Proceedings of the Annual Meeting of the International Society for Magnetic Resonance in Medicine*, Honolulu, Hawaii. April 22–27, 2017; 3523
- Hirsch J, Kohn A, Hoinkiss D, et al. **Quality assessment in the multicenter MR imaging study of the German national cohort.** In: *Proceedings of the Annual Meeting of the International Society for Magnetic Resonance in Medicine*, Honolulu, Hawaii. April 22–27, 2017; 4458
- Guehring J, Weale P, Zuehlsdorff S, inventors. System for dynamically improving medical image acquisition quality. US patent US 8,520,920 B2, 2010
- Blumenthal JD, Zijdenbos A, Molloy E, et al. **Motion artifact in magnetic resonance imaging: implications for automated analysis.** *Neuroimage* 2002;16:89–92 CrossRef Medline
- Kelly C. **Transfer learning and convolutional neural net fusion for motion artifact detection.** In: *Proceedings of the Annual Meeting of the International Society for Magnetic Resonance in Medicine*, Honolulu, Hawaii. April 22–27, 2017; 3523
- Lorch B, Vaillant G, Baumgartner C, et al. **Automated detection of motion artefacts in MR imaging using decision forests.** *J Med Eng* 2017;2017:4501647 CrossRef Medline
- Meding K, Lokyushin A, Hirsch M. **Automatic detection of motion artifacts in MR images using CNNs.** In: *Proceedings of the IEEE Conference on Acoustics, Speech and Signal Processing*, New Orleans, Louisiana. March 5–9, 2017
- Küstner T, Liebgott A, Mauch L, et al. **Automated reference-free detection of motion artifacts in magnetic resonance images.** *MAGMA* 2018;31:243–56 CrossRef Medline
- Esses S, Lu X, Zhao T, et al. **Automated image quality evaluation of T2-weighted liver MRI utilizing deep learning architecture.** *J Magn Reson Imaging* 2018;47:723–28 CrossRef Medline
- Chollet F. Keras Documentation. 2017 <https://keras.io/> Accessed December 5, 2018
- He K, Zhang X, Ren S, et al. **Deep residual learning for image recognition.** In: *Proceedings of the IEEE Conference on Computer Vision and Pattern Recognition*, Las Vegas, Nevada. June 26 to July 1, 2016
- Karpathy A. Convolutional Neural Networks for Visual Recognition. 2018 <http://cs231n.github.io/> Accessed December 9, 2018

Improving the Quality of Synthetic FLAIR Images with Deep Learning Using a Conditional Generative Adversarial Network for Pixel-by-Pixel Image Translation

A. Hagiwara, Y. Otsuka, M. Hori, Y. Tachibana, K. Yokoyama, S. Fujita, C. Andica, K. Kamagata, R. Irie, S. Koshino, T. Maekawa, L. Chougar, A. Wada, M.Y. Takemura, N. Hattori, and S. Aoki



ABSTRACT

BACKGROUND AND PURPOSE: Synthetic FLAIR images are of lower quality than conventional FLAIR images. Here, we aimed to improve the synthetic FLAIR image quality using deep learning with pixel-by-pixel translation through conditional generative adversarial network training.

MATERIALS AND METHODS: Forty patients with MS were prospectively included and scanned (3T) to acquire synthetic MR imaging and conventional FLAIR images. Synthetic FLAIR images were created with the SyMRI software. Acquired data were divided into 30 training and 10 test datasets. A conditional generative adversarial network was trained to generate improved FLAIR images from raw synthetic MR imaging data using conventional FLAIR images as targets. The peak signal-to-noise ratio, normalized root mean square error, and the Dice index of MS lesion maps were calculated for synthetic and deep learning FLAIR images against conventional FLAIR images, respectively. Lesion conspicuity and the existence of artifacts were visually assessed.

RESULTS: The peak signal-to-noise ratio and normalized root mean square error were significantly higher and lower, respectively, in generated-versus-synthetic FLAIR images in aggregate intracranial tissues and all tissue segments (all $P < .001$). The Dice index of lesion maps and visual lesion conspicuity were comparable between generated and synthetic FLAIR images ($P = 1$ and $.59$, respectively). Generated FLAIR images showed fewer granular artifacts ($P = .003$) and swelling artifacts (in all cases) than synthetic FLAIR images.

CONCLUSIONS: Using deep learning, we improved the synthetic FLAIR image quality by generating FLAIR images that have contrast closer to that of conventional FLAIR images and fewer granular and swelling artifacts, while preserving the lesion contrast.

ABBREVIATIONS: cGAN = conditional generative adversarial network; DL = deep learning; GAN = generative adversarial network; NRMSE = normalized root mean square error; PSNR = peak signal-to-noise ratio

The synthetic MR imaging technique can be used to create any contrast-weighted image, including T1-weighted, T2-weighted, and FLAIR images, based on the R1 and R2 relaxation rates (inverse of T1 and T2 relaxation times) and proton density.¹ Syn-

thetic MR imaging has become clinically feasible due to the development of rapid and simultaneous relaxometric methods,² which have high repeatability and reproducibility across different vendors.³ The synthetic MR imaging quality⁴⁻⁶ and its clinical utility for evaluating brain diseases⁷⁻¹⁰ have been widely investigated. Synthetic MR imaging has the potential to reduce scan times in clinical settings, where multiple contrast-weighted images are usually required. Although the synthetic T1-weighted and T2-weighted image quality is comparable with that of conventional images, the synthetic FLAIR image quality is generally inferior to that of conventional FLAIR images,^{4,6} thus hindering the introduction of synthetic MR imaging into routine clinical practice. Synthetic FLAIR images reportedly show more artifacts than other contrasts,⁶ including hyperintensity on the brain-CSF inter-

Received September 6, 2018; accepted after revision November 15.

From the Departments of Radiology (A.H., Y.O., M.H., Y.T., S.F., C.A., K.K., R.I., S.K., T.M., L.C., A.W., M.Y.T., S.A.) and Neurology (K.Y., N.H.), Juntendo University School of Medicine, Tokyo, Japan; Department of Radiology (A.H., R.I., S.K., T.M.), Graduate School of Medicine, University of Tokyo, Tokyo, Japan; Milliman Inc (Y.O.), Tokyo, Japan; Applied MRI Research (Y.T.), Department of Molecular Imaging and Theragnostics, National Institute of Radiological Sciences, Chiba, Japan; Department of Radiology (L.C.), Hopital Saint-Joseph, Paris, France; and Department of Radiological Sciences.

This work was supported by Japan Society for the Promotion of Science KAKENHI grant No. 16K19852; grant No. 16K10327; grant No. JP16H06280, Grant-in-Aid for Scientific Research on Innovative Areas, resource and technical support platforms for promoting research "Advanced Bioimaging Support"; the Japanese Society for Magnetic Resonance in Medicine; the Impulsing Paradigm Change through Disruptive Technologies (ImPACT) Program of the Council for Science, Technology and Innovation (cabinet office, Government of Japan); the program for Brain Mapping by Integrated Neurotechnologies for Disease Studies (Brain/MINDS) from the Japan Agency for Medical Research and Development (AMED); and AMED under grant number JP18lk1010025.

Please address correspondence to Akifumi Hagiwara, MD, Department of Radiology, Juntendo University School of Medicine, 1-2-1, Hongo, Bunkyo-ku, Tokyo, Japan, 113-8421; e-mail: a-hagiwara@juntendo.ac.jp

Indicates open access to non-subscribers at www.ajnr.org

<http://dx.doi.org/10.3174/ajnr.A5927>

face with apparently swollen brain parenchyma,^{7,11} and granular hyperintensities in the CSF, neither of which have been reported for conventional FLAIR.⁶ Hence, methods that can improve the synthetic FLAIR image quality are necessary.

One such method, deep learning (DL), has been applied to medical images for various purposes,^{12,13} particularly generative adversarial networks (GANs),¹⁴ which have been used for noise reduction¹⁵ and resolution improvement.¹⁶ The GAN technique uses an image generator, which generates a new image similar to the input target image, and a discriminator, which differentiates the target and generated images. The image generator and discriminator are simultaneously trained to transcend each other. A conditional GAN (cGAN) is a newly proposed technique that conditions the output on the input to render the same underlying information between the input and output, ultimately keeping the generated image realistic.¹⁷ However, a problem in applying DL to clinical image processing is its generative nature, which is driven by down/up sampling operations, including convolution and deconvolution. When DL is used to process nonmedical images, it often generates artificial objects in empty space or eliminates observed objects.¹⁷ While these are useful features when using DL to synthesize photos from label maps and colorize images,¹⁷ these features may be harmful when applied to clinical images.

To solve these issues, we propose using a pixel-by-pixel neural network function as a generator to improve the synthetic FLAIR image quality. This pixel-by-pixel neural network operation sets the kernel size and stride of all convolutional layers to 1, thus minimizing the possibility of generating artificial objects or erasing true information by ensuring that the 2 identical input pixel values become the same output pixel value. Because conventional FLAIR images, which were used as the target, were acquired separately from the input images, we trained the generator model with a cGAN-type learning system to avoid any adverse misregistration effects between the input and target images.

MATERIALS AND METHODS

Study Participants

This prospective study recruited 40 patients with MS between December and May 2017. Patients were diagnosed according to standard criteria.¹⁸ The MR imaging data were screened for severe motion artifacts. The first 30 consecutive subjects (11 men; mean age, 43.37 ± 9.36 years; median Expanded Disability Status Scale score, 1; range, 0–6; mean disease duration, 10.6 ± 6.94 years) were used as a training set, and the last 10 subjects (2 men; mean age, 44.7 ± 12.27 years; median Expanded Disability Status Scale score, 2.5; range, 0–4.5; mean disease duration, 10.56 ± 8.62 years) were used as a test set. The institutional review board of Juntendo University Hospital, Japan, approved this Health Insurance Portability and Accountability–compliant study, and all participants provided written informed consent.

Image Acquisition

All MR imaging was performed on a 3T system (Discovery MR750w; GE Healthcare, Milwaukee, Wisconsin) with a 19-channel head coil. All patients underwent synthetic MR imaging and conventional FLAIR imaging. We performed MR relaxometry with a 2D axial pulse sequence. This is a multisection, multi-

echo, multisaturation delay saturation-recovery turbo spin-echo acquisition method in which images are collected with different TE and saturation delay time combinations.² Typically, 2 TEs and 4 delay times are used to generate a matrix of 8 complex images, which are then used to quantify the longitudinal R1 relaxation and transverse R2 relaxation rates and proton density.¹⁹ The acquisition parameters for quantitative synthetic MR imaging were as follows: TE, 16.9 and 84.5 ms; delay times, 146, 546, 1879, and 3879 ms; TR, 4.0 seconds; FOV, 240 × 240 mm; matrix, 320 × 320; echo-train length, 10; bandwidth, 31.25 kHz; section thickness/gap, 4.0/1.0 mm; slices, 30; and acquisition time, 7 minutes 12 seconds. The SyMRI software (Version 8.0; SyntheticMR, Linköping, Sweden) was used to retrieve the R1, R2, and proton-density maps on the basis of the acquired data and to create synthetic FLAIR (with postprocessing TR, 15,000 ms; TE, 100 ms; TI, 3000 ms) and T1-weighted (with postprocessing TR, 500 ms; TE, 10 ms) images. Intracranial tissue masks were also created with the SyMRI software.²⁰ Postprocessing time on the SyMRI software was around 30 seconds in total using a workstation (HP Z230 Tower Workstation; Hewlett-Packard Japan, Tokyo, Japan) comprising Windows 7 (64-bit version; 16 GB memory) and a central processing unit (Xeon Processor E3–1281 v3; Intel, Santa Clara, California).

The acquisition parameters for conventional FLAIR imaging were as follows: TR, 9000 ms; TE, 124 ms; TI, 2472 ms; FOV, 240 × 240 mm; matrix, 320 × 224; echo-train length, 16; section thickness/gap, 4.0/1.0 mm; number of slices, 30; and acquisition time, 2 minutes 33 seconds.

DL Framework

We designed a pixel-wise translation network that receives raw synthetic MR imaging data and outputs FLAIR images by translating the input signal intensities into FLAIR images pixel by pixel using the same weight function across all pixels. Because some of the raw data information may have been lost when creating the synthetic FLAIR images using previous Bloch simulation-based algorithms,² we supposed that using the raw data as the DL input would improve the synthetic FLAIR image quality. Figure 1A shows the precise architecture of the generator model. The image generator used herein includes 2 parallel fully connected neural network streamlines that accept the same input from their common former layer. Each of the parallel networks outputs 1 value; then, these are multiplied by each other to rejoin the divided streamlines immediately before the final output. One of the 2 networks contains 1 hidden layer consisting of 128 nodes with logistic sigmoid activation and 1 output node with squaring activation to ensure that the output value is non-negative. Squaring activation was chosen here to simulate FLAIR contrast that usually takes the absolute signal values from the acquired data while keeping the differential coefficients continuous. However, this network generated T2-weighted-like images rather than FLAIR-like images. Hence, to suppress the signals of CSF, we applied 1 more network that contains 1 hidden layer consisting of 128 nodes with exponential linear unit activation and 1 output node with logistic sigmoid activation to ensure that the output value is between 0 and 1. We used the exponential linear unit here rather than the rectified linear unit because the exponential linear

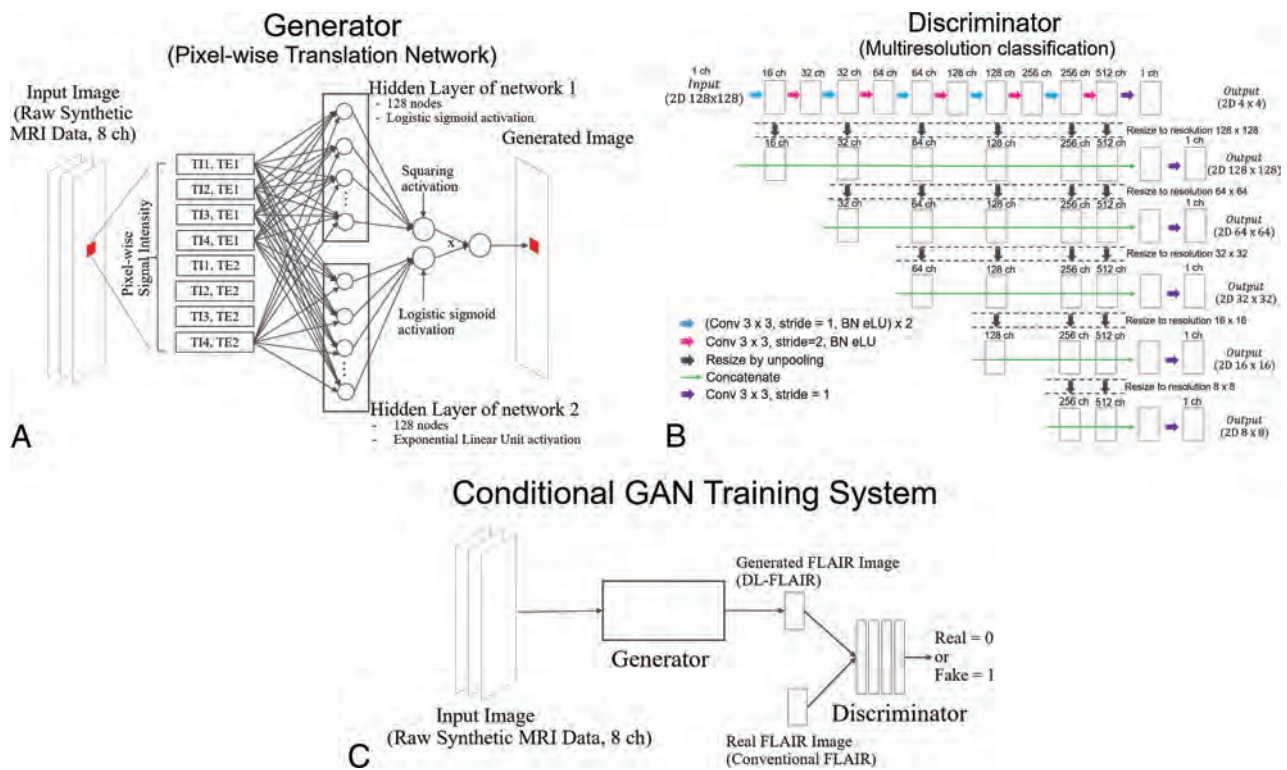


FIG 1. A, Illustration describing the generator. B, Illustration describing the discriminator. C, The framework describing the training phase of our proposed cGAN model for improving the synthetic FLAIR image quality. BN indicates batch normalization; Conv, convolution; eLU, exponential linear unit; ch, channel.

unit is less nonlinear and the learning process may become more stable.²¹

The training routine is divided into 2 steps: In the first step, the generator produces coarse FLAIR images, which allow the next GAN optimization to start with a condition that is relatively close to the convergent state. The training model is also constructed in this step to minimize the mean absolute error compared with the corresponding synthetic FLAIR images. These synthetic FLAIR images were preprocessed before this step with additional signal suppression of some specific areas, namely part of the CSF, to avoid misleading the generator to create hyperintense signals on the brain surface, a known major artifact in synthetic FLAIR images. Specifically, we roughly estimated the apparent inversion recovery time and T2 signal intensity of each voxel and then manually modified the original synthetic FLAIR pixel value to zero where the inversion recovery time was >0.3 and the T2 signal intensity was >0.7 . We estimated the apparent inversion recovery time by subtracting the signal intensity ratio of the fifth-to-seventh raw data images from 1. Similarly, the apparent T2 signal intensity was estimated by subtracting the signal intensity ratio of the eighth-to-seventh raw data images from 1. Although this estimation process was rough, it was sufficient to achieve the first step because miscalibration and suppression of signals in other areas similar to those of CSF, if any, are supposed to be corrected in the GAN training step 2. During the training step 1, fifteen patches (128×128 pixels) were randomly selected from the synthetic MR imaging raw data (512×512 pixels) as a batch, and the model was trained batch-wise for 100,000 iterations with updating of the generator by the Adam²² rule with $\alpha = 0.0005$, $\beta_1 = 0.9$,

and $\beta_2 = 0.999$. Simultaneously, for efficiency, the discriminator used in step 2 was pretrained by receiving generated and target images of the same size and updated by the Adam rule with $\alpha = 0.000001$, $\beta_1 = 0.9$, and $\beta_2 = 0.999$. Figure 1B shows the precise architecture of the discriminator.

In the second phase of the 3 training steps, we set up a cGAN training strategy with patches. Figure 1C shows a conceptual description of the cGAN training system. We set the pretrained discriminator as the initial state and continued the training to allow it to discriminate generated images and conventional true FLAIR images while also updating the generator. From the synthetic MR imaging raw data, 15 patches were randomly selected as a batch and fed into generator to yield FLAIR images. The generated images were again fed into the discriminator, which received target images (conventional FLAIR patches) and minimized the classification loss. Classification loss was determined as the average of $C(D) - C(1 - D)$, where C is the cross-entropy item and D is the logistic sigmoid output of the discriminator. This averaging operation was performed along both batches and pixels to normalize the loss. From the discriminator, the generator received the negative of the classification loss for its generated images. To stabilize the training, the discriminator was designed to return the classification results pixel by pixel in different resolutions. We used multiresolution classification that is similar to the structure of U-Net (<https://lmb.informatik.uni-freiburg.de/people/ronneber/u-net/>), which has been mainly used for semantic segmentation.²³ With this segmentation task-like architecture of the discriminator, the mode collapse phenomenon that frequently occurs in GAN training²⁴ was not observed in this study.

Although several techniques for stabilizing GAN training have been discussed in the field of machine learning,²⁵⁻²⁷ the discriminator architecture devised herein for stabilizing GAN training has not been reported previously. In this study, we used the same weight across different pixels and resolutions. For training, 15 patches (128 × 128 pixels) were randomly selected from the synthetic MR imaging raw data (512 × 512 pixels) as a batch and 100,000 iterations were performed with updating of the generator by the Adam rule in which $\alpha = 0.00001$, $\beta_1 = 0.5$, and $\beta_2 = 0.999$ and updating of the discriminator by the Adam rule where $\alpha = 0.000001$, $\beta_1 = 0.9$, and $\beta_2 = 0.999$. All model training was performed on a computer with 64 GB of CPU memory, Xeon E5-2670 v3 CPU (Intel), and a TITAN Xp graphics processing unit (NVIDIA, Santa Clara, California). The computer program was coded with Python 3.6 (<https://www.python.org/downloads/release/python-360/>) and the DL framework of Chainer 3.2.0 (<http://chainer.org/>). The FLAIR images generated by the proposed DL scheme are hereafter denoted as DL-FLAIR images.

Evaluation of the Model

Quantitative Evaluation. To quantitatively compare the synthetic and DL-FLAIR image quality, we used the peak signal-to-noise ratio (PSNR), normalized root mean square error (NRMSE), and lesion maps derived from these images. Conventional FLAIR images were registered to synthetic FLAIR images using the FMRIB Software Library (FSL; <http://www.fmrib.ox.ac.uk/fsl>).²⁸ First, mean square error maps were calculated for synthetic and DL-FLAIR images against registered conventional FLAIR images, and the PSNR was defined as:

$$PSNR = 20 \log_{10} \frac{25,500}{\sqrt{MSE}},$$

where 25,500 is the maximum range of the FLAIR signal intensity. Next the squared root of the mean square errors was calculated and scaled by dividing by the mean signal intensity of synthetic and DL-FLAIR images, respectively, after applying the intracranial masks, to produce NRMSE maps. Notably, images with a higher PSNR and lower NRMSE theoretically exhibit higher image quality.²⁹ Synthetic T1-weighted images, which were inherently aligned to synthetic FLAIR images, were skull-stripped by the intracranial masks and segmented into GM, WM, and CSF using the FMRIB Automated Segmentation Tool (FAST; <http://fsl.fmrib.ox.ac.uk/fsl/fslwiki/fast>). No gross error was visually observed in this segmentation step. Each tissue map and intracranial mask were used to extract the PSNR and NRMSE metrics in the GM, WM, CSF, and aggregate intracranial tissues.

Conventional FLAIR images were linearly coregistered to synthetic FLAIR images using SPM 12 software (<http://www.fil.ion.ucl.ac.uk/spm>). The WM lesions on these images were automatically segmented using a lesion-prediction algorithm³⁰ in the Lesion Segmentation Toolbox, Version 2.0.15 (<http://www.applied-statistics.de/lst.html>),³¹ running under SPM 12. Lesion maps were manually corrected by an experienced neuroradiologist (A.H.) with 7 years of experience. The Dice index, which represents the percentage of overlap between 2 image sets, of lesion maps was calculated between synthetic or DL-FLAIR images and conventional FLAIR images.

Qualitative Evaluation. We screened the training and test DL-FLAIR image sets for artificial object creation or large signal drop-outs and confirmed that no DL-FLAIR image had these artifacts. Image quality was visually assessed by an experienced neuroradiologist (C.A.) with 8 years of experience. Synthetic and DL-FLAIR images were assessed in random order. Lesion conspicuity in each patient was rated on a 5-point scale (1, very bad; 2, bad; 3, acceptable; 4, good; and 5, excellent). The existence of artifacts (surface hyperintensity, granular artifacts, and other artifacts that substantially degrade image quality) was also rated as follows: 1, none; 2, minimal; 3, moderate; 4, remarkable; and 5, highly remarkable. Because parenchymal swelling artifacts were difficult to evaluate on separate images, synthetic and DL-FLAIR images for each patient were simultaneously shown to the neuroradiologist (C.A.) for further evaluation using the overlay function of the FSLeyes viewer (<https://fsl.fmrib.ox.ac.uk/fsl/fslwiki/FSLeyes>).

Statistical Analysis

Statistics were computed using R (version 3.2.1; <http://www.r-project.org/>). Because not all the datasets were normally distributed when analyzed by the Shapiro-Wilk test, we used the non-parametric Wilcoxon signed rank test to compare the quantitative and qualitative scores between synthetic and DL-FLAIR images. The PSNR and NRMSE values were also compared among the GM, WM, and CSF on synthetic or DL-FLAIR images. Significance was set at $P < .05$ (2-sided). Multiple comparison correction was not performed.

RESULTS

Figure 2 shows images from a representative patient. The Table shows the PSNR and NRMSE of synthetic and DL-FLAIR images calculated against conventional FLAIR images. The PSNR was significantly higher for DL-FLAIR than synthetic FLAIR images in GM, WM, CSF, and aggregate intracranial tissues (all $P < .001$). The PSNR of synthetic and DL-FLAIR images was the lowest in GM, with WM showing lower values than CSF (all $P < .001$). The NRMSE was significantly lower for DL-FLAIR than synthetic FLAIR images in GM, WM, CSF, and aggregate intracranial tissues (all $P < .001$). The NRMSE of synthetic and DL-FLAIR images was the highest in GM, with WM showing higher values than CSF (all $P < .001$). The mean Dice index of lesion maps against conventional FLAIR images was comparable between DL-FLAIR (0.57 ± 0.17) and synthetic FLAIR images (0.55 ± 0.14) ($P = 1$).

No significant differences in lesion conspicuity, existence of surface hyperintensity artifacts, or the presence of other artifacts were identified between synthetic FLAIR and DL-FLAIR images (3.8 ± 0.40 versus 3.7 ± 0.46 , $P = .59$; 3 ± 0.77 versus 3.1 ± 1.04 , $P = .78$; and 1 ± 0 versus 1 ± 0 ; $P = 1$, respectively). However, fewer granular artifacts were present in the CSF of DL-FLAIR (2.3 ± 0.90) than synthetic FLAIR (4 ± 1.1) images ($P = .003$; Fig 3). During the simultaneous evaluation of synthetic and DL-FLAIR images, the neuroradiologist agreed that though hyperintensity artifacts were still visible in some parts of the brain surface on DL-FLAIR images, the brain parenchyma looked grossly swollen on all synthetic FLAIR images compared with the DL-FLAIR images (Fig 4).

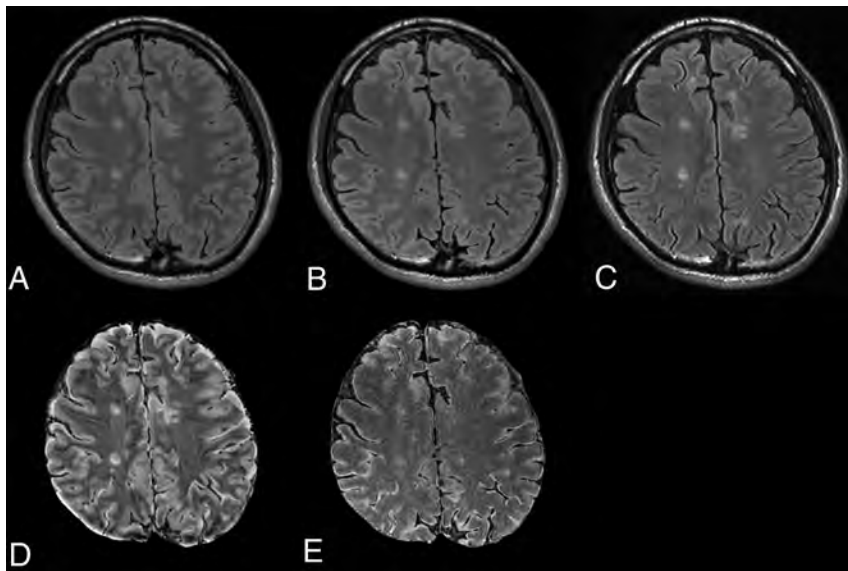


FIG 2. Synthetic FLAIR (A), DL-FLAIR (B), and conventional FLAIR (C) images of a representative patient. The overall image contrast of the DL-FLAIR image is more similar to that of the conventional FLAIR image than the contrast of the synthetic FLAIR image, while preserving the lesion contrast. The NRMSE maps of synthetic FLAIR (D) and DL-FLAIR (E) images against conventional FLAIR images are also shown. The NRMSE in the intracranial tissues is much larger in the synthetic FLAIR image than in the DL-FLAIR image. Note that the parenchymal surface shows patchy high NRMSE values on the synthetic FLAIR image, which are reduced but still visible in the DL-FLAIR image.

The PSNR and NRMSE of synthetic FLAIR and DL-FLAIR images against conventional FLAIR images in various regions^a

	Synthetic FLAIR Images	DL-FLAIR Images
GM		
PSNR	27.16 ± 0.54 ^{b,c}	34.03 ± 1.33 ^{b,c} (+25.31%)
NRMSE	0.47 ± 0.039 ^{b,c}	0.33 ± 0.028 ^{b,c} (-30.44%)
WM		
PSNR	29.51 ± 0.44 ^{b,c}	35.45 ± 1.48 ^{b,c} (+20.14%)
NRMSE	0.37 ± 0.025 ^{b,c}	0.27 ± 0.024 ^{b,c} (-27.32%)
CSF		
PSNR	34.83 ± 1.37 ^{b,c}	40.47 ± 1.37 ^{b,c} (+16.21%)
NRMSE	0.29 ± 0.027 ^{b,c}	0.21 ± 0.017 ^{b,c} (-27.36%)
Aggregate intracranial tissues		
PSNR	29.79 ± 0.71 ^b	35.90 ± 1.21 ^b (+20.54%)
NRMSE	0.38 ± 0.024 ^b	0.27 ± 0.016 ^b (-28.66%)

^a Values are means ± SD. Percentage changes in the PSNR and NRMSE for DL-FLAIR vs synthetic FLAIR images are in parentheses.

^b P < .001 for synthetic FLAIR vs DL-FLAIR images.

^c P < .001 for GM vs WM, GM vs CSF, and WM vs CSF.

DISCUSSION

To our knowledge, our study is the first to use a DL algorithm to improve the synthetic FLAIR image quality. Here, the PSNR and NRMSE were higher and lower, respectively, in all tissue segments in DL-FLAIR than in synthetic FLAIR images, meaning that DL-FLAIR images more accurately replicated conventional true FLAIR images. Although synthetic FLAIR images rely on the well-established Bloch equation,^{2,32} this approach may not be the best for replicating true FLAIR images.

In our study, lesion delineation was comparable between synthetic and DL-FLAIR images in patients with MS. Hence, the proposed DL scheme might enable reliable delineation of parenchymal lesions. However, this should be confirmed by a future study with a

systematic reading session for various diseases including brain tumors or encephalitis.

Herein, while some perceived surface hyperintensity remained, brain parenchymal swelling artifacts were improved in all patients. Hagiwara et al⁷ reported that 3 false-positives and 157 true MS plaques were detected by an experienced neuroradiologist on synthetic MR images. Because these false-positives were located in the sulci, our proposed model may decrease the number of false-positives in clinical practice. Although it has not been previously discussed, these artifacts may derive from the unavoidable partial volume effects at tissue boundaries, considering that the NRMSE on synthetic FLAIR images in our study was the highest in the GM compared with the WM and CSF. However, the current synthetic MR imaging technique adopted a monoexponential decay model assuming a homogeneous voxel² and may not appropriately produce the

FLAIR signal in a voxel with >1 tissue compartment. While our proposed DL model may have succeeded in partially solving the multiexponential signal decay at tissue boundaries, applying the single function to all voxels may not be ideal, especially for voxels with different tissue mixtures. Future studies should focus on using different weight functions for different tissue mixtures in a voxel using DL.

In the current study, granular artifacts in the CSF were minimized by the DL model. Although the exact origin of such artifacts remains unknown, Tanenbaum et al⁶ reported that they were observed in up to 59.2% of synthetic FLAIR images and typically disappeared on rescanning. The DL model proposed herein can reduce the number of rescans to avoid these artifacts. However, when the possibility of CSF pathology is minimal on the basis of clinical history, one may just ignore these granular artifacts. While prior studies confirmed the high repeatability of quantitative values derived from quantitative synthetic MR imaging,^{3,33} the evaluated value ranges mainly focused on brain tissues; hence, quantitative values in the CSF range may not be precisely measured by quantitative synthetic MR imaging, resulting in granular artifacts in the CSF on synthetic FLAIR images.

Our GAN training approach using a pixel-wise simple neural network as a generator was successful in this study. Our model did not generate obvious artificial objects because its architecture ensured that the 2 identical pixel values in the input became the same output pixel values. This property is essential for medical imaging because it will not mislead clinicians. An important contribution of our study is the implementation of such a structurally restricted generator trained by a GAN. Recently, a pixel-wise neural network translation model was used to approximate the dictionary in MR fingerprinting,³⁴ and the training method used the same acquired data for the input and target, allowing it to learn the time-

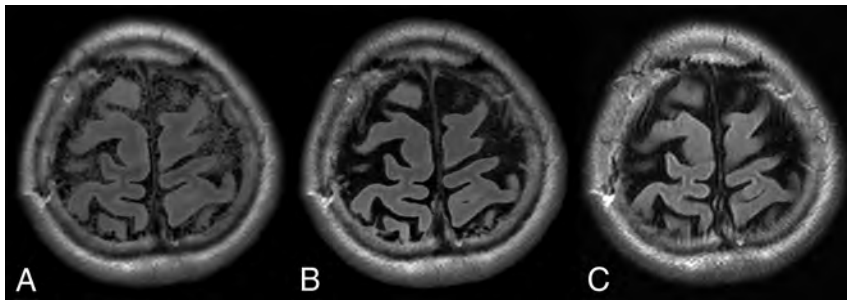


FIG 3. A, Granular artifacts in the CSF on a synthetic FLAIR image. B, The artifact is almost invisible (successfully deleted) on the DL-FLAIR image. C, Conventional FLAIR image is shown for comparison.

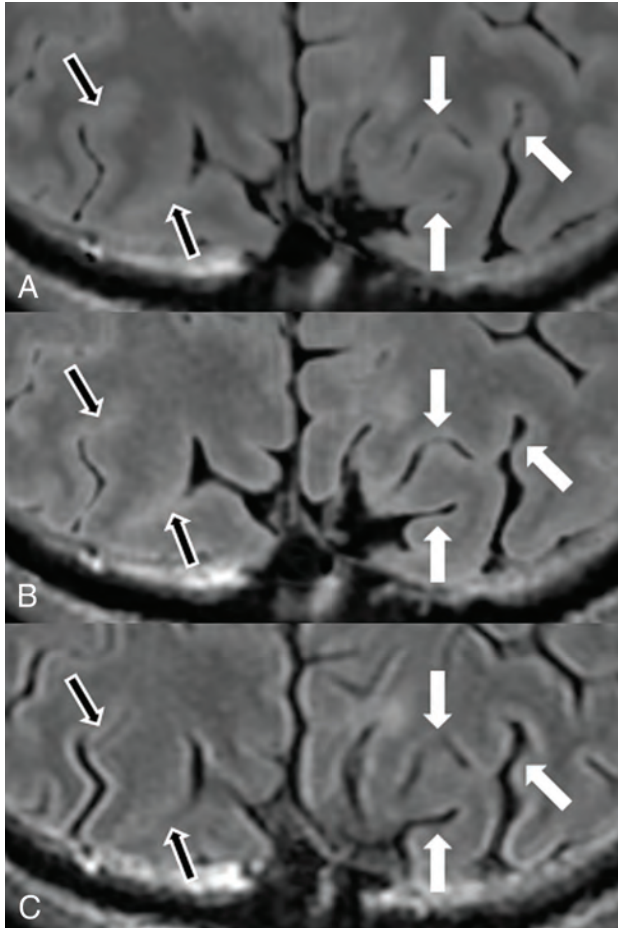


FIG 4. Magnified images from Fig 2. Synthetic FLAIR (A), DL-FLAIR (B), and conventional FLAIR (C) images are shown. Sulci are wider in B and C in some areas than they are in A (white arrows). However, for areas with tight sulci on the conventional FLAIR image (C), the sulci are tighter and more hyperintense on both synthetic FLAIR (A) and DL-FLAIR (B) images than they are on the conventional FLAIR image (black arrows).

consuming conventional reconstruction method of MR fingerprinting by DL. Because we aimed to train the generator to create FLAIR images resembling conventional FLAIR images from raw synthetic MR imaging data, positional differences between the input and target data were unavoidable. The 2 approaches for overcoming positional difference were to use a GAN based on patches and to calibrate the positional deviation and take the absolute error as a loss.

In the first approach based on patches, adversarial loss represents the complex reality expressions of generated patches by comparing them with patches of target images (conventional true FLAIR images herein) rather than pixel-wise similarity between generated images and target images. Thus, the GAN trains a generator to create visually realistic images while ignoring the effects of positional differences between input and target images. Conversely, the latter method to take error as a loss reportedly leads a generator to create unrealistic blurry images.³⁵

Therefore, we adopted a GAN approach based on patches. Because there was an imbalance of power in the competing generator and discriminator owing to fewer parameters in the generator without a convolutional architecture, the training required various stabilization measures, including learning-rate adjustments, guidance to the initial state by a mean absolute error loss function with synthetic FLAIR images, and segmentation-like discriminator architecture. To our knowledge, this study is the first to train a generator using a GAN without down/up sampling operations.

The present study has some limitations. First, we did not explicitly compare the qualities of DL-FLAIR and conventional FLAIR images. Additional studies are required to investigate whether DL-FLAIR images with further image-quality improvement can serve as substitutes for conventional FLAIR images in clinical settings. Second, data from only 1 scanner were used in this study. Hence, future studies should assess the generalizability of our results using more patients and several scanners. Third, we did not perform a reading study to count the number of MS plaques. This was due to broad diffusely abnormal white matter and/or fused plaques in some of our patient data. Fourth, only 30 cases were used for training the DL algorithm used in this study. Considering the large number of pixels per case, we thought that 30 scans could substantially cover the possible signal distributions of the synthetic MR imaging raw data. However, this assumption should be confirmed by checking the signal distributions of large datasets. In the future, the products of the DL algorithm in our study should also be applied to and validated with disease processes spanning various appearances and tissue compartments.

CONCLUSIONS

We successfully improved the synthetic FLAIR image quality using DL, thus creating FLAIR images that have contrast similar to that of conventional FLAIR images, with fewer swelling artifacts and minimal granular artifacts in the CSF, while preserving lesion contrast. The proposed DL algorithm may facilitate the introduction of synthetic MR imaging into clinical practice.

Disclosures: Akifumi Hagiwara—RELATED: Grant: Japan Society for the Promotion of Science KAKENHI, ABiS, Japanese Society for Magnetic Resonance in Medicine, Impulsing Paradigm Change through Disruptive Technologies, Agency for Medical Research and Development, UNRELATED: Payment for Lectures Including Service on Speakers Bureaus: GE Healthcare, Comments: luncheon seminar. Yujiro Otsuka—UNRELATED: Employment: Milliman Inc, Comments: I am receiving a salary as an employee. Yasuhiko Tachibana—UNRELATED: Employment: National Institute of Radiological Sciences, QST; Grants/Grants Pending: Grant-in-Aid for Scientific Re-

search, from the Japan Society for the Promotion of Science, *Comments*: KAKENHI No. 17K10385. This grant is for a research in the same field as this article but is unrelated to the current study. Koji Kamagata—UNRELATED: *Grants/Grants Pending*: Japan Society for the Promotion of Science KAKENHI (JP16K19854). Shigeki Aoki—RELATED: *Grant*: Japan Society for the Promotion of Science KAKENHI, ABIS, Japanese Society for Magnetic Resonance in Medicine, Impulsing Paradigm Change through Disruptive Technologies, Agency for Medical Research and Development, UNRELATED: *Grants/Grants Pending*: Nihon Medi-Physics, Toshiba, Bayer Yakuhin, Daiichi Sankyo, Eisai, Fujiyakuin, FUJIFILM RI Pharma, Toshiba, Canon, Japan Society for the Promotion of Science KAKENHI, ABIS, Japanese Society for Magnetic Resonance in Medicine, Impulsing Paradigm Change through Disruptive Technologies, Agency for Medical Research and Development, *Payment for Lectures Including Service on Speakers Bureaus*: honorarium for lectures/chair from GE Healthcare, Toshiba, Hitachi, Siemens, Bayer Yakuhin, Daiichi Sankyo, Eisai, Fujiyakuin, FUJIFILM RI Pharma, Nihon Medi-Physics, Meiji Seika Pharma, Canon, Guerbet. Mariko Takemura—RELATED: *Grant*: Japan Society for the Promotion of Science KAKENHI, *Comments*: grant No. 16K10327.

REFERENCES

- Bobman SA, Riederer SJ, Lee JN, et al. **Cerebral magnetic resonance image synthesis.** *AJNR Am J Neuroradiol* 1985;6:265–69 Medline
- Warntjes JB, Leinhard OD, West J, et al. **Rapid magnetic resonance quantification on the brain: optimization for clinical usage.** *Magn Reson Med* 2008;60:320–29 CrossRef Medline
- Hagiwara A, Hori M, Cohen-Adad J, et al. **Linearity, bias, intrascanner repeatability, and interscanner reproducibility of quantitative multidynamic multiecho sequence for rapid simultaneous relaxometry at 3 T: a validation study with a standardized phantom and healthy controls.** *Invest Radiol* 2019;54:39–47 CrossRef Medline
- Blystad I, Warntjes JB, Smedby O, et al. **Synthetic MRI of the brain in a clinical setting.** *Acta Radiol* 2012;53:1158–63 CrossRef Medline
- Granberg T, Uppman M, Hashim F, et al. **Clinical feasibility of synthetic MRI in multiple sclerosis: a diagnostic and volumetric validation study.** *AJNR Am J Neuroradiol* 2016;37:1023–29 CrossRef Medline
- Tanenbaum LN, Tsiouris AJ, Johnson AN, et al. **Synthetic MRI for clinical neuroimaging: results of the Magnetic Resonance Image Compilation (MAGiC) prospective, multicenter, multireader trial.** *AJNR Am J Neuroradiol* 2017;38:1103–10 CrossRef Medline
- Hagiwara A, Hori M, Yokoyama K, et al. **Synthetic MRI in the detection of multiple sclerosis plaques.** *AJNR Am J Neuroradiol* 2017;38:257–63 CrossRef Medline
- Hagiwara A, Hori M, Yokoyama K, et al. **Analysis of white matter damage in patients with multiple sclerosis via a novel in vivo magnetic resonance method for measuring myelin, axons, and g-ratio.** *AJNR Am J Neuroradiol* 2017;38:1934–40 CrossRef Medline
- Andica C, Hagiwara A, Nakazawa M, et al. **Synthetic MR imaging in the diagnosis of bacterial meningitis.** *Magn Reson Med Sci* 2017;16:91–92 CrossRef Medline
- Wallaert L, Hagiwara A, Andica C, et al. **The advantage of synthetic MRI for the visualization of anterior temporal pole lesions on double inversion recovery (DIR), phase-sensitive inversion recovery (PSIR), and myelin images in a patient with CADASIL.** *Magn Reson Med Sci* 2018;17:275–76 CrossRef Medline
- Helmersson T. *Evaluation of Synthetic MRI for Clinical Use* [master's thesis]. Department of Medical and Health Sciences. Linköping: Linköping University; 2010. <http://liu.diva-portal.org/smash/record.jsf?pid=diva2%3A389732&id=9594>. Accessed August 30, 2018:71
- Yasaka K, Akai H, Kunimatsu A, et al. **Deep learning with convolutional neural network in radiology.** *Jpn J Radiol* 2018;36:257–72 CrossRef Medline
- Nakao T, Hanaoka S, Nomura Y, et al. **Deep neural network-based computer-assisted detection of cerebral aneurysms in MR angiography.** *J Magn Reson Imaging* 2018;47:948–53 CrossRef Medline
- Goodfellow I, Pouget-Abadie J, Mirza M, et al. **Generative adversarial nets.** In: *Proceedings of Advances in Neural Information Processing Systems*; 2014:2672–80
- Wolterink JM, Leiner T, Viergever MA, et al. **Generative adversarial networks for noise reduction in low-dose CT.** *IEEE Trans Med Imaging* 2017;36:2536–45 CrossRef Medline
- Kim KH, Do WJ, Park SH. **Improving resolution of MR images with an adversarial network incorporating images with different contrast.** *Med Phys* 2018;45:3120–31 CrossRef Medline
- Isola P, Zhu J, Zhou T, et al. **Image-to-image translation with conditional adversarial networks.** arXiv:161107004 2017. <http://adsabs.harvard.edu/abs/2016arXiv161107004I>. Accessed August 13, 2018
- Polman CH, Reingold SC, Banwell B, et al. **Diagnostic criteria for multiple sclerosis: 2010 revisions to the McDonald criteria.** *Ann Neurol* 2011;69:292–302 CrossRef Medline
- Hagiwara A, Warntjes M, Hori M, et al. **SyMRI of the brain: rapid quantification of relaxation rates and proton density, with synthetic MRI, automatic brain segmentation, and myelin measurement.** *Invest Radiol* 2017;52:647–57 CrossRef Medline
- Ambarki K, Lindqvist T, Wählin A, et al. **Evaluation of automatic measurement of the intracranial volume based on quantitative MR imaging.** *AJNR Am J Neuroradiol* 2012;33:1951–56 CrossRef Medline
- Clevert D, Unterthiner T, Hochreiter S. **Fast and accurate deep network learning by exponential linear units (ELUs).** arXiv:151107289 2015. <http://adsabs.harvard.edu/abs/2015arXiv151107289C>. Accessed October 5, 2018
- Kingma D, Ba J. **Adam: a method for stochastic optimization.** arXiv:1412.6980 2014. <https://arxiv.org/abs/1412.6980>. Accessed August 22, 2018
- Ronneberger O, Fischer P, Brox T. **U-Net: convolutional networks for biomedical image segmentation.** arXiv:150504597 2015. <http://adsabs.harvard.edu/abs/2015arXiv150504597R>. Accessed October 6, 2018
- Lin G, Khetan G, Fanti G, et al. **PacGAN: the power of two samples in generative adversarial networks.** arXiv:171204086 2017. <https://arxiv.org/abs/1712.04086>. Accessed August 23, 2018
- Salimans T, Goodfellow I, Zaremba W, et al. **Improved techniques for training GANs.** arXiv:160603498 2016. <http://adsabs.harvard.edu/abs/2016arXiv160603498S>. Accessed August 28, 2018
- Huszár F. **How (not) to train your generative model: scheduled sampling, likelihood, adversary?** arXiv:151105101 2015. <http://adsabs.harvard.edu/abs/2015arXiv151105101H>. Accessed August 28, 2018
- Arjovsky M, Bottou L. **Towards principled methods for training generative adversarial networks.** arXiv:170104862 2017. <http://adsabs.harvard.edu/abs/2017arXiv170104862A>. Accessed August 28, 2018
- Jenkinson M, Beckmann CF, Behrens TE, et al. **FSL.** *Neuroimage* 2012;62:782–90 CrossRef Medline
- Wang Y, Yu B, Wang L, et al. **3D conditional generative adversarial networks for high-quality PET image estimation at low dose.** *Neuroimage* 2018;174:550–62 CrossRef Medline
- Egger C, Opfer R, Wang C, et al. **MRI FLAIR lesion segmentation in multiple sclerosis: does automated segmentation hold up with manual annotation?** *Neuroimage Clin* 2017;13:264–70 CrossRef Medline
- Schmidt P, Gaser C, Arsic M, et al. **An automated tool for detection of FLAIR-hyperintense white-matter lesions in multiple sclerosis.** *Neuroimage* 2012;59:3774–83 CrossRef Medline
- Maitra R, Riddles JJ. **Synthetic magnetic resonance imaging revisited.** *IEEE Trans Med Imaging* 2010;29:895–902 CrossRef Medline
- Krauss W, Gunnarsson M, Andersson T, et al. **Accuracy and reproducibility of a quantitative magnetic resonance imaging method for concurrent measurements of tissue relaxation times and proton density.** *Magn Reson Imaging* 2015;33:584–91 CrossRef Medline
- Cohen O, Zhu B, Rosen MS. **MR fingerprinting Deep Reconstruction Network (DRONE).** *Magn Reson Med* 2018;80:885–94 CrossRef Medline
- Welander P, Karlsson S, Eklund A. **Generative adversarial networks for image-to-image translation on multi-contrast MR images: a comparison of CycleGAN and UNIT.** arXiv:180607777 2018. <https://arxiv.org/abs/1806.07777>. Accessed August 28, 2018

Effect of Gadolinium on the Estimation of Myelin and Brain Tissue Volumes Based on Quantitative Synthetic MRI

T. Maekawa, A. Hagiwara, M. Hori, C. Andica, T. Haruyama, M. Kuramochi, M. Nakazawa, S. Koshino, R. Irie, K. Kamagata, A. Wada, O. Abe, and S. Aoki



ABSTRACT

BACKGROUND AND PURPOSE: The effect of gadolinium on the estimation of myelin has not been reported. The aim of the current study was to investigate the effects of gadolinium on automatic myelin and brain tissue volumetry via quantitative synthetic MR imaging.

MATERIALS AND METHODS: The study included 36 patients who were referred for brain metastases screening, and quantitative synthetic MR imaging data before and after gadolinium-based contrast agent administration were analyzed retrospectively. Brain metastases were detected in 17 patients. WM volume, GM volume, CSF volume, non-WM/GM/CSF volume, myelin volume, brain parenchymal volume, myelin fraction (myelin volume/brain parenchymal volume), and intracranial volume were estimated. T1 and T2 relaxation times, proton density, and myelin partial volume per voxel averaged across the brain parenchyma were also analyzed.

RESULTS: In patients with and without metastases after gadolinium-based contrast agent administration, measurements of WM and myelin volumes, and myelin fraction were significantly increased (+26.65 and +29.42 mL, +10.14 and +12.46 mL, +0.88% and +1.09%, respectively), whereas measurements of GM, CSF, brain parenchymal, and intracranial volumes were significantly decreased (−36.23 and −34.49 mL, −20.77 and −18.94 mL, −6.76 and −2.84 mL, −27.41 and −21.84 mL, respectively). Non-WM/GM/CSF volume did not show a significant change. T1, T2, and proton density were significantly decreased (−51.34 and −46.84 ms, −2.67 and −4.70 ms, −1.05% and −1.28%, respectively) after gadolinium-based contrast agent administration, whereas measurements of myelin partial volume were significantly increased (+0.78% and +0.75%, respectively).

CONCLUSIONS: Gadolinium had a significant effect on the automatic calculation of myelin and brain tissue volumes using quantitative synthetic MR imaging, which can be explained by decreases in T1, T2, and proton density.

ABBREVIATIONS: GBCA = gadolinium-based contrast agent; ICV = intracranial volume; PD = proton density; T1 = longitudinal relaxation time; T2 = transverse relaxation time; V_{MY} = myelin partial volume

Synthetic MR imaging has recently been introduced into clinical practice.^{1–4} It generates adjustable T1-weighted, T2-weighted, and FLAIR images on the basis of simultaneous

quantification of longitudinal relaxation time (T1), transverse relaxation time (T2), and proton density (PD) in a scan time of approximately 6 minutes for full head coverage with good accuracy and reproducibility.^{5,6} In contrast, only 1 predetermined contrast-weighted image per acquisition is generated by conventional MR imaging. Furthermore, quantitative measurement potentially removes imperfections and dependencies of MR imaging on scanner settings that are difficult to eliminate from conventional MR imaging.³ Moreover, automatic segmentation of brain tissue via the synthetic tissue-mapping method based on synthetic MR imaging–derived quantitative values has been reported to be

Received July 4, 2018; accepted after revision November 12.

From the Department of Radiology (T.M., A.H., M.H., C.A., T.H., M.K., M.N., S.K., R.I., K.K., A.W., S.A.), Juntendo University School of Medicine, Tokyo, Japan; Department of Radiology (T.M., A.H., S.K., R.I., O.A.), Graduate School of Medicine and Faculty of Medicine, University of Tokyo, Tokyo, Japan; and Department of Radiological Sciences (T.H., M.K.), Graduate School of Human Health Sciences, Tokyo Metropolitan University, Tokyo, Japan.

Tomoko Maekawa and Akifumi Hagiwara contributed equally to this work.

This work was supported by the Japan Society for Promotion of Science, KAKENHI grant No. 16K19852; and grant No. JP16H06280, Grant-in-Aid for Scientific Research on Innovative Areas, resource and technical support platforms for promoting research, “Advanced Bioimaging Support.” This work was funded by the Impulsing Paradigm Change through Disruptive Technologies (ImPACT) program of the Council for Science, Technology and Innovation (Cabinet Office, Government of Japan). This work was also supported by the program for Brain Mapping by Integrated Neurotechnologies for Disease Studies (Brain/MINDS) from the Japan Agency for Medical Research and Development.

Please address correspondence to Akifumi Hagiwara, MD, Department of Radiology, Juntendo University School of Medicine, 2-1-1 Hongo, Bunkyo-ku, Tokyo, 113-8421, Japan; e-mail: a-hagiwara@juntendo.ac.jp

Indicates open access to non-subscribers at www.ajnr.org

Indicates article with supplemental on-line table.

<http://dx.doi.org/10.3174/ajnr.A5921>

precise and robust^{7,8} with a postprocessing time of <1 minute, which is much shorter than that of the widely used volumetric methods associated with conventional T1-weighted images.⁹

Recently, brain myelin and edema estimation models have been developed using T1, T2, and PD values obtained via quantitative synthetic MR imaging.¹⁰ The myelin estimation model is based on predetermined parameters derived from healthy subjects for T1, T2, and PD in 4 partial volume compartments in the brain, the myelin partial volume (V_{MY}), the cellular partial volume, the free water partial volume, and the excess parenchymal water partial volume. The model postulates that each compartment has its own quantitative values and contributes to the effective quantitative values of each specific acquisition voxel, while exchanging magnetization with other partial volume compartments. In diseased brain, decreased V_{MY} indicating decreased myelin or increased excess parenchymal water partial volume indicating edema occurs in this model.¹¹ Correlations between V_{MY} and histologic myelin¹² and other myelin measurement methods¹³ were recently confirmed.

The effect of gadolinium-based contrast agent (GBCA) administration on the measurement of quantitative synthetic MR imaging tissue mapping was investigated by Warntjes et al.¹⁴ However, the effect of GBCA on the estimation of myelin has not been reported. In routine clinical practice using synthetic MR imaging, we noticed that measurement of V_{MY} increased after the administration of GBCA. Furthermore, the subjects included in their study did not have any enhancing lesions in the brain. The aim of the current study was to investigate the effect of GBCA on automatic myelin and brain tissue volumetry determined via quantitative synthetic MR imaging in patients with or without enhancing cerebral lesions.

MATERIALS AND METHODS

Subjects

MR imaging data from 36 patients (21 men, 15 women; mean age, 63 ± 11 years) who were referred for brain metastases screening between April 2015 and November 2015 were retrospectively analyzed. The patients had undergone quantitative MR imaging and conventional T1-weighted inversion recovery fast spin-echo MR imaging before and after the administration of GBCA. The study was approved by the institutional review board of Juntendo University Hospital, Japan, and the requirement for written informed consent was waived due to its retrospective nature. The patient cohort in the present study partially overlapped that in a previous publication.¹⁵

Scanning Protocol

In all patients, quantitative synthetic MR imaging was performed via a procedure described in Warntjes et al¹ involving quantification of relaxation times and PD by multiecho acquisition of saturation recovery using a turbo spin-echo readout, on a 3T MR imaging scanner (Discovery MR750w; GE Healthcare, Milwaukee, Wisconsin) with a 19-channel head coil. T1 and T2 relaxation and PD were retrieved simultaneously. The procedure involves collection with different combinations of 2 TEs and 4 delay times. The TEs used were 16.9 and 84.5 ms, and the delay times were 146, 546, 1879, and 3879 ms. The other parameters used for

quantitative MR imaging were the following: TR = 4000 ms, FOV = 240×240 mm, matrix = 320×320 , section thickness/gap = 4.0/1.0 mm, number of sections = 30, and acquisition time = approximately 6 minutes. The parameters used to obtain conventional T1-weighted inversion recovery fast spin-echo images were the following: TR = 3294 ms, TE = 18 ms, TI = 908 ms, FOV = 240×216 mm, matrix = 352×256 , echo-train length = 8, slice thickness/gap = 4/1 mm, number of slices = 30, and acquisition time = 1 minute 50 seconds. The dose of contrast medium was 0.1 mmol/kg (0.2 mL/kg), and the GBCAs administered were ProHance (gadoteridol; Bracco Diagnostics, Princeton, New Jersey; 26 patients), Omniscan (gadodiamide; Daiichi-Sankyo, Tokyo, Japan; 6 patients), and Magnevist (gadopentetate dimeglumine; Bayer HealthCare Pharmaceuticals, Wayne, New Jersey; 4 patients). The patients received a single dose of GBCA after the first acquisition, 7 minutes before the second acquisition.

Image Postprocessing

Synthetic MR imaging data were postprocessed with SyMRI software, Version 8.0 (SyntheticMR, Linköping, Sweden). T1, T2, and PD maps were acquired and then used for automatic brain tissue segmentation of WM volume, GM volume, CSF volume, the remaining unclassified non-WM/GM/CSF tissue volume within the intracranial volume (ICV), brain parenchymal volume, and ICV.⁷ Synthetic T1-weighted images were also created with TR = 500 ms and TE = 10 ms. An experienced neuroradiologist (A.H.) determined the presence or absence of brain metastases in each patient on the basis of pre-contrast-enhanced and post-contrast-enhanced conventional and synthetic T1-weighted images. The region-growing algorithm includes volume that does not match the defined WM, GM, or CSF characteristics. This remaining tissue was defined as the unclassified non-WM/GM/CSF tissue volume within the ICV, comprising unspecified tissue such as blood vessels, other pathologic tissue, or motion artifacts. The threshold for the ICV was set at PD = 50%, using the definition of the tissue interface between CSF (PD = 100%) and bone (PD = 0%). The ICV comprised all recognized WM volume, GM volume, CSF volume, and unclassified non-WM/GM/CSF tissue volume within the ICV. The brain parenchymal volume was defined as the ICV minus the CSF volume. An example of automatic tissue segmentation is shown in Fig 1.

With the assumption that all the T1, T2, and PD values of V_{MY} , cellular partial volume, free water partial volume, and excess parenchymal water partial volume contribute to the effective T1, T2, and PD in each acquisition voxel, we estimated partial volumes of these 4 compartments.¹⁰ This process was performed by running Bloch equations and optimizing model parameters in a spatially normalized and averaged brain from healthy controls. V_{MY} maps, myelin volume in the whole brain, and myelin fraction defined as myelin volume divided by brain parenchymal volume were obtained from T1, T2, and PD maps.

We also investigated changes in T1, T2, PD, and V_{MY} before and after GBCA administration, averaged across voxels in the brain parenchyma. GM and WM segmented by the FMRIB Automated Segmentation Tool (FAST; <http://fsl.fmrib.ox.ac.uk/fsl/fslwiki/fast>)¹⁶ using synthetic T1-weighted images were aggre-

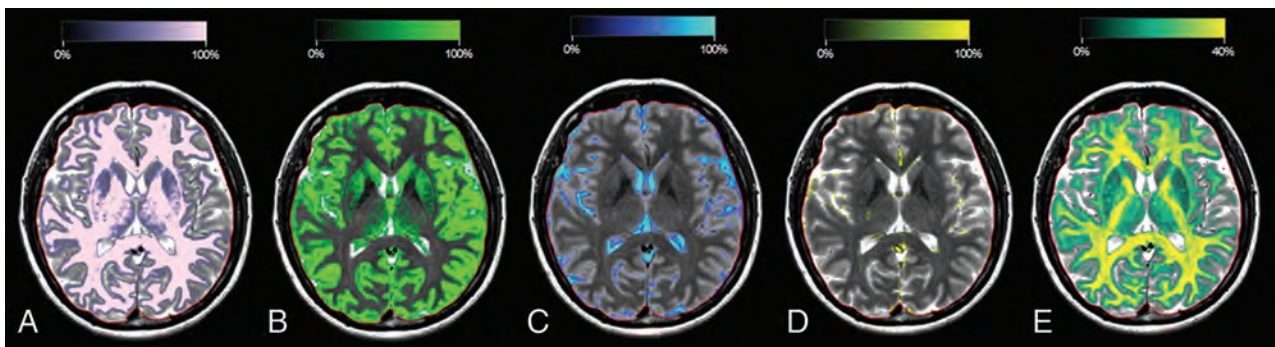


FIG 1. Typical images of a patient without brain metastases derived via automatic segmentation software. A, WM segmentation overlaid on a T2-weighted image, in which the intensity of the light-pink color overlay corresponds to the calculated WM partial volume per voxel. The red line indicates the intracranial volume. Similar images are shown for GM in green (B), CSF in blue (C), non-WM/GM/CSF in yellow (D), and myelin partial volume in yellow and green (E).

gated to be used as the whole-brain ROI, and mean values were recorded in each subject.

To investigate the effect of enhancing lesions on the measurement of myelin volume in the brain, an investigator (T.H.) manually segmented the brain metastases on post-contrast-enhanced synthetic T1-weighted images using the MRIcron software (<http://people.cas.sc.edu/rorden/mricron/index.html>). The total volume of brain metastases in each patient was recorded.

Statistical Analysis

The Shapiro-Wilk test was used to assess normality. Because not all data were normally distributed, we used the Wilcoxon signed rank test to compare tissue volumes and mean quantitative values in the brain before and after GBCA administration. These comparisons were performed separately in patients with or without metastasis. For patients with brain metastases, we used the Spearman rank order correlation coefficient to investigate the correlation between change in measured myelin volume and total volume of brain metastases. A 2-sided $P < .05$ was considered significant. All statistical analyses were performed using SPSS, Version .25 (IBM, Armonk, New York).

RESULTS

Brain metastases were detected in 17 patients (11 men, 6 women; mean age, 61 ± 10 years), and no brain metastases were detected in 19 patients (10 men, 9 women; mean age, 66 ± 10 years). Among patients with brain metastases, the total volume of metastases was 4.84 ± 6.61 mL. Results of the automatic tissue-volume measurements are shown in the On-line Table, part of which is summarized in Fig 2. After GBCA administration, measurements of WM volume, myelin volume, and myelin fraction in patients with and without metastases were significantly increased ($+26.65$ and $+29.42$ mL, $+10.14$ and $+12.46$ mL, $+0.88\%$ and $+1.09\%$, respectively); and GM volume, CSF volume, brain parenchymal volume, and ICV were significantly decreased (-36.23 and -34.49 mL, -20.77 and -18.94 mL, -6.76 and -2.84 mL, -27.41 and -21.84 mL, respectively), regardless of the presence of metastases. Measurement of unclassified non-WM/GM/CSF tissue volume within the ICV was increased, but the increase was not statistically significant.

The effects of GBCA administration on T1, T2, and PD values are shown in the Table. In patients with and without metastasis,

measurement of V_{MY} was significantly increased ($+0.78\%$ and $+0.75\%$, respectively), and measurements of T1, T2, and PD were significantly decreased after GBCA administration (-51.34 and -46.84 ms, -2.67 and -4.70 ms, and -1.05% and -1.28% , respectively). Visually obvious increases in V_{MY} were observed in some patients (Fig 3). However, the correlation between change in measured myelin volume and total volume of brain metastases was not significant (Spearman $\rho = -0.12$, $P = .64$).

DISCUSSION

In this study, we investigated the effects of GBCA on automatic brain tissue and myelin volumetry using quantitative synthetic MR imaging. The administration of GBCA had significant effects on both automatic brain tissue and myelin volumetry determined via quantitative synthetic MR imaging, with the exception of unclassified non-WM/GM/CSF tissue volume within the ICV. GBCA administration was followed by decreased T1, T2, and PD in the whole brain in ROI analysis.

GBCA administration decreased T1 and T2 in the whole brain in our study; this decrease can be explained by the shortening effect of GBCA on relaxation times. This effect was observed regardless of the presence of metastases, even in the absence of enhancing lesions. A previous study reported enhancement of perivascular spaces at 4 hours after intravenous administration of GBCA even in subjects without renal insufficiency.¹⁷ This suggests that the GBCA in blood vessels may have permeated the perivascular space and glymphatic system in the brain, thus resulting in decreases in T1, T2, and PD in the current study, even though post-GBCA MR imaging was performed only 7 minutes after GBCA administration. The exact cause of decreased PD after GBCA administration is unknown, but it has been suggested that the slight reduction in T1 relaxation of brain tissue due to the presence of GBCA in the capillary network may result in a slight decrease in the PD calculated, though PD should not be theoretically affected by T1.¹⁴ Furthermore, decreased PD in the CSF may have led to decreased measurement of ICV, which was determined at $PD = 50\%$,¹⁸ also resulting in a decrease in apparent CSF volume.

To our knowledge, this is the first study that has evaluated the effects of GBCA on myelin measurement via MR imaging. Our study showed significantly increased myelin volume, myelin fraction, and V_{MY} after GBCA administration. On synthetic MR im-

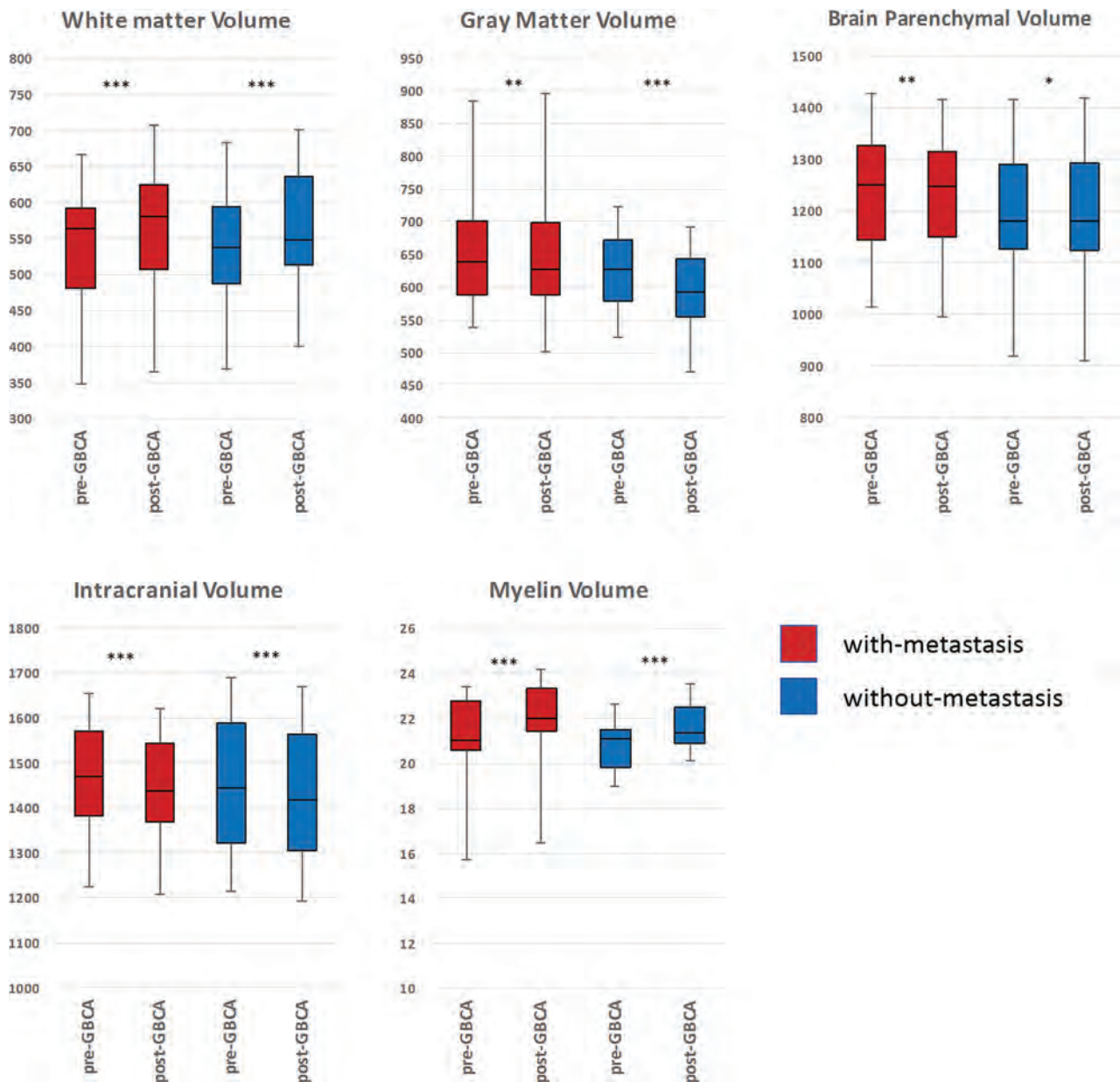


FIG 2. Comparison of volumetric and myelin measurements derived via quantitative synthetic MR imaging pre- and postadministration of a gadolinium-based contrast agent. Based on the Wilcoxon signed rank test, *asterisk* = $P < .05$; *double asterisks* = $P < .01$; and *triple asterisks* = $P < .001$.

T1, T2, PD values, and V_{MY} determined via quantitative synthetic MRI pre- and postadministration of gadolinium-based contrast agent^a

	V_{MY} (%)	T1 (ms)	T2 (ms)	PD (%)
With metastases pre-GBCA	21.14 ± 1.83	1061.68 ± 59.80	99.26 ± 12.37	75.90 ± 1.99
With metastases post-GBCA	21.92 ± 1.67	1010.35 ± 54.57	95.59 ± 13.75	74.85 ± 2.02
Difference	0.78 ± 0.85 ^b	-51.34 ± 43.44 ^b	-2.67 ± 9.35 ^c	-1.05 ± 1.26 ^b
Without metastases pre-GBCA	20.84 ± 1.08	1076.41 ± 75.40	98.43 ± 13.42	75.87 ± 1.79
Without metastases post-GBCA	21.59 ± 1.01	1029.58 ± 70.97	93.73 ± 15.39	74.59 ± 2.03
Difference	0.75 ± 0.53 ^d	-46.84 ± 31.23 ^d	-4.70 ± 12.21 ^b	-1.28 ± 1.35 ^b

^a Data are mean ± SD.

^b Wilcoxon signed rank test $P < .01$.

^c Wilcoxon signed rank test $P < .05$.

^d Wilcoxon signed rank test $P < .001$.

aging, myelin estimation is performed using predetermined parameters adjusted to healthy subjects for T1, T2, and PD in 4 partial volume compartments; V_{MY} , cellular partial volume, free water partial volume, and excess parenchymal water partial vol-

ume, with V_{MY} showing lower T1, T2, and PD values than the other compartments.¹⁰ Thus, decreases in T1, T2, and PD in the brain parenchyma should have contributed to increases in apparent myelin volume in the brain. Investigators and clinicians

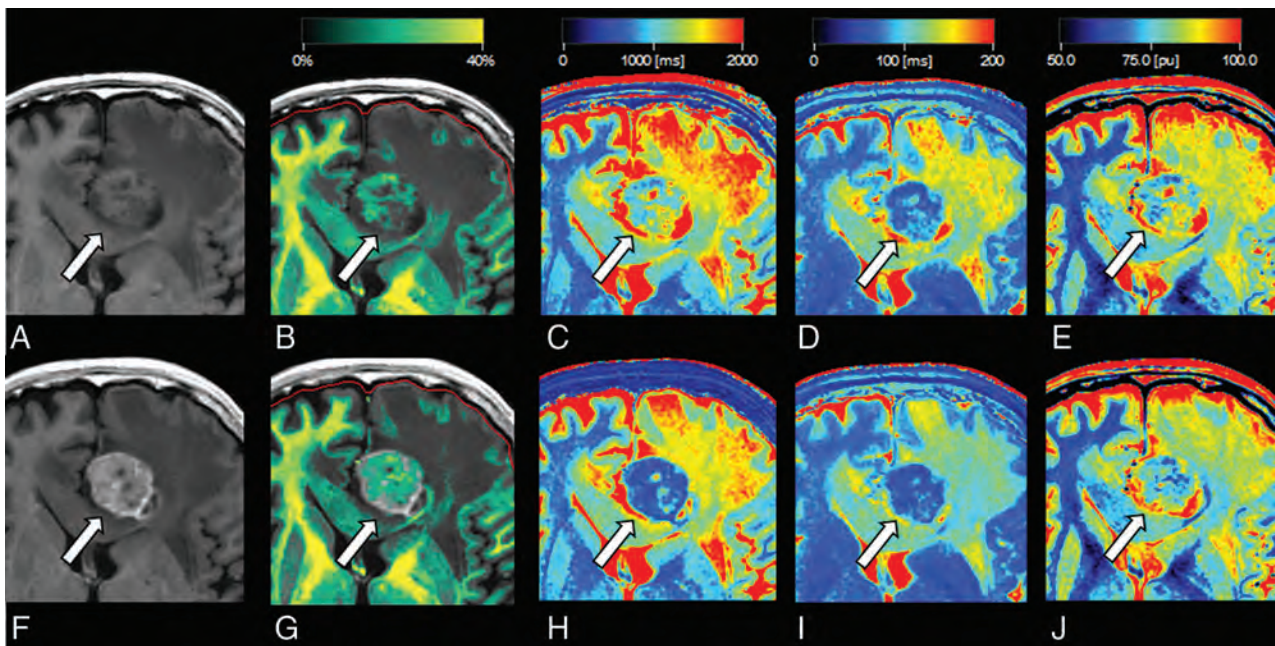


FIG 3. Representative quantitative maps of a patient with brain metastasis. T1-weighted image before (A) and after (F) administration of gadolinium-based contrast agent and quantitative maps overlaid on the T1-weighted image before (B–E) and after (G–J) administration of gadolinium-based contrast agents are shown. The brain metastasis shows contrast enhancement (arrows in A and F). The increase in myelin partial volume is clear in the brain metastasis on the myelin partial volume maps (arrows in B and G). The decreases in T1, T2, and proton density are clear in the brain metastasis on the T1 (arrows in C and H), T2 (arrows in D and I), and proton-density (arrows in E and J) maps.

should be cautious when assessing V_{MY} measured via quantitative synthetic MR imaging in patients in whom GBCA was administered. In particular, estimated myelin of some brain metastases was apparently increased in quantitative synthetic MR imaging after GBCA administration in the current study; thus, it is necessary to be cautious when measuring V_{MY} in enhanced lesions. However, in the current study, the total volume of brain metastases did not significantly correlate with the measured total myelin volume in the brain.

Several other methods have been proposed for myelin imaging,^{19,20} and GBCA may have different effects on other methods than it had on the methods used in the current study. The effects of GBCA on other myelin measurement methods remain to be determined, but methods based on relaxometry (eg, macromolecular tissue volume,²¹ myelin water imaging,²⁰ and the ratio of T1-weighted and T2-weighted images²²) are expected to be affected by GBCA, as implied by the results of ROI analysis in the present study. Notably, the absolute myelin content value in a voxel is especially important when calculating the g-ratio, which is the inner-to-outer diameter of a myelinated nerve fiber, in combination with diffusion MR imaging.²³

Apparently increased WM volume and decreased GM volume, CSF volume, brain parenchymal volume, and ICV after GBCA administration in the current study are partially concordant with a report by Warntjes et al.¹⁴ In that study, there were no statistically significant differences in WM volume, GM volume, or brain parenchymal volume after GBCA administration, even though they used a sample size of 20, which is similar to the number of subjects included in our study. This result could be partly due to the differences in imaging time delay after GBCA administration and acquisition time, which were 3 minutes and 1 min-

ute longer than those in the present study, respectively. It has been reported that imaging time delays of 1 minute and 5 minutes after GBCA administration lead to higher contrast of brain metastases than a 10-minute delay.²⁴ Furthermore, differences in the age of the patients and selected patient groups and use of a greater variety of contrast agents in our study may have also contributed to the differences in the size of effects caused by GBCA in our study and theirs. Tissue clusters in synthetic tissue mapping are derived using predetermined T1, T2, and PD values in the T1-T2-PD space, with T1, T2, and PD higher for GM than for WM.⁷ Thus, the decreases in T1, T2, and PD values revealed by ROI analysis in the present study should all have contributed to increased measurements of WM volume and decreased GM volume.

Even though differences in the measured WM volume, CSF volume, non-WM/GM/CSF, and brain parenchymal volume between pre- and postadministration of GBCA in our study were much smaller than the differences in patients with MS and matched healthy controls as reported by Warntjes et al,¹⁴ differences in measured GM volume (–36 mL without metastasis and –34 mL with metastasis) between pre- and postadministration of GBCAs in our study were slightly larger than the difference in measured GM volume in patients with MS and matched healthy controls observed in their study (–22 mL). Thus, GM volume should be more cautiously evaluated than other tissue volumes in patients with MS after administration of GBCA. Changes in brain parenchymal volume after administration of GBCA (–0.55% without metastasis and –0.24% with metastasis) in our study were comparable with those previously observed in patients with MS for the atrophy rate per year (–0.273%) using synthetic MR imaging.²⁵ Therefore, caution is warranted when evaluating lon-

itudinal changes in brain parenchymal volume of patients with MS after administration of GBCA. However, these changes are also comparable with repeatability of up to 0.40%, calculated as the coefficient of variation reported in brain parenchymal volume measured by synthetic MR imaging.⁶

A limitation of the current study was that only a single dose of GBCA and a single time point after administration were investigated. Although we controlled these variables carefully, the absolute GBCA concentration may have varied among patients due to weight, blood volume, and renal function. In addition, the number of times GBCAs had been administered to the patients in the current study in the past was unknown. Recently, the deposition of gadolinium in the brain has been extensively investigated,²⁶⁻³¹ and the more GBCAs are administered, the more gadolinium is deposited in the brain. Therefore, past administration of GBCA may have some effect on the automatic calculation of brain tissue and myelin volumes via quantitative synthetic MR imaging.

CONCLUSIONS

The administration of GBCA had significant effects on the automatic calculation of brain tissue and myelin volumes using quantitative synthetic MR imaging. Measurement of V_{MY} was increased in ROI analysis, and T1, T2, and PD were decreased in the whole brain after GBCA administration. It is necessary for researchers, clinicians, and interpreting radiologists to be cautious when investigating brain tissue volumes and myelin based on quantitative synthetic MR imaging after GBCA administration.

Disclosures: Akifumi Hagiwara—RELATED: Grant: Japan Society for Promotion of Science KAKENHI, Comments: grant No. 16K19852. Shigeki Aoki—RELATED: Grant: government funding*; UNRELATED: Grants/Grants Pending: Bayer, Daiichi Sankyo, Eisai, Fujiyaku, Fujifilm, Nihon Medi-Physics, Comments: grant for diagnostic radiology*; Payment for Lectures Including Service on Speakers Bureaus: GE Healthcare, Toshiba, Canon, Siemens, Bayer Yakuhin, Daiichi Sankyo, Eisai, Fujiyaku, Fuji Film RI, Medipysics, Guerbet, Novartis, Comments: honorarium for lectures/chair*; Travel/Accommodations/Meeting Expenses Unrelated to Activities Listed: GE Healthcare, Comments: GE Healthcare provided support to visit Wisconsin and Mayo Clinic to see the new MR imaging machines. *Money paid to the institution.

REFERENCES

1. Warntjes JB, Leinhard OD, West J, et al. **Rapid magnetic resonance quantification on the brain: optimization for clinical usage.** *Magn Reson Med* 2008;60:320–29 CrossRef Medline
2. Blystad I, Warntjes JB, Smedby O, et al. **Synthetic MRI of the brain in a clinical setting.** *Acta Radiol* 2012;53:1158–63 CrossRef Medline
3. Hagiwara A, Warntjes M, Hori M, et al. **SyMRI of the brain: rapid quantification of relaxation rates and proton density, with Synthetic MRI, automatic brain segmentation, and myelin measurement.** *Invest Radiol* 2017;52:647–57 CrossRef Medline
4. Wallaert L, Hagiwara A, Andica C, et al. **The advantage of synthetic MRI for the visualization of anterior temporal pole lesions on double inversion recovery (DIR), phase-sensitive inversion recovery (PSIR), and myelin images in a patient with CADASIL.** *Magn Reson Med Sci* 2018;17:275–76 CrossRef Medline
5. Krauss W, Gunnarsson M, Andersson T, et al. **Accuracy and reproducibility of a quantitative magnetic resonance imaging method for concurrent measurements of tissue relaxation times and proton density.** *Magn Reson Imaging* 2015;33:584–91 CrossRef Medline
6. Hagiwara A, Hori M, Cohen-Adad J, et al. **Linearity, bias, intra-scanner repeatability, and inter-scanner reproducibility of quantitative multi-dynamic multi-echo sequence for rapid simultaneous relaxometry at 3T: a validation study with a standardized phantom**

and healthy controls. *Invest Radiol* 2018 Sep 5. [Epub ahead of print] CrossRef Medline

7. West J, Warntjes JB, Lundberg P. **Novel whole brain segmentation and volume estimation using quantitative MRI.** *Eur Radiol* 2012;22:998–1007 CrossRef Medline
8. Andica C, Hagiwara A, Hori M, et al. **Automated brain tissue and myelin volumetry based on quantitative MR imaging with various in-plane resolutions.** *J Neuroradiol* 2018;45:164–68 CrossRef Medline
9. Granberg T, Uppman M, Hashim F, et al. **Clinical feasibility of synthetic MRI in multiple sclerosis: a diagnostic and volumetric validation study.** *AJNR Am J Neuroradiol* 2016;37:1023–29 CrossRef Medline
10. Warntjes M, Engström M, Tisell A, et al. **Modeling the presence of myelin and edema in the brain based on multi-parametric quantitative MRI.** *Front Neurol* 2016;7:16 CrossRef Medline
11. Hagiwara A, Hori M, Yokoyama K, et al. **Utility of a multiparametric quantitative MRI model that assesses myelin and edema for evaluating plaques, periplaque white matter, and normal-appearing white matter in patients with multiple sclerosis: a feasibility study.** *AJNR Am J Neuroradiol* 2017;38:237–42 CrossRef Medline
12. Warntjes JBM, Persson A, Berge J, et al. **Myelin detection using rapid quantitative MR imaging correlated to macroscopically registered Luxol fast blue-stained brain specimens.** *AJNR Am J Neuroradiol* 2017;38:1096–102 CrossRef Medline
13. Hagiwara A, Hori M, Kamagata K, et al. **Myelin measurement: comparison between simultaneous tissue relaxometry, magnetization transfer saturation index, and T1w/T2w ratio methods.** *Sci Rep* 2018;8:10554 CrossRef Medline
14. Warntjes JB, Tisell A, Landtblom AM, et al. **Effects of gadolinium contrast agent administration on automatic brain tissue classification of patients with multiple sclerosis.** *AJNR Am J Neuroradiol* 2014;35:1330–36 CrossRef Medline
15. Hagiwara A, Hori M, Suzuki M, et al. **Contrast-enhanced synthetic MRI for the detection of brain metastases.** *Acta Radiol Open* 2016;5:2058460115626757 CrossRef Medline
16. Zhang Y, Brady M, Smith S. **Segmentation of brain MR images through a hidden Markov random field model and the expectation-maximization algorithm.** *IEEE Trans Med Imaging* 2001;20:45–57 CrossRef Medline
17. Naganawa S, Nakane T, Kawai H, et al. **Gd-based contrast enhancement of the perivascular spaces in the basal ganglia.** *Magn Reson Med Sci* 2017;16:61–65 CrossRef Medline
18. Ambarki K, Lindqvist T, Wåhlin A, et al. **Evaluation of automatic measurement of the intracranial volume based on quantitative MR imaging.** *AJNR Am J Neuroradiol* 2012;33:1951–56 CrossRef Medline
19. Duval T, Stikov N, Cohen-Adad J. **Modeling white matter microstructure.** *Funct Neurol* 2016;31:217–28 Medline
20. Alonso-Ortiz E, Levesque IR, Pike GB. **MRI-based myelin water imaging: a technical review.** *Magn Reson Med* 2015;73:70–81 CrossRef Medline
21. Mezer A, Yeatman JD, Stikov N, et al. **Quantifying the local tissue volume and composition in individual brains with magnetic resonance imaging.** *Nat Med* 2013;19:1667–72 CrossRef Medline
22. Glasser MF, Van Essen DC. **Mapping human cortical areas in vivo based on myelin content as revealed by T1- and T2-weighted MRI.** *J Neurosci* 2011;31:11597–616 CrossRef Medline
23. Hagiwara A, Hori M, Yokoyama K, et al. **Analysis of white matter damage in patients with multiple sclerosis via a novel in vivo MR method for measuring myelin, axons, and g-ratio.** *AJNR Am J Neuroradiol* 2017;38:1934–40 CrossRef Medline
24. Jeon JY, Choi JW, Roh HG, et al. **Effect of imaging time in the magnetic resonance detection of intracerebral metastases using single dose gadobutrol.** *Korean J Radiol* 2014;15:145–50 CrossRef Medline
25. Warntjes JB, Tisell A, Håkansson I, et al. **Improved precision of automatic brain volume measurements in patients with clinically isolated syndrome and multiple sclerosis using edema correction.** *AJNR Am J Neuroradiol* 2018;39:296–302 CrossRef Medline

26. Kanda T, Ishii K, Kawaguchi H, et al. **High signal intensity in the dentate nucleus and globus pallidus on unenhanced T1-weighted MR images: relationship with increasing cumulative dose of a gadolinium-based contrast material.** *Radiology* 2014;270:834–41 CrossRef Medline
27. Errante Y, Cirimele V, Mallio CA, et al. **Progressive increase of T1 signal intensity of the dentate nucleus on unenhanced magnetic resonance images is associated with cumulative doses of intravenously administered gadodiamide in patients with normal renal function, suggesting dechelation.** *Invest Radiol* 2014;49:685–90 CrossRef Medline
28. Adin ME, Kleinberg L, Vaidya D, et al. **Hyperintense dentate nuclei on T1-weighted MRI: relation to repeat gadolinium administration.** *AJNR Am J Neuroradiol* 2015;36:1859–65 CrossRef Medline
29. McDonald RJ, McDonald JS, Kallmes DF, et al. **Intracranial gadolinium deposition after contrast-enhanced MR imaging.** *Radiology* 2015;275:772–82 CrossRef Medline
30. Kanda T, Fukusato T, Matsuda M, et al. **Gadolinium-based contrast agent accumulates in the brain even in subjects without severe renal dysfunction: evaluation of autopsy brain specimens with inductively coupled plasma mass spectroscopy.** *Radiology* 2015;276:228–32 CrossRef Medline
31. Murata N, Gonzalez-Cuyar LF, Murata K, et al. **Macrocyclic and other non-group 1 gadolinium contrast agents deposit low levels of gadolinium in brain and bone tissue: preliminary results from 9 patients with normal renal function.** *Invest Radiol* 2016;51:447–53 CrossRef Medline

FDG-PET and MRI in the Evolution of New-Onset Refractory Status Epilepticus

T. Strohm, C. Steriade, G. Wu, S. Hantus, A. Rae-Grant, and M. Larvie



ABSTRACT

BACKGROUND AND PURPOSE: New-onset refractory status epilepticus is a clinical condition characterized by acute and prolonged pharmacoresistant seizures without a pre-existing relevant neurologic disorder, prior epilepsy, or clear structural, toxic, or metabolic cause. New-onset refractory status epilepticus is often associated with antineuronal antibodies and may respond to early immunosuppressive therapy, reflecting an inflammatory element of the condition. FDG-PET is a useful diagnostic tool in inflammatory and non-inflammatory encephalitis. We report here FDG-PET findings in new-onset refractory status epilepticus and their correlation to disease activity, other imaging findings, and outcomes.

MATERIALS AND METHODS: Twelve patients who met the criteria for new-onset refractory status epilepticus and who had FDG-PET and MR imaging scans and electroencephalography at a single academic medical center between 2008 and 2017 were retrospectively identified. Images were independently reviewed by 2 radiologists specialized in nuclear imaging. Clinical characteristics and outcome measures were collected through chart review.

RESULTS: Twelve patients underwent 21 FDG-PET scans and 50 MR imaging scans. Nine (75%) patients were positive for autoantibodies. All patients had identifiable abnormalities on the initial FDG-PET in the form of hypermetabolism (83%) and/or hypometabolism (42%). Eight (67%) had medial temporal involvement. All patients ($n = 3$) with *N*-methyl-D-aspartic acid receptor antibodies had profound bilateral occipital hypometabolism. Initial MR imaging findings were normal in 6 (50%) patients. Most patients had some degree of persistent hyper- (73%) or hypometabolism (45%) after immunosuppressive therapy. FDG-PET hypometabolism was predictive of poor outcome (mRS 4–6) at hospital discharge ($P = .028$).

CONCLUSIONS: Both FDG-PET hypometabolism and hypermetabolism are seen in the setting of new-onset refractory status epilepticus and may represent markers of disease activity.

ABBREVIATIONS: ALE = autoimmune limbic encephalitis; EEG = electroencephalography; GABA-B = γ -aminobutyric acid B; LGI1 = leucine-rich glioma inactivated 1; NMDA = *N*-methyl-D-aspartate; NMDA-R = *N*-methyl-D-aspartate receptor; NORSE = new-onset refractory status epilepticus; VGKC = voltage-gated potassium channel

New-onset refractory status epilepticus (NORSE) is a clinical condition characterized by prolonged pharmacoresistant seizures in an individual without active epilepsy or other pre-

existing relevant neurologic disorders.^{1,2} Other terms such as acute encephalitis with refractory, repetitive partial seizures; devastating epileptic encephalopathy in school-aged children; and febrile infection-related epilepsy syndrome describe the same disease entity. Although the absence of a clear acute or active toxic, metabolic, or structural cause is necessary for the diagnosis, the neuropathology of NORSE includes patients with viral infections (such as herpes simplex virus 1) and autoimmune syndromes such as autoimmune limbic encephalitis (ALE).²⁻⁵ Typical findings include the following: hippocampal or neocortical T2-hyperintense MR imaging lesions, mild pleocytosis and/or elevated protein in the CSF, and periodic and epileptiform discharges on electroencephalography (EEG).^{1,6} An underlying inflammatory mechanism has been suggested by the following findings: 1) Up to two-thirds of patients are found to have an associated neuronal

Received July 15, 2018; accepted after revision November 19.

From the Department of Neurology (T.S.), Neurovascular Stroke Center, Ohio State University, Columbus, Ohio; Department of Epilepsy (C.S., S.H.), Department of Nuclear Medicine (G.W., M.L.), Department of Neuroradiology (M.L.), and Department of Neuroimmunology (A.R.-G.), Cleveland Clinic, Cleveland, Ohio. Dr. Strohm was formerly at Cleveland Clinic.

Previously presented as a poster at: Annual Meeting of the Neurocritical Care Society, October 9–13, 2017; Waikoloa, Hawaii.

Please address correspondence to Tamara Strohm, MD, Department of Neurology, Neurovascular Stroke Center, Ohio State University, 3172A Graves Hall, 333 W 10th Ave, Columbus, OH 43210; e-mail: tamara.strohm@gmail.com

Indicates article with supplemental on-line tables.

<http://dx.doi.org/10.3174/ajnr.A5929>

cell surface or intracellular antibody,¹ 2) a proportion of patients may respond to early immunosuppressive therapy,⁷⁻¹¹ and 3) elevated levels of cytokines interleukin-6 and interleukin-8 return to normal after treatment, corresponding to clinical improvement.¹² Given the substantial morbidity (neurologic disability, subsequent epilepsy) and mortality associated with the diagnosis of NORSE, this hypothesis is of interest. The therapeutic implications, in the setting of prolonged intensive care unit and hospital stays and frequent anesthetic treatment, highlight a need for the development of biomarkers to track disease activity and response to therapies.

Abnormal findings on FDG-PET have been demonstrated in conditions such as ALE associated with a NORSE syndrome; however, typical findings and their relevance to disease activity and outcomes have not been established.^{13,14} Meanwhile, the use of FDG-PET is well-established in chronic epilepsy, with interictal hypometabolism suggesting an abnormal function of neuronal networks.¹⁵⁻¹⁷

We sought to describe FDG-PET characteristics and association of FDG-PET findings with MR imaging, EEG, clinical course, treatment, and outcome measures in a cohort of patients with NORSE.

MATERIALS AND METHODS

Patient Selection

We retrospectively identified patients at a single academic institution from November 2008 to July 2017 in an ALE data base containing patients with autoimmune encephalitis, rapidly progressive dementia, and unexplained new-onset seizures. The data base was searched using the keyword “seizures.” Among 26 patients with seizures, 12 patients were identified as fulfilling the consensus definition of NORSE,² all of whom had undergone both FDG-PET and MR imaging. The mean age was 40 years (range, 14–78 years), and 10 (83%) patients were female.

Antineuronal antibody panels were performed from serum and/or CSF of all patients (7 [58%] with both) by commercial laboratories (Athena Laboratories, ARUP; Mayo Medical Laboratories, Rochester, Minnesota) and included a combination of the following: glutamic acid decarboxylase 65; voltage-gated potassium channel (VGKC); leucine-rich glioma inactivated 1 (LGI1); contactin-associated protein 2; γ -aminobutyric acid B (GABA-B); α -amino-3-hydroxy-5-methyl-4-isoxazolepropionic acid; *N*-methyl-D-aspartate (NMDA); antineuronal nuclear antibody 1, 2, 3; antiglial nuclear antibody 1, 2; Purkinje-cell antibody 1, 2; and amphiphysin and anti-Tr antibodies. Eleven (92%) had NMDA antibody testing, and all patients had VGKC antibody testing. EEG was performed within 24 hours of FDG-PET in 11 (92%) patients. All patients received immunosuppressive therapy, with 11 (92%) undergoing FDG-PET following treatment.

The electronic medical record was reviewed for patient characteristics, hospital course, results of diagnostic testing, treatment, and outcome at hospital discharge and last follow-up appointment. Three patients did not have follow-up after hospital discharge.

Approval from the Cleveland Clinic IRB was obtained, and consent was waived due to the retrospective nature of this study.

FDG-PET Imaging

[¹⁸F] FDG (185–370 MBq) was injected intravenously. Imaging was performed approximately 45–60 minutes later using a Biograph 6 PET/CT scanner (Siemens, Erlangen, Germany). The PET emission scan was obtained using a 15-minute acquisition with 1 bed position. PET images were reconstructed using the following parameters: CT attenuation-correction Fourier rebinning, trim sonogram (brain mode), ordered subset expectation maximization, 6 iterations, 8 subsets, 3-mm Gaussian filter, matrix size = 168 × 168, zoom = 2×, and match CT slice location using 2-mm slice thickness. Reconstructed images were reviewed both with and without attenuation correction. Attenuation-correction CT parameters were the following: extended FOV = 700 mm, 130 kV(peak), 20 mAs, 3.0-mm slice thickness, 2.0-mm slice increment, 3 × 6 mm collimation, B31s kernel.

MR Imaging Acquisition

All MR imaging was performed using clinical protocols. Scans were performed on 1.5T and 3T scanners (Siemens) with protocols designed to provide comparable imaging results from all scanners used for patients in this study; accordingly, no effort was made to use a single scanner. T1, T2, T2 FLAIR, and diffusion-weighted images were routinely obtained. SWI or another susceptibility sequence was performed in most scans. Postcontrast T1-weighted images were obtained following intravenous administration of gadoterate meglumine.

Imaging Review

All FDG-PET and MR imaging scans were independently reviewed by 2 board-certified radiologists specialized in nuclear imaging. Qualitative evaluation was performed by visual inspection using FDG-PET images coregistered with the most recent MR imaging scan. Semiquantitative analysis was performed using a parametric data base comparison with age-matched control subjects as implemented in syngo.via (Siemens). Abnormal findings were characterized as hypermetabolism or hypometabolism and classified according to the brain structure involved, including lobes and, when appropriate, substructures such as the perirolandic region, hippocampus, amygdala, striatum, and cerebellar hemispheres.

Statistical Analysis

Descriptive statistics were performed for each variable, including means, medians, and SDs for continuous variables and frequencies for categorical variables. Fisher exact tests (2-tailed) were used for comparisons of categorical variables. Significance was set at $P < .05$.

RESULTS

Patient Characteristics

Patient characteristics, presenting clinical features, and serum and CSF findings are summarized in On-line Table 1. Most patients (75%) were positive for autoantibodies (GABA-B, $n = 1$; glutamic acid decarboxylase 65, $n = 3$; *N*-methyl-D-aspartate receptor (NMDA-R), $n = 3$; VGKC, $n = 1$; and LGI1, $n = 1$), and all patients were treated with immunosuppressive therapy at a median of 12.5 days of hospitalization. Most patients had a pro-

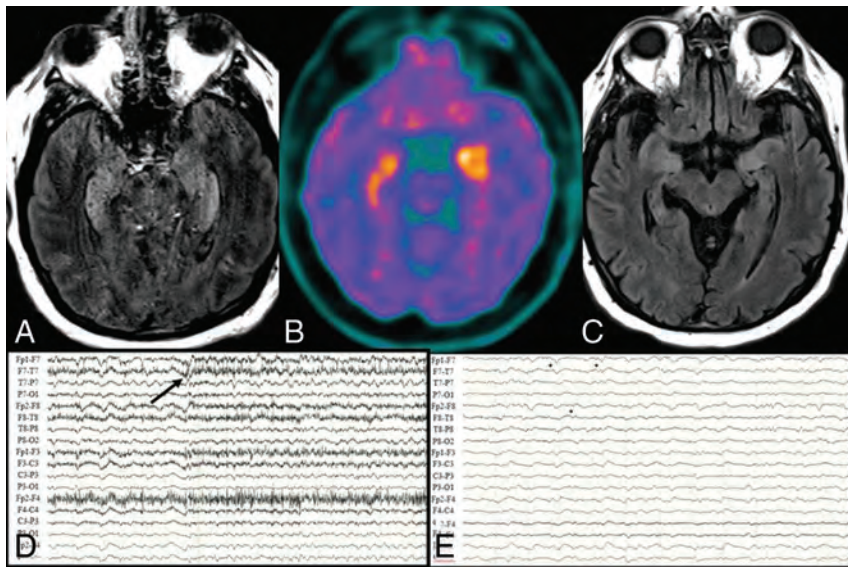


FIG 1. Brain MR imaging, FDG-PET, and EEG findings for P2, a 63-year-old man with glutamic acid decarboxylase 65 encephalitis and normal brain MR imaging findings at the onset of seizures. *A*, Axial T2-weighted FLAIR image at day 12 of status epilepticus shows bilateral hippocampal and insula T2-weighted hyperintense lesions. *B*, Axial FDG-PET image at day 12 of status epilepticus shows bilateral hippocampus, amygdala, and insula hypermetabolism. *C*, Axial T2-weighted FLAIR image at day 49 of status epilepticus shows resolution of hippocampal and insula T2-weighted hyperintense lesions with diffuse atrophy. *D*, EEG shows left frontotemporal seizures (onset at *black arrow*) with bilateral periodic discharges before seizure. *E*, EEG shows bilateral independent periodic discharges (*black asterisks*).

tracted hospital course (median, 48.5 days; range, 19–199 days) with prolonged status epilepticus (median, 12 days, range, 3–106 days). The clinical examination (correlated with the time of MR imaging and FDG-PET) is noted in On-line Table 2. All patients received immunosuppressive therapy (see On-line Table 3 for details).

FDG-PET and MR Imaging Findings

FDG-PET, MR imaging, EEG, and clinical examination findings are summarized in On-line Table 2 with a highlighted case in Fig 1.

All patients had at least 1 FDG-PET scan, obtained a mean of 13 days after the onset of status epilepticus, (range, –5–53 days). All patients had at least 1 abnormal finding on the FDG-PET scan: Seven (58%) had hypermetabolism only, 2 (17%) had hypometabolism only, and 3 (25%) had both. Eight (67%) had bilateral abnormalities, and 6 (50%) had unilateral amygdala and/or hippocampal hypermetabolism. One patient with VGKC-complex antibody and faciobrachial dystonic seizures secondary to a presumed LGI1 antibody (not tested) had bilateral basal ganglia hypermetabolism. Three patients (25%, all with NMDA-R antibodies) had marked bilateral occipital hypometabolism, and 2 of them (67%) also had perirolandic hypometabolism. Three patients (27%) had EEG evidence of seizure at the time of the initial FDG-PET. There was no association between hypermetabolism and EEG seizure at the time of FDG-PET acquisition (Fisher exact test, $P = .49$).

Six patients had multiple FDG-PET scans. Of these 6, four (67%) showed new hypermetabolism and 2 (33%) had new hypometabolism, so a total of 5 (83% of patients with repeat FDG-PET scans) had new abnormalities. Furthermore, of patients with

a repeat FDG-PET scan, 4 (67%) had resolution of hypermetabolic foci and 1 (17%) had resolution of a hypometabolic focus. One complex patient with NMDA-R antibody encephalitis underwent 5 FDG-PET scans from the onset of status epilepticus to day 234 (Fig 2). At seizure onset, his FDG-PET scan showed marked bilateral occipital and parietal hypometabolism, which persisted throughout his disease course.

In comparison, initial MR imaging findings were normal in 6 (50%) patients and remained normal in 3 (25%) patients on a second MR imaging. All patients had abnormal findings by the third MR imaging scan. The most common finding was unilateral amygdala and/or hippocampal T2 hyperintensity, with or without associated swelling. All patients with an initial abnormal finding on MR imaging also had hypermetabolism on the first FDG-PET. No correlation was found between FDG-PET hypometabolism or hypermetabolism and abnormal findings on MR imaging (Fisher exact tests $P = 1$ and .45, respectively).

Other MR imaging findings included superficial cerebral venous thrombosis with or without a small subarachnoid hemorrhage in 2 (17%) and leptomeningeal thickening and enhancement in 2 (17%). Hippocampal or diffuse atrophy or both occurred in 9 (75%) patients, with a median delay from symptom onset to the time of identification of the imaging findings of 48 days (range, 19–937 days).

Eleven patients underwent FDG-PET after immunosuppressive therapy (Fig 3). Eight (73%) and 5 (45%) patients had hypermetabolism or hypometabolism, respectively, following treatment.

Outcome

The mean modified Rankin Scale score at hospital discharge was 4 (median, 4; range, 2–5). Nine patients (75%) followed up at our institution, with a mean follow-up time of 672 days. The mean mRS score improved to 2 (median, 1; range, 0–6) at last follow-up, by which time 5 (56%) patients had returned to baseline or near-baseline (mRS range, 0–1), 3 (33%) had some deficits but remained ambulatory (mRS range, 2–3), and 1 patient had died. Five (56%) continued to have clinical seizures at last follow-up and were treated with a mean of 2.5 antiepileptic drugs (range, 1–4).

Imaging Predictors of Outcome

FDG-PET hypometabolism (when seen in the initial FDG-PET obtained) was predictive of poor outcome (defined as mRS 4–6) at hospital discharge (Fisher exact 2-tailed test, $P = .028$), while abnormal findings on MR imaging were not predictive of poor outcome at discharge (Fisher exact 2-tailed test, $P = 1$). No ab-

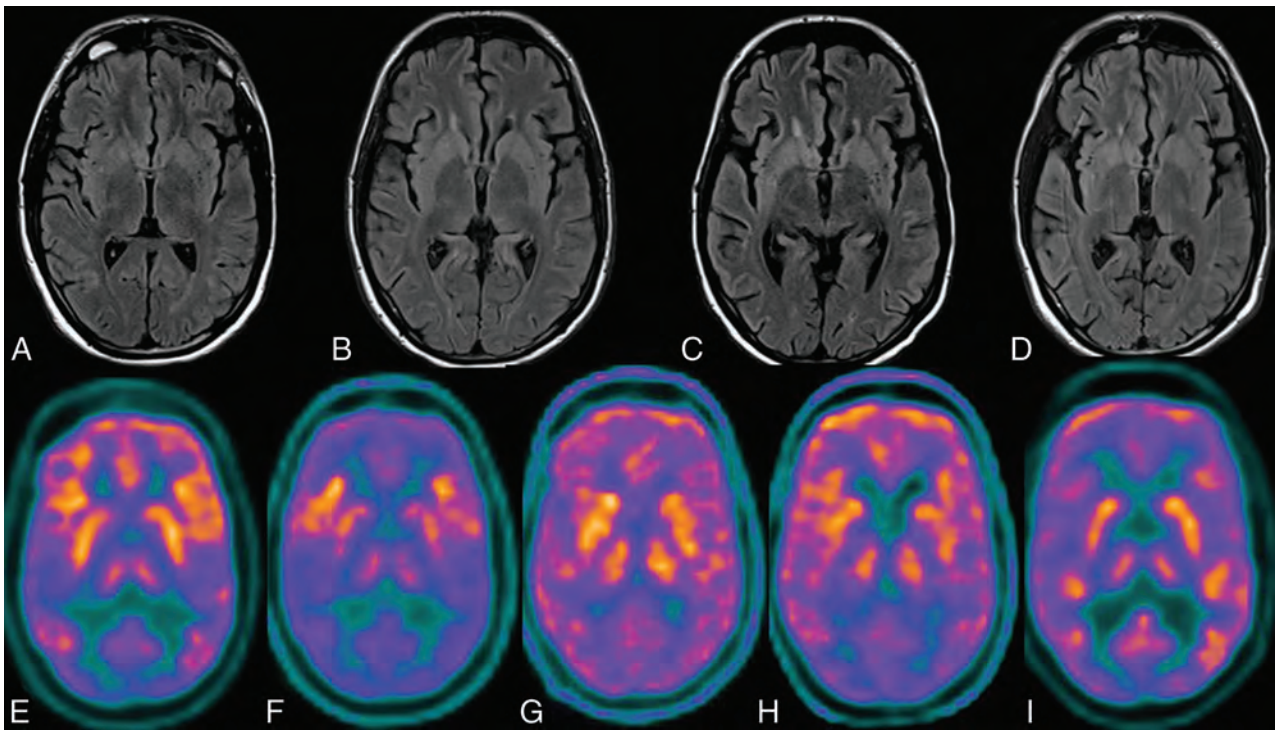


FIG 2. Brain MR imaging and FDG-PET findings for P5, a 22-year-old man with NMDA-R antibody encephalitis. A, Axial T2-weighted FLAIR image 7 days before the onset of status epilepticus with normal findings. B, Axial T2-weighted FLAIR image 2 days before the onset of status epilepticus with normal findings. C, Axial T2-weighted FLAIR image at day 28 of status epilepticus shows mild diffuse atrophy. D, Axial T2-weighted FLAIR image at day 63 of status epilepticus shows moderate diffuse atrophy. E, Axial FDG-PET image at day zero of status epilepticus shows marked bilateral occipital-greater than-parietal hypometabolism. F, Axial FDG-PET image at day 12 of status epilepticus shows bilateral inferolateral frontal hypermetabolism with diffuse hypometabolism. G, Axial FDG-PET image at day 56 of status epilepticus shows resolution of bilateral inferolateral frontal hypermetabolism with diffuse cortical hypometabolism. H, Axial FDG-PET image at day 88 of status epilepticus shows moderate bilateral occipital-greater than-parietal hypometabolism. I, Axial FDG-PET image at day 234 following status epilepticus shows mild bilateral occipital hypometabolism.

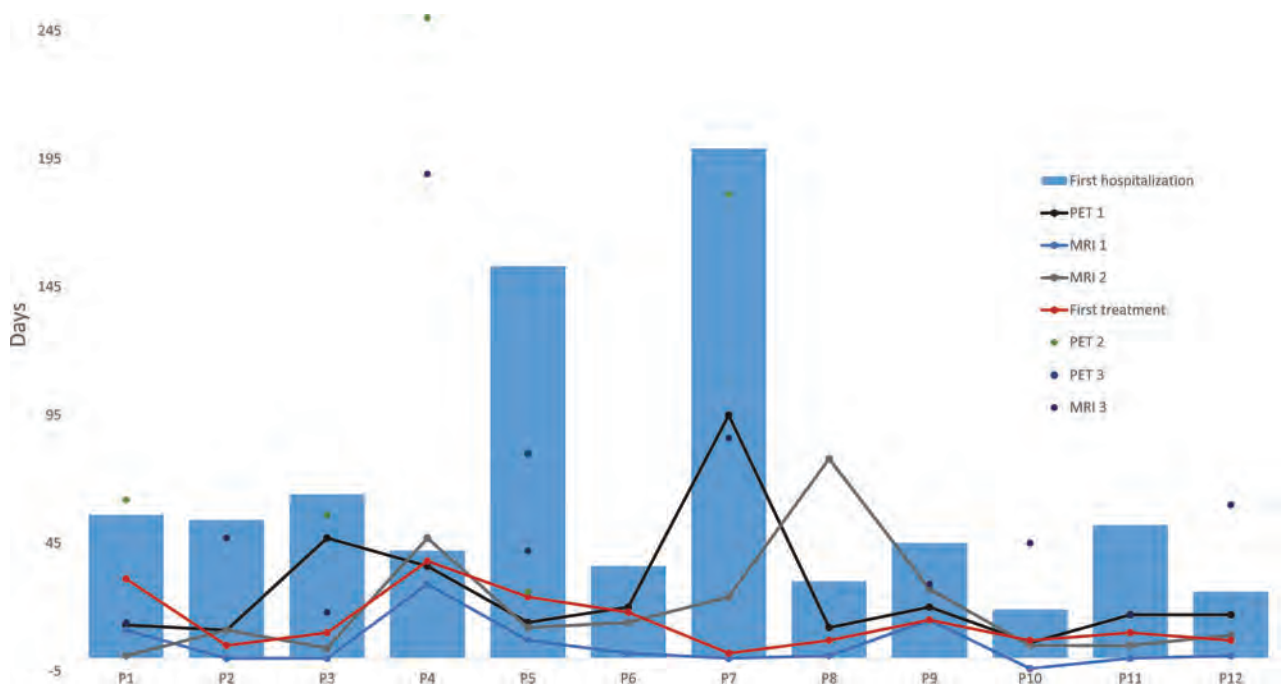


FIG 3. Timeline of brain MR imaging, FDG-PET, and the first immunotherapy treatment during initial hospitalization. Not depicted are FDG-PET 2 of P10 at 1397 days and MR imaging 3 of P8 at 415 days.

normal findings on imaging were predictive of persistent seizures at last follow-up. Indeed, we did not find an association between PET hypometabolism (2-tailed Fisher exact test, $P = .52$) and abnormal findings on MR imaging (2-tailed Fisher exact test, $P = 1$) and persistent seizures.

DISCUSSION

We describe FDG-PET and MR imaging findings spanning the disease course in a cohort of 12 patients with NORSE. We propose a role for FDG-PET as a biomarker of disease activity in NORSE by the following: 1) determining regions of brain vulnerable to encephalitic involvement (amygdala, hippocampus, occipital cortex, sensorimotor cortex, striatum) and discussing the biologic plausibility in the setting of our understanding of mechanisms of NORSE; 2) demonstrating an evolution of FDG-PET findings during the disease course; 3) exploring FDG-PET findings as predictors of outcome; and 4) finally, highlighting a higher proportion of abnormal findings on FDG-PET compared with MR imaging early in the disease course independent of EEG findings.

Regional Vulnerability

Our findings illustrate a predilection of certain brain regions for abnormal metabolism. The most common regions of metabolic abnormality, as identified on FDG-PET, are the amygdala and hippocampus (67% of cases), which are also regions where MR imaging abnormalities were frequently identified (42% of cases). In the setting of ALE, medial temporal and limbic hypermetabolism or hypometabolism has also been reported,^{18,19} mirroring abnormalities of the hippocampus and amygdala on MR imaging.²⁰⁻²³ This regional predilection on neuroimaging may reflect an underlying neuroinflammatory pathology preferentially affecting the hippocampus, which may be common not only to ALE but also to NORSE. Infiltration of inflammatory cells and complement activation have been shown to lead to parenchymal edema in histopathologic studies of VGKC-antibody-associated ALE, demonstrating limbic T-cell infiltration with perivascular and parenchymal B-cells in the hippocampus.²⁴ Regional predilection may reflect antigen expression topography and/or, on a broader level, regional susceptibility to neuroinflammation.²⁵ The latter is supported by the finding in this study that FDG-PET medial temporal hypermetabolism was present with multiple types of antibodies (NMDA-R, glutamic acid decarboxylase 65, VGKC, GABA-B) as well as cases negative for antibodies.

Other regional vulnerabilities were found in association with specific antibodies. Bilateral occipital and perirolandic hypometabolism were noted in patients with NMDA-R antibodies, consistent with previous reports of a frontotemporal-to-occipital gradient with hypermetabolism in the frontal and temporal lobes and profound hypometabolism in the occipital lobes.^{13,26,27} Similarly, striatal hypermetabolism was noted in 1 patient with VGKC-LGI1, similar to previous reports of abnormalities in the cortical sensorimotor and basal ganglia metabolism in the VGKC-antibody ALE.²⁸ Quartuccio et al²⁹ hypothesized that antibodies against intracellular antigens were more likely to cause a T-cell-mediated release of cytokines and

chemokines in the limbic system manifesting as FDG-PET hypermetabolism. They proposed that FDG-PET hypometabolism, conversely, was secondary to cell-surface antibody-mediated capping and internalization leading to a decrease in neuronal activity.

Finally, widespread findings without region predilection have been reported in a cohort of children with febrile infection-related epilepsy syndrome, in whom widespread hypometabolism in the bilateral temporoparietal and orbitofrontal cortices was found to correspond with EEG findings and neuropsychological deficits.³⁰

Evolution of FDG-PET Findings during the Disease Course

Most patients with serial FDG-PET and MR imaging scans showed evolution, with resolution of prior findings and new abnormalities on subsequent imaging (Figs 1 and 2). While the main driver of the evolution in FDG-PET findings is unclear, one may hypothesize a role for severity of illness, treatment effect, and underlying pathology. Other findings including leptomeningeal thickening and enhancement, subarachnoid hemorrhage, and cerebral venous thrombosis on MR imaging have been described in ALE. Cerebral venous thrombosis and subarachnoid hemorrhage may reflect abnormalities in the coagulation cascade secondary to an underlying inflammatory process or immunosuppressive therapy.

FDG-PET as a Predictor of Outcome

FDG-PET abnormalities were correlated with poor outcome at hospital discharge. Conversely, both cases with normal FDG-PET on serial imaging had good (mRS, 0–3) outcomes at hospital discharge. Others have reported normalization of cerebral glucose metabolism with recovery.³¹ The variability in outcomes reported (for instance, 20% mortality, 30% debilitated with mRS 4–5, and 50% with mRS 0–3 at 1 year in Kantanen et al,³² in 2017) may reflect variability in underlying pathophysiology and treatment practices (aggressiveness of anesthetic and barbiturate use, use and escalation of immunosuppressive therapy). At the heart of variation in treatment practices is a lack of biomarkers beyond EEG to guide clinical decision-making. In this cohort, abnormal findings on FDG-PET were present independent of the persistence of EEG seizures. This finding suggests that abnormal FDG-PET metabolism may be more directly related to the pathophysiology of the disease process than seizure activity or other metrics routinely followed in clinical practice.

Comparative Value of FDG-PET and MR Imaging as Imaging Modalities in NORSE

Others have reported increased sensitivity of FDG-PET versus MR imaging during the initial evaluation.^{29,33,34} Our findings mirrored this: Fifty percent of MR imaging scans initially had abnormal findings compared with 100% of FDG-PET scans. With time, an increasing proportion of MRIs showed some abnormal findings. The higher chance of an abnormality on an FDG-PET scan early in the disease course not only increases its diagnostic value but also raises the possibility that it may be a more useful biomarker.

Limitations

Limitations include the retrospective nature of this study, small sample size, and heterogeneity in patient characteristics. Given that NORSE is a clinical diagnosis, diversity among autoantibodies and disease processes may limit the ability to generalize. Excepting cases with NMDA-R antibodies, we found that abnormal findings on FDG-PET were not segregated by antibody type or seropositive groups. Additionally, the retrospective nature of the study was associated with variability in the timing of FDG-PET and MR imaging scans. The variability in treatment received, both antiepileptic including barbiturate and immunotherapeutic, could also have impacted glucose metabolism on FDG-PET.

CONCLUSIONS

Evolving patterns of brain hypermetabolism and hypometabolism, as revealed by FDG-PET, are seen in NORSE, with a predilection for the amygdala and hippocampus in cases with a diversity of autoantibodies. In the cohort presented here, FDG-PET often showed patterns of mixed hypermetabolism and hypometabolism in the earlier, more acute phases, with evolution to hypometabolism in the later, more chronic phases. We propose an independent role for FDG-PET as a complementary marker of disease activity in NORSE.

REFERENCES

1. Gaspard N, Foreman BP, Alvarez V, et al. Critical Care EEG Monitoring Research Consortium (CCEMRC). **New-onset refractory status epilepticus: etiology, clinical features, and outcome.** *Neurology* 2015;85:1604–13 CrossRef Medline
2. Hirsch LJ, Gaspard N, van Baalen A, et al. **Proposed consensus definitions for new-onset refractory status epilepticus (NORSE), febrile infection-related epilepsy syndrome (FIRES), and related conditions.** *Epilepsia* 2018;59:739–44 CrossRef Medline
3. Graus F, Titulaer MJ, Balu R, et al. **A clinical approach to diagnosis of autoimmune encephalitis.** *Lancet Neurol* 2016;15:391–404 CrossRef Medline
4. Ismail FY, Kossoff EH. **AERRPS, DESC, NORSE, FIRES: Multi-labeling or distinct epileptic entities?** *Epilepsia* 2011;52:e185–89 CrossRef Medline
5. Sakuma H, Awaya Y, Shiomi M, et al. **Acute encephalitis with refractory, repetitive partial seizures (AERRPS): a peculiar form of childhood encephalitis.** *Acta Neurol Scand* 2010;121:251–56 CrossRef Medline
6. Costello DJ, Kilbride RD, Cole AJ. **Cryptogenic new onset refractory status epilepticus (NORSE) in adults: infectious or not?** *J Neurol Sci* 2009;277:26–31 CrossRef Medline
7. Byun J, Lee S, Jung K, et al. **Effect of immunotherapy on seizure outcome in patients with autoimmune encephalitis: a prospective observational registry study.** *PLoS One* 2016;11:e0146455 CrossRef Medline
8. Gall CR, Jumma O, Mohanraj R. **Five cases of new onset refractory status epilepticus (NORSE) syndrome: outcomes with early immunotherapy.** *Seizure* 2013;22:217–20 CrossRef Medline
9. Iizuka T, Kanazawa N, Kaneko J, et al. **Cryptogenic NORSE: its distinctive clinical features and response to immunotherapy.** *Neurol Neuroimmunol Neuroinflamm* 2017;4:e396 CrossRef Medline
10. Khawaja AM, DeWolfe JL, Miller DW, et al. **New-onset refractory status epilepticus (NORSE): the potential role for immunotherapy.** *Epilepsy Behav* 2015;47:17–23 CrossRef Medline
11. Li J, Saldivar C, Maganti RK. **Plasma exchange in cryptogenic new onset refractory status epilepticus.** *Seizure* 2013;22:70–73 CrossRef Medline
12. Kenney-Jung DL, Vezzani A, Kahoud RJ, et al. **Febrile infection-related epilepsy syndrome treated with anakinra.** *Ann Neurol* 2016; 80:939–45 CrossRef Medline
13. Leypoldt F, Buchert R, Kleiter I, et al. **Fluorodeoxyglucose positron emission tomography in anti-N-methyl-D-aspartate receptor encephalitis: distinct pattern of disease.** *J Neurol Neurosurg Psychiatry* 2012;83:681–86 CrossRef Medline
14. Titulaer M, Soffiatti R, Dalmau J, et al; European Federation of Neurological Societies. **Screening for tumours in paraneoplastic syndromes: report of an EFNS task force.** *Eur J Neurol* 2011;18:19–e3 CrossRef Medline
15. Cole AJ. **Status epilepticus and periictal imaging.** *Epilepsia* 2004;45: 72–77 Medline
16. Kim S, Mountz JM. **SPECT imaging of epilepsy: an overview and comparison with F-18 FDG PET.** *Int J Mol Imaging* 2011;2011: 813028 CrossRef Medline
17. Sarria-Estrada S, Toledo M, Lorenzo-Bosquet C, et al. **Neuroimaging in status epilepticus secondary to paraneoplastic autoimmune encephalitis.** *Clin Radiol* 2014;69:795–803 CrossRef Medline
18. Baumgartner A, Rauer S, Mader I, et al. **Cerebral FDG PET and MRI findings in autoimmune limbic encephalitis: correlation with autoantibody types.** *J Neurol* 2013;260:2744–53 CrossRef Medline
19. Probasco JC, Solnes L, Nalluri A, et al. **Abnormal brain metabolism on FDG PET/CT is a common early finding in autoimmune encephalitis.** *Neurol Neuroimmunol Neuroinflamm* 2017;4:e352 CrossRef Medline
20. Finke C, Prüss H, Heine J, et al. **Evaluation of cognitive deficits and structural hippocampal damage in encephalitis with leucine-rich, glioma-inactivated 1 antibodies.** *JAMA Neurol* 2017;74:50–59 CrossRef Medline
21. Heine J, Prüss H, Bartsch T, et al. **Imaging of autoimmune encephalitis—relevance for clinical practice and hippocampal function.** *Neuroscience* 2015;309:68–83 CrossRef Medline
22. Miller TD, Chong TT, Aimola Davies AM, et al. **Focal CA3 hippocampal subfield atrophy following LGI1 VGKC-complex antibody limbic encephalitis.** *Brain* 2017;140:1212–19 CrossRef Medline
23. Wagner J, Schoene-Bake J, Malter MP, et al. **Quantitative FLAIR analysis indicates predominant affection of the amygdala in antibody-associated limbic encephalitis.** *Epilepsia* 2013;54:1679–87 CrossRef Medline
24. Khan NL, Jeffrey MA, Good C, et al. **Histopathology of VGKC antibody-associated limbic encephalitis.** *Neurology* 2009;72:1703–05 CrossRef Medline
25. Vincent A, Bien CG, Irani SR, et al. **Autoantibodies associated with diseases of the CNS: new developments and future challenges.** *Lancet Neurol* 2011;10:759–72 CrossRef Medline
26. Maeder-Ingvar M, Prior JO, Irani SR, et al. **FDG PET hyperactivity in basal ganglia correlating with clinical course in anti-NMDA-R antibodies encephalitis.** *J Neurol Neurosurg Psychiatry* 2011;82:235–36 CrossRef Medline
27. Probasco JC, Solnes L, Nalluri A, et al. **Decreased occipital lobe metabolism by FDG PET/CT: an anti-NMDA receptor encephalitis biomarker.** *Neurol Neuroimmunol Neuroinflamm* 2018;5:e413 CrossRef Medline
28. Dodich A, Cerami C, Iannaccone S, et al. **Neuropsychological and FDG-PET profiles in VGKC autoimmune limbic encephalitis.** *Brain Cogn* 2016;108:81–87 CrossRef Medline
29. Quartuccio N, Caobelli F, Evangelista L, et al; Young AIMN Working Group. **The role of FDG PET/CT in the evaluation of patients affected by limbic encephalitis: a systematic review of the literature.** *J Neuroimmunol* 2015;284:44–48 CrossRef Medline
30. Mazzuca M, Jambaque I, Hertz-Pannier L, et al. **18F-FDG PET reveals frontotemporal dysfunction in children with fever-induced refractory epileptic encephalopathy.** *J Nucl Med* 2011;52:40–47 CrossRef Medline
31. Nardetto L, Zoccarato M, Santelli L, et al. **(18)F-FDG PET/MRI in cryptogenic new-onset refractory status epilepticus: a potential**

- marker of disease location, activity and prognosis? *J Neurol Sci* 2017; 381:100–02 CrossRef Medline
32. Kantanen A, Reinikainen M, Parviainen I, et al. **Long-term outcome of refractory status epilepticus in adults: a retrospective population-based study.** *Epilepsy Res* 2017;133:13–21 CrossRef Medline
33. Solnes LB, Jones KM, Rowe SP, et al. **Diagnostic value of 18F-FDG PET/CT versus MRI in the setting of antibody-specific autoimmune encephalitis.** *J Nucl Med* 2017;58:1307–13 CrossRef Medline
34. Newey C, Sarwal A, Hantus S. **[18F]-fluoro-deoxy-glucose positron emission tomography scan should be obtained early in cases of autoimmune encephalitis.** *Autoimmune Dis* 2016;2016:9450452 CrossRef Medline

Alterations in Brain Metabolites in Patients with Epilepsy with Impaired Consciousness: A Case-Control Study of Interictal Multivoxel ¹H-MRS Findings

Z. Tan, X. Long, F. Tian, L. Huang, F. Xie, and S. Li

ABSTRACT

BACKGROUND AND PURPOSE: Previous studies have shown perfusion abnormalities in the thalamus and upper brain stem in patients with epilepsy with impaired consciousness. We hypothesized that these areas associated with consciousness will also show metabolic abnormalities. However, metabolic abnormalities in those areas correlated with consciousness has not been characterized with multivoxel ¹H-MRS. In this study, we investigated the metabolic alterations in these brain regions and assessed the correlation between seizure features and metabolic alterations.

MATERIALS AND METHODS: Fifty-seven patients with epilepsy and 24 control subjects underwent routine MR imaging and 3D multivoxel ¹H-MRS. Patients were divided into 3 subgroups: focal impaired awareness seizures ($n = 18$), primary generalized tonic-clonic seizures ($n = 19$), and secondary generalized tonic-clonic seizures ($n = 20$). The measured metabolite alterations in NAA/Cr, NAA/(Cr + Cho), and Cho/Cr ratios in brain regions associated with the consciousness network were compared between the patient and control groups. ROIs were placed in the bilateral inferior frontal gyrus, supramarginal gyrus, cingulate gyrus, precuneus, thalamus, and upper brain stem. Correlations between clinical parameters (epilepsy duration and seizure frequency) and metabolite alterations were analyzed.

RESULTS: Significantly lower NAA/Cr and NAA/(Cho + Cr) ratios ($P < .05$ and $< .01$, respectively) were observed in the bilateral thalamus and upper brain stem in all experimental groups, and significantly high Cho/Cr ratios ($P < .05$) were observed in the right thalamus in the focal impaired awareness seizures group. There were no significant differences in metabolite ratios among the 3 patient groups ($P > .05$). The secondary generalized tonic-clonic seizures group showed a negative correlation between the duration of epilepsy and the NAA/(Cr + Cho) ratio in the bilateral thalamus ($P < .05$).

CONCLUSIONS: Metabolic alterations were observed in the brain stem and thalamus in patients with epilepsy with impaired consciousness.

ABBREVIATIONS: FIAS = focal impaired awareness seizures; PGTCs = primary generalized tonic-clonic seizures; SGTCs = secondary generalized tonic-clonic seizures

Epilepsy is a devastating illness of the nervous system. Studies have shown that uncontrolled seizures impair the quality of life of patients with epilepsy, particularly those who have seizures with impaired consciousness.^{1,2} Impaired consciousness during seizure episodes may have adverse consequences, such as accidental injuries or even death. Given its potential hazards, investigation of the underlying mechanisms of impaired consciousness during seizures is imperative.

With rapid advances in neuroimaging technology and knowledge of brain electrophysiology, structural and functional alterations in some specific areas of the brain have been shown to be associated with the status of consciousness in the course of focal impaired awareness seizures (FIAS) and generalized tonic-clonic seizures.³⁻⁵ These specific structures constitute the consciousness system,⁶⁻⁸ including the bilateral medial and lateral frontoparietal association cortex and subcortical arousal systems.

Blumenfeld et al⁹ reported widespread bilateral cerebral blood flow alterations in the course of human FIAS arising from the temporal lobe; they suggested that impaired consciousness during temporal lobe seizures may result from focal abnormal activity in the temporal and subcortical networks linked to widespread impaired function of the association cortex, as assessed by SPECT and electroencephalography. Lee et al¹⁰ have shown perfusion alterations in the bilateral thalamus and upper brain stem in patients with epilepsy

Received June 28, 2018; accepted after revision December 1.

From the Departments of Neurology (Z.T., X.L., F.T., L.H., S.L.) and Radiology (F.X.), Xiangya Hospital, Central South University, Changsha, China.

Zheren Tan and Xiaoyan Long contributed equally to this work.

Please address correspondence to Shuyu Li, MD, Central South University, Department of Neurology, 87 Xiangya Rd, Changsha 410008, China; e-mail: xysnlsy@sina.com/409685656@qq.com

<http://dx.doi.org/10.3174/ajnr.A5944>

with impaired consciousness using SPECT. Marie et al¹¹ reported that impaired consciousness during temporal lobe seizures is characterized by increased long-distance synchronization between the thalamus and parietal cortices based on stereoelectroencephalography. Xie et al¹² used DTI to demonstrate long-lasting neuronal dysfunction of the bilateral dorsal thalamus and posterosuperior aspect of the midbrain in patients with epilepsy.

¹H-MR spectroscopy is a noninvasive MR imaging technique that can detect NAA, Cho, Cr, and other metabolites in brain tissues.^{13–20} Previous studies have confirmed hippocampal metabolic alterations in patients with temporal lobe epilepsy by ¹H-MRS.^{15,21} Therefore, we hypothesized that the areas associated with consciousness may also show metabolic alterations in patients with epilepsy with impaired consciousness. However, the metabolic alterations in these brain regions of patients with epilepsy have not been characterized with multiple-voxel ¹H-MR spectroscopy. In the present study, we evaluated the specific brain regions of patients with epilepsy for metabolic alterations using multivoxel ¹H-MRS and assessed the correlation between seizure features and metabolic alterations.

MATERIALS AND METHODS

Participants

This study was conducted at the Xiangya Hospital, Central South University, Changsha, China, from August 2011 to January 2012. All patients were diagnosed with epilepsy at the Department of Neurology. The inclusion criteria were the following: 1) patients with a confirmed diagnosis of epilepsy based on clinical assessment, neuroimaging, and electroencephalography (using the latest criteria of the International League Against Epilepsy for classification of seizures²²); 2) the availability of complete clinical data and interictal MR imaging/MR spectroscopy findings; 3) a history of loss of consciousness during seizures; 4) ≥ 2 seizure episodes per year; and 5) right-handed patients with no abnormal MR imaging findings. The exclusion criteria were the following: 1) patients with a history of diseases that can affect consciousness, such as syncope, neuropsychiatric disorders, and transient ischemic attacks; 2) patients with serious systemic diseases or metabolic disorders; 3) patients with conditions that are contraindications for MR imaging; and 4) patients who refused to undergo ¹H-MRS.

Not all seizures are associated with loss of consciousness. Seizure types associated with impaired consciousness include absence seizures, focal impaired awareness seizures, and secondary generalized tonic-clonic seizures (SGTCS)⁶; the last type includes primary generalized tonic-clonic seizures (PGTCS) and SGTCSs. All 3 seizure types converge on a common set of structures, including the frontoparietal association cortex and the subcortical arousal systems in the thalamus and upper brain stem, which seem to be vital centers for loss of consciousness in epilepsy.⁶ However, the number of patients diagnosed with absence seizures at the Xiangya Hospital who fulfilled the inclusion criteria was relatively small; therefore, only data pertaining to patients with FIAS, PGTCS, and SGTCS were collected. A total of 57 patients were included in the present study and were divided into 3 groups: FIAS ($n = 18$; mean age, 28 ± 10 years); SGTCS ($n = 20$; mean age, 27 ± 13 years), and PGTCS ($n = 19$; mean age, 26 ± 10 years). The antiepileptic drugs received by the patients included

oxcarbazepine, valproic acid, and levetiracetam. Twenty-four age-, sex-, and handedness-matched healthy subjects (16 men, 8 women; mean age, 27 ± 9 years) served as the control group. None of the subjects in the control group had any systemic or neurologic illness, history of head trauma, or any family history of neurologic diseases. The protocol for this study was approved by the Research Ethics Committee of the Xiangya Hospital. Written informed consent was obtained from all subjects before their enrollment.

MR Imaging Acquisition

The study was performed on a Signa HDX 3T MR imaging scanner (GE Healthcare, Milwaukee, Wisconsin); an 8-channel head coil was used for all MR imaging/MR spectroscopy studies. All subjects initially underwent conventional brain MR imaging evaluation. We used the following sequences: axial T1-weighted (TE/TR, 24/1750 ms; 384×256 ; slice thickness, 5 mm; slice gap, 2 mm); axial T2-weighted with fast spin-echo (TE/TR, 120/4480 ms; 384×256 ; slice thickness, 5 mm; slice gap 2 mm); axial T2 FLAIR (TE/TR, 168/8500 ms; 384×256 ; slice thickness, 5 mm; slice gap, 2 mm); and sagittal T1-weighted (TE/TR, 24/2650 ms; 384×256 ; slice thickness, 5 mm; slice gap, 2 mm).

Proton MR Spectroscopy

3D chemical shift imaging using a point-resolved spectroscopy pulse was performed. To obtain the spectrum, we placed the VOI of the multivoxel MR spectroscopy sections over the brain regions related to the consciousness network. The first multivoxel section (Fig 1A–H) encompassed the bilateral inferior frontal gyrus, supramarginal gyrus, cingulate gyrus, and precuneus. The second multivoxel section (Fig 1I, -J) included the bilateral thalamus. The last multivoxel MR spectroscopy section (Fig 1K) included the upper brain stem. The positioning of the multivoxel sections (3 transverse sections) was performed on voxels graphically prescribed from conventional axial T2-weighted images. Eleven VOIs from 3 sections were obtained. The acquisition parameters used were the following: TE, 144 ms; TR, 1000 ms; NEX, 1.0; FOV, 12×12 cm; phase-encoding matrix, 8×8 ; slice thickness, 10 mm; voxel size, $15 \times 15 \times 10$ mm; degree of water suppression, $\geq 85\%$; full width at half maximum, < 10 Hz. The total scan time was 8 minutes and 36 seconds. Water suppression was also applied using the chemical shift selective suppression method.

FuncTool (GE Healthcare) was used to automatically calculate and analyze the integral peak of the corresponding chemical shift of NAA, Cr, and Cho and to measure the metabolite ratios (Figs 1–4). Spectra were excluded if they matched the following criteria: 1) water suppression of $< 85\%$, 2) full width at half maximum of ≥ 10 Hz, and 3) unstable baseline.

Statistical Analyses

Data processing and analyses were conducted using SPSS 23.0 for Windows (IBM, Armonk, New York). Continuous variables are expressed as mean \pm SD. To meet the requirements for a normal distribution, we examined each variable independently with a Shapiro-Wilk test. For homogeneity of variance, the Levene test was used. Differences between the patient and control groups with respect to the measured metabolite ratios, including NAA/Cr, NAA/(Cr + Cho), and Cho/Cr of the ROIs, were assessed

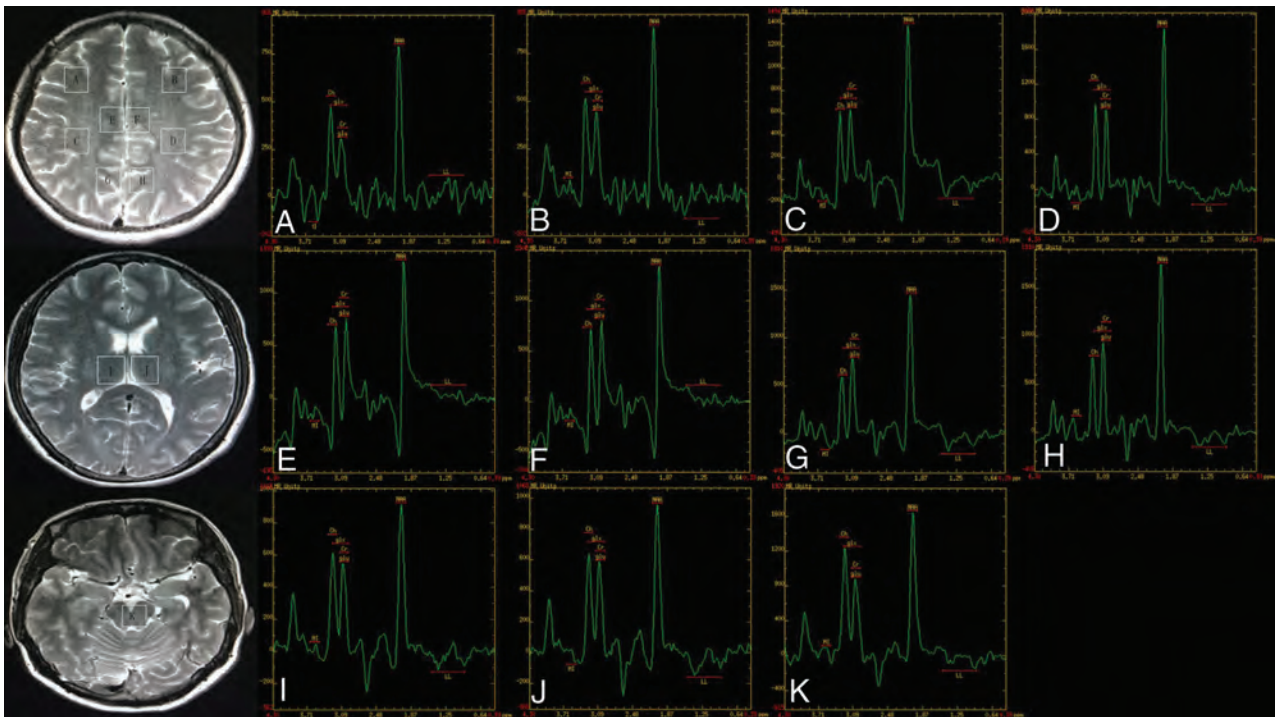


FIG 1. MR spectroscopy maps show the ROIs including the bilateral inferior frontal (A and B), supramarginal gyrus (C and D), cingulate gyrus (E and F), precuneus (G and H), thalamus (I and J), and the upper brain stem (K) of a patient with FIAS.

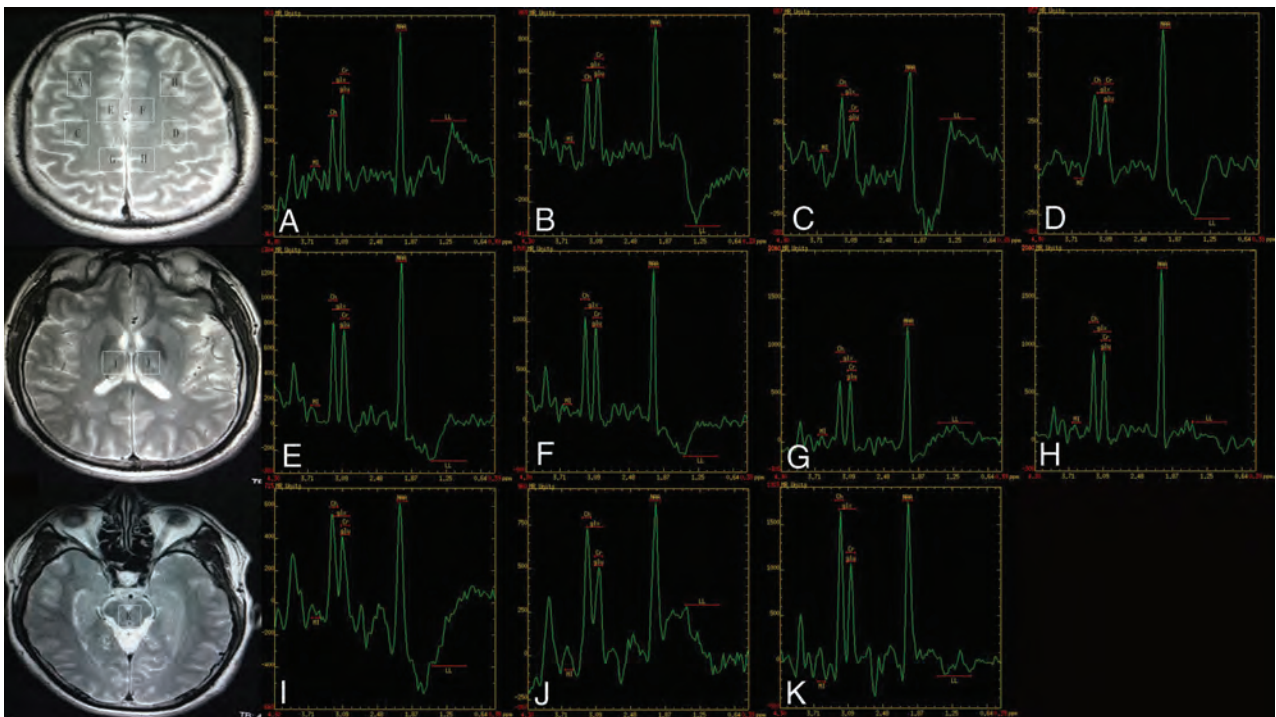


FIG 2. MR spectroscopy maps show the ROIs including the bilateral inferior frontal (A and B), supramarginal gyrus (C and D), cingulate gyrus (E and F), precuneus (G and H), thalamus (I and J), and the upper brain stem (K) of a patient with PGTCs.

using the Kruskal-Wallis ANOVA test. Pair-wise comparisons using the Dunn-Bonferroni approach are presented for any dependent variables for which the Kruskal-Wallis test was significant. Last, the Spearman rank correlation test was performed to explore the correlation between clinical parameters (epilepsy duration and seizure frequency) and corresponding metabolic alterations

of patients with 3 different seizure types. $P < .05$ was considered indicative of a significant between-group difference.

RESULTS

There was no significant difference among the 4 groups with respect to age or sex ($P > .05$ for both). The characteristics of the study

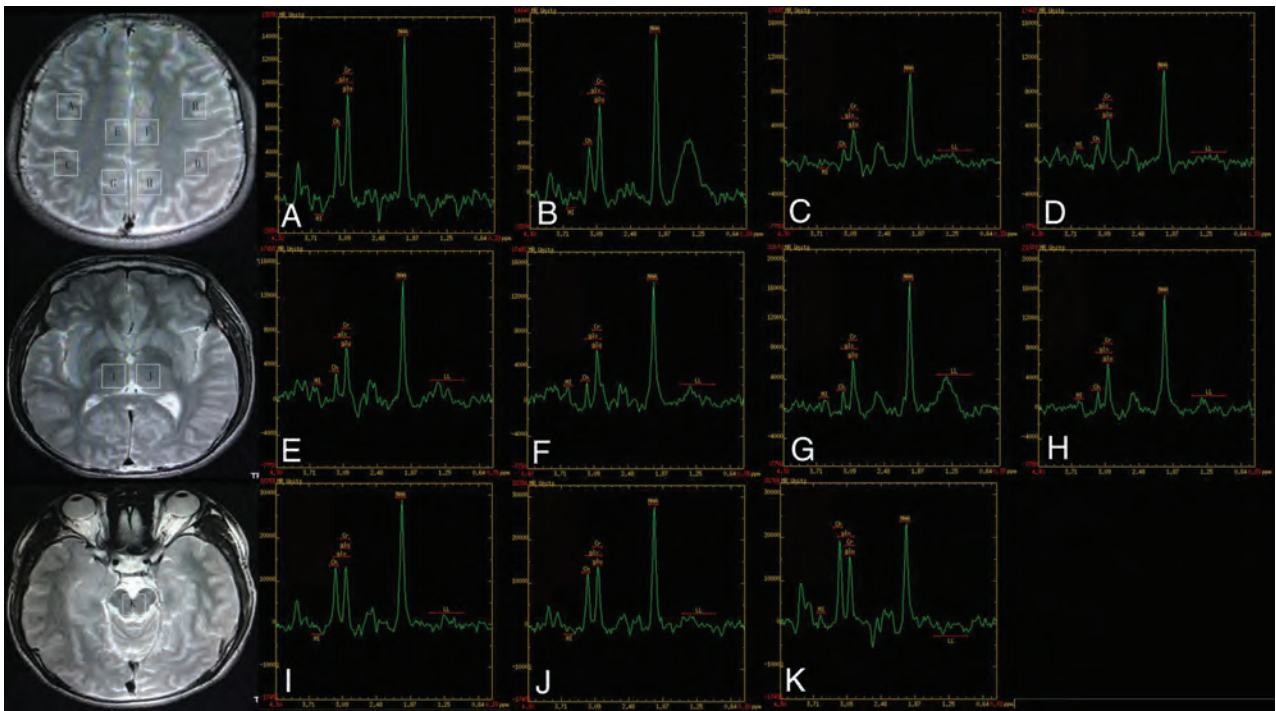


FIG 3. MR spectroscopy maps show the ROIs including the bilateral inferior frontal (A and B), supramarginal gyrus (C and D), cingulate gyrus (E and F), precuneus (G and H), thalamus (I and J), and the upper brain stem (K) of a patient with SGTCs.

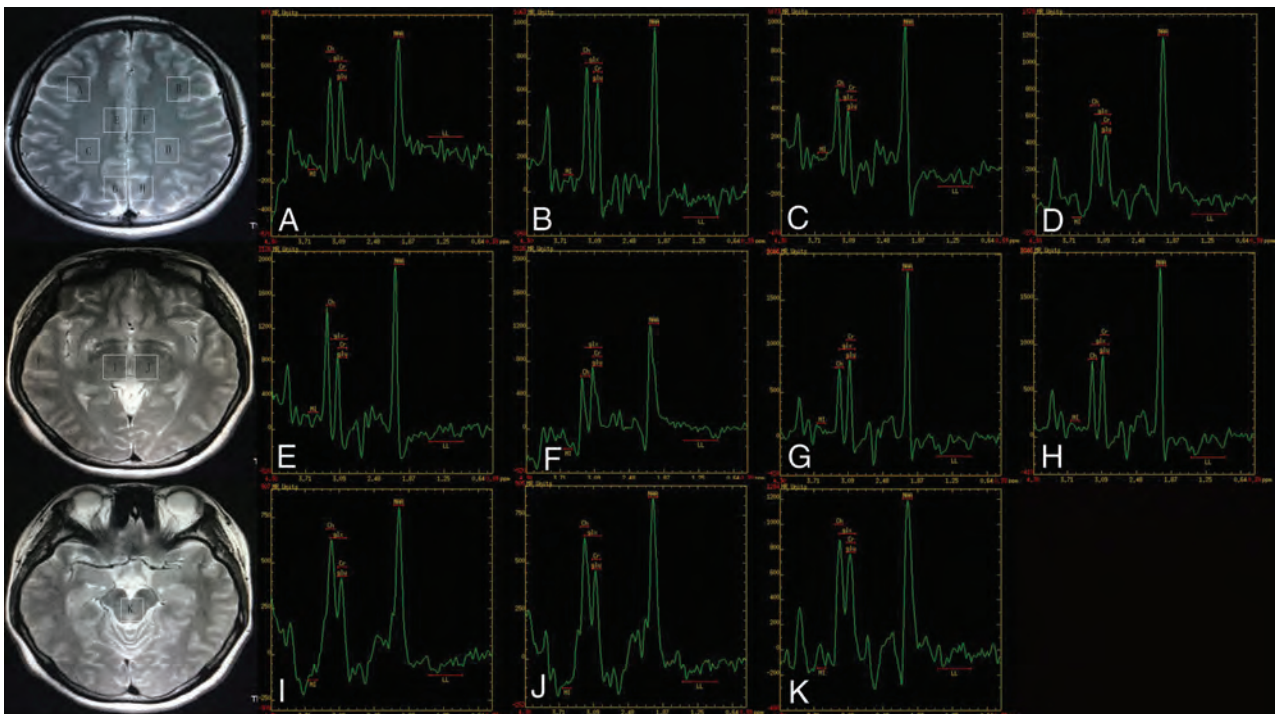


FIG 4. MR spectroscopy maps show the ROIs including the bilateral inferior frontal (A and B), supramarginal gyrus (C and D), cingulate gyrus (E and F), precuneus (G and H), thalamus (I and J), and the upper brain stem (K) of a healthy subject (control group).

subjects are shown in the Table. Significant differences were observed among the 4 groups with respect to the measured metabolite ratios in the thalamus and upper brain stem. The NAA/Cr ratio and NAA/Cho + Cr ratio in the bilateral thalamus and upper brain stem in all patient groups were significantly lower than those in the control group (Figs 5 and 6). The Cho/Cr ratio in the right thalamus in the

FIAS group was significantly higher than that in the control group (Fig 7). No significant differences were observed among the 3 patient groups with respect to the metabolite ratios.

The SGTCs group showed a negative correlation between epilepsy duration and the NAA/(Cr + Cho) ratio in the left ($P = .03$) and right thalamus ($P = .04$); however, no significant correlation

between seizure frequency and metabolic alterations was observed in any of the patient groups ($P > .05$ for both).

DISCUSSION

Multivoxel MR spectroscopy was used in the present study. Compared with single-voxel MR spectroscopy, disadvantages of multivoxel MR spectroscopy include the following: 1) relatively longer setup and scan time, 2) difficulties in obtaining homogeneous shim over the entire region, 3) lower signal-to-noise and spectral quality for individual voxels, and 4) spectral contamination from adjacent voxels. However, multivoxel MR spectroscopy offers higher spatial resolution and a larger total coverage area, which facilitate assessment of multiple regions of the brain at the same time. Therefore, multivoxel MR spectroscopy is more suitable for comparing metabolic alterations among different regions involved in the consciousness system, which conformed to the requirement of this study.

As in MR imaging, the TE affects the information obtained with MR spectroscopy. In general, long-TE methods could sup-

press short-T2 macromolecules and lipid signals, resulting in a more rectilinear baseline and more simplified spectra, which facilitate interpretation and quantitation of peak areas of major metabolites.²³⁻²⁵ Therefore, we used a long TE.

¹H-MRS has been shown to be a reliable method for measurement of intracellular metabolite concentrations (eg, NAA, Cr, and Cho) in patients with epilepsy.^{13,26} Alterations in brain metabolite levels determined by ¹H-MRS were shown to be consistent with the pathologic characteristics.²⁷

The Cr peak in the ¹H spectrum represents both creatine and its phosphorylated form, phosphocreatine. These are found in high concentrations in metabolically active tissues such as the brain that produce energy by oxidative/aerobic metabolism.²⁸ Cr is a multifunctional molecule in the brain. It reflects energy metabolism and is particularly important for the maintenance of membrane potential.^{29,30} It is well-established that the level of Cr is relatively constant in the brain under physiologic conditions; therefore, it is often used as the internal concentration reference.^{15,20,31} While brain Cr concentration stays constant in many diseases, pathologic conditions that disturb cell energetics (such as stroke, tumors, and neurodegenerative diseases) may disturb the Cr concentration.³¹

The NAA level reflects the amount and functional metabolic status of neurons; its concentration decreases with neuronal damage and/or dysfunction.^{20,26} In the

Demographic and clinical characteristics of subjects disaggregated by study group^a

	FIAS	PGTCS	SGTCS	Control
Age (yr)	28 ± 10	26 ± 10	27 ± 13	27 ± 9
Sex (M/F)	14:4	10:9	13:7	16:8
Duration of epilepsy (yr)	8.25 ± 7.85	7.56 ± 9.16	6.18 ± 7.57	—
Seizure frequency (No./yr)	55 ± 42	15 ± 25	36 ± 59	—

Note:—indicates there is no value.

^a Data represented as mean ± SD.

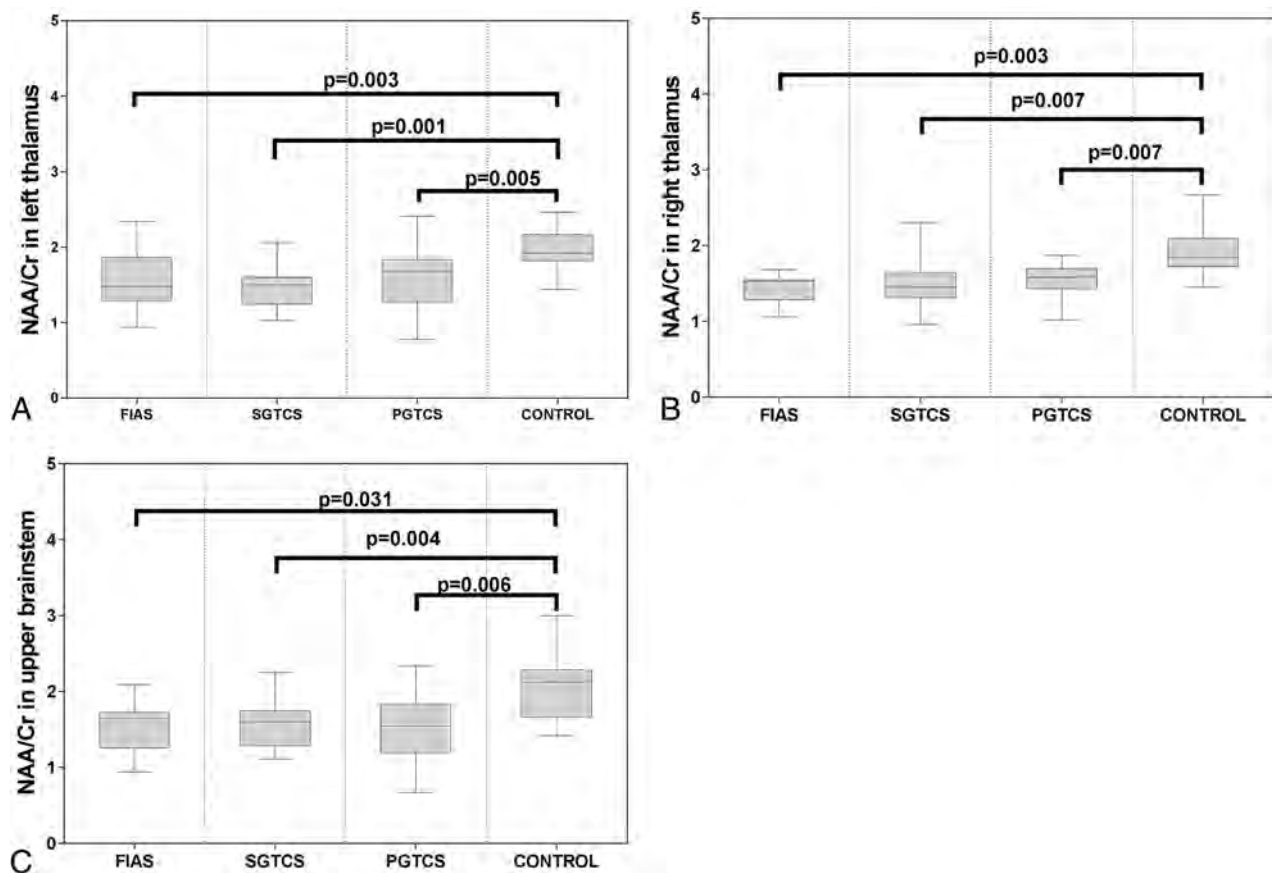


FIG 5. Boxplot for pair-wise comparison of ratios of NAA/Cr. Significant intergroup differences were observed in the bilateral thalamus (A and B) and upper brain stem (C).

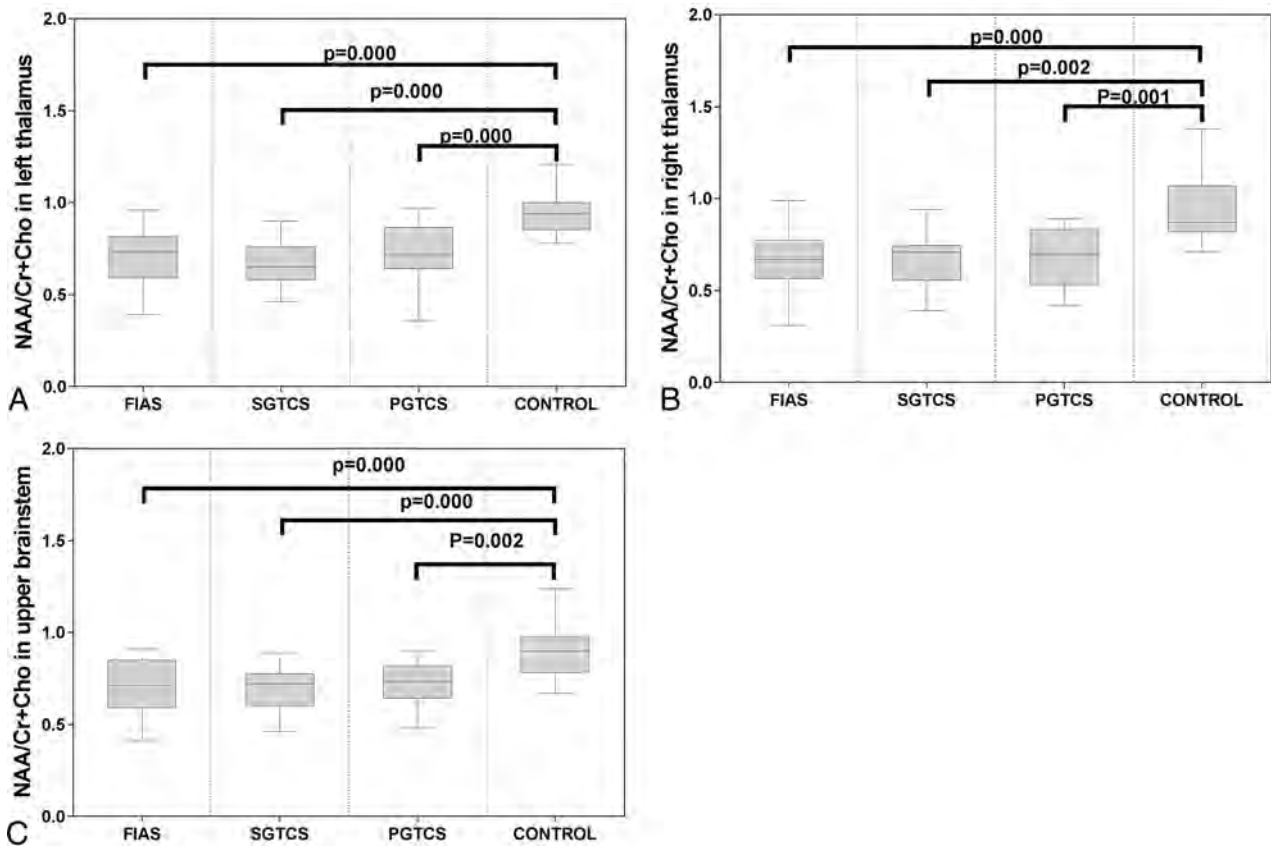


FIG 6. Boxplot for pair-wise comparison of ratios of NAA/Cr + Cho. Significant intergroup differences were observed in the bilateral thalamus (A and B) and upper brain stem (C).

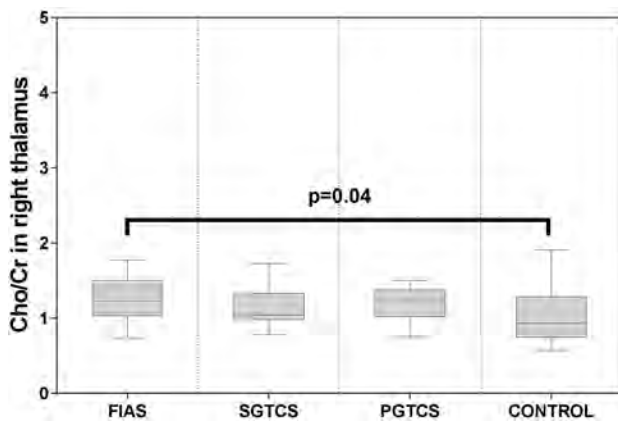


FIG 7. Boxplot for pair-wise comparison of ratios of Cho/Cr. Significant intergroup differences were observed in the right thalamus.

present study, importantly lower NAA/Cr and NAA/(Cr + Cho) ratios, which imply a decrease in the NAA level, were observed in the thalamus and upper brain stem in all 3 patient subgroups. Hammen et al²¹ and Hugg et al³² have already demonstrated the association of a reduced NAA level (as determined by ¹H-MR spectroscopy) with neuronal loss in patients with temporal lobe epilepsy; these findings indicate that the NAA spectra is a valuable predictor of cell loss. Furthermore, Duc et al³³ showed an association between altered NAA metabolism in mesial temporal lobe epilepsy and the degree of neuronal loss. However, Petroff et al³⁴ found no significant association between hippocampal neuronal loss and the cellular content of NAA

and Cr in their ¹H-MR spectroscopy study of hippocampal specimens; they proposed that neuronal dysfunction rather than neuronal loss results in a decrease in total NAA concentration due to mitochondrial damage. In a study by Dautry et al,³⁵ total NAA concentration was reduced by the mitochondrial toxin 3-nitropropionic acid in an animal model; however, no signs of neuronal cell degeneration or neuronal loss were observed in the subsequent postmortem histologic examination. On the basis of these findings, we speculate that there is neuronal loss or dysfunction in these regions. Further research is required to draw definitive conclusions in this respect.

In the present study, a significantly higher Cho/Cr ratio was observed in the right thalamus of patients in the PGTCs and FIAS groups. Cho content in the brain has been shown to mainly comprise free choline, glycerophosphocholine, and phosphocholine,³⁶ which are markers of cell membrane integrity; their concentration increases in conditions that involve cell membrane turnover or destruction (eg, tumors and demyelinating diseases).^{20,29} However, Hammen et al²¹ characterized the metabolic alterations in the hippocampus of patients with temporal lobe epilepsy using single-voxel MR spectroscopy, and the alterations in Cho did not correlate with neuronal loss in any hippocampal subregion confirmed by neuropathology. Whether an increase in the Cho/Cr ratio may indicate neuronal loss is open to debate and further research.

Consistent with this observation, previous DTI studies have shown significantly higher ADC values in the bilateral thalamus

and upper brain stem in patients with FIAS, PGTCS, and SGTCS; these findings indicate neuronal dysfunction in the bilateral dorsal thalamus and upper brain stem of these patients.¹¹ This conclusion is consistent with those of previous studies that showed that neuronal damage or dysfunction of the thalamus and upper brain stem may impair consciousness.^{37,38} Regardless of the seizure type, metabolite alterations are observed in common specific regions of the brain, which indicate their involvement in the mechanism of a variety of seizures with conscious disturbance.

However, there was no significant metabolic alteration in regions other than the bilateral thalamus and upper brain stem in all experimental groups. Compared with the spectra from voxels that cover the bilateral thalamus and upper brain stem, the spectra from other voxels are more susceptible to contamination from CSF and white matter around other ROIs, which may affect the accuracy of spectra from those voxels; this may have resulted in the observed lack of a significant metabolic alteration.

Several previous studies have described a correlation between structural abnormalities of the hippocampus and the duration of epilepsy in patients with temporal lobe epilepsy^{39,40}; this indicates that repeat seizures cause progressive damage to specific regions. Therefore, it is conceivable that patients with a longer duration of epilepsy and more frequent seizures have more severe metabolic abnormalities. Indeed, epilepsy duration and seizure frequency were shown to be associated with the level of NAA in the temporal lobe in previous studies focused on temporal lobe epilepsy.^{41,42} Consistent with this finding, we found a significant inverse correlation between epilepsy duration and the NAA/(Cr + Cho) ratio in the bilateral thalamus in the SGTCS group, but not in the FIAS group. In the present study, seizure frequency was not a significant predictor of the degree of metabolic abnormality; however, the lack of association may be attributable to the small sample size. Thus, the association between seizure frequency and the degree of metabolic abnormality requires further study involving a larger cohort of patients.

In several previous studies, the influence of antiepileptic drugs was analyzed. However, no statistically significant effects of antiepileptic drugs were found in most previous studies. Simister et al¹³ found no significant difference in gamma-aminobutyric acid plus homocarnosine values between patients with idiopathic generalized epilepsy receiving antiepileptic drugs and those not receiving antiepileptic drugs. Lin et al¹⁴ found no significant effects of medication on NAA/Cr. Whether antiepileptic drugs have an effect on alterations in brain metabolites is open to debate and further research.

In the present study, significantly lower NAA/Cr and NAA/(Cr + Cho) ratios were observed in the thalamus in all patient groups, while a significantly high Cho/Cr ratio was only observed in the right thalamus ($P < .05$) in the FIAS group. However, when patients with PGTCS were compared with healthy subjects, a trend toward higher values of Cho/Cr ($P = .06$) was observed in the PGTCS group. In addition, previous studies that focused on idiopathic generalized epilepsy or generalized tonic-clonic seizures have demonstrated the thalamic metabolic abnormalities using ¹H-MRS.^{43,44} These findings indicate that the thalamus may be involved in the underlying mechanism of impaired con-

sciousness in all forms of epilepsy that were studied in our research.

Several studies have described a relationship between structural abnormalities and the duration of epilepsy.^{39,41} In addition, previous neuroimaging studies have reported a negative association between epilepsy duration and thalamic NAA/Cr ratios.^{14,43} It could be expected that patients with a longer duration of epilepsy may show more severe metabolic abnormalities. However, our data failed to show any association between thalamic metabolic alterations and epilepsy duration in any of the groups except the SGTCS group. It will therefore be necessary to replicate the findings in a larger population.

Some limitations of our study should be noted. These include the single-center design, small sample size, and heterogeneity among the patient groups with respect to antiepileptic treatment and the interval between the last known seizure and the scan. These limitations may have impacted the results such as the observed lack of correlation between seizure frequency and metabolic alterations. Use of FuncTool to analyze the data is suboptimal; a more sophisticated approach such as the LCModel (<http://www.s-provencher.com/lcmodel.shtml>) would be preferable because it also includes uncertainty estimates. Cr or Cr + Cho concentrations were used as an internal concentration reference to simplify quantification; however, it is difficult to rule out the possibility that the metabolic abnormalities were due to elevated Cr and/or Cho concentrations rather than to the reduced NAA concentration. Therefore, an alternative would be to use water concentration as an internal reference in further research. A small proportion of the data were from the edge of the volume, which may have impacted the accuracy of the spectra.

Further studies are required to examine the pre- and posttreatment metabolic alterations in epilepsy associated with loss of consciousness and to determine the influence of other factors on metabolic alterations in regions associated with loss of consciousness (eg, the type of antiepileptic drug and the interval between the last seizure and the scan).

CONCLUSIONS

¹H-MRS is a noninvasive neuroradiology technique that is more sensitive than routine brain MR imaging for the detection of metabolic alterations in patients with epilepsy. Our research demonstrated altered levels of NAA and Cho in the thalamus and upper brain stem of patients with epilepsy, which is indicative of neuronal dysfunction and/or neuronal loss. Neuronal dysfunction in these areas may contribute to the loss of consciousness in these patients. Furthermore, patients with a longer duration of epilepsy may have more severe metabolic abnormalities.

ACKNOWLEDGMENTS

We thank all our colleagues at the Department of Radiology for the permission to use GE Signa HDX 3T MR imaging scanner.

REFERENCES

1. Sperling MR. **The consequences of uncontrolled epilepsy.** *CNS Spectr* 2004;9:98–101, 106–09 Medline
2. Vickrey BG, Berg AT, Sperling MR, et al. **Relationships between seizure severity and health-related quality of life in refractory localization-related epilepsy.** *Epilepsia* 2000;41:760–64 CrossRef Medline

3. Bagshaw AP, Cavanna AE. **Brain mechanisms of altered consciousness in focal seizures.** *Behav Neurol* 2011;24:35–41 CrossRef Medline
4. Cavanna AE, Monaco F. **Brain mechanisms of altered conscious states during epileptic seizures.** *Nat Rev Neurol* 2009;5:267–76 CrossRef Medline
5. Seri S, Brazzo D, Thai NJ, et al. **Brain mechanisms of altered consciousness in generalised seizures.** *Behav Neurol* 2011;24:43–46 CrossRef Medline
6. Blumenfeld H. **Impaired consciousness in epilepsy.** *Lancet Neurol* 2012;11:814–26 CrossRef Medline
7. Yu L, Blumenfeld H. **Theories of impaired consciousness in epilepsy.** *Ann of N Y Acad Sci* 2009;1157:48–60 CrossRef Medline
8. Blumenfeld H. **Epilepsy and the consciousness system: transient vegetative state?** *Neurol Clin* 2011;29:801–23 CrossRef Medline
9. Blumenfeld H, McNally KA, Vanderhill SD, et al. **Positive and negative network correlations in temporal lobe epilepsy.** *Cereb Cortex* 2004;14:892–902 CrossRef Medline
10. Lee KH, Meador KJ, Park YD, et al. **Pathophysiology of altered consciousness during seizures: subtraction SPECT study.** *Neurology* 2002;59:841–46 CrossRef Medline
11. Marie A, Luc V, Jean R, et al. **Impaired consciousness during temporal lobe seizures is related to increased long-distance cortical-subcortical synchronization.** *Brain* 2009;132:2091–101 CrossRef Medline
12. Xie F, Xing W, Wang X, et al. **Altered states of consciousness in epilepsy: a DTI study of the brain.** *Int J Neurosci* 2017;127:667–72 CrossRef Medline
13. Simister RJ, McLean MA, Barker GJ, et al. **A proton magnetic resonance spectroscopy study of metabolites in the occipital lobes in epilepsy.** *Epilepsia* 2003;44:550–58 CrossRef Medline
14. Lin K, Carrete H Jr, Lin J, et al. **Magnetic resonance spectroscopy reveals an epileptic network in juvenile myoclonic epilepsy.** *Epilepsia* 2009;50:1191–200 CrossRef Medline
15. Mueller SG, Ebel A, Barakos J, et al. **Widespread extrahippocampal NAA/(Cr+Cho) abnormalities in TLE with and without mesial temporal sclerosis.** *J Neurol* 2011;258:603–12 CrossRef Medline
16. Kabay SC, Gumustas OG, Karaman HO, et al. **A proton magnetic resonance spectroscopic study in juvenile absence epilepsy in early stages.** *Eur J Paediatr Neurol* 2010;14:224–28 CrossRef Medline
17. Striano P, Caranci F, Di Benedetto R, et al. **(1)H-MR spectroscopy indicates prominent cerebellar dysfunction in benign adult familial myoclonic epilepsy.** *Epilepsia* 2009;50:1491–97 CrossRef Medline
18. de Araújo Filho GM, Lin K, Lin J. **Are personality traits of juvenile myoclonic epilepsy related to frontal lobe dysfunctions? A proton MRS study.** *Epilepsia* 2009;50:1201–09 CrossRef Medline
19. Hajek M, Dezortova M, Krsek P, et al. **(1)H MR spectroscopy in epilepsy.** *Eur J Radiol* 2008;67:258–67 CrossRef Medline
20. McLean MA, Cross JJ. **Magnetic resonance spectroscopy: principles and applications in neurosurgery.** *Br J Neurosurg* 2009;23:5–13 Medline
21. Hammen T, Hildebrandt M, Stadlbauer A, et al. **Non-invasive detection of hippocampal sclerosis: correlation between metabolite alterations detected by (1)H-MRS and neuropathology.** *NMR Biomed* 2008;21:545–52 CrossRef Medline
22. Fisher RS, Cross JH, French JA, et al. **Operational classification of seizure types by the International League Against Epilepsy: Position Paper of the ILAE Commission for Classification and Terminology.** *Epilepsia* 2017;58:522–30 CrossRef Medline
23. Hancu I, Zimmerman EA, Sailasuta N, et al. **(1)H-MR spectroscopy using TE averaged PRESS: a more sensitive technique to detect neurodegeneration associated with Alzheimer's disease.** *Magn Reson Med* 2005;53:777–82 CrossRef Medline
24. Hurd R, Sailasuta N, Srinivasan R, et al. **Measurement of brain glutamate using TE-averaged PRESS at 3T.** *Magn Reson Med* 2004;51:435–40 CrossRef Medline
25. Cendes F, Knowlton RC, Novotny E. **Magnetic resonance spectroscopy in epilepsy: clinical issues.** *Epilepsia* 2002;43(Suppl 1):32–39
26. Xu M, Ergene E, Zagardo M, et al. **Proton MR spectroscopy in patients with structural MRI-negative temporal lobe epilepsy.** *J Neuroimaging* 2015;25:1030–37 CrossRef Medline
27. Maton BM, Kuzniecky RI. **Proton MRS: N-acetyl aspartate, creatine, and choline.** *Adv Neurol* 2000;83:253–59 Medline
28. Stovell MG, Yan JL, Sleight A, et al. **Assessing metabolism and injury in acute human traumatic brain injury with magnetic resonance spectroscopy: current and future applications.** *Front Neurol* 2017;8:426 CrossRef Medline
29. Wyss M, Kaddurah-Daouk R. **Creatine and creatinine metabolism.** *Physiol Rev* 2000;80:1107–213 CrossRef Medline
30. Béard E, Braissant O. **Synthesis and transport of creatine in the CNS: importance for cerebral functions.** *J Neurochem* 2010;115:297–313 CrossRef Medline
31. Rackayova V, Cudalbu C, Pouwels PJ, et al. **Creatine in the central nervous system: from magnetic resonance spectroscopy to creatine deficiencies.** *Anal Biochem* 2017;529:144–57 CrossRef Medline
32. Hugg JW, Laxer KD, Matson GB, et al. **Neuron loss localizes human temporal lobe epilepsy by in vivo proton magnetic resonance spectroscopic imaging.** *Ann Neurol* 1993;34:788–94 CrossRef Medline
33. Duc CO, Trabesinger AH, Weber OM, et al. **Quantitative (1)H MRS in the evaluation of mesial temporal lobe epilepsy in vivo.** *Magn Reson Imaging* 1998;16:969–79 CrossRef Medline
34. Petroff OA, Errante LD, Kim JH, et al. **N-acetyl-aspartate, total creatine, and myo-inositol in the epileptogenic human hippocampus.** *Neurology* 2003;60:1646–51 CrossRef Medline
35. Dautry C, Vaufray F, Brouillet E, et al. **Early N-acetyl aspartate depletion is a marker of neuronal dysfunction in rats and primates chronically treated with the mitochondrial toxin 3-nitropropionic acid.** *J Cereb BloodFlow Metab* 2000;20:789–99 CrossRef Medline
36. Barker PB, Breiter SN, Soher BJ, et al. **Quantitative proton spectroscopy of canine brain: in vivo and in vitro correlations.** *Magn Reson Med* 1994;32:157–63 CrossRef Medline
37. Greenberg MK, Barsan WG, Starkman S. **Neuroimaging in the emergency patient presenting with seizure.** *Neurology* 1996;47:26–32 CrossRef Medline
38. Greicius MD, Krasnow B, Reiss AL, et al. **Functional connectivity in the resting brain: a network analysis of the default mode hypothesis.** *Proc Natl Acad Sci U S A* 2003;100:253–58 CrossRef Medline
39. McDonald CR, Hagler DJ Jr, Ahmadi ME, et al. **Regional neocortical thinning in mesial temporal lobe epilepsy.** *Epilepsia* 2008;49:794–803 CrossRef Medline
40. Coan A, Appenzeller S, Bonilha L, et al. **Seizure frequency and lateralization affect progression of atrophy in temporal lobe epilepsy.** *Neurology* 2009;73:834–42 CrossRef Medline
41. Garcia PA, Laxer KD, van der Grond J, et al. **Correlation of seizure frequency with N-acetyl-aspartate levels determined by (1)H magnetic resonance spectroscopic imaging.** *Magn Reson Imaging* 1997;15:475–78 CrossRef Medline
42. Tasch E, Cendes F, Li L, et al. **Neuroimaging evidence of progressive neuronal loss and dysfunction in temporal lobe epilepsy.** *Ann Neurol* 1999;45:568–76 CrossRef Medline
43. Bernasconi A, Bernasconi N, Natsume J, et al. **Magnetic resonance spectroscopy and imaging of the thalamus in idiopathic generalized epilepsy.** *Brain* 2003;126:2447–54 CrossRef Medline
44. Haki C, Gümüştaş OG, Bora I, et al. **Proton magnetic resonance spectroscopy study of bilateral thalamus in juvenile myoclonic epilepsy.** *Seizure* 2007;16:287–95 CrossRef Medline

Utility of Dynamic Susceptibility Contrast Perfusion-Weighted MR Imaging and ¹¹C-Methionine PET/CT for Differentiation of Tumor Recurrence from Radiation Injury in Patients with High-Grade Gliomas

Z. Qiao, X. Zhao, K. Wang, Y. Zhang, D. Fan, T. Yu, H. Shen, Q. Chen, and L. Ai



ABSTRACT

BACKGROUND AND PURPOSE: Both ¹¹C-methionine PET/CT and DSC-PWI could be used to differentiate radiation injury from recurrent brain tumors. Our aim was to assess the performance of MET PET/CT and DSC-PWI for differentiation of recurrence and radiation injury in patients with high-grade gliomas and to quantitatively analyze the diagnostic values of PET and PWI parameters.

MATERIALS AND METHODS: Forty-two patients with high-grade gliomas were enrolled in this study. The final diagnosis was determined by histopathologic analysis or clinical follow-up. PWI and PET parameters were recorded and compared between patients with recurrence and those with radiation injury using Student *t* tests. Receiver operating characteristic and logistic regression analyses were used to determine the diagnostic performance of each parameter.

RESULTS: The final diagnosis was recurrence in 33 patients and radiation injury in 9. PET/CT showed a patient-based sensitivity and specificity of 0.909 and 0.556, respectively, while PWI showed values of 0.667 and 0.778, respectively. The maximum standardized uptake value, mean standardized uptake value, tumor-to-background maximum standardized uptake value, and mean relative CBV were significantly higher for patients with recurrence than for patients with radiation injury. All these parameters showed a high discriminative power in receiver operating characteristic analysis. The optimal cutoff values for the tumor-to-background maximum standardized uptake value and mean relative CBV were 1.85 and 1.83, respectively, and corresponding sensitivities and specificities for the diagnosis of recurrence were 0.97 and 0.667 and 0.788 and 0.88, respectively. Areas under the curve for the tumor-to-background maximum standardized uptake value and mean relative CBV were 0.847 ± 0.077 and 0.845 ± 0.078 , respectively. Combined assessment of the tumor-to-background maximum standardized uptake value and mean relative CBV showed the largest area under the curve (0.953 ± 0.031), with corresponding sensitivity and specificity of 0.848 and 1.0, respectively.

CONCLUSIONS: Both ¹¹C-methionine PET/CT and PWI are equally accurate in the differentiation of recurrence from radiation injury in patients with high-grade gliomas, and a combination of the 2 modalities could result in increased diagnostic accuracy.

ABBREVIATIONS: AUC = area under the curve; MET = ¹¹C-methionine; HGG = high-grade glioma; max = maximum; rCBV = relative CBV; SUV = standardized uptake value; TBR = tumor-to-background

Gliomas are the most common primary brain tumors. Tumor resection followed by postoperative chemotherapy and radiation therapy is the primary treatment for gliomas. However, radiation therapy may damage normal brain tissue and result in

adverse effects involving the brain. Classically, radiation injury can be classified into acute and delayed reactions. Radiation-induced necrosis is the most severe form of radiation injury and usually occurs 3–12 months after radiation therapy, though it can also occur years after treatment. The incidence of radiation-induced necrosis is reportedly 3%–24%.¹ The recurrence rate for gliomas, particularly high-grade gliomas (HGGs), is extremely high. The differentiation of tumor recurrence from radiation injury is an important part of clinical management. However, both recurrent active tumors and necrotic inflammation result in

Received May 29, 2018; accepted after revision November 24.

From the Departments of Nuclear Medicine (Z.Q., X.Z., K.W., Y.Z., D.F., Q.C., L.A.) and Radiology (H.S.), Beijing Tian Tan Hospital, Capital Medical University, Beijing, China; Department of Medical Imaging (T.Y.), Cancer Hospital of China Medical University, Shenyang, China; and Department of Medical Imaging (T.Y.), Liaoning Cancer Hospital and Institute, Shenyang, China.

Zhen Qiao and Xiaobin Zhao contributed equally to this work and should be considered co-first authors

This work was supported by the Beijing Natural Science Foundation(7184207); the Clinical Capability Construction Project for Liaoning Provincial Hospitals (LNCCC-B06–2014); the National Basic Research Program of China (2015CB755500); and the Youth Research Fund of Beijing Tian Tan Hospital (2016-YQN-02).

Please address correspondence to Lin Ai, Beijing Tian Tan Hospital, Capital Medical University, 6, Tiantanxili, Beijing, 100050, China; e-mail: ailin@bjtth.org

Indicates open access to non-subscribers at www.ajnr.org

Indicates article with supplemental on-line table.

<http://dx.doi.org/10.3174/ajnr.A5952>

breakdown of the BBB; therefore, both conditions show similar enhancement in gadolinium-enhanced MR imaging. As a result, discrimination between them can be challenging. More advanced imaging strategies have thus been developed, mainly advanced MR imaging techniques and novel PET radiotracers to target the biologic activity of tumor cells.^{2,3}

PWI can demonstrate the characteristics of the vascular physiology and hemodynamics of tumors and has been used to differentiate recurrence from radiation injury.⁴⁻⁷ Dynamic contrast-enhanced MR imaging can quantitatively measure the permeability of immature microvessels in tumors by generating quantitative parameters such as the volumetric transfer constant, fractional plasma volume, and fractional volume of the extracellular extravascular space. Dynamic contrast-enhanced imaging is used less frequently in clinical practice. DSC-MR imaging is the most commonly used perfusion MR imaging technique in clinical practice; it is a standard method for measuring cerebral blood volume and cerebral blood flow. Because of treatment-induced vascular endothelial damage and coagulation necrosis, radiation injury is associated with hypoperfusion. Accordingly, the relative CBV (rCBV) tends to be lower with radiation necrosis than with tumor recurrence.

Amino acid PET is useful for the noninvasive differentiation of tumor and nontumoral lesions because tumors have significantly higher uptake than nontumoral tissue. ¹¹C-methionine (MET) is one of the most widely studied amino acid tracers for brain tumor imaging. The uptake of MET by recurrent tumors is associated with cellular proliferation and microvessel count and is different from uptake by radiation necrosis lesions, which is associated with passive diffusion across the broken BBB. Therefore, MET PET/CT has the potential to differentiate radiation injury from recurrent brain tumors. Previous studies have demonstrated that PWI might be similar or even superior to PET/CT for the differentiation of recurrence from radiation injury.^{8,9} However, each technique has its strengths and limitations, and validation in clinical trials is mandatory for the successful implementation of these techniques.⁹⁻¹¹

We conducted the present study to evaluate the usefulness of MET PET/CT and PWI for the differentiation of recurrence from radiation injury in patients with HGGs and quantitatively analyze the diagnostic values of MET PET/CT and PWI parameters. We also aimed to assess the combined diagnostic performance of the 2 modalities with regard to the therapeutic response of tumors.

MATERIALS AND METHODS

Patient Population

This retrospective study was approved by the ethics committee of Beijing Tiantan Hospital. The subjects were selected from a total of 235 patients with gliomas who underwent MET PET/CT at our institution between June 2015 and June 2017. The inclusion criteria were as follows: histopathologic diagnosis of HGGs (III-IV) according to the World Health Organization criteria; use of radiation therapy (3D conformal radiation therapy) or gamma knife surgery followed by tumor resection, with an interval of >3 months between radiation therapy and PET scanning; perfor-

mance of contrast-enhanced and DSC-PWI, with an interval of <1 month between PET and PWI; and a clinical follow-up duration of >3 months. The exclusion criterion consisted of an unclear follow-up diagnosis. Ultimately, 42 patients were enrolled in our study.

Determination of Lesions

Clinical follow-up, follow-up MR imaging, or histopathologic analysis was performed to determine whether the lesions represented recurrence or radiation injury. Recurrence was defined by any of the following: progression of symptoms or death caused by brain tumor progression; a progressive increase (diameter increase, >25%) in the size of the contrast-enhancing lesion with or without antitumor treatment, which was consistent with an increase in the MET uptake area on follow-up MR imaging studies (with an interval of no less than 3 months), after the initial progress seen on the first follow-up MR imaging or new enhancing lesions on follow-up MR imaging; pathologic confirmation after tumor resection or biopsy; and progression of symptoms or a progressive increase in the lesion size (diameter increase, <25%) that could not be attributed to radiation injury or other disease. Radiation injury was diagnosed by pathologic examination or by a decrease in the size or stabilization of the contrast-enhancing lesion for a minimum of 6 months on follow-up MR imaging studies for patients without antitumor therapy.

PET/CT Protocol and Analysis

MET was synthesized by a solid-phase reaction. ¹¹CO₂ was obtained by cyclotron (HM-10; Sumitomo, Hokkaido, Japan) and transferred to a carbon multifunctional synthesis module (CFN-C; Sumitomo, Tokyo, Japan). After methylation, a highly reactive methylation precursor, ¹¹CH₃I, was obtained and then reacted with L-cysteine thioketone (Sigma, St. Louis, Missouri) to obtain MET at room temperature. MET was sterilized by passage through 0.22- μ m sterile filters before injection. PET/CT was performed using the Discovery Elite (GE Healthcare, Milwaukee, Wisconsin) 10 minutes after intravenous injection of 370-738.8 MBq of MET using the 3D acquisition mode for a 10-minute static scan. The data were reconstructed using the ordered subset expectation maximization algorithm, and the images were viewed on an AW4.5 Workstation (GE Healthcare).

Fused PET/CT images were visually assessed by 2 nuclear medicine physicians using contrast-enhanced brain MR images as references. Finally, the results of visual assessments were reclassified by consensus between 2 observers with respective experience in nuclear medicine of 6 and 13 years. The regional MET uptake was expressed as the standardized uptake value (SUV). An ROI for each lesion was outlined by 40% of the isocontour of the uptake maximum. In case no abnormality was detected on PET, the ROI was drawn on the area corresponding to the abnormality on MR imaging. As a normal control, an identical ROI was drawn over the contralateral cerebral cortex. The mean and maximum SUVs (SUV_{mean} and SUV_{max}, respectively) were measured for each ROI. The tumor-to-background SUV_{max} ratio (TBR_{SUV_{max}}) was defined as the ratio of the SUV_{max} of the lesion to the SUV_{max} of the contralateral normal cortex. In case of multiple lesions, the lesion with the highest uptake was analyzed.

MR Image Acquisition and Analysis

DSC-PWI was performed for all patients using an echo-planar imaging sequence during intravenous injection of the contrast agent. One of 2 MR imaging devices was used (Tim Trio and Verio; Siemens, Erlangen, Germany). The PWI parameters were as follows: TR, 1400–1500 ms; TE, 30–32 ms; echo-train length, 1 *k*-space; position angle, 90°; matrix, 128 × 128. The MR imaging data were digitally transferred to a personal computer for further analyses. Dynamic curves were determined using a software package (Perfusion Mismatch Analyzer, Version 5.0.0.0, ASIST-Japan; <http://asist.umin.jp/index-e.htm>). CBV, TTP, MTT, and CBF maps were extracted using numeric integration of the curves. These maps, mainly CBF and CBV maps, were visually assessed by 2 physicians with respective experience in radiology of 7 and >15 years. ROIs of lesions were drawn on each slice of the CBV maps by connecting the dotted lines with the software using contrast-enhanced MR images as a reference. Areas containing small vessels and necrosis were carefully excluded from the ROIs. Control ROIs were drawn in the contralateral normal region, excluding lesions or vessels. The relative parameters were calculated from the lesion-to-normal ratio. The mean rCBV (rCBV_{mean}) of lesions was calculated from the mean of the relative parameters for each slice. In case of multiple lesions, the lesion with the highest rCBV_{mean} was analyzed.

Statistical Analysis

Continuous parameters with normal distribution were presented as means ± SDs. Mean differences were assessed between the 2 groups, and the significance of mean differences was evaluated using the Student *t* test. The McNemar test was used to compare differences in the diagnostic performance between the 2 modalities. Logistic regression analysis was used to determine the best predictors of recurrence or radiation injury, and receiver operating characteristic analysis was performed to determine the best cutoff values for parameters that proved to be substantial predictors of recurrence or radiation injury. All statistical analyses were performed using SPSS software, Version 24 (IBM, Armonk, New York). We also determined the diagnostic performance of a combination of the best predictors. Areas under the receiver operating characteristic curves (AUCs) for different parameters were compared with the DeLong test¹² using MedCalc for Windows (MedCalc Software, Mariakerke, Belgium). *P* < .05 indicated statistical significance.

RESULTS

The demographic and clinical characteristics of the included patients are shown in the On-line Table. Four of 42 patients were treated with temozolomide (patient Nos. 1, 11, 16, and 27). Of the 42 patients, 33 and 9 were diagnosed with recurrence and radiation injury, respectively, by histopathologic analysis (*n* = 9 and *n* = 1, respectively) or clinical follow-up (*n* = 24 and *n* = 8, respectively).

Visual Assessments of MET PET/CT images

Findings for 34 of the 42 patients were suggestive of recurrence, 6 scans were equivocal, and 2 scans were negative for recurrent tumors. When equivocal scans were reclassified as having negative findings, MET PET/CT showed a patient-based sensitivity

Table 1: Results of visual assessments of MET PET/CT for patients with HGGs

Final Diagnosis	Visual Assessment			Total
	Positive	Equivocal	Negative	
Recurrence	30	3	0	33
Radiation injury	4	3	2	9
Total	34	6	2	42

Table 2: Results of visual assessments of PWI for patients with HGGs

Final Diagnosis	Visual Assessment			Total
	Positive	Equivocal	Negative	
Recurrence	22	8	3	33
Radiation injury	2	1	6	9
Total	24	9	9	42

Table 3: Results of semiquantitative analysis of MET PET/CT and PWI parameters for the differentiation of recurrence from radiation injury in patients with HGGs

	Final Diagnosis		<i>P</i> Value ^a
	Recurrence	Radiation Injury	
SUV _{max}	5.10 ± 2.41	2.41 ± 1.67	.003
SUV _{mean}	2.83 ± 1.27	1.39 ± 0.9	.003
TBRSUV _{max}	3.48 ± 1.17	1.96 ± 0.96	.003
rCBV _{mean}	2.68 ± 1.14	1.33 ± 0.77	.004

^a All *P* values for discrimination between recurrence and radiation injury are significant.

and specificity of 0.909 and 0.556, respectively, with corresponding positive and negative predictive values of 0.882 and 0.625, respectively. Table 1 shows the findings of visual assessments of PET/CT images.

Visual Assessments of DSC-PWI

The findings of visual assessments of PWI are summarized in Table 2. Findings for 24 of the 42 patients were suggestive of recurrence, 9 scans were equivocal, and 9 were negative for recurrent tumors. When equivocal scans were reclassified as having negative findings, PWI showed a patient-based sensitivity and specificity of 0.667 and 0.778, respectively, with corresponding positive and negative predictive values of 0.917 and 0.389, respectively.

Results of Semiquantitative Analysis

Detailed data pertaining to semiquantitative analysis of imaging parameters for the 2 groups are summarized in Table 3. SUV_{max}, SUV_{mean}, TBRSUV_{max}, and rCBV_{mean} were significantly higher for patients with recurrence than for patients with radiation injury. All the above parameters showed a significant discriminative power in receiver operating characteristic analysis (Fig 1). The optimal cutoff values for TBRSUV_{max} and rCBV_{mean} were determined as 1.85 and 1.83, respectively. When 1.85 was used as the optimal cutoff TBRSUV_{max} value for differentiating recurrence from radiation injury, the sensitivity and specificity of MET PET/CT were 0.970 and 0.667, respectively. When 1.83 was used as the optimal cutoff value for rCBV_{mean}, PWI showed a patient-based sensitivity and specificity of 0.788 and 0.889, respectively. The McNemar test revealed statistically significant differences between TBRSUV_{max} and rCBV_{mean} (*P* = .039). Disagreement between MET PET/CT and PWI was observed for 8 patients with recurrence and 4 with radiation injury (Figs 2 and 3). No patient

with recurrence had negative findings on both MET PET/CT and perfusion-weighted images, while no patient with radiation injury showed positive findings on both image sets (Table 4).

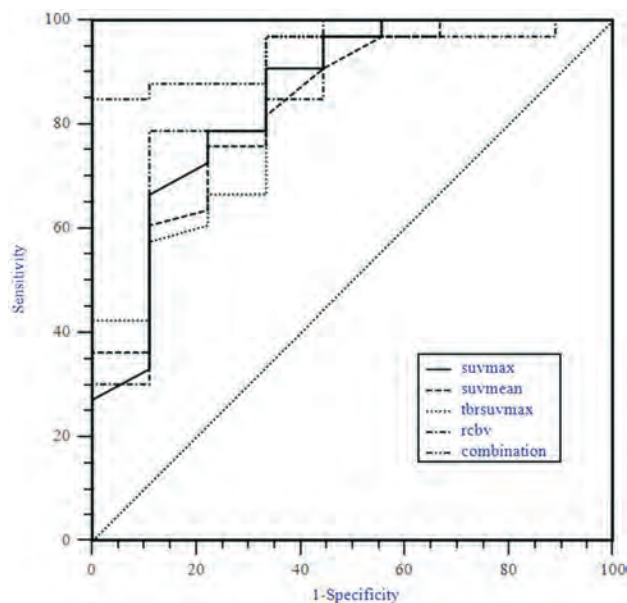


FIG 1. Receiver operating curves for perfusion-weighted MR imaging and MET PET/CT parameters for the differentiation of recurrence and radiation injury in patients with high-grade gliomas.

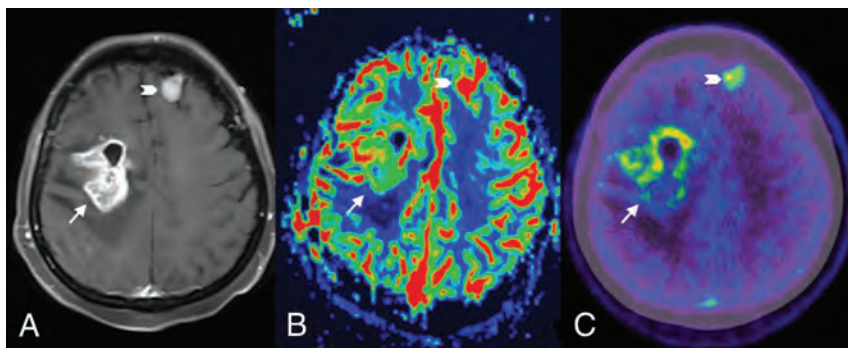


FIG 2. Contrast-enhanced T1-weighted MR image (A) and a relative CBV map (B) and an MET PET/CT image (C) for a 41-year-old woman with recurrent glioblastoma. The lesion in the right frontal lobe (arrow) shows enhancement (A) and positive findings on both the rCBV map (B) and MET PET/CT image (C). The lesion localized in the left frontal lobe (chevron) might be a meningioma, which has been stable for several years.

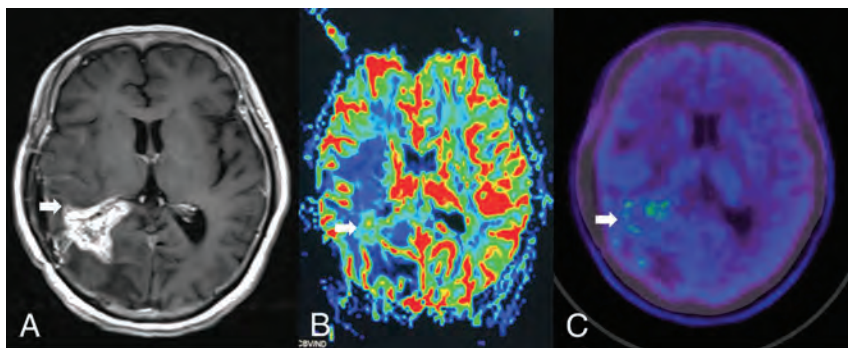


FIG 3. Contrast-enhanced T1-weighted MR image (A) and relative CBV map (B) and MET PET/CT image (C) for a 44-year-old man with necrosis. The lesion in the right parietal lobe (arrow) shows enhancement (A) and negative findings on both the rCBV map (B) and the MET PET/CT image (C).

Agreement between visual assessments and semiquantitative analyses was observed for 37 of the 42 (88%) patients when MET PET/CT was used and for 29 of the 42 (69%) patients when PWI was used. The corresponding κ coefficients were 0.595 and 0.355, respectively.

AUCs for TBR_{SUV}_{max} and rCBV_{mean} were 0.847 ± 0.077 and 0.845 ± 0.078 , respectively, with no significant differences. Logistic regression and receiver operating characteristic analysis revealed the largest AUC (0.953 ± 0.031) for a combination of TBR_{SUV}_{max} and rCBV_{mean}, with corresponding sensitivity and specificity of 0.848 and 1.0, respectively.

DISCUSSION

In the present study, we evaluated the usefulness of MET PET/CT and PWI for the differentiation of recurrence from radiation injury in patients with HGGs and quantitatively analyzed the diagnostic values of MET PET/CT and PWI parameters. Similar findings were observed for the 2 modalities, and it was observed that the accuracy was the highest when they were combined.

Several studies have shown that MET PET/CT is useful for distinguishing tumor recurrence from radiation-induced necrosis.¹³⁻¹⁵ The major advantage of this technique is that the tracer is thought to accumulate preferentially in tumor tissue, resulting in good contrast against the normal tissue in the background. Similar to a previous study,¹⁶ all cases that

showed negative results on visual assessment were those with radiation injury. Three cases of radiation injury showed equivocal findings and 4 showed positive findings on visual assessments; these findings can be explained by the mild MET uptake in some cases of necrosis. The mechanism underlying MET uptake by radiation necrosis lesions remains unclear. A possible mechanism is increased methionine metabolism and permeability induced by gliosis mediated by astrocytes and microglial cells, which are commonly observed in cases of radiation injury.¹⁶ Furthermore, radiation injury may break the BBB, resulting in passive diffusion of MET, and this may explain the false-positive PET findings. Theoretically, the uptake by recurrence should exceed that by radiation injury lesions; however, one should not preclude the possibility of similar uptakes. According to suggestions in previous studies,¹⁷⁻¹⁹ we assumed that semiquantitative analysis of MET PET/CT parameters might be helpful in the present study, which showed that visual-assessment findings were not very different from those of semiquantitative analysis with a cutoff value for the differentiation of

Table 4: Comparison of patients with recurrence with patients with radiation injury, according to cutoff values for TBR_{SUV}_{max} and rCBV_{mean}

PET	Recurrence PWI			Radiation Injury PWI		
	+	-	Total	+	-	Total
+	25	7	32	0	3	3
-	1	0	1	1	5	6
Total	26	7	33	1	8	9

Note:—+ indicates TBR_{SUV}_{max} ≥ 1.85 or rCBV_{mean} ≥ 1.83; —, TBR_{SUV}_{max} < 1.85 or rCBV_{mean} < 1.83.

recurrence from radiation injury. According to our results, we expect that visual assessment may be useful for a rapid diagnosis.

It is difficult to determine the appropriate parameter to evaluate accumulation rates in the semiquantitative analysis of MET PET/CT. SUV produced a high SD, even in normal gray matter¹⁶; notably, TBR can reduce individual differences. Tsuyuguchi et al¹⁶ showed no significant difference between recurrence and necrosis groups with respect to TBR or SUV. Terakawa et al¹⁸ reported significant differences in all indices (SUV_{mean}, SUV_{max}, and TBR_{mean}), with the exception of the TBR_{max} between glioma recurrence and radiation necrosis. The difference may depend on the type and number of patients included in the study. The former involved a small number of patients, while the latter involved patients with both high- and low-grade gliomas. It has been shown that MET uptake in glioblastoma is higher than in low-grade gliomas,²⁰ resulting in a better diagnostic ability for HGG recurrence than for recurrence of low-grade gliomas. Although the TBR has been used for differentiation, the cutoff ratio differs among studies, probably due to the variation of the PET scan protocol, which has not been standardized.

Terakawa et al¹⁸ reported that a mean lesion-to-normal uptake ratio of >1.58 resulted in the best sensitivity and specificity (75% and 75%, respectively) for the differentiation of recurrent gliomas (including HGGs and low-grade gliomas) from radiation necrosis. The reference region in the study of Terakawa et al was placed in the region of uptake in the contralateral normal frontal lobe gray matter, which was different from that in our study. In the present study, we used the ratio of the maximum lesion uptake to a reference uptake value instead of the mean uptake value. Previous studies using different cutoff values for the TBR to differentiate patients with glioma (all grades) recurrence from those with radiation injury have reported sensitivities ranging from 75% to 100% and specificities ranging from 60% to 100%.^{21,22}

PWI can demonstrate the characteristics of the vascular physiology and the hemodynamics of tumors. Tumor recurrence is accompanied by abundant abnormal blood vessels with increased permeability, while necrosis is associated with treatment-induced vascular endothelial damage and coagulation necrosis. It has been reported that PWI correlated with vascularity could be used to differentiate recurrence from necrosis. In 2017, Patel et al⁵ summarized 28 articles on PWI-based differentiation of recurrent tumors and posttreatment changes and reported that the accuracy was similar among the best-performing DSC and dynamic contrast-enhanced parameters from each study. DSC and dynamic contrast-enhanced techniques each have their own limitations.

DSC has poorer spatial resolution and is more sensitive to the effects of susceptibility. Dynamic contrast-enhanced imaging requires complex pharmacokinetic models to maintain robustness with respect to nonlinearity between signal intensity and contrast agent concentration. The pooled sensitivities and specificities of the best-performing DSC-PWI parameters from all studies were 90% and 88%. Within individual studies, PWI parameters distinguished viable tumor tissue from treatment changes with relatively good sensitivity and specificity. The most commonly evaluated PWI parameters are rCBV_{mean} and rCBV_{max}. Patel et al⁵ also calculated the pooled sensitivities and specificities of rCBV_{mean} (threshold range, 0.9–2.15) and rCBV_{max} (threshold range, 1.49–3.1) for the detection of recurrence.

In the present study, we used a cutoff value of 1.83 for rCBV_{mean}, which resulted in a sensitivity and specificity of 0.788 and 0.889, respectively. Differences in cutoff values between our study and the previous studies could be attributed to differences in image-acquisition techniques, machines, processing techniques, and analysis tools. Young et al²³ and Prager et al²⁴ reported that rCBV individually showed the highest sensitivity and specificity to discriminate recurrence from radiation injury in patients with HGG when the cutoff values were 1.8 and 1.4, respectively. The present study showed that the agreement between visual assessments and semiquantitative analyses of parameters was better with MET PET/CT than with PWI in the discrimination of recurrence from radiation injury, probably because of the high background intensity in PWI that impaired accurate visual assessment.

Deng et al⁸ conducted a meta-analysis of 11 studies assessing MET PET/CT and 7 studies assessing DSC-PWI and showed that the AUC for PWI was larger than that for MET PET/CT (*P* < .01). Another meta-analysis⁹ conducted in 2010 also reported that PWI may be superior to MET PET/CT for the differentiation of recurrence from radiation necrosis. Various types and grades of gliomas included in the meta-analysis may cause bias. In contrast, the present study derived similar AUCs for PWI and MET PET/CT. These discrepant findings could be attributed to differences in acquisition parameters and PWI being performed using 2 different MR imaging units in the present study. Although receiver operating characteristic curve analysis with an rCBV of >3.69 representing tumor recurrence showed 100% sensitivity and 100% specificity, Kim et al⁹ failed to show statistical significance in the HGG diagnostic accuracy of PWI and MET due to the small number of analyzed cases (*n* = 10). D'Souza et al²⁵ compared MET PET/CT and advanced MR imaging (inclusion of MR spectroscopy and PWI) in the identification of tumor recurrence in 41 patients with HGGs; that study indicated that MET PET seemed more sensitive, whereas advanced MR imaging seemed more specific. There was no statistically significant difference in the diagnostic performance of either technique. Similar to the present study, the diagnosis of recurrence was determined by histology or follow-up. Concordant results of PWI, MET PET, and histology were shown in 7 cases with HGGs in the study by Dandois et al²⁶; not all patients had a histologic diagnosis. This study was analyzed on the basis of the imaging process, and 31 of 33 combined MR and PET studies showed same diagnostic results.

Our study was based on patients, and 12/42 cases of disagree-

ment were observed between MET PET and PWI. Most interesting, all cases showing negative findings in both imaging modalities were those of radiation injury, while all cases showing positive findings in both imaging modalities were those of recurrence. Collectively, these findings suggest that agreement of MET PET/CT and PWI may be helpful in the determination of recurrence. In case of disagreement between MET PET/CT and PWI findings, the diagnosis may be unclear. In addition, MET PET/CT in this study has a higher sensitivity than PWI but exhibits a lower specificity; this may be related to the cutoff value selected. We found that the AUC for a combination of TBR_{SUV}_{max} and rCBV_{mean} was the largest, though there was no significant difference. This finding suggests that the accuracy of a combination of MET PET/CT and PWI parameters is better than that of individual parameters for the differentiation of radiation necrosis and recurrence in patients with HGGs.

Our effort to determine which of the 2 methods is better was inconclusive; good use of each method is effective. PET/MR imaging combines 2 imaging modalities and has the advantages of high spatial resolution and numerous biologically relevant tracers. However, the method for PET/MR imaging attenuation correction, which affects quantitative reliability, has yet to be optimized. Rausch et al²⁷ proposed that ultrashort TE-based and BD-based attenuation correction (BD, noncommercial prototype software by Siemens Healthcare) is clinically acceptable for SUV calculations of tracer uptake in lesions within the brain. In addition, the more recent developments in attenuation correction for MR imaging-based methods (eg, RESOLUTE) are promising.²⁸ However, the use of PET/MR imaging has some unclear drawbacks: Patient comfort is decreased and communication with the patient is hampered. Thus, movement artifacts are more common in PET/MR imaging. Although the application of PET/MR imaging may play a greater role in the combination of PET and advanced MR imaging using hybrid systems, the drawbacks of PET/MR imaging still need to be overcome.

The findings of this study suggest that MET PET/CT and PWI are equally accurate in the differentiation of recurrence from radiation injury in patients with HGGs, and a combination of the 2 modalities could be helpful.

This study has some limitations. First, it was a retrospective study. Second, histopathologic analysis was not performed for all patients. Third, PWI was performed using 2 different machines with varied acquisition parameters. Fourth, the proportion of patients with radiation injury in our study population was small. Thus, our results should be interpreted with caution.

CONCLUSIONS

This study compared MET PET/CT and PWI for the differentiation of recurrence from radiation injury in patients with HGGs. Both imaging techniques had similar diagnostic performance in discriminating recurrence and radiation injury, and combining the 2 may be helpful. Meanwhile, semiquantitative analysis can be helpful in cases in which visual assessment yields equivocal results. Further studies with a larger sample size, a better study design, and using machines with identical image-acquisition parameters are warranted to confirm our results.

REFERENCES

1. Verma N, Cowperthwaite MC, Burnett MG, et al. **Differentiating tumor recurrence from treatment necrosis: a review of neuro-oncologic imaging strategies.** *Neuro Oncol* 2013;15:515–34 CrossRef Medline
2. Hyare H, Thust S, Rees J. **Advanced MRI techniques in the monitoring of treatment of gliomas.** *Curr Treat Options Neurol* 2017;19:11 CrossRef Medline
3. Galldiks N, Law I, Pope WB, et al. **The use of amino acid PET and conventional MRI for monitoring of brain tumor therapy.** *Neuroimage Clin* 2017;13:386–94 CrossRef Medline
4. Mangla R, Singh G, Ziegelitz D, et al. **Changes in relative cerebral blood volume 1 month after radiation-temozolomide therapy can help predict overall survival in patients with glioblastoma.** *Radiology* 2010;256:575–84 CrossRef Medline
5. Patel P, Baradaran H, Delgado D, et al. **MR perfusion-weighted imaging in the evaluation of high-grade gliomas after treatment: a systematic review and meta-analysis.** *Neuro Oncol* 2017;19:118–27 CrossRef Medline
6. Barajas RF Jr, Chang JS, Segal MR, et al. **Differentiation of recurrent glioblastoma multiforme from radiation necrosis after external beam radiation therapy with dynamic susceptibility-weighted contrast-enhanced perfusion MR imaging.** *Radiology* 2009;253:486–96 CrossRef Medline
7. Bisdas S, Naegele T, Ritz R, et al. **Distinguishing recurrent high-grade gliomas from radiation injury: a pilot study using dynamic contrast-enhanced MR imaging.** *Acad Radiol* 2011;18:575–83 CrossRef Medline
8. Deng SM, Zhang B, Wu YW, et al. **Detection of glioma recurrence by ¹¹C-methionine positron emission tomography and dynamic susceptibility contrast-enhanced magnetic resonance imaging: a meta-analysis.** *Nucl Med Commun* 2013;34:758–66 CrossRef Medline
9. Kim YH, Oh SW, Lim YJ, et al. **Differentiating radiation necrosis from tumor recurrence in high-grade gliomas: assessing the efficacy of 18F-FDG PET, 11C-methionine PET and perfusion MRI.** *Clin Neurol Neurosurg* 2010;112:758–65 CrossRef Medline
10. Hojjati M, Garg V, Badve CA, et al. **Differentiation of recurrent spinal ependymoma from postradiation treatment necrosis through multiparametric PET-MR and perfusion MRI.** *Clin Imaging* 2017;41:48–52 CrossRef Medline
11. Wang X, Hu X, Xie P, et al. **Comparison of magnetic resonance spectroscopy and positron emission tomography in detection of tumor recurrence in posttreatment of glioma: a diagnostic meta-analysis.** *Asia Pac J Clin Oncol* 2015;11:97–105 CrossRef Medline
12. DeLong ER, DeLong DM, Clarke-Pearson DL. **Comparing the areas under two or more correlated receiver operating characteristic curves: a nonparametric approach.** *Biometrics* 1988;44:837–45 CrossRef Medline
13. Nihashi T, Dahabreh IJ, Terasawa T. **Diagnostic accuracy of PET for recurrent glioma diagnosis: a meta-analysis.** *AJNR Am J Neuroradiol* 2013;34:944–50, S1–11 CrossRef Medline
14. Minamimoto R, Saginoya T, Kondo C, et al. **Differentiation of brain tumor recurrence from post-radiotherapy necrosis with 11C-methionine PET: visual assessment versus quantitative assessment.** *PLoS One* 2015;10:e0132515 CrossRef Medline
15. Skvortsova TY, Brodskaya ZL, Gurchin AF. **PET using 11C-methionine in recognition of pseudoprogression in cerebral glioma after combined treatment [in English, Russian].** *Zh Vopr Neurokhir Im N N Burdenko* 2014;78:50–58 CrossRef Medline
16. Tsuyuguchi N, Takami T, Sunada I, et al. **Methionine positron emission tomography for differentiation of recurrent brain tumor and radiation necrosis after stereotactic radiosurgery: in malignant glioma.** *Ann Nucl Med* 2004;18:291–96 CrossRef Medline
17. Herrmann K, Czernin J, Cloughesy T, et al. **Comparison of visual and semiquantitative analysis of 18F-FDOPA-PET/CT for recurrence detection in glioblastoma patients.** *Neuro Oncol* 2014;16:603–09 CrossRef Medline
18. Terakawa Y, Tsuyuguchi N, Iwai Y, et al. **Diagnostic accuracy of**

- ¹¹C-methionine PET for differentiation of recurrent brain tumors from radiation necrosis after radiotherapy.** *J Nucl Med* 2008;49:694–99 CrossRef Medline
19. Martínez-Amador N, Jimenez-Bonilla J, Martínez-Rodríguez I, et al. **Value of the visual and semiquantitative analysis of carbon-11-methionine PET/CT in brain tumors' recurrence versus post-therapeutic changes.** *Nucl Med Commun* 2017;38:1125–32 CrossRef Medline
 20. Kaschten B, Stevenaert A, Sadzot B, et al. **Preoperative evaluation of 54 gliomas by PET with fluorine-18-fluorodeoxyglucose and/or carbon-11-methionine.** *J Nucl Med* 1998;39:778–85 Medline
 21. Tripathi M, Sharma R, Varshney R, et al. **Comparison of F-18 FDG and C-11 methionine PET/CT for the evaluation of recurrent primary brain tumors.** *Clin Nucl Med* 2012;37:158–63 CrossRef Medline
 22. Deuschl C, Kirchner J, Poeppel TD, et al. **¹¹C-MET PET/MRI for detection of recurrent glioma.** *Eur J Nucl Med Mol Imaging* 2018;45:593–601 CrossRef Medline
 23. Young RJ, Gupta A, Shah AD, et al. **MRI perfusion in determining pseudoprogression in patients with glioblastoma.** *Clin Imaging* 2013;37:41–49 CrossRef Medline
 24. Prager AJ, Martinez N, Beal K, et al. **Diffusion and perfusion MRI to differentiate treatment-related changes including pseudoprogression from recurrent tumors in high-grade gliomas with histopathologic evidence.** *AJNR Am J Neuroradiol* 2015;36:877–85 CrossRef Medline
 25. D'Souza MM, Sharma R, Jaimini A, et al. **¹¹C-MET PET/CT and advanced MRI in the evaluation of tumor recurrence in high-grade gliomas.** *Clin Nucl Med* 2014;39:791–98 CrossRef Medline
 26. Dandois V, Rommel D, Renard L, et al. **Substitution of ¹¹C-methionine PET by perfusion MRI during the follow-up of treated high-grade gliomas: preliminary results in clinical practice.** *J Neuroradiol* 2010;37:89–97 CrossRef Medline
 27. Rausch I, Rischka L, Ladefoged CN, et al. **PET/MRI for oncologic brain imaging: a comparison of standard MR-based attenuation corrections with a model-based approach for the Siemens mMR PET/MR System.** *J Nucl Med* 2017;58:1519–25 CrossRef Medline
 28. Ladefoged CN, Andersen FL, Kjaer A, et al. **RESOLUTE PET/MRI attenuation correction for O-(2-¹⁸F-fluoroethyl)-L-tyrosine (FET) in brain tumor patients with metal implants.** *Front Neurosci* 2017;11:453 CrossRef Medline

Standardized MR Perfusion Scoring System for Evaluation of Sequential Perfusion Changes and Surgical Outcome of Moyamoya Disease

Y.-H. Lin, M.-F. Kuo, C.-J. Lu, C.-W. Lee, S.-H. Yang, Y.-C. Huang, H.-M. Liu, and Y.-F. Chen



ABSTRACT

BACKGROUND AND PURPOSE: Simple-but-precise evaluation of cerebral perfusion is crucial for the treatment of Moyamoya disease. We aimed to develop a standardized scoring system for MR perfusion suitable for Moyamoya disease evaluation and investigate the postoperative serial changes and outcome predictors.

MATERIALS AND METHODS: From January 2013 to December 2016, patients diagnosed with Moyamoya disease and receiving indirect revascularization were recruited prospectively. Clinical data and serial imaging studies were analyzed. The TTP maps were standardized using cerebellar reference values. We developed a scoring system of standardized TTP maps: 14 points for each hemisphere with higher points indicating better perfusion.

RESULTS: In total, 24 children (4–17 years of age, 41 hemispheres) and 20 adults (18–51 years of age, 34 hemispheres) were included. The mean preoperative TTP scores were higher in children (7.34 ± 3.90) than in adults (4.88 ± 3.24). The standardized TTP maps revealed dynamic improvement with an increase in the corresponding scores at the 1-, 3-, and 6-month postoperative follow-ups; the scores stabilized after 6 months. The mean improvement in the 6-month scores of the pediatric and adult groups was 4.15 ± 3.55 and 6.03 ± 3.04 , respectively. The 6-month TTP score improvements were associated with Matsushima grades. If we took score improvement as the outcome, the preoperative TTP score was the only significant predictor in multivariable analysis.

CONCLUSIONS: The standardized TTP maps and scoring system facilitated the quantification of the sequential perfusion changes during Moyamoya disease treatment. The preoperative perfusion status was the only predictor of indirect revascularization outcome.

ABBREVIATIONS: EDAS = encephaloduroarteriosynangiosis; EPS = encephalopericraniosynangiosis; MMD = Moyamoya disease; MRP = MR perfusion

Moyamoya disease (MMD) is a progressive occlusive disease of the supraclinoid segment of the ICA associated with collateral vessel formation at the base of the brain. MMD has 2 age peaks: at approximately 10 years and at 30–40 years. The major clinical presentation is ischemic stroke in both children and

adults.¹ Surgical revascularization is the only effective therapy for patients with MMD to reduce their risk of subsequent strokes. Although the clinical response to surgical treatment appears to be favorable in most cases, there is considerable debate regarding the advantages and disadvantages of direct and indirect revascularizations, particularly for adult patients.^{2–4} The effectiveness of indirect revascularization in adult patients with MMD, however, has been supported by clinical and angiographic evaluations.^{5–7}

Evaluation of MMD severity has largely depended on conventional angiography. Suzuki and Takaku⁸ proposed 6 stages of angiographic evolution in MMD. However, only some patients follow this stepwise progression, and the staging is not correlated with the clinical symptoms. Thus far, the evaluation of surgical outcome after revascularization for MMD depends on angiography using the Matsushima grading system.⁹ However, conventional angiography is invasive, and the Matsushima grading system focuses only on the outer aspect of cerebral hemispheres.

Brain perfusion studies provide cross-sectional imaging through SPECT, Xe-CT, ¹⁵O-H₂O PET, MR perfusion (MRP),

Received August 18, 2018; accepted after revision December 1.

From the Department of Medical Imaging (Y.-H.L., C.-J.L., C.-W.L., Y.-F.C.) and Division of Neurosurgery (M.-F.K., S.-H.Y.), Department of Surgery, National Taiwan University Hospital, Taiwan; Department of Medical Imaging (Y.-C.H.), Min-Sheng General Hospital, Taoyuan, Taiwan; and Department of Radiology (H.-M.L.), Fu Jen Catholic University Hospital, New Taipei City, Taiwan.

This work was supported by grants from Ministry of Science and Technology, Taiwan to Dr. Y.-F. Chen (MOST-103-2321-B-002-032) and Dr. M.-F. Kuo (MOST 105-2314-B-002-004-MY2 and 103-2321-B-002-033).

Yen-Heng Lin and Meng-Fai Kuo contributed equally to the article.

Paper previously presented in poster form at: XXI Symposium Neuroradiologicum, March 19–23, 2018; Taipei, Taiwan.

Please address correspondence to Ya-Fang Chen, MD, Department of Medical Imaging, National Taiwan University Hospital, Hsin-Chu Branch, No. 25, Lane 442, Section 1, Jingguo Rd, HsinChu City 300, Taiwan; e-mail: joannayfc@gmail.com

Indicates open access to non-subscribers at www.ajnr.org

<http://dx.doi.org/10.3174/ajnr.A5945>

and CT perfusion in MMD.¹⁰⁻¹⁴ Given the adverse effect of radiation, MRP is an efficient, noninvasive tool for evaluation. A study comparing MTT measured through DSC MR imaging and the oxygen extraction fraction measured through PET revealed that an MTT delay of 2 seconds (compared with the cerebellum) suggested misery perfusion.¹⁵ Changes in TTP maps after revascularization surgery were reported to be correlated with clinical outcome in patients with MMD.¹⁶ In clinical practice, the evaluation of the TTP map is generally qualitative rather than quantitative. A scoring system serving as a simple method of communication among clinicians, such as ASPECTS¹⁷ for acute stroke treatment, would be helpful for the treatment of MMD.

In this study, our purpose was 2-fold: First, develop a scoring system for standardized TTP maps of MRP that is suitable for evaluation of longitudinal perfusion changes; and second, on the basis of the proposed scoring system, investigate the outcome predictors for indirect revascularization in patients with MMD.

MATERIALS AND METHODS

The institutional review board of National Taiwan University Hospital approved this study, and written informed consent was obtained from all participants.

Participants

From January 2013 to December 2016, patients with MMD were prospectively recruited and operated on by a single neurosurgeon at our institution. The diagnosis of MMD was made according to the criteria stated by the Research Committee on Spontaneous Occlusion of the Circle of Willis in Japan.¹⁸ Preoperative MR imaging and MRP were part of our study. The patients who did not have a preoperative MRP result of sufficient quality or had undergone previous revascularization surgery were excluded.

All patients were scheduled for MR imaging and MRP follow-ups at 1, 3, 6, and 12 months after the operation. Conventional angiography was performed before each operation and 6–12 months after the last operation. The age, sex, presenting symptoms, associated diseases, operative methods, neuroimaging and clinical results, and surgical complications were recorded. Only the operated hemispheres were analyzed in this study.

MR Imaging and MRP

MR imaging and MRP were performed using a 1.5T MR imaging scanner, Signa Excite HDx (GE Healthcare, Milwaukee, Wisconsin). The scanning protocol involved axial FLAIR, T2WI, DWI of 5-mm thickness, TOF-MRA, and precontrast and postcontrast 3D-T1WI (inversion recovery spoiled gradient recalled). We used DSC MR imaging for MRP (TR/TE = 1000/40 ms, flip angle = 90°, FOV = 24 × 24 cm, in-plane resolution = 1.9 × 1.9 mm, thickness = 5 mm, gap = 3–5 mm depending on the head size, 12 slices covering half of the cerebellum to the top of the cerebrum, 50 phases). The MRP was aligned to the subcallosal line with a slice through the subcallosal line. Gadovist (gadobutrol; 0.1 mmol/kg; Bayer Schering Pharma, Berlin, Germany) was injected 5 seconds after the DSC MR imaging commenced (injection rate = 3 cm³/s) followed by a 20-cm³ saline flush. The follow-up MR imaging and MRP followed the slice location of the preoperative study.

Semiquantitative TTP Scoring System

Postprocessing of DSC MR imaging data was performed using the Perfusion Mismatch Analyzer (PMA; Version 5.0.0.0; Advanced Medical Science Center, Iwate Medical University, Iwate, Japan). TTP maps were generated and input to OsiriX Imaging Software (<http://www.osirix-viewer.com>). We used the National Institutes of Health color bar for display and adjusted the window level and width for each brain according to the value of the TTP of the cerebellum. The numeric range of the color bar was fixed to 15 seconds, whereas the lower end was adjusted to 4 seconds lower than the cerebellar average TTP value so that the cerebellum would appear blue. The areas of prolonged TTP (≥ 2 seconds) would appear green to red on color maps. Figure 1 depicts the sequential change of a patient's standardized color maps before and after surgical revascularization.

We developed a scoring system for semiquantification of the TTP maps, the TTP scoring system. MRP at 14 regions in 3 levels (ie, ganglionic, ventricular roof, and high convexity) was selected for scoring (Fig 2). For each region, if blue occupied more than half of the area, it was given 1 point. Each healthy cerebral hemisphere would score 14 points. The infarcted areas were not excluded from evaluation. Two neuroradiologists read the standardized TTP color maps independently and provided the scores according to the color in the 14 regions of each hemisphere.

Conventional Angiography

A complete angiographic study of the common carotid, external carotid, and ICAs of each hemisphere, and vertebral angiography of the dominant side was performed. Preoperative and postoperative angiography was assessed using the Suzuki staging (I–VI) and Matsushima grading (A–C) systems, respectively, for each cerebral hemisphere.^{8,9}

Surgical Procedure

All participants underwent encephaloduroarteriosynangiosis (EDAS) or encephalomyosynangiosis of the temporal region, with or without additional encephalopericraniosynangiosis (EPS) of the frontal or parietal regions. Patients requesting a 1-stage operation underwent multiple burr-hole operations for both cerebral hemispheres. During EPS and multiple burr-hole operations, craniotomy windows (diameter, 3–4 cm) were created to facilitate the exposure of the arteries located in the cerebral sulci and obtain effective contact with the donor vascular tissue. During EDAS, the horizontal width of the craniotomy window was >3 cm to expose at least 1 sulcus and the vertical length was >7 cm to acquire a long superficial temporal artery flap. An anchoring suture between the superficial temporal artery flap and dura was created at the 4 corners of the craniotomy window. In addition, duroplexy was performed by infolding the dural flap into the cerebral sulci in every craniotomy window.

Statistical Analysis

Descriptive statistics for demographic data, clinical manifestation, radiologic evaluation, operative method, periprocedural complications, and follow-up data are provided. The TTP scores were treated as continuous data, without violating the assumption of normality. TTP score improvement was considered a radio-

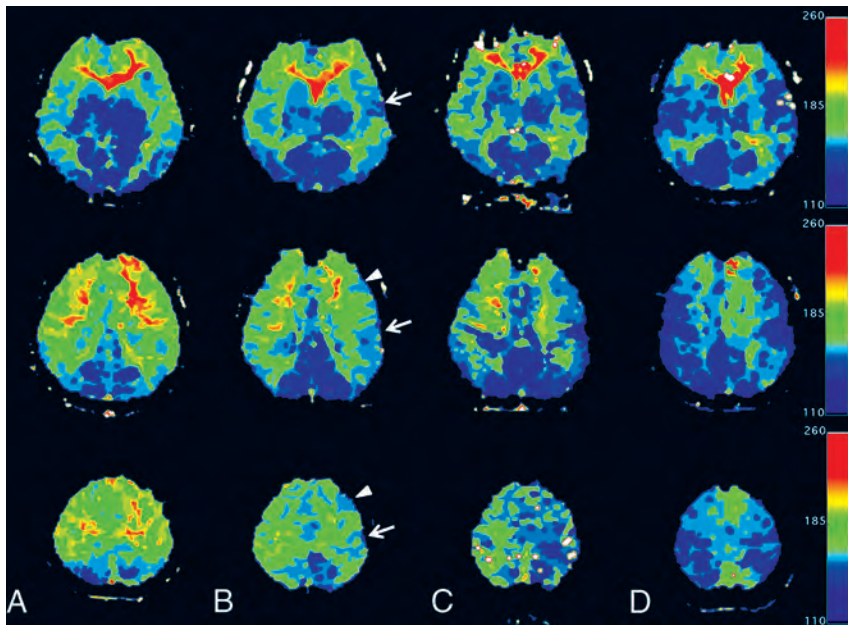


FIG 1. Serial changes in 3 levels in standardized TTP maps of an 18-year-old female patient with MMD. Preoperatively (A) and 1 (B) and 3 (C) months after left temporal EDAS and frontal EPS and a 6-month map after a right-sided operation (D). Preoperative maps show large areas of prolonged TTP in the anterior cerebral artery and MCA territories bilaterally (A). Areas of normalized TTP near the craniotomy site (arrows: temporal EDAS; arrowheads: frontal EPS) are shown in the 1-month postoperative map (B) and are enlarged in the 3-month map (C). The contralateral hemisphere shows simultaneous improvement. After a subsequent right-sided operation, the right cerebrum shows increased areas of TTP normalization. The final maps show only small areas of TTP prolongation at the bilateral medial cerebrum (D).

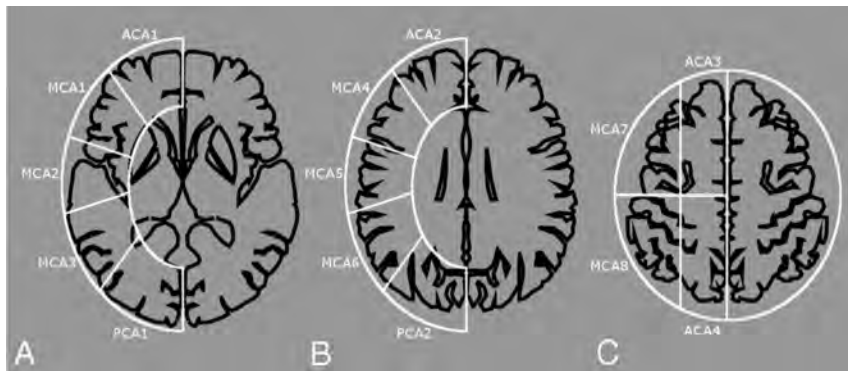


FIG 2. TTP scoring system. We counted and totaled 14 cortical regions in 3 levels of cerebral hemispheres: ganglionic level (A), ventricular roof level (B), and high convexity (C). Each level is approximately 2 cm apart. An area of blue larger than one-half of 1 region is counted as 1 point, otherwise, it is counted as 0 points. The total TTP score of 1 hemisphere ranges from 0 to 14 points: 4, 8, and 2 for the anterior cerebral artery, MCA, and posterior cerebral artery areas, respectively.

logic outcome. The interrater reliability of the TTP score was assessed using the intraclass correlation coefficient. To investigate the predictor for this radiologic outcome, we used a linear mixed-regression model to control the correlation between hemispheres of the same subject. Categorical predictors were coded as dummy variables. If the predictor was a continuous variable, standardization of the variable was performed to facilitate direct comparison of coefficients. Univariable and multivariable analyses were conducted using the Wald test for the coefficients. The significance level was set at .05. All statistical analyses were performed on SAS (Version 9.4; SAS Institute, Cary, North Carolina).

RESULTS

Patients' Clinical and Radiologic Data

During the study period, 31 pediatric and 23 adult patients with MMD were operated on at our institution; of them, 2 were excluded because of insufficient preoperative MRP quality and 8 due to previous revascularization. Finally, 44 patients (24 pediatric and 20 adult) were included. Among the 88 hemispheres, there were 75 operated hemispheres (41 pediatric and 34 adult) included in the analysis. Table 1 shows the patient characteristics.

The pre- and postoperative features of the operated hemispheres are shown in Table 2. Among the 75 hemispheres, an additional EPS was performed in the frontal or parietal area in 15 (36%) pediatric and 30 (88%) adult hemispheres, respectively. Three adults had immediate postoperative stroke related to relatively low blood pressure and diabetic ketoacidosis; however, they were stabilized thereafter. No periprocedural infarction occurred in the pediatric patients.

The mean follow-up duration for pediatric and adult patients was 38 ± 16.57 and 29.85 ± 15.11 months, respectively. Three pediatric patients had new asymptomatic MR imaging–demonstrated infarctions after the operation: Two developed the infarction on the nonoperated side, whereas 1 had it in the posterior cerebral artery territory of the operated side. MRA showed enlargement of superficial temporal arteries and middle meningeal arteries on the operative sides with reciprocal change of the smaller anterior cerebral artery and MCA. MRA and MRP revealed disease progression in the posterior cerebral artery territories of 3 children during the follow-up period; 2 of them received

adjuvant EPS to cover the posterior cerebral artery territory later. The patients presenting with transient ischemic attacks, cerebral infarction, hemorrhage, or syncope had no new attacks. The patients presenting with headaches had partial-to-complete symptom relief. One of the 7 patients with seizures was still taking 1 type of antiepileptic drug, whereas the other 6 were symptom-free.

Postoperative Sequential Changes of TTP Scores with Angiographic Correlation

The intraclass correlation coefficients of preoperative and postoperative TTP scores were 0.95 (95% CI, 0.925–0.967) and 0.86

(95% CI, 0.789–0.909), respectively. Only the results of scorer 1 were further analyzed.

The mean preoperative TTP score for each hemisphere was 7.34 ± 3.90 and 4.88 ± 3.24 in pediatric and adult patients, respectively. The sequential changes in postoperative 1-, 3-, 6-, and 12-month TTP scores in all patients with available data were assessed. The mean pediatric hemisphere score improvement was

1.19 ± 1.64 , 3.24 ± 2.36 , 4.15 ± 3.55 , and 4.17 ± 3.51 at the 1-, 3-, 6-, and 12-month follow-ups, respectively, compared with the preoperative score. Furthermore, the mean adult hemisphere score improvement was 3.18 ± 2.69 , 5.08 ± 2.72 , 6.03 ± 3.04 , and 6.34 ± 2.93 at the 1-, 3-, 6-, and 12-month follow-ups, respectively (Fig 3). In both groups, the postoperative perfusion changes were more robust at 0–3 months than at 3–6 months of follow-up. The changes stabilized after 6 months. The difference between the 6- and 12-month scores was minor (mean difference, 0.08) and nonsignificant using the paired *t* test ($P = .2$). According to the color maps, the earliest perfusion changes occurred in the MCA territory around the craniotomy sites and grew larger on the follow-up maps (Fig 1). After unilateral revascularization, the contralateral cerebrum would also show perfusion improvement.

Most of the cerebral infarctions were small or in the white matter, which would not influence the TTP scores. Among the patients with cerebral infarction, only 7 of them (including 3 preoperatively, 3 immediately after operation, and 1 with disease progression) showed infarctions sizable enough to influence the TTP scores in the range of 1–3 points. These areas showed parenchymal defects on the follow-up studies, and the points were permanently lost.

Postoperative angiography was performed in 56 cerebral hemispheres (33 pediatric hemispheres and 23 adult hemispheres). We selected the 6-month TTP data after the final operation to evaluate the surgical outcome for both hemispheres. In these hemispheres, higher Matsushima grades (grade A being the highest) demonstrated higher TTP score improvement (Table 3). Matsushima grade A or B is usually considered adequate or satisfactory collateral formation; thus, the proportions of adult and pediatric patients with adequate results were similar (83% and 82%, respectively). The mean TTP score improvement in the 8 pediatric and 11 adult hemispheres without postoperative angiography was 4.13 ± 2.62 and 5.73 ± 2.69 , respectively, which was close to that of Matsushima grade B in adult patients and between Matsushima grades A and B in pediatric patients, suggesting satisfactory results.

Postoperative angiography was performed in 56 cerebral hemispheres (33 pediatric hemispheres and 23 adult hemispheres). We selected the 6-month TTP data after the final operation to evaluate the surgical outcome for both hemispheres. In these hemispheres, higher Matsushima grades (grade A being the highest) demonstrated higher TTP score improvement (Table 3). Matsushima grade A or B is usually considered adequate or satisfactory collateral formation; thus, the proportions of adult and pediatric patients with adequate results were similar (83% and 82%, respectively). The mean TTP score improvement in the 8 pediatric and 11 adult hemispheres without postoperative angiography was 4.13 ± 2.62 and 5.73 ± 2.69 , respectively, which was close to that of Matsushima grade B in adult patients and between Matsushima grades A and B in pediatric patients, suggesting satisfactory results.

Analyses of Postoperative TTP Score Improvement

To compare the TTP score improvement across the hemispheres, linear mixed-model analysis was performed with random intercepts. To keep reasonable statistical power more than 0.8, we chose only 4 predictors in analyses. Age, male sex, preoperative TTP score, and additional EPS to the areas other than the temporal region were input as

Table 1: Patient demographic and clinical data

	Pediatric Patients (n = 24)	Adult Patients (n = 20)
Age (mean) (yr)	9.21 ± 3.59	32.4 ± 10.94
Sex (male) (No.) (%)	16 (67)	3 (15)
Clinical presentation (No.) (%)		
Focal neurologic symptoms	17 (71)	13 (65)
Seizure	3 (13)	4 (20)
Headache	5 (21)	3 (15)
Infarction	9 (38)	14 (70)
Hemorrhage	0 (0)	1 (5)
Comorbidities (No.) (%) ^a	3 (8)	0 (0)

^a There were 2 patients with neurofibromatosis type 1 and 1 patient with systemic lupus erythematosus.

Table 2: Pre- and postoperative radiologic characteristics

	Pediatric Hemispheres (n = 41)	Adult Hemispheres (n = 34)
Preoperative Suzuki stage (No.) (%)		
I	1 (2)	0 (0)
II	7 (17)	5 (15)
III	18 (44)	11 (32)
IV	12 (29)	10 (29)
V	3 (7)	3 (9)
VI	0 (0)	5 (15)
Preoperative TTP score (points) (mean)	7.34 ± 3.90	4.88 ± 3.24
Additional EPS (No.) (%)	15 (36)	30 (88)
Periprocedural infarction (No.) (%)	0 (0)	3 (9)
Duration of follow-up (mean) (mo)	38.00 ± 16.57	29.85 ± 5.11
Progressive PCA disease (No.) (%)	3 (7)	0 (0)
Recurrent stroke during follow-up (No.) (%) ^a	3 (7)	0 (0)

Note:—PCA indicates posterior cerebral artery.

^a Between 2 operations: 2 on the nonoperated side, 1 in the PCA territory on the operated side.

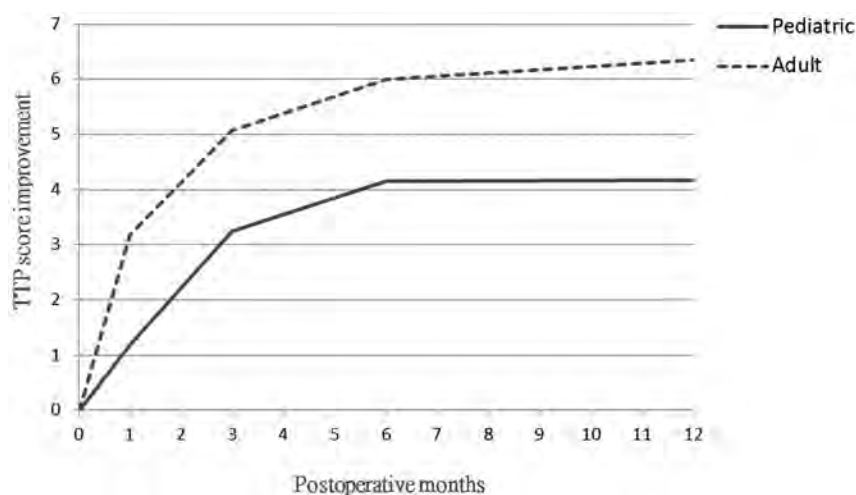


FIG 3. Line chart revealing postoperative sequential changes of TTP score improvement. In both pediatric and adult groups, the score improvements are most robust at 0–3 months followed by 3–6 months and reach a plateau at the 6-month follow-up. Our adult group has more score improvement than the pediatric group, probably related to more severe preoperative disease status.

Table 3: Postoperative Matsushima grading and TTP score improvement (6 months after the operation) indicating that TTP score improvement is correlated with Matsushima grading

	Pediatric		Adult	
	No. of Hemispheres (%)	Score Improvement (Mean)	No. of Hemispheres (%)	Score Improvement (Mean)
Matsushima grade				
A	17 (52)	5.94 ± 3.72	10 (44)	7.40 ± 2.37
B	10 (30)	3.50 ± 2.83	9 (39)	6.00 ± 2.96
C	6 (18)	0.17 ± 1.17	4 (17)	3.50 ± 4.73
Unknown ^a	8	4.13 ± 2.62	11	5.73 ± 2.69

^a The patients did not undergo postoperative catheter angiography.

Table 4: Linear mixed regression model analyses of predictors for postoperative 6-month TTP score improvement^a

Variable	Univariable		Multivariable	
	Coefficient (SD)	P Value ^b	Coefficient (SD)	P Value ^b
Age	0.92 (0.40)	.03	-0.28 (0.24)	.26
Sex (male)	-2.47 (0.76)	.002	-0.51 (0.44)	.26
Preoperative TTP score	-3.03 (0.19)	<.001	-2.93 (0.21)	<.001
Additional EPS ^c	3.03 (0.75)	<.001	0.58 (0.47)	.21

^a Linear mixed regression model with random intercepts and standardized age and preoperative TTP scores were used.

^b P values were obtained with the Wald test.

^c EPS to the hypoperfusion area at frontal or parietal regions in addition to temporal EDAS in the same procedure.

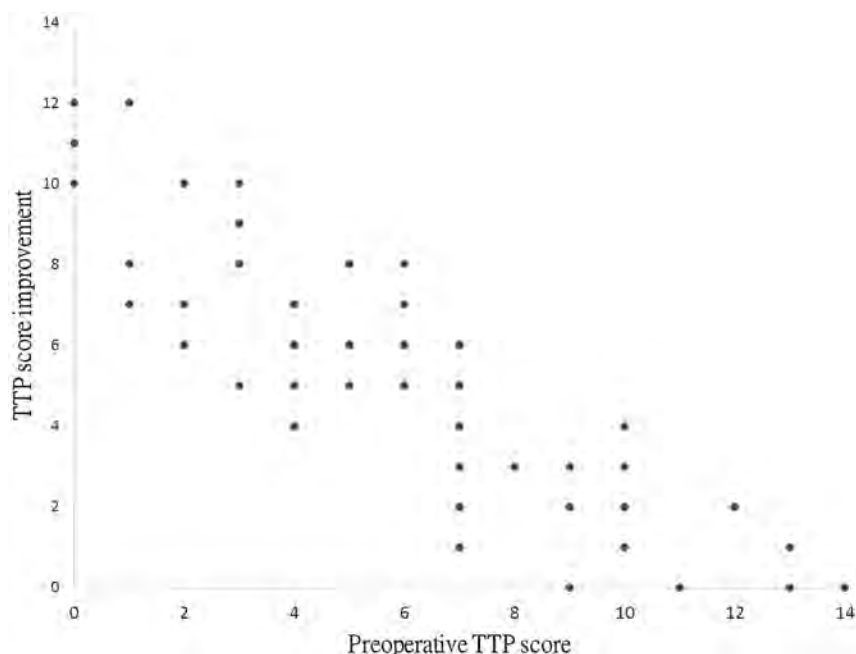


FIG 4. Scatter diagram indicating that the preoperative TTP score is inversely correlated with the TTP score improvement after the operation.

predictors. In univariable analyses, all 4 predictors were significant. After further controlling the correlation among these predictors, multivariable analyses were performed. The results indicated that only the preoperative TTP score was significant (coefficient = -2.93; $P < .001$). Regarding the point estimate of the coefficient, the absolute values of age, sex, and EPS decreased considerably, and that for age changed from a positive to a negative value. The detailed results are listed in Table 4. The results indicated that only the preoperative TTP score mattered when taking all predictors into account. Figure 4 illustrates the pre-

sumed linear relationship between the improvements in the preoperative and postoperative TTP scores.

DISCUSSION

The standard evaluation before and after surgical revascularization for MMD has been dependent on conventional angiography, which is an invasive procedure. Although MRP studies have also been applied in the follow-up of MMD, no standardized scoring method has been widely accepted for long-term use. Similar to previous reports,^{19,20} our pediatric participants experienced more disease progression during the follow-up period, suggesting ongoing disease activity, while our adult patients presented with more severe disease and with more posterior circulation involvement, which also suggest a more advanced stage.²¹ The standardized TTP maps and scoring system, providing an understanding of the extent and severity of cerebral perfusion impairment, are suitable for long-term follow-up of subjects with MMD, particularly for the children in whom disease progression is expected and radiation risk is a particular concern.

Our study indicated that an improvement in cerebral perfusion after indirect revascularization can be seen as early as 1 month after the operation, and the postoperative 6-month TTP scores increased to approximately 11 points in each cerebral hemisphere. Multivariable analysis suggested that hemispheres with more severe perfusion impairment would benefit more from indirect revascularization, regardless of patient age. A higher level of vascular plasticity and the angiogenic potential are hallmarks of MMD compared with vascular narrowing of other etiologies.^{22,23} The ischemic brain may provoke revascularization if a vascularized graft is present nearby.

Therefore, the hemispheres with poorer initial perfusion are supposed to improve more postoperatively if optimal revascularization coverage is provided. By contrast, the hemispheres with less perfusion impairment may not benefit much from revascularization surgery. Whether a preset EDAS or other revascularized flaps can provide collaterals if the cerebral perfusion deteriorates at a later time remains unknown. The optimal surgical timing should thus be carefully determined with the help of TTP maps and MRA.

Ishii et al²⁴ reported that a preoperative MTT delay predicted

the degree of postoperative revascularization and that no difference existed between adults and children in the degree of revascularization. The authors used ROIs to measure different cortical areas and obtain the MTT relative to the cerebellum. Ladner et al²⁵ developed a complex scoring system to incorporate the prior infarcts, angiography, and cerebral reactivity to measure hemodynamic severity in MMD. We used the standardized TTP map, which is an easily obtainable method to evaluate perfusion independent of the deconvolution algorithms. This simple scoring system uses visual assessment rather than ROIs. The standardized TTP maps enable rapid detection of the abnormal perfusion areas. Although we used the PMA and OsiriX viewers, the generation of TTP maps and standardization of the color maps can be achieved in every MR imaging workstation for routine clinical use. By using standardized TTP maps and the scoring systems, semiquantifying perfusion changes during follow-up are feasible. Early detection of disease progression would be easier by comparing the interval changes on the standardized TTP maps and the MRA. Conventional angiography might be best reserved for preoperative evaluation and surgical planning.

Our study did not provide data comparing the effects of direct and indirect revascularization; however, the 6-month MRP and clinical outcomes indicated that indirect revascularization in the adult group seemed to be as safe and effective as in the pediatric group. For adult patients with MMD with sizable areas of cerebral perfusion impairment, indirect revascularization can serve as a safe and effective means to reconstitute cerebral perfusion. Whether direct revascularization or combined direct and indirect revascularization is a superior method for adult patients remains unclear. Our standardized TTP maps and scoring system may offer an effective imaging tool to evaluate revascularized areas and to quantitatively analyze the effects of different operation methods.

Our study had the following limitations: First, our sample size was small. Therefore, the number of predictors in regression analyses was limited because of concern of statistical power. However, it was a prospective study, and all procedures were performed by the same senior neurosurgeon. Our results provided an insight into how cerebral perfusion changes after indirect revascularization for MMD. Second, the mean follow-up duration was 2–3 years in our patients. A longer follow-up period is vital, particularly in growing children. Third, a stress test was not applied in our perfusion study because the intravenous form of acetazolamide was not available at our institution. Another consideration is the potential hazards of the stress test to the brain with impaired perfusion. Fourth, we had only 12 slices to cover the brain because of the limitation of our 1.5T scanner with TR = 1000 ms. However, we aligned our slices to the subcallosal line and placed a slice through the subcallosal line, and the gap and slice thickness of follow-up examinations also followed the preoperative ones; therefore, the differences in slice locations among examinations should have been minimized. Finally, the scoring system alone may not reflect the true perfusion condition. In this TTP scoring system, we could not further differentiate more pronounced perfusion impairment from modest perfusion impairment in a single region if the perfusion impairment area was larger than one-half

of the region. However, we can simply compare the colors on the standardized maps to resolve the problem.

CONCLUSIONS

We developed a TTP scoring system that helped in quantitative evaluation of the preoperative severity and sequential changes in MRP of patients with MMD. The preoperative perfusion status was the only outcome predictor of indirect revascularization. The indirect revascularization has a favorable outcome in both pediatric and adult patients with MMD.

ACKNOWLEDGMENTS

The authors acknowledge statistical assistance provided by the Department of Medical Research in the National Taiwan University Hospital.

REFERENCES

1. Chen PC, Yang SH, Chien KL, et al. **Epidemiology of moyamoya disease in Taiwan: a nationwide population-based study.** *Stroke* 2014;45:1258–63 CrossRef Medline
2. Teo MK, Madhugiri VS, Steinberg GK. **Editorial: direct versus indirect bypass for moyamoya disease—ongoing controversy.** *J Neurosurg* 2017;126:1520–22 CrossRef Medline
3. Macyszyn L, Attiah M, Ma TS, et al. **Direct versus indirect revascularization procedures for moyamoya disease: a comparative effectiveness study.** *J Neurosurg* 2017;126:1523–29 CrossRef Medline
4. Uchino H, Kim JH, Fujima N, et al. **Synergistic interactions between direct and indirect bypasses in combined procedures: the significance of indirect bypasses in moyamoya disease.** *Neurosurgery* 2017;80:201–09 CrossRef Medline
5. Dusick JR, Gonzalez NR, Martin NA. **Clinical and angiographic outcomes from indirect revascularization surgery for moyamoya disease in adults and children: a review of 63 procedures.** *Neurosurgery* 2011;68:34–43; discussion 43 CrossRef Medline
6. Park SE, Kim JS, Park EK, et al. **Direct versus indirect revascularization in the treatment of moyamoya disease.** *J Neurosurg* 2018;129:480–89 CrossRef Medline
7. Lin N, Aronson JP, Manjila S, et al. **Treatment of moyamoya disease in the adult population with pial synangiosis.** *J Neurosurg* 2014;120:612–17 CrossRef Medline
8. Suzuki J, Takaku A. **Cerebrovascular “moyamoya” disease: disease showing abnormal net-like vessels in base of brain.** *Arch Neurol* 1969;20:288–99 CrossRef Medline
9. Matsushima Y, Inaba Y. **Moyamoya disease in children and its surgical treatment: introduction of a new surgical procedure and its follow-up angiograms.** *Childs Brain* 1984;11:155–70 Medline
10. Miller JH, Khonsary A, Raffel C. **The scintigraphic appearance of childhood moyamoya disease on cerebral perfusion imaging.** *Pediatr Radiol* 1996;26:833–38 CrossRef Medline
11. Lee SK, Kim DI, Jeong EK, et al. **Postoperative evaluation of moyamoya disease with perfusion-weighted MR imaging: initial experience.** *AJNR Am J Neuroradiol* 2003;24:741–47 Medline
12. Kang KH, Kim HS, Kim SY. **Quantitative cerebrovascular reserve measured by acetazolamide-challenged dynamic CT perfusion in ischemic adult moyamoya disease: initial experience with angiographic correlation.** *AJNR Am J Neuroradiol* 2008;29:1487–93 CrossRef Medline
13. Touho H, Karasawa J, Ohnishi H. **Preoperative and postoperative evaluation of cerebral perfusion and vasodilatory capacity with ^{99m}Tc-HMPAO SPECT and acetazolamide in childhood moyamoya disease.** *Stroke* 1996;27:282–89 CrossRef Medline
14. Kuroda S, Kashiwazaki D, Hirata K, et al. **Effects of surgical revascularization on cerebral oxygen metabolism in patients with moyamoya disease: an 15O-gas positron emission tomographic study.** *Stroke* 2014;45:2717–21 CrossRef Medline

15. Tanaka Y, Nariai T, Nagaoka T, et al. **Quantitative evaluation of cerebral hemodynamics in patients with moyamoya disease by dynamic susceptibility contrast magnetic resonance imaging: comparison with positron emission tomography.** *J Cereb Blood Flow Metab* 2006;26:291–300 CrossRef Medline
16. Yun TJ, Cheon JE, Na DG, et al. **Childhood moyamoya disease: quantitative evaluation of perfusion MR imaging—correlation with clinical outcome after revascularization surgery.** *Radiology* 2009;251:216–23 CrossRef Medline
17. Barber PA, Demchuk AM, Zhang J, et al. **Validity and reliability of a quantitative computed tomography score in predicting outcome of hyperacute stroke before thrombolytic therapy: ASPECTS Study Group—Alberta Stroke Programme Early CT Score.** *Lancet* 2000;355:1670–74 CrossRef Medline
18. Research Committee on the Pathology and Treatment of Spontaneous Occlusion of the Circle of Willis; Health Labour Sciences Research Grant for Research on Measures for Intractable Diseases. **Guidelines for diagnosis and treatment of moyamoya disease (spontaneous occlusion of the circle of Willis).** *Neurol Med Chir (Tokyo)* 2012;52:245–66 CrossRef
19. Kim SK, Cho BK, Phi JH, et al. **Pediatric moyamoya disease: an analysis of 410 consecutive cases.** *Ann Neurol* 2010;68:92–101 CrossRef Medline
20. Ishii K, Isono M, Kobayashi H, et al. **Temporal profile of angiographical stages of moyamoya disease: when does moyamoya disease progress?** *Neurol Res* 2003;25:405–10 CrossRef Medline
21. Lee JY, Kim SK, Phi JH, et al. **Posterior cerebral artery insufficiency in pediatric moyamoya disease.** *J Korean Neurosurg Soc* 2015;57:436–39 CrossRef Medline
22. Acker G, Fekonja L, Vajkoczy P. **Surgical management of moyamoya disease.** *Stroke* 2018;49:476–82 CrossRef Medline
23. Bedini G, Blecharz KG, Nava S, et al. **Vasculogenic and angiogenic pathways in moyamoya disease.** *Curr Med Chem* 2016;23:315–45 CrossRef Medline
24. Ishii Y, Nariai T, Tanaka Y, et al. **Practical clinical use of dynamic susceptibility contrast magnetic resonance imaging for the surgical treatment of moyamoya disease.** *Neurosurgery* 2014;74:302–09 CrossRef Medline
25. Ladner TR, Donahue MJ, Arteaga DF, et al. **Prior Infarcts, Reactivity, and Angiography in Moyamoya Disease (PIRAMD): a scoring system for moyamoya severity based on multimodal hemodynamic imaging.** *J Neurosurg* 2017;126:495–503 CrossRef Medline

Acute Toxic Leukoencephalopathy: Etiologies, Imaging Findings, and Outcomes in 101 Patients

C. Özütemiz, S.K. Roshan, N.J. Kroll, J.C. Benson, J.B. Rykken, M.C. Oswood, L. Zhang, and A.M. McKinney



ABSTRACT

BACKGROUND AND PURPOSE: Prior studies regarding acute toxic leukoencephalopathy (ATL) are either small, or preliminary. Our aim was to evaluate etiologies of and differences in imaging severity and outcomes among various etiologies of ATL.

MATERIALS AND METHODS: MRIs of patients with suspected ATL over 15 years were retrospectively reviewed; inclusion criteria were: MRI <3 weeks of presentation with both DWI and FLAIR. These were jointly graded by two neuroradiologists via a previously described score of severity. Clinical outcome was evaluated via both modified Rankin (mRS) and ATL outcome (ATLOS) scores, each being correlated with the DWI and FLAIR scores. Etiologic subgroups of $n > 6$ patients were statistically compared.

RESULTS: Of 101 included patients, the 4 subgroups of $n > 6$ were the following: chemotherapy ($n = 35$), opiates ($n = 19$), acute hepatic encephalopathy ($n = 14$), and immunosuppressants ($n = 11$). Other causes ($n = 22$ total) notably included carbon monoxide ($n = 3$), metronidazole ($n = 2$), and uremia ($n = 1$). The mean DWI/FLAIR severity scores were 2.6/2.3, 3.3/3.3, 2.1/2.1 and 2.0/2.5 for chemotherapeutics, opiates, AHE and immunosuppressants, respectively, with significant differences in both imaging severity and outcome ($P = .003-.032$) among subgroups, particularly immunosuppressant versus chemotherapy-related ATL and immunosuppressants versus opiates ($P = .004-.032$) related ATL. DWI and FLAIR severity weakly correlated with outcome ($\rho = 0.289-.349$, $P < .005$) but correlated stronger in the chemotherapy ($\rho = 0.460-.586$, $P < .010$) and opiate ($\rho = .472-.608$, $P < .05$) subgroups, which had the worst outcomes. ATL clinically resolved in 36%, with severe outcomes in 23% (coma or death, 9/16 deaths from fludarabine). Notable laboratory results were elevated CSF myelin basic protein levels in 8/9 patients and serum blood urea nitrogen levels in 24/91.

CONCLUSIONS: Clinical outcomes of ATL vary on the basis of etiology, being worse in chemotherapeutic- and opiate-related ATL. Uremia may be a predisposing or exacerbating factor.

ABBREVIATIONS: AHE = acute hepatic/hyperammonemic encephalopathy; ATL = acute toxic leukoencephalopathy; ATLOS = acute toxic leukoencephalopathy outcome score; CTL = chronic toxic leukoencephalopathy; MBP = myelin basic protein; NAWM = normal appearing white matter; PRES = posterior reversible encephalopathy syndrome; PVWM = periventricular white matter

The term “toxic leukoencephalopathy” refers to nonspecific neurologic symptoms (such as altered mental status) due to injury of the cerebral white matter, occurring from a variety of conditions.¹⁻³ This can exist in either the acute form as acute toxic leukoencephalopathy (ATL) or in the chronic form as chronic toxic leukoencephalopathy (CTL). Notably, patients have more subtle and slower development of neurologic symptoms and MR imaging findings in CTL.³ On the other hand, ATL is a relatively uncommon condition in acute encephalopathic (i.e. obtunded) patients, particularly in those who are post-chemotherapy or im-

munosuppression for marrow transplantation, with a shared imaging appearance on DWI from multiple potential etiologies.⁴ The clinical features of ATL are quite variable but are abrupt in onset, ranging from minor cognitive impairment to severe neurologic dysfunction, depending on the extent of involved areas of the brain.¹⁻³ Notably, while this damage is best initially depicted on DWI, with focal or symmetric reduced diffusion in the periventricular white matter (PVWM) with or without accompanying lesions on FLAIR, histopathology has noted both intramyelinic and oligodendroglial swelling.²⁻⁴ Recognizing this condi-

Received August 29, 2018; accepted after revision December 3.

From the Department of Radiology (C.Ö., S.K.R., J.C.B., J.B.R., A.M.M.) and Faculty of Medicine (N.J.K.), University of Minnesota, Minneapolis, Minnesota; Department of Radiology (M.C.O.), Hennepin County Medical Center, Minneapolis, Minnesota; and Biostatistics Design and Analysis Center (L.Z.), Clinical and Translational Science Institute, University of Minnesota, Minneapolis, Minnesota.

Please address correspondence to Can Özütemiz, MD, Department of Radiology, University of Minnesota MMC 292, 420 Delaware St, SE Minneapolis, MN 55455; e-mail: ozutemiz@umn.edu; @CanOzutemiz

Indicates open access to non-subscribers at www.ajnr.org

Indicates article with on-line appendix.

<http://dx.doi.org/10.3174/ajnr.A5947>

tion is crucial because it is a clinoradiologic diagnosis in which the symptoms and imaging findings may reverse abruptly upon removal of the underlying cause; alternatively, ATL can be fatal.²

Various toxic etiologies have been reported to cause ATL, including chemotherapeutic and immunosuppressive agents, substance abuse (particularly opiates), antimicrobials, environmental toxins, hepatic failure, and others.^{2,4-10} Notably, ATL has an overall worse prognosis than posterior reversible encephalopathy syndrome (PRES), another potentially reversible disorder that can also occur with chemotherapy or immunosuppression.⁴ However, it is unknown whether the outcomes from these various causes of ATL are similar and whether they have differences in initial imaging severity; it is plausible that severe imaging findings could portend worse outcome in particular settings, which would emphasize the importance of prompt recognition of ATL in particular clinical scenarios.

Given that prior studies were smaller and preliminary, the goal of this larger study was to evaluate various causes of ATL, to determine whether the imaging severity correlates with the clinical outcome, to evaluate differences in imaging severity and outcome among various etiologies/subgroups of ATL, and, secondarily, to describe any new causes of ATL.

MATERIALS AND METHODS

Patients: Inclusion/Exclusion Criteria

This retrospective, observational study was approved by the institutional review boards of University of Minnesota Medical Center and Hennepin County Medical Center (a quaternary care and a level I trauma center). Patients with suspected ATL were identified by PACS archives over 16 years (June 2002 to June 2018), as well as a radiological information system report search for the terms “leukoencephalopathy” or “toxic” in patients having undergone MR imaging, using 2 software programs: Vitrea Intelligence (Vital Images, Minnetonka, Minnesota) and Primordial communicator module of Powerscribe (Nuance Communications, Burlington, Massachusetts). These 2 methods yielded 172 patients suspected of having ATL on MR imaging before in-depth electronic health record review; thereafter, their electronic health records were reviewed by a quartet of a neuroradiology fellow, a radiology resident, a research fellow, and a medical student (C.O., J.C.B., S.K.R., N.J.K.) to assess whether patients were also clinically confirmed as having ATL or whether there was any positive clinical finding correlating with imaging such as withdrawal of the culprit agent and subsequent resolution of imaging/symptoms. The MR images were then reviewed separately by 2 staff neuroradiologists (A.M.M. and J.B.R. in University of Minnesota Medical Center and A.M.M. and M.C.O. in Hennepin County Medical Center, each with >10 years’ experience) to include those with ATL on MR imaging. Because there are overlapping etiologies that may cause both ATL and PRES, the neuroradiologists ensured that there was no cortical edema, which has been described as the earliest manifestation of PRES; thus, patients were included only if they had reduced diffusion involving the white matter.¹¹⁻¹³

Inclusion criteria for formal review (of imaging severity and outcome) included, at a minimum, the following: MR imaging within 3 weeks of presentation, including DWI with ADC maps,

and FLAIR images obtained in the acute setting when patients were still symptomatic, either in the pretreatment or early treatment era, as well as MR imaging with reduced diffusion in the white matter suspicious for ATL.² Patients were excluded if there was a lack of DWI or ADC maps, lack of measured ADC reduction, CTL or MR imaging findings not suggestive of ATL (eg, predominantly cortical edema), other PVWM disorders with reduced diffusion (eg, lymphoma, primary brain tumor, infarction, trauma); or they were younger than 10 years of age or had infectious disorders, hypoxic-ischemic insults, leukodystrophies, severely compromised MR imaging data, clinical findings not indicating ATL (eg, lack of acute neurologic symptoms, discordance between clinical and radiologic findings), and potential confounding conditions (eg, cranial metastasis or the presence of leptomeningeal enhancement) (Fig 1).

MR Imaging Acquisition

During a 15-year period, multiple 1.5T and 3T MR imaging units were used, so the sequence parameters varied. However, the general ranges were as follows for FLAIR, DWI, SWI, postcontrast T1WI, and MRA—FLAIR: TR/TE/TI/NEX/echo-train length at 1.5T: 6000–9000 ms/105–110 ms/2000–2200 ms/1–2/15–23; at 3T: 8000–11,000 ms/100–120 ms/2000–2200 ms/1–2/11–25; on 1.5T DWI: TR/TE, 3100–4000 ms/70–120 ms; on 3T: TR/TE, 2700–3000 ms/60–100 ms; gradient strength $b=1000$ s/mm²; SWI: TR/TE/NEX/flip angle at 1.5T: 49 ms/40 ms/1/15°; at 3T: 20 ms/27 ms/1/15°; postcontrast T1WI: TR/TE/NEX/echo-train length at 1.5T: 420–500 ms/12–15 ms/2–3/35; at 3T: 500–650 ms/11–15 ms/1–2/35; TOF-MRA: TR/TE/NEX at 1.5T, 35–40 ms/7 ms/1; at 3T, 20–25 ms/3–4 ms/1. The slice thickness for FLAIR, DWI, and postcontrast T1WI was 5 mm; for SWI, it was 2 mm; and for TOF-MRA, it was 0.9 mm (4 slabs).

MR Imaging Review, Grading of Radiologic Severity, and ADC Measurements

ADC measurements were obtained from the lowest ADC value region and averaging 3 ROIs from these abnormal regions. ROI sizes were selected as either the smallest or the default size allowed by the PACS, varying between 0.165 and 0.371 cm² for standardization of the measurements. If ATL was bilateral, the ROIs were averaged between sides; if unilateral, the 3 ROIs were averaged from that lesion. The percentage ADC reduction in visibly affected regions was calculated and compared with normal-appearing white matter, usually being the anterior frontal PVWM, by averaging ≥ 3 ADC-value ROIs. All ADC measurements were obtained by a neuroradiology fellow (C.O.) separately, before MR imaging severity scoring.

The initial MR imaging severity of DWI and FLAIR was graded independently by 2 staff neuroradiologists using a previously described system, ranging from grades 0 to 4 (0 = normal, 4 = severe; see the On-line Appendix for more information).^{2,14} In a few cases in which scoring was different, these images were evaluated jointly by the 2 neuroradiologists in a separate session. SWI and postcontrast T1WI were also assessed, as well as follow-up MR imaging, when available. CTA or MRA was also evaluated, if available, for any additional positive findings.

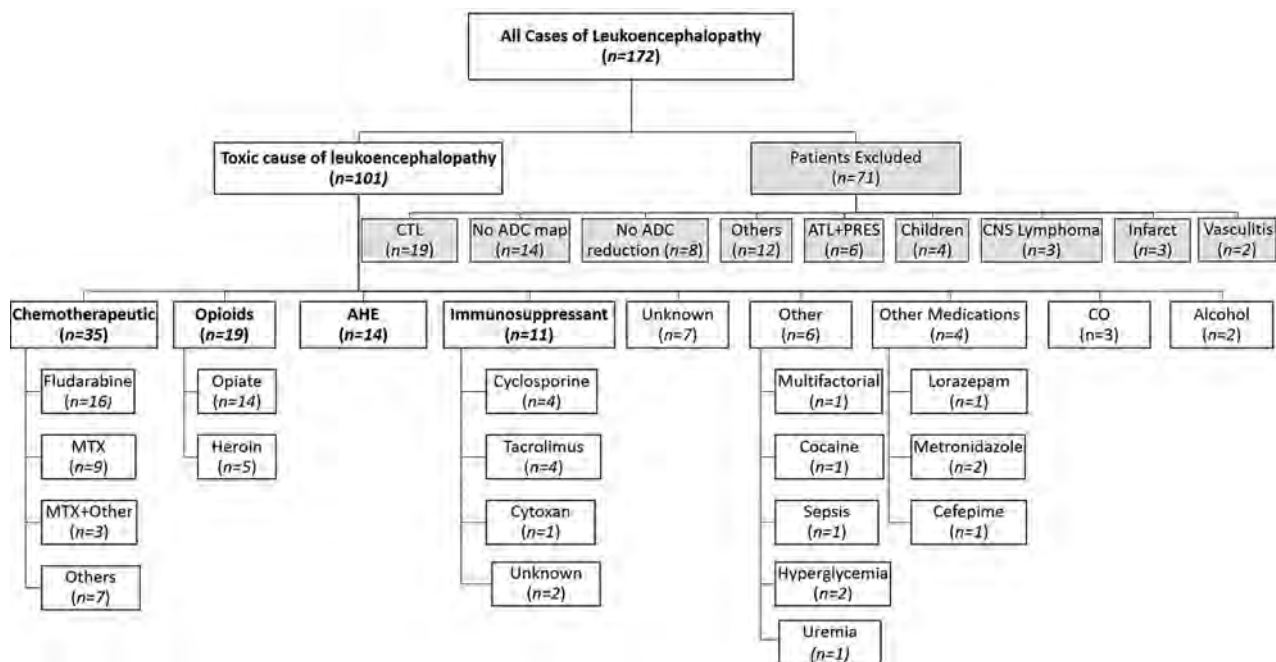


FIG 1. Organizational chart of inclusion of 101 patients with ATL in this study. MTX = Methotrexate; CO = carbon monoxide; CTL = Chronic toxic leukoencephalopathy; ATL+PRES = Acute toxic leukoencephalopathy with concomitant posterior reversible encephalopathy syndrome.

Table 1: Summary of variables with respect to groups of cause of ATL

Variable	Statistic	All ATL (n = 101)	CTX (n = 35)	O/H (n = 19)	AHE (n = 14)	ID (n = 11)	Unknown (n = 7)	Other (n = 6)	PM ^a (n = 4)	CO (n = 3)	Alcohol (n = 2)
Sex	Male	50	17	11	7	2	2	4	2	3	2
	Female	51	18	8	7	9	5	2	2	0	0
Age (years)	Mean (SD)	40.72 (17.6)	41.3 (18.9)	34.6 (14.7)	44.6 (14.2)	52.1 (19.7)	33.6 (13.0)	36.4 (21.2)	49.0 (20–68) ^b	31.3 (20–44) ^b	31.0 (25–37) ^b
mRS score	Mean (SD)	1.97 (2.1)	2.71 (2.2)	2.33 (2.0)	2.07 (2.2)	0.40 (0.5)	1.50 (1.6)	1.80 (2.5)	0.25 (0–1) ^b	1.67 (0–5) ^b	0.50 (0–1) ^b
ATLOS score	Mean (SD)	1.60 (1.6)	2.29 (1.7)	1.67 (1.4)	1.57 (1.7)	0.60 (0.97)	1.17 (1.2)	1.40 (2.0)	0.25 (0–1) ^b	1.33 (0–4) ^b	0.50 (0–1) ^b
DWI severity	Mean (SD)	2.59 (1.1)	2.63 (1.0)	3.26 (1.1)	2.07 (0.9)	2.00 (0.77)	2.14 (1.2)	3.20 (1.3)	2.75 (2–4) ^b	2.67 (1–4) ^b	2.00 (1–3) ^b
FLAIR severity	Mean (SD)	2.52 (1.2)	2.34 (1.3)	3.32 (0.9)	2.15 (1.0)	2.55 (0.5)	2.00 (1.3)	3.40 (1.3)	1.67 (1–3) ^b	2.33 (0–4) ^b	1.50 (1–2) ^b
ADC % loss	Mean (SD)	35.6% (17.9)	34.0% (20.1)	41.3% (16.2)	30.5% (14.2)	28.2% (13.7)	32.4% (20.0)	34.3% (13.7)	44.4% (20.8–62.1) ^b	63.8% (58.9–71.6) ^b	38.9% (29.5–48) ^b

Note:—CTX indicates Chemotherapeutics; O/H, Opiates/Heroin; AHE, Acute Hepatic Encephalopathy; ID, Immunosuppressive drugs; PM, Prescribed medications; CO, Carbon Monoxide.

^a Including metronidazole (n = 2), lorazepam (n = 1), and cefepime (n = 1).

^b Minimum-Maximum.

Clinical Outcome Scoring

To score the clinical outcome, 2 scoring methods were used: the mRS (based on a clinical follow-up time at >90 days) and a previously published ATL outcome score (ATLOS, based on clinical follow-up of >30 days).^{2,15} During the electronic health record review, the etiology of ATL was explained if clearly identified. Regarding laboratory tests, results of a basic metabolic panel and CSF tests obtained within a time window of 1 week before and after the initial brain MR imaging were evaluated if available and clinically important abnormal values were recorded.

Statistical Evaluation

A biostatistician performed the calculations. For statistical comparison among subgroups, subcategories of ATL etiologies were

compared consisting of >6 patients; these subgroups were compared using the Kruskal-Wallis (continuous variables), Fisher exact (categorical variables), and pair-wise comparison (subgroup-subgroup) tests, to evaluate significant differences in MR imaging severity or outcomes among subgroups. For pair-wise comparisons, Kruskal-Wallis (with 2 groups) tests were used. The Wilcoxon test was used to compare MR imaging measures of the subjects with the most severe clinical outcomes, with those with complete symptom resolution. To adjust for multiple pair-wise comparisons, the *P* value threshold for significance was set to *P* < .0083 using Bonferroni's method. Spearman correlations were then obtained separately between each of the following variables, including age, FLAIR MRI severity, DWI MRI severity, mRS and ATLOS outcome scores, while the Wilcoxon test was

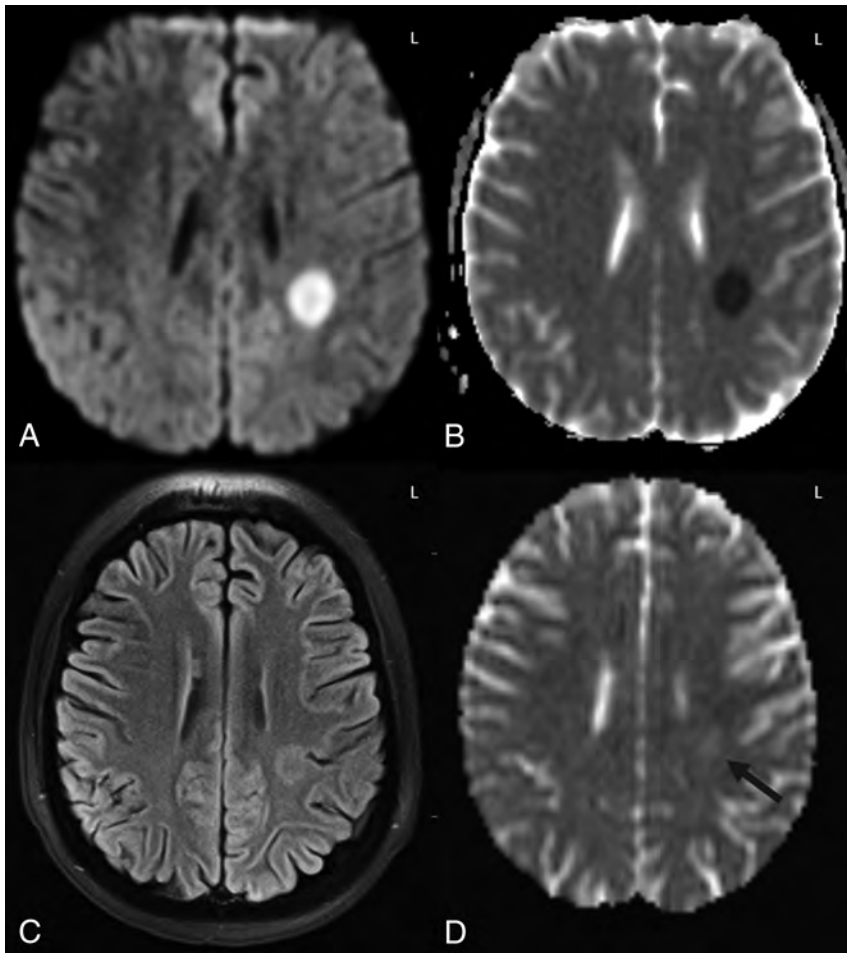


FIG 2. Example of grade 1 DWI-FLAIR ATL severity. A 16-year-old girl with acute leukemia after 5 days of high-dose cytarabine and clofarabine combined chemotherapy, presented with acute right upper extremity weakness. An initial head CT (not shown) was unremarkable. On DWI (A) and ADC (B), unilateral diffusion reduction was present in the left PVWM with 60% ADC loss compared with NAWM and corresponding faint FLAIR hyperintensity (C). Accompanying MRA study (not shown) was normal. D, On follow-up MR imaging at 2 weeks after withdrawal of the chemotherapy, there was normalization of diffusion reduction with faint residual hyperintensity on DWI (not shown), ADC map (D, black arrow), and FLAIR (not shown), with a resultant T2-shinethrough effect on DWI. The symptoms had resolved at long-term clinical follow-up with both the ATLOS and mRS clinical scores being 0.

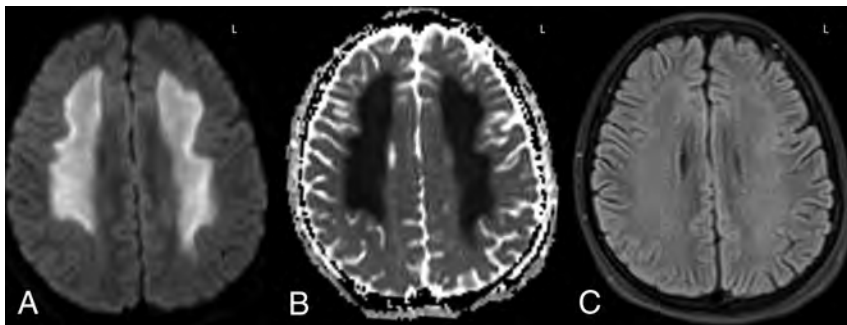


FIG 3. Example of a grade 2 DWI-FLAIR ATL severity from uremia. A previously healthy 16-year-old boy with coma had renal failure of unknown cause, blood urea nitrogen level of >115 mg/dL (normal <25 mg/dL), creatinine level of 18.34 mg/dL (normal, <1.2 mg/dL), glomerular filtration rate of 5 (normal, >90), and systolic blood pressure of >160 mm Hg. MR imaging revealed PVWM abnormalities sparing the basal ganglia on DWI (A and B), with a normal appearance on FLAIR (C) and normal MRA (not shown). Laboratory work-up only revealed uremia. Clinically, the symptoms resolved with dialysis, and MR imaging 2 days later (not shown) noted continued diffusion reduction, while the ADC values rose with complete resolution of symptoms (the ATLOS and mRS scores were 0).

used to evaluate for differences between gender ($P < .05$ used for both the Spearman and Wilcoxon tests). All analyses were obtained using SAS (Version 9.4; SAS Institute, Cary, North Carolina).

RESULTS

Patient Demographics and Subcategories of ATL

Ultimately, 101 patients with ATL were included, with 71 excluded, most commonly due to CTL ($n = 19$), as shown in Fig 1. The subcategories of causes with $n > 6$ were chemotherapy ($n = 35$), opiates ($n = 19$), acute hepatic encephalopathy (AHE, $n = 14$), and immunosuppressive drugs ($n = 11$), as shown in Table 1. There were no significant differences in sex or age among each of the 4 subgroups of >6 (each, $P > .05$). Samples of patients' MR images are depicted in Figs 2–5.

MR Imaging Severity Scoring and Subgroup Comparisons

Table 1 depicts the mean severities on DWI and FLAIR of all patients. There were significant differences overall between the mean DWI ($P = .003$) and FLAIR ($P = .009$) MR imaging severity scores among the 4 major subgroups. Notably, opiate abuse had the highest mean severity on both sequences, while patients who were immunosuppressed and those with AHE had the least mean severity on DWI and FLAIR, respectively. Pair-wise intergroup comparisons of the MR imaging severities and outcomes of the 4 subgroups are provided in Table 2. Notably, 6/101 patients with ATL had only reversible splenial lesions (grade 1 severity) with complete symptom resolution; of these, the causes in 4 different patients were the following: chemotherapy, immunosuppressive medication, sepsis, and alcohol toxicity, while in the remaining 2 patients, the etiology was unknown.

Clinical Outcome Severities and Subgroup Comparisons

Table 1 provides the mean clinical outcome score on mRS at >90 days and on ATLOS at >30 days for each subgroup; in 7 patients, outcomes could not be discerned. Overall, significant differences were found among the 4 major sub-

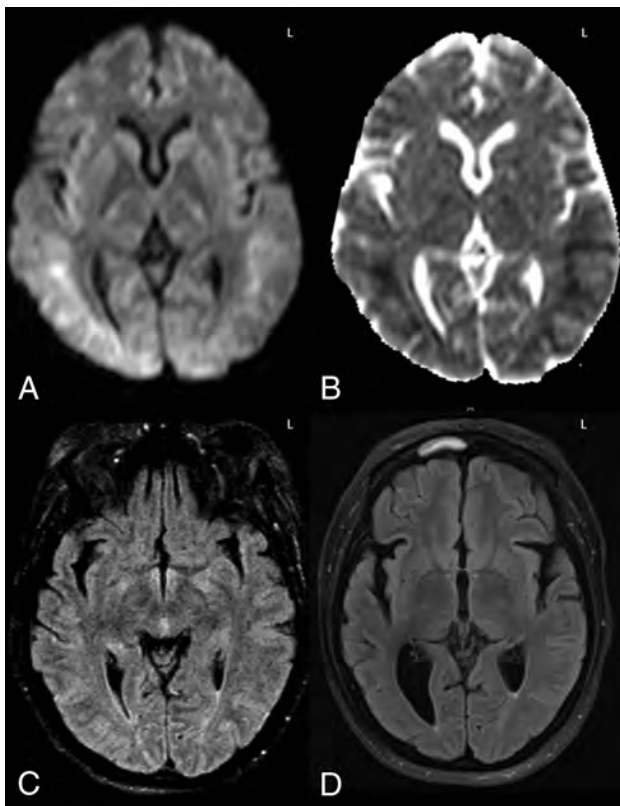


FIG 4. A 40-year-old woman with altered mentation 1 month post-liver transplantation, who was immunosuppressed with tacrolimus. MR imaging demonstrated extensive diffusion reduction bilaterally in the PVWM and subcortical white matter on DWI and ADC (A and B), with 58% ADC loss (versus NAWM) and slight hyperintensity on FLAIR (C) involving 3 lobes, consistent with grade 3 ATL imaging severity on DWI and FLAIR. Note that there was no apparent cortical edema on FLAIR to suggest PRES. After the withdrawal of tacrolimus and supportive therapy, the long-term ATLOS and mRS scores were both 0. D, An MR imaging 12 years later (obtained for chronic headaches) showed mild-moderate right PVWM loss and ex-vacuo dilation of the occipital horn of the right lateral ventricle as sequelae of ATL, without cortical encephalomalacia.

groups for both the mRS ($P = .025$) and ATLOS ($P = .032$) scores. When we compared these subgroup outcomes against each other (Table 2), there were significant differences between the chemotherapy-versus-immunosuppressed subgroups for both scores, and between opiate-versus-immunosuppressed groups based on the mRS only; the other intergroup comparisons did not have significant differences (each, $P > .0083$).

Severe outcomes (grade 4 on ATLOS or grade 5–6 on mRS) were noted in 22/94 (23.4%) patients with available data in this study, 16 of whom died and 6 being comatose at 90 days postpresentation; 13 of these 22 patients had severe outcomes from chemotherapy. In the 16 patients who died, the etiologies were the following: fludarabine ($n = 9$), AHE ($n = 3$), and 1 each of methotrexate, opiates, hyperglycemia, and rituximab. In the 16 patients who died, the cause of death was often other comorbidities such as sepsis, organ failure, cardiac arrest, or diffuse malignancy, though their neurologic symptoms related to ATL never subsided. At the other end of the clinical outcome spectrum, there was symptom resolution (ATLOS or mRS grade 0) in 34/94 (36.1%) patients with ATL, with 26/94 (27.6%) having only minimal se-

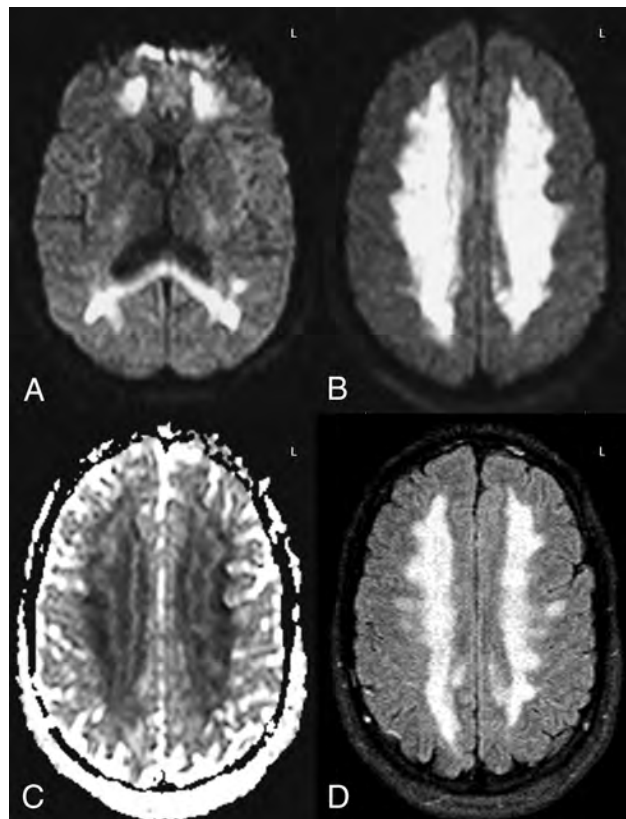


FIG 5. Example of opiate-related grade 4 DWI-FLAIR ATL severity. A 26-year-old comatose man with urine toxicology positive for propoxyphene (an opioid analgesic) had diffuse and confluent DWI-ADC (A–C) and FLAIR (D) abnormalities with 67% ADC loss versus NAWM. The patient had moderate long-term neurologic sequelae, with the ATLOS at 1 month being 2 and the mRS at 3 months being 3. Follow-up MR imaging was not performed.

quela (ATLOS grade 1 or mRS grades 1–2). When we compared the subjects with the most severe clinical outcomes ($n = 22$) with those with complete symptom resolution ($n = 34$) regardless of different etiologies, DWI and FLAIR imaging scores were higher in the severe-outcomes group compared with the symptom-resolution group. DWI_{mean} was 3.1 versus 2.2 ($P = .002$), and $FLAIR_{\text{mean}}$ was 3 versus 2 ($P = .005$), respectively.

Correlation of MR Imaging Severity of Subgroups with Outcomes

There was a strong correlation between DWI and FLAIR severity ($\rho = 0.731, P < .0001$) and between the mRS and ATLOS scores ($\rho = 0.978, P < .0001$). There were mild-moderate correlations between both the DWI and FLAIR severity with both the mRS and ATLOS ($\rho = 0.289–.349, P \leq .005$) as shown in Table 3. Regarding the 4 subcategories of >6 , both DWI and FLAIR severity mildly to moderately correlated with the outcome scores for opiates ($\rho = 0.472–0.608, P < .05$) and chemotherapy ($\rho = 0.460–0.586, P < .05$). There was no significant correlation of age or sex with either DWI or FLAIR severity or with either clinical outcome score (each, $P > .005$).

ADC Measurements and Other MR Imaging/MRA Findings

A boxplot (Fig 6) shows that the greatest percentage ADC reduction was noted in the affected PVWM of carbon monoxide toxicity

Table 2: Pair-wise intergroup comparison of clinical outcomes among the 4 largest subgroups causing ATL^a

	P Values for Pair-wise Comparison					
	Chemotherapy vs Immunosuppressant	Chemotherapy vs AHE	Chemotherapy vs Opiates	Immunosuppressant vs AHE	Immunosuppressant vs Opiates	Opiates vs AHE
mRS	.004 ^b	.32	.62	.07	.007 ^b	.61
ATLOS	.006 ^b	.16	.23	.19	.031	.66
DWI severity	.08	.08	.03	.93	.003 ^b	.003 ^b
FLAIR severity	.90	.50	.006 ^b	.25	.015	.003 ^b

^a Multiple comparisons were adjusted with a Bonferroni correction ($P = .0083$).

^b Significant.

Table 3: Correlation between MRI severity and clinical outcome severity

	All Patients		Chemotherapeutics		Opiates		AHE		Immunosuppressants	
	mRS	ATLOS	mRS	ATLOS	mRS	ATLOS	mRS	ATLOS	mRS	ATLOS
DWI severity										
ρ	.349	.289	.478	.460	.608	.573	-.123	-.240	.000	-.103
P	.001 ^a	.005 ^a	.006 ^a	.009 ^a	.007 ^a	.012 ^a	.674	.408	1.00	.777
FLAIR severity										
ρ	.336	.332	.543	.586	.472	.412	.123	.135	.000	.079
P	.001 ^a	.001 ^a	.001 ^a	.001 ^a	.047 ^a	.088	.689	.659	1.00	.826

^a Significant.

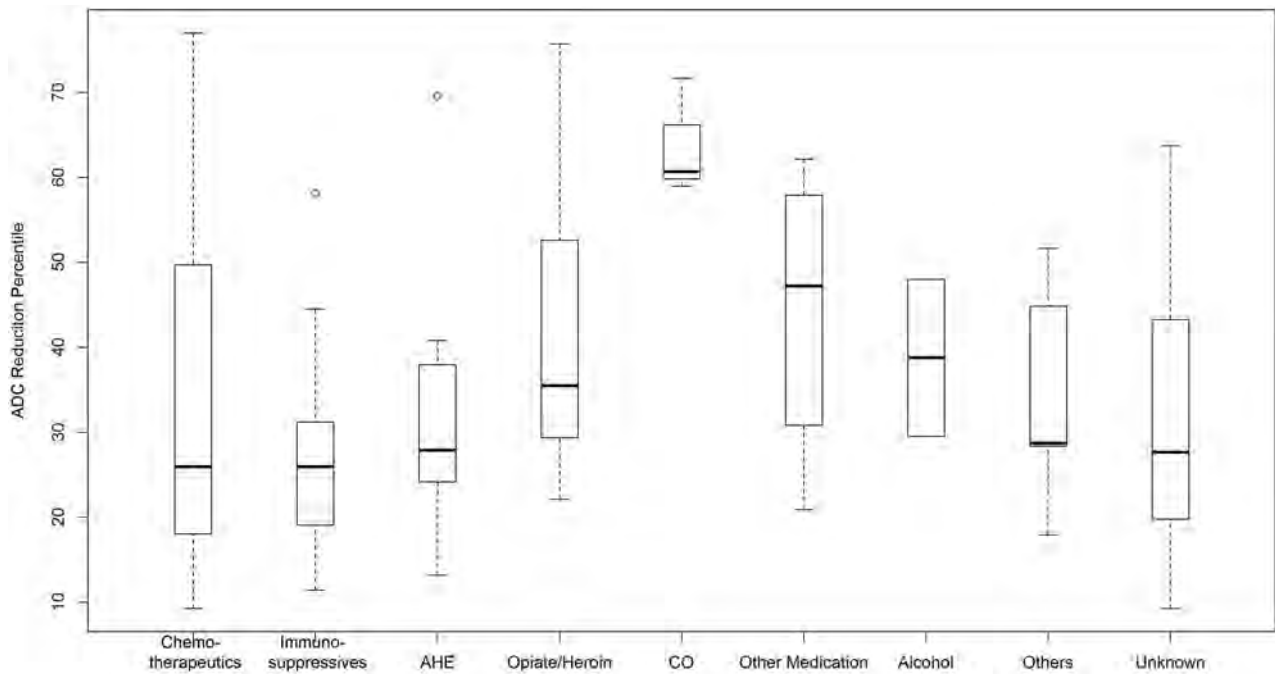


FIG 6. Boxplot of each etiologic subgroup with the percentage ADC reduction of affected regions compared with NAWM. ATL from carbon monoxide (CO, a small subgroup of 3) had a much greater percentage ADC reduction versus the other subgroups.

(mean, 64.0%), while the least was the immunosuppressive medication subgroup (mean, 28.2%). Regarding other MR imaging findings, contrast-enhanced T1WI was available in 72 patients, without any >1-cm-size enhancing foci, though punctate foci were found in 7/72 (9.0%) amid the PVWM lesions on DWI. SWI was available in 52 patients (T2*WI, in 8 others), with punctate microhemorrhages in 9/60 patients (15%); 5 of these 9 had an mRS ≤ 1 . MRA was available in 23/101 patients, and the findings of only 1 were positive (an incidental aneurysm).

Additional Laboratory Findings

Of 101 patients with ATL, 45 had a lumbar puncture; 24/45 had positive CSF findings. Most notably, in the 9 patients with an

available myelin basic protein (MBP) level, 8 had increased MBP (4 from fludarabines, 3 from opiates, 1 unknown), 9 had increased total protein, 9 had increased glucose, and 2 had findings positive for oligoclonal bands. A metabolic panel was available in 91 patients; 54/91 had a positive finding—most notably, the blood urea nitrogen level was increased in 24 of these 91 patients.

DISCUSSION

ATL is an uncommon condition that should be considered in the differential diagnosis of patients with acute encephalopathy. It is a clinicoradiologic diagnosis characterized by cerebral WM injury on DWI from a toxic substance and should be distinguished from

other clinical disorders such as PRES, hypoxic-ischemic encephalopathy, meningitis, encephalitis, tumor recurrence, metastasis, stroke, acute disseminated encephalomyelitis, and other metabolic syndromes. Recognizing this uncommon disorder is vital because it can be potentially reversible with prompt removal of the underlying cause and supportive therapy, while the clinical outcome varies among etiologies. Given the shared imaging appearance on DWI of the various causes of ATL, it is important to both diagnose this condition and assist the ordering physician in determining an underlying etiology, given the differences in outcomes among causes. However, to our knowledge, no larger study has as yet evaluated differences in outcomes among different etiologies of ATL.

Many etiologies have been reported for ATL, including a variety of chemotherapeutic and immunosuppressive medications, opiate ingestion (whether prescribed or illicit), some antimicrobial medications, various metabolic disorders (such as hyperammonemia from AHE or hyperglycemia), carbon monoxide poisoning, and, recently, even a commercially available dietary supplement.^{2-10,16-18} In this study, chemotherapy was the most common cause, followed by opioids, AHE, and immunosuppressants, while the cause was unknown in 7%. According to these results, each cause may affect each age group and sex equally, but the imaging severity and clinical outcomes differ among the types of etiologies.

The exact pathophysiology of ATL is also unknown, but the evidence shows that white matter damage may occur directly from toxic injury on the myelin sheath or indirectly from capillary endothelial injury or a combination of both.^{2-4,13} For example, carbon monoxide and inhaled opiates may cause either toxic demyelination or spongiform degeneration of the PVWM.^{5,19} While chemotherapeutics such as fludarabine and methotrexate can cause direct toxic damage of the axons and myelin sheath, chemotherapeutic agents, such as methotrexate and 5-fluorouracil, and immunosuppressive agents, such as tacrolimus and cyclosporine, were shown to disrupt the cerebral microvasculature.^{4,20-24} Regardless of the culprit agent, diffusion reduction in the PVWM may appear due to pathologic changes in the myelin from intramyelinic edema or toxic demyelination.^{2,3,5,8}

The conditions of about one-third of the patients with ATL in this study were from chemotherapy, with fludarabine (16%) being most common and methotrexate in 12%. Fludarabine was also the most common cause of death from ATL (9/16 patients with ATL who died), in accord with prior literature that showed that fludarabine can cause severe, late-onset ATL (weeks after chemotherapy) and that ATL from fludarabine has worse outcomes relative to PRES from fludarabine.^{4,25} Thus, fludarabine likely accounts for the chemotherapy-related subgroup having the worst outcome.

Opioids were the second most common cause of ATL in this study (18.8%), having the second worst outcomes of the 4 ATL subgroups that consisted of >6 patients, while this group tends to have the most severe extent on DWI. Opioids are lipophilic substances that can cross through the BBB and accumulate in fat-rich myelin when in high doses, thus causing cerebral or cerebellar symmetric spongiform degeneration.^{19,26} Particularly in the case of "chasing the dragon," the inhaled substance bypasses other

organs, thus allowing faster, direct passage to the brain relative to the intravenous route. In addition, potentially superimposed hypoxia may induce BBB disruption, thus aggravating the toxic effects.²⁷ Notably, opiate toxicity/overdose may present with several imaging patterns (such as basal ganglia injury), perhaps due to anoxic injury; hence, because this study focused solely on the PVWM pattern of injury of ATL, these results may not be extrapolated onto other imaging patterns.

AHE (13.8%) was the third most common cause of ATL. Notably, AHE most commonly involves the insula or thalami, with variable PVWM involvement.⁹ Thus, this study included only AHE with solely PVWM lesions, which occurs in 15% of the cases of AHE.⁹ The outcomes of AHE-related ATL in this study tended to be slightly better than those of chemotherapy- and opiate-related ATL.

The fourth largest subgroup was immunosuppressant medications (10.9%). With the increasing implementation of marrow transplantation, ATL from immunosuppressants may be increasing in frequency in a fashion similar to that of another potentially reversible disorder, PRES.^{11,12,14,28} Thus, immunosuppressant-related ATL had the best outcomes relative to the other subgroups of known causes in this study. However, both this study and prior ones have shown that ATL from immunosuppressive medications such as cyclosporine is still relatively uncommon.^{4,12}

Another subgroup of ATL was carbon monoxide toxicity ($n = 3$), which has at least 3 previously described patterns of involvement on DWI: PVWM, basal ganglia, or hippocampal (least common).^{5,29} Concomitant anoxic injury causing such lesions may also occur, but the PVWM variant was present in only a few patients in this study ($n < 6$), thus preventing a correlation of the clinical outcomes to the imaging severity.

Regarding the intergroup comparisons of imaging severity, the DWI severity was worse in the opiate subgroup versus the AHE and immunosuppressant subgroups, where ATL from opiates and chemotherapy tended to have more diffuse WM involvement. Meanwhile, ATL from AHE and immunosuppressants was milder and more focal. In most patients with ATL, the FLAIR lesions were less evident than on DWI or developed later, as shown previously.²

Regarding other imaging findings, contrast enhancement is not a common feature in ATL, being punctate and observed in only 9% of patients in this study, with differing outcomes; thus, the presence of enhancement likely neither changes the diagnosis nor affects outcome. Similarly, the presence of microhemorrhages (in 15%) does not correlate with outcome and likely does not have clinical significance but may be related to underlying vasculopathy.³⁰ MRA findings were largely negative, and only 1 patient had an incidental aneurysm.

Regarding the clinical outcomes from ATL and comparisons between subgroups, chemotherapy- and opiate-related ATL had significantly worse outcomes, despite the potentially reversible nature of ATL. Again, fludarabine likely accounts for the chemotherapy subgroup having the worst outcomes overall. In comparison, immunosuppressant-related ATL was less common in our population, with milder imaging severity and better outcomes, which is of note because one might expect that the comorbidities in immunosuppressed patients would precipitate worse out-

comes. Although chemotherapy- and opiate-related ATL has worse clinical outcome scores compared with immunosuppressant-related ATL in pair-wise comparison (Table 2), only the opiate subgroup showed significant differences regarding imaging severity compared with the immunosuppressant group, which also supports the opiate-related ATL having the most severe and extensive DWI findings.

Regarding the AHE and immunosuppressant subgroups, the severity of imaging findings and clinical outcome did not significantly correlate in either of these 2 subgroups; this finding likely confirms the potentially reversible nature of ATL within these 2 subgroups. On the other hand, the opiate and chemotherapy subgroups of ATL had overall more severe MR imaging scores/extent, with moderate correlations between the imaging severity and outcome, suggesting that more diffuse brain involvement is likely to result in neurologic sequelae. Regardless of different etiologies, when the extent of abnormal DWI and FLAIR findings reached grade 3 or 4 (On-line Appendix), there was a higher possibility of severe outcomes.

The review of the laboratory values yielded interesting findings of MBP and blood urea nitrogen levels that may further elucidate the underlying pathophysiology of ATL. MBP is an important component of CNS myelin formation, and though its presence in CSF is nonspecific, increased levels of CSF-MBP suggest active demyelination in some syndromes, such as multiple sclerosis.^{31,32} In this regard, a prior study focused on transplant neurotoxicity may have been the first of fludarabine-related ATL (having 4 patients from this study's cohort), and described high CSF-MBP levels.⁴ In addition, the current study may be the first description of elevated CSF-MBP in opiate-related ATL (3 patients) in humans, suggesting myelin damage; notably, CNS MBP is reduced with chronic demyelination in mice chronically exposed to opiates.³³ Hence, CSF-MBP could be a potential marker to support the diagnosis of and evaluate the extent of myelin damage in ATL.

Another value, serum blood urea nitrogen, was increased in 26% of the patients with available values, secondary to either impaired kidney function or tumor lysis in patients in oncology. Most interesting, uremia has been described in association with PRES, whereas uremic encephalopathy may present on MR imaging with symmetric T2 hyperintensity of the basal ganglia.³⁴ To our knowledge, the patient with uremia-related ATL described herein with PVWM involvement but sparing the basal ganglia may be the second such patient with uremia described with that imaging appearance (Fig 3).³⁵ Furthermore, a recent study focused on concomitant ATL and PRES in a small cohort (a subset of patients excluded from this study) in which most had kidney failure and perhaps uremia.¹³ It is not known how uremia causes toxic leukoencephalopathy; however, diffusion tensor imaging studies found premature PVWM disease, especially in the anterior PVWM in patients with chronic kidney disease, and various uremic toxins may cause both endothelial dysfunction and cognitive impairment, especially via neuroexcitatory uremic-guanidine compounds.^{36,37} Given the number of patients with uremia in this study, it is plausible that uremia may exacerbate ATL or even predispose to ATL in the absence of other toxins.

There are several limitations to this study, the predominant

one being that it was retrospective; for example, the clinical outcomes were based on retrospective evaluation of the patients' records. In addition, many patients, particularly within the chemotherapeutic and immunosuppressant groups, had multiple confounding factors that could affect the clinical outcome. Also, in the case of exposure to multiple potential toxic agents or medications, the MR imaging findings could vary due to superimposed nontoxic etiologies such as anoxia, sepsis, or renal failure. However, the authors note that this study focused on the outcomes from a common, shared imaging appearance of ATL involving the PVWM and included patients on that basis, not on the basis of etiology. Finally, multiple MRIs from different machines with 1.5T and 3T strengths were performed, whereas the differences in appearances and ADC values between 1.5T and 3T were not assessed in this study.

CONCLUSIONS

ATL is an imaging appearance that can arise from various etiologies, with potentially reversible reduced diffusion predominantly affecting the PVWM. Given the shared DWI appearance among this heterogeneous array of etiologies, their outcomes may differ. Thus, the neurologic symptoms completely resolved in 36%, while severe outcomes occurred in 23%. The clinical outcome was most severe with chemotherapy-related ATL (mostly due to fludarabine), whereas opiate toxicity had the second worst outcome and tends to have more severe extent on DWI. In contrast, immunosuppressive-related ATL tends to be more focal and clinically milder. These observations point to a need to study other clinical factors or comorbidities that influence the outcomes of ATL, such as the presence of uremia.

Disclosures: Mark C. Oswood—UNRELATED: Payment for Lectures Including Service on Speakers Bureaus: Philips Healthcare, Comments: sponsored lectures and speakers bureau in 2016–2017. Alexander M. McKinney—UNRELATED: Board Membership: VEEV, Inc., Minneapolis, MN, Comments: president and owner, informatics company; Patents (Planned, Pending or Issued): informatics patents; Royalties: Springer Nature, Cham, Switzerland, Comments: book royalties.

REFERENCES

1. Filley CM, Kleinschmidt-DeMasters BK. **Toxic leukoencephalopathy.** *N Engl J Med* 2001;345:425–32 CrossRef Medline
2. McKinney AM, Kieffer SA, Paylor RT, et al. **Acute toxic leukoencephalopathy: potential for reversibility clinically and on MRI with diffusion-weighted and FLAIR imaging.** *AJR Am J Roentgenol* 2009;193:192–206 CrossRef Medline
3. Rimkus Cde M, Andrade CS, Leite Cda C, et al. **Toxic leukoencephalopathies, including drug, medication, environmental, and radiation-induced encephalopathic syndromes.** *Semin Ultrasound CT MR* 2014;35:97–117 CrossRef Medline
4. Beitinjaneh A, McKinney AM, Cao Q, et al. **Toxic leukoencephalopathy following fludarabine-associated hematopoietic cell transplantation.** *Biol Blood Marrow Transplant* 2011;17:300–08 CrossRef Medline
5. Teksam M, Casey SO, Michel E, et al. **Diffusion-weighted MR imaging findings in carbon monoxide poisoning.** *Neuroradiology* 2002; 44:109–13 CrossRef Medline
6. Keogh CF, Andrews GT, Spacey SD, et al. **Neuroimaging features of heroin inhalation toxicity: “chasing the dragon.”** *AJR Am J Roentgenol* 2003;180:847–50 CrossRef Medline
7. Sandoval C, Kutscher M, Jayabose S, et al. **Neurotoxicity of intrathecal methotrexate: MR imaging findings.** *AJNR Am J Neuroradiol* 2003;24:1887–90 Medline

8. Lucato LT, McKinney AM, Short J, et al. **Reversible findings of restricted diffusion in 5-fluorouracil neurotoxicity.** *Australas Radiol* 2006;50:364–68 CrossRef Medline
9. McKinney AM, Lohman BD, Sarikaya B, et al. **Acute hepatic encephalopathy: diffusion-weighted and fluid-attenuated inversion recovery findings, and correlation with plasma ammonia level and clinical outcome.** *AJNR Am J Neuroradiol* 2010;31:1471–79 CrossRef Medline
10. Kim E, Na DG, Kim EY, et al. **MR imaging of metronidazole-induced encephalopathy: lesion distribution and diffusion-weighted imaging findings.** *AJNR Am J Neuroradiol* 2007;28:1652–58 CrossRef Medline
11. Casey SO, Sampaio RC, Michel E, et al. **Posterior reversible encephalopathy syndrome: utility of fluid-attenuated inversion recovery MR imaging in the detection of cortical and subcortical lesions.** *AJNR Am J Neuroradiol* 2000;21:1199–206 Medline
12. McKinney AM, Short J, Truwit CL, et al. **Posterior reversible encephalopathy syndrome: incidence of atypical regions of involvement and imaging findings.** *AJR Am J Roentgenol* 2007;189:904–12 CrossRef Medline
13. Özütemiz C, Roshan SK, Kroll NJ, et al. **Concomitant acute toxic leukoencephalopathy and posterior reversible encephalopathy syndrome.** *J Neuroimaging* 2018;28:535–41 CrossRef Medline
14. Karia SJ, Rykken JB, McKinney ZJ, et al. **Utility and significance of gadolinium-based contrast enhancement in posterior reversible encephalopathy syndrome.** *AJNR Am J Neuroradiol* 2016;37:415–22 CrossRef Medline
15. Banks JL, Marotta CA. **Outcomes validity and reliability of the modified Rankin Scale: implications for stroke clinical trials—a literature review and synthesis.** *Stroke* 2007;38:1091–96 CrossRef Medline
16. Bartlett E, Mikulis DJ. **Chasing “chasing the dragon” with MRI: leukoencephalopathy in drug abuse.** *Br J Radiol* 2005;78:997–1004 CrossRef Medline
17. Schuurin J, Wesseling P, Verrips A. **Severe tacrolimus leukoencephalopathy after liver transplantation.** *AJNR Am J Neuroradiol* 2003;24:2085–88 Medline
18. Escamilla-Ocañas CE, Cámara-Lemarroy CR, Cantú-Martínez L, et al. **Acute toxic leukoencephalopathy associated with a non-prescription weight loss supplement: a report of two cases.** *Neurol Sci* 2017;38:2199–201 CrossRef Medline
19. Wolters EC, van Wijngaarden GK, Stam FC, et al. **Leukoencephalopathy after inhaling “heroin” pyrolysate.** *Lancet* 1982;2:1233–37 Medline
20. Akiba T, Okeda R, Tajima T. **Metabolites of 5-fluorouracil, alpha-fluoro-beta-alanine and fluoroacetic acid, directly injure myelinated fibers in tissue culture.** *Acta Neuropathol* 1996;92:8–13 CrossRef Medline
21. Shibutani M, Okeda R. **Experimental study on subacute neurotoxicity of methotrexate in cats.** *Acta Neuropathol* 1989;78:291–300 CrossRef Medline
22. Okeda R, Shibutani M, Matsuo T, et al. **Experimental neurotoxicity of 5-fluorouracil and its derivatives is due to poisoning by the monofluorinated organic metabolites, monofluoroacetic acid and alpha-fluoro-beta-alanine.** *Acta Neuropathol* 1990;81:66–73 CrossRef Medline
23. Aydin K, Donmez F, Tuzun U, et al. **Diffusion MR findings in cyclosporin-a induced encephalopathy.** *Neuroradiology* 2004;46:822–24 CrossRef Medline
24. Wilasrusmee C, Da Silva M, Singh B, et al. **Morphological and biochemical effects of immunosuppressive drugs in a capillary tube assay for endothelial dysfunction.** *Clin Transplant* 2003;17 (Suppl 9):6–12 CrossRef Medline
25. Lee MS, McKinney AM, Brace JR, et al. **Clinical and imaging features of fludarabine neurotoxicity.** *J Neuroophthalmol* 2010;30:37–41 CrossRef Medline
26. Kaiko RF, Wallenstein SL, Rogers A, et al. **Relative analgesic potency of intramuscular heroin and morphine in cancer patients with postoperative pain and chronic pain due to cancer.** *NIDA Res Monogr* 1981;34:213–19 Medline
27. Offiah C, Hall E. **Heroin-induced leukoencephalopathy: characterization using MRI, diffusion-weighted imaging, and MR spectroscopy.** *Clin Radiol* 2008;63:146–52 CrossRef Medline
28. Rykken JB, McKinney AM. **Posterior reversible encephalopathy syndrome.** *Semin Ultrasound CT MR* 2014;35:118–35 CrossRef Medline
29. Jeon SB, Sohn CH, Seo DW, et al. **Acute brain lesions on magnetic resonance imaging and delayed neurological sequelae in carbon monoxide poisoning.** *JAMA Neurol* 2018;75:436–43 CrossRef Medline
30. Benson JC, Payabvash S, Thalken GL, et al. **Delineation of microhemorrhage in acute hepatic encephalopathy using susceptibility-weighted imaging.** *Eur J Radiol* 2016;85:629–34 CrossRef Medline
31. Boggs JM. **Myelin basic protein: a multifunctional protein.** *Cell Mol Life Sci* 2006;63:1945–61 CrossRef Medline
32. Whitaker JN. **Myelin basic protein in cerebrospinal fluid and other body fluids.** *Mult Scler* 1998;4:16–21 Medline
33. Fan R, Schrott LM, Arnold T, et al. **Chronic oxycodone induces axonal degeneration in rat brain.** *BMC Neurosci* 2018;19:15 CrossRef Medline
34. Kim DM, Lee IH, Song CJ. **Uremic encephalopathy: MR imaging findings and clinical correlation.** *AJNR Am J Neuroradiol* 2016;37:1604–09 CrossRef Medline
35. Kang E, Jeon SJ, Choi SS. **Uremic encephalopathy with atypical magnetic resonance features on diffusion-weighted images.** *Korean J Radiol* 2012;13:808–11 CrossRef Medline
36. Drew DA, Koo BB, Bhadelia R, et al. **White matter damage in maintenance hemodialysis patients: a diffusion tensor imaging study.** *BMC Nephrol* 2017;18:213 CrossRef Medline
37. Bugnicourt JM, Godefroy O, Chillon JM, et al. **Cognitive disorders and dementia in CKD: the neglected kidney-brain axis.** *J Am Soc Nephrol* 2013;24:353–63 CrossRef Medline

Sexual Dimorphism and Hemispheric Asymmetry of Hippocampal Volumetric Integrity in Normal Aging and Alzheimer Disease

 B.A. Ardekani,  S.A. Hadid,  E. Blessing, and  A.H. Bachman

ABSTRACT

BACKGROUND AND PURPOSE: Asymmetric atrophy of the hippocampus is an important clinical finding in normal aging and Alzheimer disease. In this study, we investigate the associations between the magnitude and asymmetry of hippocampal volumetric integrity and age, sex, and dementia severity.

MATERIALS AND METHODS: We have recently developed a rapid fully automatic algorithm to measure the hippocampal parenchymal fraction, an index of hippocampal volumetric integrity on structural MR imaging of the brain. We applied this algorithm to measure the hippocampal parenchymal fraction bilaterally on 775 MR imaging volumes scanned from 198 volunteers in a publicly available data base. All subjects were right-handed and older than 60 years of age. Subjects were categorized as cognitively healthy ($n = 98$), with mild cognitive impairment ($n = 70$), or with mild/moderate Alzheimer disease ($n = 30$). We used linear mixed-effects models to analyze the hippocampal parenchymal fraction and its asymmetry with respect to age, sex, dementia severity, and intracranial volume.

RESULTS: After controlling for age, sex, and intracranial volume, we found that the magnitude of the hippocampal parenchymal fraction decreased and its asymmetry increased significantly with dementia severity. Also, hippocampal parenchymal fraction asymmetry was significantly higher in men after controlling for all other variables, but there was no sex effect on hippocampal parenchymal fraction magnitude. The magnitude of the hippocampal parenchymal fraction decreased and its asymmetry increased significantly with age in subjects who were cognitively healthy, but associations with age were different in nature in the mild cognitive impairment and Alzheimer disease groups.

CONCLUSIONS: Hippocampal atrophy progresses asymmetrically with age in cognitively healthy subjects. Hippocampal parenchymal fraction asymmetry is significantly higher in men than women and in mild cognitive impairment/Alzheimer disease relative to cognitively healthy individuals.

ABBREVIATIONS: AD = Alzheimer disease; AI = asymmetry index; ART = Automatic Registration Toolbox; CN = cognitively normal; DX = diagnostic group factor; ICV = intracranial volume; HPF = hippocampal parenchymal fraction; LHPF = left HPF; MCI = mild cognitive impairment; RHPF = right HPF

Alzheimer disease (AD) is the most common form of dementia, accounting for 60%–80% of all cases.¹ Age is the greatest risk factor for late-onset AD; and with an aging population, it is projected that the annual number of new AD cases in the United States will double by 2050.¹ There also appears to be a connection between AD and sex because women have an estimated double the

lifetime risk for developing AD,¹ and this cannot be solely explained by their higher average life expectancy of about 5 years.²

The hippocampus is a medial temporal lobe brain structure that plays a decisive role in the formation and retention of episodic memory and, in AD, is one of the first regions of the brain to experience atrophy.³ Structural MR imaging changes in the medial temporal lobe have been detected up to 10 years before clinical manifestations of AD.⁴ It is imperative to accurately characterize the patterns of hippocampal atrophy related to both normal aging and early AD, which would be extremely useful for developing new therapeutic interventions and monitoring disease progression. Numerous studies have shown significant reductions of hippocampal volume in mild cognitive impairment (MCI) and AD.^{5,6} Furthermore, many studies have reported hippocampal volume asymmetry in normal aging, MCI, and AD, with most reporting a right-greater-than-left asymmetry.^{6–10}

Received June 21, 2018; accepted after revision December 9.

From Center for Brain Imaging and Neuromodulation, The Nathan S. Kline Institute for Psychiatric Research (B.A.A., S.A.H., A.H.B.), Orangeburg, New York; and Department of Psychiatry (B.A.A., E.B.), New York University School of Medicine, New York, New York.

Please address correspondence to Babak A. Ardekani, PhD, Center for Brain Imaging and Neuromodulation, The Nathan S. Kline Institute for Psychiatric Research, 140 Old Orangeburg Rd, Orangeburg, NY 10962; e-mail: ardekani@nki.rfmh.org

<http://dx.doi.org/10.3174/ajnr.A5943>

Table 1: Cohort demographics^a

Group	CN	MCI	AD
CDR	0	0.5	1 (<i>n</i> = 28), 2 (<i>n</i> = 2)
No. of subjects	98	70	30
Sex (female:male)	72:26	39:31	20:10
Age (yr)	75.9 ± 9.0 (60–94)	76.2 ± 7.2 (62–92)	78.0 ± 6.9 (65–96)
Education (yr)	14.5 ± 2.9 (8–23)	13.8 ± 3.2 (6–20)	12.8 ± 3.2 (7–20)
ICV (cm ³)	1439 ± 150 (1132–1818)	1485 ± 187 (1171–1992)	1480 ± 118 (1274–1732)
MMSE	29.0 ± 1.2 (25–30)	25.6 ± 3.5 (14–30)	21.2 ± 4.0 (15–29)

Note:—CDR indicates Clinical Dementia Rating; MMSE, Mini-Mental State Examination.

^a Values given are means and range.

However, there have been some discrepancies in the literature over the nature of this putative hippocampal asymmetry. Some studies suggest that the observed asymmetry, at least in part, is due to a visual perception bias if the volumes are manually traced.^{11,12} Left-versus-right bias is also possible in automatic atlas-based hippocampal segmentation methods if care is not taken to ensure that a “symmetric method” is applied to measuring the bilateral hippocampi.^{8,10}

Sex is an important factor to consider for an accurate study of hippocampal asymmetry. The possibility that sex may determine asymmetry in brain structure and function is supported by known examples, including sex-dependent patterns of regional asymmetry in medial temporal lobe areas^{13,14} and in lateralization of blood oxygen level–dependent fMRI activation in response to emotional¹⁵ and semantic processing tasks.¹⁶ Whether asymmetry in the hippocampus per se is affected by sex is not clear. Most studies do not report any sex-related differences in their measured asymmetries.^{6,8–10} Maller et al⁷ did examine this question but did not find any sex difference in the degree of bilateral hippocampal asymmetry. Lucarelli et al,¹⁷ however, reported that men had greater asymmetry than women. There is also uncertainty as to whether the extent of asymmetry is the same between healthy subjects and MCI and AD groups,⁶ or whether asymmetry increases⁸ or decreases⁹ with increasing disease severity. These findings underline the need to further investigate the relationship among hippocampal asymmetry, sex, and disease severity. An improved understanding of these interactions toward a more precise patient-specific definition of disease-related changes was recently emphasized as a goal of the Alzheimer Precision Medicine Initiative.¹⁸

Hippocampal volume per se is not ideal for characterizing hippocampal degeneration. While atrophy of the hippocampus reduces its volume, the converse is not necessarily true—that is, a small volume does not necessarily indicate abnormality. For example, the raw hippocampal volumes in women are generally smaller than in men but the level of hippocampal atrophy is not different.⁷ Also, normal hippocampal volume is quite variable across subjects and is strongly influenced by intracranial volume (ICV) as a proxy for premorbid brain size.^{7,19,20} Due to these factors, it is difficult to detect subtle differences in hippocampal volume. To overcome this issue, we have recently developed a method to characterize the volumetric integrity of the hippocampus by measuring the hippocampal parenchymal fraction (HPF), an index that attempts to mimic how neuroradiologists visually identify abnormal-appearing hippocampi on MR imaging²¹—that is, when the hippocampal region contains larger-than-expected amounts of CSF.

In both AD²² and in first-episode psychosis,²³ the HPF has been shown to be more sensitive than pure hippocampal volume

in differentiating patients and controls. A cognitively normal (CN) versus early AD classification task using the HPF and its time rate of change achieved an accuracy of 97%.²² The same task using hippocampal volume and its time rate of change obtained from FreeSurfer, Version 5.3 (<http://surfer.nmr.mgh.harvard.edu>)²⁴ achieved a lower accuracy of 89%.²² A group comparison of

healthy controls versus medication-naïve patients with first-episode psychosis showed a significantly lower HPF in first-episode psychosis.²³ However, hippocampal volume in the same subjects as measured by FreeSurfer, Version 6.0, failed to find any group differences.²³ Furthermore, a follow-up scan after 8 weeks of treatment with antipsychotic medication showed a significantly reduced HPF from baseline in first-episode psychosis, whereas FreeSurfer volumes did not detect any longitudinal changes.²³ The HPF has also been found to be a better predictor of future cognitive decline than volume.²⁵

In this article, we measured the bilateral HPF on 3D volumetric MR imaging scans acquired from older adult subjects with and without AD-type dementia obtained through a publicly available data base. We then used linear mixed-effects statistical models to study the relationship between the magnitude and bilateral asymmetry of the HPF with respect to subject age, sex, and dementia severity.

MATERIALS AND METHODS

Study Subjects

We obtained data from the publicly available Open Access Series of Imaging Studies,^{26,27} phase 1 (OASIS1, <http://oasis-brains.org/>), a cross-sectional collection of 416 right-handed subjects 18–96 years of age. In this study, we retained only a subset of 198 subjects who were 60 years of age or older. The 198 older subjects in the OASIS1 data base with and without dementia were recruited from the longitudinal pool of the Washington University Alzheimer’s Disease Research Center. Subjects with a primary cause of dementia unrelated to AD such as vascular dementia, major depression, head injuries, strokes, and the use of psychoactive drugs and those with obvious lesions or other unrelated abnormalities in their MR images were excluded. Cohort demographics are shown in Table 1. Subjects were divided into 3 diagnostic groups: 1) cognitively normal (*n* = 98) with a Clinical Dementia Rating of zero; 2) mild cognitive impairment (*n* = 70) with a Clinical Dementia Rating of 0.5; and 3) AD (*n* = 30), twenty-eight subjects with a Clinical Dementia Rating of 1, and 2 with a Clinical Dementia Rating of 2.

MR Imaging Protocol

For each subject, 3 or 4 (six in 1 subject) individual sagittal 3D-T1-weighted MPRAGE structural MR imaging volumes were acquired in a single acquisition session using a 1.5T Magnetom Vision scanner (Siemens, Erlangen, Germany). The total number of volumes acquired from the 198 subjects in this study was 775. One hundred seventy-eight subjects had 4 volumes each, 19 subjects had 3 volumes each, and 1 subject had 6 volumes. The MPRAGE

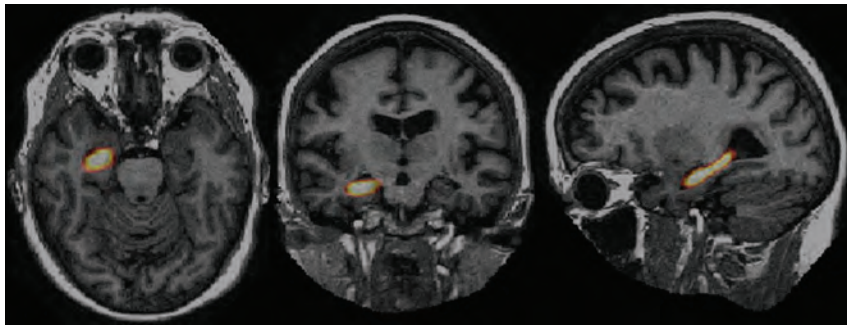


FIG 1. Axial (left), coronal (middle), and sagittal (right) slices through a 3D structural MR imaging scan of a subject. The right hippocampus probabilistic VOI is superimposed on the image in native space.

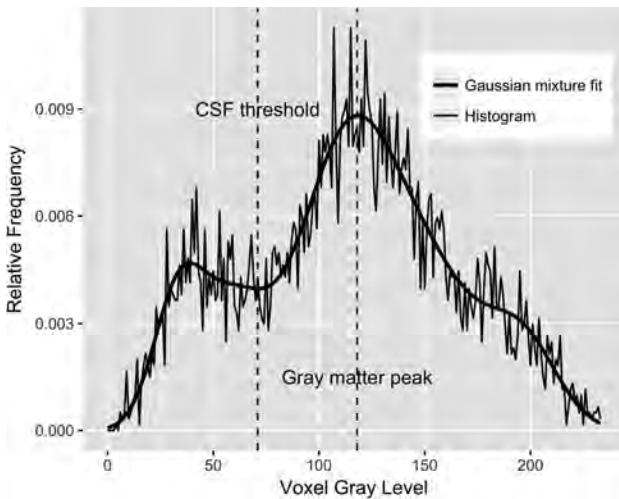


FIG 2. Histogram of the voxels with nonzero probabilities on the VOI in Fig 1 (thin line) along with a fitted Gaussian mixture model (thick line) using the expectation-maximization algorithm. The automatically determined CSF threshold is shown as a vertical line approximately located at the intensity value of 70. The HPF is defined as the fraction of voxels in the VOI whose intensities are greater than the CSF threshold.

pulse sequence parameters were the following: matrix size = $256 \times 256 \times 128$, voxel size = $1 \times 1 \times 1.25 \text{ mm}^3$, TR = 9.7 ms, TE = 4.0 ms, TI = 20 ms, delay time = 200 ms, flip angle = 10° with a zero interslice gap. A more detailed description of image acquisition protocol can be found in Marcus et al.²⁶

Imaging Processing

Image processing was performed using the Automatic Registration Toolbox (ART; <https://www.nitrc.org/projects/art>)²⁸ software package in 2 steps. The 3–4 scans from each subject (6 scans in 1 case) were registered using the Automatic Temporal Registration Algorithm module of ART, an unbiased symmetric rigid-body affine registration algorithm. Registration results were visually inspected for accuracy.

Following intrasubject registration, bilateral HPFs were measured on each of the 775 volumes using the KAIBA module in ART. The HPF estimates the fraction of brain parenchyma in a VOI that is automatically defined around each hippocampus. The VOI is the projection of a hippocampal probability map onto the MR imaging volume in its native orientation based on automatic detection of >100 landmarks near each hippocampus. The prob-

ability map is defined by the average of 65 manually traced hippocampi on a group of young healthy individuals. In a sense, the projection of this hippocampal probability map onto the subject's MR imaging volume indicates the location where one would expect to find the hippocampus in a healthy young individual. Because atrophy of the hippocampus is associated with a commensurate increase in the surrounding CSF, the HPF quantifies the extent to which brain tissue, as opposed to CSF, is found in the VOI. Figure 1 shows the projection of the probabilistic right hippocampal VOI onto the native space of a raw 3D MPRAGE volume.

KAIBA examines the voxel-intensity histogram in the VOI. A Gaussian mixture model is fitted to the histogram using the expectation-maximization algorithm. The fitted mixture model is then analyzed to obtain a CSF threshold as shown in Fig 2. Finally, the HPF is computed as the ratio of the volume of the suprathreshold voxels to the total VOI.

KAIBA is carefully designed to avoid any possible left-right bias in measuring the HPF by computing the bilateral HPF twice, once in the original volume and a second time in a duplicate volume obtained by flipping through the left-right axis and then averaging the measured HPFs for each hemisphere.

On the basis of the measured left HPF (*LHPF*) and right HPF (*RHPF*), we computed an overall bilateral measure of hippocampal volumetric integrity as the average:

$$1) \quad HPF = \frac{LHPF + RHPF}{2},$$

and a percentage asymmetry index (AI):

$$2) \quad AI = \frac{|RHPF - LHPF|}{HPF} \times 100\%.$$

As with Lucarelli et al,¹⁷ in this study, the *AI* measures the magnitude of asymmetry without regard to its direction.

Statistical Analysis

We used the *lmer* function of the *lme4* package (Version 1.1–17; <https://cran.r-project.org/web/packages/lme4/index.html>) in the R statistical computing and graphics language (Version 3.5.0; <http://www.r-project.org>) to fit linear mixed-effects models to the response variables *HPF* and *AI* to analyze their relationships to covariates: age, sex, diagnostic group, and estimated total intracranial volume. The significance of the fixed-effects parameters was tested using the ANOVA function of the *lmerTest* package (Version 3.0–1; <https://cran.r-project.org/web/packages/lmerTest/index.html>) with the Satterthwaite method for computing the denominator degrees of freedom and *F* statistics.

Examination of model residuals following fitting of the mixed-effects models indicated considerable departure from the assumed normality of the residuals. The problem was mitigated by applying the logit transformation (3a) and the Box-Cox transfor-

Table 2: Definitions of all mathematic terms used in the mixed-effects model equation (Equation 4)

i	Volume index $i = 1, 2, \dots, 775$
j	Subject identification index $j = 1, 2, \dots, 198$
y_i	$\text{logit}(HPF)$ or $\log(AI)$ for volume i as the response variable
ID_i	Subject index of volume i where $ID_i \in \{1, 2, \dots, 198\}$
Age_i	Age of subject ID_i , minus 76.34, the average age of all 198 subjects
ICV_i	Estimated total intracranial volume of subject ID_i minus 1461.5, the average ICV of all 198 subjects
DX_i	Diagnostic group of subject ID_i , a factor with 3 levels $\{CN, MCI, AD\}$
Sex_i	Sex of subject ID_i , a factor with 2 levels $\{Male, Female\}$
$I\{statement\}$	Indicator function that takes on values of 1 or 0 depending on whether the <i>statement</i> is true or false
$\beta_0 \dots \beta_7$	Model fixed-effects parameters to be estimated and tested against null hypotheses of type $\sum_k \beta_k = 0$
b_j	Model random effects assumed to be independent and identically distributed Gaussian with mean 0 and variance σ_b^2
e_i	Random residuals assumed to be independent and identically distributed Gaussian with mean 0 and variance σ_e^2

mation²⁹ (3b) to the response variables *HPF* and *AI*, respectively, as follows:

$$3A) \quad y = \text{logit}(HPF) = \log\left(\frac{HPF}{1 - HPF}\right)$$

$$3B) \quad y = \text{boxcox}(AI) = \frac{(AI)^\lambda - 1}{\lambda},$$

where the Box-Cox transformation parameter λ in 3b was estimated using the R *boxcoxmix* package (Version 0.20; <https://cran.r-project.org/web/packages/boxcoxmix/boxcoxmix.pdf>) to be $\lambda = 0.4$.

Because we have 775 MR imaging volumes, we denote our response variable by y_i ($i = 1, 2, \dots, 775$), where y_i represents either $\text{logit}(HPF)$ or $\text{boxcox}(AI)$. We fitted the following mixed-effects model:

$$4) \quad y_i = \beta_0 + b_j I\{ID_i = j\} + \beta_1 Age_i + \beta_2 I\{DX_i = MCI\} + \beta_3 I\{DX_i = AD\} + \beta_4 Age_i I\{DX_i = MCI\} + \beta_5 Age_i I\{DX_i = AD\} + \beta_6 ICV_i + \beta_7 I\{Sex_i = Male\} + e_i.$$

This model involves 10 unknown parameters that are estimated. These are the 8 fixed effects, β_0 – β_7 , and 2 variance components σ_b^2 and σ_e^2 associated with random effects b_j and residuals e_i , respectively. In this model, the diagnostic group factor (*DX*) is a fixed factor with 3 levels, *CN*, *MCI*, and *AD*, indicating the diagnostic group; *ID* is a random factor with 198 levels $j = 1, 2, \dots, 198$, corresponding to the individual study subjects with b_j as the corresponding random effects. *Sex* is a fixed factor with 2 levels; and *Age* and *intracranial volume (ICV)* are continuous mean-centered covariates. The precise definitions of all mathematic terms and notations in Equation 4 are given in Table 2.

RESULTS

Image Processing

The Automatic Temporal Registration Algorithm relies on methods for automatic detection of the midsagittal plane and anterior/posterior commissure. Visual inspection revealed that in 13 of the 775 volumes (1.7%), the midsagittal plane anterior/posterior commissure detection failed. These volumes belonged to 4 different subjects in our cohort of 198 (2%). In the 13 failed cases, we supplied the program with 3 manually identified landmarks on the midsagittal plane, following which the program proceeded to successfully complete the registrations. Following Automatic

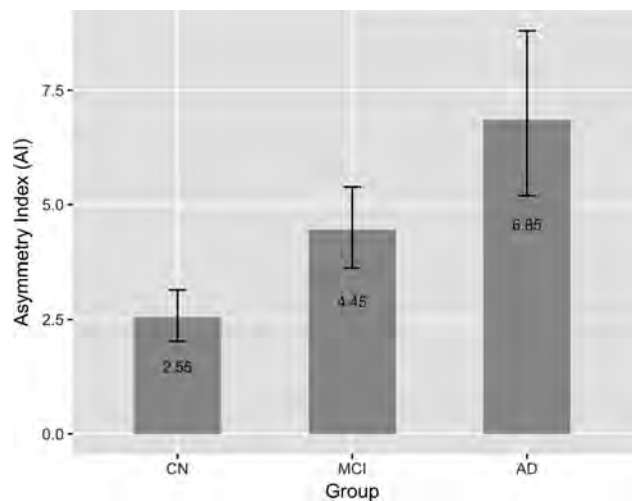


FIG 3. Predicted marginal means of the asymmetry index in different diagnostic groups. AI was found to be significantly different between the CN versus MCI ($P < .001$), CN versus AD ($P < .001$), and MCI versus AD ($P = .03$) groups. AI increased with increasing dementia severity. Error bars indicate 95% CI.

Temporal Registration Algorithm registrations, KAIBA successfully computed LHPF and RHPF on all 775 volumes. All the following statistical results pertain to the transformed response variables *HPF* and *AI* using Equations 3a and 3b.

Statistical Analysis of AI

Statistically significant variance in AI was explained by the *DX* ($P < .001$), *Sex* ($P < .01$), and *ICV* ($P = .02$). In addition, there was a significant *DX*-by-*Age* interaction ($P < .001$).

AI versus Diagnostic Group

Figure 3 shows the predicted marginal mean and 95% confidence interval of AI in the *CN*, *MCI*, and *AD* groups. Pair-wise comparisons among the 3 diagnostic groups showed a significant increase in asymmetry with dementia severity: *CN* vs *MCI* ($P < .001$), *CN* vs *AD* ($P < .001$), and *MCI* vs *AD* ($P = .03$). The *P* values are adjusted using the Tukey method for comparing a family of 3 estimates.

AI versus Sex and ICV

Figure 4 shows the predicted marginal mean and 95% CI of AI in men and women. There was a significant main effect of sex on AI as indicated by β_7 in the fitted Equation 4 that was significantly different from zero ($P < .01$), showing higher asymmetry in men.

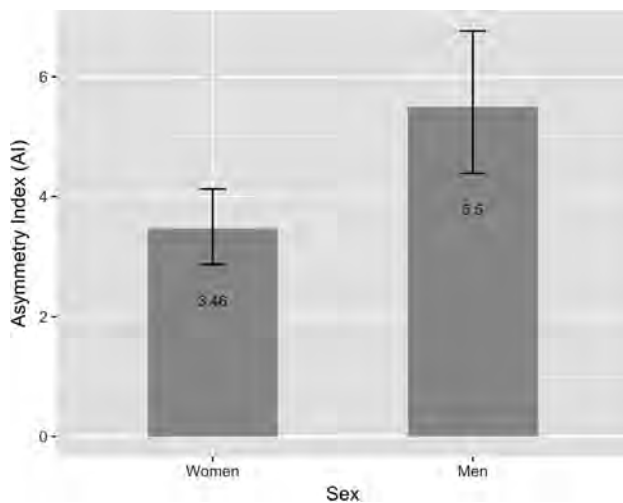


FIG 4. Predicted marginal means of the asymmetry index in men and women. The AI was found to be significantly higher in men ($P < .01$) after controlling for age, intracranial volume, and diagnostic group. Error bars indicate 95% CI.

Our analysis also suggested that asymmetry decreased with increasing ICV as indicated by the significantly negative β_6 ($P = .02$) in the fitted Equation 4.

AI versus Age and Diagnostic Group

Fitting of Equation 4 to AI also revealed significant age-by-diagnosis interactions. In CN, asymmetry increased significantly with age as indicated by a positive β_1 ($P < .001$). However, in the MCI group, asymmetry decreased with age as indicated by a significantly negative linear combination $\beta_1 + \beta_4$ ($P < .05$). Finally, in the AD group, we found no significant age effect on AI by testing the linear combination $\beta_1 + \beta_5$ ($P = .13$).

Statistical Analysis of HPF

Statistically significant variance in the HPF was explained by the DX ($P < .001$), Age ($P < .001$), and ICV ($P = .001$). In addition, there was significant DX-by-Age interaction ($P < .01$).

HPF versus Diagnostic Group

Figure 5 shows the predicted marginal mean and 95% CI of HPF in the CN, MCI, and AD groups. Pair-wise comparisons among the 3 diagnostic groups showed significant decrease in the HPF with dementia severity: CN vs MCI ($P < .001$), CN vs AD ($P < .001$), and MCI vs AD ($P < .001$), in which the P values are adjusted using the Tukey method for comparing a family of 3 estimates.

HPF versus Sex and ICV

There was no significant sex effect on the HPF as indicated by a β_7 estimate, which was not significantly different from zero ($P = .23$). Our analysis showed that the HPF decreased with increasing ICV as indicated by a significantly negative β_6 ($P = .001$).

HPF versus Age and Diagnostic Group

Fitting of Equation 4 to the HPF revealed significant age-by-diagnosis interactions. In the cognitively healthy group, HPF decreased significantly with age as indicated by a negative β_1 ($P < .001$).

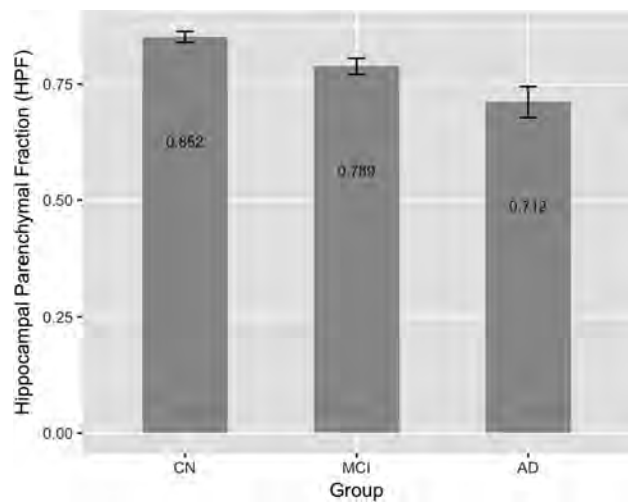


FIG 5. Predicted marginal means of the HPF (averaged across hemispheres) in different diagnostic groups. The HPF was found to be significantly different between the CN versus MCI ($P < .001$), CN versus AD ($P < .001$), and MCI versus AD ($P < .001$) groups. The HPF decreased with increasing dementia severity. Error bars indicate 95% CI.

.001). The HPF also decreased with age in the MCI group as indicated by a significantly negative linear combination $\beta_1 + \beta_4$ ($P < .001$). Finally, in the AD group, we found no significant age effect on the HPF by testing the linear combination $\beta_1 + \beta_5$ ($P = .13$).

DISCUSSION

In this article, we examined the magnitude and asymmetry of hippocampal volumetric integrity in normal aging, MCI, and AD-type dementia based on measurement of the hippocampal parenchymal fraction. We found that the asymmetry of hippocampal atrophy increased with age in subjects who were cognitively normal and it was more asymmetric in men than women (Fig 4). These findings agree with the results of Lucarelli et al,¹⁷ who found that the asymmetry of hippocampal volume increased with age and that men had greater asymmetry than women.

Our findings also concur with the recent longitudinal study by Fraser et al,³⁰ who reported the rate of decline of hippocampal volume measured by very reliable manual tracing by the same highly trained neurologist in 244 middle-aged and 199 older-aged healthy adults based on a pair of baseline and follow-up structural MR images from each individual scanned 8 years apart. They found that the rate of decline of the left hippocampus was higher than that of the right hippocampus in both groups, which indicates increasing AI in normal aging. Sex differences in the rates of decline were not examined.

We also found that both the MCI and AD groups had significantly higher hippocampal asymmetry than the CN group and that the AD group had significantly higher hippocampal asymmetry than the MCI group (Fig 3). Therefore, we conclude that the extent of hippocampal asymmetry as measured by AI is positively correlated with dementia severity. These results are consistent with those of Wachinger et al,⁸ who reported an increase in hippocampal asymmetry concurrent with disease severity beyond an aging effect.

Examining the definition of AI given by Equation 2, we can see

that *AI* can increase with decreasing *HPF* in the denominator or increasing $|RHPF-LHPF|$ in the numerator or both. We have shown in this study that the *HPF* decreases with dementia severity (Fig 5); therefore, the increase in *AI* is, in part, due to decreasing *HPF*. We also examined the relationship between $|RHPF-LHPF|$ and disease severity (results not reported) and determined that this quantity increased significantly in both MCI and AD groups relative to CN. An increase in the mean value of $|RHPF-LHPF|$ itself can be attributed to 2 factors. Assuming that the difference between the right and left *HPF* is normally distributed, the probability distribution of $|RHPF-LHPF|$ would be the so-called folded normal distribution whose expected value depends on both the mean and variance of *RHPF-LHPF*. In other words, the increasing *AI* with disease severity could also be partly due to a larger variance in right-left differences in the MCI/AD groups.

We also found an interaction between age and diagnostic group on asymmetry. While asymmetry increased with age in the group that was cognitively normal, asymmetry was observed to decrease with age in both MCI and AD groups, though the association between age and asymmetry in AD did not reach statistical significance, likely due to the smaller sample size in this group. The finding of a negative correlation between age and asymmetry in the MCI and AD groups indicates that hippocampal asymmetry is higher in those with earlier onset of the disease, suggesting that those who experience earlier onset are more acutely impaired. This finding is consistent with the observation that those with earlier disease onset have a more severe disease course.³¹

Furthermore, we found that the *HPF* decreased significantly from CN to MCI and from MCI to AD (Fig 5). This is consistent with numerous previous publications that report a compromised hippocampal volumetric integrity in AD compared with controls.^{5,6} We also found that the *HPF* significantly decreased with age in both the CN and MCI groups, but the association between the *HPF* and AD did not reach statistical significance. The latter result may be due to the smaller sample size ($n = 30$) in this group; and second, the more advanced dementia in this group means that the compromised hippocampal volumetric integrity is more influenced by the time since dementia onset than by subject age. This finding is consistent with previous reports indicating that the loss of hippocampal volume and changes in shape are more closely related to age in the healthy controls than in patients with dementia.³²

Taken together, our results suggest that decreased magnitude and increased asymmetry of the *HPF* beyond what is expected in normal aging have the potential to be used as early imaging biomarkers of AD. Our results also confirm a sexual dimorphism in asymmetric hippocampal atrophy patterns in both normal aging and AD, with men having significantly more asymmetry.

In this article, we have considered only hippocampal degeneration. Future work is required to determine whether the asymmetric pattern of neurodegeneration is specific to the hippocampus or whether it extends to other brain regions.

We used cross-sectional data in this study and therefore were not able to ascertain the rates of change of *HPF* asymmetry. A future direction of research is to use longitudinal data bases to study dynamic changes in asymmetry in subjects with normal aging and AD. Previously, we used the magnitude of *HPF* and its

rate of change with respect to time as features in machine learning algorithms used for differentiating healthy subjects from those with AD,²² as well as for differentiating stable patients with MCI from those with an incipient AD diagnosis.³³ Future studies will need to be conducted to assess the influence of including *HPF* asymmetry and its rate of change as additional classification features on the performance of machine learning algorithms.

CONCLUSIONS

In this article, we analyzed the hippocampal volumetric integrity as measured by *HPF* and its asymmetry as measured by *AI* with respect to age, sex, and dementia severity. We found that the extent of *HPF* asymmetry is greater in patients with AD than in normally aging subjects and that men had more hippocampal asymmetry than women. We also found that the extent of hippocampal asymmetry is positively correlated with age in cognitively healthy subjects but no statistically significant relationship between *HPF* asymmetry and aging was found within the AD group and that asymmetry diminished with aging within the MCI group. In addition to the level of hippocampal volumetric integrity, its asymmetry can potentially be used as an early biomarker of AD.

REFERENCES

- 2018 Alzheimer's Disease Facts and Figures. <https://www.alz.org/media/HomeOffice/Facts%20and%20Figures/facts-and-figures.pdf>. Accessed June 13, 2018
- Fisher DW, Bennett DA, Dong H. **Sexual dimorphism in predisposition to Alzheimer's disease.** *Neurobiol Aging* 2018;70:308–24 CrossRef Medline
- Braak H, Braak E. **Neuropathological staging of Alzheimer-related changes.** *Acta Neuropathol* 1991;82:239–59 CrossRef Medline
- Tondelli M, Wilcock GK, Nichelli P, et al. **Structural MRI changes detectable up to ten years before clinical Alzheimer's disease.** *Neurobiol Aging* 2012;33:825.e25–36 CrossRef Medline
- Frisoni GB, Fox NC, Jack CR Jr, et al. **The clinical use of structural MRI in Alzheimer disease.** *Nat Rev Neurol* 2010;6:67–77 CrossRef Medline
- Shi F, Liu B, Zhou Y, et al. **Hippocampal volume and asymmetry in mild cognitive impairment and Alzheimer's disease: meta-analyses of MRI studies.** *Hippocampus* 2009;19:1055–64 Medline
- Maller JJ, Anstey KJ, Réglade-Meslin C, et al. **Hippocampus and amygdala volumes in a random community-based sample of 60–64 year olds and their relationship to cognition.** *Psychiatry Res* 2007; 156:185–97 Medline
- Wachinger C, Salat DH, Weiner M, et al. **Whole-brain analysis reveals increased neuroanatomical asymmetries in dementia for hippocampus and amygdala.** *Brain* 2016;139:3253–66 CrossRef Medline
- Barnes J, Scallin RI, Schott JM, et al. **Does Alzheimer's disease affect hippocampal asymmetry? Evidence from a cross-sectional and longitudinal volumetric MRI study.** *Dement Geriatr Cogn Disord* 2005; 19:338–44 Medline
- Schmidt MF, Storrs JM, Freeman KB, et al. **A comparison of manual tracing and FreeSurfer for estimating hippocampal volume over the adult lifespan.** *Hum Brain Mapp* 2018;39:2500–13 CrossRef Medline
- Maltbie E, Bhatt K, Paniagua B, et al. **Asymmetric bias in user guided segmentations of brain structures.** *Neuroimage* 2012;59:1315–23 CrossRef Medline
- Rogers BP, Sheffield JM, Luksik AS, et al. **Systematic error in hippocampal volume asymmetry measurement is minimal with a manual segmentation protocol.** *Front Neurosci* 2012;6:179 CrossRef Medline

13. Hamilton LS, Narr KL, Luders E, et al. **Asymmetries of cortical thickness: effects of handedness, sex, and schizophrenia.** *Neuroreport* 2007;18:1427–31 Medline
14. Kong XZ, Mathias SR, Guadalupe T et al; ENIGMA Laterality Working Group. **Mapping cortical brain asymmetry in 17,141 healthy individuals worldwide via the ENIGMA Consortium.** *Proc Natl Acad Sci U S A* 2018;115:E5154–63 CrossRef Medline
15. Schneider S, Peters J, Bromberg U, et al; AGEN consortium. **Boys do it the right way: sex-dependent amygdala lateralization during face processing in adolescents.** *Neuroimage* 2011;56:1847–53 CrossRef Medline
16. Kansaku K, Kitazawa S. **Imaging studies on sex differences in the lateralization of language.** *Neurosci Res* 2001;41:333–37 Medline
17. Lucarelli RT, Peshock RM, McColl R, et al. **MR imaging of hippocampal asymmetry at 3T in a multiethnic, population-based sample: results from the Dallas Heart Study.** *AJNR Am J Neuroradiol* 2013;34:752–57 CrossRef Medline
18. Hampel H, Vergallo A, Giorgi FS, et al; Alzheimer Precision Medicine Initiative (APMI). **Precision medicine and drug development in Alzheimer's disease: the importance of sexual dimorphism and patient stratification.** *Front Neuroendocrinol* 2018;50:31–51 CrossRef Medline
19. Geuze E, Vermetten E, Bremner JD. **MR-based in vivo hippocampal volumetrics, 1: review of methodologies currently employed.** *Mol Psychiatry* 2005;10:147–59 Medline
20. Hansen TI, Brezova V, Eikenes L, et al. **How does the accuracy of intracranial volume measurements affect normalized brain volumes? Sample size estimates based on 966 subjects from the HUNT MRI Cohort.** *AJNR Am J Neuroradiol* 2015;36:1450–56 CrossRef Medline
21. Gama HP, da Rocha AJ, Valerio RM, et al. **Hippocampal abnormalities in an MR imaging series of patients with tuberous sclerosis.** *AJNR Am J Neuroradiol* 2010;31:1059–62 CrossRef Medline
22. Ardekani BA, Convit A, Bachman AH. **Analysis of the MIRIAD data shows sex differences in hippocampal atrophy progression.** *J Alzheimers Dis* 2016;50:847–57 CrossRef Medline
23. Goff DC, Zeng B, Ardekani BA, et al. **Association of hippocampal atrophy with duration of untreated psychosis and molecular biomarkers during initial antipsychotic treatment of first-episode psychosis.** *JAMA Psychiatry* 2018;75:370–78 CrossRef Medline
24. Fischl B. **FreeSurfer.** *Neuroimage* 2012;62:774–81 CrossRef Medline
25. Bruno D, Ciarleglio A, Grothe MJ, et al. **Hippocampal volume and integrity as predictors of cognitive decline in intact elderly.** *Neuroreport* 2016;27:869–73 CrossRef Medline
26. Marcus DS, Wang TH, Parker J, et al. **Open Access Series of Imaging Studies (OASIS): cross-sectional MRI data in young, middle aged, nondemented, and demented older adults.** *J Cogn Neurosci* 2007;19:1498–507 Medline
27. OASIS. Open-Access Series Of Imaging Studies. www.oasis-brain-s.org. Accessed April 12, 2018
28. Neuroimaging Tools and Resources Collaboratory. Automatic Registration Toolbox. www.nitrc.org/projects/art. Accessed May 17, 2018
29. Box GEP, Cox DR. **An analysis of transformations.** *Journal of the Royal Statistical Society. Series B (Methodological)* 1964;26:211–52
30. Fraser MA, Shaw ME, Anstey KJ, et al. **Longitudinal assessment of hippocampal atrophy in midlife and early old age: contrasting manual tracing and semi-automated segmentation (FreeSurfer).** *Brain Topogr* 2018;31:949–62 CrossRef Medline
31. Reid W, Broe G, Creasey H, et al. **Age at onset and pattern of neuropsychological impairment in mild early-stage Alzheimer disease: a study of a community-based population.** *Arch Neurol* 1996;53:1056–61 Medline
32. Xu Y, Valentino DJ, Scher AI, et al. **Age effects on hippocampal structural changes in old men: the HAAS.** *Neuroimage* 2008;40:1003–15 Medline
33. Ardekani BA, Bermudez E, Mubeen AM, et al; Alzheimer's Disease Neuroimaging Initiative. **Prediction of incipient Alzheimer's disease dementia in patients with mild cognitive impairment.** *J Alzheimers Dis* 2017;55:269–81 CrossRef Medline

Clinical Outcome after Thrombectomy in Patients with Stroke with Premorbid Modified Rankin Scale Scores of 3 and 4: A Cohort Study with 136 Patients

F. Seker, J. Pfaff, S. Schönenberger, C. Herweh, S. Nagel, P.A. Ringleb, M. Bendszus, and M.A. Möhlenbruch

ABSTRACT

BACKGROUND AND PURPOSE: We aimed to analyze the clinical outcome after mechanical thrombectomy in patients with premorbid mRS 3 and 4 because there are currently no data on this patient group.

MATERIALS AND METHODS: Between January 2009 and November 2017, all patients with premorbid mRS 3 or 4 undergoing mechanical thrombectomy due to anterior circulation stroke were selected. Good outcome was defined as a clinical recovery to the status before stroke onset (ie, equal premorbid mRS and mRS at 90 days). In addition, mortality at discharge and at 90 days was analyzed.

RESULTS: One hundred thirty-six patients were included, of whom 81.6% presented with premorbid mRS 3; and 18.4%, with premorbid mRS 4; 24.0% of patients with premorbid mRS 4 achieved clinical recovery compared with 20.7% of patients with premorbid mRS 3 ($P = .788$). However, the proportion of hospital mortality and mortality at 90 days was nonsignificant, but markedly higher in patients with premorbid mRS 4. Multivariate analysis identified low NIHSS scores (OR, 0.92; 95% CI, 0.85–0.99; $P = .040$), high ASPECTS (OR, 1.45; 95% CI, 1.02–2.16; $P = .049$), and TIC1 2b–3 (OR, 7.11; 95% CI, 1.73–49.90; $P = .017$) as independent predictors of good outcome.

CONCLUSIONS: Good outcome in patients with premorbid mRS 3 and 4 is less frequent compared with premorbid mRS 0–2. Nevertheless, about 20% of the patients return to their premorbid mRS, which may justify endovascular treatment. The most important predictor of good outcome is successful recanalization.

ABBREVIATION: MT = mechanical thrombectomy

The mRS is a commonly used outcome measure in stroke treatment (Table 1).¹ In addition, it is also used to assess the premorbid/prestroke disability of patients with stroke. Most randomized controlled trials on mechanical thrombectomy (MT) published in recent years excluded patients with premorbid mRS > 1.² Only the Endovascular Therapy Following Imaging Evaluation for Ischemic Stroke 3 (DEFUSE-3) included patients with premorbid mRS 0–2.³ Therefore, the American Heart Association/American Stroke Association briefly addressed this issue in their latest guidelines, stating that MT in patients with premorbid mRS > 1 has uncertain benefits and further randomized controlled trials are necessary.⁴

Nevertheless, many stroke centers regularly perform MT in patients with premorbid mRS 2 (ie, in patients with slight disability but functional independence before stroke onset). However,

there are uncertainties about the efficacy of thrombectomy in patients with moderate and moderately severe disability (ie, premorbid mRS 3 and 4). To our knowledge, there are no randomized controlled trials or cohort studies addressing this issue. Therefore, we analyzed clinical outcomes of patients with anterior circulation stroke and premorbid mRS 3 and 4 undergoing MT at our comprehensive stroke center.

MATERIALS AND METHODS

Patient Selection

Between January 2009 and November 2017, all patients with stroke undergoing MT at our institution were prospectively collected in a stroke data base. For these patients, we performed a single-center, observational, retrospective cohort study. Inclusion criteria were the following: 1) occlusion of the intracranial internal carotid artery or M1 or M2 segment of the middle cerebral artery, and 2) premorbid mRS 3 or 4. Our institutional review board approved this study. Informed consent was waived.

Treatment

The decision for treatment was made in consensus between the neurologist and neuroradiologist on duty, mostly depending on

Received May 21, 2018; accepted after revision November 7.

From the Departments of Neuroradiology (F.S., J.P., C.H., M.B., M.A.M.) and Neurology (S.S., S.N., P.A.R.), Heidelberg University Hospital, Heidelberg, Germany.

Please address correspondence to Markus A. Möhlenbruch, MD, Im Neuenheimer Feld 400, 69120 Heidelberg, Germany; e-mail: markus.moehlenbruch@med.uni-heidelberg.de

<http://dx.doi.org/10.3174/ajnr.A5920>

the imaging findings and the probable or explicit patient preference. Patients received intravenous thrombolysis, if eligible. Patients underwent MT with the intention to achieve TICI 2b–3.

Image Analysis

The baseline ASPECTS was determined on either nonenhanced CT scans or diffusion-weighted images before MT by a radiologist. The occlusion site was determined on digital subtraction angiograms. Successful recanalization was defined as TICI 2b–3 on the final angiogram.

Outcome Measures

The primary outcome parameter was good clinical outcome defined as a clinical recovery to the status before stroke onset (ie, premorbid mRS and mRS scores at 90 days were equal). Poor outcome was defined as any worsening of the mRS score at 90 days. Secondary outcome parameters were hospital mortality and mortality at 90 days.

Table 1: Modified Rankin Scale

Score	Description
0	No symptoms at all
1	No significant disability despite symptoms: able to carry out all usual duties and activities
2	Slight disability: unable to carry out all previous activities, but able to look after own affairs without assistance
3	Moderate disability: requiring some help, but able to walk without assistance
4	Moderately severe disability: unable to walk without assistance and unable to attend own bodily needs without assistance
5	Severe disability: bedridden, incontinent, and requiring constant nursing care and attention
6	Death

Originally published in van Swieten J, Koudstaal P, Visser M, et al. "Interobserver agreement for the assessment of handicap in stroke patients." *Stroke* 1988;19:604-07.

Table 2: Patient characteristics

	Good Outcome			P Value ^a
	Total (n = 136)	(n = 29)	Poor Outcome (n = 107)	
Age (mean) (SD)	80.6 (10.1)	79.5 (13.2)	81.0 (9.2)	.585
Female (No.) (%)	90 (66.2)	20 (69.0)	70 (65.4)	.827
Diabetes (No.) (%)	34 (25.0)	5 (17.2)	29 (27.1)	.340
Hypertension (No.) (%)	102 (75.0)	21 (72.4)	81 (75.7)	.809
Arrhythmia (No.) (%)	84 (61.8)	19 (65.5)	65 (60.7)	.674
Coronary heart disease (No.) (%)	41 (30.1)	8 (27.6)	33 (30.8)	.822
Hypercholesterolemia (No.) (%)	41 (30.1)	8 (27.6)	33 (30.8)	.822
Premorbid mRS (No.) (%)				.719
3	111 (81.6)	23 (79.3)	88 (82.2)	
4	25 (18.4)	6 (20.7)	19 (17.8)	
Baseline NIHSS (median) (IQR)	18 (15–22)	15 (12–19)	19 (15–23)	.009
ASPECTS (median) (IQR)	9 (8–10)	10 (9–10)	9 (8–10)	.051
Intravenous thrombolysis (No.) (%)	61 (44.9)	13 (44.8)	48 (44.9)	1.000
Onset-to-groin (median) (IQR)	240 (180–344)	232 (182–280)	247 (180–357)	.250
Groin-to-TICI (median) (IQR)	75 (41–108)	63 (32–97)	77 (46–117)	.142
Occlusion site (No.) (%)				
ICA	31 (22.8)	2 (6.9)	29 (27.1)	.024
M1	78 (57.4)	15 (51.7)	63 (58.9)	.530
M2	30 (22.1)	12 (41.4)	18 (16.8)	.010
TICI 2b–3	103 (75.7)	27 (93.1)	76 (71.0)	.014

Note:—IQR indicates interquartile range.

^a Comparison between patients with good and poor outcomes.

Statistical Methods

R Version 3.4.3 and RStudio Version 1.1.414 (RStudio; <https://www.rstudio.com/>) were used for statistical analysis. Numeric baseline characteristics were described in medians and interquartile ranges or means and SDs. Patients achieving good clinical outcome were compared with those with poor outcome in a univariate analysis. All variables with $P < .1$ were included in a multivariate binary logistic regression analysis to identify independent predictors of good clinical outcome. Comparisons between groups were performed using Student t tests or the Mann-Whitney U test for continuous data and the Fisher exact test for categorical variables. The Kruskal-Wallis test was used for group comparisons. A P value $< .05$ was considered statistically significant.

RESULTS

Of 1223 patients within the above-mentioned timeframe who underwent MT, a total of 136 consecutive patients (11.1%) met the inclusion criteria of this study. Of these, 111 patients (81.6%) presented with a premorbid mRS of 3 and 25 patients (18.4%) presented with a premorbid mRS of 4. The mean age of our cohort was 80.6 ± 10.1 years.

Of these 136 patients, 12 (8.8%) were treated with aspiration only, 111 (81.6%) were treated using stent retrievers under proximal aspiration, and 13 (9.6%) were treated with aspiration attempts and stent-retriever attempts under proximal aspiration.

Good-versus-Poor Outcome

In our cohort, 21.3% achieved good clinical outcome—that is, the mRS at 90 days after stroke onset was the same as the premorbid mRS. First, we compared patients achieving good clinical outcome with those achieving poor outcome (78.7%). Age, proportion of risk factors, premorbid mRS, rate of intravenous thrombolysis treatment, and time from onset to groin puncture and from groin puncture to TICI were similar in both groups (Table 2).

Multivariate analysis identified low NIHSS scores (OR, 0.92; 95% CI, 0.85–0.99; $P = .040$), high ASPECTS (OR, 1.45; 95% CI, 1.02–2.16; $P = .049$), and TICI 2b–3 (OR, 7.11; 95% CI, 1.73–49.90; $P = .017$) as independent predictors of good clinical outcome. The occlusion site was not an independent predictor. Nonetheless, patients with good outcome had a significantly lower rate of ICA occlusion (6.9% versus 27.1%, $P = .024$) and a significantly higher rate of M2 occlusion (41.4% versus 16.8%, $P = .010$). The proportion of M1 occlusions was nonsignificantly smaller in patients with good outcome (51.7% versus 58.9%, $P = .530$) (Table 3).

Premorbid mRS 3 versus 4

Finally, we compared clinical outcomes in patients with premorbid mRS 3 and 4. The rate of successful recanalization was similar in both groups. Ninety-day mRS was significantly higher in patients with

Table 3: Multivariate analysis—Independent predictors of good outcome

	Odds Ratio (95% CI)	Adjusted P Value
Baseline NIHSS	0.92 (0.85–0.99)	.040
ASPECTS	1.45 (1.02–2.16)	.049
ICA occlusion	0.31 (0.04–1.30)	.152
M2 occlusion	2.35 (0.86–6.52)	.097
TICI 2b–3	7.11 (1.73–49.90)	.017

Table 4: Comparison of outcome in patients with premorbid mRS 3 and 4

	Premorbid mRS 3 (n = 111)	Premorbid mRS 4 (n = 25)	P Value
TICI 2b–3 (No.) (%)	85 (76.6)	18 (72.0)	.614
90-Day mRS (median) (IQR)	5 (3.5–6)	6 (4–6)	<.001
Good outcome (No.) (%)	23 (20.7)	6 (24.0)	.788
Hospital mortality (No.) (%)	17 (15.3)	6 (24.0)	.231
Mortality at 90 days (No.) (%)	52 (46.8)	16 (64.0)	.183

premorbid mRS 4 compared with mRS 3 (median mRS of 6 versus mRS 5, $P < .001$). The proportion of good outcome was slightly but nonsignificantly higher in patients with premorbid mRS 4 (24.0% versus 20.7%, $P = .7877$). Hospital mortality and mortality at 90 days were nonsignificantly but markedly higher in patients with premorbid mRS 4 (24.0% versus 15.3%, $P = .231$; and 64.0% versus 46.8%, $P = .183$) (Table 4).

DISCUSSION

In this study, we analyzed clinical outcome in a stroke cohort that has been excluded from previous randomized controlled trials on neurothrombectomy: patients with stroke with moderate and moderately severe premorbid disability.

As a main finding, about one-fifth of our cohort achieved good clinical outcome: These patients returned to their prestroke condition 90 days after stroke onset without the need for further assistance or additional costs. Indeed, worsening of clinical status is associated with increasing health care costs.⁵ Dewilde et al,⁶ for instance, report that mRS 4 at 90 days after stroke onset was associated with significantly higher care costs compared with mRS 3 (\$4008 versus \$1639, $P < .001$). Therefore, MT can prevent an increase of long-term health care costs in patients with elevated premorbid mRS.

The relatively low rate of good outcome compared with the results of thrombectomy in premorbid mRS 0–2 might be attributed to old age and age-related frailty.⁷ While mean age in our cohort was 80.6 years, median age in the Highly Effective Reperfusion evaluated in Multiple Endovascular Stroke Trials (HERMES) meta-analysis was 68 years.²

Hospital mortality and mortality at 90 days were nonsignificantly higher in patients with premorbid mRS 4 compared with premorbid mRS 3. This difference is probably not significant due to the low number of patients with premorbid mRS 4 in our cohort ($n = 25$). A possible explanation is that treatment in patients with premorbid mRS 4 might be terminated earlier compared with patients with premorbid mRS 3.

Successful recanalization was the most powerful predictor of good outcome (OR, 7.11; 95% CI, 1.73–49.90; $P = .0171$). Furthermore, increasing stroke severity (high NIHSS score) and increasing infarct size (low ASPECTS) were associated with lower

chances of achieving good outcome in our cohort. This finding has been previously described by Hui et al.⁸ Although both parameters were statistically independent predictors, they might nevertheless be related to the occlusion site because proximal occlusions are usually associated with worse outcome compared with distal occlusions.⁹ In our cohort, M2 occlusions were more frequent in patients with good outcome, and ICA occlusions were more frequent in patients with poor outcome.

Our study has limitations, mainly due its retrospective non-randomized design. There might be a selection bias because patients with stroke with premorbid mRS 3 and 4 not undergoing MT were not included in this study. Because we did not have a control group, it is not possible to determine the benefit of MT compared with best medical care. MT may possibly have little benefit in patients with premorbid mRS 3 and 4. Also, only a small group of 25 patients with premorbid mRS 4 were analyzed in this study. Moreover, using the mRS for prestroke assessment is controversial because the mRS is primarily designed to assess post-treatment clinical status. Fearon et al¹⁰ have reported that inter-observer reliability and validity of premorbid mRS are limited. In some cases, assessing the premorbid status is not even possible because of missing or incorrect information. Nonetheless, mRS is the most frequently used measure to assess the premorbid status of patients with acute stroke.

CONCLUSIONS

Overall, good clinical outcome, defined as unchanged disability, is less frequent in premorbid mRS 3 and 4 compared with patients with premorbid mRS 0–2. Nevertheless, about 20% of the patients return to their premorbid mRS, which may justify endovascular treatment. Because we did not have a control group, it is not possible to determine the benefit of MT compared with best medical care. MT may possibly have little benefit in patients with premorbid mRS 3 and 4. The most important predictor of good outcome is successful recanalization.

Disclosures: Johannes Pfaff—UNRELATED: Travel/Accommodations/Meeting Expenses Unrelated to Activities Listed: Stryker, MicroVention. Christian Herweh—UNRELATED: Consultancy: Brainomix. Simon Nagel—UNRELATED: Consultancy: Brainomix; Payment for Lectures Including Service on Speakers Bureaus: Medtronic, Pfizer, Bayer, Boehringer Ingelheim. Peter A. Ringleb—UNRELATED: Consultancy: Boehringer Ingelheim. Comments: Advisory Board member; Payment for Lectures Including Service on Speakers Bureaus: Boehringer Ingelheim, Bayer, Daiichi Sankyo, Pfizer. Comments: lecture fee, travel support. Martin Bendszus—UNRELATED: Board Membership: Data and Safety Monitoring Board for Vascular Dynamics, Guerbet, Boehringer Ingelheim; Consultancy: Codman, Roche, Guerbet, Boehringer Ingelheim, B. Braun; Grants/Grants Pending: DFG, Hopp Foundation, Novartis, Siemens, Guerbet, Stryker, Covidien*; Payment for Lectures Including Service on Speakers Bureaus: Novartis, Roche, Guerbet, Teva Pharmaceutical Industries, Bayer, Codman. Markus A. Möhlenbruch—UNRELATED: Board Membership: Codman; Consultancy: Medtronic, MicroVention, Stryker; Grants/Grants Pending: Balt, MicroVention*; Payment for Lectures Including Service on Speakers Bureaus: Medtronic, MicroVention, Stryker. *Money paid to the institution.

REFERENCES

- Swieten JC van, Koudstaal PJ, Visser MC, et al. **Interobserver agreement for the assessment of handicap in stroke patients.** *Stroke* 1988; 19:604–07 CrossRef Medline
- Goyal M, Menon BK, van Zwam WH, et al. **Endovascular thrombectomy after large-vessel ischaemic stroke: a meta-analysis of individual patient data from five randomised trials.** *Lancet* 2016; 387:1723–31 CrossRef Medline

3. Albers GW, Marks MP, Kemp S, et al. **Thrombectomy for stroke at 6 to 16 hours with selection by perfusion imaging.** *N Engl J Med* 2018; 378:708–18 CrossRef Medline
4. Powers WJ, Rabinstein AA, Ackerson T, et al; American Heart Association Stroke Council. **2018 Guidelines for the Early Management of Patients with Acute Ischemic Stroke: A Guideline for Healthcare Professionals from the American Heart Association/American Stroke Association.** *Stroke* 2018;49:e46–110
5. Wilson A, Bath PM, Berge E, et al. **Understanding the relationship between costs and the modified Rankin Scale: a systematic review, multidisciplinary consensus and recommendations for future studies.** *Eur Stroke J* 2017;2:3–12 CrossRef Medline
6. Dewilde S, Annemans L, Peeters A, et al. **Modified Rankin scale as a determinant of direct medical costs after stroke.** *Int J Stroke* 2017; 12:392–400 CrossRef Medline
7. Knoflach M, Matosevic B, Rucker M, et al. **Functional recovery after ischemic stroke: a matter of age—data from the Austrian Stroke Unit Registry.** *Neurology* 2012;78:279–85 CrossRef Medline
8. Hui FK, Obuchowski NA, John S, et al. **ASPECTS discrepancies between CT and MR imaging: analysis and implications for triage protocols in acute ischemic stroke.** *J Neurointerv Surg* 2017;9: 240–43 CrossRef Medline
9. Behme D, Kowoll A, Weber W, et al. **M1 is not M1 in ischemic stroke: the disability-free survival after mechanical thrombectomy differs significantly between proximal and distal occlusions of the middle cerebral artery M1 segment.** *J Neurointerv Surg* 2015;7:559–63 CrossRef Medline
10. Fearon P, McArthur KS, Garrity K, et al. **Prestroke modified Rankin Stroke Scale has moderate interobserver reliability and validity in an acute stroke setting.** *Stroke* 2012;43:3184–88 CrossRef Medline

Selection of Patients with Stroke for Thrombectomy Must Be Judicious and Should Not Be Offered to Any Patient with Large-Vessel Occlusion with a Femoral Pulse

In this issue of the *American Journal of Neuroradiology (AJNR)*, the authors reported their findings in the retrospective study, “Clinical Outcome after Thrombectomy in Patients with Stroke with Premorbid Modified Rankin Scale Scores of 3 and 4: A Cohort Study with 136 Patients.”¹ The authors examined outcomes of patients with notable premorbid impaired functional status who underwent endovascular thrombectomy for the treatment of acute ischemic stroke. The bottom line was that approximately 20% of patients returned to their baseline premorbid function, and the authors concluded that endovascular thrombectomy could be justified in this group of patients.

The authors’ conclusion represented a notable departure from current guidelines, which were derived from the successful randomized controlled thrombectomy studies dating from 2015, culminating in 2 further successful trials extending the time window for intervention up to 24 hours after stroke onset.² To briefly recapitulate, the American Stroke Association guidelines stipulated that the group of patients most likely to benefit was those with premorbid modified Rankin Scale scores of 0–2. The downstream effect of the guidelines was that those patients with notable pre-morbid impairment mRS of 3 to 5 (excluding those with mRS 6 which equated death) were essentially excluded from thrombectomy. This generated debate in some quarters whether the strict adherence of guidelines “denied” treatment to a subgroup of patients who might have benefitted from treatment.

It is important to reflect on the classification of patients into different groups of the mRS. mRS 3 describes a patient with moderate disability and specifically “requiring some help but able to walk without assistance,” and mRS 4 describes moderate-to-severe disability with the patient “unable to walk without assistance and unable to attend to own bodily needs without assistance.”³ The assessment of patients according to the mRS does allow room for flexible interpretation, but a patient with mRS 4 is essentially an individual who requires 24-hour supervision and is likely to reside in a high-level-care environment.

The philosophical question of treatment should also take into account the wishes of the patients, who, with premorbid function of mRS 3 or 4, will differ substantially from those with premorbid

functional independence. Pearlman et al⁴ in a study involving 342 patients with a mixture of stroke survivors and nursing home residents examined this salient question and found that those with notable premorbid impairment viewed their health function as “states worse than death” and clearly voiced strong reluctance to undergoing life-prolonging treatment.⁴ These findings are sobering in that perhaps as clinicians we have frequently adopted, sometimes justifiably in emergency situations, patriarchal standpoints and have not adequately taken into account the reluctance of patients for invasive treatment.

I commend the authors of the study in this issue of the *AJNR* for their investigation of thrombectomy outcomes in a group of patients with notable premorbid dysfunction. However, the results do not support a motion to alter current clinical guidelines, and I believe that the triage of patients with stroke for thrombectomy must remain judicious and that we should avoid falling into the trap of treating any patient with large-artery occlusion and a femoral pulse.

REFERENCES

1. Seker F, Pfaff J, Schönenberger S, et al. **Clinical outcome after thrombectomy in patients with stroke with premorbid modified Rankin Scale scores of 3 and 4: a cohort study with 136 patients.** *AJNR Am J Neuroradiol* 2018; CrossRef
2. Powers WJ, Rabinstein AA, Ackerson T, et al; American Heart Association Stroke Council. **2018 guidelines for the early management of patients with acute ischemic stroke: a guideline for healthcare professionals from the American Heart Association/American Stroke Association.** *Stroke* 2018;49: e46–110 CrossRef Medline
3. Quinn TJ, Dawson J, Walters M. **Dr John Rankin; his life, legacy, and the 50th anniversary of the Rankin Stroke Scale.** *Scott Med J* 2008;53: 44–47 CrossRef Medline
4. Pearlman RA, Cain KC, Starks H, et al. **Preferences for life-sustaining treatments in advance care planning and surrogate decision making.** *J Palliat Med* 2000;3:37–48 CrossRef Medline

© B. Yan

Comprehensive Stroke Center
Royal Melbourne Hospital
Parkville, Melbourne, Victoria, Australia

<http://dx.doi.org/10.3174/ajnr.A5928>

Ostium Ratio and Neck Ratio Could Predict the Outcome of Sidewall Intracranial Aneurysms Treated with Flow Diverters

N. Paliwal, V.M. Tutino, H. Shallwani, J.S. Beecher, R.J. Damiano, H.J. Shakir, G.S. Atwal, V.S. Fennell, S.K. Natarajan, E.I. Levy, A.H. Siddiqui, J.M. Davies, and H. Meng



ABSTRACT

BACKGROUND AND PURPOSE: Incompletely occluded flow diverter treated aneurysms remain at risk of rupture and thromboembolic complications. Our aim was to identify the potential for incomplete occlusion of intracranial aneurysms treated by flow diverters. We investigated whether aneurysm ostium size in relation to parent artery size affects angiographic outcomes of flow diverter–treated sidewall aneurysms.

MATERIALS AND METHODS: Flow diverter–treated sidewall aneurysms were divided into “occluded” and “residual” (incomplete occlusion) groups based on 6-month angiographic follow-up. We calculated the ostium ratio, a new parameter defined as the aneurysm ostium surface area versus the circumferential surface area of the parent artery. We also calculated the neck ratio, defined as clinical aneurysm neck diameter versus parent artery diameter from pretreatment 2D DSA, as a 2D surrogate. We compared the performance of these ratios with existing aneurysm morphometrics (size, neck diameter, volume, aspect ratio, size ratio, undulation index, nonsphericity index, ellipticity index, bottleneck factor, aneurysm angle, and parent vessel angle) and flow diverter–related parameters (metal coverage rate and pore density). Statistical tests and receiver operating characteristic analyses were performed to identify significantly different parameters between the 2 groups and test their predictive performances.

RESULTS: We included 63 flow diverter–treated aneurysms, 46 occluded and 17 residual. The ostium ratio and neck ratio were significantly higher in the residual group than in the occluded group ($P < .001$ and $P = .02$, respectively), whereas all other parameters showed no statistical difference. As discriminating parameters for occlusion, ostium ratio and neck ratio achieved areas under the curve of 0.912 (95% CI, 0.838–0.985) and 0.707 (95% CI, 0.558–0.856), respectively.

CONCLUSIONS: High ostium ratios and neck ratios could predict incomplete occlusion of flow diverter–treated sidewall aneurysms. Neck ratio can be easily calculated by interventionists to predict flow-diverter treatment outcomes.

ABBREVIATIONS: CND = clinical neck diameter; FD = flow diverter; MCR = metal coverage rate; NR = neck ratio; OsR = ostium ratio; VSW = virtual stenting workflow

Flow diverters (FDs) are used to treat an increasing diversity of intracranial aneurysms.^{1–3} These devices are self-expanding, densely braided metallic stents that are deployed across the aneu-

rysm neck. The goal of flow diversion is to reconstruct the parent artery by diverting blood flow from the aneurysm, subsequently initiating thrombus formation in the aneurysm sac and endothelialization across the parent vessel defect (ie, the ostium). Despite the success of this strategy, up to 15% of FD-treated aneurysms have incomplete thrombosis within the sac,⁴ meaning that a persistent risk for aneurysm rupture and further complications exists.^{5,6}

Physicians look to morphologic metrics to predict outcomes

Received June 21, 2018; accepted after revision November 7.

From the Department of Mechanical and Aerospace Engineering (N.P., R.J.D., H.M.), Canon Stroke and Vascular Research Center (N.P., V.M.T., R.J.D., E.I.L., A.H.S., J.M.D., H.M.), and Department of Biomedical Engineering (V.M.T., H.M.), University at Buffalo, Buffalo, New York; Departments of Neurosurgery (V.M.T., H.S., J.S.B., H.J.S., G.S.A., V.S.F., S.K.N., E.I.L., A.H.S., J.M.D., H.M.), Radiology (E.I.L., A.H.S.), and Biomedical Informatics (J.M.D.), Jacobs School of Medicine, University at Buffalo, Buffalo, New York; Department of Neurosurgery (H.S., J.S.B., H.J.S., G.S.A., V.S.F., S.K.N., A.H.S., J.M.D.), Gates Vascular Institute at Kaleida Health, Buffalo, New York, and Jacobs Institute (A.H.S., J.M.D.), Buffalo, New York.

This work was supported by Canon Medical Systems Corporation and National Institutes of Health grant R01-NS-091075. J.M.D. was supported by the National Center for Advancing Translational Sciences of the National Institutes of Health under award number KL2TR001413 to the University at Buffalo.

The content is solely the responsibility of the authors and does not necessarily represent the official views of the National Institutes of Health.

Please address correspondence to Hui Meng, PhD, Canon Stroke and Vascular Research Center, Clinical Translational Research Center, 875 Ellicott St, Buffalo, NY 14214; e-mail: huimeng@buffalo.edu

Indicates open access to non-subscribers at www.ajnr.org

Indicates article with supplemental on-line appendix.

Indicates article with supplemental on-line photos.

<http://dx.doi.org/10.3174/ajnr.A5953>

and tailor treatment. Our goal was to identify metrics that could be measured before treatment that may indicate potential incomplete occlusion of FD-treated aneurysms. For coil embolization, surgeons have used aneurysm dome and neck measurements to gauge treatment options.^{7,8} However, these metrics do not necessarily equate to success with flow diversion. Mut et al⁹ demonstrated that aneurysm neck diameter, size, volume, and aspect ratio do not indicate the occlusion outcome of FD-treated aneurysms. These parameters only consider measurements of the aneurysm sac and not the parent vessel or its relationship to the aneurysm. Gentric et al¹⁰ showed that flow-diversion effects vary with the size of the aneurysm ostium (ie, the defect in the parent artery made by the aneurysm). They also postulated that larger defects might cause deformation of the struts of the FD, affecting FD porosity across the aneurysmal defect, thus leading to ineffective flow diversion.

In this study, we hypothesized that the aneurysmal defect on the parent artery and the extent to which it circumferentially envelops the parent artery affect the ability of the FD to redirect flow away from the aneurysm and thus may reduce the likelihood of occlusion. To quantify this concept, we defined a novel parameter, ostium ratio (OsR), which is the ratio of the area of the ostium surface of the aneurysm to the circumferential parent vessel area. A 2D surrogate, the neck ratio (NR), was also defined as the ratio of the aneurysm neck diameter to the parent artery diameter. The OsR and NR were evaluated in 63 sidewall aneurysms treated with FDs. Forty-six aneurysms had complete occlusion, and 17 had residual filling on angiographic imaging at the 6-month follow-up. Other aneurysm morphometrics and FD parameters were also compared between the 2 groups. Linear regression analysis was performed to check for correlation of the OsR with FD parameters.

MATERIALS AND METHODS

Patient Selection and Aneurysm Model Generation

A data base of a consecutive series of patients with aneurysms treated using the Pipeline Embolization Device (Covidien, Irvine, California) has been maintained at the University at Buffalo. From this data base, we retrospectively identified patients treated between 2009 and 2017 who satisfied the inclusion criteria of our study. These criteria included the following: imaging evidence of a sidewall ICA aneurysm treated using a single Pipeline Embolization Device, no previous treatment of the aneurysm, pretreatment 3D rotational DSA images with sufficient quality for accurate reconstruction and segmentation for precise morphologic modeling, and 6-month 2D DSA follow-up available. We excluded previously treated aneurysms to avoid confounding of the healing due to the presence of an existing endovascular device with the healing associated with FD treatment. The pretreatment 3D DSA images were segmented using an open-source software package, Vascular Modeling Toolkit (www.vmtk.org), to obtain accurate surface representation of the vascular geometry of each aneurysm.

Approval for the collection and review of patient data was obtained from the institutional review board. Consent from the individual patients was waived by the board.

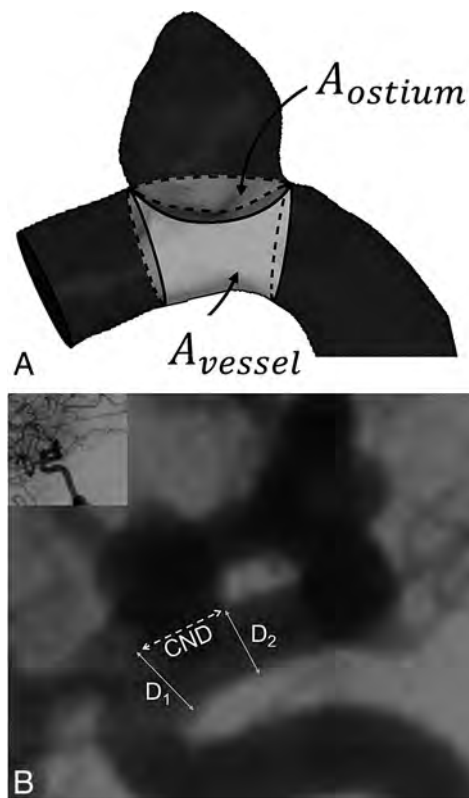


FIG 1. Definitions of OsR and NR on the 3D model and 2D DSA image for a representative patient-specific aneurysm. *A*, The illustration shows the area of the ostium surface (within the *dashed curves*) and the area of the circumferential parent artery (within the *solid lines*) for OsR calculations. *B*, CND and parent vessel diameters (D_1 , D_2) are calculated on the most perpendicular projection of the pretreatment 2D DSA imaging. D_1 and D_2 are measured at the proximal and distal extremes, respectively, of the line that measures the CND.

Ostium Ratio

The OsR was defined as the area of the reconstructed aneurysm ostium surface (A_{ostium}) divided by the area of the circumferential section of the remaining parent vessel (A_{vessel}). The circumferential section of the parent vessel was determined by drawing 2 planes at the proximal and distal extremities of the aneurysmal ostium surface in the parent vessel. Regions representing A_{ostium} and A_{vessel} are illustrated on a representative sidewall aneurysm in Fig 1A.

$$OsR = \frac{A_{ostium}}{A_{vessel}}$$

The ostium and parent vessel surfaces for calculating the OsR are obtained in 3 steps: parent vessel reconstruction, ostium surface generation, and corresponding parent vessel isolation. Details on each step for calculation of the OsR are described in the On-line Appendix.

Neck Ratio

Because complex computations of the 3D aneurysm geometry are required to calculate the OsR, we devised a surrogate, the NR, which can easily be calculated by interventionists. The NR is the ratio of the clinical neck diameter (CND) to the average parent vessel diameter. To obtain this ratio, we used pretreatment 2D

angiographic images, and the image with the most perpendicular projection was identified for each aneurysm. Then, CND and the proximal (D_1) and distal (D_2) ends of the aneurysm neck in the parent artery were measured on each image as shown in Fig 1B. The calculation is as follows:

$$NR = \frac{CND}{\left(\frac{D_1 + D_2}{2}\right)}$$

For NR measurements on 2D-DSA images, a line to measure the CND was first drawn across the aneurysmal neck. A line at the proximal end and a line at the distal end of the CND were then drawn in the parent vessel to measure D_1 and D_2 , respectively (Fig 1B).

Other Morphology-Based Parameters

Other common morphologic parameters calculated for each case were aneurysm size (size), neck diameter, aneurysm volume, aspect ratio, and size ratio. "Aspect ratio" is defined as the ratio of the aneurysm size to the neck diameter, and "size ratio" is defined as the ratio of aneurysm size to the parent vessel diameter.¹¹⁻¹³ AView software was used to calculate these morphologic parameters to assess differences between the occluded and residual groups.¹⁴⁻¹⁶ Furthermore, as shown by Darsaut et al,¹⁷ the curvature of the aneurysm and parent vessel affects the occlusion outcome of FD-treated aneurysms. Therefore, we calculated the aneurysm angle and parent vessel angle for each aneurysm.^{11,17} To quantify aneurysm shapes in both groups, we calculated the following shape indices for each aneurysm: undulation index, non-sphericity index, ellipticity index, and bottleneck factor.^{11,12}

FD-Related Parameters

Two FD-related parameters, metal coverage rate (MCR) and pore density, were calculated for each case to assess associations with occlusion status and the OsR. MCR quantifies the percentage area of the aneurysm neck covered by the FD wire struts, and pore density quantifies the number of FD pores per unit area at the neck plane.^{1,18,19} MCR and pore density could not be measured accurately from posttreatment images due to imaging artifacts after FD implantation. Therefore, virtual FD deployment was performed on each case to simulate clinical FD deployment and quantify MCR and pore density. We used an expansion-based in-house virtual stenting workflow to perform virtual FD deployment on these cases.²⁰⁻²² MCR and pore density were quantified from the FD deployment results at the aneurysm neck. Details of the virtual stenting workflow, FD deployment, and quantification of the MCR and pore density are provided in the On-line Appendix.

FD deployments and subsequent MCR and pore density calculations are extremely variable and depend on the size of the device and the curvature and morphology of the artery.^{23,24} Therefore, to validate the MCR and pore density calculated after virtual stent placement, we performed experimental validation using physical deployment of FDs in 3 patient-specific aneurysm models fabricated using optically clear silicone.²⁵ Validation results showed that the MCR and pore density from the virtual stenting workflow were within 10% of the physical

Table 1: Demographic and clinical information for patients in the occluded and residual groups

Parameter	Occluded	Residual	P Value
Age (average \pm SE) (yr)	57.6 \pm 2.4	62.2 \pm 2.9	.28
Female sex (No. of patients)	37	15	.12
Hypertension (No. of patients)	10	8	.26
Smoking (No. of patients)	15	9	.48

Note:—SE indicates standard error.

deployment range for all 3 aneurysms. Details of validation analysis and results are included in the On-line Appendix.

Researchers involved in calculating the morphologic parameters (including the OsR and NR) and the FD-related parameters were blinded to the clinical outcome of the aneurysms.

Statistical Analyses

FD-treated aneurysms were dichotomized as "occluded" or "residual" based on the 6-month 2D-DSA images. Completely occluded aneurysms were included in the occluded group, and aneurysms with neck or dome remnants were included in the residual group. For statistical analysis, we performed the Shapiro-Wilk test to check for normal distribution of the continuous variables. A Mann-Whitney U test (for non-normally distributed data) or a Student t test (for normally distributed data) was used to distinguish differences in OsR, NR, size, neck diameter, volume, aspect ratio, size ratio, MCR, and pore density between the 2 groups. For categorical variables, a χ^2 test was used to test statistically significant differences between the groups. All values were expressed as mean \pm standard error. Statistical significance was defined as a $P < .05$. Area under the receiver operating characteristic curve (area under the curve) and 95% CI were used to assess the predictable power of statistically significant parameters.²⁶ The optimal cutoff point was determined by the Youden Index (J statistic),²⁷ which indicates the point in the receiver operating characteristic curve with maximum specificity and sensitivity. To determine whether the OsR and NR were related to the MCR and pore density, we performed linear regression analysis and defined correlation as $R^2 > 0.80$. Statistical analysis was performed using the commercial SPSS software package (Version 24.0; IBM, Armonk, New York).

RESULTS

A total of 63 aneurysms in 60 patients met the study inclusion criteria. At the time of FD treatment, 4 of 63 aneurysms were ruptured. At 6-month follow-up, 46 aneurysms were occluded, whereas 17 aneurysms had some residual contrast filling. No significant differences were found in age, sex, hypertension, or smoking status between the occluded and residual groups (Table 1). OsR was significantly higher in the residual group than in the occluded group (0.58 \pm 0.03 versus 0.35 \pm 0.02, $P < .001$, Fig 2). OsR values ranged from 0.13 to 0.66 and from 0.41 to 0.87 in the occluded and residual groups, respectively.

Apart from the OsR, the NR was the only morphologic parameter that was significantly higher in the residual group than the occluded group (1.74 \pm 0.18 versus 1.30 \pm 0.07, $P = .02$) (Table 2). Although values for size, neck diameter, volume, aspect ratio, and size ratio were higher in the residual group than in the occluded group, none of these parameters

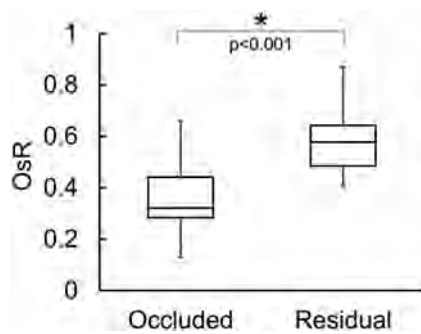


FIG 2. Box-and-whisker plot of the OsR ($P < .001$) shows a statistically significant difference in the OsR between the occluded and residual groups. The horizontal line within each box indicates the median, boundaries of the box indicate the 25th and 75th percentiles, and whisker bars represent the highest and lowest values of the OsR in each group.

Table 2: Aneurysmal morphologic and FD-related parameters in the occluded and residual groups^a

Parameter	Occluded	Residual	P Value
OsR	0.35 ± 0.02	0.58 ± 0.03	<.001 ^b
NR	1.30 ± 0.07	1.74 ± 0.18	.02 ^b
Size (mm)	5.6 ± 0.6	6.6 ± 1.1	.29
Neck diameter (mm)	4.67 ± 0.26	6.06 ± 0.62	.06
Aneurysm volume (mm ³)	251.52 ± 105.48	502.75 ± 239.77	.35
AR	1.01 ± 0.08	1.12 ± 0.16	.53
SR	1.48 ± 0.19	2.00 ± 0.43	.27
UI	0.06 ± 0.01	0.07 ± 0.02	.77
NSI	0.23 ± 0.01	0.27 ± 0.03	.43
EI	0.21 ± 0.01	0.24 ± 0.02	.33
BF	1.26 ± 0.07	1.23 ± 0.08	.15
AA	89.39 ± 2.98	89.32 ± 2.63	.34
PVA	3.17 ± 4.14	4.61 ± 6.27	.84
MCR (%)	27.46 ± 0.51	26.93 ± 1.02	.64
PD (1/mm ²)	28.35 ± 0.86	25.79 ± 1.7	.19

Note:—AA indicates aneurysm angle; AR, aspect ratio; BF, bottleneck factor; EI, ellipticity index; PD, pore density; PVA, parent vessel angle; SR, size ratio, UI, undulation index; NSI, nonsphericity index.

^a Values expressed as average ± standard error.

^b Significant difference.

reached statistically significant differences. There was no statistical difference between aneurysm angle ($P = .34$) and parent vessel angle ($P = .84$) in the occluded and residual groups. In terms of shape indices, the undulation index, nonsphericity index, and ellipticity index were higher in the residual group, and bottleneck factor was higher in the occluded group. However, no shape index was significantly different in the occluded and residual groups. For FD-related parameters, the MCR and pore density were higher in the occluded group, but the differences between the groups were not statistically significant for either parameter (Table 2).

Figure 3 shows a comparison between the OsR and NR in the 2 groups (normalized by the values in the occluded group) (Fig 3A) and the receiver operating characteristic curve to assess their predictive powers (Fig 3B). There were larger differences between the normalized OsR in the occluded and residual groups compared with the normalized NR (Fig 3A). In the receiver operating characteristic analysis, the area under the curve for the OsR was 0.912 (95% CI, 0.838–0.985) and the NR was 0.707 (95% CI, 0.558–0.856) (Fig 3B). On the basis of the Youden Index (J statistic)²⁷ for maximal sensitivity and specificity, the optimum pre-

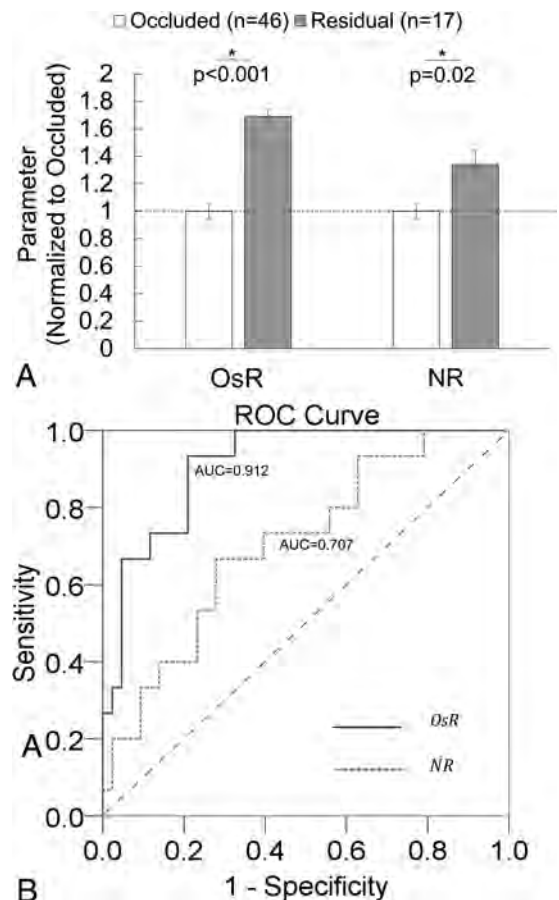


FIG 3. Comparison of the OsR and NR mean (± standard error) normalized by the occluded group and receiver operating characteristic curves of the OsR and NR for occlusion status. A, Larger differences in the OsR between the occluded and residual groups ($P < .001$) compared with the NR ($P = .02$). B, Receiver operating characteristic curve (ROC) of the OsR (solid line) and NR (dotted line) against the occlusion status, with an area under the curve of 0.912 for the OsR and 0.707 for the NR. The asterisk indicates statistically significant difference.

dictive cutoff to distinguish occluded-versus-residual cases occurred at OsR = 0.46 and NR = 1.3.

Linear regression analysis of FD-related parameters against the OsR and NR showed a statistically insignificant correlation between MCR and OsR, pore density and OsR, MCR and NR, and pore density and NR (Fig 4).

DISCUSSION

In this study, we sought to determine whether the relationship between aneurysm and parent artery morphology influences occlusion rates with FD treatment. We hypothesized that when a larger percentage of the parent vessel requires reconstruction and healing, the occlusion rate would fall. To test this hypothesis, we defined the novel metric, OsR, that captures this concept of the percentage of the parent vessel involved and found that a higher OsR correlates with aneurysm residual (incomplete occlusion) at 6 months. Our results suggest that aneurysms with higher OsR are less amenable to treatment with a single FD and may require alternate/adjunctive treatment paradigms. The predictive ability of the OsR was high, and previously described morphologic parameters (size, neck diameter, volume, aspect ratio, and size ratio) do not capture this complexity.

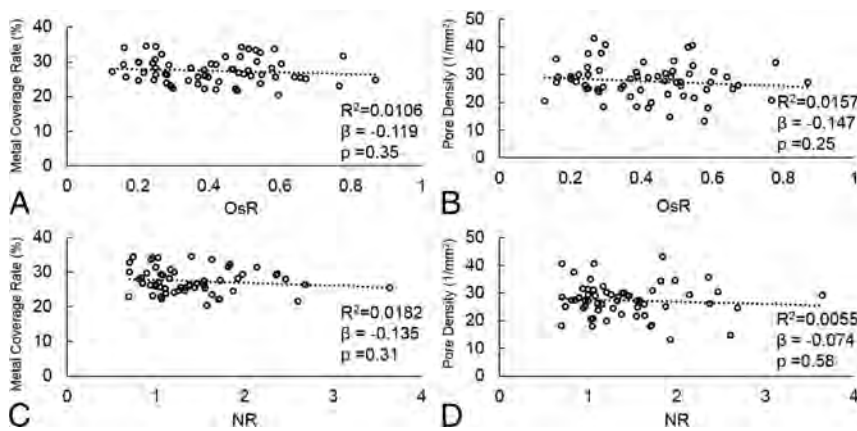


FIG 4. Linear regression analysis to test for correlation of the OsR and NR with FD parameters, MCR (%) (A and C) and pore density ($1/\text{mm}^2$) (B and D). A and B, MCR ($R^2 = 0.0106$) and pore density ($R^2 = 0.0157$) were independent of the OsR. C and D, MCR ($R^2 = 0.0182$) and pore density ($R^2 = 0.0055$) were also independent of the NR. Corresponding β and P values are also provided.

Large OsR Is Associated with Incompletely Occluded FD-Treated Aneurysms

OsR, the ratio of the surface area of the aneurysm ostium to the remaining circumferential surface area of the corresponding parent artery, essentially quantifies the fraction of the area of an FD that will be exposed at the aneurysm ostium. An aneurysm ostium is defined by complex 3D curves, and OsR accurately quantifies this curvature and represents the patient-specific aneurysm defect relative to the parent artery. Higher OsR in our residual cases suggests that a larger proportion of the parent vessel (ie, a larger parent vessel defect) provided the inlet for blood flow into aneurysms in the residual group. This would lead to a higher flow rate into the aneurysmal sac, which poses more burden for flow diversion and hence less effective flow-diversion treatment using a single FD in these cases. This premise is confirmed by a recent study from our group in which aneurysms with a higher OsR had a significantly higher inflow rate into the aneurysmal sac both before and after FD implantation, and all 3 parameters (OsR, pretreatment inflow rate, and posttreatment inflow rate) were negatively correlated with treatment outcome.²⁸ Thus, the OsR reflects flow-diversion effectiveness influenced by vascular morphology. It could potentially identify those aneurysms that are unsuitable for single-FD treatment.

A larger ostium has been correlated to the speed and degree of aneurysm occlusion after flow diversion in studies performed in animal models.^{10,29} For example, Chung et al²⁹ deployed FDs in an elastase-induced rabbit aneurysm model and found that aneurysms with smaller ostia occluded faster than aneurysms with larger ostia. Additionally, Gentric et al¹⁰ deployed FDs in large and giant sidewall aneurysms in a canine model and found that aneurysms with larger ostia showed worse angiographic outcome than aneurysms with small ostia. To our knowledge, our study is the first to show a correlation between the aneurysm ostium and angiographic outcome of FD-treated aneurysms using clinical data. Our results mirror those of the previous animal studies, albeit we correlated angiographic imaging findings to OsR not just the surface area or length of the ostium. We postulate that the OsR, which represents how much of the parent vessel is covered by the aneurysm, may be a better indicator of outcome than the ostium area or length alone.

NR as a Practical Surrogate for OsR

For the OsR concept to be clinically useful, it must be readily obtained by clinicians when they are making treatment decisions. To this end, we devised the NR as a clinical surrogate for the OsR in predicting the success of flow diversion (NR area under the curve = 0.707; 95% CI, 0.558–0.856). Although the OsR had better performance, it is currently difficult to implement in the catheterization laboratory, whereas clinicians can easily measure neck diameter and parent vessel diameter to compute the NR (see the illustration in Fig 1B).

On the basis of the cutoff values of the OsR and NR, it can be interpreted that ICA aneurysms with $\text{OsR} \geq 0.46$ or

$\text{NR} \geq 1.3$ might not be amenable to treatment with a single FD. We suspect that in practice, clinicians will find that smaller OsR and NR values indicate that an aneurysm may occlude fully with a single FD. Conversely, larger values of the OsR and NR may indicate a need for alternative treatment strategies, such as additional FDs or adjunctive coils,³⁰ to achieve similar rates of occlusion. Clinical studies have shown better success rates for FDs with adjunctive coils compared with FDs alone.^{31,32} Alternatively, for cases with a high OsR and NR, FD deployment techniques can change device properties. Catheter manipulations, such as “push-pull,” during the deployment of an FD can locally compress and provide optimal metal coverage across the neck, and this may increase flow diversion away from the aneurysm, compared with normal FD-deployment technique.^{18,33} The push-pull technique enables localized compaction of the FD, increasing the MCR across the neck.^{33,34} However, prospective studies are required to assess the reliability of the OsR and NR in predicting the success of flow diversion.

FD-Device Parameters Do Not Correlate with OsR or Angiographic Outcome

In our study, we virtually deployed FDs in all aneurysm cases to investigate whether the device configuration in cases with larger OsRs may play a role in treatment outcome. On the basis of our results, we found no significant association between the OsR and the device-related metrics, MCR and pore density. This finding is in contrast to those of Gentric et al,¹⁰ who used FD deployment in silicone tubes to show larger deformation of the FD struts in aneurysms with larger ostia. They suggested that larger ostia modify the FD configuration, increasing porosity and potentiating ineffective flow diversion. However, we did not find any correlation of porosity with angiographic outcome or OsR. Further studies investigating how FD-deployment configuration is related to poor clinical outcome are required.

Limitations

First, our analysis was performed on retrospectively collected data; a prospective study with a larger cohort is required to validate

the power of the OsR and NR in predicting the outcome of FD-treated aneurysms. Second, due to the limited FD data base at our single center, we included only sidewall aneurysms located at the ICA and our results might not be applicable to sidewall aneurysms at other anatomic locations. Future studies of different aneurysm types at different anatomic locations are required to confirm our findings. Third, due to a steep learning curve for clinical FD deployment, deployment strategies have been optimized across time, resulting in higher success of FD treatment as operator experience increases.³⁵ However, we did not consider operator experience in our study. Fourth, because the OsR and NR are independent on the FD device used, the effect of optimized FD-deployment strategies such as compacting the device at the aneurysm neck¹⁸ cannot be predicted by either the OsR or NR. Fifth, as demonstrated by Farzin et al,³⁶ measurements of the MCR and pore density could be subjective and depend on the operator. Thus, our MCR and pore density measurements might not represent actual values but may provide a good estimate for each case, as shown by our experimental validation in the On-line Appendix.

CONCLUSIONS

We defined OsR, a novel metric that correlates with the occlusion status of flow-diverted sidewall aneurysms. We also defined a 2D surrogate, NR, as the ratio of aneurysm neck diameter to the parent vessel diameter. Retrospective analysis of 63 FD-treated aneurysms showed that a high OsR and NR are correlated with incomplete occlusion at 6-month follow-up. Common morphologic and device-related parameters (size, neck diameter, volume, aspect ratio, size ratio, MCR, and pore density) did not show an association with the angiographic outcome of FD-treated aneurysms. Receiver operating characteristic analysis showed the high predictive power of the OsR and NR to discriminate occluded and residual aneurysms. Prospective investigation is necessary to validate the OsR and NR as predictors of occlusion in FD-treated aneurysms.

ACKNOWLEDGMENTS

We thank Palak K. Patel for technical assistance; Paul H. Dressel, BFA, for preparation of the illustrations; and W. Fawn Dorr, BA, and Debra J. Zimmer for editorial assistance.

Disclosures: Vincent M. Tutino—*OTHER RELATIONSHIPS*: cofounder of Neurovascular Diagnostics, Elad I. Levy—*UNRELATED: Board Membership*: Stryker, NeXtGen Biologics, MEDX, Cognition Medical Systems, EndoStream Medical, *Comments*: on the advisory board, no money paid; *Consultancy*: Claret Medical, Gerson Lehman Group Consulting, Guidepoint Global, Imperative Care, Medtronic, Rebound Therapeutics, StimMed; *Expert Testimony*: I render medicolegal opinions as an expert witness for various attorneys; *Payment for Lectures Including Service on Speakers Bureaus*: Medtronic (formerly Covidien), *Comments*: honorarium for training and lectures; *Stock/Stock Options*: NeXtGen Biologics, Rapid Medical, Claret Medical, Cognition Medical Systems, Imperative Care, Rebound Therapeutics, StimMed, Three Rivers Medical Center, *Comments*: shareholder/ownership interest. Adnan H. Siddiqui—*UNRELATED: Consultancy*: Amnis Therapeutics, Boston Scientific, Canon Medical Systems USA, Cerebrotech Medical Systems, Cerenovus, Claret Medical, Corindus, EndoStream Medical, Guidepoint Global, Imperative Care, Integra Life-Sciences, Medtronic, MicroVention, Northwest University, Data and Safety Monitoring Board Chair for the HEAT Trial, Penumbra, Rapid Medical, Rebound Therapeutics, Silk Road Medical, StimMed, Stryker, Three Rivers Medical Center, VasSol, W.L. Gore & Associates; *Grants/Grants Pending*: coinvestigator: National Institutes of Health/National Institute of Neurological Disorders and Stroke 1R01NS091075, Virtual Intervention of Intracranial Aneurysms; *Stock/Stock Options*: Amnis Therapeutics,

Apama Medical, Blinktbi, Buffalo Technology, Cardinal Health, Cerebrotech Medical Systems, Claret Medical, Cognition Medical Systems, EndoStream Medical, Imperative Care, International Medical Distribution Partners, Rebound Therapeutics, Silk Road Medical, StimMed, Synchron, Three Rivers Medical Center, Viseon Spine; *Other*: National Principal Investigator/Steering Committees: Cerenovus LARGE trial and ARISE II trial, Medtronic SWIFT PRIME and SWIFT DIRECT trials, MicroVention FRED trial and CONFIDENCE study, MUSC POSITIVE trial, Penumbra 3D Separator Trial, COMPASS trial, INVEST trial. Jason M. Davies—*RELATED: Grant*: UB CTSA, *Comments*: KL2*; *UNRELATED: Consultancy*: Cerevenous, Medtronic*; *Payment for Lectures Including Service on Speakers Bureaus*: Penumbra; *Stock/Stock Options*: Rist Neurovascular, Inc. Hui Meng—*RELATED: Grant*: National Institutes of Health/National Institute of Neurological Disorders and Stroke, *Comments*: 5R01NS091075-01*; *UNRELATED: Employment*: cofounder of Neurovascular Diagnostics. Gursant S. Atwal—*UNRELATED: Consultancy*: Imperative Care, *Comments*: consultant for a company about stroke care. *Money paid to the institution.

REFERENCES

1. D'Urso PI, Lanzino G, Cloft HJ, et al. **Flow diversion for intracranial aneurysms: a review.** *Stroke* 2011;42:2363–68 CrossRef Medline
2. Becske T, Kallmes DF, Saatci I, et al. **Pipeline for uncoilable or failed aneurysms: results from a multicenter clinical trial.** *Radiology* 2013; 267:858–68 CrossRef Medline
3. Becske T, Potts MB, Shapiro M, et al. **Pipeline for uncoilable or failed aneurysms: 3-year follow-up results.** *J Neurosurg* 2017;127:81–88 CrossRef Medline
4. Kallmes DF, Brinjikji W, Cekirge S, et al. **Safety and efficacy of the Pipeline embolization device for treatment of intracranial aneurysms: a pooled analysis of 3 large studies.** *J Neurosurg* 2017;127:775–80 CrossRef Medline
5. Kulcsár Z, Houdart E, Bonafé A, et al. **Intra-aneurysmal thrombosis as a possible cause of delayed aneurysm rupture after flow-diversion treatment.** *AJNR Am J Neuroradiol* 2011;32:20–25 CrossRef Medline
6. Siddiqui AH, Abla AA, Kan P, et al. **Panacea or problem: flow diverters in the treatment of symptomatic large or giant fusiform vertebrobasilar aneurysms.** *J Neurosurg* 2012;116:1258–66 CrossRef Medline
7. Turjman F, Massoud TF, Sayre J, et al. **Predictors of aneurysmal occlusion in the period immediately after endovascular treatment with detachable coils: a multivariate analysis.** *AJNR Am J Neuroradiol* 1998;19:1645–51 Medline
8. Johnston SC, Higashida RT, Barrow DL, et al; Committee on Cerebrovascular Imaging of the American Heart Association Council on Cardiovascular Radiology. **Recommendations for the endovascular treatment of intracranial aneurysms: a statement for healthcare professionals from the Committee on Cerebrovascular Imaging of the American Heart Association Council on Cardiovascular Radiology.** *Stroke* 2002;33:2536–44 CrossRef Medline
9. Mut F, Raschi M, Scrivano E, et al. **Association between hemodynamic conditions and occlusion times after flow diversion in cerebral aneurysms.** *J Neurointerv Surg* 2015;7:286–90 CrossRef Medline
10. Gentric JC, Darsaut TE, Makoyeva A, et al. **The success of flow diversion in large and giant sidewall aneurysms may depend on the size of the defect in the parent artery.** *AJNR Am J Neuroradiol* 2014;35: 2119–24 CrossRef Medline
11. Dhar S, Tremmel M, Mocco J, et al. **Morphology parameters for intracranial aneurysm rupture risk assessment.** *Neurosurgery* 2008; 63:185–96; discussion 196–97 CrossRef Medline
12. Raghavan ML, Ma B, Harbaugh RE. **Quantified aneurysm shape and rupture risk.** *J Neurosurg* 2005;102:355–62 Medline
13. Ujiie H, Tamano Y, Sasaki K, et al. **Is the aspect ratio a reliable index for predicting the rupture of a saccular aneurysm?** *Neurosurgery* 2001;48:495–503; discussion 502–03 CrossRef Medline
14. Rajabzadeh-Oghaz H, Varble N, Davies JM, et al. **Computer-assisted adjuncts for aneurysmal morphologic assessment: toward more precise and accurate approaches.** *Proc SPIE Int Soc Opt Eng* 2017; 10134 CrossRef Medline
15. Xiang J, Antiga L, Varble N, et al. **AView: an image-based clinical computational tool for intracranial aneurysm flow visualization**

- and clinical management. *Ann Biomed Eng* 2016;44:1085–96 CrossRef Medline
16. Xiang J, Varble N, Davies JM, et al. **Initial clinical experience with AView: a clinical computational platform for intracranial aneurysm morphology, hemodynamics, and treatment management.** *World Neurosurg* 2017;108:534–42 CrossRef Medline
 17. Darsaut TE, Bing F, Salazkin I, et al. **Flow diverters failing to occlude experimental bifurcation or curved sidewall aneurysms: an in vivo study in canines.** *J Neurosurg* 2012;117:37–44 CrossRef Medline
 18. Damiano R, Tutino V, Paliwal N, et al. **Compacting a single flow diverter versus overlapping flow diverters for intracranial aneurysms: a computational study.** *AJNR Am J Neuroradiol* 2017;38:603–10 CrossRef Medline
 19. Wang K, Huang Q, Hong B, et al. **Correlation of aneurysm occlusion with actual metal coverage at neck after implantation of flow-diverting stent in rabbit models.** *Neuroradiology* 2012;54:607–13 CrossRef Medline
 20. Paliwal N, Yu H, Damiano R, et al. **Fast virtual stenting with vessel-specific initialization and collision detection.** In: *Proceedings of the ASME International Design Engineering Technical Conferences and Computers and Information in Engineering Conference*, Buffalo, New York. August 17–20, 2014; V003T12A14–V03T12A14
 21. Paliwal N, Yu H, Xu J, et al. **Virtual stenting workflow with vessel-specific initialization and adaptive expansion for neurovascular stents and flow diverters.** *Comput Methods Biomech Biomed Engin* 2016;19:1423–31 CrossRef Medline
 22. Larrabide I, Kim M, Augsburger L, et al. **Fast virtual deployment of self-expandable stents: method and in vitro evaluation for intracranial aneurysmal stenting.** *Med Image Anal* 2012;16:721–30 CrossRef Medline
 23. Bing F, Darsaut TE, Salazkin I, et al. **Stents and flow diverters in the treatment of aneurysms: device deformation in vivo may alter porosity and impact efficacy.** *Neuroradiology* 2013;55:85–92 CrossRef Medline
 24. Makoyeva A, Bing F, Darsaut T, et al. **The varying porosity of braided self-expanding stents and flow diverters: an experimental study.** *AJNR Am J Neuroradiol* 2013;34:596–602 CrossRef Medline
 25. Paliwal N, Damiano RJ, Varble NA, et al. **Methodology for computational fluid dynamic validation for medical use: application to intracranial aneurysm.** *J Biomech Eng* 2017;139 CrossRef Medline
 26. Hanley JA, McNeil BJ. **The meaning and use of the area under a receiver operating characteristic (ROC) curve.** *Radiology* 1982;143:29–36 CrossRef Medline
 27. Youden WJ. **Index for rating diagnostic tests.** *Cancer* 1950;3:32–35 CrossRef
 28. Paliwal N, Jaiswal P, Tutino VM, et al. **Outcome prediction of intracranial aneurysm treatment by flow diverters using machine learning.** *Neurosurg Focus* 2018;45:E7 CrossRef Medline
 29. Chung B, Mut F, Kadirvel R, et al. **Hemodynamic analysis of fast and slow aneurysm occlusions by flow diversion in rabbits.** *J Neurointerv Surg* 2015;7:931–35 CrossRef Medline
 30. Damiano RJ, Ma D, Xiang J, et al. **Finite element modeling of endovascular coiling and flow diversion enables hemodynamic prediction of complex treatment strategies for intracranial aneurysm.** *J Biomech* 2015;48:3332–40 CrossRef Medline
 31. Lin N, Brouillard AM, Krishna C, et al. **Use of coils in conjunction with the Pipeline Embolization Device for treatment of intracranial aneurysms.** *Neurosurgery* 2015;76:142–49 CrossRef Medline
 32. Nossek E, Chalif DJ, Chakraborty S, et al. **Concurrent use of the Pipeline Embolization Device and coils for intracranial aneurysms: technique, safety, and efficacy.** *J Neurosurg* 2015;122:904–11 CrossRef Medline
 33. Xiang J, Ma D, Snyder KV, et al. **Increasing flow diversion for cerebral aneurysm treatment using a single flow diverter.** *Neurosurgery* 2014;75:286–94; discussion 294 CrossRef Medline
 34. Ma D, Xiang J, Choi H, et al. **Enhanced aneurysmal flow diversion using a dynamic push-pull technique: an experimental and modeling study.** *AJNR Am J Neuroradiol* 2014;35:1779–85 CrossRef Medline
 35. Jabbour P, Chalouhi N, Tjoumakaris S, et al. **The Pipeline Embolization Device: learning curve and predictors of complications and aneurysm obliteration.** *Neurosurgery* 2013;73:113–20; discussion 120 CrossRef Medline
 36. Farzin B, Brosseau L, Jamali S, et al. **Flow diverters: inter and intrarater reliability of porosity and pore density measurements.** *J Neurointerv Surg* 2015;7:734–39 CrossRef Medline

Endothelialization following Flow Diversion for Intracranial Aneurysms: A Systematic Review

 K. Ravindran,  M.M. Salem,  A.Y. Alturki,  A.J. Thomas,  C.S. Ogilvy, and  J.M. Moore



ABSTRACT

BACKGROUND: The underlying mechanism of action of flow diverters is believed to be the induction of aneurysm thrombosis and simultaneous endothelial cell growth along the device struts, thereby facilitating aneurysm exclusion from the circulation. Although extensive attention has been paid to the role of altered cerebrovascular hemodynamics using computational fluid dynamics analyses, relatively less emphasis has been placed on the role of the vascular endothelium in promoting aneurysm healing.

PURPOSE: Our aim was to systematically review all available literature investigating the mechanism of action of flow diverters in both human patients and preclinical models.

DATA SOURCES: A systematic search of PubMed, Cochrane Central Register of Controlled Trials MEDLINE, EMBASE, and the Web of Science electronic data bases was conducted in accordance with the Preferred Reporting Items for Systematic Reviews and Meta-Analyses guidelines.

STUDY SELECTION: We selected articles assessing the role of endothelialization in flow-diverter treatment of cerebral aneurysms, including both preclinical and clinical studies.

DATA ANALYSIS: Ten articles were eligible for inclusion in this review. Two assessed endothelialization in human patients, while the other 8 used preclinical models (either rabbits or pigs).

DATA SYNTHESIS: Methods used to assess endothelialization included optical coherence tomography and scanning electron microscopy.

LIMITATIONS: A limitation was the heterogeneity of studies.

CONCLUSIONS: Current data regarding the temporal relationship to flow-diverter placement has largely been derived from work in preclinical animal models. Whether these cells along the device struts originate from adjacent endothelial cells or are the result of homing of circulating endothelial progenitor cells is equivocal.

ABBREVIATIONS: Ang-1 = angiotensin-1; CD31 = cluster of differentiation 31; CD34 = cluster of differentiation 34; EPCs = endothelial progenitor cells; PED = Pipeline Embolization Device; PRISMA = Preferred Reporting Items for Systematic Reviews and Meta-Analyses; Tie2 = cell-surface receptor that binds and is activated by the angiotensins

Flow diversion has revolutionized the treatment of select intracranial aneurysms, representing both a safe and efficacious alternative to open microsurgery and other endovascular modalities.^{1,2} In contrast to devices used in other vascular beds, the

cellular and molecular mechanisms underpinning their mechanism of action have not been as well-characterized, despite an exponential increase in their use in recent years. Aneurysm occlusion via flow diversion has traditionally been proposed to occur by 2 predominant overarching processes: 1) intra-aneurysmal thrombosis following device-related disruption of blood flow, and 2) provision of a scaffold for endothelial cell growth at the aneurysmal neck by the device itself.³ However, it remains unclear which of these processes is most critical in promoting aneurysmal obliteration.

Initial global endothelialization along the flow-diverting stent and device endothelialization across the neck are crucial events

Received October 3, 2018; accepted after revision December 8.

From the Neurosurgical Service, Beth Israel Deaconess Medical Center, Harvard Medical School, Boston, Massachusetts.

Please address correspondence to Justin M. Moore, MD, PhD, Neurosurgical Service, Beth Israel Deaconess Medical Center, 110 Francis St, Suite 3B, Boston, MA 02215-5501; e-mail: justinmurraymoore@gmail.com

 Indicates article with supplemental on-line table.

<http://dx.doi.org/10.3174/ajnr.A5955>

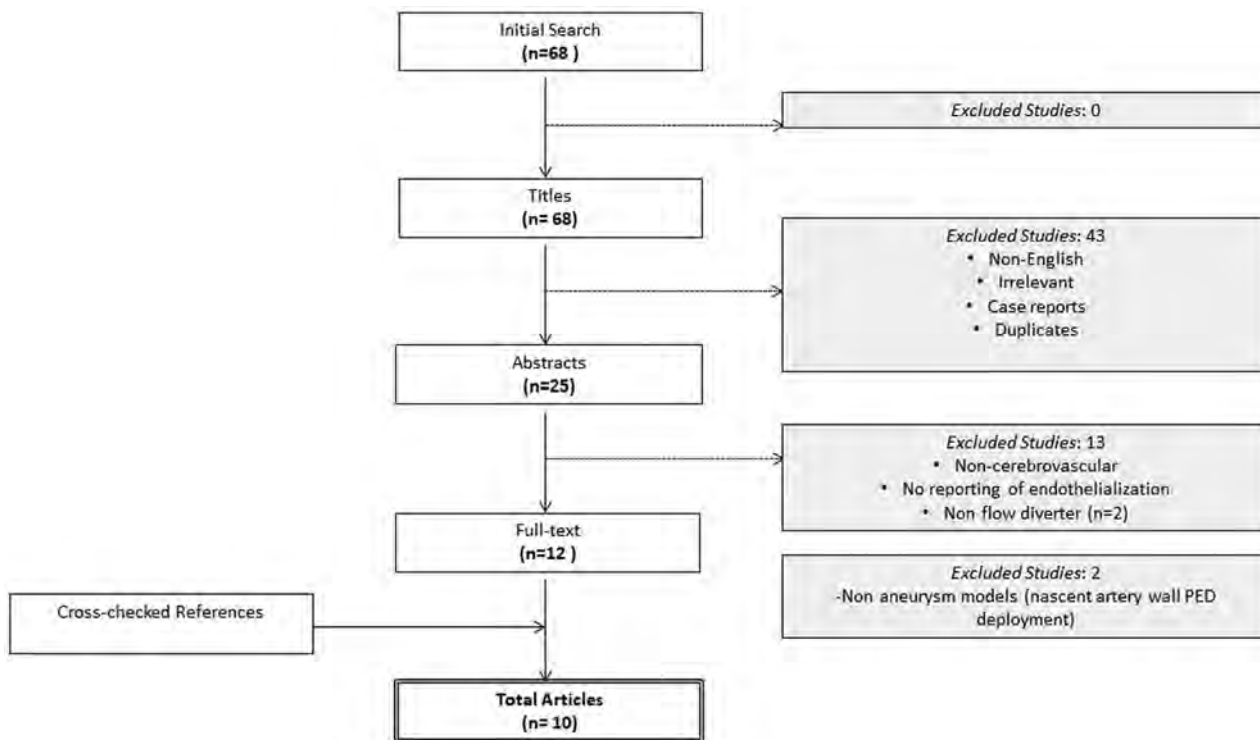


FIG 1. PRISMA flow chart of articles.

for facilitating aneurysm healing; the aneurysm remains at risk of rupture while this process occurs.^{4,5} Mismatch between successful angiographic aneurysm occlusion and MR imaging-visible aneurysm residual and controversy regarding optimal dual-antiplatelet therapy and its duration suggest that greater understanding of flow-diverter endothelialization may aid in optimizing successful aneurysm treatment. Furthermore, an improved understanding of endothelialization may help identify patients whose aneurysms are unlikely to be obliterated or to recur following flow-diverter placement. Thus, we performed a systematic review of all available literature investigating the overall device endothelialization of flow diverters in both human patients and preclinical models.

MATERIALS AND METHODS

Literature Search Strategy

This review was conducted according to the Preferred Reporting Items for Systematic Reviews and Meta-Analyses (PRISMA) guidelines. Electronic searches were conducted using Ovid MEDLINE, PubMed, EMBASE, the Cochrane Central Register of Controlled Trials, and the Web of Science from dates of inception until April 2018. To maximize the sensitivity of the search criteria, we combined the following terms: “flow diverter,” “flow diversion,” “flow-diverting stent,” “Pipeline Embolization Device,” “mechanism,” “endothelial,” and “endothelialization” as either key words or MeSH terms. References from multiple articles were additionally searched to retrieve any studies examining outcomes not found during the initial literature search.

Selection Criteria

Inclusion criteria for eligible studies in this systematic review were all studies reporting the use of any flow-diverting stent and any

mention of endothelial healing. All abstracts were independently screened by 2 reviewers (K.R., M.M.S.). Case reports, conference presentations, editorials, and non-English studies were excluded.

RESULTS

A total of 68 references were identified through a search of 5 electronic data bases (Fig 1). Following exclusion of duplicate and irrelevant references and after detailed abstract and title screening, 10 references directly relating to endothelialization were included per the search criteria (On-line Table).⁵⁻¹⁴ Two of the included references studied endothelialization in human patients.^{7,14} The remainder of the included articles used preclinical animal models, constituting pigs ($n = 1$) and rabbits ($n = 7$). Methods used to investigate endothelial coverage of flow-diverting stents included scanning electron microscopy and optical coherence tomography.

DISCUSSION

Mechanisms of Aneurysm Occlusion: Animal Data

Animal models of aneurysms have proved critical at providing histopathologic data following Pipeline Embolization Device (PED; Covidien, Irvine, California) deployment, given the difficulty in obtaining human data. However, limitations in translating results from animal models into human patients still exist due to subtle anatomic variances and different hemodynamic environments.

Computational fluid dynamics analyses of elastase-induced aneurysms in rabbits have suggested that a reduction of flow velocity with secondary induction of thrombosis is the foremost mechanism of aneurysm exclusion.¹⁵ At least at the aneurysmal

dome, diminished flow velocity may thus serve as the key driver of aneurysm healing. The close relationship between lower aneurysmal flow velocities and shorter occlusion times further supports this argument.¹⁶ In a 2007 study, Kallmes et al³ used a rabbit elastase model of saccular aneurysms to histologically demonstrate the presence of unorganized thrombus in aneurysm domes at 1 month, with an 88% rate of complete occlusion. Although the study was limited to only 6 subjects, intimal hyperplasia along the struts across the aneurysm neck was observed in 4 subjects at 6 months following PED deployment, with minimal intimal hyperplasia observed along the parent artery distal to the aneurysm. Moreover, in this study, scanning electron micrography demonstrated contiguity between the endothelium of the parent artery and the endothelial cells covering the stent. However, the patency of smaller branch arteries led the authors to conclude that intra-aneurysmal thrombosis was the foremost mechanism of aneurysmal exclusion, despite intimal hyperplasia being observed along device struts at 1 month posttreatment.

A similar study in rabbits by Kadirvel et al⁵ showed complete endothelialization on the PED surface as early as 1 week following deployment in the setting of complete occlusion, as well as at 8 weeks posttreatment. This appears to suggest that endothelialization following PED placement occurs in 2 phases: rapidly, at the parent artery and slowly at the aneurysmal neck, with the latter requiring an underlying scaffold of smooth-muscle cells.⁵ In particular, angiopoietin-1 (Ang-1) is an established proangiogenic factor, capable of inducing vessel remodeling following injury through interactions with the cell-surface receptor that binds and is activated by the angiopoietins (Tie2), expressed at the vascular endothelial surface.¹⁷ Most important, in the bone marrow, the subsequent Ang-1/Tie2 complex signaling maintains the undifferentiated state of hematopoietic stem cells, precursors to bone marrow-derived endothelial progenitor cells, and is also upregulated in brain endothelial cells following cerebral ischemia.¹⁸⁻²⁰ Vascular endothelial growth factor released by local endothelium in response to injury and foreign matter is also shown to upregulate Ang-1 locally, and additionally, both factors are expressed by bone marrow stem cell subtypes.^{21,22} Most important, histopathologic analyses failed to reveal the presence of solitary thrombi in the absence of overlying smooth-muscle and endothelial cells.

Where tissue islands were observed, these were composed primarily of monocytes and macrophages. Notably, the antiplatelet regimen commonly used in animals has been premedication with aspirin and clopidogrel with maintenance of dual-antiplatelet therapy for 1 month following PED placement. With experimental aneurysms tending toward occlusion at around 2 months post-PED in the rabbit model, the duration of the dual antiplatelets may be somewhat short. Endothelialization, therefore, may, accordingly, be limited due to presence of organized thrombus and platelets along the device struts hindering effective neointima formation. In incompletely occluded aneurysms, patchy islands of endothelial cells are observed in rabbits after cessation of dual-antiplatelet therapy.⁵ The role of the clopidogrel response and pharmacogenomic profiles in the rabbit model is also another factor that perhaps warrants consideration and may influence endothelialization profiles.

Recently, the Pipeline Flex with Shield technology (Medtronic Neurovascular, Irvine, CA) a second-generation flow-diverter adaptation of the PED Flex incorporating a phosphorylcholine coating along the device struts to reduce thrombogenicity has been studied in pre-clinical models. Preliminary work in a pig aneurysm model has demonstrated significantly higher neointimal thickness with Shield-versus-non-surface-modified flow diverters and a trend toward earlier neointima formation, as determined by optical coherence tomography.¹² The surface modification of the Shield technology with phosphorylcholine polymers allows greater adsorption of fibronectin, a cell-cell adhesion molecule that is normally present on the subendothelium and is exposed following endothelial injury.²³ Fibronectin binds to sites on the modified stent and is able to stimulate local angiogenesis through integrin binding on endothelial cells.²⁴ Thus, the surface-modified Shield may (in theory) accelerate endothelialization, though this has yet to be clinically demonstrated.

Although this study provides some insight into the time course of endothelialization along flow-diverting stents in large-mammal animal models, the ability to draw further conclusions is hampered by the lack of aneurysm creation in this model. As indicated by computational fluid dynamics analyses, the vascular environment at the aneurysm neck is substantially different from that in the nascent arterial wall.²⁵ Secretion of matrix metalloproteinases and transforming growth factor β by fibroblasts and myofibroblasts, in particular, creates an inflammatory milieu that leads to a prothrombotic, activated vascular endothelium.

Conversely, Parameswaran et al²⁶ have recently shown the presence of cluster of differentiation 31 (CD31+) cells in aneurysmal segments from a rabbit experimental aneurysmal model, in the absence of any endovascular intervention. Most interesting, the authors demonstrated a temporal relationship in unintervened aneurysm endothelialization, with an initial endothelial denudation occurring up to 4–8 weeks following aneurysm creation—as evidenced by the qualitative reduction in whole-mount en face immunostaining for CD31+ cells—and subsequent repopulation by endothelial cells occurring at 12 weeks.

Perhaps some of the strongest evidence of flow-diverter endothelialization in animals has been provided by work done in a rabbit aneurysm model, using immunogold labelling scanning electron microscopy to visualize endothelial coverage in harvested arteries.¹¹ Using biotinylated cluster of differentiation 34 (CD34+) antibodies, a surface marker of endothelial progenitor cells, conjugated to streptavidin gold nanoparticles in an indirect immunolabeling assay, the study authors showed 87%–90% total tissue coverage along the flow diverters up to 60 days postimplantation. In contrast to prior work, these results suggest that circulating endothelial progenitor cells may provide a greater contribution to initial endothelialization than previously believed. However, this study is limited by the following: 1) use of custom-made flow diverters with different porosities compared with commercially available devices, and 2) the histology was performed on harvested arterial segments, and it is unclear whether the flow diverter was wholly contained within the harvested segment. Finally, lack of assaying for mature endothelial cells (CD31+ CD34–) early on may have overlooked any hyperacute contribu-

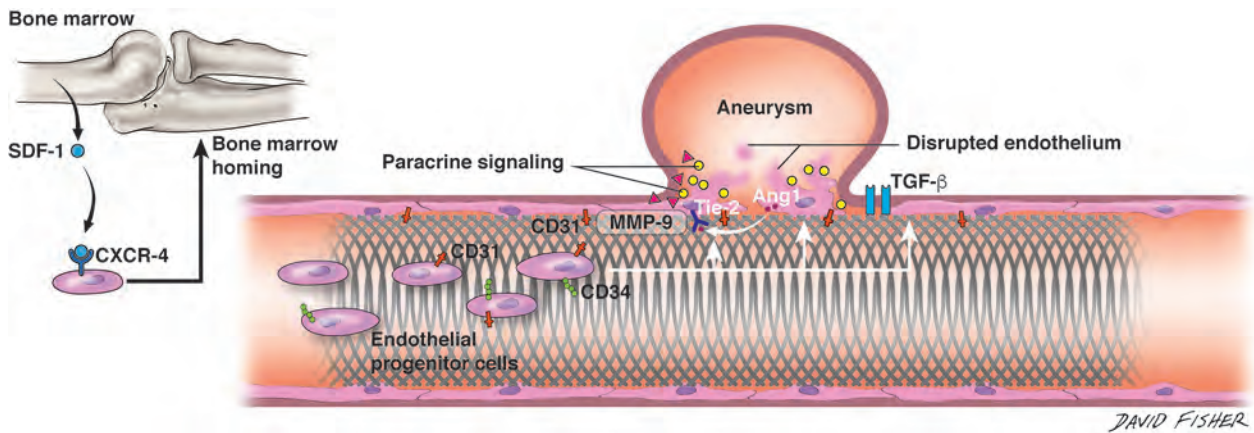


FIG 2. Endothelialization along the flow-diverting stent. Interplay among the flow-diverting stent, native vessel endothelium, molecular factors at aneurysm dome, and circulating endothelial progenitor cells is depicted in cartoon format. Stromal cell-derived factor 1 (SDF-1) released from the bone marrow binds to the C-X-C chemokine receptor type 4 (CXCR-4) receptor on circulating EPCs and directs homing of these cells to the bone marrow. At the site of flow-diverter placement, circulating EPCs (shown as CD31+ CD34+) are seen along device struts. At the aneurysm dome, several molecules, including matrix metalloproteinase-9 (MMP-9), act to stimulate vascular repair. Ang-1 is furthermore released from the disrupted endothelium, where its prorepair action is mediated by the Tie2 receptor expressed on the vascular endothelium. TGF- β indicates transforming growth factor β . Artist: David Fisher, Dept of Neurosurgery, University of Alabama-Birmingham. Published with permission.

tion to endothelialization by the action of locally derived endothelial cells (Fig 2).

Wall Apposition

In the coronary vasculature, incomplete stent apposition has been strongly associated with in-stent thrombosis.²⁷ Congruently, in a study of 41 elastase-induced saccular aneurysms in rabbits, aneurysms with histologically graded good wall apposition following PED treatment had higher angiographic occlusion rates than those with poor wall apposition treatment.¹³

Device Sizing, Pore Density, Metal Coverage: How Do They Affect Occlusion?

To achieve good proximal apposition, conventionally operators tend to choose “oversized” devices to attain adequate metal coverage at the ostium, thus enhancing aneurysmal occlusion. In comparison with the large repository of data that exists in the coronary literature regarding stent endothelialization, it would appear that both density and material influence subsequent endothelialization. However, it has been reported that neither pore density nor metal coverage has significant association with aneurysmal occlusion.²⁸ The study authors noted, expectedly, that ostial diameter was inversely correlated with occlusion.

Mechanisms of Aneurysm Occlusion: Human Data

Attempts at elucidating the interplay between thrombosis and endothelialization as pivotal mechanisms for aneurysmal exclusion in human patients have been restricted to a handful of studies with small sample sizes. The requisite for a histopathologic demonstration of the endothelial cell phenotype along the stent has thus largely limited investigations to postmortem analyses of harvested arterial segments.

The relative contribution of intra-aneurysmal thrombus formation, as a mechanism of aneurysm exclusion, has been supported by computational fluid dynamics analyses of post-PED-treated hemodynamics. Flow-diverter therapy results in reductions in aneurysmal inflow and wall shear stress that provide

an environment for promoting parent vessel remodeling.²⁹ Intracranial aneurysms treated with flow diversion with shorter times to occlusion have also been reported to exhibit different hemodynamic conditions than those with longer occlusion times, with a significantly lower mean aneurysmal velocity, inflow rate, and shear rate observed in this former group.¹⁶

Currently, meaningful histopathologic data of intracranial aneurysms treated with flow diverting stents remain scant. Studies to date in human patients have largely been confined to occlusion rates based on angiographic correlation. Dai et al³⁰ have reported the histopathologic results of a solitary case of a basilar tip aneurysm treated with the PED and demonstrated neointimal hyperplasia along the aneurysm neck interface. Further postmortem histopathologic analysis of 5 giant fusiform aneurysms treated with PEDs by Szikora et al,¹⁴ in 2015, failed to demonstrate any organized thrombus at 13 months posttreatment, despite angiographic evidence of complete occlusion. Indeed, portions of the PED within the parent artery were shown to be covered with neointima, even in the absence of detectable smooth-muscle cells. Most important, endothelialization was not observed in sections of the stent placed inside the aneurysm itself, suggesting that contact with a physiologically intact vascular wall may be necessary.¹⁴ However, in a study of 13 aneurysms that were initially treated with the PED but subsequently ruptured, intra-aneurysmal thrombus was identified in all cases.³¹ The authors hypothesized that persisting intraluminal thrombus, triggering autolytic vessel wall degradation, contributed to aneurysmal rupture. Of note, only 2 cases in this study were examined histopathologically, with both exhibiting unorganized thrombi (On-line Table).

Recent work by our group has demonstrated the angiographic appearance of separation of the parent vessel from aneurysms following PED placement, termed the “collar sign,” in incompletely occluded aneurysms.⁷ We have hypothesized that this represents endothelialization along the stent surface in juxtaposition to the aneurysmal neck. Paradoxical incomplete aneurysm occlusion following PED placement at 6-month follow-up may be po-

tentially explained via the existence of interspersed channels between regions of neointimal hyperplasia, still allowing blood flow, corroborated by a case report by Dai et al.³⁰ Similarly, endothelialization has been shown to be a driving factor in determining aneurysmal exclusion in intracranial aneurysms treated by coil embolization.³² However, histologic analyses suggest that organized thrombus formation is a greater driver of healing following coil deployment compared with flow diversion. Not only does the time course and natural history of healing appear to differ with coil treatment versus flow diversion, the cell mediators also appear to be different, with the fibroblasts and myofibroblasts playing larger roles.⁴ Histopathologic analysis of aneurysm tissue harvested postmortem from human patients treated with bare platinum coils has shown the presence of early neointima, along with collagen-rich tissue along device coils.³³ Following aneurysm treatment with bioactive coil deployment, further postmortem studies have failed to demonstrate the presence of endothelium within harvested tissue in the acute period.³⁴

Endothelial Cells on Stents: Where Do They Come From?

The origin of endothelial cell strut coverage observed following flow-diverter therapy remains unclear. Endothelial cells along the stent may either arise *de novo* through paracrine signaling from adjacent endothelial cells or via differentiation of peripherally circulating bone marrow–derived endothelial progenitor cells (EPCs). To date, studies have used an array of immunohistochemical techniques in animal models to demonstrate cell origin by assaying for CD34 and CD31 surface expression, adhesion molecules expressed at the cell surface of undifferentiated EPCs, and mature endothelial cells, respectively.

In the coronary vasculature, *in situ* endothelialization following stent placement is believed to occur through a combination of cell migration from surrounding endothelium in conjunction with the adhesion of circulating EPCs to stent struts under the influence of secreted angiogenic factors.³⁵ The stromal-derived factor 1/C-X-C chemokine receptor type 4 axis plays an important role in the migration of EPCs in the context of both angiogenesis and vascular repair.

Few studies have examined the source of endothelial coverage on flow-diverter stents used in intracranial aneurysms. The autologous transfusion of cultured fluorescently labeled EPCs in a rabbit model of flow diverter–treated aneurysms demonstrated the localization of fluorescence signal to the subendothelial space and device struts, though there was no statistically significant difference in the number of endothelial cells between transfused and nontransfused groups.¹⁰ The study of Kadirvel et al⁵ using a similar animal model, however, failed to demonstrate any CD34+ cells along device struts, suggesting that observed endothelial cells had not originated from circulating EPCs. The absence of cells derived from EPCs even at 8 weeks following aneurysmal occlusion is intriguing, though only accurately demonstrable through bone marrow transplantation experiments, which were not performed in the study. While comparisons are often made between coronary stents and even aortic grafts, the porosity and composition of the flow-diverting stent—and indeed cerebrovascular hemodynamics—arguably make extrapolation on underlying mechanisms difficult. Indeed, in the coronary vasculature, exper-

ience with stents coated with antibodies specific for blood-derived endothelial progenitor cells has shown increased stent endothelial coverage.³⁶ Notably, in the postmortem series of Szikora et al,¹⁴ no endothelial cells staining positive for CD34, a marker of circulating endothelial progenitor cells, were observable along the flow diverter; this finding was similarly corroborated in the rabbit aneurysm model.^{3,16}

In a recent follow-up study by Li et al,⁹ administration of a pharmacologic antagonist of the stromal cell–derived factor-1/CXC chemokine receptor type 4, AMD 3100, showed increased neointimal thickness along the flow-diverting stent in a rabbit aneurysm model. Moreover, quantitative polymerase chain reaction determination of messenger RNA in the neointimal cells growing along the stent surface showed increased Tie2 and vascular endothelial cadherin expression levels. However, the pharmacodynamics of AMD 3100 have not yet been clearly elucidated, and whether extramedullary C-X-C chemokine receptor type 4 expression may have contributed to the observed effect was not completely discussed. Despite early enthusiasm surrounding their potential, the putative role of EPCs, in the context of capture stents coated with an anti-CD34 antibody, has not yet been convincingly demonstrated in the coronary literature.

Limitations

Our study has several limitations. First, the heterogeneity of the studies and lack of standardized protocols hinder the scope of the analysis and make comparisons difficult. The small sample size of most available articles is an additional limitation. Most data are drawn from animal models, in which subtle anatomic and hemodynamic differences from human circulation could question the generalizability of such drawn conclusions. The included human studies were, moreover, small case series and reports, with the small sample size making it difficult to extrapolate and draw meaningful conclusions. Indeed, there was an overall paucity of data on the subject, despite the widespread use of the PED.

Future Directions

The vascular endothelium lies at a critical interface that, when exposed to subtle alterations in the hemodynamic state, becomes vasoactive. The intimate interaction between stent struts and endothelium thus makes this structure an ideal therapeutic target for optimizing aneurysm occlusion. Current translational research is aimed at designing low-profile stents that maximize endothelialization, while balancing the risk of in-stent stenosis and ensuing endothelial hyperplasia. While in-stent restenosis remains a persisting problem in the coronary vasculature, the incidence following flow-diverting stent placement is low. Thus, the endothelium may provide the source of a potential biomarker that, if identified, may predict successful aneurysm occlusion based on patient biology. In the coronary literature, several key molecules have drawn attention in recent years, including C-reactive protein, eosinophilic cationic protein, matrix metalloproteinases, and the lectins, though difficulties in providing quick, commercially available laboratory assays have slowed efforts.³⁷ An effective biomarker must have certain characteristics, including high specificity and sensitivity and cost-effectiveness. However, further mechanistic insight into the key signaling pathways

involved in flow diverter–induced aneurysm healing is warranted, to better identify therapeutic targets. Application of high-throughput “omics” analyses may allow an increased understanding of these cellular and molecular mechanisms.

CONCLUSIONS

Stent endothelial cell coverage is a predominant mechanism by which aneurysm healing occurs following flow-diverter treatment. Current data regarding the temporal relationship to flow-diverter placement has largely been derived from work in preclinical animal models. Whether these cells originate from adjacent endothelial cells or are the result of homing of circulating endothelial progenitor cells is equivocal. Further investigation into the underlying signaling mechanisms is required to identify potential therapeutic targets for optimizing aneurysm occlusion.

REFERENCES

1. Becske T, Kallmes DF, Saatci I, et al. **Pipeline for uncoilable or failed aneurysms: results from a multicenter clinical trial.** *Radiology* 2013; 267:858–68 CrossRef Medline
2. Kallmes DF, Hanel R, Lopes D, et al. **International retrospective study of the Pipeline embolization device: a multicenter aneurysm treatment study.** *AJNR Am J Neuroradiol* 2015;36:108–15 CrossRef Medline
3. Kallmes DF, Ding YH, Dai D, et al. **A new endoluminal, flow-disrupting device for treatment of saccular aneurysms.** *Stroke* 2007;38: 2346–52 CrossRef Medline
4. Brinjikji W, Kallmes DF, Kadirvel R. **Mechanisms of healing in coiled intracranial aneurysms: a review of the literature.** *AJNR Am J Neuroradiol* 2015;36:1216–22 CrossRef Medline
5. Kadirvel R, Ding YH, Dai D, et al. **Cellular mechanisms of aneurysm occlusion after treatment with a flow diverter.** *Radiology* 2014;270: 394–99 CrossRef Medline
6. Ding Y, Dai D, Kallmes DF, et al. **Preclinical testing of a novel thin film nitinol flow-diversion stent in a rabbit elastase aneurysm model.** *AJNR Am J Neuroradiol* 2016;37:497–501 CrossRef Medline
7. Griessenauer CJ, Gupta R, Shi S, et al. **Collar sign in incompletely occluded aneurysms after Pipeline embolization: evaluation with angiography and optical coherence tomography.** *AJNR Am J Neuroradiol* 2017;38:323–26 CrossRef Medline
8. Li Z, Zhao R, Fang X, et al. **Recombinant human SDF-1 α administration accelerates aneurysm neck reendothelialization in rabbit saccular aneurysms after flow diverter treatment.** *Acta Biochim Biophys Sin (Shanghai)* 2017;49:246–53 CrossRef Medline
9. Li Z, Zhao R, Fang X, et al. **AMD3100 accelerates reendothelialization of neointima in rabbit saccular aneurysm after flow diverter treatment.** *World Neurosurg* 2017;107:416–23 CrossRef Medline
10. Li ZF, Fang XG, Yang PF, et al. **Endothelial progenitor cells contribute to neointima formation in rabbit elastase-induced aneurysm after flow diverter treatment.** *CNS Neurosci Ther* 2013;19:352–57 CrossRef Medline
11. Marosfoi M, Langan ET, Strittmatter L, et al. **In situ tissue engineering: endothelial growth patterns as a function of flow diverter design.** *J Neurointerv Surg* 2017;9:994–98 CrossRef Medline
12. Matsuda Y, Chung J, Lopes DK. **Analysis of neointima development in flow diverters using optical coherence tomography imaging.** *J Neurointerv Surg* 2018;10:162–67 CrossRef Medline
13. Rouchaud A, Ramana C, Brinjikji W, et al. **Wall apposition is a key factor for aneurysm occlusion after flow diversion: a histologic evaluation in 41 rabbits.** *AJNR Am J Neuroradiol* 2016;37:2087–91 CrossRef Medline
14. Szikora I, Turányi E, Marosfoi M. **Evolution of flow-diverter endothelialization and thrombus organization in giant fusiform aneurysms after flow diversion: a histopathologic study.** *AJNR Am J Neuroradiol* 2015;36:1716–20 CrossRef Medline
15. Cebral JR, Mut F, Raschi M, et al. **Analysis of hemodynamics and aneurysm occlusion after flow-diverting treatment in rabbit models.** *AJNR Am J Neuroradiol* 2014;35:1567–73 CrossRef Medline
16. Chung B, Mut F, Kadirvel R, et al. **Hemodynamic analysis of fast and slow aneurysm occlusions by flow diversion in rabbits.** *J Neurointerv Surg* 2015;7:931–35 CrossRef Medline
17. Koh GY. **Orchestral actions of angiotensin-1 in vascular regeneration.** *Trends Mol Med* 2013;19:31–39 CrossRef Medline
18. Brindle NP, Saharinen P, Alitalo K. **Signaling and functions of angiotensin-1 in vascular protection.** *Circ Res* 2006;98:1014–23 CrossRef Medline
19. Pang D, Wang L, Dong J, et al. **Integrin $\alpha 5 \beta 1$ -Ang-1/Tie2 receptor cross-talk regulates brain endothelial cell responses following cerebral ischemia.** *Experimental & Molecular Medicine* 2018;50:117 CrossRef
20. Fukuhara S, Sako K, Minami T, et al. **Differential function of Tie2 at cell-cell contacts and cell-substratum contacts regulated by angiotensin-1.** *Nat Cell Biol* 2008;10:513–26 CrossRef Medline
21. Hattori K, Dias S, Heissig B, et al. **Vascular endothelial growth factor and angiotensin-1 stimulate postnatal hematopoiesis by recruitment of vasculogenic and hematopoietic stem cells.** *J Exp Med* 2001; 193:1005–14 CrossRef Medline
22. Benest AV, Salmon AH, Wang W, et al. **VEGF and angiotensin-1 stimulate different angiogenic phenotypes that combine to enhance functional neovascularization in adult tissue.** *Microcirculation* 2006;13:423–37 CrossRef Medline
23. Chin-Queue SL, Hsu SH, Nguyen-Ehrenreich KL, et al. **Endothelial cell recovery, acute thrombogenicity, and monocyte adhesion and activation on fluorinated copolymer and phosphorylcholine polymer stent coatings.** *Biomaterials* 2010;31:648–57 CrossRef Medline
24. Cseh B, Fernandez-Sauze S, Grall D, et al. **Autocrine fibronectin directs matrix assembly and crosstalk between cell-matrix and cell-cell adhesion in vascular endothelial cells.** *J Cell Sci* 2010;123(Pt 22): 3989–99 CrossRef Medline
25. Cebral JR, Mut F, Raschi M, et al. **Aneurysm rupture following treatment with flow-diverting stents: computational hemodynamics analysis of treatment.** *AJNR Am J Neuroradiol* 2011;32:27–33 CrossRef Medline
26. Parameswaran PK, Dai D, Ding YH, et al. **Assessment of endothelialization of aneurysm wall over time in a rabbit model through CD31 scoring.** *JNIS* 2018;10:888–91
27. Cook S, Wenaweser P, Togni M, et al. **Incomplete stent apposition and very late stent thrombosis after drug-eluting stent implantation.** *Circulation* 2007;115:2426–34 CrossRef Medline
28. Hodis S, Ding YH, Dai D, et al. **Relationship between aneurysm occlusion and flow diverting device oversizing in a rabbit model.** *J Neurointerv Surg* 2016;8:94–98 CrossRef Medline
29. Larrabide I, Aguilar ML, Morales HG, et al. **Intra-aneurysmal pressure and flow changes induced by flow diverters: relation to aneurysm size and shape.** *AJNR Am J Neuroradiol* 2013;34:816–22 CrossRef Medline
30. Dai D, Ding YH, Kelly M, et al. **Histopathological findings following Pipeline embolization in a human cerebral aneurysm at the basilar tip.** *Interv Neuroradiol* 2016;22:153–57 CrossRef Medline
31. Kulcsár Z, Houdart E, Bonafé A, et al. **Intra-aneurysmal thrombosis as a possible cause of delayed aneurysm rupture after flow-diversion treatment.** *AJNR Am J Neuroradiol* 2011;32:20–25 CrossRef Medline
32. Pandey AS, San Antonio JD, Addya S, et al. **Mechanisms of endothelial cell attachment, proliferation, and differentiation on 4 types of platinum-based endovascular coils.** *World Neurosurg* 2014;82:684–95 CrossRef Medline
33. Bavinszki G, Talazoglu V, Killer M, et al. **Gross and microscopic histopathological findings in aneurysms of the human brain treated with Guglielmi detachable coils.** *J Neurosurg* 1999;91:284–93 Medline
34. Szikora I, Seifert P, Hanzely Z, et al. **Histopathologic evaluation of**

- aneurysms treated with Guglielmi detachable coils or matrix detachable microcoils. *AJNR Am J Neuroradiol* 2006;27:283–88
35. Werner N, Kosiol S, Schiegl T, et al. **Circulating endothelial progenitor cells and cardiovascular outcomes.** *N Engl J Med* 2005;353:999–1007 CrossRef Medline
36. den Dekker WK, Houtgraaf JH, Onuma Y, et al. **Final results of the HEALING IIB trial to evaluate a bio-engineered CD34 antibody coated stent (GenousStent) designed to promote vascular healing by capture of circulating endothelial progenitor cells in CAD patients.** *Atherosclerosis* 2011;219:245–52 CrossRef Medline
37. Niccoli G, Montone RA, Ferrante G, et al. **The evolving role of inflammatory biomarkers in risk assessment after stent implantation.** *J Am Coll Cardiol* 2010;23 56:1783–93 CrossRef Medline

High-Definition Zoom Mode, a High-Resolution X-Ray Microscope for Neurointerventional Treatment Procedures: A Blinded-Rater Clinical-Utility Study

S.V. Setlur Nagesh, V. Fennel, J. Krebs, C. Ionita, J. Davies, D.R. Bednarek, M. Mokin, A.H. Siddiqui, and S. Rudin



ABSTRACT

BACKGROUND AND PURPOSE: Quality of visualization of treatment devices during critical stages of endovascular interventions, can directly impact their safety and efficacy. Our aim was to compare the visualization of neurointerventional procedures and treatment devices using a 194- μm pixel flat panel detector mode and a 76- μm pixel complementary metal oxide semiconductor detector mode (high definition) of a new-generation x-ray detector system using a blinded-rater study.

MATERIALS AND METHODS: Deployment of flow-diversion devices for the treatment of internal carotid artery aneurysms was performed under flat panel detector and high-definition-mode image guidance in a neurointerventional phantom simulating patient cranium and tissue attenuation, embedded with 3D-printed intracranial vascular models, each with an aneurysm in the ICA segment. Image-sequence pairs of device deployments for each detector mode, under similar exposure and FOV conditions, were evaluated by 2 blinded experienced neurointerventionalists who independently selected their preferred image on the basis of visualization of anatomic features, image noise, and treatment device. They rated their selection as either similar, better, much better, or substantially better than the other choice. Inter- and intrarater agreement was calculated and categorized as poor, moderate, and good.

RESULTS: Both raters demonstrating good inter- and intrarater agreement selected high-definition-mode images with a frequency of at least 95% each and, on average, rated the high-definition images as much better than flat panel detector images with a frequency of 73% from a total of 60 image pairs.

CONCLUSIONS: Due to their higher resolution, high-definition-mode images are sharper and visually preferred compared with the flat panel detector images. The improved imaging provided by the high-definition mode can potentially provide an advantage during neurointerventional procedures.

ABBREVIATIONS: DA = digital angiography; FPD = flat panel detector; HiDef = high definition; PED = Pipeline Embolization Device; RP = reference point

The technologic advances in neuroendovascular devices have led to fluoroscopically guided endovascular treatment of intracranial aneurysms becoming the preferred treatment. The constantly evolving design of stents and coils, and recent de-

velopment of new technologies such as flow diversion and intrasaccular and bifurcation devices now offer neurointerventionalists a variety of treatment options. However, the commercial x-ray imaging detector technology used during neuroendovascular interventions has not kept up with the increased requirements of image resolution.

The flat panel detector (FPD) used in most angiographic and fluoroscopy suites consists of an array of square pixels based on thin-film transistor technology, with sizes varying from 140 to 200 μm .¹ During the most critical steps of aneurysm treatment, such as deploying or repositioning a stent or flow-diversion devices or manipulating the microcatheter within a coil mass to achieve op-

Received August 21, 2018; accepted after revision November 12.

From the Canon (formerly Toshiba) Stroke and Vascular Research Center (S.V.S.N., J.K., C.I., D.R.B., A.H.S., S.R.), and Departments of Biomedical Engineering (C.I., S.R.), Mechanical and Aerospace Engineering (S.R.), and Electrical Engineering (S.R.), University at Buffalo, State University of New York; Buffalo, New York; Department of Neurosurgery (V.F., J.D.), Gates Vascular Institute at Kaleida Health, Buffalo, New York; Departments of Neurosurgery (S.V.S.N., V.F., C.I., J.D., D.R.B., A.H.S.), Bioinformatics (J.D.), and Radiology (D.R.B., A.H.S., S.R.), Jacobs School of Medicine and Biomedical Sciences, University at Buffalo, State University of New York, Buffalo, New York; Jacobs Institute (J.D., A.H.S.), Buffalo, New York; and Department of Neurosurgery and Brain Repair (M.M.), University of South Florida, Tampa, Florida.

This work was supported by National Institutes of Health grant No. R01EB2873 and equipment support from Canon Medical Systems.

Please address correspondence to Swetadri Vasan Setlur Nagesh, MS, PhD, Canon Stroke and Vascular Research Center, University at Buffalo, 875 Ellicott St, Buffalo, NY 14203; e-mail: ss438@buffalo.edu

Indicates open access to non-subscribers at www.ajnr.org

Indicates article with supplemental on-line table and appendix.

Indicates article with supplemental on-line photos.

Indicates article with supplemental on-line video.

<http://dx.doi.org/10.3174/ajnr.A5922>

timal coil structure, it is critical to have high-quality images of the treatment area to guide device deployment. To provide such improved imaging, a new detector system (On-line Fig 1) consisting of the conventional large-FOV regular-resolution FPD mode (194- μm pixel size at the detector) and a smaller FOV high-resolution complementary metal oxide semiconductor high definition (HiDef) mode (76- μm pixel size at the detector) has been developed.

Early experience with the HiDef mode in imaging a standard line-pair phantom (On-line Fig 2) demonstrated improved spatial resolution over the standard FPD mode, with line pairs as high as 5.6 line pairs/mm distinctly visualized without loss in information in the HiDef images. However, the objective evaluation of how this new technology with improved performance affects the decision-making during neurointerventional procedures and, specifically, aneurysm embolization with the flow-diversion approach has not been performed. In this study, we present a blinded-rater study comparing the visualization of neurointerventional procedures and treatment devices using the 194- μm pixel FPD and 76- μm pixel HiDef mode of the new-generation x-ray detector system.

METHODS AND MATERIALS

Detector Description

The new x-ray imaging system has both a regular-resolution 194- μm pixel FPD mode and a high-resolution 76- μm pixel HiDef mode in 1 single unit. The FPD mode has larger FOVs, varying from 30×30 cm to 15×15 cm. Smaller FOVs up to 6.3×6.3 cm are available using digital interpolation. In the high-resolution HiDef mode, only smaller FOVs are available, ranging from 8.9×8.9 to 3.8×3.8 cm.

At any given point in time, 1 of the 2 modes is active, and when needed, the image acquisition between the 2 modes can be quickly changed using an FOV switch, without adding any additional delay to the procedure.

Intervention Model Description

An x-ray image is formed by the differential attenuation of the x-ray beam within a patient's body. During an endovascular neurointervention, the major sources of x-ray attenuation are the human bone (skull) and the soft tissue (including the human cerebral cortex and skin tissue). To simulate this, a neurointervention phantom was developed by placing a human skull (simulating bone attenuation) in-between a total stack of five 1-inch acrylic layers (simulating tissue attenuation²). To simulate the cerebral circulation, we embedded a 3D-printed model of patient-based intracranial vasculature, consisting of the internal carotid artery segment, the middle cerebral artery, and the anterior cerebral artery segments closely representing the human circle of Willis region, inside the skull and connected it to a pulsatile flow loop, with water used as circulation fluid. The process of fabricating 3D-printed phantoms was previously described in Ionita et al³ and Russ et al.⁴ The neurointervention phantom setup and its attenuation comparison with 3 commercially available anthropomorphic phantoms are presented in the On-line Appendix.

Neurointerventional Treatment Simulation

For this study, endovascular treatment of intracranial aneurysms of the internal carotid artery with the flow-diversion approach

using the Pipeline Embolization Device (PED; Covidien, Irvine, California) was simulated.⁵ Five different 3D-printed models with aneurysms in the ICA segment were fabricated and treated with a 4.75×30 mm PED. Due to limitations in the availability of the PED and its high cost, we only partially deployed the device to approximately 50% of its length and then resheathed and reused it for subsequent simulated interventions.

Image Acquisition and Display Setup

The main purpose of the study was to qualitatively evaluate the simulated clinical image sequences of PED deployment acquired using both FPD and HiDef modes of the new detector system. The image acquisitions were divided into the following 2 categories:

Deployment Image Sequences. First, for a particular aneurysm geometry, a PED was partially deployed using a background (bone) subtracted roadmap and an unsubtracted (native) image guidance from 1 of the 2 detector modes (FPD or HiDef). The stent was then resheathed and repositioned to its initial location before deployment. Then, the PED was partially redeployed under road-mapping and native image guidance from the other detector mode. During clinical neurointerventions, the roadmap images and the native images complement each other and are displayed and viewed simultaneously. For comparison, the roadmap images along with the corresponding native images from 1 detector mode form a deployment image sequence.

For the same aneurysm geometry, the 2 deployment imaging sequences, 1 from each detector mode, are considered an image sequence pair.

For a total of 5 aneurysm geometries with 2 C-arm views per geometry (anteroposterior [frontal] and posteroanterior [lateral]), a total of 10 image-sequence pairs under fluoroscopy and 10 image pairs under digital angiography (DA) exposure conditions were obtained. On-line Fig 4 shows frames obtained from a sample image sequence pair acquired under fluoroscopic conditions, and On-line Fig 5 shows frames obtained from a sample image sequence pair acquired under DA conditions. On-line videos 1 and 2 show the PED deployment sequence acquired using HiDef and FPD modes, respectively, for the anatomy and exposure conditions presented in On-line Fig 5.

DSA Image Sequences. For a particular aneurysm geometry, with the PED partially deployed, DSA image sequences using the FPD and HiDef modes each were acquired. 80% iodine and 20% water were used as a contrast agent. Similar to the deployment image sequences, the bone-subtracted image along with the unsubtracted native image from 1 detector formed a DSA image sequence. For the same aneurysm geometry, the 2 DSA image sequences, 1 from each detector, were considered an image-sequence pair.

Ten DSA image sequence pairs were obtained. Similar to On-line Fig 5 (and On-line Fig 4), Fig 1 shows a sample image-sequence pair acquired under DSA conditions.

A 0.3-mm focal spot size and an average geometric magnification of 1.2 were maintained for all the acquisitions. Within an image-sequence pair, the distance between the neurointervention phantom and the detector panel and the view angle (C-arm angle) were kept the same. The exposure conditions as determined by the

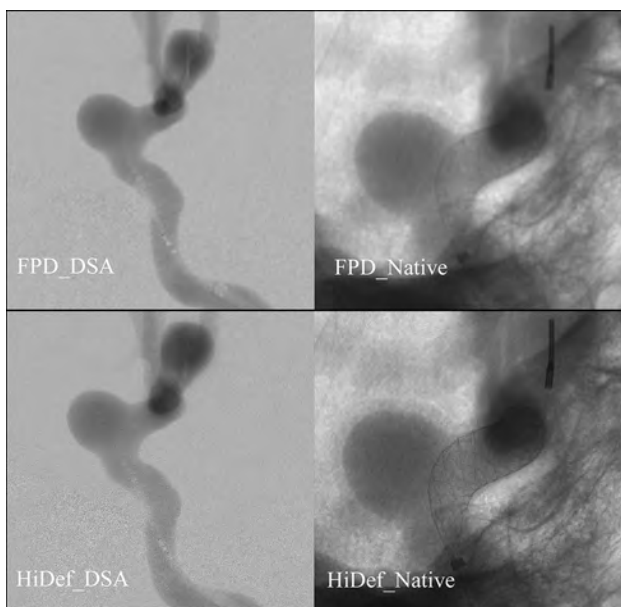


FIG 1. Sample single-image sequence pair acquired under DSA exposures. The average RP air kerma per frame for DSA was calculated to be 1.40 mGy for the FPD mode and 1.34 mGy for the HiDef mode. Due to more quanta reaching the detector, the image quality is improved for both the FPD and HiDef modes compared with On-line Fig 4 and On-line Fig 5. The amount of information available in the HiDef native image is higher than in the FPD native image. For the reader to appreciate the difference between HiDef and FPD images, especially the visualization of the stent, the native images are zoomed-in to the ROI showing the stent area.

automatic exposure control of the imaging system were also kept similar.

For each acquisition, by dividing the cumulative reference-point (RP) air kerma (reported by the angiography machine at a reference point 15 cm from the isocenter toward the x-ray source to approximate the patient entrance air kerma) by the number of frames in the acquisition, we calculated the reference point air kerma per frame. The average of the RP air kerma for both FPD and HiDef modes for fluoroscopy, DA, and DSA acquisitions is reported in the beginning of the Results section.

Image-Quality Evaluation

For rater evaluation, 30 image sequence pairs were acquired, 10 in fluoroscopy, 10 in DA, and 10 in DSA. With each image-sequence pair repeated twice, 60 image-sequence pairs were presented to 2 experienced practicing neurointerventionalist raters. The raters were asked to select their preferred image sequence within a pair based on a comparison of the following 2 criteria—C1: overall image preference in terms of visualization of anatomic features and image noise and C2: the visual quality of the stent.

Different raters can perceive the difference between the images within a pair differently; thus, the raters were asked to score (rater-assigned scores) their selected image as either similar, better, much better, or substantially better than the other image. By means of this rater-assigned score, the detector from which the selected image was acquired was recorded as the preferred detector (detector-preference scores).

Image Display

Two display monitors with the same pixel resolution and similar brightness and contrast levels were used to display the image pairs. For a fair and unbiased comparison, the display monitor stations showing the HiDef and FPD images within an image sequence pair were not the same but were randomized for all the pairs and not made known to the raters.

The detector FOV between the FPD and HiDef modes was kept comparable, 6.3×6.3 cm in the FPD mode and 5.8×5.8 cm in the HiDef mode. The display brightness and contrast between the 2 image sets were adjusted to be similar to avoid any bias. The raters were also free to choose and adjust the display brightness and contrast for each image pair independently. For a fair image comparison, the image processing was kept similar for both HiDef and FPD modes.

Statistical Analysis

For each of the criteria, histogram analysis was performed on the rater-assigned scores as well as the detector-preference score. Intrarater agreement for the rater-assigned scores and interrater agreement for the detector-preference scores for each of the criteria were determined using the binomial exact confidence interval test. Assessment of the degree of agreement was based on the 95% upper confidence values (0–0.49 = poor, 0.50–0.74 = moderate, 0.75–1.0 = good). To establish statistical significance between the FPD and HiDef modes, we conducted a 1-sample *t* test on all rater-assigned scores and the detector preference scores for all criteria. For each of the criteria and all the image pairs, an assumption that both raters would select similar image quality between the 2 detector modes within an image pair was used as the null hypothesis. A *P* value < .05 was considered statistically significant.

RESULTS

The average RP air kerma per frame for fluoroscopy was 0.02 mGy for the FPD mode and 0.03 mGy for the HiDef mode; for DA, it was 0.16 mGy for the FPD mode and 0.17 mGy for the HiDef mode; and for DSA, it was 1.40 mGy for the FPD mode and 1.34 mGy for the HiDef mode.

The histogram distribution of the rater-assigned scores for the 2 criteria for fluoroscopy, DA, and DSA exposures is presented in Fig 2. For fluoroscopic exposures, rater A selected the HiDef images as better than FPD images with a frequency of at least 60% for both criteria, whereas rater B selected the HiDef images as much better than FPD images with a frequency of 50% for both criteria. For DA and DSA exposures, both raters selected the HiDef images as much better than FPD images with an average frequency of 90%.

Combining the rater-assigned scores for both criteria and all 3 exposure modes, both raters, on average, rated the HiDef images as much better than FPD images with a frequency of 73% for both criteria.

The distribution for the detector-preference scores is shown in Fig 3. In all 3 exposure modes for both criteria, both raters preferred HiDef images over FPD images with a frequency of at least 95%.

The results from the binomial exact CI test and 1-sample *t* test are summarized in Tables 1 and 2. For all criteria, both raters had

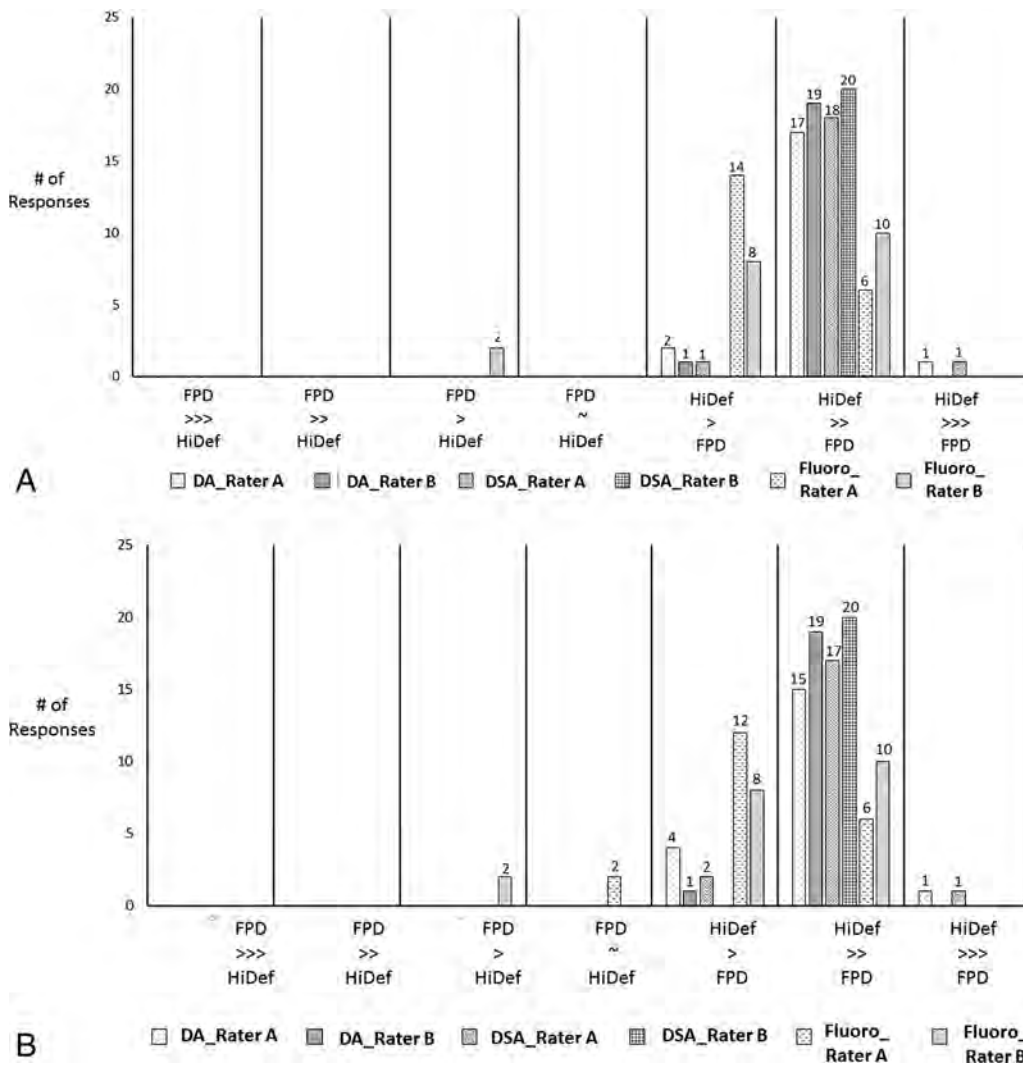


FIG 2. Histogram distribution of rater-assigned scores (raters A and B) for all 5 aneurysm geometries, *A*, The first criterion: overall image preference in terms of visualization of anatomic features and image noise. *B*, The second criterion: visual quality of the stent for all 3 exposure modes: fluoroscopy (Fluoro), DA, and DSA. The raters were asked to score their image preference as either similar (~), better (>), much better (>>), or substantially better (>>>) than the other image.

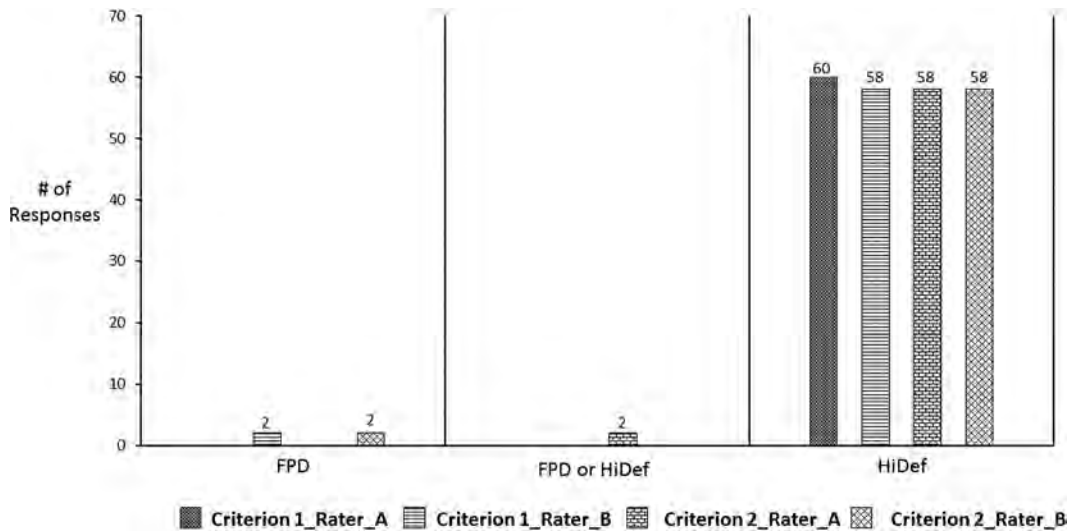


FIG 3. Distribution of detector preference scores for 60 image sequence pairs (all 5 aneurysm geometries) for both criteria. On the basis of the rater-assigned scores (Fig 2), the detector from which the selected image was acquired was recorded as the preferred detector.

Table 1: Statistical test results—binomial exact CI test for intrarater agreement^a

Criteria	Rater-Assigned Scores							
	Intrarater Agreement						1-Sample T Test	
	Rater 1			Rater 2			Rater 1 P Value	Rater 2 P Value
P(agr)	95% LC	95% UC	P(agr)	95% LC	95% UC			
C1	.7	0.50	0.85	.83	0.65	0.94	<.001	<.001
C2	.56	0.37	0.75	.83	0.65	0.94	<.001	<.001

Note:—P(agr) indicates probability of agreement; LC, lower confidence; UC, upper confidence; C1, overall image preference in terms of visualization of anatomic features and image noise; C2, the visual quality of stent.

^a One-sample t test for analysis of the scores.

Table 2: Statistical test results—binomial exact CI test for interrater agreement^a

Criteria	Detector-Preference Scores				
	Interrater Agreement			1-Sample T Test	
	P(agr)	95% LC	95% UC	Rater 1 P Value	Rater 2 P Value
C1	.96	0.82	0.99	<.001	<.001
C2	.9	0.73	0.97	<.001	<.001

Note:—P(agr) indicates probability of agreement; LC, lower confidence; UC, upper confidence; C1, overall image preference in terms of visualization of anatomic features and image noise; C2, the visual quality of stent.

^a One-sample t test for analysis of the scores.

good intrarater agreement and were consistent. From the detector-preference scores for each criterion, good interrater agreement was determined, further substantiating the results from Fig 3 that both raters generally preferred the HiDef images over the FPD images.

From the 1-sample *t* test for all rater-assigned scores and detector-preference scores for both criteria, a *P* value < .001 was calculated for both raters. This indicates that the null hypothesis assumption that the image quality of HiDef and FPD images is similar is wrong and statistically they are significantly different.

DISCUSSION

The improvement in visualization due to use of a surgical microscope was one of the key reasons for its adoption during open craniotomies for treatment of vascular diseases such as brain aneurysms in the late 1960s and 1970s.⁶ Similarly, the optimization of laparoscopic visualization has ushered in the standardization of minimalist approaches compared with major open laparotomy procedures during general urologic and gynecologic surgery.⁷ Likewise, enhanced visualization during critical aspects of endovascular interventions, such as during microcatheterization and stent or coil deployment, directly impacts the safety and efficacy of neurointerventional procedures.

Previously, high-resolution fluoroscopy systems based on charge-couple devices⁸ and complementary metal oxide semiconductors⁹ were developed to provide improved imaging of the treatment area compared with existing FPD systems during neurovascular interventions. Successful use of the high-resolution fluoroscopy systems based on charge-couple devices during 2 clinical neurointerventional studies was reported.^{10,11} In both cases, high-resolution fluoroscopy provided improved visualization of the endovascular devices. Another study¹² reported that the high-resolution fluoroscopy was particularly beneficial during the treatment of partially thrombosed aneurysms. However, the high-resolution fluoroscopy detector systems were separate

from the FPD panels and were mounted on a mechanical changer. Whenever high-resolution imaging was needed, the high-resolution fluoroscopy was deployed into the active FOV using the changer system.

In the new detector system presented in this work, the higher resolution HiDef mode and the regular-resolution mode are available in 1 single unit and can be selected by an FOV switch, which gives it a distinct advantage over the high-resolution fluoroscopy systems. From On-line Fig 2, it can be seen that due to smaller pixel size, the high-resolution HiDef mode has a distinct advantage over the regular-resolution FPD mode and up to 5.6 line pairs/mm can be easily visualized. The aim of our study was to determine whether this added advantage provided by the HiDef mode can actually improve imaging of a treatment device such as a PED, a flow-diverter stent used for the treatment of intracranial aneurysms. When deployed, the PED induces a modification of blood flow within and around the inflow zone of an aneurysm that leads to gradual intra-aneurysmal thrombosis and subsequent atrophy, while preserving flow in the parent vessel and perforating branches.¹³

The subjective assessment of 2 comparable clinical images using image-quality rating scores is a standard practice and has been previously used to compare images from 2 different detectors such as comparing computed radiography with screen films¹⁴ and in comparing selenium-based digital radiography with conventional film-screen (100-speed) radiography.¹⁵

From the detector-preference score distribution shown in Fig 3, both raters in good agreement (interrater agreement in Tables 1 and 2) preferred the HiDef images over the FPD images for both criteria. For both criteria, from the rater-assigned scores shown in Fig 2, it can be seen that in fluoroscopic exposures, both interventionalists, on average, rated the HiDef image quality as better compared with the FPD quality, whereas in DA and DSA exposures, they rated the HiDef image quality as much better compared with the FPD quality. This is consistent because the image SNR in DA is higher than in fluoroscopy, and in DSA, it is higher than in DA due to increased quanta reaching the detector. During an intervention, it is critical for interventionalists to have optimal visualization of devices such as stents and flow diverters to ascertain their placement along the course of the vessel, ensure proper deployment and wall apposition of the treatment device, and recognize impending kinking or twisting, which can result in unexpected complications.¹⁶

From On-line Fig 4 acquired in fluoroscopy-exposure conditions, it can be seen that due to higher spatial resolution, visualization of stent and other anatomic features is better in the HiDef mode compared with the regular FPD mode. When we compared

On-line Fig 5 when the PED is deployed with DA with On-line Fig 4 for the same aneurysm geometry, it can be seen that due to higher quanta reaching the detector, while the image quality is improved in both FPD and HiDef images, the amount of information available in HiDef images, especially the visualization of the stent structure including the individual struts, is greater compared with the corresponding FPD image. Such information can be critical during the intervention because devices such as the PED place additional constraints on imaging technology because manipulations during deployment induce changes in the structure of the PED, which may affect treatment outcomes. For instance, with the information provided in HiDef images in On-line Fig 5, one could selectively compress the device to preferentially increase its metal coverage over the aneurysm ostia to induce higher mesh attenuation, aiding occlusion without inducing compression over side branches and perforators, preventing the risk of branch occlusion and postprocedural stroke.^{17,18} In the DSA exposure mode shown in Fig 1, the image quality in both FPD and HiDef images is further improved due to higher quanta; however, the information available in HiDef images is much higher than in the FPD images. During the deployment process, a DSA with contrast injection is performed to visualize the flow in the aneurysm and proximal and distal vasculature. With the information in HiDef images, one could visualize the flow not only inside the stent but also around the stent walls in places with poor stent-to-vessel wall apposition.

Furthermore, from the *P* values presented in Tables 1 and 2 for both the rater-assigned and detector-preference scores, it can be deduced that for all criteria, both raters concluded that PED images from the HiDef mode were significantly improved over those from the FPD mode.

Intracranial arteries range from 5 to <1 mm in diameter; and because the treatment devices are continually evolving to enable greater accuracy of treatment in such areas, the imaging technology should also evolve. Flow-diversion devices are being increasingly used for distally located aneurysms with smaller diameter parent arteries.^{19,20} With the conventional FPD imaging systems, the images can be digitally interpolated to provide a zoomed-in view of the treatment area and devices when needed. However, the resulting image might still have poor resolution and lower image quality. In the new detector system, when a zoomed-in view is needed, the high-resolution HiDef mode can be turned on electronically. The results of the study show that the HiDef-mode images are significantly improved over the zoomed-in FPD mode. This improvement gives the new detector system a unique advantage over the conventional FPD systems.

The purpose of the study was to evaluate x-ray image quality of the new detector system during neurointerventional treatment. To that extent, the use of a 3D “patient-specific” printed model with appropriate x-ray attenuation simulation can offer a viable alternative to preclinical animal studies. With the advancement in 3D printing technology, an accurate replica of the human vasculature can be easily reproduced. Use of animal studies could provide more information about the actual treatment procedure, such as the biologic interaction of the treatment device and the blood vessels, but this is not within the scope of this work. In this study, we assumed that the treatment would be performed with

the patient under general anesthesia, similar to treatment in the study of Nelson et al,⁵ thus minimizing patient motion. In both FPD and HiDef modes at high image magnifications, significant patient motion could affect the visibility in background subtracted images due to mask misregistration. Studies involving other neurointerventional treatment devices such as coils, high-porosity stents, and balloons are currently being performed.

CONCLUSIONS

The HiDef mode of the new detector system is equivalent to a microscope that can be used during critical stages of the intervention when superior imaging over the magnified view of the treatment area and devices is required. Due to the high resolution of the HiDef mode, the images are sharper and visually preferred compared with the lower resolution images of the FPD. This is supported by the results of the comparative study presented. Neurointerventions may be performed with a greater degree of accuracy using the improved imaging provided by the new detector system.

Disclosures: Ciprian Ionita—*RELATED: Grant:* Canon Medical Systems*; *UNRELATED: Consultancy:* Jacobs Institute; *Employment:* University at Buffalo, *Comments:* Assistant Professor; *Grants/Grants Pending:* National Institutes of Health*. Daniel R. Bednarek—*UNRELATED: Grants/Grants Pending:* Canon Medical Systems*; *Royalties:* Canon Medical Systems, *Comments:* dose-tracking system licensed through the University at Buffalo Technology Transfer Office.* Maxim Mokin—*UNRELATED: Consultancy:* Penumbra, Cerebrotech Medical Systems, Canon Medical Systems. Adnan H. Siddiqui—*UNRELATED: Consultancy:* Amnis Therapeutics, Boston Scientific, Canon Medical Systems, Cerebrotech Medical Systems, Cerenovus, Claret Medical, Corindus, EndoStream Medical, Guidepoint Global, Imperative Care, Integra, Medtronic, MicroVention, Northwest University Data and Safety Monitoring Board Chair for the HEAT trial, Penumbra, Rapid Medical, Rebound Therapeutics, Serenity Medical Evaluations, Silk Road Medical, StimMed, Stryker, Three Rivers Medical, VasSol, W.L. Gore & Associates; *Employment:* Jacobs Institute, University at Buffalo Neurosurgery; *Stock/Stock Options:* Amnis Therapeutics, Apama Medical, Blinktbi, Buffalo Technology Partners, Cardinal Health, Cerebrotech Medical Systems, Claret Medical, Cognition Medical, EndoStream Medical, Imperative Care, International Medical Distribution Partners, Rebound Therapeutics, Rist Neurovascular, Serenity Medical, Silk Road Medical, StimMed, Synchron, Three Rivers Medical, Viseon Spine; *Other:* Cerenovus, LARGE trial and ARISE II trial; Medtronic, SWIFT PRIME and SWIFT DIRECT trials; MicroVention, FRED trial and CONFIDENCE study, MUSC POSITIVE trial; Penumbra, Separator 3D Trial, COMPASS trial, INVEST trial, *Comments:* National Principal Investigator/Steering Committees. Stephen Rudin—*RELATED: Grant:* Canon Medical Systems, *Comments:* Also, previous work was supported by a grant from National Institutes of Health to the University at Buffalo (Toshiba Medical is now Canon Medical)*; *UNRELATED: Patents (Planned, Pending or Issued):* Canon Medical Systems*; *Royalties:* Canon Medical Systems, *Comments:* coauthor on Dose-Tracking System licensed to Canon by the University at Buffalo.* Jason Davies—*RELATED: Grant:* University at Buffalo Clinical and Translational Science Award (CTSA) UL1TR001412 KL2*; *UNRELATED: Stock/Stock Options:* RIST NEUROVASCULAR, INC. *Money paid to the institution.

REFERENCES

- Nickoloff EL. AAPM/RSNA physics tutorial for residents: physics of flat-panel fluoroscopy systems—survey of modern fluoroscopy imaging: flat-panel detectors versus image intensifiers and more. *Radiographics* 2011;31:591–602 CrossRef Medline
- Schropp L, Alyass NS, Wenzel A, et al. Validity of wax and acrylic as soft-tissue simulation materials used in vitro radiographic studies. *Dentomaxillofac Radiol* 2012;41:686–90 CrossRef Medline
- Ionita CN, Mokin M, Varble N, et al. Challenges and limitations of patient-specific vascular phantom fabrication using 3D Polyjet printing. *Proc SPIE Int Soc Opt Eng* 2014;9038:90380M CrossRef Medline
- Russ M, O'Hara R, Setlur Nagesh SV, et al. Treatment planning for image-guided neuro-vascular interventions using patient-specific

- 3D printed phantoms.** *Proc SPIE Int Soc Opt Eng* 2015;9417 CrossRef Medline
5. Nelson PK, Lylyk P, Szikora I, et al. **The Pipeline Embolization Device for the intracranial treatment of aneurysms trial.** *AJNR Am J Neuroradiol* 2011;32:34–40 CrossRef Medline
 6. Uluc K, Kujoth GC, Baskaya MK. **Operating microscopes: past, present, and future.** *Neurosurg Focus* 2009;27:E4 Medline
 7. Rassweiler JJ, Teber D. **Advances in laparoscopic surgery in urology.** *Nat Rev Urol* 2016;13:387–99 CrossRef Medline
 8. Jain A, Bednarek DR, Ionita C, et al. **A theoretical and experimental evaluation of the microangiographic fluoroscope: a high-resolution region-of-interest x-ray imager.** *Med Phys* 2011;38:4112–26 CrossRef Medline
 9. Jain A, Bednarek DR, Rudin S. **Experimental and theoretical performance analysis for a CMOS-based high-resolution image detector.** *Proc SPIE Int Soc Opt Eng* 2014;9033:90333P CrossRef Medline
 10. Kan P, Yashar P, Ionita CN, et al. **Endovascular coil embolization of a very small ruptured aneurysm using a novel microangiographic technique: technical note.** *J Neurointerv Surg* 2013;5:e2 CrossRef Medline
 11. Binning MJ, Orion D, Yashar P, et al. **Use of the microangiographic fluoroscope for coiling of intracranial aneurysms.** *Neurosurgery* 2011;69:1131–38 CrossRef Medline
 12. Starke RM, Turk A, Ding D, et al. **Technology developments in endovascular treatment of intracranial aneurysms.** *J Neurointerv Surg* 2016;8:135–44 CrossRef Medline
 13. Eller JL, Dumont TM, Sorkin GC, et al. **The Pipeline embolization device for treatment of intracranial aneurysms.** *Expert Rev Med Devices* 2014;11:137–50 CrossRef Medline
 14. Swee RG, Gray JE, Beabout JW, et al. **Screen-film versus computed radiography imaging of the hand: a direct comparison.** *AJR Am J Roentgenol* 1997;168:539–42 CrossRef Medline
 15. Piraino DW, Davros WJ, Lieber M, et al. **Selenium-based digital radiography versus conventional film-screen radiography of the hands and feet: a subjective comparison.** *AJR Am J Roentgenol* 1999;172:177–84 CrossRef Medline
 16. Mitchell B, Jou LD, Mawad M. **Retrieval of distorted Pipeline embolic device using snare-loop.** *J Vasc Interv Neurol* 2014;7:1–4 Medline
 17. Xiang J, Damiano RJ, Lin N, et al. **High-fidelity virtual stenting: modeling of flow diverter deployment for hemodynamic characterization of complex intracranial aneurysms.** *J Neurosurg* 2015;123:832–40 CrossRef Medline
 18. Shapiro M, Raz E, Becske T, et al. **Variable porosity of the Pipeline embolization device in straight and curved vessels: a guide for optimal deployment strategy.** *AJNR Am J Neuroradiol* 2014;35:727–33 CrossRef Medline
 19. Nossek E, Zumofen DW, Setton A, et al. **Treatment of distal anterior cerebral artery aneurysms with the Pipeline Embolization Device.** *J Clin Neurosci* 2017;35:133–38 CrossRef Medline
 20. Puri AS, Massari F, Asai T, et al. **Safety, efficacy, and short-term follow-up of the use of Pipeline Embolization Device in small (<2.5 mm) cerebral vessels for aneurysm treatment: single institution experience.** *Neuroradiology* 2016;58:267–75 CrossRef Medline

Percutaneous CT-Guided Skull Biopsy: Feasibility, Safety, and Diagnostic Yield

A. Tomasian, T.J. Hillen, and J.W. Jennings

ABSTRACT

BACKGROUND AND PURPOSE: Although percutaneous musculoskeletal biopsies are routinely performed in the axial and appendicular skeleton, there are no published data on the systematic evaluation of the feasibility, safety, and diagnostic accuracy of percutaneous skull biopsy. In certain clinical encounters such as patients with primary skull tumors or patients with known cancer and isolated skull lesions suspected of calvarial metastasis or synchronous primary tumor, percutaneous skull biopsy may be considered a viable option. The purpose of this study was to evaluate the feasibility, safety profile, and diagnostic yield of percutaneous CT-guided skull biopsy.

MATERIALS AND METHODS: Percutaneous CT-guided skull biopsy was performed in 14 patients. Patient demographics, cancer history, indication for initial imaging, imaging technique of diagnosis, skull tumor anatomic location, and final histologic diagnosis were documented. Preprocedural imaging of each skull lesion was reviewed to determine tumor size and characteristics. Procedural notes were reviewed to determine the total conscious sedation time or anesthesia time, type of biopsy needle, and the number and length of obtained core specimens. Procedure-related complications were also documented according to the Society of Interventional Radiology classification.

RESULTS: All CT-guided percutaneous skull biopsy procedures were performed as preoperatively planned and were technically successful. Procedures were performed with the patient under conscious sedation in 93% (13/14) of cases. Definitive histologic diagnosis was achieved in 86% (12/14) of cases. There were no acute or delayed procedure-related complications.

CONCLUSIONS: The results of this retrospective initial study suggest that percutaneous CT-guided skull biopsy is feasible with an excellent safety profile, affords a high diagnostic yield for histologic characterization, and may obviate more invasive open skull biopsies.

Skull lesions are uncommonly encountered in clinical practice and are often asymptomatic and discovered incidentally on routine imaging studies acquired for unrelated reasons. Calvarial tumors may also be identified during the work-up of localized symptoms such as pain and palpable masses or defects, as well as on staging studies of other diseases. Primary skull neoplasms comprise approximately 0.8% of all bone tumors, and although benign lesions are reported to be more common than malignant tumors, the exact prevalence of each has not been established.¹ Most calvarial lesions have no characteristic imaging features, and correlation of clinical data, particularly a history of cancer, with imaging findings may help direct the diagnostic and therapeutic

approach. Most clinical oncology protocols and treatment guidelines require that histologic specimens be obtained for proof of diagnosis, as well as genetic and/or molecular testing. Imaging-guided percutaneous biopsy of bone lesions has gained wide acceptance as the preferred approach in lieu of open biopsies due to its cost-effectiveness, better safety profile, and high diagnostic accuracy.²⁻⁶

Although percutaneous biopsies are routinely performed in the axial and appendicular skeleton, there are no published data on the systematic evaluation of the feasibility, safety, and diagnostic accuracy of percutaneous skull biopsy, in part, because there are commonly safer skeletal sites that may be targeted for tissue sampling, particularly in patients with cancer. However, in certain clinical encounters such as patients with primary skull tumors or patients with known cancer and isolated skull lesions suspected of calvarial metastasis or synchronous primary tumor, percutaneous skull biopsy may be considered a viable option.

The purpose of this study was to evaluate the feasibility, safety profile, and diagnostic yield of percutaneous CT-guided skull biopsy.

Received September 30, 2018; accepted after revision December 8.

From the Department of Radiology (A.T.), University of Southern California, Los Angeles, California; and Mallinckrodt Institute of Radiology (T.J.H., J.W.J.), St. Louis, Missouri.

Please address correspondence to Anderanik Tomasian, MD, Department of Radiology, University of Southern California, 1500 San Pablo St, Los Angeles, CA 90033; e-mail: tomasian.andy@gmail.com

<http://dx.doi.org/10.3174/ajnr.A5949>

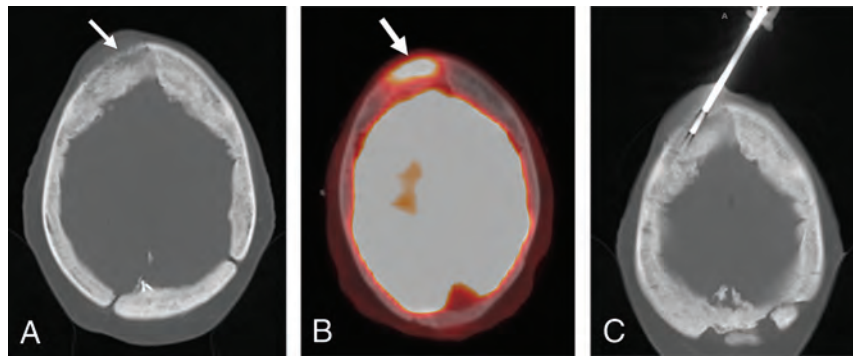


FIG 1. A 58-year-old woman with a history of index finger chondrosarcoma and a right frontal bone mass. Axial CT (A) and FDG-PET/CT (B) images show an aggressive permeative and hypermetabolic bone marrow–replacing lesion in the right frontal bone with an aggressive periosteal reaction (A and B, arrow). Axial CT image during percutaneous biopsy (C) shows positioning of a coaxial bone-biopsy needle within the lesion. The total conscious sedation time was 29 minutes, and histologic evaluation confirmed intrasosseous meningioma.

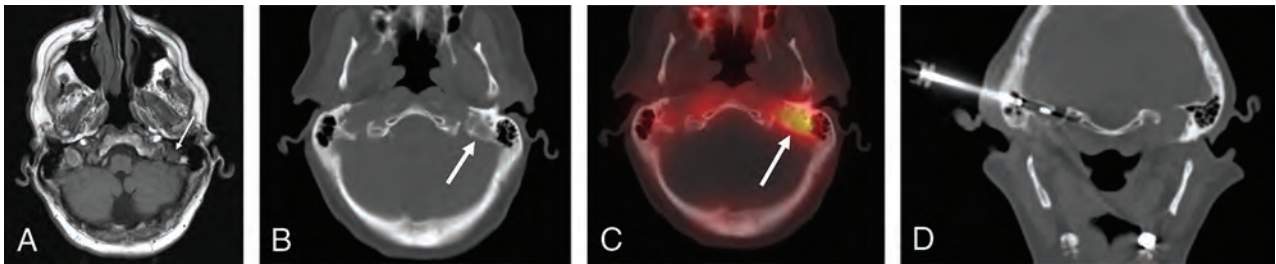


FIG 2. A 65-year-old man with poorly differentiated salivary gland sarcomatoid carcinoma with a left temporal bone lesion. Axial T1-weighted MR imaging (A), CT (B), and technetium 99m methylene diphosphonate SPECT-CT (C) images show an osteolytic bone marrow–replacing lesion with increased radiopharmaceutical uptake in the petrous portion of the left temporal bone (A–C, arrow). Note the surrounding vital tissues. Coronal CT image (D) during percutaneous biopsy shows coaxial positioning of a soft-tissue biopsy needle, through an OnControl bone introducer cannula, within the lesion through the mastoid air cells. The total conscious sedation time was 40 minutes, and histologic evaluation confirmed metastasis from a known primary salivary gland tumor.

MATERIALS AND METHODS

Mallinckrodt Institute of Radiology (IRB) approval was obtained to retrospectively review the institutional data base for all patients who underwent percutaneous CT-guided skull biopsy between 2014 and 2018. Informed consent was waived for retrospective participation in the study. Recorded data included patient demographics, cancer history, indication for initial imaging, imaging technique for diagnosis, skull tumor anatomic location, and final histologic diagnosis. Preprocedural imaging of each skull lesion was reviewed to determine tumor size and characteristics (osteolytic, osteoblastic, or mixed). Procedural notes were reviewed to determine the total conscious sedation or anesthesia time, type of biopsy needle, and the number and length of obtained core specimens.

Biopsy Planning and Procedure

To ensure safety and minimize the risk of potential complications, the operator must have detailed knowledge of the skull anatomy, and during periprocedural planning and biopsy, attention should be paid to the critical structures, particularly the skull base neurovascular foramina and canals as well as important components of the temporal bone that may be technically more challenging to access and pose higher risks of complications. The authors recommend preprocedural discussions with neurologic surgery or ear, nose, and throat surgery services in all cases to minimize such potential risks.

Preprocedural imaging was reviewed to determine the optimal

biopsy approach in all cases. Written informed consent was obtained before all procedures. All procedures were performed using CT guidance with patients either under conscious sedation using midazolam and fentanyl or general anesthesia and were supervised by 2 attending musculoskeletal radiologists, one with >10 years of experience and the other with >8 years of experience in performing musculoskeletal biopsies. A combination of anatomic landmarks and skin BB markers was used to localize the needle entry site. The implemented measures to reduce the patient radiation dose included decreasing the tube current and gantry rotation time (milliamperes-second), decreasing the x-ray beam energy (kilovolt [peak]), increasing the pitch (at a set tube current), central patient positioning at the CT isocenter, and limiting the scan length to the volume of interest. Following the initial guidance scan, which was performed with standard-dose CT parameters for optimal assessment of the ROI, a reduced CT dose protocol was used for the subsequent scans, which included 100 mAs, 100 kV(p), and pitch of 1.0–1.2, with a 2-mm section thickness. Both bone and soft-tissue CT windows were used for needle guidance. Superficial and deep soft-tissue and periosteal anesthesia were achieved with 50:50 dilution of 1% lidocaine and 0.25% bupivacaine.

The procedures were performed using 1 of 2 coaxial biopsy needle systems, each with a 6-cm introducer cannula and a 10-cm biopsy needle: 1) a coaxial battery-powered hand drill with a 10 (11)-ga introducer cannula and 12 (13)-ga inner diamond-tipped needle (Arrow OnControl; Vidacare, Shavano Park, Texas). The

inner needle is then exchanged for a 12(13)-ga hollow biopsy needle. This needle system was used in 86% (12/14) of cases; or 2) a coaxial soft-tissue core biopsy system with a 13-ga introducer cannula and 14-ga spring-loaded biopsy needle (Bard Marquee, C.R. Bard, Tempe, Arizona; or Achieve, Merit Medical, South Jordan, Utah) was used. The soft-tissue core biopsy system was used if the lesion was entirely osteolytic with extensive cortical destruction or a soft-tissue component. In addition, in cases in which lesion access was achieved with the bone core biopsy system and no specimen could be obtained due to the destructive nature of the mass, a hollow soft-tissue core biopsy needle was placed coaxially through the existing bone core introducer cannula to obtain tissue (Fig 1 and 2).

Contraindications to imaging-guided skull biopsies included percutaneously inaccessible lesions, coagulopathy (platelet count of <50,000 per microliter and an international normalized ratio of >1.5), and allergy to conscious sedation or general anesthesia medications.

Outcome Assessment

Procedural complications were documented according to Society of Interventional Radiology classification.⁷ Patients were clinically monitored for a minimum of 2 hours after each procedure for evidence of acute complications, such as hematoma formation or neurologic injury. A follow-up phone call was performed 24 hours following the biopsy by a nurse coordinator, and electronic medical records were also reviewed for evidence of delayed complications within 30 days of the biopsy. Procedures were considered technically successful if the biopsy needle was visualized within the target lesion and core specimens were obtained. Surgical pathology reports were reviewed to assess the diagnostic yield. Negative biopsy results were not pursued further when follow-up imaging confirmed lesion stability or a negative result was considered concordant with a low pretest probability of an aggressive etiology. Surgical pathology reports were also reviewed for the presence of crush artifacts. If crush artifacts were present, the specimen was considered histologically adequate if it could still be used to confirm or exclude the diagnosis in question.

RESULTS

All biopsy procedures were performed as preoperatively planned and were technically successful. According to the Society of Interventional Radiology classification, there were no acute or delayed procedure-related complications. Percutaneous CT-guided skull biopsy was performed on 14 patients (men, $n = 5$, and women, $n = 9$) with an age range of 35–84 years. Fifty-seven percent (8/14 patients) of patients had a history of cancer. Indications for imaging included oncologic staging (57%, 8/14 patients), palpable mass (7%, 1/14 patients), cranial nerve dysfunction (7%, 1/14 patients), and imaging for unrelated reasons (incidental diagnosis) (29%, 4/14 patients). Preprocedural imaging included PET/CT ($n = 4$), MR imaging ($n = 7$), CT ($n = 9$), and bone scintigraphy ($n = 3$), including SPECT ($n = 1$). Procedures were performed with the patient under conscious sedation in 93% (13/14) of cases and under general anesthesia in 7% (1/14) of cases. The median conscious sedation duration was 40 minutes (range,

27–75 minutes). The median midazolam and fentanyl doses administered were 2.5 mg (range, 1–4 mg) and 150 μg (range, 75–300 μg), respectively. The total anesthesia time was 30 minutes for procedures performed with the patient under general anesthesia. Definitive histologic diagnosis was achieved in 86% (12/14) of cases.

There was no biopsy specimen with crush artifacts. In 1 patient with a palpable left frontal bone mass that was characterized on MR imaging, histologic analysis showed blood products with benign bone and soft tissue that were considered concordant with imaging findings suggestive of hemangioma. In 1 patient with a left frontal bone osteolytic lesion incidentally identified on head CT and subsequently characterized on bone scintigraphy demonstrating increased radiopharmaceutical uptake, histologic analysis showed no evidence of malignancy with benign bone and soft tissue. The lesion remained unchanged on 2-year follow-up imaging; this finding was considered concordant with the biopsy results. The details of the patient cohort including skull lesion anatomic location, tumor size, tumor characteristics, type of biopsy needle, number and length of obtained core specimens, and final histologic diagnosis are shown in the Table.

DISCUSSION

The results of the present study demonstrate that percutaneous CT-guided skull biopsy is feasible and safe with a high diagnostic yield. Although percutaneous imaging-guided biopsy of musculoskeletal lesions, including appendicular and spinal bone tumors, has been well-established and accepted as a safe and cost-effective approach with high diagnostic accuracy for histologic characterization,^{2–6} to our knowledge, there is essentially no published literature to date on the systematic evaluation of the safety profile and diagnostic yield of percutaneous imaging-guided skull biopsy. This is, in part, because there are often other skeletal lesions that are safer and less technically challenging to target for biopsy, particularly in oncologic patients. However, with progressively increasing use of routine cross-sectional imaging and oncologic staging imaging in clinical practice, isolated skull lesions in patients with or without a history of cancer may be identified more frequently, and percutaneous tissue sampling of a calvarial lesion may be the only minimally invasive viable option to both establish a new diagnosis such as new or synchronous primary tumor or confirm metastasis. Percutaneous imaging-guided skull biopsy poses a unique challenge due to the proximity of brain tissue, critical facial structures, and vital neurovascular structures in the skull base, which may discourage both clinicians and radiologists from requesting and performing such procedures, respectively.

In this initial experience, all procedures were technically successful with excellent safety profiles, characterized by lack of procedure-related complications according to the Society of Interventional Radiology classification.⁷ The median conscious sedation duration was 40 minutes (range, 27–75 minutes), which is within the reasonable range for imaging-guided percutaneous bone biopsies.^{5,6} Diagnostic yield refers to the likelihood that a test or procedure will provide the information needed to establish a diagnosis and is defined as diagnostic results divided by the sum of diagnostic results and nondiagnostic results. Therefore, diagnostic yield is the most direct and accurate representation of the biopsy success rate. In our study, definitive histologic diagnosis

Details of skull lesions, biopsy parameters, and final diagnosis^a

Patient No.	Anatomic Site	Tumor Size (mm)	Tumor Feature	Biopsy Needle	Specimen No.	Core Length (mm)	Final Diagnosis
1	Right frontal	50 × 46 × 22	Permeative	Bone	3	20	Intraosseous meningioma
2	Left frontal	13 × 9 × 5	Osteolytic	Bone	1	10	Blood products and benign tissue
3	Left frontal	61 × 42 × 13	Osteoblastic	Bone	7	2–10	B-cell lymphoma
4	Right frontal	9 × 9 × 5	Osteolytic	Bone	1	6	Hemangioma
				Soft tissue	1	5	
5	Left frontal	11 × 10 × 4	Osteolytic	Bone	1	5	Benign bone and soft tissue
				Soft tissue	2	10	
6	Skull base and occipital	Diffuse	Mixed	Bone, soft tissue	6	15–20	Fibrous dysplasia
7	Left temporal	19 × 14 × 10	Osteolytic	Bone	1	15	Metastatic salivary sarcomatoid carcinoma
				Soft tissue	1	20	
8	Right temporal	21 × 15 × 7	Osteolytic	Soft tissue	5	10–20	Plasmocytoma
9	Left parietal	38 × 34 × 10	Mixed	Bone	1	10	Metastatic breast carcinoma
				Soft tissue	1	20	
10	Right occipital	12 × 8 × 8	Osteolytic	Bone	1	20	Osteonecrosis
11	Left occipital	27 × 20 × 19	Osteolytic	Soft tissue	2	20	Metastatic thyroid carcinoma
12	Right parietal	24 × 18 × 13	Mixed	Bone	2	4–6	Metastatic breast carcinoma
13	Left parietal	Most of parietal bone	Permeative	Bone	1	5	Radiation-induced sarcoma
				Soft tissue	6	10–20	
14	Left frontal	27 × 17 × 14	Osteoblastic	Bone	2	15	Xanthoma with osteosclerosis

^a Data for patients 3 and 6 have been previously published.⁸

was achieved in 86% (12/14) of patients, which directly influenced patients' management by confirming metastasis, new primary tumor, synchronous primary tumor (patient 3), or benign histology (Table). In 2 patients with no definitive histologic diagnosis, biopsy results were considered concordant with imaging features indicating a benign etiology.

The authors used a coaxial bone-biopsy needle system with a battery-powered hand drill in 86% (12/14) of patients (with or without a soft-tissue biopsy needle), which facilitates needle purchase and advancement within the bone by providing the operator greater control over the needle trajectory via recruitment of wrist and hand muscles with more fine-movement capabilities compared with standard manual techniques in which direct pushing and rotation of the biopsy needle knob or handle are implemented and proximal arm and shoulder musculature are used. This system is particularly important in skull biopsies because it results in more accurate targeting of lesions and avoidance of injury to surrounding critical structures. In 2 patients, due to the extensive destructive nature of the target lesions, soft-tissue needles were used to perform the biopsy. In addition, if a skull lesion is accessed with a coaxial bone-biopsy system and the initial biopsy attempt results in no specimen, which is not unusual in destructive osteolytic lesions, the authors recommend coaxial placement of a soft-tissue biopsy needle through the existing bone biopsy introducer cannula for improved sample yield. In 2015, Wallace et al⁸ reported 2 cases of successful percutaneous CT-guided skull biopsy confirming histologic diagnoses with no complications, and the authors suggested the feasibility and safety of the procedure.

The major limitations of the present study include the retrospective methodology and the small number in the patient cohort.

CONCLUSIONS

The results of this retrospective initial study suggest that percutaneous CT-guided skull biopsy is feasible with an excellent safety

profile and affords a high diagnostic yield for histologic characterization and may obviate more invasive open-skull biopsies.

Disclosures: Travis J. Hillen—UNRELATED: Consultancy: Medtronic. Jack W. Jennings—RELATED: Consulting Fee or Honorarium: Bard, Comments: The consulting was for a device that has not yet gone to market; UNRELATED: Consultancy: Merit, BTG, Medtronic; Payment for Lectures Including Service on Speakers Bureaus: Merit, payment made to individual.

REFERENCES

- Shah MV, Haines SJ. Pediatric skull, skull base, and meningeal tumors. *Neurosurg Clin N Am* 1992;3:893–924 CrossRef Medline
- Skrzynski MC, Biermann JS, Montag A, et al. Diagnostic accuracy and charge-savings of outpatient core needle biopsy compared with open biopsy of musculoskeletal tumors. *J Bone Joint Surg Am* 1996;78:644–49 CrossRef Medline
- Fraser-Hill MA, Renfrew DL. Percutaneous needle biopsy of musculoskeletal lesions, 1: effective accuracy and diagnostic utility. *AJR Am J Roentgenol* 1992;158:809–12 CrossRef Medline
- Fraser-Hill MA, Renfrew DL, Hilsenrath PE. Percutaneous needle biopsy of musculoskeletal lesions, 2: cost-effectiveness. *AJR Am J Roentgenol* 1992;158:813–18 CrossRef Medline
- Traina F, Errani C, Toscano AJ, et al. Current concepts in the biopsy of musculoskeletal tumors: AAOS exhibit selection. *Bone Joint Surg Am* 2015;97:e7 CrossRef Medline
- Wallace AN, McWilliams SR, Wallace A, et al. Drill-assisted biopsy of the axial and appendicular skeleton: safety, technical success, and diagnostic efficacy. *J Vasc Interv Radiol* 2016;27:1618–22 CrossRef Medline
- Ahmed M, Solbiati L, Brace CL, et al; International Working Group on Image-Guided Tumor Ablation, Interventional Oncology Sans Frontières Expert Panel, Technology Assessment Committee of the Society of Interventional Radiology, Standard of Practice Committee of the Cardiovascular and Interventional Radiological Society of Europe. Image-guided tumor ablation: standardization of terminology and reporting criteria: a 10-year update. *J Vasc Interv Radiol* 2014;25:1691–705 CrossRef Medline
- Wallace AN, Tomasian A, Hsi AC, et al. CT-guided percutaneous skull biopsy using a drill-assisted system: technical report of two cases. *Interv Neuroradiol* 2015;21:774–79 CrossRef Medline

Transient Ischemic Attack and Carotid Web

H. Hu, X. Zhang, J. Zhao, Y. Li, and Y. Zhao



ABSTRACT

BACKGROUND AND PURPOSE: Carotid web was recognized as a cause of ischemic stroke. We sought to determine the clinical and imaging profiles of patients with a carotid web as well as its association with TIA.

MATERIALS AND METHODS: A retrospective review of carotid CT angiography studies and brain MR imaging in patients with TIA during the past 3 years ($n = 135$) was performed to determine the presence of carotid webs by 2 experienced neuroradiologists according to previously published criteria. Demographics and clinical and imaging characteristics are shown by descriptive statistics for patients with an identified carotid web. The agreement in the detection of carotid webs between 2 neuroradiologists was examined using κ statistics.

RESULTS: There were 12 (8.9%) carotid webs at the symptomatic bifurcation and 1 carotid web (0.7%) at the asymptomatic bifurcation, and no hyperintensity was seen on DWI of these 12 patients. Eight of these 12 (75%) patients with a carotid web were women. None of the 12 patients with a carotid web had major risk factors or other causes of TIA. Fair-to-good interobserver agreement ($\kappa = 0.87$) was seen for diagnosing a carotid web with CT angiography. The rate (10/12, 83.3%) of short-term recurrent episodes of TIA in patients with TIA with a carotid web was significantly higher than that of patients without a carotid web (15/123, 12.2%) ($P < .001$).

CONCLUSIONS: The incidence of carotid web in patients with TIA was 8.9%. There is an association between carotid web and patients with TIA without other identified risks. Carotid web may be an underestimated risk factor for TIA.

Transient ischemic attack is a common ischemic cerebrovascular disease. According to the guidelines proposed by the American Heart Association and American Stroke Association in 2009,¹ TIA is defined as a transient episode of neurologic dysfunction caused by focal brain, spinal cord, or retinal ischemia, without acute infarction. The probability of stroke occurring at 2, 7, 30, and 90 days after TIA onset was approximately 2%–4%, 6%,

4%–10%, and 10%–20% in previous studies.^{2,3} If the patient is treated properly, the risk of stroke at 90 days after TIA could be reduced to 1%–3%.⁴ Therefore, TIA is a stroke-warning event requiring urgent intervention, and its occurrence is also a good time for secondary prevention.

Decisions about TIA treatment and secondary prevention rely on identification of the main cause of the disease. However, in one-third of patients with TIA, the cause cannot be identified.⁵ In several recent case series, carotid webs were identified as a possible cause of ischemic stroke in a predominantly female population with no otherwise known reason for stroke.^{6–9} A carotid web is defined as a thin intraluminal filling defect along the posterior wall of the carotid bulb in oblique sagittal reformats, and, most important, with a septum evident on the axial section on CTA.^{6–9} However, there are few reports on the relationship between a carotid web and TIA. Is carotid web one of the causes of TIA?

Therefore, we hypothesized that a carotid web may be one of the risk factors for TIA without identifiable cause. We retrospectively analyzed carotid CTA data to explore the incidence of carotid webs in patients with TIA and to determine the clinical and imaging profiles of patients with carotid webs as well as their association with TIA.

Received August 25, 2018; accepted after revision December 3.

From the Institute of Diagnostic and Interventional Radiology (H.H., X.Z., J.Z., Y.L.), and Department of Neurology (Y.Z.), Shanghai Jiao Tong University Affiliated Sixth People's Hospital, Shanghai, People's Republic of China.

This work was supported by National Natural Science Foundation of China No. 81871329; National Natural Science Foundation of China No. 81471656; Shanghai Talent Development Fund, No. 201555; Shanghai Key Discipline of Medical Imaging grant No. 2017ZZ02005; Shanghai Municipal Education Commission-Gaofeng Clinical Medicine Grant Support No. 2016427; Clinical Science and Technology Innovation Project of Shanghai Shen Kang Hospital Development Center No. SHDC22015038; and Shanghai Municipal Science and Technology Commission Medical Guide Project No. 16411968900.

Please address correspondence to Yuehua Li, MD, Institute of Diagnostic and Interventional Radiology, Shanghai Jiao Tong University Affiliated Sixth People's Hospital, 600, Yishan Rd, Shanghai, 200233, China; e-mail: liyuehua312@163.com

Indicates open access to non-subscribers at www.ajnr.org

<http://dx.doi.org/10.3174/ajnr.A5946>

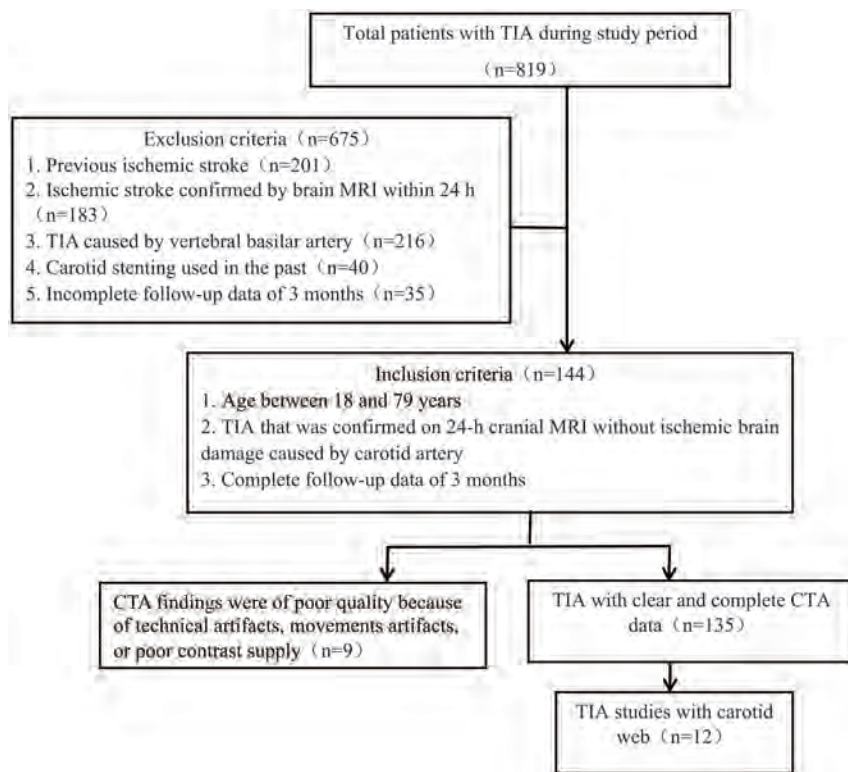


FIG 1. Flow chart of inclusion criteria.

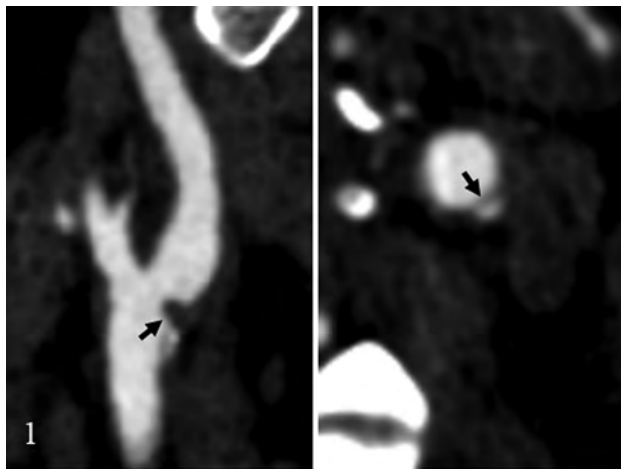


FIG 2. Carotid web diagnosis by the classic appearance on CTA, which shows a thin intraluminal filling defect along the posterior wall of the carotid bulb on an oblique sagittal section and a corresponding septum on axial images (arrow).

MATERIALS AND METHODS

Patients

This retrospective study was approved by the ethics committee of the Sixth People's Hospital of Shanghai Jiao Tong University; the need for informed consent was waived. A chart review of all patients ($n = 819$) presenting to our hospital with TIA from January 1, 2015, to December 31, 2017, was undertaken. Figure 1 provides details of patient selection for the study.

Clinical Information

Data on age, sex, history of hypertension, diabetes mellitus, cardiac insufficiency, atrial fibrillation, and current smoking were

retrospectively collected. All patients were treated with antiplatelet therapy. Data on routine follow-up within 3 months after discharge were also collected. A short-term recurrent episode was considered if TIA relapse occurred during the first hospitalization or within 3 months, and short-term progression of acute cerebral infarction was considered if an ischemic stroke was confirmed on MR imaging.

Image Evaluation

Carotid CTA was performed on a 128–multidetector row CT scanner with 1-mm thick sections and was acquired from the aortic arch through the circle of Willis. Scanning parameters included the following: gantry rotation time, 0.5 seconds; pitch, 1; voltage, 120 kV(peak); and current, 360 mAs. Intravenous contrast material (80 mL of iohexol, 300 mg/mL, Omnipaque; GE Healthcare, Piscataway, New Jersey) and a 50-mL saline flush were administered at a rate of 4 mL/s with a power injector. Images were reconstructed with axial, coronal,

sagittal, and 3D volume reconstructions.

An independent review of these studies was then performed by 2 experienced neuroradiologists with 6–8 years of experience in carotid CTA imaging and analysis. The readers were blinded to patient age and sex. The presence of a carotid web was evaluated by each reader at the baseline CTA. A carotid web was identified when there was a thin, smooth, membrane-like intraluminal filling defect along the posterior wall of the carotid bulb on oblique sagittal images and a corresponding thin septum on axial images (Fig 2).^{5–8} Then, there was a consensus reading of all webs identified by the 2 radiologists independently. A carotid web was diagnosed only if both radiologists agreed regarding the presence of a web on sagittal and axial images. The degree of carotid stenosis and the length of the carotid web were measured according to NASCET criteria¹⁰ and the study of Hausseen et al.¹¹ The differential diagnosis was performed, as shown in Fig 3, when calcified atherosclerotic plaques, carotid artery embolism, carotid artery dissection, or typical fibromuscular dysplasia at 3 cm above and below the carotid bifurcation was detected. FLAIR and DWI imaging were used to assess the presence of TIA-induced brain tissue damage. Follow-up brain MR imaging (DWI and FLAIR) was assessed for the presence of stroke.

Statistical Analysis

Demographic data and clinical information were presented as medians. For patients both with and without a carotid web on CTA, group differences in age were assessed using the Mann-Whitney U test. For other baseline values (demographics and risk factors), group differences were assessed using the Fisher exact test. The proportion of carotid webs at the symptomatic and asymptomatic bifurcations was estimated using conditional logis-



FIG 3. The differential diagnosis includes calcified atherosclerotic plaques (A), carotid artery embolism (B), and carotid artery dissection (C).

tic regression, in which odds ratios were calculated with 95% confidence intervals. The Cohen κ statistic was used to calculate the interobserver agreement for identifying carotid webs for all patients. Statistical significance was defined as $P < .05$. Analyses were performed with SPSS 22.0 (IBM, Armonk, New York).

RESULTS

Of the 135 patients with TIA with complete carotid CTA data included in this study, both readers agreed on 12 cases of carotid web (Cohen coefficient, 0.87; 95% CI, 0.55–1). Disagreement was encountered in 2 patients. Furthermore, the 2 cases were both rejected as webs because the 2 readers could not reach an agreement. Radiologically, the typical appearance of a carotid web on CTA is a thin intraluminal filling defect arising from the posterior wall of the carotid bulb on oblique sagittal images and a corresponding thin septum on axial images (Fig 4). There were 12 (8.9%; 95% CI, 4%–13.8%) carotid webs at the symptomatic bifurcation and 1 (0.7%; 95% CI, 0%–2.2%) at the asymptomatic bifurcation (odds ratio, 3.4; 95% CI, 1.9–6.26; $P < .001$). As shown in Table 1, the median age (58 years) of patients with a carotid web at the symptomatic carotid bifurcation differed ($P = .026$) from those (64 years) without a carotid web at the symptomatic carotid bifurcation. We found that carotid webs in the symptomatic carotid artery were more often observed in female patients ($n = 9$) than in male patients ($n = 3$; $P < .015$). However, there were no differences in symptomatic carotid artery location between the right and left sides ($P = .548$). Among 12 patients with a carotid web at the symptomatic side, 1 had a history of smoking (case 2), one had a history of diabetes (case 3), and 10 had no risk factors for TIA such as hypertension, diabetes, atrial fibrillation, and myocardial infarction.

All 135 patients with TIA underwent brain MR imaging within 24 hours after admission. Carotid CTA was performed within 1 week. There was no hyperintensity detected on DWI, in both patients with symptomatic carotid webs and those without carotid webs. The rate (10/12, 83.3%) of short-term recurrent episodes of TIA in patients with TIA with a carotid artery web was significantly higher than that of patients without a carotid artery web (15/123, 12.2%) ($P < .00$).

As shown in Table 2, the degree of carotid artery stenosis (NASCET criteria)¹⁰ was $<50\%$ (range, 0%–20%), and the aver-

age length of the carotid web was 3.9 ± 1.1 mm (range, 2.9–6.5 mm) in all 12 patients with carotid webs. Furthermore, the average size (3.5 ± 0.8 mm) of the carotid artery web in patients with a carotid web without recurrent TIA and progressive ischemic stroke within 3 months was smaller than that (4.1 ± 1.2 mm) in patients with carotid web with recurrent TIA and deteriorating ischemic stroke within 3 months ($P = .416$). All 12 patients with a carotid web had no typical medial fibromuscular dysplasia. Three of 12 patients had nonstenotic calcification at the carotid bifurcation.

DISCUSSION

Our findings showed a prevalence of 8.9% of symptomatic carotid webs at the carotid bifurcation in patients with TIA due to carotid system disease. Other notable major risk factors for TIA could not be identified in most patients with a symptomatic carotid web. These findings support our hypothesis that a carotid web may be an important risk factor for ischemic TIA when no other cause is found.

We found a higher prevalence (8.9%) of carotid webs in patients with TIA than in previously reported data (1.2%⁶ and 2.5%⁹) according to a hospital-based sample of patients suspected of having stroke and intracranial large-vessel occlusion, respectively. TIA, a precursor of ischemic stroke, carries a high risk of recurrent stroke within 90 days from the event,¹² which could explain the higher prevalence. In addition, the previously reported prevalence of a carotid web was 9.4%, 21.2%, and 37%, respectively, in patients with cryptogenic ischemic stroke^{7,8,13} and 23%¹³ in all patients with carotid ischemic stroke. Our result was similar to the earlier reported prevalence (9.4%) of carotid webs in patients with cryptogenic ischemic stroke, but lower than the prevalence of 21.2%, 37%, and 23% in patients with cryptogenic ischemic stroke and all patients with carotid ischemic stroke, respectively. Differences in methodology and population characteristics may explain discrepancies in these findings because the prevalence of a carotid web is thought to be increased in African American and Afro-Caribbean compared with white and Asian populations.^{8,13}

In our data, 2 patients with TIA and a carotid web each had a history of smoking and diabetes. While smoking and diabetes were independent risk factors for TIA,^{14–16} no atheromatous changes were seen on CTA. Thus, a carotid web was the main identifiable cause of our patients' TIAs. Existing literature about the relation of carotid web and TIA is scarce. Morgenlander and Goldstein¹⁷ reported that a young female patient with a carotid web but without other identifiable risk factors for stroke progressed to acute ischemic stroke after a recurrent TIA. Thus, our findings are in line with those in the literature.

In our study, carotid webs were more frequently found at the ipsilateral symptomatic bifurcation and in female patients without cardiovascular risk factors or other major risk factors for TIA.

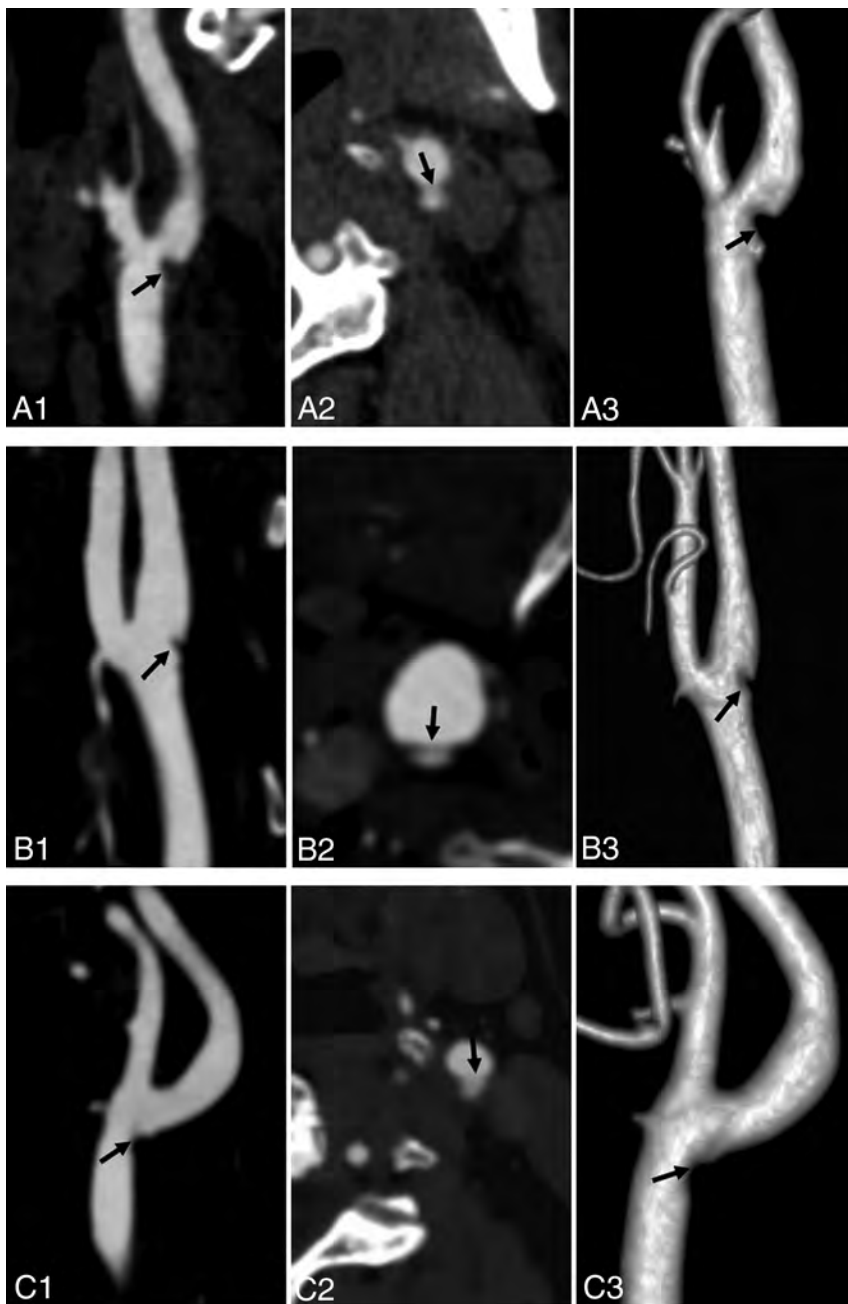


FIG 4. Carotid artery web in 3 patients with TIA (A–C). Sagittal oblique CTA (A1, B1, and C1) shows a shelf-like intraluminal protrusion arising from the posterior wall of the carotid bulb (arrow). Axial CTA (A2, B2, and C2) shows that the membrane is shelf-like, consistent with a carotid artery web (arrow); volume reconstruction (A3, B3, and C3) shows the same web inside the vessel (arrow).

This result was consistent with literature reports about patients with stroke with carotid webs.^{6–9,13} However, the median age (58 years) of patients with TIA with a carotid web in our study was higher than that previously reported for patients with stroke with a carotid web,^{6–9,13} which may be related to an older age of onset in patients with TIA.

In this study, the rate of short-term recurrent episodes of TIA within 3 months in patients with TIA with carotid webs was 83.3%, higher than that of patients with TIA without a carotid artery web (12.2%) ($P < .001$) and higher than the average reported in the literature.^{2,3} Moreover, the degree of carotid artery

stenosis (NASCET criteria)¹⁰ of all 12 patients with carotid webs was $<50\%$ (range, 0%–20%). Generally, the degree of carotid artery stenosis $<50\%$ is not considered a risk factor for TIA or ischemic stroke.⁷ Thus, studies have postulated that carotid web–induced ischemic stroke may be mediated by an embolic mechanism, with sluggish/turbulent blood flow produced by the filling defect increasing the thrombogenicity and risk of artery-to-artery embolism.^{6–9,13,18} Therefore, we speculated that the presence of a carotid web might lead to changes of carotid hemodynamics, which was related to recurrence of TIA and progression to acute ischemic stroke within 3 months in patients with TIA with carotid webs.

However, because of the limitation of small samples and lack of fluid dynamics data, the relation between the thrombogenicity of webs and the size of the “shelf” of the web was not clear in this study. Although the average size of a carotid web (4.1 ± 1.2 mm) in patients with recurrence of TIA and progression to stroke within 3 months was larger than that (3.5 ± 0.8 mm) in patients without recurrence of TIA and progression to stroke within 3 months, there were no statistically significant differences between the 2 groups ($P = .416$). Hence, the relation between the change of carotid hemodynamics and the size of the shelf of the carotid web in patients with TIA deserves further study.

In our study, the agreement between the 2 neuroradiologists on the CTA-based diagnosis of carotid webs was good ($\kappa = 0.87$). The carotid web had characteristics on CTA, and it can be definitely diagnosed. Carotid webs could be distinguished from dissection and atherosclerotic plaques by their characteristic location and appearance, being thin and focal in nature and exclu-

sively located in the posterior wall of the carotid bulb. In contrast, dissection is typically located beyond the carotid bulb and may be related to intramural hematomas and/or pseudoaneurysms. Soft carotid plaques often, but not necessarily, are seen as focal areas of vessel wall thickening, confined to the posterior wall of the carotid bulb.⁹ Histopathologically, carotid web has been referred to as an atypical variant of fibromuscular dysplasia, though without actual evidence of fibromuscular dysplasia in other vessels, which is different from the typical presentation of fibromuscular dysplasia.^{6,13} Typical myofibroblastic dysplasia mainly involves the arterial media,

Table 1: Demographics and clinical characteristics of patients in our study

Parameter	Patients with TIA without Carotid Web (n = 123)	Patients with TIA with Carotid Web (n = 12)	P Value
Median age (yr)	64	58	.028
Sex (male)	77 (62.6%)	3 (25%)	.015
Ethnicity (No.) (%)			
Chinese	123 (100%)	12 (100%)	
Other	0	0	
Right-hemisphere stroke	56 (45.5%)	4 (33.3%)	.548
Risk factors			
Hypertension	26 (21.1%)	0	.122
Diabetes	16 (13.0%)	1 (8.3%)	1.0
Atrial fibrillation	9 (7.3%)	0	1.0
Myocardial infarction	2 (1.6%)	0	1.0
Smoking	20 (16.3%)	1 (8.3%)	.691
Alcohol abuse	10 (8.1%)	0	.599
MRI (DWI hyperintensity)	0	0	
Recurrent episode within 3 mo	15 (12.2%)	10 (83.3%)	.00

Note:—Unless otherwise indicated, data are absolute values with percentages in parentheses.

Table 2: Detailed imaging/clinical features of 12 patients with TIA with a carotid web

Patient No.	Degree of Carotid Artery Stenosis (%) and Carotid Web (mm)	Nonstenosis Calcification of Carotid Bifurcation	Recurrent TIA	Progression to Cerebral Infarction (within 3 mo)
1	0, 3.5	No	Yes	No
2	20, 6.5	Yes	Yes	Yes
3	0, 3.5	No	Yes	Yes
4	10, 3.0	No	Yes	Yes
5	0, 2.9	No	No	No
6	10, 5.8	Yes	Yes	Yes
7	5, 3.6	No	Yes	Yes
8	0, 3.3	No	Yes	Yes
9	15, 3.9	No	Yes	Yes
10	0, 3.0	Yes	Yes	Yes
11	0, 4.6	No	No	No
	0, 2.9	No	No	No
12	10, 4	No	Yes	Yes

with a classic “string of beads” imaging appearance, and is not associated with ischemic stroke.^{6–9,13}

Proper detection of carotid webs could help optimize the management of TIA and stroke; in particular, for patients with TIA and acute ischemic stroke without other clear risk factors. Several treatment options have been proposed, such as carotid endarterectomy and stent placement.^{10,11,19,20} However, optimal treatment strategies need to be investigated in clinical trials.

Our research had several limitations. First, the study design was a retrospective analysis with a small sample size. Second, all patients with carotid webs were identified on the basis of carotid CTA, without histologic observation. Third, although small protruding lesions of a carotid bifurcation were considered a risk factor in previous studies,^{6,9} they were not included in our study because of lower interobserver agreement of assessment during carotid CTA.

CONCLUSIONS

Our study showed that the incidence of a carotid web in patients with TIA was 8.9% and the rate of progression to ischemic stroke in the short term was high. Therefore, carotid webs should be considered in patients with TIA who do not have other major risk factors.

REFERENCES

- Easton JD, Saver JL, Albers GW, et al; American Heart Association, American Stroke Association Stroke Council, Council on Cardiovascular Surgery and Anesthesia, Council on Cardiovascular Radiology and Intervention, Council on Cardiovascular Nursing, Interdisciplinary Council on Peripheral Vascular Disease. **Definition and evaluation of transient ischemic attack: a scientific statement for health-care professionals from the American Heart Association/American Stroke Association Stroke Council; Council on Cardiovascular Surgery and Anesthesia; Council on Cardiovascular Radiology and Intervention; Council on Cardiovascular Nursing; and the Interdisciplinary Council on Peripheral Vascular Disease—The American Academy of Neurology affirms the value of this statement as an educational tool for neurologists.** *Stroke* 2009;40:2276–93 CrossRef Medline
- Wu CM, McLaughlin K, Lorenzetti DL, et al. **Early risk of stroke after transient ischemic attack: a systematic review and meta-analysis.** *Arch Intern Med* 2007;167:2417–22 CrossRef Medline
- Giles MF, Rothwell PM. **Risk of stroke early after transient ischemic attack: a systematic review and meta-analysis.** *Lancet Neurol* 2007;6:1063–72 CrossRef Medline
- Sanders LM, Srikanth VK, Jolley DJ, et al. **Monash transient ischemic attack triaging treatment: safety of a transient ischemic attack mechanism-based outpatient model of care.** *Stroke* 2012;43:2936–41 CrossRef Medline
- Li L, Yiin GS, Geraghty OC, et al. **Incidence, outcome, risk factors, and long-term prognosis of cryptogenic transient ischaemic attack**

- and ischaemic stroke: a population-based study. *Lancet Neurol* 2015;14:903–13 CrossRef Medline
6. Choi PM, Singh D, Trivedi A, et al. **Carotid webs and recurrent ischemic strokes in the era of CT angiography.** *AJNR Am J Neuroradiol* 2015;36:2134–39 CrossRef Medline
 7. Coutinho JM, Derkatch S, Potvin AR, et al. **Carotid artery web and ischemic stroke: a case-control study.** *Neurology* 2017;88:65–69 CrossRef Medline
 8. Sajedi PI, Gonzalez JN. **Carotid bulb webs as a cause of “cryptogenic” ischemic stroke.** *AJNR Am J Neuroradiol* 2017;38:1399–404 CrossRef Medline
 9. Compagne KCJ, van Es AC, Berkhemer OA, et al; MR CLEAN Trial Investigators. **Prevalence of carotid web in patients with acute intracranial stroke due to intracranial large vessel occlusion.** *Radiology* 2018;286:1000–07 CrossRef Medline
 10. Barnett HJ, Taylor DW, Eliasziw M, et al. **Benefit of carotid endarterectomy in patients with symptomatic moderate or severe stenosis: North American Symptomatic Carotid Endarterectomy Trial Collaborators.** *N Engl J Med* 1998;339:1415–25 CrossRef Medline
 11. Haussen DC, Grossberg JA, Bouslama M, et al. **Carotid web (intimal fibromuscular dysplasia) has high stroke recurrence risk and is amenable to stenting.** *Stroke* 2017;48:3134–37 CrossRef Medline
 12. Cruz-Flores S. **Acute stroke and transient ischemic attack in the outpatient clinic.** *Med Clin North Am* 2017;101:479–94 CrossRef Medline
 13. Joux J, Boulanger M, Jeannin S, et al. **Association between carotid bulb diaphragm and ischemic stroke in young Afro-Caribbean patients: a population-based case-control study.** *Stroke* 2016;47:2641–44 CrossRef Medline
 14. Wong SW, McGrath NN. **Screening, prevalence and ethnic variation of diabetes mellitus in people with acute stroke and transient ischaemic attack: a cross-sectional study in Northland, New Zealand.** *N Z Med J* 2016;129:62–66 Medline
 15. Daubail B, Durier J, Jacquin A, et al. **Factors associated with early recurrence at the first evaluation of patients with transient ischemic attack.** *J Clin Neurosci* 2014;21:1940–44 CrossRef Medline
 16. Strom JO, Tavosian A, Appelros P. **Cardiovascular risk factors and TIA characteristics in 19,872 Swedish TIA patients.** *Acta Neurol Scand* 2016;134:427–33 CrossRef Medline
 17. Morgenlander JC, Goldstein LB. **Recurrent transient ischemic attacks and stroke in association with an internal carotid artery web.** *Stroke* 1991;22:94–98 CrossRef Medline
 18. Kim SJ, Nogueira RG, Haussen DC. **Current understanding and gaps in research of carotid webs in ischemic strokes: a review.** *JAMA Neurol* 2018 Nov 5. [Epub ahead of print] CrossRef Medline
 19. Lenck S, Labeyrie MA, Saint-Maurice JP, et al. **Diaphragms of the carotid and vertebral arteries: an under-diagnosed cause of ischaemic stroke.** *Eur J Neurol* 2014;21:586–93 CrossRef Medline
 20. Elmokadem AH, Ansari SA, Sangha R, et al. **Neurointerventional management of carotid webs associated with recurrent and acute cerebral ischemic syndromes.** *Interv Neuroradiol* 2016;22:432–37 CrossRef Medline

Resting-State Functional Connectivity of the Middle Frontal Gyrus Can Predict Language Lateralization in Patients with Brain Tumors

S. Gohel, M.E. Laino, G. Rajeev-Kumar, M. Jenabi, K. Peck, V. Hatzoglou, V. Tabar, A.I. Holodny, and B. Vachha



ABSTRACT

BACKGROUND AND PURPOSE: A recent study using task-based fMRI demonstrated that the middle frontal gyrus is comparable with Broca's area in its ability to determine language laterality using a measure of verbal fluency. This study investigated whether the middle frontal gyrus can be used as an indicator for language-hemispheric dominance in patients with brain tumors using task-free resting-state fMRI. We hypothesized that no significant difference in language lateralization would occur between the middle frontal gyrus and Broca area and that the middle frontal gyrus can serve as a simple and reliable means of measuring language laterality.

MATERIALS AND METHODS: Using resting-state fMRI, we compared the middle frontal gyrus with the Broca area in 51 patients with glial neoplasms for voxel activation, the language laterality index, and the effect of tumor grade on the laterality index. The laterality index derived by resting-state fMRI and task-based fMRI was compared in a subset of 40 patients.

RESULTS: Voxel activations in the left middle frontal gyrus and left Broca area were positively correlated ($r = 0.47, P < .001$). Positive correlations were seen between the laterality index of the Broca area and middle frontal gyrus regions ($r = 0.56, P < .0005$). Twenty-seven of 40 patients (67.5%) showed concordance of the laterality index based on the Broca area using resting-state fMRI and the laterality index based on a language task. Thirty of 40 patients (75%) showed concordance of the laterality index based on the middle frontal gyrus using resting-state fMRI and the laterality index based on a language task.

CONCLUSIONS: The middle frontal gyrus is comparable with the Broca area in its ability to determine hemispheric dominance for language using resting-state fMRI. Our results suggest the addition of resting-state fMRI of the middle frontal gyrus to the list of noninvasive modalities that could be used in patients with gliomas to evaluate hemispheric dominance of language before tumor resection. In patients who cannot participate in traditional task-based fMRI, resting-state fMRI offers a task-free alternate to presurgically map the eloquent cortex.

ABBREVIATIONS: BA = Broca area; BOLD = blood oxygen level–dependent; ICA = independent component analysis; LI = laterality index; MFG = middle frontal gyrus; rsfMRI = resting-state fMRI

The determination of hemispheric language dominance is a critical part of the presurgical evaluation of patients with brain tumors. Studies have shown blood oxygen level–dependent (BOLD) task-based functional MR imaging to be an excellent

noninvasive alternative to the intracarotid amobarbital procedure or Wada test.^{1–4} However, the usefulness and reliability of task-based fMRI are limited in cognitively impaired patients, pediatric patients, and patients with language barriers for whom task completion poses a major challenge. To overcome this limitation, resting-state fMRI (rsfMRI) is emerging as an alternative paradigm-free extraction of brain networks, including language networks, using low-frequency fluctuations in the BOLD signal.⁵

The Wernicke area and Broca area (BA) are considered

Received July 16, 2018; accepted after revision November 12.

From the Department of Health Informatics (S.G.), Rutgers University School of Health Professions, Newark, New Jersey; Departments of Radiology (M.E.L., M.J., K.P., V.H., A.I.H., B.V.), Medical Physics (K.P.), and Neurosurgery (V.T.), Memorial Sloan Kettering Cancer Center, New York, New York; Department of Radiology (M.E.L.), Catholic University of the Sacred Heart, Rome, Italy; and Icahn School of Medicine at Mount Sinai (G.R.-K.), New York, New York.

This research was funded, in part, through the National Institutes of Health/National Cancer Institute Cancer Center support grant P30 CA008748. Research reported in this study was also supported by the National Cancer Institute of the National Institutes of Health under award No. R25CA020449 and, in part, by a grant to Maria Elena Laino, Principal Investigator, from the Department of Radiology at Memorial Sloan Kettering Cancer Center for a European School of Radiology Visiting Scholarship in oncologic imaging.

The content is solely the responsibility of the authors and does not necessarily represent the official views of the National Institutes of Health.

Please address correspondence to Behroze A. Vachha, MD, PhD, Department of Radiology, Memorial Sloan Kettering Cancer Center, 1275 York Ave, New York, NY 10021; e-mail: vachhab@mskcc.org

Indicates open access to non-subscribers at www.ajnr.org

<http://dx.doi.org/10.3174/ajnr.A5932>

primary language centers, and activations in these regions are commonly evaluated for language laterality.^{1,6,7} However, the presence of abnormal tumor neovasculature and resultant neurovasculature uncoupling can contribute to false-negative signals from the disruption and subsequent diversion of BOLD signals ipsilateral to the tumor.^{8,9} To overcome this problem, studies are investigating the use of secondary language areas supplementary to, or as substitutes for, primary language areas to determine hemispheric dominance.¹⁰ The middle frontal gyrus (MFG) is one of the secondary language areas implicated in nuances of language expression such as semantics, grammar and syntax, verbal fluency, and verbal working memory among other cognitive functions, including attention orientation.¹¹⁻¹⁹ Prior research has noted that the MFG consistently activates during fMRI language tasks,^{4,20,21} and a recent study using task-based fMRI demonstrated that the MFG is comparable with the BA in its ability to indicate hemispheric dominance for language using a measure of verbal fluency.¹⁸

To the best of our knowledge, no previous study has used rsfMRI to estimate language laterality using the MFG. The purpose of this study, therefore, was to investigate whether the MFG can be used as an indicator of language-hemisphere dominance in patients with brain tumors using paradigm-free resting-state fMRI. We hypothesized no significant difference in language lateralization between the MFG and BA and that the MFG can serve as a simple and reliable means of measuring language laterality.

MATERIALS AND METHODS

Subjects

The study was approved by the institutional review board at Memorial Sloan Kettering Cancer Center. Fifty-one patients with brain tumors (age range, 22–78 years; mean, 51 ± 14.2 years; 31 men) referred for presurgical functional mapping by fMRI were included in this retrospective study. All patients were native English speakers and had no pre-existing language impairment per chart review. Handedness was determined by the Edinburgh Handedness Inventory with 47 patients determined to be right-handed and 4 determined to be left-handed. All patients had subsequent pathologically confirmed intra-axial primary glial tumors. Pathology revealed 20 low-grade (World Health Organization I and II) and 31 high-grade (World Health Organization III and IV) tumors. In 28 patients, the lesion was located in the left hemisphere (7 in the temporal lobe, 15 in the frontal lobe, and 6 in the parietal lobe). In 23 patients, the lesion was located in the right hemisphere (5 in the temporal lobe, 17 in the frontal lobe, and 1 in the parietal lobe).

Data Acquisition

Each patient underwent resting-state fMRI as part of the routine presurgical work-up. Scanning was performed on 3T scanners (GE 750W Discovery, Milwaukee, Wisconsin) using an 24-channel head coil. For task-based and rsfMRI, T2*-weighted images were acquired with a single-shot gradient-echo echo-planar sequence in an axial orientation (TR/TE = 2500/30 ms, flip angle = 80°, slice thickness = 4 mm, FOV = 240 mm², matrix = 64 × 64) covering the whole brain. 3D T1-weighted images were acquired with a spoiled gradient-recalled sequence (TR/TE = 22/4 ms, matrix = 256 × 256 matrix, flip angle = 30°, slice thickness = 1.5

mm). For the resting-state fMRI scan, patients were instructed to leave their eyes open, focus on looking at a crosshair, and not think about anything during the scan. A total of 160 volumes were acquired. Of the 51 patients included in the study, 40 also performed a silent word-generation task in the same session as part of presurgical language mapping. The language tasks were used to determine language laterality (right-dominant, left-dominant, or bihemispheric dominance) using methodology previously used by Dong et al,¹⁸ and the results were documented in the patients' final presurgical mapping report.

Resting-State fMRI Data Analysis

In the current study, we implemented a data-processing scheme as outlined in Bharath et al.²² Data processing was based on SPM12 (<http://www.fil.ion.ucl.ac.uk/spm/software/spm12/>). In the first step, we discarded the first 5 time points from the functional MR imaging data to allow T1 relaxation. Next head-motion correction was performed to reduce the effect of within-scan head motion. During head-motion correction, we extracted the motion parameters, which describe the subject's motion in 6 different directions. Following motion correction, the subject's fMRI data were coregistered with the subject-specific anatomic images to improve normalization into Montreal Neurological Institute space. Following coregistration, we segmented each subject's anatomic images into gray matter, white matter, and CSF images. During the segmentation procedure, deformation fields were derived to transfer functional images into Montreal Neurological Institute standard space. We performed segmentation using the new segment procedures in SPM12. Each subject's segmentation maps were manually inspected to ensure successful segmentation. Finally, we used this subject-specific deformation field to transform the functional images into standard space images. In the next step, we implemented a linear regression to remove the effects of motion-related noise from the BOLD fMRI data. A general linear model-based regression approach was implemented using 24 motion regressors. This consisted of 6 motion parameters derived in the motion correction step, 6 squared of the original motion parameters, 6 one-time-points delayed version of the motion parameters and finally 6 squared of the delayed motion parameters. No regressors from the CSF or white matter region were included in the regression model. Following regression, residual data were derived and a temporal filtering between the frequency bands of 0.01 and 0.1 Hz was applied. Finally, 6-mm spatial smoothing was applied to the filtered fMRI data.

Spatial Extent of the MFG and BA

To identify active voxels in the BA and MFG regions, we implemented an independent component analysis (ICA)-based approach. In the first step, we performed a single-subject ICA on the filtered fMRI data. For each of the subjects, we performed a separate ICA and extracted 40 independent components. To identify ICAs representing the MFG and BA, we implemented a 2-step process. First, we calculated Dice coefficients between each of the independent components and the BA and MFG mask derived from the Harvard-Oxford Atlas.^{23,24} Next, we identified the top 5 independent components with the highest Dice coefficient. Each of these 5 independent components was then manually inspected

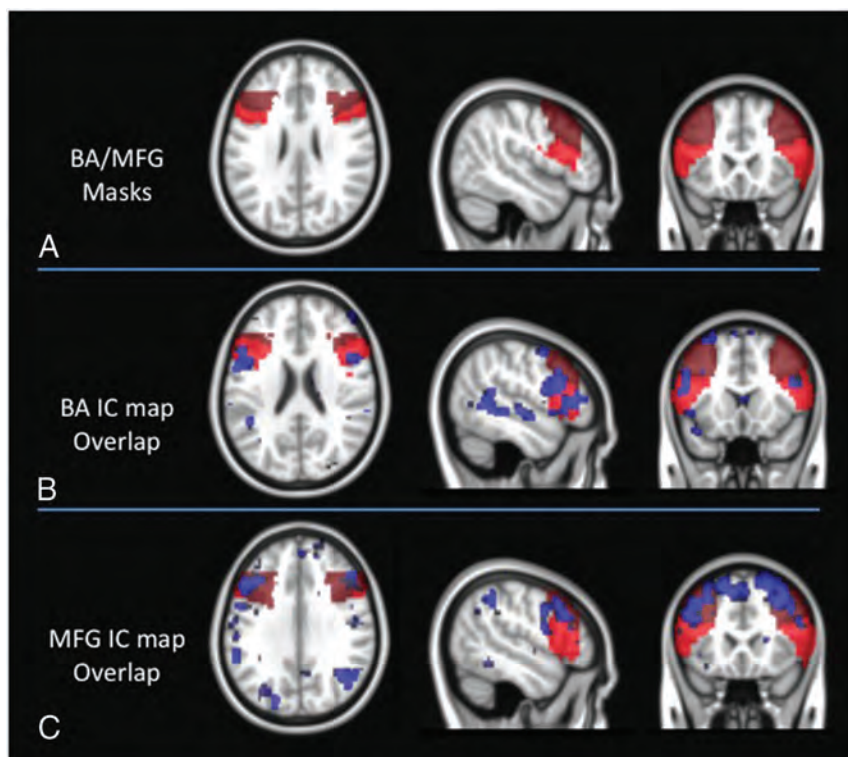


FIG 1. A, Broca area and middle frontal gyrus masks overlaid on the Montreal Neurological Institute standard brain. B, ICA maps representing the BA network are overlaid on the BA/MFG masks for a representative subject. C, ICA maps representing the MFG network are overlaid on the BA/MFG masks for a representative subject.

using consensus viewing by 2 neuroradiologists with 4–15 years of fMRI experience to identify independent components representing the functional connectivity of the MFG and BA. After identifying these components, active voxels within the left MFG were calculated as the overlap between the independent component representing the MFG and the MFG region derived through the Harvard-Oxford atlas. The same process was repeated for the right MFG, as well as the left and right BAs to calculate the active voxels for each of the ROIs. Figure 1 illustrates the masks for BA and MFG regions, as well as independent components from a representative patient. The mean activated voxels in the MFG and BA were calculated for each patient. To account for differences in the size of MFG and BA masks, we divided active voxels by the number of voxels in the Harvard-Oxford atlas. We compared the ratio of active voxels using a paired *t* test. The possible relationship of voxel count between the left MFG and the left BA was shown using a scatterplot, and correlation was tested using the Pearson correlation analysis. For all statistical analyses, a significance level of .001 was used.

Laterality Index in the MFG and BA

The laterality index (LI) for the MFG and BA was calculated using the standard LI formula^{2,7,25}: $LI = (L - R) / (L + R)$, where L and R are the number of active voxels in given ROIs (MFG and BA) in the left and right hemispheres, respectively. The LI ranged from -1 (complete right dominance) to +1 (complete left dominance). Consistent with prior studies,²⁶⁻²⁸ we defined right-hemispheric laterality as $-1 \leq LI < -0.2$, bilaterality as $-0.2 \leq LI \leq 0.2$, and left-hemispheric language laterality as $0.2 < LI \leq 1$.

In addition, we also calculated the functional connectivity be-

tween the MFG and BA ROIs. For each of the subjects, the filtered fMRI signal was extracted from the active voxels. The Pearson correlation coefficient was calculated between these time-series to derive functional connectivity between the MFG and BA ROIs.

Effect of Tumor Grade and Location on the LI

Tumors in each of the left and right hemispheres were categorized as high-grade (World Health Organization grades III and IV) or low-grade (World Health Organization grades I and II). For each hemisphere, LIs of the BA and MFG were compared between the high-grade and low-grade tumor groups. Differences in the LI of the BA and MFG between tumors in the left-versus-right hemisphere were also compared. LI differences were assessed using a 2-sample *t* test with the significance level set at $<.05$.

Comparison of the LI between rsfMRI and Task-Based fMRI

Forty of the 51 patients included in this study had both rsfMRI and language task-based data obtained in the same session as

part of presurgical language mapping. For each of these 40 patients, the LI of the MFG and BA based on rsfMRI was compared with the LI based on task-based fMRI so that a match (eg, left-versus-left) was scored as 100% accurate, while a mismatch (eg, left-versus-right) was scored as 0% accurate.

RESULTS

Spatial Extent of the MFG and BA

In the first step, we compared the number of active voxels between the left BA and left MFG regions. The scatterplot between the number of active voxels for the left BA and the left middle frontal gyrus is shown in Fig 2. We observed significant correlation for the number of active voxels between the left MFG and left BA ($r = 0.47, P < .001$). The number of active voxels was found to be significantly higher in the MFG regions (376.92) compared with the BA regions (218.09); however, when we corrected for the size of the MFG and BA masks, these differences were not statistically significant. Similarly, a significantly higher number of voxels was found in the right MFG region (218.09) compared with the right BA region (99.35); however, these differences were also not significant when correcting for the size of the MFG and BA masks (Fig 2).

Laterality Index in the MFG and BA

On the basis of the values for the number of active voxels, we calculated laterality indices for both the MFG and BA regions. Figure 3 shows the LI for each of the subjects calculated using these active voxels. We observed significant correlation ($r = 0.56, P < .0005$) between the LI of the BA and the LI of the MFG regions. As evident from Fig 3, many patients were identified as

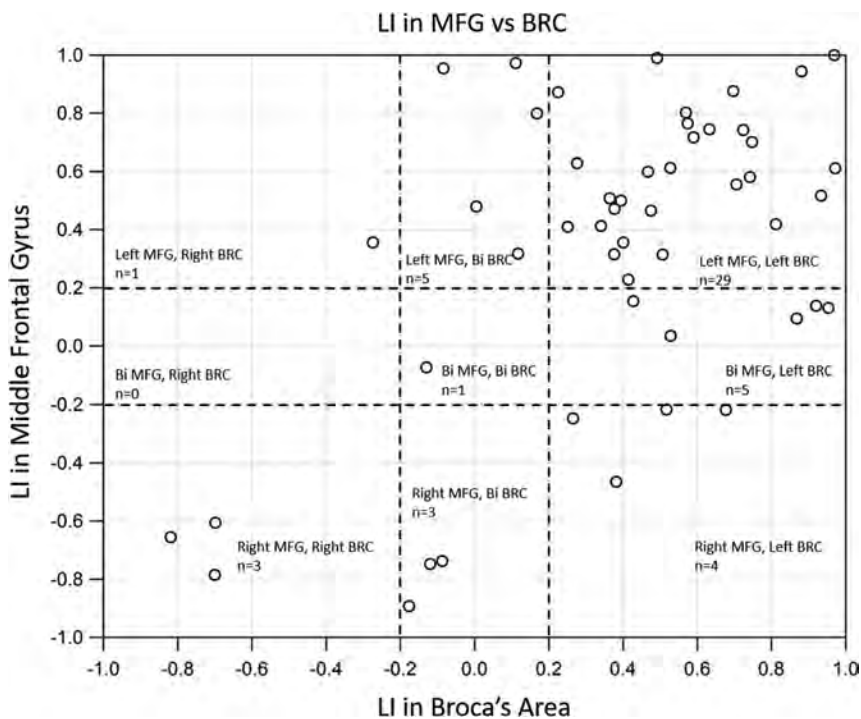


FIG 2. Scatterplot between the percentage of BA voxels and the percentage of middle frontal gyrus voxels across participants. Significant correlation was observed between the percentage of MFG and BA voxels across patients.

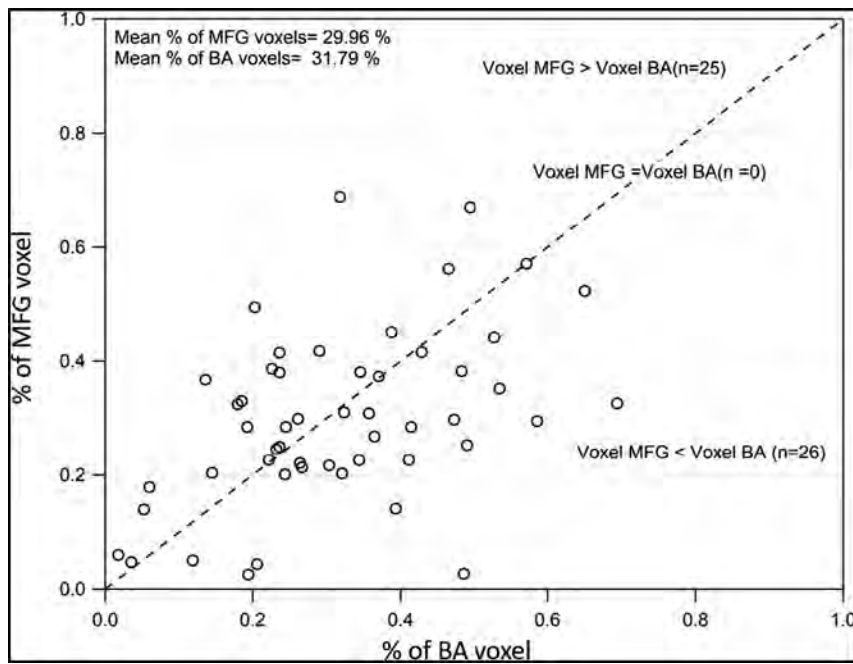


FIG 3. Scatterplot of the LIs in the middle frontal gyrus versus the BA. A significant positive correlation was observed between the LI of MFG and BA regions.

left-lateralized for both the MFG and BA, while only 3 patients were found to be right-lateralized in both groups.

We observed significantly higher functional connectivity between the left and right BAs and the left MFG, while the functional connectivity between the left BA regions and the right MFG was the lowest. Significantly high functional connectivity between right BA regions and the right MFG was noted. Figure 4 depicts

group-level functional connectivity between the BA and the MFG regions.

Effect of Tumor Grade and Location on the LI

In patients with tumors in the left hemisphere, the mean LI in the MFG was 0.06 ± 0.50 for low-grade tumors and 0.26 ± 0.52 for high-grade tumors ($P = .3577$, two-sample t test), while the mean LI in the BA was 0.26 ± 0.45 for low-grade tumors and 0.30 ± 0.47 for high-grade tumors ($P = .8383$, two-sample t test). For right-hemisphere tumors, the mean LI in the MFG was 0.38 ± 0.60 for low-grade tumors and 0.58 ± 0.33 for high-grade tumors ($P = .3353$, two-sample t test), while the mean LI in the BA was 0.56 ± 0.37 for low-grade tumors and 0.43 ± 0.35 for high-grade tumors ($P = .3917$, two-sample t test).

Tumor location in the left-versus-right hemisphere regardless of grade did not significantly contribute to the LI in both the BA and MFG. The mean LI in the BA for left-hemisphere tumors was 0.29 ± 0.46 , and 0.49 ± 0.36 for right-hemisphere tumors ($P = .09$, two-sample t test). The mean LI in the MFG for left-hemisphere tumors was 0.19 ± 0.52 , and 0.48 ± 0.49 for right-hemisphere tumors ($P = .04$, two-sample t test). However, tumor location in the left hemisphere (frontal-versus-nonfrontal) contributed to differences in the LI in the BA and MFG. The mean LI in the BA for left-frontal tumors was 0.12 ± 0.53 , and 0.47 ± 0.28 for left nonfrontal tumors ($P = .0472$, two-sample t test). The mean LI of the MFG for left-frontal tumors was -0.02 ± 0.49 , and 0.44 ± 0.42 for left nonfrontal tumors ($P = .0113$, 2-sample t test). Tumor location in the right hemisphere (frontal-versus-nonfrontal) also contributed to differences in the LI in the BA but not in the MFG. The mean LI in the BA for right frontal tumors was 0.58 ± 0.26 , and 0.14 ± 0.47 for right nonfrontal tumors ($P = .0119$, two-sample t test). The mean LI in the MFG for right-frontal tumors was 0.56 ± 0.37 , and

0.18 ± 0.74 for right nonfrontal tumors ($P = .12$, two-sample t test).

Comparison of the LI between rsfMRI and Task-Based fMRI

To derive the reliability of the laterality index through resting-state fMRI, we directly compared it with the task-based laterality

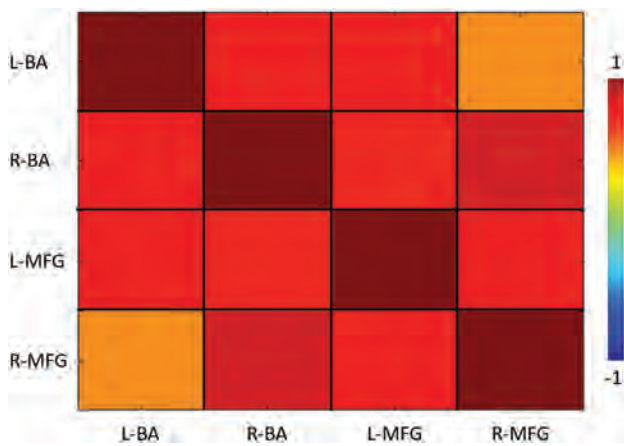


FIG 4. Group-level functional connectivity between the bilateral BA and MFG regions across patients. Positive functional connectivity was observed between the bilateral BA and bilateral MFG regions.

index. We observed overlap between the laterality index derived from rsfMRI and task-based fMRI. Specifically, when we derived the LI on the basis of the BA using rsfMRI, 27/40 patients (67.5%) showed concordance with the laterality index based on a silent word-generation task. Similarly, when we derived the LI using the MFG and rsfMRI, 30/40 patients (75%) showed concordance with the laterality index based on a silent word-generation task.

DISCUSSION

This study is the first to demonstrate that the MFG is a reliable means of lateralizing language networks using rsfMRI in patients with brain tumors. Our study demonstrated that voxel activation in the MFG correlated with that in the BA. Similarly, the LIs in the MFG correlated with LIs in the BA so that the greater the LI in the BA, the greater it was in the MFG. While the MFG had a slightly higher average LI than the BA, we found no statistically significant differences in language lateralization between the MFG and BA. Most important, LIs calculated from rsfMRI showed significant overlap with the LI determined from task-based fMRI.

Although the MFG is a well-known secondary language area,²⁹⁻³¹ research characterizing its exact role in presurgical mapping is limited.^{11,12,14,32,33} In a study of patients with temporal lobe epilepsy, Lehericy et al¹⁴ demonstrated that asymmetric activation in the MFG correlated with hemispheric-dominance determination based on Wada testing. Task-based fMRI has shown similar activation patterns of the MFG in patients with brain tumors who were provided language tasks.^{20,21} The results of our study support these prior findings and suggest that the MFG can be used as an additional indicator in determining language-hemispheric dominance in clinically difficult cases in which a brain tumor could result in false-negative activation in the BA.

In contrast to prior studies that used task-based paradigms to study the MFG, this study provided a comparative measure of the utility of the MFG relative to the BA in determining language lateralization using task-free resting-state fMRI. In those patients with significant physical or cognitive deficits, performing a task can be challenging; rsfMRI has risen as a promising alternate. This study adds to the growing body of evidence that suggests that rsfMRI can be potentially useful for presurgical mapping of elo-

quent cortices.^{5,34-42} Furthermore, in contrast to prior studies that have used a priori seed-based methods for presurgical mapping of language functions with rsfMRI, this study uses a model-free ICA approach that avoided some of the pitfalls of seed-based analysis, including subjective expertise in seed placement.

Our study found no significant effects of tumor grade on language lateralization. However, not unexpectedly, tumor location contributed to language lateralization so that patients with left-hemisphere tumors that were located in the frontal region had lower lateralization compared with those with nonfrontal left-hemisphere tumors. Previous studies have suggested that tumor neovascularity diminished fMRI activation in the tumor hemisphere^{8,43,44} and consequently affected the fMRI determination of true lateralization for language in patients with brain tumors. Our findings are consistent with previous literature that demonstrated that right-handed patients with neoplasms affecting language areas in the left hemisphere had lower LIs compared with healthy controls.⁴⁵

Some limitations to this study merit further research. First, the sample size was small, especially in terms of patients with atypical or right-sided language laterality. Second, although we excluded patients with an operation, we acknowledge that this method may not be generalizable to patients after surgery or patients with major structural lesions that may affect the consistency of standardized anatomic templates. Third, we used a model-free ICA approach; specific parameters such as the number of ICA components could have influenced the results of ICA-based functional MR imaging analyses.

Before surgery, it is important to map the eloquent areas close to a tumor to avoid damaging those areas. Generally, direct cortical stimulation has been the method of choice for making this assessment, but it is limited to detecting mainly the cortical surface areas. Moreover, direct cortical stimulation determination of language-hemisphere dominance is not perfect. There is no one method that can provide a completely accurate lateralization of language. Therefore, multiple modalities must be used to determine lateralization of language with as much accuracy and certainty as possible. This recommendation is especially important in cases in which lateralization based on the BA can be misleading and additional markers are needed. Our results suggest the addition of rsfMRI of the MFG to the list of noninvasive modalities that could be used in patients with gliomas to evaluate hemispheric dominance of language before tumor resection.

CONCLUSIONS

Activation in the MFG parallels that in the BA in non-task-based rsfMRI assessing hemispheric dominance of language. Task-based and rsfMRI comparisons of the BA and MFG are similar. Therefore, clinical use of rsfMRI for language lateralization, specifically by assessing MFG activity, should be considered in patients with brain tumors.

Disclosures: Suril Gohel—UNRELATED: Grants/Grants Pending: National Institutes of Health, Department of Defense. Maria Elena Laino—RELATED: Grant: National Institutes of Health/National Cancer Institute Cancer Center support grant P30 CA008748.* Andrei I. Holodny—RELATED: Grant: National Institutes of Health, Comments: National Institutes of Health—National Institute of Biomedical Imaging and Bioengineering 1R01EB022720-01 (H. Makse and A.I. Holodny, Multiple Principal Investigators), National Institutes of Health—National Cancer Institute 1 R21

CA220144–01 (A.I. Holodny and K. Peck, Multiple Principal Investigators), and subaward on U54 CA 137788 (T. Ahles, Principal Investigator)*; *OTHER RELATIONSHIPS*: President of fMRI Consulting, LLC, a purely educational entity. Behroze Vachha—*RELATED*: Grant: National Institutes of Health/National Cancer Institute Cancer Center support grant P30 CA008748, National Cancer Institute/National Institutes of Health award support number R25CA020449.* *Money paid to the institution.

REFERENCES

- Janecek JK, Swanson SJ, Sabsevitz DS, et al. **Language lateralization by fMRI and Wada testing in 229 patients with epilepsy: rates and predictors of discordance.** *Epilepsia* 2013;54:314–22 CrossRef Medline
- Desmond JE, Sum JM, Wagner AD, et al. **Functional MRI measurement of language lateralization in Wada-tested patients.** *Brain* 1995;118(Pt 6):1411–19 CrossRef Medline
- Dym RJ, Burns J, Freeman K, et al. **Is functional MR imaging assessment of hemispheric language dominance as good as the Wada test?: a meta-analysis.** *Radiology* 2011;261:446–55 CrossRef Medline
- Lehéricy S, Cohen L, Bazin B, et al. **Functional MR evaluation of temporal and frontal language dominance compared with the Wada test.** *Neurology* 2000;54:1625–33 CrossRef Medline
- Tie Y, Rigolo L, Norton IH, et al. **Defining language networks from resting-state fMRI for surgical planning: a feasibility study.** *Hum Brain Mapp* 2014;35:1018–30 CrossRef Medline
- Frost JA, Binder JR, Springer JA, et al. **Language processing is strongly left lateralized in both sexes: evidence from functional MRI.** *Brain* 1999;122 (Pt 2):199–208 CrossRef Medline
- Szaflarski JP, Binder JR, Possing ET, et al. **Language lateralization in left-handed and ambidextrous people: fMRI data.** *Neurology* 2002;59:238–44 CrossRef Medline
- Ulmer JL, Hacein-Bey L, Mathews VP, et al. **Lesion-induced pseudodominance at functional magnetic resonance imaging: implications for preoperative assessments.** *Neurosurgery* 2004;55:569–79, discussion 580–81 Medline
- Hou BL, Bradbury M, Peck KK, et al. **Effect of brain tumor neovascularity defined by rCBV on BOLD fMRI activation volume in the primary motor cortex.** *Neuroimage* 2006;32:489–97 CrossRef Medline
- Sanai N, Mirzadeh Z, Berger MS. **Functional outcome after language mapping for glioma resection.** *N Engl J Med* 2008;358:18–27 CrossRef Medline
- Brown S, Martinez MJ, Parsons LM. **Music and language side by side in the brain: a PET study of the generation of melodies and sentences.** *Eur J Neurosci* 2006;23:2791–803 CrossRef Medline
- Wang S, Zhu Z, Zhang JX, et al. **Broca's area plays a role in syntactic processing during Chinese reading comprehension.** *Neuropsychologia* 2008;46:1371–78 CrossRef Medline
- Abrahams S, Goldstein LH, Simmons A, et al. **Functional magnetic resonance imaging of verbal fluency and confrontation naming using compressed image acquisition to permit overt responses.** *Hum Brain Mapp* 2003;20:29–40 CrossRef Medline
- Leung HC, Gore JC, Goldman-Rakic PS. **Sustained mnemonic response in the human middle frontal gyrus during on-line storage of spatial memoranda.** *J Cogn Neurosci* 2002;14:659–71 CrossRef Medline
- Smolker HR, Depue BE, Reineberg AE, et al. **Individual differences in regional prefrontal gray matter morphometry and fractional anisotropy are associated with different constructs of executive function.** *Brain Struct Funct* 2015;220:1291–306 CrossRef Medline
- Steinmann E, Schmalor A, Prehn-Kristensen A, et al. **Developmental changes of neuronal networks associated with strategic social decision-making.** *Neuropsychologia* 2014;56:37–46 CrossRef Medline
- Brennan NP, Peck KK, Holodny A. **Language mapping using fMRI and direct cortical stimulation for brain tumor surgery: the good, the bad, and the questionable.** *Top Magn Reson Imaging* 2016;25:1–10 CrossRef Medline
- Dong JW, Brennan NM, Izzo G, et al. **fMRI activation in the middle frontal gyrus as an indicator of hemispheric dominance for language in brain tumor patients: a comparison with Broca's area.** *Neuroradiology* 2016;58:513–20 CrossRef Medline
- Japee S, Holiday K, Satyshur MD, et al. **A role of right middle frontal gyrus in reorienting of attention: a case study.** *Front Syst Neurosci* 2015;9:23 Medline
- Roux FE, Boulanouar K, Lotterie JA, et al. **Language functional magnetic resonance imaging in preoperative assessment of language areas: correlation with direct cortical stimulation.** *Neurosurgery* 2003;52:1335–45, discussion 1345–47 Medline
- Kamada K, Sawamura Y, Takeuchi F, et al. **Expressive and receptive language areas determined by a non-invasive reliable method using functional magnetic resonance imaging and magnetoencephalography.** *Neurosurgery* 2007;60:296–305, discussion 305–06 Medline
- Bharath RD, Munivenkatappa A, Gohel S, et al. **Recovery of resting brain connectivity ensuing mild traumatic brain injury.** *Front Hum Neurosci* 2015;9:513 CrossRef Medline
- Taylor PA, Gohel S, Di X, et al. **Functional covariance networks: obtaining resting-state networks from intersubject variability.** *Brain Connect* 2012;2:203–17 CrossRef Medline
- Taylor PA, Saad ZS. **FATCAT: (an efficient) functional and tractographic connectivity analysis toolbox.** *Brain Connect* 2013;3:523–35 CrossRef Medline
- Binder JR, Sabsevitz DS, Swanson SJ, et al. **Use of preoperative functional MRI to predict verbal memory decline after temporal lobe epilepsy surgery.** *Epilepsia* 2008;49:1377–94 CrossRef Medline
- Seghier ML. **Laterality index in functional MRI: methodological issues.** *Magn Reson Imaging* 2008;26:594–601 CrossRef Medline
- Deblaere K, Boon PA, Vandemaele P, et al. **MRI language dominance assessment in epilepsy patients at 1.0 T: region of interest analysis and comparison with intracarotid amytal testing.** *Neuroradiology* 2004;46:413–20 Medline
- Springer JA, Binder JR, Hammelke TA, et al. **Language dominance in neurologically normal and epilepsy subjects: a functional MRI study.** *Brain* 1999;122 (Pt 11):2033–46 CrossRef Medline
- Rogalski E, Cobia D, Harrison TM, et al. **Anatomy of language impairments in primary progressive aphasia.** *J Neurosci* 2011;31:3344–50 CrossRef Medline
- Fertonani A, Rosini S, Cotelli M, et al. **Naming facilitation induced by transcranial direct current stimulation.** *Behav Brain Res* 2010;208:311–18 CrossRef Medline
- Grossman M, Cooke A, DeVita C, et al. **Age-related changes in working memory during sentence comprehension: an fMRI study.** *Neuroimage* 2002;15:302–17 CrossRef Medline
- Acheson DJ, MacDonald MC. **Verbal working memory and language production: common approaches to the serial ordering of verbal information.** *Psychol Bull* 2009;135:50–68 CrossRef Medline
- Baddeley A. **Working memory and language: an overview.** *J Commun Disord* 2003;36:189–208 CrossRef Medline
- DeSalvo MN, Douw L, Takaya S, et al. **Task-dependent reorganization of functional connectivity networks during visual semantic decision making.** *Brain Behav* 2014;4:877–85 CrossRef Medline
- Mitchell TJ, Hacker CD, Breshears JD, et al. **A novel data-driven approach to preoperative mapping of functional cortex using resting-state functional magnetic resonance imaging.** *Neurosurgery* 2013;73:969–82, discussion 982–83 CrossRef Medline
- Rosazza C, Aquino D, D'Incerti L, et al. **Preoperative mapping of the sensorimotor cortex: comparative assessment of task-based and resting-state FMRI.** *PLoS One* 2014;9:e98860 CrossRef Medline
- Doucet GE, Pustina D, Skidmore C, et al. **Resting-state functional connectivity predicts the strength of hemispheric lateralization for language processing in temporal lobe epilepsy and normals.** *Hum Brain Mapp* 2015;36:288–303 CrossRef Medline
- Zhang D, Johnston JM, Fox MD, et al. **Preoperative sensorimotor mapping in brain tumor patients using spontaneous fluctuations in neuronal activity imaged with functional magnetic resonance imaging: initial experience.** *Neurosurgery* 2009;65(6 Suppl):226–36 CrossRef Medline
- Liu H, Buckner RL, Talukdar T, et al. **Task-free presurgical mapping**

- using functional magnetic resonance imaging intrinsic activity. *J Neurosurg* 2009;111:746–54 CrossRef Medline
40. Kokkonen SM, Nikkinen J, Remes J, et al. **Preoperative localization of the sensorimotor area using independent component analysis of resting-state fMRI.** *Magn Reson Imaging* 2009;27:733–40 CrossRef Medline
41. Shimony JS, Zhang D, Johnston JM, et al. **Resting-state spontaneous fluctuations in brain activity: a new paradigm for presurgical planning using fMRI.** *Acad Radiol* 2009;16:578–83 CrossRef Medline
42. Leuthardt EC, Roland J, Breshears JD, et al. **Listening to the brain: new techniques in intraoperative brain mapping.** *Neurosurgery* 2013;60(Suppl 1):64–69 CrossRef Medline
43. Holodny AI, Schulder M, Liu WC, et al. **The effect of brain tumors on BOLD functional MR imaging activation in the adjacent motor cortex: implications for image-guided neurosurgery.** *AJNR Am J Neuroradiol* 2000;21:1415–22 Medline
44. Schreiber A, Hubbe U, Ziyeh S, et al. **The influence of gliomas and nonglial space-occupying lesions on blood-oxygen-dependent contrast enhancement.** *AJNR Am J Neuroradiol* 2000;21:1055–63 Medline
45. Partovi S, Jacobi B, Rapps N, et al. **Clinical standardized fMRI reveals altered language lateralization in patients with brain tumor.** *AJNR Am J Neuroradiol* 2012;33:2151–57 CrossRef Medline

Treatment Response Prediction of Nasopharyngeal Carcinoma Based on Histogram Analysis of Diffusional Kurtosis Imaging

N. Tu, Y. Zhong, X. Wang, F. Xing, L. Chen, and G. Wu



ABSTRACT

BACKGROUND AND PURPOSE: The prediction of treatment response is important in planning and modifying the chemoradiation therapy regimen. This study aimed to explore the quantitative histogram indices for treatment-response prediction of nasopharyngeal carcinoma based on diffusional kurtosis imaging compared with a standard ADC value (ADC_{standard}).

MATERIALS AND METHODS: Thirty-six patients with an initial diagnosis of locoregionally advanced nasopharyngeal carcinoma and diffusional kurtosis imaging acquisitions before and after neoadjuvant chemotherapy were enrolled. Patients were divided into respond-versus-nonrespond groups after neoadjuvant chemotherapy and residual-versus-nonresidual groups after radiation therapy. Histogram parameters of diffusional kurtosis imaging–derived parameters (ADC, ADC coefficient corrected by the non-Gaussian model [D], apparent kurtosis coefficient without a unit [K]) were calculated. The ADC_{standard} was calculated on the basis of intravoxel incoherent movement data. The intraclass correlation coefficient, Kolmogorov-Smirnov test, Student *t* test or Mann-Whitney *U* test, and receiver operating characteristic analysis were performed.

RESULTS: Most of the parameters had good-to-excellent consistency (intraclass correlation coefficient = 0.675–0.998). The pre- ADC_{standard} , pre-ADC (10th, 25th, 50th percentiles), pre-D (10th, 25th, 50th percentiles), and pre- $K_{50\text{th}}$ were significantly different between the respond and nonrespond groups, while the pre- $ADC_{10\text{th}}$, pre- $K_{90\text{th}}$, post- $ADC_{50\text{th}}$, post- $K_{75\text{th}}$, post- $K_{90\text{th}}$, and the percentage change of parameters before and after neoadjuvant chemotherapy ($\Delta ADC_{50\text{th}}\%$) were significantly different between the residual and nonresidual groups (all $P < .05$). Receiver operating characteristic analysis indicated that setting pre- $D_{50\text{th}} = 0.875 \times 10^{-3} \text{mm}^2/\text{s}$ as the cutoff value could result in optimal diagnostic performance for neoadjuvant chemotherapy response prediction (area under the curve = 0.814, sensitivity = 0.70, specificity = 0.92), while the post- $K_{90\text{th}} = 1.035$ (area under the curve = 0.829, sensitivity = 0.78, specificity = 0.72), and $\Delta ADC_{50\text{th}}\% = 0.253$ (area under the curve = 0.833, sensitivity = 0.94, specificity = 0.72) were optimal for radiation therapy response prediction.

CONCLUSIONS: Histogram analysis of diffusional kurtosis imaging may potentially predict the neoadjuvant chemotherapy and short-term radiation therapy response in locoregionally advanced nasopharyngeal carcinoma, therefore providing evidence for modification of the treatment regimen.

ABBREVIATIONS: CR = complete response; D = ADC coefficient corrected by the non-Gaussian model; DKI = diffusional kurtosis imaging; IMRT = intensity-modulated radiation therapy; K = apparent kurtosis coefficient without a unit; NAC = neoadjuvant chemotherapy; NPC = nasopharyngeal carcinoma; PR = partial response; SD = stable disease; $\Delta ADC_{50\text{th}}\%$ = the percentage change of parameters before and after neoadjuvant chemotherapy

Nasopharyngeal carcinoma (NPC) is a territorial epidemic in southern China and Southeast Asia; in 2012, seventy-one percent of new NPC cases were in these areas.¹ Neoadjuvant chemotherapy (NAC) followed by intensity-modulated radiation

therapy (IMRT) has currently been widely accepted as the preferred treatment for NPC. NAC improves quality of life by optimizing the IMRT plan² due to reducing the overall tumor volume and boosting radiation therapy sensitivity, thereby facilitating local control and reducing the rate of distant metastases.³ However, the resistance of patients with locoregionally advanced NPC to the

Received January 18, 2018; accepted after revision November 16.

From the Departments of Radiology (N.T., X.W., F.X., G.W.) and Radiation and Medical Oncology (Y.Z., L.C.), Zhongnan Hospital of Wuhan University, Wuhan University, Hubei, China.

This study received funding from the National Key Basic Research Program of the National Natural Science Foundation of China (grant No. 2016YFC1304702 to Guangyao Wu).

Ning Tu, Yahua Zhong, and Xiangyu Wang contributed equally to this work.

Please address correspondence to Guangyao Wu, MD, No. 169, Donghu Rd, Department of Radiology, Zhongnan Hospital of Wuhan University, Wuhan 430071, Hubei, China; e-mail: wuguangyao2002@163.com

Indicates open access to non-subscribers at www.ajnr.org

Indicates article with supplemental on-line tables.

<http://dx.doi.org/10.3174/ajnr.A5925>

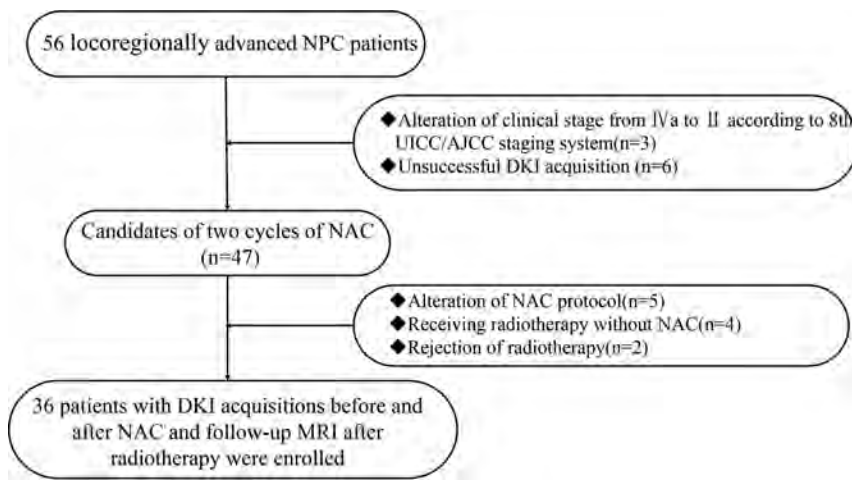


FIG 1. Flowchart of patient selection.

conventional NAC-plus-IMRT regimen leads to poor survival and poor quality of life after retreatment.⁴ The prediction of treatment response can offer important references for individualized treatment-strategy planning. The treatment response after 2 NAC cycles has been reported as a valuable time point to choose patients who respond well to chemoradiation therapy.^{5,6}

Diffusion-weighted imaging, based on free diffusion of water molecules following Gaussian distribution, is the most widely used functional MR imaging technology.^{7,8} However, water molecular diffusion in biologic tissues is restricted by various barriers, resulting in not following a Gaussian distribution. By means of a non-Gaussian distribution model, diffusional kurtosis imaging (DKI) can yield kurtosis and diffusion coefficients corrected by the non-Gaussian model.^{9,10} The histogram analysis can reflect the whole-tumor heterogeneity¹¹ and has the potential for treatment-response prediction.¹² The predictive value of histogram analysis of DKI-derived parameters in assessing the treatment response is still unclear. Therefore, in this study, we aimed to use the histogram analysis of DKI parameters in comparison with a standard ADC value (ADC_{standard}) to explore the quantitative indices for prediction of treatment-response assessment in patients with NPC.

MATERIALS AND METHODS

Patient Selection and Treatment Protocols

Our institutional review board approved the protocol of this retrospective study and waived the requirement for obtaining informed consent. Between December 2015 and March 2017, 56 newly diagnosed patients with locoregionally advanced NPC (clinical stages III and IV) with no pretreatment were retrospectively recruited. All patients' Tumor, Node, Metastasis status and clinical stage were re-evaluated by oncologists referring to the eighth edition of the American Joint Committee on Cancer/Union for International Cancer Control *TNM Classification for Nasopharyngeal Cancers* (<https://emedicine.medscape.com/article/2048007-overview>).¹³ Nine patients were excluded (3 for alteration of clinical stage from stage IVa to stage II after restaging, 6 for unsuccessful DKI acquisitions).

Forty-seven individuals were candidates for 2 cycles of NAC (21 days per cycle). In each cycle, patients were given a dose of

25 mg/m² of cisplatin (DDP) on days 1, 2, and 3 and 75 mg/m² of docetaxel (DOC) on day 1. Eleven patients were excluded (5 for stopping treatment due to severe complications, 4 for receiving radiation therapy directly without NAC, 2 for refusal of further radiation therapy). The remaining 36 patients then received IMRT with a total dose of 70 Gy in 31 fractions. Among them, 20 patients received concurrent chemotherapy with nedaplatin (50 mg/m² per week). The flow diagram of patient selection is shown in Fig 1.

MR Imaging Acquisition

MR imaging examinations were performed using a 3T MR imaging scanner (Magnetom Prisma; Siemens, Erlangen, Germany) with 20-channel head and neck combined coil. The routine MR imaging protocol includes sagittal and axial T1-weighted imaging using a turbo spin-echo technique (TR/TE = 670/9 ms, section thickness/gap = 5/1 mm, FOV = 220 mm, matrix = 240 × 320) before and after contrast injection, axial T2-weighted imaging using Dixon techniques (TR/TE = 4070/81 ms, section thickness/gap = 4/1 mm, FOV = 220 mm, matrix = 224 × 320), and oblique coronal T2WI with fat suppression using a turbo inversion recovery technique (TR/TE = 3300/37ms, section thickness/gap = 3/0.3 mm, FOV = 240 mm, matrix = 224 × 320).

For DKI acquisitions, a single-shot echo-planar imaging diffusion sequence was used (TR/TE = 4900/60 ms, section thickness/gap = 5/0 mm, FOV = 280 mm, matrix = 116 × 128, concatenation = 1) in 3 orthogonal directions, with 5 b-values (200, 500, 1000, 1500, 2000 /mm²). The total acquisition time of DKI was 3 minutes 26 seconds.

Standard ADC using $b = 0$ and $b = 1000$ mm²/s was calculated on the basis of intravoxel incoherent movement data. Intravoxel incoherent movement was acquired by a ZOOMIT (Siemens) single-shot-EPI diffusion sequence (TR/TE = 3000/62.4 ms, section thickness/gap = 4/0 mm, FOV = 200 mm, matrix = 44 × 90, concatenation = 1) in 3 orthogonal directions, with 11 b-values (0, 50, 100, 150, 200, 300, 400, 500, 700, 900, 1000 s/mm²). The total acquisition time of intravoxel incoherent movement was 5 minutes 26 seconds.

Dynamic contrast-enhanced imaging was also performed. The intravoxel incoherent movement and dynamic contrast-enhanced imaging analysis were not assessed in this study.

The routine and DKI protocols were performed before starting NAC treatment and within 3 days after 2 cycles of NAC. Routine MR imaging protocols were performed 3 months after radiation therapy.

DKI Data Analysis

The entire image-analysis algorithm was achieved using an in-house program written in Matlab (Version R2013b; MathWorks, Natick, Massachusetts). The DKI parameter was fitted according to the following equation¹⁴:

$$1) \quad \frac{S_b}{S_0} = \exp(-b \times D + \frac{1}{6} \times b^2 \times D^2 \times K).$$

S_0 is signal intensity at $b = 0$, S_b is signal intensity for a given b -value. D is the apparent diffusion coefficient corrected by the non-Gaussian model, K is the apparent kurtosis coefficient without units.

The DKI-derived ADC value in this study was a mean value obtained using all b -values fitting a conventional monoexponential model according to the following equation¹⁴:

$$2) \quad S_b = S_0 \times \exp(-b \times ADC).$$

We drew ROIs manually on all the sections involving tumors in DKI, avoiding the large vessels and parapharyngeal lymph nodes; they subsequently were copied automatically onto the DKI-derived parameter maps (ADC, ADC coefficient corrected by the non-Gaussian model [D], and apparent kurtosis coefficient without a unit [K] maps) by software. In tumors with muscle and skull base invasion, the involved skull base and muscle were excluded.

Histogram analysis of the DKI-derived parameters (ADC, D, and K) was performed using SPSS Statistics 24.0 (IBM, Armonk, New York). On the basis of the whole-tumor-volume ROIs, we derived the following parameters: 1) 10th percentile; 2) 25th percentile; 3) 50th percentile (median); 4) 75th percentile; 5) 90th percentile; 6) mean; 7) standard deviation; 8) skewness; and 9) kurtosis.¹⁵

All ROI placements were performed by 2 experienced radiologists (with 8 and 10 years of experience in head and neck MR imaging) who were blinded to the study design, with reference to T2-fat suppression, contrast-enhanced T1WI, and dynamic contrast-enhanced MR images. The measurement results of the 2 radiologists were used to assess the interreader reproducibility. The average of the 2 measurement results was used for further statistical analysis.

Standard ADC Analysis

Because the DKI protocol only contains b -values of $>200 \text{ s/mm}^2$, the standard ADC value (ADC_{standard}) using $b = 0$ and $b = 1000 \text{ mm/s}^2$ was calculated on the basis of intravoxel incoherent movement data with the Z420 workstation (syngo VH22B; Siemens). ROIs were manually drawn on the maximum cross-sectional area of primary lesions. Limited by the workstation, we collected only the mean value of standard ADC for analysis.

Evaluation of NAC Response

After 2 NAC cycles, shrinking ratios of the target lesions, including primary tumor and pathologic lymph nodes with diameters of $>15 \text{ mm}$, were calculated on the basis of RECIST 1.1 criteria (<http://recist.eortc.org/recist-1-1-2/>).¹⁶ Compared with initial target lesions, a reduction of the sum of the longest diameter of $\geq 30\%$ after treatment was considered as a partial response (PR), and the others who did not reach 30% were regarded as having stable disease (SD). The absence of visible and viable tumors with no lymph nodes having a diameter of $>10 \text{ mm}$ based on the MR imaging assessment was considered a complete response (CR).

After 2 NAC cycles, patients achieving CR or PR were categorized as the respond group (Fig 2), while SD was the nonrespond group (Fig 3).

Evaluation of Radiation Therapy Response

After the whole chemoradiotherapy protocol (2 NAC cycles and IMRT), the radiation therapy response was calculated on the basis RECIST 1.1 criteria¹⁶ compared with initial target lesions. Patients who achieved CR were recategorized as the nonresidual group (Fig 2), while those with PR or SD were in the residual group (Fig 3).

Statistical Analysis

Statistical analysis was performed using SPSS Statistics 24.0 and Medcalc 11.4. The parameters before and after NAC were marked as $\text{preparameter}_{\text{histogram parameter}}$ and $\text{postparameter}_{\text{histogram parameter}}$. Experimental data were presented as arithmetic means unless otherwise stated. Interobserver consistency of the parameters between the 2 readers was assessed using the intraclass correlation coefficient with 95% confidence intervals. The Kolmogorov-Smirnov test was used to assess the normality of data distribution. Then the statistical comparisons between the respond and nonrespond groups and between the residual and nonresidual groups was performed using the independent-samples t test or Mann-Whitney U test accordingly. Receiver operating characteristic analyses and areas under the curve were used to assess the diagnostic efficiency of parameters in the prediction of treatment response. The cutoff value was established by maximizing the Youden index (Youden index = sensitivity + specificity - 1). $P < .05$ was considered as statistically significant.

RESULTS

Clinical Results

Thirty-six patients (27 males, and 9 females, with a mean age of 48.5 years; range, 17–67 years) with successful DKI acquisitions before and after NAC and MR imaging follow-up acquisitions after radiation therapy were included. Patient characteristics are shown in On-line Table 1 in detail. No obvious differences of clinical characteristics, involving age, sex, Tumor, Node, Metastasis staging, and clinical staging were found between the NAC and radiation therapy response subgroups. The MR images and DKI parameter maps of representative patients with NPC are shown in Figs 2 and 3.

Interreader Agreement

The interreader intraclass correlation coefficient for the measurements of DKI-derived histogram parameters between 2 radiologists revealed that the $\text{pre-}ADC_{\text{skew}}$, $\text{post-}ADC_{\text{skew}}$, $\text{post-}D_{\text{mean}}$, $\text{post-}K_{\text{standard deviation}}$, $\text{post-}K_{\text{skew}}$, and $\text{post-}K_{\text{kurtosis}}$ had poor-to-moderate consistency (intraclass correlation = 0.001–0.576), $\text{post-}D_{\text{standard deviation}}$ had good consistency (intraclass correlation = 0.675), and other parameters had excellent consistency (intraclass correlation > 0.81). After excluding the parameters with poor-to-moderate consistency, the average values of the other parameters measured by the 2 radiologists were calculated for further statistical analysis.

Parameters before NAC for Prediction of NAC Response

After 2 NAC cycles, 1 patient who achieved CR and 22 patients who achieved PR were classified as the respond group, while the

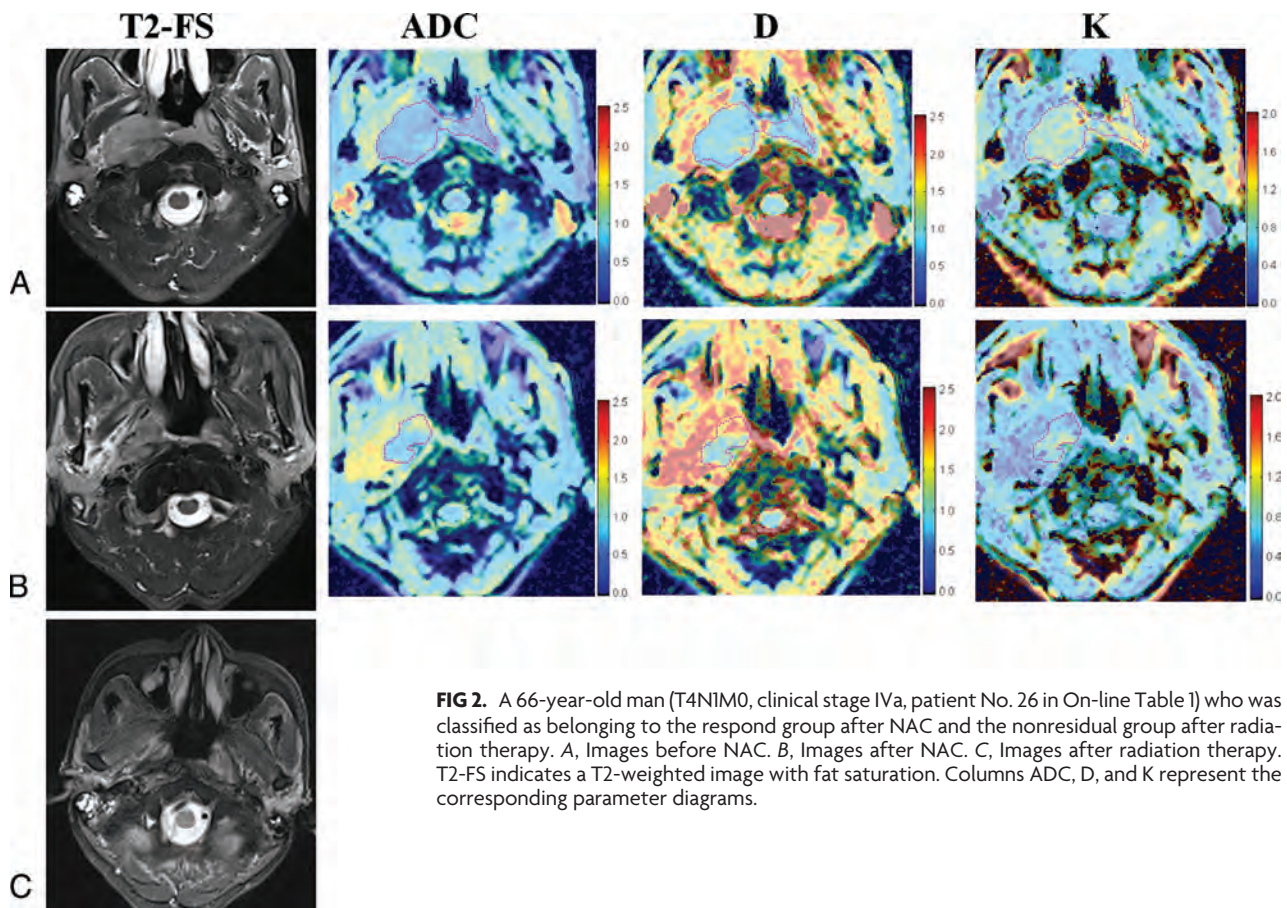


FIG 2. A 66-year-old man (T4N1M0, clinical stage IVa, patient No. 26 in On-line Table 1) who was classified as belonging to the respond group after NAC and the nonresidual group after radiation therapy. *A*, Images before NAC. *B*, Images after NAC. *C*, Images after radiation therapy. T2-FS indicates a T2-weighted image with fat saturation. Columns ADC, D, and K represent the corresponding parameter diagrams.

other 13 patients who achieved SD were classified as the nonrespond group.

Compared with the nonrespond group, the respond group demonstrated higher ADC values, higher D values, and lower K values. The pre-ADC_{standard} was significantly higher in the respond group than in the nonrespond group (0.95 ± 0.12 versus 0.83 ± 0.14 , $P = .008$). The pre-ADC_{mean} and pre-ADC_{50th} were significantly lower than the pre-ADC_{standard} (0.63 ± 0.09 , 0.60 ± 0.10 versus 0.91 ± 0.14 , $P < .001$). The correlation between pre-ADC_{mean} and pre-ADC_{standard} was weak ($r = 0.104$, $P = .545$), while that between pre-ADC_{50th} and pre-ADC_{standard} was good ($r = 0.525$, $P = .001$).

After Bonferroni-Holm correction, pre-ADC (10th, 25th, 50th percentiles) and pre-D (10th, 25th, 50th percentiles) were significantly higher in the respond group than in the nonrespond group (P value = .002–.047), while the pre-K_{50th} was significantly lower ($P = .018$). Details are presented in On-line Table 2 and Fig 4.

Receiver operating characteristic analysis (On-line Table 3 and Fig 5) indicated that the setting $\text{pre-D}_{50th} \times 10^{-3} = 0.875 \text{ mm}^2/\text{s}$ as the cutoff value could obtain optimal diagnostic performance (area under the curve = 0.814, sensitivity = 0.70, specificity = 0.92) for the prediction of the NAC treatment response.

Parameters before and after NAC for Prediction of Radiation-Therapy Response

After radiation therapy with or without concurrent chemotherapy ($n = 20$ versus 16), 18 patients who achieved CR were classified as the nonresidual group, while 10 patients who achieved PR

and 8 patients who achieved SD were classified as the residual group. With a Fisher exact test (double-tailed $P = .315$), our study showed no significant difference in the treatment response to radiation therapy between subgroups with or without concurrent chemotherapy.

Compared with the residual group, the nonresidual group had higher ADC values, higher D values, and lower K values both before and after NAC. The ADC and D values significantly increased, while the K value significantly decreased after NAC (all $P < .05$). After Bonferroni-Holm correction, the pre-ADC_{10th}, pre-K_{90th}, and post-ADC_{50th} were significantly higher, while the post-K_{75th} and post-K_{90th} were significantly lower in the nonresidual group compared with the residual group (all, $P < .005$).

The pre-ADC_{standard} value was slightly higher in the residual group compared with the nonresidual group ($P = .397$), while the post-ADC_{standard} had no statistical significance ($P = .959$).

The analysis of percentage change of parameters before and after NAC showed that there were 8 percentage change parameters with P values $< .05$ (P value = .005–.04), including ADC (25th, 50th, 90th percentiles), D (25th percentile, standard deviation) and K (50th, 75th, 90th percentiles). After Bonferroni-Holm correction, only the percentage change of parameters before and after neoadjuvant chemotherapy ($\Delta\text{ADC}_{50th}\%$) was significantly different between groups ($P = .005$). Details are presented in On-line Table 4 and Fig 4.

Receiver operating characteristic analysis (On-line Table 3 and Fig 6) indicated that among all time point parameters, setting

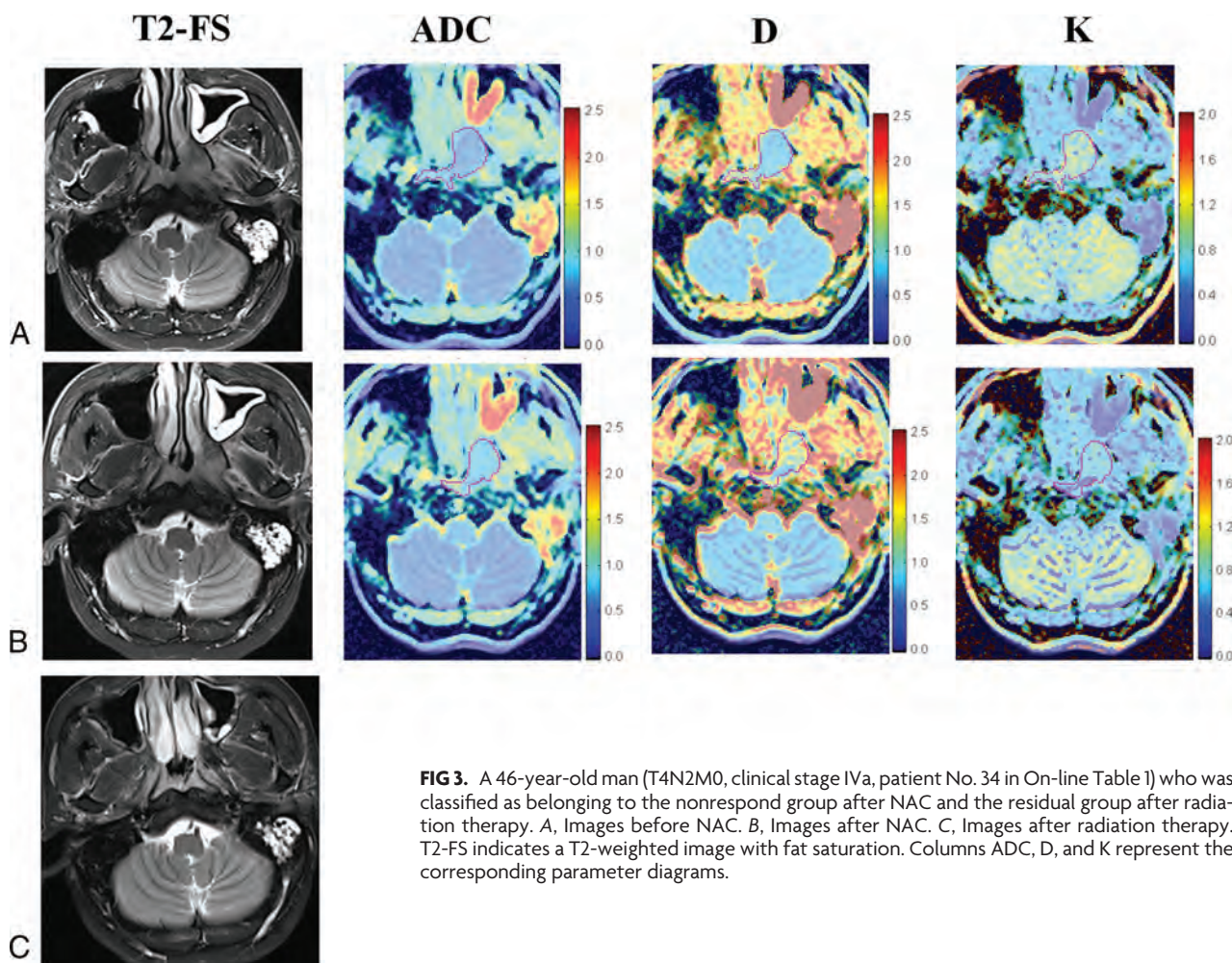


FIG 3. A 46-year-old man (T4N2M0, clinical stage IVa, patient No. 34 in On-line Table 1) who was classified as belonging to the nonrespond group after NAC and the residual group after radiation therapy. *A*, Images before NAC. *B*, Images after NAC. *C*, Images after radiation therapy. T2-FS indicates a T2-weighted image with fat saturation. Columns ADC, D, and K represent the corresponding parameter diagrams.

post- $K_{90th} = 1.035$ as the cutoff value could obtain optimal diagnostic performance (area under the curve = 0.829, sensitivity = 0.78, specificity = 0.72) for the prediction of the treatment response to radiation therapy, while the setting $\Delta ADC_{50th}\% = 0.253$ could obtain even better diagnostic performance (area under the curve = .833, sensitivity = 0.94, specificity = 0.72), though with no significance ($P > .05$).

DISCUSSION

Our study demonstrated that the histogram parameters derived from the DKI technique were feasible for predicting the tumor response of NAC and short-term radiation therapy in patients with NPC, while standard ADC can only predict the NAC response.

Prediction of treatment response has crucial importance in treatment-strategy planning and modification. The advantage and protocol of NAC have not been completely established. Although the necessity of the combination of docetaxel, cisplatin, and fluorouracil remains controversial,¹⁷⁻¹⁹ low-dose regimens of docetaxel, cisplatin, and fluorouracil were reported to have substantially good tolerance and compliance rates.²⁰ Moreover, molecular-targeted therapy in patients with NPC has become a research hot point. The addition of bevacizumab²¹ or nimotuzumab^{4,22} to the conventional docetaxel and cisplatin²³ protocol has been reported to have the potential to delay the progression of subclinical distant disease and modify the long-term survival. The

early identification of patients who may have resistance to NAC or IMRT can provide evidence for treatment-regimen modification. Our study demonstrated no significant difference in the radiation therapy response between the IMRT group with or without concurrent chemotherapy. Similarly, Zhang et al²⁴ reported that concurrent chemotherapy with IMRT after NAC for locoregionally advanced NPC is probably not necessary. However, this observation needs further evidence from multicenter clinical trials.

A previous study based on long-term clinical outcomes has reported that the skewness of the ADC distribution curve was a predictor of local failure in patients with NPC.²⁵ Another retrospective study demonstrated more positive results, indicating that the mean and median values of pretreatment ADC might provide useful information for predicting outcome and selecting high-risk patients appropriate for more aggressive therapy.⁸ Our study demonstrated that $ADC_{standard}$ and ADC derived from the DKI model before initiating NAC were both able to predict the NAC response. However, the prediction value of $ADC_{standard}$ and ADC derived from the DKI model in short-term radiation therapy was limited. The method of response evaluation and the time interval of follow-up may contribute to this controversial result. The relationship between short-term and long-term outcomes after chemoradiotherapy has not been studied. The difference in the prediction efficiency of the radiation therapy response between our study and previous studies may suggest that the short-term radi-

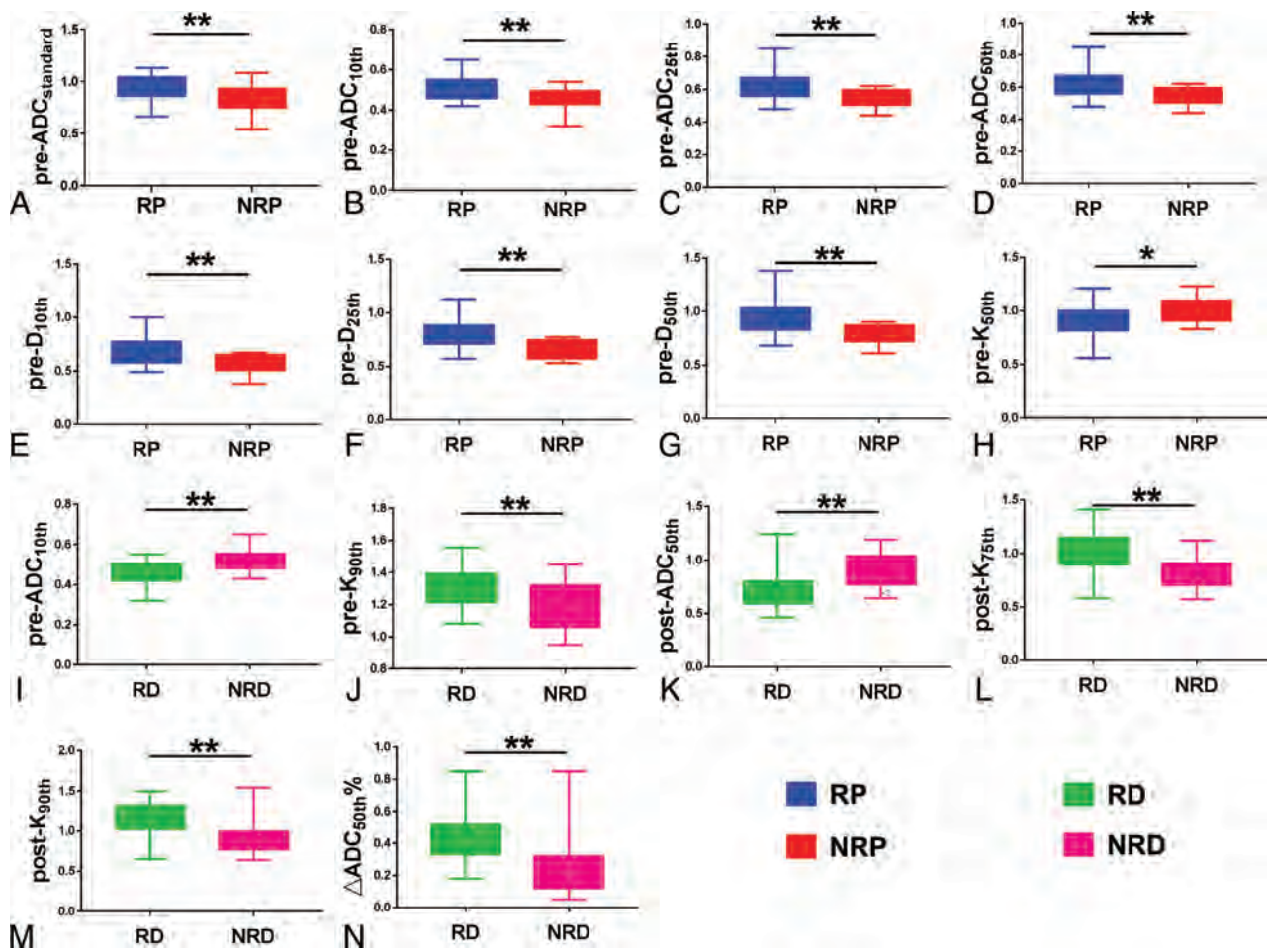


FIG 4. Parameters that were significantly different between the respond (RP) and nonrespond (NRP) groups (A–H) and between residual (RD) and nonresidual (NRD) groups (I–N). The asterisk indicates $P < .05$; double asterisks, $P < .01$.

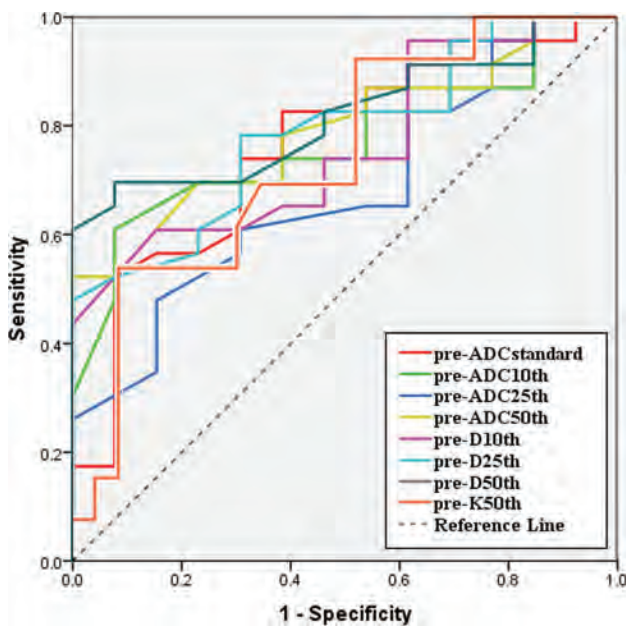


FIG 5. Receiver operating characteristic analysis curves for parameters in the prediction of NAC treatment response. The setting pre-D_{50th} = 0.875 mm²/s as the cutoff value could yield optimal diagnostic performance (area under the curve = 0.814, sensitivity = 0.70, specificity = 0.92).

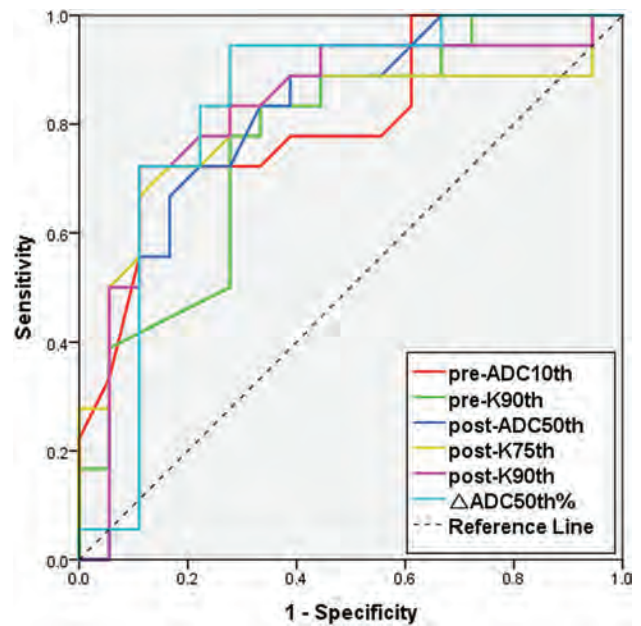


FIG 6. Receiver operating characteristic analysis curves for parameters in the prediction of treatment response to radiation therapy. The setting Δ ADC_{50th}% = 0.253 as the cutoff value could obtain optimal diagnostic performance (area under the curve = 0.833, sensitivity = 0.94, specificity = 0.72).

ation therapy (3 months after the whole chemoradiotherapy protocol) response may have a weak correlation with long-term outcome.

In our study, the correlation between mean ADC values derived from DKI models covering whole tumor and ADC_{standard} covering the largest level of tumor was weak, while the correlation between median ADC derived from DKI models and ADC_{standard} was good and these two parameters both have good diagnostic efficiency in NAC response assessment. As the selection of ROIs varies between these two parameters, it may suggest that when calculating ADC value, the median value is prior in whole-tumor ROI drawing, while mean value prior in one-slice ROI.

Our study has demonstrated that higher ADC values, higher D values, and lower K values are related to positive NAC and radiation therapy responses, consistent with previous studies in NPC^{6,27,28} and head and neck squamous cell carcinoma.^{29,30} Moreover, an increase in ADC was seen after NAC. Previous studies have reported that the Δ ADC was significantly lower in patients with later tumor recurrence than in those with complete remission, similar to our results.^{30,31} Similarly, in our study, Δ ADC_{50th} demonstrated the highest diagnostic performance in the prediction of radiation therapy response. Although this trend appears to be the norm, there have been cases in which a decrease, rather than an increase, in ADC measurements has been reported to correlate with a positive response to NAC.³² Tumors consist of a complex microenvironment composed of immune, stromal, and cancer cells, any mediator of which can foster cancer growth and therapy resistance.³³ Previous study has demonstrated that low ADC values correlate well with a high clinical stage and high tumor aggressiveness, which are characterized by more vascular hyperplasia and necrosis, which may result in therapy resistance.^{11,34–36}

As the complexity of tumor microenvironment increases, the water molecular diffusion restriction increases, resulting in a higher deviation of the Gaussian distribution. Current state-of-the-art multiparametric MR imaging introduces the kurtosis model to reflect the non-Gaussian water molecular diffusion, which may reflect physiologic features and pathologic changes by investigating tissue cellularity and heterogeneity at the micron level,³⁴ and can monitor its changes after therapy.³⁷ A recent clinical study showed that DKI was the best technique, with a diagnostic accuracy of 0.93 in predicting local control in nasal or sinonasal squamous cell carcinoma.¹² Previous studies have reported that the D parameter excludes the perfusion-related signal in pixels and reflects more detail about tumor microstructure complexity than ADC.^{34,38,39} Fujima et al¹² suggested that the low treatment-response area represents a lower D value area, while higher treatment sensitivity areas had increased D values. In our study, the pre-D_{50th} value was lower than the mean value, representing components with lower D values, which may lead to treatment resistance and have the highest diagnostic ability in NAC treatment-response assessment.

The apparent diffusional kurtosis (K parameter, unitless) reflects the peaked distribution of tissue diffusivity that occurs in the context of non-Gaussian diffusion behavior and increases with the microstructural complexity of tissue.^{40,41} Similarly, our study showed that the nonrespond and residual groups are asso-

ciated with higher K values. Among time point parameters, the post-K_{90th}, which represents higher K value components that may lead to treatment resistance, has the best predictive value for the assessment of radiation therapy response.

Although this study revealed the feasibility of DKI parameters in the prediction of NAC and radiation therapy outcome, the accurate biologic mechanism of treatment resistance remains unclear. This study may provide a novel perspective to explore the mechanism of treatment resistance of tumors in consideration of the histogram distribution of water diffusion characteristics.

Limitations

This study has some limitations. First, our study was retrospective with a small sample size and short-term follow-up, enrolling only patients with locoregionally advanced NPC. Second, the assessment of the treatment response to radiation therapy in our study included only patients who received radiation therapy after NAC, causing selection bias and limiting the reliability of this study in the assessment of the treatment response to radiation therapy. Third, the measurement of change in primary tumor size was based on dimensions. Choosing the same level and site before and after treatment was difficult; therefore, volume measurement for treatment response assessment should be emphasized in a future study.

CONCLUSIONS

Histogram analysis of diffusional kurtosis imaging may potentially predict the response of NAC and short-term radiation therapy, therefore providing evidence for modification of the treatment regimen.

ACKNOWLEDGMENTS

We would like to acknowledge the assistance of Tong San Koh, Haijun Yu, Hongyan Zhang, Zheng Li, Yong Huang, and Liu Shi.

REFERENCES

1. Chua ML, Wee JT, Hui EP, et al. **Nasopharyngeal carcinoma.** *Lancet* 2016;387:1012–24 CrossRef Medline
2. Yang H, Chen X, Lin S, et al. **Treatment outcomes after reduction of the target volume of intensity-modulated radiotherapy following induction chemotherapy in patients with locoregionally advanced nasopharyngeal carcinoma: a prospective, multi-center, randomized clinical trial.** *Radiother Oncol* 2018;126:37–42 CrossRef Medline
3. Cao SM, Yang Q, Guo L, et al. **Neoadjuvant chemotherapy followed by concurrent chemoradiotherapy versus concurrent chemoradiotherapy alone in locoregionally advanced nasopharyngeal carcinoma: a phase III multicentre randomised controlled trial.** *Eur J Cancer* 2017;75:14–23 CrossRef Medline
4. Yao JJ, Zhang LL, Gao TS, et al. **Comparing treatment outcomes of concurrent chemoradiotherapy with or without nimotuzumab in patients with locoregionally advanced nasopharyngeal carcinoma.** *Cancer Biol Ther* 2018;1–6. [Epub ahead of print] CrossRef Medline
5. Zheng D, Chen Y, Liu X, et al. **Early response to chemoradiation therapy for nasopharyngeal carcinoma treatment: value of dynamic contrast-enhanced 3.0 T MRI.** *J Magn Reson Imaging* 2015;41:1528–40 CrossRef Medline
6. Zheng D, Lai G, Chen Y, et al. **Integrating dynamic contrast-enhanced magnetic resonance imaging and diffusion kurtosis imaging for neoadjuvant chemotherapy assessment of nasopharyngeal carcinoma.** *J Magn Reson Imaging* 2018;48:1208–16 CrossRef Medline
7. Ai QY, King AD, Law BK, et al. **Diffusion-weighted imaging of na-**

- sopharyngeal carcinoma to predict distant metastases. *Eur Arch Otorhinolaryngol* 2017;274:1045–51 CrossRef Medline
8. Zhang Y, Liu X, Zhang Y, et al. Prognostic value of the primary lesion apparent diffusion coefficient (ADC) in nasopharyngeal carcinoma: a retrospective study of 541 cases. *Sci Rep* 2015;5:12242 CrossRef Medline
 9. Jensen JH, Helpert JA, Ramani A, et al. Diffusional kurtosis imaging: the quantification of non-Gaussian water diffusion by means of magnetic resonance imaging. *Magn Reson Med* 2005;53:1432–40 CrossRef Medline
 10. Sun K, Chen X, Chai W, et al. Breast cancer: diffusion kurtosis MR imaging: diagnostic accuracy and correlation with clinical-pathologic factors. *Radiology* 2015;277:46–55 CrossRef Medline
 11. Xu XQ, Ma G, Wang YJ, et al. Histogram analysis of diffusion kurtosis imaging of nasopharyngeal carcinoma: correlation between quantitative parameters and clinical stage. *Oncotarget* 2017;8:47230–38 CrossRef Medline
 12. Fujima N, Yoshida D, Sakashita T, et al. Prediction of the treatment outcome using intravoxel incoherent motion and diffusional kurtosis imaging in nasal or sinonasal squamous cell carcinoma patients. *Eur Radiol* 2017;27:956–65 CrossRef Medline
 13. Kang M, Zhou P, Li G, et al. Validation of the 8th edition of the UICC/AJCC staging system for nasopharyngeal carcinoma treated with intensity-modulated radiotherapy. *Oncotarget* 2017;8:70586–94 CrossRef Medline
 14. Jensen JH, Helpert JA. MRI quantification of non-Gaussian water diffusion by kurtosis analysis. *NMR Biomed* 2010;23:698–710 CrossRef Medline
 15. Just N. Improving tumour heterogeneity MRI assessment with histograms. *Br J Cancer* 2014;111:2205–13 CrossRef Medline
 16. Eisenhauer EA, Therasse P, Bogaerts J, et al. New response evaluation criteria in solid tumours: revised RECIST guideline (version 1.1). *Eur J Cancer* 2009;45:228–47 CrossRef Medline
 17. Fangzheng W, Chuner J, Lei W, et al. Addition of 5-fluorouracil to first-line induction chemotherapy with docetaxel and cisplatin before concurrent chemoradiotherapy does not improve survival in locoregionally advanced nasopharyngeal carcinoma. *Oncotarget* 2017;8:91150–61 CrossRef Medline
 18. Peng H, Tang LL, Chen BB, et al. Optimizing the induction chemotherapy regimen for patients with locoregionally advanced nasopharyngeal carcinoma: a big-data intelligence platform-based analysis. *Oral Oncol* 2018;79:40–46 CrossRef Medline
 19. Sun Y, Li WF, Chen NY, et al. Induction chemotherapy plus concurrent chemoradiotherapy versus concurrent chemoradiotherapy alone in locoregionally advanced nasopharyngeal carcinoma: a phase 3, multicentre, randomised controlled trial. *Lancet Oncol* 2016;17:1509–20 CrossRef Medline
 20. Jin T, Zhang Q, Jiang F, et al. Neoadjuvant chemotherapy with different dose regimens of docetaxel, cisplatin and fluorouracil (TPF) for locoregionally advanced nasopharyngeal carcinoma: a retrospective study. *Oncotarget* 2017;8:100764–72 CrossRef Medline
 21. Lee NY, Zhang Q, Pfister DG, et al. Addition of bevacizumab to standard chemoradiation for locoregionally advanced nasopharyngeal carcinoma (RTOG 0615): a phase 2 multi-institutional trial. *Lancet Oncol* 2012;13:172–80 CrossRef Medline
 22. Wang F, Jiang C, Ye Z, et al. Treatment outcomes of 257 patients with locoregionally advanced nasopharyngeal carcinoma treated with nimotuzumab plus intensity-modulated radiotherapy with or without chemotherapy: a single-institution experience. *Transl Oncol* 2018;11:65–73 CrossRef Medline
 23. Zhong YH, Dai J, Wang XY, et al. Phase II trial of neoadjuvant docetaxel and cisplatin followed by intensity-modulated radiotherapy with concurrent cisplatin in locally advanced nasopharyngeal carcinoma. *Cancer Chemother Pharmacol* 2013;71:1577–83 CrossRef Medline
 24. Zhang L, Shan GP, Li P, et al. The role of concurrent chemotherapy to intensity-modulated radiotherapy (IMRT) after neoadjuvant docetaxel and cisplatin treatment in locoregionally advanced nasopharyngeal carcinoma. *Med Oncol* 2015;32:41 CrossRef Medline
 25. Law BK, King AD, Bhatia KS. Diffusion-weighted imaging of nasopharyngeal carcinoma: can pretreatment DWI predict local failure based on long-term outcome? *AJNR Am J Neuroradiol* 2016;37:1706–12 CrossRef Medline
 26. Blazic IM, Lilic GB, Gajic MM. Quantitative assessment of rectal cancer response to neoadjuvant combined chemotherapy and radiation therapy: comparison of three methods of positioning region of interest for ADC measurements at diffusion-weighted MR imaging. *Radiology* 2017;282:615 CrossRef Medline
 27. Chen Y, Ren W, Zheng D, et al. Diffusion kurtosis imaging predicts neoadjuvant chemotherapy responses within 4 days in advanced nasopharyngeal carcinoma patients. *J Magn Reson Imaging* 2015;42:1354–61 CrossRef Medline
 28. Yan DF, Zhang WB, Ke SB, et al. The prognostic value of pretreatment tumor apparent diffusion coefficient values in nasopharyngeal carcinoma. *BMC Cancer* 2017;17:678 CrossRef Medline
 29. Jansen JF, Parra C, Lu Y, et al. Evaluation of head and neck tumors with functional MR imaging. *Magn Reson Imaging Clin N Am* 2016;24:123–33 CrossRef Medline
 30. Vandecaveye V, Dirix P, De Keyser F, et al. Diffusion-weighted magnetic resonance imaging early after chemoradiotherapy to monitor treatment response in head-and-neck squamous cell carcinoma. *Int J Radiat Oncol Biol Phys* 2012;82:1098–107 CrossRef Medline
 31. Zhang GY, Wang YJ, Liu JP, et al. Pretreatment diffusion-weighted MRI can predict the response to neoadjuvant chemotherapy in patients with nasopharyngeal carcinoma. *Biomed Res Int* 2015;2015:307943 CrossRef Medline
 32. Ryoo I, Kim JH, Choi SH, et al. Squamous cell carcinoma of the head and neck: comparison of diffusion-weighted MRI at b-values of 1,000 and 2,000 s/mm² to predict response to induction chemotherapy. *Magn Reson Med Sci* 2015;14:337–45 CrossRef Medline
 33. Obenaus AC, Zou Y, Ji AL, et al. Therapy-induced tumour secretomes promote resistance and tumour progression. *Nature* 2015;520:368–72 CrossRef Medline
 34. Raab P, Hattingen E, Franz K, et al. Cerebral gliomas: diffusional kurtosis imaging analysis of microstructural differences. *Radiology* 2010;254:876–81 CrossRef Medline
 35. Wang X, Tu N, Qin T, et al. Diffusion kurtosis imaging combined with DWI at 3-T MRI for detection and assessment of aggressiveness of prostate cancer. *AJR Am J Roentgenol* 2018;211:797–804 CrossRef Medline
 36. Tamada T, Prabhu V, Li J, et al. Prostate cancer: diffusion-weighted MR imaging for detection and assessment of aggressiveness: comparison between conventional and kurtosis models. *Radiology* 2017;284:100–08 CrossRef Medline
 37. Peeters F, Rommel D, Abarca-Quinones J, et al. Early (72-hour) detection of radiotherapy-induced changes in an experimental tumor model using diffusion-weighted imaging, diffusion tensor imaging, and Q-space imaging parameters: a comparative study. *J Magn Reson Imaging* 2012;35:409–17 CrossRef Medline
 38. Beaulieu C. The basis of anisotropic water diffusion in the nervous system: a technical review. *NMR Biomed* 2002;15:435–55 CrossRef Medline
 39. Xiao Y, Pan J, Chen Y, et al. Intravoxel incoherent motion-magnetic resonance imaging as an early predictor of treatment response to neoadjuvant chemotherapy in locoregionally advanced nasopharyngeal carcinoma. *Medicine (Baltimore)* 2015;94:e973 CrossRef Medline
 40. Kuang F, Yan Z, Wang J, et al. The value of diffusion-weighted MRI to evaluate the response to radiochemotherapy for cervical cancer. *Magn Reson Imaging* 2014;32:342–49 CrossRef Medline
 41. Roethke MC, Kuder TA, Kuru TH, et al. Evaluation of diffusion kurtosis imaging versus standard diffusion imaging for detection and grading of peripheral zone prostate cancer. *Invest Radiol* 2015;50:483–89 CrossRef Medline

Contrast-Enhanced 3D-FLAIR Imaging of the Optic Nerve and Optic Nerve Head: Novel Neuroimaging Findings of Idiopathic Intracranial Hypertension

E. Golden, R. Krivochenitser, N. Mathews, C. Longhurst, Y. Chen, J.-P.J. Yu, and T.A. Kennedy



ABSTRACT

BACKGROUND AND PURPOSE: The sensitivity of contrast-enhanced 3D-FLAIR has not been assessed in patients with idiopathic intracranial hypertension. The purpose of this study was to evaluate whether hyperintensity of the optic nerve/optic nerve head on contrast-enhanced 3D-FLAIR imaging is associated with papilledema in patients with idiopathic intracranial hypertension.

MATERIALS AND METHODS: A retrospective review was conducted from 2012 to 2015 of patients with clinically diagnosed idiopathic intracranial hypertension and age- and sex-matched controls who had MR imaging with contrast-enhanced 3D-FLAIR. Two neuroradiologists graded each optic nerve/optic nerve head on a scale of 0–3. This grade was then correlated with the Frisén Scale, an ophthalmologic scale used for grading papilledema from 0 (normal) to 5 (severe edema). To estimate the correlation between the MR imaging and Frisén scores, we calculated the Kendall τ coefficient.

RESULTS: Forty-six patients (3 men, 43 women) with idiopathic intracranial hypertension and 61 controls (5 men, 56 women) with normal findings on MR imaging were included in this study. For both eyes, there was moderate correlation between the 2 scales (right eye: $\tau = 0.47$; 95% CI, 0.31–0.57; left eye: $\tau = 0.38$; 95% CI, 0.24–0.49). Interreader reliability for MR imaging scores showed high interreader reliability (right eye: $\kappa = 0.76$; 95% CI, 0.55–0.88; left eye: $\kappa = 0.87$; 95% CI, 0.78–0.94). Contrast-enhanced 3D-FLAIR imaging correlates with the Frisén Scale for moderate-to-severe papilledema and less so for mild papilledema.

CONCLUSIONS: Hyperintensity of the optic nerve/optic nerve head on contrast-enhanced 3D-FLAIR is sensitive for the detection of papilledema in patients with idiopathic intracranial hypertension, which may be useful when prompt diagnosis is crucial.

ABBREVIATIONS: CE = contrast-enhanced; ICP = intracranial pressure; IIH = idiopathic intracranial hypertension; OD = right eye; ON = optic nerve; ONH = optic nerve head; OS = left eye

Idiopathic intracranial hypertension (IIH) is an uncommon neurologic condition characterized by elevated intracranial pressure (ICP), which is associated with headaches, diplopia, and papilledema. In rare cases, vision loss has been described in IIH; in cases of fulminant IIH, this deficit has been documented to occur within days of symptom onset.¹ Vision loss, however, can be halted or even reversed if detected in time, making prompt diag-

nosis of IIH critical.² IIH is diagnosed clinically using the updated Modified Dandy Criteria, the clinical criterion standard that consists of the following: papilledema or other signs and symptoms related to generalized increased ICP, elevated ICP with normal CSF composition, and a neuroimaging study performed to exclude a cause of elevated ICP.¹ The severity of papilledema in patients with IIH is graded by the Frisén Scale, the ophthalmologic scale for papilledema severity, which ranges from 0 to 5 and denotes normal, very early, early, moderate, marked, and severe papilledema.^{3–5}

In contrast to the clinical diagnosis of IIH, the neuroimaging diagnosis of IIH remains a diagnosis of exclusion. Historically, the role of imaging in IIH has been to exclude secondary causes of

Received August 2, 2018; accepted after revision November 23.

From the Departments of Radiology (E.G., J.-P.J.Y., T.A.K.), Ophthalmology (R.K., N.M., Y.C.), and Psychiatry (J.-P.J.Y.), University of Wisconsin School of Medicine and Public Health, Madison, Wisconsin; and Department of Biostatistics and Medical Informatics (C.L.), Department of Biomedical Engineering (J.-P.J.Y.), College of Engineering, and Neuroscience Training Program (J.-P.J.Y.), Wisconsin Institutes for Medical Research, University of Wisconsin-Madison, Madison, Wisconsin.

J.-P.J.Y. was supported by the University of Wisconsin School of Medicine and Public Health and the Department of Radiology, the Brain and Behavior Research Foundation Young Investigator Grant, and by the Clinical and Translational Science Award program, through the National Institutes of Health National Center for Advancing Translational Sciences, grant ULTR002373.

The content is solely the responsibility of the authors and does not necessarily represent the official views of the National Institutes of Health.

Please address correspondence to Tabassum A. Kennedy, MD, Department of Radiology, Division of Neuroradiology, University of Wisconsin School of Medicine and Public Health, 600 Highland Ave, Madison, WI 53792-3252; e-mail: tkennedy@uwhealth.org; @tabby_kennedy

Indicates open access to non-subscribers at www.ajnr.org

<http://dx.doi.org/10.3174/ajnr.A5937>

increased ICP in patients with clinically diagnosed papilledema.³ However, patients presenting with visual changes or other signs of increased ICP have undergone imaging before fundoscopic examination.³ This has created an opportunity for neuroimaging to serve as a primary diagnostic tool for clinically suspected IIH. Several radiologic findings of papilledema and IIH have been previously described, including flattening of the globe, protrusion of the optic nerve (ON), a partially empty sella, and transverse sinus stenosis.⁶⁻¹² Postcontrast enhancement of the optic nerve head (ONH) is also a known finding in IIH.^{6,10} Additionally, hyperintensity of the ONH on diffusion-weighted imaging has also been described.³ However, DWI has several intrinsic limitations, which may restrict its use in the diagnosis of IIH. DWI is typically performed with thick sections limiting the visualization of the optic nerve and thereby decreasing the overall sensitivity of the imaging study; additionally, field distortions and other artifacts often seen with DWI in the region of the orbit further limit the sensitivity of DWI for the detection of ONH signal abnormalities.³

In the catalogue of descriptions of the radiologic findings of IIH, the MR imaging pulse sequences used in the previous studies are widely varying, with no study to date systematically evaluating the potential role of contrast-enhanced (CE) 3D-FLAIR imaging for the sensitive and specific detection of IIH. Hyperintensity of the ON on CE FLAIR imaging has been used previously in evaluating other abnormalities of the optic nerve, including neuropathy, neuritis, and atrophy.^{13,14} We present the first systematic investigation of CE 3D-FLAIR hyperintensity for the evaluation of the ON and ONH for the detection of papilledema in patients with IIH and also present corroborating clinical data that demonstrate both the sensitivity and specificity of our neuroimaging findings.

MATERIALS AND METHODS

Subject Population and Controls

This retrospective study was approved by the University of Wisconsin-Madison institutional review board. A retrospective chart review was performed on consecutive patients with known disease seen in our neuro-ophthalmology clinic between January 2012 and December 2015. The inclusion criteria were patients who had been diagnosed with IIH by a staff neuro-ophthalmologist using the Modified Dandy Criteria and who also had contemporaneous contrast-enhanced MR imaging of the brain with CE 3D-FLAIR imaging. The severity of papilledema in the subject group was graded by a neuro-ophthalmologist using the Frisén Scale, the ophthalmologic scale for papilledema severity, which ranges from 0 to 5 and denotes normal, very early, early, moderate, marked, and severe papilledema.³⁻⁵

Age- and sex-matched control subjects were identified sequentially and in chronologic order from a list of MR imaging studies of patients without IIH, retrieved by conducting a text search of the Radiology Information System of our institution. The search criteria for the text search included the desired age \pm 2 years, sex parameters, the key words “unremarkable study” in the radiology report, and completion of the study between January 2012 and December 2015. A subsequent chart review was then performed on all identified control patients to further exclude control subjects with a history of intracranial pathology, increased

Table 1: Demographic and clinical information of study and control cohorts

	Study Cohort (n = 46)	Control Cohort (n = 61)
Mean age (yr)	29.6 \pm 11	30.9 \pm 11.7
Sex		
Male	3	5
Female	43	56
Frisén Scale papilledema grade OD (mean)	2.32 \pm 1.3	Not available
Frisén Scale papilledema grade OS (mean)	2.32 \pm 1.3	Not available

ICP, a history of neurologic surgery, or any other history to suggest a possible diagnosis of IIH. This chart review included any clinic notes from the ordering physician as well as any neurology, neurosurgery, or ophthalmology notes if applicable. Clinical and demographic data were collected for all patients with IIH and controls (Table 1). All control patients were considered negative controls and were presumed to have normal fundoscopic examination findings, given that there was no indication in the patient chart that the controls met the Modified Dandy Criteria.

Brain MR Imaging Acquisition

MR imaging was performed on 1.5T and 3T MR imaging scanners (GE Optima MR450w, GE Signa HDxt, GE Discovery MR750w; GE Healthcare, Milwaukee, Wisconsin). An 8-channel receiver head coil was used for image acquisition. All MR imaging contained the following sequence: contrast-enhanced 3D sagittal T2-weighted FLAIR images acquired on 1.5T and 3T magnets. The sagittal 3D-FLAIR sequence was performed as the initial sequence following the intravenous contrast injection of 0.1 mmol/kg of gadobenate dimeglumine (MultiHance; Bracco Diagnostics, Princeton, New Jersey). Coronal and axial reconstructions were subsequently created. The sagittal, coronal, and axial series were available for image review.

Neuroimaging Evaluation

A grading scheme for evaluation of the ON and ONH on CE 3D-FLAIR imaging was modeled on the 3- and 4-point scales used in previous studies to evaluate hyperintensity.^{3,6} The grading scale is as follows: 0 = normal; 1 = mild hyperintensity of the ON without involvement of the ONH; 2 = moderate hyperintensity of the ON and ONH as well as mild inversion of the ONH; and 3 = marked hyperintensity of the ON and ONH with severe inversion of the ONH (Fig 1). The degree of hyperintensity was ultimately a subjective evaluation of optic nerve signal intensity in relation to the signal intensity of the temporal lobe white matter. Two experienced neuroradiologists with Certificates of Added Qualification, blinded to clinical and demographic data, evaluated the signal intensity of the ON and ONH on CE 3D-FLAIR imaging for both patients with IIH and controls. The images for both the patients with IIH and controls were intermixed and presented to each blinded neuroradiologist in random order. Each ON was evaluated independently and was individually scored with the aforementioned grading scale. An ophthalmologic diagnosis of IIH using the Modified Dandy Criteria was viewed as the criterion standard; therefore, both the true presence and the true severity of the disease were determined by the ophthalmologic examination.

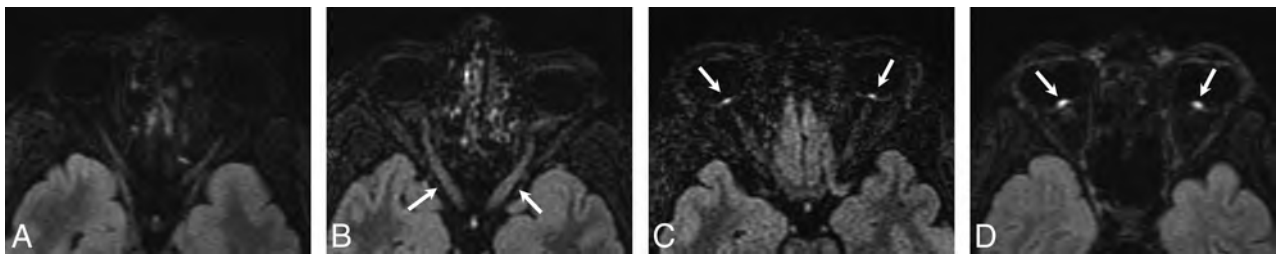


FIG 1. CE 3D-FLAIR images obtained in 4 different patients illustrate the grades of edema seen within the optic nerve and optic nerve head on MR imaging: 0 = normal (A), 1 = mild hyperintensity of the ON without involvement of the ONH (arrows, B), 2 = moderate hyperintensity of the ONH as well as mild inversion of the ONH (arrows, C), and 3 = marked hyperintensity of the ONH with severe inversion of the ONH (arrows, D).

True disease severity was graded by the neuro-ophthalmologist using the Frisén Scale.

Statistical Methods

To assess interrater reliability (2 readers) for MR imaging on the 0- to 3-point grading scale and binary scale interpretation, we estimated the Cohen κ (quadratically weighted and unweighted, respectively) using the ‘psych’ package (Version 1.7.8; <https://cran.r-project.org/web/packages/psych/psych.pdf>) in R (Version 3.4.3; <http://www.r-project.org/>) along with 95% bias-corrected and accelerated–bootstrapped confidence intervals.¹⁵ For the binary MR imaging scale only, sensitivity and specificity estimates were calculated for each reader along with 95% Agresti–Coull confidence intervals. To estimate the correlation between MR imaging and Frisén Scale scores, we calculated a nonparametric correlation coefficient (Kendall τ) along with the associated 95% bias-corrected and accelerated–bootstrapped confidence interval (4000 iterations) for each eye. Because optic nerve appearance on MR imaging and funduscopy is thought to be temporally associated with one another, a sensitivity analysis was conducted via bootstrap simulation to determine whether patients whose MR imaging and funduscopy images were obtained >30 days apart were significantly influencing the estimated correlation between MR imaging and Frisén Scale scores.

RESULTS

Demographic and Clinical Characteristics

During the study period, 78 patients were clinically diagnosed with IIH on the basis of their clinical funduscopy examination findings by our neuro-ophthalmology colleagues. Following the application of exclusion criteria (no imaging performed, imaging performed at a referring facility, imaging without CE 3D-FLAIR, date of imaging outside the study parameters, and a history of intracranial pathology or instrumentation), 46 patients were included in our study. The study population consisted of 3 men and 43 women with a mean age of 29.6 ± 11 years. The incidence of IIH is significantly higher among women, especially young women and women with obesity. That disparity is reflected therefore in both our patient population and also in our control sample. Frisén Scale scores for the study patients ranged from 0 to 5, with a histogram pictured in Fig 2. Sixty-one patients with normal findings on MR imaging were included in this study. The control population consisted of 5 men and 56 women, with a mean age of 30.9 ± 11.7 years. The indications for MR imaging in these patients were the following: headache ($n = 26$; 42.6%), inner ear

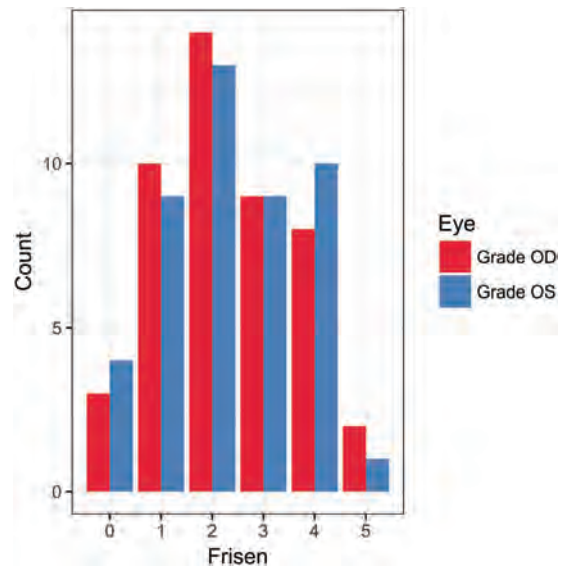


FIG 2. Histogram of observed Frisén Scale scores in the patient group for both OD and OS.

symptoms such as hearing loss or vertigo ($n = 11$; 18.0%), non-specific neurologic symptoms such as confusion ($n = 5$; 8.2%), vision changes ($n = 4$; 6.6%), neuropathies ($n = 4$; 6.6%), screening for masses in oncology or patients with transplants ($n = 3$; 4.9%), trauma ($n = 2$; 3.3%), pituitary symptoms ($n = 2$; 3.3%), seizures ($n = 2$; 3.3%), and anosmia ($n = 1$; 1.6%).

ON and ONH CE FLAIR Imaging Evaluation

Following blinding of clinical and demographic data, the ON and ONH in each patient (IIH and controls) were independently evaluated by both readers. MR imaging findings were considered positive if given any nonzero score on the scale in our study. Each reader found that there was a greater incidence of hyperintensity of the ON/ONH on CE 3D-FLAIR imaging among the patients with IIH than among the control group. For reader 1, hyperintensity of at least 1 ON was 84.4% sensitive (95% CI, 75.7%–90.4%) and 100% specific (95% CI, 96.3%–100%) for the presence of papilledema. The correlation between reader 1’s evaluation of the papilledema grade as measured on the scale of our study and the papilledema grade per the neuro-ophthalmologic Frisén Scale was as follows: right eye (OD): $\tau = 0.48$; 95% CI, 0.32–0.61; left eye (OS): $\tau = 0.43$; 95% CI, 0.24–0.57. For reader 2, hyperintensity of at least 1 ON was 77.1% sensitive (95% CI, 67.7%–84.4%) and 87.7% specific (95% CI, 80.6%–92.5%) for the presence of papilledema. The correlation between reader 2’s evaluation of the

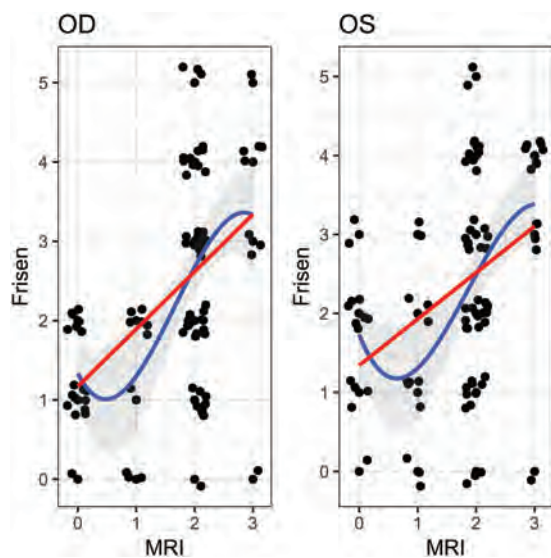


FIG 3. Measured Frisén Scale and MR imaging scores for patients positive for IIH (with added jitter) for both OD and OS. The *blue line* represents the estimated cubic polynomial of best fit (with a 95% confidence band) and the *red line* represents the estimated linear regression.

Table 2: P values for differences in the study population correlation coefficient and the restricted group correlation coefficient

	P Value
$T_{reader\ 1\ OD} - T_{reader\ 1\ OD}$.453
$T_{reader\ 1\ OS} - T_{reader\ 1\ OS}$.553
$T_{reader\ 2\ OD} - T_{reader\ 2\ OD}$.612
$T_{reader\ 2\ OS} - T_{reader\ 2\ OS}$.533

Note:— T indicates the study population correlation coefficient; T , the restricted group correlation coefficient.

papilledema grade as measured on the scale of our study and the papilledema grade per the neuro-ophthalmologic Frisén Scale was as follows: OD: $\tau = 0.46$; 95% CI, 0.13–0.61; OS: $\tau = 0.33$; 95% CI, 0.05–0.50. When we combined the scores from both readers, the correlation between the 2 scales was as follows: OD: $\tau = 0.47$; 95% CI, 0.31–0.57; OS: $\tau = 0.38$; 95% CI, 0.24–0.49 (Fig 3).

Interreader reliability for the detection of abnormal signal intensity within the ON of those with IIH was assessed using a Cohen κ unweighted score and showed moderate-to-substantial agreement between the 2 readers (OD: $\kappa = 0.73$; 95% CI, 0.36–0.92; OS: $\kappa = 0.76$; 95% CI, 0.36–0.94). Interreader reliability for MR imaging grades on the scale of our study was assessed using the Cohen unweighted κ (quadratic) and showed substantial-to-almost-perfect agreement between the 2 readers (OD: $\kappa = 0.76$; 95% CI, 0.55–0.88; OS: $\kappa = 0.87$; 95% CI, 0.78–0.94).

The range of time between the fundoscopic evaluation and MR imaging in our study population was 0–86 days. Subgroup analysis conducted on a restricted group of patients with IIH who had undergone imaging or fundoscopy within 30 days of one another did not yield any statistically significant differences in results. The *P* values for the differences in the correlation coefficients between the study population and the restricted group are listed in Table 2.

DISCUSSION

In this retrospective study, we sought to determine the sensitivity and specificity of CE 3D-FLAIR imaging to detect papilledema in patients with IIH and to further quantify the relationship between our proposed imaging measures of papilledema and the Frisén Scale, a clinical neuro-ophthalmologic grading scale of papilledema severity. Our results demonstrate that postcontrast FLAIR hyperintensity of the ON and ONH is strongly correlated with a clinical diagnosis of IIH and that postcontrast FLAIR hyperintensity of at least 1 ON is at once a robust, sensitive, and specific sign of papilledema. In an extension of our work, we present additional evidence of a positive correlation between the Frisén Scale and our proposed imaging measures of papilledema, highlighting both the clinical utility of our study and its translational potential.

3D-FLAIR imaging affords several built-in advantages when imaging the ON because it addresses many of the well-known challenges that come with optic nerve imaging. Optimal imaging of the optic nerve includes suppression of the orbital fat surrounding the optic nerve to circumvent high signal intensity and chemical shift artifacts, and fluid suppression to suppress the high signal from the CSF surrounding the optic nerve. Both fluid and fat suppression can be easily achieved with FLAIR imaging.¹⁶ While FLAIR can be acquired with a 2D or 3D acquisition, 3D-FLAIR has been shown to be superior to 2D-FLAIR for imaging optic neuropathy, highlighted by its ability to generate multiplanar reconstructions to follow tortuous ONs as well as the high spatial resolution afforded by 3D-FLAIR imaging.¹⁶ Because FLAIR imaging is also a standard feature of many brain imaging protocols, findings related to IIH in the optic nerve may be detected even if clinical concern has not yet prompted a request for orbit-specific imaging. Other sequences such as steady-state free precession sequences (eg, FIESTA or CISS) have been shown to adequately detect optic nerve findings seen with IIH, but unlike FLAIR, are often supplementary sequences performed for a specific indication.

Our neuroimaging findings of high postcontrast FLAIR signal in the optic nerve and optic nerve head are also consistent with prevailing biologic and biomechanical models of elevated intracranial pressure in which elevated intracranial pressure leads to axoplasmic stasis and subsequent neurotoxicity.^{17–22} Axoplasmic stasis is a phenomenon of interrupted axonal transport that results in swelling of nerve fibers, organelle aggregation, and subsequent metabolic waste accumulation leading to cytotoxicity.²² Elevated intracranial pressure is hypothesized to lead to the mechanical transduction of increased pressure along the optic nerve sheath that leads to compression of the surrounding vasculature and the resultant venous stasis.²² This venous stasis potentially accounts for the enhancement often seen at the optic nerve head in IIH.^{10,23} Other similar hypotheses and models propose the development of axonal ischemia occurring in the setting of increased ICP, which mechanically compresses the ciliary circulation.^{3,24} It is likely that multiple factors contribute to the edema and enhancement seen at the level of the optic nerve head.

Several studies in the literature have shown increased conspicuity of changes related to optic neuropathy in patients with suspected optic neuritis using a CE FLAIR technique.^{13,14} They theorized that the increased conspicuity on CE FLAIR is predom-

inantly related to T2/FLAIR signal prolongation, with alternative potential contributions from enhancing scar, ongoing demyelination, or other mechanisms resulting in blood-brain barrier breakdown.¹³ We hypothesized that the observed hyperintensity within the ON and ONH in patients with IIH is related to synergistic effects between the edematous changes within the ON and ONH manifested on FLAIR and concomitant venous stasis, which may also be seen as enhancement, thus likely contributing to the observed increased sensitivity of this imaging sign on CE 3D-FLAIR. Venous status may result in breakdown of the blood-retinal barrier, ultimately leading to enhancement that is isolated to the optic nerve head in patients with IIH.^{10,23} It is unknown, however, how the timing of contrast relative to the acquisition of the 3D-FLAIR sequence affects the signal hyperintensity appreciated in the optic nerve and optic nerve head in these patients. At our institution, the 3D-FLAIR sequence is performed as the initial sequence after the administration of gadobenate dimeglumine (MultiHance). To fully understand the relative contribution of the T2 effects seen on FLAIR versus postcontrast effects, future investigation is needed to evaluate the sensitivity and specificity of 3D-FLAIR without contrast in patients with IIH.^{10,25}

While CE 3D-FLAIR imaging shows evidence of papilledema in patients with IIH, with a reasonable amount of sensitivity and specificity, the correlation between the Frisén Scale and our scale was only moderately positive. The correlation differs with the different degrees of severity, with a more linear correlation for cases of moderate-to-severe papilledema and no correlation for cases of mild papilledema. This discrepancy could be partially due to the inherent subjectivity of our scale and reader disagreement on the subtleties of mild hyperintensity in the optic nerve versus normal signal. Image noise present in the axial and coronal reconstructions may also be a contributing factor to the discrepancy observed between the readers in cases of mild papilledema, but it is likely not a confounding factor in more severe cases of papilledema. The variability and discrepancy in mild states of disease have also been shown in previous studies.³ Viets et al,³ who investigated increased diffusion signal on DWI as an indicator of papilledema in patients with IIH, also found that their sign became more sensitive as the Frisén Scale grade increased. This finding suggests that hyperintensity of the optic nerve on FLAIR imaging cannot be used for a definitive diagnosis of all severities of IIH but may be useful for the detection of more severe IIH.

Whether the papilledema grade correlates with visual outcome is controversial.^{4,26} The papilledema grade has not been found to be correlated with the severity of visual impairment.^{27,28} However, some studies have also found that only patients who present with “obvious” papilledema on physical examination ever develop clinically meaningful visual impairment.²⁸ In this subset of patients, the evidence suggests that the papilledema grade does correlate with the amount of vision loss at higher grades of papilledema.^{28,29} Additionally, patients who present with vision loss at the time of diagnosis also tend to have poor visual outcomes.²⁴ This finding would suggest that the most useful diagnostic imaging study would be one that detects papilledema in patients who would ultimately be found to have moderate-to-severe papilledema on funduscopic examination.

The limitations of our study are those primarily related to the

retrospective study design. It was not possible to obtain funduscopic photographs for the control group; therefore, the controls were assumed to have negative funduscopic examination findings (Frisén Scale = 0). Therefore, despite the best attempts to exclude control patients with a history of IIH, intracranial pathology, or instrumentation, a chart review cannot fully ensure that all control patients were true-negative controls. Another potential limitation is that a designated temporal relationship between a funduscopic photograph and MR imaging was not one of the inclusion criteria for this study. However, a subgroup analysis of patients who underwent MR imaging and had funduscopic photos within 30 days of one another did not show markedly different results than those presented here. Another limitation of this study is that the FLAIR images were not compared with postcontrast T1-weighted sequences. This limitation was due to the heterogeneity in neuroimaging protocols used in both the study and control populations, leading to a variety of different postcontrast sequences performed, thus limiting the ability to directly compare sequences.

CONCLUSIONS

Herein, we present the first application of CE 3D-FLAIR imaging for the detection of papilledema in patients with clinically diagnosed IIH and demonstrate that hyperintensity of the optic nerve on CE 3D-FLAIR is a sensitive and specific sign for papilledema in patients with IIH. Additionally, we show a moderately positive correlation between the degree of hyperintensity and the severity of papilledema as measured on the neuro-ophthalmologic Frisén Scale and demonstrate that this correlation is strongest in patients with severe papilledema. Therefore, significant hyperintensity of the optic nerve on CE 3D-FLAIR imaging is a useful detection tool for IIH in high-risk patients in whom prompt diagnosis is critical but neuro-ophthalmologic evaluation is not readily available.

Disclosures: John-Paul J. Yu—RELATED: Grant: National Institutes of Health KL2 Award, Brain and Behavior Research Foundation.* *Money paid to the institution.

REFERENCES

1. Shaikh AG, Bates JH, Yeates SW, et al. **Fulminant idiopathic intracranial hypertension.** *JAMA Neurol* 2013;70:937–38 CrossRef Medline
2. Bidot S, Bruce BB. **Update on the diagnosis and treatment of idiopathic intracranial hypertension.** *Semin Neurol* 2015;35:527–38 CrossRef Medline
3. Viets R, Parsons M, Van Stavern G, et al. **Hyperintense optic nerve heads on diffusion-weighted imaging: a potential imaging sign of papilledema.** *AJNR Am J Neuroradiol* 2013;34:1438–42 CrossRef Medline
4. Wall M, Kupersmith MJ, Kiebertz KD, et al; NORDIC Idiopathic Intracranial Hypertension Study Group. **The idiopathic intracranial hypertension treatment trial: clinical profile at baseline.** *JAMA Neurol* 2014;71:693–701 CrossRef Medline
5. Frisén L. **Swelling of the optic nerve head: a backstage view of a staging scheme.** *J Neuroophthalmol* 2017;37:3–6 CrossRef Medline
6. Padhye LV, Van Stavern GP, Sharma A, et al. **Association between visual parameters and neuroimaging features of idiopathic intracranial hypertension.** *J Neurol Sci* 2013;332:80–85 CrossRef Medline
7. Salvay DM, Padhye LV, Huecker JB, et al. **Correlation between papilledema grade and diffusion-weighted magnetic resonance imaging in idiopathic intracranial hypertension.** *J Neuroophthalmol* 2014;34:331–35 CrossRef Medline

8. Hirfanoglu T, Aydin K, Serdaroglu A, et al. **Novel magnetic resonance imaging findings in children with intracranial hypertension.** *Pediatr Neurol* 2015;53:151–56 CrossRef Medline
9. Morris PP, Lachman N, Black DF, et al. **Increased curvature of the tentorium cerebelli in idiopathic intracranial hypertension.** *AJNR Am J Neuroradiol* 2017;38:1789–93 CrossRef Medline
10. Degan AJ, Levy LM. **Pseudotumor cerebri: brief review of clinical syndrome and imaging findings.** *AJNR Am J Neuroradiol* 2011;32:1986–93 CrossRef Medline
11. Agid R, Farb RI, Willinsky RA, et al. **Idiopathic intracranial hypertension: the validity of cross-sectional neuroimaging signs.** *Neuroradiology* 2006;48:521–27 CrossRef Medline
12. Morris PP, Black DF, Port J, et al. **Transverse sinus stenosis is the most sensitive MR imaging correlate of idiopathic intracranial hypertension.** *AJNR Am J Neuroradiol* 2017;38:471–77 CrossRef Medline
13. Boegel KH, Tyan AE, Iyer VR, et al. **Utility of coronal contrast-enhanced fat-suppressed FLAIR in the evaluation of optic neuropathy and atrophy.** *Eur J Radiol Open* 2017;4:13–18 CrossRef Medline
14. Pino-Lopez L, Wenz H, Bohme J, et al. **Contrast-enhanced fat-suppressed FLAIR for the characterization of leptomeningeal inflammation in optic neuritis.** *Mult Scler* 2018 Apr 1. [Epub ahead of print] CrossRef Medline
15. Revelle WR (photographer). *psych: Procedures for Personality and Psychological Research*. 2017. <https://www.scholars.northwestern.edu/en/publications/psych-procedures-for-personality-and-psychological-research>. Accessed July 26 2018
16. Aiken AH, Mukherjee P, Green AJ, et al. **MR imaging of optic neuropathy with extended echo-train acquisition fluid-attenuated inversion recovery.** *AJNR Am J Neuroradiol* 2011;32:301–05 CrossRef Medline
17. Killer HE, Jaggi GP, Flammer J, et al. **Cerebrospinal fluid dynamics between the intracranial and the subarachnoid space of the optic nerve: is it always bidirectional?** *Brain* 2007;130:514–20 CrossRef Medline
18. Jonas JB, Wang NL, Yang DY, et al. **Facts and myths of cerebrospinal fluid pressure for the physiology of the eye.** *Prog Retin Eye Res* 2015;46:67–83 CrossRef Medline
19. Killer HE, Jaggi GP, Miller NR. **Papilledema revisited: is its pathophysiology really understood?** *Clin Exp Ophthalmol* 2009;37:444–47 CrossRef Medline
20. Tso MO, Hayreh SS. **Optic disc edema in raised intracranial pressure, IV: axoplasmic transport in experimental papilledema.** *Arch Ophthalmol* 1977;95:1458–62 CrossRef Medline
21. Radius RL, Anderson DR. **Morphology of axonal transport abnormalities in primate eyes.** *Br J Ophthalmol* 1981;65:767–77 CrossRef Medline
22. Hayreh SS. **Pathogenesis of optic disc edema in raised intracranial pressure.** *Prog Retin Eye Res* 2016;50:108–44 CrossRef Medline
23. Manfré L, Lagalla R, Mangiameli A, et al. **Idiopathic intracranial hypertension: orbital MRI.** *Neuroradiology* 1995;37:459–61 CrossRef Medline
24. Corbett JJ, Savino PJ, Thompson HS, et al. **Visual loss in pseudotumor cerebri: follow-up of 57 patients from five to 41 years and a profile of 14 patients with permanent severe visual loss.** *Arch Neurol* 1982;39:461–74 CrossRef Medline
25. Brodsky MC, Vaphiades M. **Magnetic resonance imaging in pseudotumor cerebri.** *Ophthalmology* 1998;105:1686–93 CrossRef Medline
26. Obi EE, Lakhani BK, Burns J, et al. **Optic nerve sheath fenestration for idiopathic intracranial hypertension: a seven-year review of visual outcomes in a tertiary centre.** *Clin Neurol Neurosurg* 2015;137:94–101 CrossRef Medline
27. Trobe JD. **Papilledema: the vexing issues.** *J Neuroophthalmol* 2011;31:175–86 CrossRef Medline
28. Wall M. **Idiopathic intracranial hypertension.** *Neurol Clin* 2010;28:593–617 CrossRef Medline
29. Wall M, White WN 2nd. **Asymmetric papilledema in idiopathic intracranial hypertension: prospective interocular comparison of sensory visual function.** *Invest Ophthalm Vis Sci* 1998;39:134–42 Medline

Cavum Septum Pellucidum in the General Pediatric Population and Its Relation to Surrounding Brain Structure Volumes, Cognitive Function, and Emotional or Behavioral Problems

M.H.G. Dremmen, R.H. Bouhuis, L.M.E. Blanken, R.L. Muetzel, M.W. Vernooij, H.E. Marroun, V.W.V. Jaddoe, F.C. Verhulst, H. Tiemeier, and T. White



ABSTRACT

BACKGROUND AND PURPOSE: The cavum septum pellucidum, a cavity filled with CSF, is localized between the 2 lateral ventricles of the brain. The cavum is present in all neonates, but it typically closes within 5 months after birth. In some cases, this closure does not occur and a persistent or enlarged cavum septum pellucidum has been linked, in some studies, to psychiatric disorders. However, the clinical relevance in the general population is unknown. In this study, we examined the relationship between the cavum septum pellucidum and volumes of brain structures, cognitive function, and emotional and behavioral problems in children.

MATERIALS AND METHODS: This study was embedded in the Generation R Study, a prospective cohort in Rotterdam, the Netherlands. MR imaging studies of 1070 children, 6–10 years of age, were systematically evaluated for the presence and length of a persistent cavum septum pellucidum. An enlarged cavum septum pellucidum was defined as a cavum length of ≥ 6 mm. Groups without, with persistent, and with enlarged cavum septi pellucidi were compared for brain structure volumes, nonverbal intelligence, and emotional and behavioral problems.

RESULTS: The prevalence of cavum septi pellucidi in our sample was 4.6%. Children with an enlarged cavum septum pellucidum had a larger corpus callosum, greater thalamic and total white matter–to–total brain volume ratio, and smaller lateral ventricle volumes. We did not find a relationship between cavum septi pellucidi and cognitive function or emotional and behavioral problems.

CONCLUSIONS: The cavum septum pellucidum is a normal structural brain variation without clinical implications in this population-based sample of school-aged children.

ABBREVIATIONS: CBCL = Child Behavior Checklist; CSP = cavum septum pellucidum; IQ = intelligence quotient; M = marginal mean; ρ_s = Spearman partial correlation; SE = standard error

The septum pellucidum is a thin plate consisting of 2 fused laminae or septa located between the lateral ventricles of the brain. At birth, these 2 septa are separated and form the lateral walls of a cavity filled with CSF, the cavum septum pellucidum (CSP). The 2 septa of the cavum typically fuse into a single septum pellucidum within 5 months after birth, likely due to growth of

the surrounding brain structures.^{1–3} However, in some cases, the septa do not fuse and form the persistent cavum. A persistent CSP with a cavum length of < 5 mm is common in a large proportion of healthy subjects, with prevalence rates of up to 30% in the adult population,^{1,4} and is therefore considered a normal variant. In general, the size of a normal-variant septum is estimated at approximately 1–4 mm.^{1,5} There is no clear cutoff value to define enlargement of the CSP, but many previous studies used a common cutoff of ≥ 6 mm.^{2,3,5–16}

In patients with schizophrenia and an enlarged CSP, smaller amygdala volumes and smaller left posterior parahippocampal gyrus volumes compared with patients without CSP were found.¹² Other

Received August 29, 2018; accepted after revision December 1.

From the Departments of Radiology (M.H.G.D., R.H.B., M.W.V., T.W.), Epidemiology (R.L.M., M.W.V., V.W.V.J.), and Pediatrics (V.W.V.J.), Erasmus Medical Center, Rotterdam, the Netherlands; Department of Child and Adolescent Psychiatry (L.M.E.B., R.L.M., H.E.M., F.C.V., H.T., T.W.) and Generation R Study Group (L.M.E.B., R.L.M., H.E.M.), Erasmus Medical Center-Sophia, Rotterdam, the Netherlands; Department of Clinical Medicine (F.C.V.), University of Copenhagen, Copenhagen, Denmark; and Harvard School of Public Health (H.T.), Boston, Massachusetts.

Marjolein H.G. Dremmen and Roos H. Bouhuis contributed equally to this work.

This study was financially supported through Netherlands Organization for Health Research and Development TOP project No. 91211021. The general design of the Generation R Study is made possible by financial support from the Erasmus Medical Center, Rotterdam; the Erasmus University Rotterdam; the Netherlands Organization for Health Research and Development; and the Netherlands Organization for Scientific Research, the Ministry of Health, Welfare and Sport.

Please address correspondence to Marjolein Dremmen, MD, Erasmus Medical Center-Sophia, Department of Radiology, Room 5b-1654, PO Box 2060, 3000 CB Rotterdam, the Netherlands; e-mail: m.dremmen@erasmusmc.nl

Indicates open access to non-subscribers at www.ajnr.org

Indicates article with supplemental on-line tables.

Indicates article with supplemental on-line photos.

<http://dx.doi.org/10.3174/ajnr.A5939>

studies did not find a relation to global or specific brain structure volumes.^{7,9,13,17} However, because the postnatal closure of the CSP is presumed to be dependent on growing brain structures,^{2,3} we would expect the brain regions in direct or close contact with the septum pellucidum to be smaller in subjects with enlarged CSPs.

Because an enlarged CSP is considered a neurodevelopmental anomaly, it has been postulated as a potential marker for psychiatric disorders that have neurodevelopmental origins. Indeed, an enlarged CSP has been evaluated in a broad range of psychiatric adult populations, typically by measuring the anterior-to-posterior CSP length on MR imaging studies, but with mixed results. Some studies have shown significantly higher rates of enlarged CSPs in adult patients with schizophrenia,^{5,9,18} schizophrenia spectrum disorder,¹⁸ bipolar disorder,¹¹ and disruptive behavior disorder¹⁹ and opiate-dependent subjects.¹⁶ However, other studies did not find higher rates of enlarged CSPs in schizophrenia,^{2,6,10,12,20} bipolar disorder,²¹ and other psychiatric disorders, including attention deficit/hyperactivity disorder,²² borderline personality disorder,¹³ depression,¹³ or obsessive-compulsive disorder.¹⁴

The relationship between CSP and cognition is even less clear. Nopoulos et al²³ found a negative correlation between cavum length and the intelligence quotient (IQ) in patients with schizophrenia and an enlarged CSP; however, they did not show this relationship between an enlarged CSP and cognition in the control group. On the other hand, another study has found that a larger proportion of subjects evaluated for mental retardation also had an enlarged CSP.²⁴ In addition, an enlarged CSP has been found in children with syndromes that include cognitive impairments such as fetal alcohol syndrome²⁵ or Apert syndrome.²⁶ These studies may suggest that a relationship exists between an enlarged CSP and cognitive function that extends to the general population.

The heterogeneity in different cutoffs used to define the presence of an enlarged CSP could contribute to some of the mixed findings. The presence of an enlarged CSP, according to the ≥ 6 -mm cutoff varied from 0% to 19.5% in patients and from 0% to 14.7% in controls.^{2,3,6-16} Because control groups for clinical studies do not always reflect the general population, the prevalence of an enlarged CSP in the general pediatric population is unknown. Thus, the goal of this study was to determine the prevalence of a CSP in the general pediatric population and to examine the relationship between the size of a CSP and brain structure volumes, nonverbal intelligence (as a proxy for cognitive function), and emotional or behavioral problems in children.

Given the previously reported link between an enlarged CSP and behavioral or emotional disorders,^{11,15,19} we hypothesized that a relationship between the size of a CSP and behavioral problems and cognitive performance would be present in a population-based sample of children.

MATERIALS AND METHODS

Participants

The current study was embedded in the longitudinal population-based Generation R Study. An overview of the Generation R Study design is published elsewhere.^{27,28} Briefly, the Generation R Study is a prospective birth cohort study that started in Rotterdam between 2002 and 2006. After informed consent was obtained, a

total of 9778 pregnant women were included. Information on the demographic characteristics included educational levels of the mother. Multiple measurements were collected during pregnancy (eg, maternal alcohol use and smoking behavior).²⁹ A neuroimaging substudy of children 6–9 years of age was initiated in 2009 and involved 1070 children.²⁸ Exclusion criteria were general contraindications for MR imaging examination (ie, pacemaker, ferrous metal implants), severe motor or sensory disorders (deafness or blindness), neurologic disorders (ie, seizures or tuberous sclerosis), moderate-to-severe head injuries with loss of consciousness, and claustrophobia. Informed consent was obtained from the parents before participation. The study was approved by the Medical Ethics Committee at the Erasmus Medical Center-Sophia, Rotterdam.²⁸

MR Imaging Acquisition

Children were familiarized with the MR imaging scanners using a mock scanning procedure.²⁸ MR images were acquired on a 3T scanner (Discovery MR750; GE Healthcare, Milwaukee, Wisconsin) using an 8-channel head coil for signal reception. Following a 3-plane localizing and coil-intensity calibration scan, a high-resolution T1-weighted inversion recovery fast-spoiled gradient-recalled sequence was obtained with the following parameters: TR = 10.3 ms, TE = 4.2 ms, TI = 350 ms, NEX = 1, flip angle = 16°, readout bandwidth = 20.8 kHz, matrix = 256 × 256. The total scan time for the T1 was 5 minutes 40 seconds.²⁸ The MR images underwent a 6-parameter affine transformation into a study-specific template at 1 × 1 × 1 mm isotropic resolution.³⁰

CSP Assessment

The CSP was assessed in a standardized manner by a single trained neuroradiologist, blinded to subject information. Anatomic boundaries for the CSP were as follows: the genu of the corpus callosum defined the anterior boundary, the body of the corpus callosum defined the superior boundary, the rostrum of the corpus callosum and the anterior commissure defined the inferior boundary, and the anterior limb and pillars of the fornix defined the posterior boundary. On-line Fig 1 illustrates the anterior and posterior boundaries of the CSP in the sagittal plane. Similar to other studies,^{5-9,12,13,15,19,20,22,23} the anterior-to-posterior length of the CSP was measured by counting the number of coronal 1-mm slices on which a cavum was visible. A cavum was labeled as enlarged when its length was ≥ 6 slices (ie, ≥ 6 mm).^{2,3,6-16} Absence of a CSP was labeled “no CSP.” A cavum of < 6 mm in length was categorized as a normal-variant CSP. Figure 1 illustrates the presence of an enlarged CSP. Intrarater reliability was based on 50 repeat ratings and was found to be high (test-retest reliability, Cronbach $\alpha = 0.96$). Scans that were of insufficient quality to determine the existence or length of a CSP were excluded from the analyses (12.5%, $n = 134$). The insufficient scan quality was mainly due to movement artifacts, which are a well-known problem when performing MR imaging studies in unselected children at a young age.

Global and Regional Brain Structures

Volumes of global and regional brain structures were measured using FreeSurfer image analysis, Suite 5.1 (<http://surfer.nmr.mgh.harvard.edu/>). The technical details of these procedures

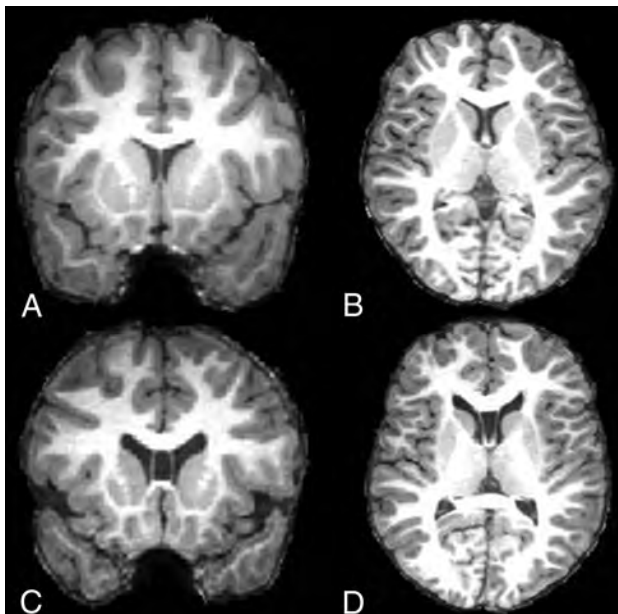


FIG 1. MR imaging of the cavum septum pellucidum. Coronal T1-weighted MR image (A) and axial T1-weighted MR image (B) show no CSP. C, Coronal T1-weighted MR image (C) and axial T1-weighted MR image (D) demonstrate an enlarged CSP.

have been described elsewhere.^{31,32} Briefly, this process included intensity normalization, the removal of nonbrain tissue, automated Talairach transformation into standard space, and segmentation of the cortical and subcortical white and gray matter volumetric structures. The volumes of brain regions in close vicinity to the CSP were selected for analysis. These regions included the corpus callosum, lateral ventricles, thalamus, hippocampus, amygdala, and the caudate nucleus. Volumes of global brain measures were also examined, including total brain, total gray matter, and total white matter volumes.

Emotional and Behavioral Problems

Emotional and behavioral problems were measured using the sum scores of the 99 items of the Child Behavior Checklist (CBCL).³³ This questionnaire, completed by the parents when the children were approximately 6 years of age, includes behavioral, emotional, and social problems in school-aged children. The items were calculated for several syndrome scales: emotionally reactive, anxious/depressed, somatic complaints, withdrawn, attention problems, and aggressive behavior. Broadband scores of internalizing symptoms and externalizing symptoms were used.

Nonverbal Intelligence

The Generation R cohort includes children from different ethnic minorities with differences in Dutch language abilities. Therefore, nonverbal intelligence was measured using 2 subtests of the Snijders-Oomen Nonverbal Intelligence Test 2.5–7-Revised.³⁴ Due to time constraints, we selected 2 subtests: Mosaics and categories for testing spatial insight and abstract reasoning abilities, respectively. Because the correlation between the sum of these 2 subtests and the full SON-R IQ battery is very high ($r = 0.86$), these subdomain scores can be used as nonverbal IQ scores.³⁵ Raw subtest scores were transformed according to population- and

age-specific norms with a mean value of 100 ± 15 .³⁶ Handedness was determined using the Edinburgh Handedness Inventory.²⁹

Statistical Analyses

Demographic differences between the no/normal-variant CSP (control group) and the enlarged CSP group were analyzed using a χ^2 test for categorical variables (sex, ethnicity, handedness, maternal education, maternal alcohol use during pregnancy, maternal smoking behavior during pregnancy) and independent t tests for continuous variables (age). Differences in brain structure volumes, nonverbal intelligence, and emotional and behavioral problems between the controls and the enlarged CSP group were tested using ANCOVAs. Covariates were added to the model if they resulted in a $>5\%$ change in the effect estimate, including the child's age, sex, ethnicity, and maternal education. The analyses of regional brain structure volumes were also adjusted for total problem score and total brain volume. Because the control group did include a small CSP (0–5 mm) and the biologic relevance of a normal-sized CSP is not clear, 2 additional sensitivity analyses were performed for brain structure volumes, nonverbal intelligence, and emotional and behavior problems. First, sensitivity analyses were performed comparing the 2 extreme categories (0 versus ≥ 6 mm), and second, an analysis was performed using a classification into 3 groups (0 versus 1–5 versus ≥ 6 mm). For certain analyses of brain structure volumes and emotional or behavioral scores, the length of the CSP was used as a continuous variable.

All analyses were performed using the Statistical Package for the Social Sciences, Version 21.0 (SPSS; IBM, Armonk, New York). In addition, a nonparametric analysis with CSP length as a continuous variable was performed using Statistical Analysis Software, Version 9.3 (SAS Institute, Cary, North Carolina). To correct for multiple testing, we calculated the effective number of tests on the basis of the covariance structure among the different outcomes.³⁷ We found the number of effective tests to be 5; thus, the corrected threshold for significance was $P < .01$. Data were missing on internalizing symptoms (10.5% missing data), externalizing symptoms (10.0%), nonverbal IQ (8.8%), and the covariates, maternal education (9.5%) and the CBCL sum score (9.5%). Missing values were estimated using a multiple imputation method with 5 imputations and 10 iterations. Finally, an additional nonresponse analysis was performed comparing the baseline characteristics of the study participants with the group of children excluded due to insufficient scan quality.

RESULTS

Sample Characteristics

Sample characteristics are presented in Table 1. Children in the control group and the enlarged CSP group did not differ in age at scanning [$t(934) = 0.26, P = .79$], sex [$\chi^2(1) = 0.03, P = .86$], ethnicity [$\chi^2(2) = 2.68, P = .26$], handedness [$\chi^2(1) = 0.001, P = .98$], maternal education [$\chi^2(2) = 0.93, P = .63$], maternal alcohol use during pregnancy [$\chi^2(3) = 1.53, P = .68$], and maternal smoking behavior during pregnancy [$\chi^2(2) = 0.23, P = .89$].

CSP

Figure 2 shows the distribution of the anterior-to-posterior cavum lengths in the entire sample. The prevalence of a CSP in the

Table 1: Sample characteristics

	Total Group (n = 936) (100%)	Controls (n = 893) (95.4%)	Enlarged CSP (n = 43) (4.6%)
Child characteristics			
Age (mean) (SD) (yr)	7.9 (1.00)	7.9 (1.00)	7.9 (0.91)
Sex (%)			
Girls	45.5	45.6	44.2
Boys	54.5	54.4	55.8
Ethnicity (%)			
Dutch	68.8	69.0	65.1
Other Western	6.8	7.1	2.3
Non-Western	24.4	24.0	32.6
Handedness (%)			
Right	90.5	90.5	90.7
Left	9.4	9.4	9.3
Maternal characteristics			
Maternal education (%) ^a			
Low	10.9	10.8	14.0
Medium	29.0	29.0	27.9
High	50.6	51.1	41.9
Alcohol during pregnancy (%) ^b			
Never	34.3	34.0	39.5
Stopped	13.7	13.8	11.6
Occasionally	35.7	35.7	34.9
Frequently	9.2	9.4	4.7
Smoking during pregnancy (%) ^c			
Never	72.2	72.1	74.4
Stopped	6.3	6.4	4.7
Continued	17.9	17.9	18.6

^a Low indicates primary school or lower vocational education; medium, intermediate vocational education; high, higher vocational education or university. Missing data on maternal education are 9.5%.

^b Frequently indicates that the mother drank ≥ 1 glass per week for at least 2 trimesters. Missing data on alcohol are 7.2%.

^c Smoking >10 cigarettes per day fluctuated between 3.6% and 5.6% throughout pregnancy, with the highest percentage in the first trimester.⁴¹ Missing data on smoking are 3.5%.

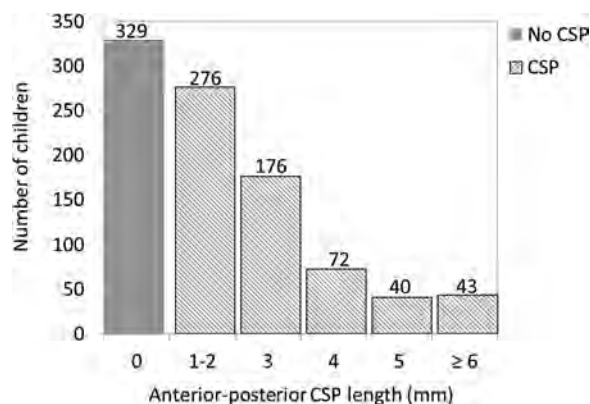


FIG 2. Distribution of no CSP, normal-variant CSP, and enlarged CSP for the whole sample ($n = 936$).

study population was 64.9%, categorized into normal-variant CSP (60.3% of total study population) and enlarged CSP (4.6% of total study population). The mean cavum length in the control group was 2.67 mm; lengths ranged from 1 to 5 mm. The mean cavum length in the enlarged CSP group was 12.56 mm; lengths in this group ranged from 6 to 37 mm. A histogram of CSP lengths in the enlarged CSP group is shown in On-line Fig 2.

Global Brain Structures

Table 2 shows the differences in global structure volumes between the controls and the enlarged CSP group. Children in the enlarged CSP group had larger total brain volumes [$F(1,93) = 3.93, P =$

0.05, partial $\eta^2 = 0.004$] and larger total white matter/total brain ratio volumes [$F(1,93) = 6.81, P = .009$, partial $\eta^2 = 0.007$] compared with the children in the control group, adjusting for the covariates. After correcting for multiple testing, only the difference in white matter/total brain ratio volume remained. Comparing the children in the controls ($n = 893$) with the those in the enlarged CSP group ($n = 43$) or comparison of the 3 groups (0 versus 1–5 versus ≥ 6 mm) showed similar results. CSP length was positively correlated with total brain volume (Spearman partial correlation, $\rho_s = 0.19, P < .001$) and white matter/total brain ratio volume (Spearman partial correlation, $\rho_s = 0.13, P < .001$).

Regional Brain Structures

Table 3 shows the difference in volumes of specific structures between the controls and the enlarged CSP group. Children in the enlarged CSP group had larger corpus callosum volumes [$F(1,93) = 6.79, P = .009$, partial $\eta^2 = 0.007$], larger thalamus volumes [$F(1,93) = 11.21, P = .001$, partial $\eta^2 = 0.012$], and smaller amygdala volumes [$F(1,93) = 4.48, P = 0.04$, partial $\eta^2 =$

0.005] compared with the children in the control group, after controlling for covariates. After we corrected for multiple testing, only differences in the corpus callosum and thalamus volumes remained. On-line Table 1 presents the results of the comparison of children in the no-CSP group ($n = 329$) with the those in the enlarged CSP group (≥ 6 mm). Additionally, children with an enlarged CSP had smaller lateral ventricle volumes compared with children with complete absence of a cavum [$F(1,36) = 8.16, P = .005$, partial $\eta^2 = 0.022$]. On-line Table 2 presents the results of the comparison of the 3 groups (0 versus 1–5 versus ≥ 6 mm). In this analysis, the difference in amygdala volume disappeared, and the 3 groups were found to differ in caudate nucleus volume [$F(2,93) = 5.33, P = .005$, partial $\eta^2 = 0.011$]. CSP length was positively correlated with the volume of the corpus callosum (Spearman partial correlation, $\rho_s = 0.12, P < .001$), thalamus (Spearman partial correlation, $\rho_s = 0.08, P = .02$), and caudate nucleus (Spearman partial correlation, $\rho_s = -.10, P = .002$) and was negatively correlated with lateral ventricle volumes (Spearman partial correlation, $\rho_s = -.20, P < .001$).

Nonverbal Intelligence

Children in the no/normal-sized CSP and the enlarged CSP groups did not differ in nonverbal IQ scores [$F(1,93) = 0.05, P = 0.82$, partial $\eta^2 = 0.000$]. Estimated marginal means (M) for nonverbal IQ were $M = 101.63$, standard error (SE) = 0.46 versus $M = 101.13$, SE = 2.08. The results of comparing the children in the no-CSP group ($n = 329$) with the enlarged CSP group ($n =$

Table 2: ANCOVA for global brain structures^a

	Marginal Mean Volumes (cm ³) (SE)		F	Sig.	Partial η^2
	Controls (n = 893)	Enlarged CSP (n = 43)			
TBV	1129.09 (4.095)	1167.00 (18.673)	3.93	.05	0.004
Total GMV/TBV	0.63 (0.001)	0.63 (0.003)	2.14	.14	0.002
Total WMV/TBV	0.33 (0.001)	0.34 (0.002)	6.81	.009 ^b	0.007

Note:—TBV indicates total brain volume; GMV, gray matter volume; WMV, white matter volume; Sig., significance.

^a Results of the first imputed dataset are reported; ranges of the other datasets can be found in On-line Tables 1 and 2. Covariates are age, sex, ethnicity, maternal education, and CBCL sum score.

^b Significant after correcting for multiple testing.

Table 3: ANCOVA for regional brain structures (control vs enlarged CSP)^a

	Marginal Mean Volumes (cm ³) (SE)		F	Sig.	Partial η^2
	Controls (n = 893)	Enlarged CSP (n = 43)			
Corpus callosum	2.71 (0.012)	2.86 (0.055)	6.79	.009 ^b	0.007
Lateral ventricles	8.94 (0.172)	7.49 (0.786)	3.22	.07	0.003
Thalamus	14.12 (0.036)	14.69 (0.165)	11.21	.001 ^b	0.012
Hippocampus	8.03 (0.024)	7.94 (0.111)	0.67	.41	0.001
Amygdala	3.17 (0.014)	3.04 (0.062)	4.48	.04	0.005
Caudate nucleus	8.44 (0.032)	8.30 (0.148)	0.91	.34	0.001

Note:—Sig. indicates significance.

^a Results of the first imputed dataset are reported; ranges of the other datasets can be found in On-line Tables 1 and 2. Covariates are age, sex, ethnicity, total brain volume, maternal education, and CBCL sum score.

^b Significant after correcting for multiple testing.

43) were also not significant. Comparing 3 groups (0 versus 1–5 versus ≥ 6 mm) did show a difference in nonverbal IQ scores [$F(1,93) = 3.37, P = 0.04, \text{partial } \eta^2 = 0.007$]. Estimated marginal means for the 3 groups were $M = 100.08, SE = 0.75$ versus $M = 102.53, SE = 0.57$ versus $M = 101.14, SE = 2.07$; however, this finding did not survive correction for multiple testing. A non-parametric test with CSP length as a continuous variable did not show a correlation between CSP length and nonverbal IQ scores.

Emotional or Behavioral Problems

Children in the control group and the enlarged CSP group did not differ in emotional [$F(1,93) = 2.35, P = 0.13, \text{partial } \eta^2 = 0.003$] or behavioral [$F(1,93) = 0.35, P = 0.55, \text{partial } \eta^2 = 0.000$] problem scores. Estimated marginal means for emotional scores were $M = 2.48, SE = 0.04$ versus $M = 2.18, SE = 0.19$. Estimated marginal means for behavioral scores were $M = 2.80, SE = 0.04$ versus $M = 2.93, SE = 0.20$. Mean scores are reported as square-root-transformed scores. Comparing the children in the no-CSP group ($n = 329$) with those in the enlarged CSP group ($n = 43$) or comparing 3 groups (0 mm 1–5 versus ≥ 6 mm) did not change the results. A Spearman correlation coefficient test with CSP length as a continuous variable also did not show a correlation between CSP length and emotional or behavioral scores.

Participant versus Excluded Analysis

Of all 1070 scans, 134 scans (12.5%) were of insufficient quality and were excluded from the analyses. Children whose scans were excluded did not differ from the current study sample ($n = 936$) in age at the time of scanning [$t(1068) = -0.81, P = .42$], sex [$\chi^2(1) = 3.18, P = .07$], ethnicity [$\chi^2(2) = 3.85, P = .15$], handedness [$\chi^2(1) = 0.43, P = .51$], nonverbal IQ [$t(980) = -0.59, P = .56$], maternal education [$\chi^2(2) = 3.83, P = .15$], maternal alcohol use during pregnancy [$\chi^2(3) = 1.12, P = .77$], and maternal smoking behavior during pregnancy [$\chi^2(2) = 5.64, P = .06$]. However, children excluded from the analyses had

higher CBCL sum scores than the included children [$t(970) = 2.53, P = .01$].

DISCUSSION

To further understand the brain structural correlates associated with an enlarged CSP, we evaluated the relationship between the CSP and the volume of global and regional brain structures. Children with enlarged CSPs were found to have larger total white matter/total brain volume ratios and corpus callosum and thalamus volumes. Similar to studies in patients with schizophrenia spectrum disorder,¹² amygdala volumes were smaller in subjects with enlarged CSPs. However, this result did not remain significant after correction for multiple testing. In addition, children with enlarged CSPs had smaller lateral ventricle volumes compared with children with a total absence of a cavum. CSP length was positively correlated

with total brain volume; white matter/total brain ratio; and corpus callosum, thalamus, and caudate nucleus volumes. CSP length was negatively correlated with lateral ventricle volumes.

It has been postulated that the postnatal closure of the CSP is a result of growth of surrounding brain structures, exerting pressure on the 2 leaflets of the septum pellucidum and thereby facilitating fusion.^{2,3} Brain development in this early postnatal period has not been extensively studied, but a recent study on infant brain development in the first 3 months after birth³⁸ presents growth rates for several ROIs of the current study. The lateral ventricles were found to grow at the highest rate, increasing around 78% in the first 90 days after birth. As hypothesized, the rapid growth of the lateral ventricles in these first months after birth could induce closure of the cavum by exerting lateral pressure on both sides of the septal leaves. We speculated that smaller growth rates in this period could cause failure of CSP closure. If these early growth rates are decisive for structure volumes at a later age, our results support this hypothesis because the lateral ventricles were smaller in children with the presence of a CSP compared with those with total absence of a cavum. Previous studies have reported an association between an enlarged CSP and syndromes including cognitive impairment such as fetal alcohol syndrome and Apert syndrome.^{25,26}

Mechanical factors that potentially play a role in the closure of the CSP in the general pediatric population could also extend to these clinical conditions. In these syndromes, there is an obvious change in brain volume and/or head size, which could cause major changes in the exerting pressure on the septal leaves, leading to a failure of CSP closure. The enlarged CSP would rather be a consequence of the anatomic and structural abnormalities in these syndromes than a marker of cognitive function itself. In addition, the larger total amount of white matter (larger total white matter/total brain volumes ratios) in the enlarged CSP group could also contribute to a change in mechanical factors that

cause the lateral ventricles to grow less rapidly in the early postnatal period. This, in turn, could modify the exerting lateral pressure on both sides of the septal leaves and alter the possible closure mechanisms of the septal leaves.

In addition, other regional brain structures were also found to be larger in children with a persistent CSP. For example, the corpus callosum is a structure that directly surrounds the CSP but was found to be larger in children with an enlarged CSP. We speculated that the exertion of lateral pressure, like the pressure of growing lateral ventricles, is more effective in facilitating the postnatal fusing process of the septum leaves if the corpus callosum is smaller. Thus, under the rubric of a mechanical closure hypothesis of the CSP, larger brain structures would require greater distributed pressure along the structure to close the septum. However, because we do not have MR imaging data available during the early postnatal period, it is not possible to draw conclusions concerning the timing and longitudinal relationship with neighboring structures related to the postnatal closure of the CSP. It is likely that multiple-yet-unknown factors play a role in this process.

Furthermore, it would be interesting to search for genetic factors that play a role in the closure of the CSP. Because the Generation R Study is currently starting to prospectively scan the parents of a subgroup of children scanned in this study, assessment of the presence and size of a CSP in the parents could be of great value to demonstrate the influence of genetics. This may well be a focus of further studies.

The prevalence of an enlarged CSP in our population-based sample of school-aged children is 4.6%. This falls within the range described in prior literature in adult populations.^{2,3,5-16} While earlier research tended to focus on psychiatric populations, the prevalence in healthy control groups in these studies varied substantially from 0% to 14.7%. Because many of these studies had small sample sizes and control groups are not always reflective of recruitment from the general population, we believe that our study provides more accurate rates of enlarged CSPs in the general pediatric population. However, we are unaware of studies assessing changes with time in the size or presence of the CSP; thus, longitudinal studies are necessary to address this question.

An enlarged CSP is considered a potential marker for neurodevelopmental abnormalities. However, in contrast to earlier studies,^{11,15,19} we did not find a relationship between an enlarged CSP and nonverbal intelligence. We also did not find a relationship between emotional or behavioral problems and an enlarged CSP. While we found no evidence for behavioral correlates of an enlarged CSP in this population-based sample of school-aged children, some neuropsychiatric disorders that show a relationship with an enlarged CSP have a typical age of onset in late adolescence and early adulthood. For example, schizophrenia spectrum disorders and bipolar disorders generally present with the first symptoms between 17 and 25 years of age.^{7,21} Thus, it is possible that the relationship between an enlarged CSP and psychopathology will emerge later, parallel to the emergence of psychiatric symptoms. The small, nonsignificant, volumetric differences of certain brain structures found in this study could theoretically indicate some structural changes in brain regions that might form the basis for these diseases.

There are some limitations in the study protocol. Only 1 rater evaluated the MR imaging studies and assessed the presence and size of the CSP. However, the rater was specifically trained to evaluate the CSP and performed all the measurements in a standardized manner. Furthermore, 1 exclusion criterion to undergo MR imaging examination in the Generation R Study design is a history of moderate-to-severe head injuries with loss of consciousness. In previous literature, a possible relationship between an enlarged CSP and traumatic brain injury has been reported in adults as well as in children.^{39,40} Therefore, exclusion of children with previous moderate-to-severe brain injury potentially resulted in selection bias. In addition, missing values on internalizing and externalizing symptoms, nonverbal IQ, and certain covariates are a potential limitation of the study design, but we applied multiple imputation methods to reduce the potential bias introduced as a result of missing data to a minimum.

The strengths of the current study are the standardized MR imaging measurements obtained in a large population-based sample of 1070 children of different ethnicities and backgrounds. The study contains an extensive data collection with a broad range of physiologic and environmental measures. Therefore, it includes valuable data representative of the pediatric population in general.

CONCLUSIONS

The CSP is a structural brain variation without cognitive or behavioral implications in this population-based sample of school-aged children. However, we did find a relationship between CSP and global and regional volumetric brain measures, but the clinical relevance of this relationship is as yet uncertain.

Disclosures: Marjolein H.G. Dremmen—*RELATED: Grant:* the Netherlands Organization for Health Research and Development*; *UNRELATED: Employment:* Pediatric Radiologist at Erasmus Medical Center, Rotterdam. Roos H. Bouhuis—*RELATED: Grant:* the Netherlands Organization for Health Research and Development.* Hanan El Marroun—*RELATED: Grant:* European Union, *Comments:* The Horizon 2020 research and innovation program (grant agreement No.633595 DynaHEALTH and No.733206 LifeCycle) of the European Union.* Frank C. Verhulst—*UNRELATED: Royalties:* distributor of the Dutch translations of the Achenbach System of Empirically Based Assessment, from which I receive remuneration. Tonya White—*RELATED: Grant:* the Netherlands Organization for Health Research and Development.* *Money paid to the institution.

REFERENCES

1. Sarwar M. **The septum pellucidum: normal and abnormal.** *AJNR Am J Neuroradiol* 1989;10:989–1005 Medline
2. Dickey CC, McCarley RW, Xu ML, et al. **MRI abnormalities of the hippocampus and cavum septi pellucidi in females with schizotypal personality disorder.** *Schizophr Res* 2007;89:49–58 CrossRef Medline
3. Choi JS, Kang DH, Park JY, et al. **Cavum septum pellucidum in subjects at ultra-high risk for psychosis: compared with first-degree relatives of patients with schizophrenia and healthy volunteers.** *Prog Neuropsychopharmacol Biol Psychiatry* 2008;32:1326–30 CrossRef Medline
4. Shunk H. **Congenital dilatations of the septi pellucidum.** *Radiology* 1963;81:610–18 CrossRef Medline
5. Nopoulos PC, Giedd JN, Andreasen NC, et al. **Frequency and severity of enlarged cavum septi pellucidi in childhood-onset schizophrenia.** *Am J Psychiatry* 1998;155:1074–79 CrossRef Medline
6. Hagino H, Suzuki M, Kurokawa K, et al. **Magnetic resonance imaging study of the cavum septi pellucidi in patients with schizophrenia.** *Am J Psychiatry* 2001;158:1717–19 CrossRef Medline
7. Rajarethinam R, Miedler J, DeQuardo J, et al. **Prevalence of cavum**

- septum pellucidum in schizophrenia studied with MRI. *Schizophr Res* 2001;48:201–05 CrossRef Medline
8. Crippa JA, Uchida R, Busatto GF, et al. **The size and prevalence of the cavum septum pellucidum are normal in subjects with panic disorder.** *Braz J Med Biol Res* 2004;37:371–74 CrossRef Medline
 9. de Souza Crippa JA, Zuardi AW, Busatto GF, et al. **Cavum septum pellucidum and adhesion interthalamica in schizophrenia: an MRI study.** *Eur Psychiatry* 2006;21:291–99 CrossRef Medline
 10. Flashman LA, Roth RM, Pixley HS, et al. **Cavum septum pellucidum in schizophrenia: clinical and neuropsychological correlates.** *Psychiatry Res* 2007;154:147–55 CrossRef Medline
 11. Kim MJ, Lyoo IK, Dager SR, et al. **The occurrence of cavum septi pellucidum enlargement is increased in bipolar disorder patients.** *Bipolar Disord* 2007;9:274–80 CrossRef Medline
 12. Takahashi T, Suzuki M, Hagino H, et al. **Prevalence of large cavum septi pellucidum and its relation to the medial temporal lobe structures in schizophrenia spectrum.** *Prog Neuropsychopharmacol Biol Psychiatry* 2007;31:1235–41 CrossRef Medline
 13. Takahashi T, Yücel M, Lorenzetti V, et al. **Midline brain structures in patients with current and remitted major depression.** *Prog Neuropsychopharmacol Biol Psychiatry* 2009;33:1058–63 CrossRef Medline
 14. Chon MW, Choi JS, Kang DH, et al. **MRI study of the cavum septum pellucidum in obsessive-compulsive disorder.** *Eur Arch Psychiatry Clin Neurosci* 2010;260:337–43 CrossRef Medline
 15. Raine A, Lee L, Yang Y, et al. **Neurodevelopmental marker for limbic maldevelopment in antisocial personality disorder and psychopathy.** *Br J Psychiatry* 2010;197:186–92 CrossRef Medline
 16. Hwang J, Kim JE, Kaufman MJ, et al. **Enlarged cavum septum pellucidum as a neurodevelopmental marker in adolescent-onset opiate dependence.** *PLoS One* 2013;8:e78590 CrossRef Medline
 17. Galarza M, Merlo AB, Ingratta A, et al. **Cavum septum pellucidum and its increased prevalence in schizophrenia: a neuroembryological classification.** *J Neuropsychiatry Clin Neurosci* 2004;16:41–46 CrossRef Medline
 18. Kasai K, McCarley RW, Salisbury DF, et al. **Cavum septi pellucidum in first-episode schizophrenia and first-episode affective psychosis: an MRI study.** *Schizophr Res* 2004;71:65–76 CrossRef Medline
 19. White SF, Brislin S, Sinclair S, et al. **The relationship between large cavum septum pellucidum and antisocial behavior, callous-unemotional traits and psychopathy in adolescents.** *J Child Psychol Psychiatry* 2013;54:575–81 CrossRef Medline
 20. Rajarethinam R, Sohi J, Arfken C, et al. **No difference in the prevalence of cavum septum pellucidum (CSP) between first-episode schizophrenia patients, offspring of schizophrenia patients and healthy controls.** *Schizophr Res* 2008;103:22–25 CrossRef Medline
 21. Takahashi T, Malhi GS, Wood SJ, et al. **Midline brain abnormalities in established bipolar affective disorder.** *J Affect Disord* 2010;122:301–05 CrossRef Medline
 22. Nopoulos P, Berg S, Castellanos FX, et al. **Developmental brain anomalies in children with attention-deficit hyperactivity disorder.** *J Child Neurol* 2000;15:102–08 CrossRef Medline
 23. Nopoulos P, Krie A, Andreasen NC. **Enlarged cavum septi pellucidum in patients with schizophrenia: clinical and cognitive correlates.** *J Neuropsychiatry Clin Neurosci* 2000;12:344–49 CrossRef Medline
 24. Bodensteiner JB, Schaefer GB, Craft JM. **Cavum septi pellucidum and cavum vergae in normal and developmentally delayed populations.** *J Child Neurol* 1998;13:120–21 CrossRef Medline
 25. Swayze VW 2nd, Johnson VP, Hansen JW, et al. **Magnetic resonance imaging of brain anomalies in fetal alcohol syndrome.** *Pediatrics* 1997;99:232–40 CrossRef Medline
 26. Renier D, Arnaud E, Cinalli G, et al. **Prognosis for mental function in Apert's syndrome.** *J Neurosurg* 1996;85:66–72 Medline
 27. Jaddoe VW, Mackenbach JP, Moll HA, et al. **The Generation R Study: design and cohort profile.** *Eur J Epidemiol* 2006;21:475–84 CrossRef Medline
 28. White T, El Marroun H, Nijs I, et al. **Pediatric population-based neuroimaging and the Generation R Study: the intersection of developmental neuroscience and epidemiology.** *Eur J Epidemiol* 2013;28:99–111 CrossRef Medline
 29. White T, Muetzel RL, El Marroun H, et al. **Paediatric population neuroimaging and the Generation R Study: the second wave.** *Eur J Epidemiol* 2018;33:99–125 CrossRef Medline
 30. Muetzel RL, Blanken LME, Thijsen S, et al. **Variability in ICA-derived resting-state networks in 6-to-10 year-old children.** *Hum Brain Mapp* 2016;37:4286–4300 CrossRef Medline
 31. White T, Jansen PR, Muetzel RL, et al. **Automated quality assessment of structural magnetic resonance images in children: comparison with visual inspection and surface-based reconstruction.** *Hum Brain Mapp* 2018;39:1218–31 CrossRef Medline
 32. Fischl B, Salat DH, Busa E, et al. **Whole brain segmentation: automated labeling of neuroanatomical structures in the human brain.** *Neuron* 2002;33:341–55 CrossRef Medline
 33. Achenbach TM, Rescorla LA. *Manual for the ASEBA Preschool Forms and Profiles.* Burlington, VT: University of Vermont, Research Center for Children, Youth, & Families; 2000
 34. Basten M, van der Ende J, Tiemeier H, et al. **Nonverbal intelligence in young children with dysregulation: the Generation R Study.** *Eur Child Adolesc Psychiatry* 2014;23:1061–70 CrossRef Medline
 35. Moore C, O'Keefe S, Lawhorn D, et al, et al. **Concurrent validity of the Snijders-Oomen Nonverbal Intelligence Test 2 1/2–7–Revised with the Wechsler Preschool and Primary Scale of Intelligence–Revised.** *Psychological Reports* 1998;82:619–25 CrossRef
 36. Snijders JH, Snijders-Oomen AW, Tellegen PJ, et al. *SON-R 21/2–7: Snijders-Oomen Niet-Verbale Intelligentietest—Handleiding en Verantwoording.* Amsterdam: Boom Testuitgevers; 2005
 37. Galwey NW. **A new measure of the effective number of tests, a practical tool for comparing families of non-independent significance tests.** *Genet Epidemiol* 2009;33:559–68 CrossRef Medline
 38. Holland D, Chang L, Ernst TM, et al. **Structural growth trajectories and rates of change in the first 3 months of infant brain development.** *JAMA Neurol* 2014;71:1266–74 CrossRef Medline
 39. Lee JK, Wu J, Banks S, et al. **Prevalence of traumatic findings on routine MRI in a large cohort of professional fighters.** *AJNR Am J Neuroradiol* 2017;38:1303–10 CrossRef Medline
 40. Silk T, Beare R, Crossley L, et al. **Cavum septum pellucidum in pediatric traumatic brain injury.** *Psychiatry Res* 2013;213:186–92 CrossRef Medline
 41. El Marroun H, White TJ, van der Knaap NJ, et al. **Prenatal exposure to selective serotonin reuptake inhibitors and social responsiveness symptoms of autism: population-based study of young children.** *Br J Psychiatry* 2014;205:95–102 CrossRef Medline

MR Imaging Scoring System for White Matter Injury after Deep Medullary Vein Thrombosis and Infarction in Neonates

K.L. Benninger, N.L. Maitre, L. Ruess, and J.A. Rusin



ABSTRACT

BACKGROUND AND PURPOSE: Advanced imaging techniques have allowed earlier and more accurate detection of cerebral deep medullary vein thrombosis and infarction. Our objective was to develop an MR imaging scoring system to evaluate the severity of white matter injury in neonates with deep medullary vein thrombosis and infarction.

MATERIALS AND METHODS: This was a retrospective study of infants born ≥ 32 weeks' gestation (2000–2016) diagnosed with deep medullary vein thrombosis and infarction on neuroimaging in the first 30 days of life. A 102-point deep medullary vein white matter injury global severity score was developed. MR images were scored by 2 pediatric radiologists. Subject clinical data and regional and global severity scores were recorded.

RESULTS: Fifty-one patients (mean gestational age, 37.3 ± 2.2 weeks; mean birth weight, 3182 ± 720 g) were included with a mean age at diagnosis via MR imaging of postnatal day 10.1 ± 6.1 . Global severity scores ranged from 1 to 53, with a median score of 11 (interquartile range, 5–25). Lesions were more common in the frontal and parietal regions and less common in the occipital and temporal regions. Fifty-five percent of the group had neonatal seizures. No difference in perinatal risk factors (gestational age, birthweight, 5-minute Apgar score, chorioamnionitis, delivery room resuscitation, ventilator, or inotrope requirement) was observed among severity score quartiles.

CONCLUSIONS: An MR imaging scoring system provides a comprehensive and objective classification of WM injury after deep medullary vein thrombosis and infarction in late preterm and term neonates. The global severity score is independent of gestational age and other antenatal risk factors, consistent with presentation in previously healthy-appearing neonates.

ABBREVIATION: DMV = deep medullary vein

Cerebral sinovenous thrombosis is an important cause of morbidity and mortality in children, with an incidence of 0.67 cases per 100,000 children, with nearly half of cases occurring in neonates.^{1,2} Neonates are at increased risk of developing throm-

bosis secondary to immature hemostatic systems.^{3,4} Other recognized predisposing risks include maternal and perinatal factors unique to the neonatal time period such as maternal preeclampsia, diabetes and chorioamnionitis, fetal distress, birth asphyxia, sepsis, cardiac defects, and inherited prothrombotic abnormalities.¹⁻³

The incidence of cerebral sinovenous thrombosis may be underestimated in neonates. Cranial sonography is still the most routinely used neuroimaging technique in this age group, yet it is insufficient to precisely identify deep or diffuse thromboses. However, central nervous system imaging using MR imaging and, in particular, SWI allows accurate localization of deep vein thrombosis or infarction in children and adults.⁵⁻⁷ In particular, linear, radially oriented, fan-shaped lesions in the periventricular WM are indicative of deep medullary vein (DMV) involvement. This particular imaging pattern is explained by the anatomic distribution of the WM venous drainage.⁸ The characteristic pattern of DMV thrombosis and ensuing infarction of the surrounding tissue has been recognized on neuroimaging with increasing frequency in the past decade.^{5,6,9}

Received September 26, 2018; accepted after revision December 1.

From the Departments of Pediatrics and Center for Perinatal Research (K.L.B., N.L.M.) and Radiology (L.R., J.A.R.), Nationwide Children's Hospital, Columbus, Ohio; and Wexner Medical Center (K.L.B., N.L.M., L.R., J.A.R.), Ohio State University, Columbus, Ohio.

This work was supported by 1R01HD081120-01A1 from the Eunice Kennedy Shriver National Institute of Child Health and Human Development to N.L.M.

The content is solely the responsibility of the authors and does not necessarily represent the official view of the funding organization.

Paper previously presented at: Annual Meeting of the Midwest Society for Pediatric Research, October 4–5, 2018, Royal Oak, Michigan; and Children's Hospitals Neonatal Consortium 10th Annual Quality & Research Symposium, October 22–24, 2018, Lewis Center, Ohio.

Please address correspondence to Kristen L. Benninger, MD, Nationwide Children's Hospital, 575 Children's Crossroad, WB5203, Columbus, OH 43215-5994; e-mail: kristen.benninger@nationwidechildrens.org

Indicates open access to non-subscribers at www.ajnr.org

<http://dx.doi.org/10.3174/ajnr.A5940>

Table 1: DMV white matter injury severity scoring system

	Points	Scoring
Cerebral edema	0–3	None = 0, right or left = 1, bilateral asymmetric = 2, bilateral symmetric = 3
Corpus callosum	0–3	1 point each for genu, body, and/or splenium lesion
Right cerebral WM		Score each cerebral hemisphere region for punctate, linear, and/or cavitory lesions
Frontal	0–12	Punctate: mild (1–3 lesions) = 1, moderate (4–6 lesions) = 2, severe (>6 lesions) = 3
Parietal	0–12	Linear: mild (1–3 lesions) = 1, moderate (4–6 lesions) = 2, severe (>6 lesions) = 3
Occipital	0–12	Cavitory: mild (1–3 lesions, <15 mm) = 2, moderate (4–6 lesions, <15 mm) = 4
Temporal	0–12	severe (>6 lesions, <15 mm, or 1+ lesion >15 mm) = 6
Left cerebral WM		
Frontal	0–12	
Parietal	0–12	
Occipital	0–12	
Temporal	0–12	
	0–102	Global severity score

Despite increasing recognition of DMV thrombosis and infarction on neuroimaging, there is no published standardized approach to evaluate or grade these lesions in neonates. Clinical outcome data related to DMV pathology in neonates or children exist only in isolated case reports of motor impairment.⁹ Fetal diagnosis of DMV thrombosis and infarction has been described; however, in all cases in utero fetal or neonatal death shortly after delivery occurred.^{10,11} Similar lesions are described more frequently in preterm neonates with germinal matrix hemorrhage and congestion and obstruction of the terminal or medullary veins with subsequent parenchymal hemorrhage.⁵ However, in term neonates, germinal matrix hemorrhage is much less frequent, but DMV congestion, thrombosis, infarction, and hemorrhage are also seen.⁵ It has been hypothesized that DMV lesions in term neonates may be related to transient hypoperfusion or impairment in cerebral blood flow.⁵ No current system classifies this problem in infants during the perinatal period.

Therefore, the aim of our study was to develop a scoring system for conventional MR imaging that comprehensively and objectively defines brain injury after DMV thrombosis and infarction, to facilitate future prospective studies of developmental outcomes. We hypothesized that we could develop a semiquantitative system to characterize both the extent and topography of insults to the neonatal brain after DMV thrombosis and infarction. To test this hypothesis, we leveraged a large retrospective neuroimaging data base at our institution and graded DMV lesions while characterizing perinatal risk factors consistent with cerebral sinovenous thrombosis.

MATERIALS AND METHODS

Study Design and Participants

We retrospectively reviewed patients with a diagnosis of DMV thrombosis and infarction in a pediatric neuroradiology data base. All subjects were admitted to the neonatal intensive care unit or other hospital units at our institution between 2000 and 2016. Included in the review were infants born at ≥ 32 weeks' gestation and diagnosed with DMV thrombosis and infarction on neuroimaging during the first 30 days after birth. We excluded infants with congenital CNS anomalies or major congenital syndromes. The electronic medical record was reviewed, and all pertinent clinical, laboratory, imaging, and follow-up data were collected. This study was approved by the institutional (Nationwide Children's Hospital) review board for human research of the hospital.

Study data were managed using REDCap electronic data capture tools (<https://www.project-redcap.org/>) hosted at our institution.¹²

MR Imaging Acquisition

All brain MR imaging scans were obtained on either 1.5T or 3T MR imaging scanners (Excite HDXT 1.5T and GE Signa MR750 3T; GE Healthcare, Milwaukee, Wisconsin; and Magnetom Espree 1.5T and Magnetom Skyra 3T; Siemens, Erlangen Germany). Due to the retrospective study design, there was variation in imaging protocols, sequences, and parameters obtained. Scans included a combination of T1, T2, T1 FLAIR, DWI, and SWI sequences. Twenty patients also had 2D time-of-flight MR venograms available for review.

MR Imaging Assessment

While all scans for all subjects were reviewed, the MR image obtained at the time of initial radiologic diagnosis of DMV thrombosis and infarction was used for scoring purposes. A standardized scoring system was developed a priori on the basis of the topography of venous supply to the WM,⁸ to describe the severity of cerebral WM injury after DMV thrombosis and infarction.

The DMV WM injury-severity scoring system identified and assigned points for the degree of injury for focal lesions within the right and left frontal, parietal, occipital, and temporal lobes, for focal infarction within the corpus callosum and for diffuse WM cerebral edema (Table 1). Focal infarction and diffuse cerebral swelling were identified as focal or diffuse WM increased T2 and/or restricted diffusion signal abnormality, respectively, and were scored as present in cerebral WM either unilaterally, bilateral symmetrically, or bilateral asymmetrically. Regions were then scored separately for any punctate, linear, and/or cavitory lesions. Punctate and linear lesions, including those in a radial pattern, were identified as T1 bright and T2 dark, with hemorrhage confirmed on SWI and scored as mild, moderate, or severe on the basis of the number of lesions. Cavitory lesions were more heavily weighted to account for their larger and more severe tissue injury. All regional scores were added to the corpus callosum and cerebral edema scores to yield a global severity score (0–102 points). A diagrammatic representation of the scoring system is shown in Figs 1–4. Two pediatric radiologists independently scored the

scans and then agreed on the final consensus scoring after review of any discrepancies.

Statistical Analysis

Continuous variables were summarized using mean \pm SD or median (interquartile range). The DMV WM injury-severity scoring

system is a sum of scaled scores with a continuous composite. Categorical variables were summarized using percentiles. ANOVA was used to compare variance in means among the 4 quartiles in continuous variables. Adjustment for multiple comparisons was through Bonferroni correction. The Kruskal-Wallis test for nonparametric variables was used to assess the frequency distribution of categorical variables. Significance was assigned at $P < .05$. All analyses were performed using SPSS Statistics for MacIntosh (Version 24.0; Release 2016; IBM, Armonk, New York).

RESULTS

Our cohort consisted of 51 patients. Infants were born at a mean gestational age of 37 weeks (range, 32–41 weeks) with a mean birth weight of 3182 ± 720 g. Sixty-three percent of the group was male. On average, infants were admitted to our hospital on day of life 4.7 ± 4.9 , with only 37% admitted within the first day of life. The most commonly identified maternal risk factors were preeclampsia or hypertension (33%), diabetes (12%), and a maternal prothrombotic disorder (6%). Fifty-five percent of the infants had no identified maternal risk factors. One-third of in-

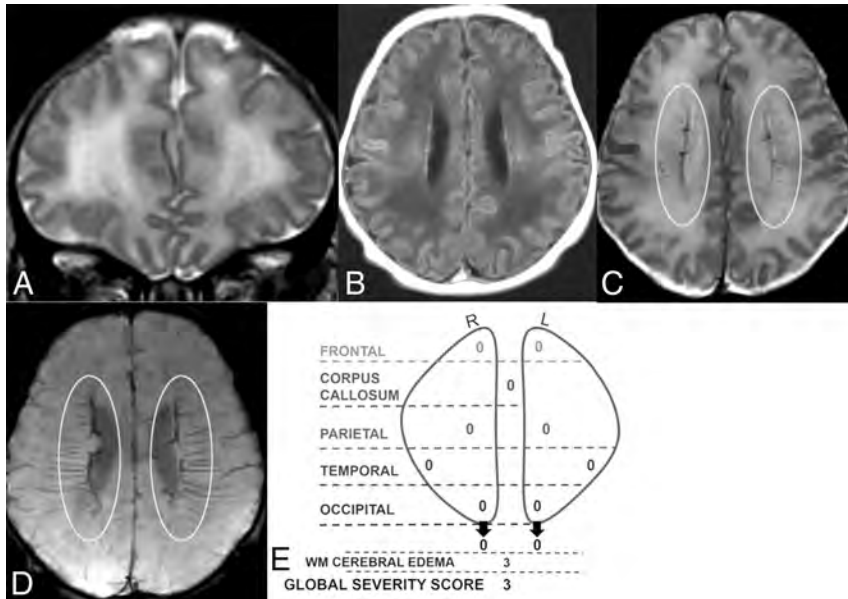


FIG 1. Coronal T2 (A) and axial T1 FLAIR (B), T2 (C), and SWI (D) MR images of a 6-day-old boy. Global severity score = 3 (first quartile) (E). There is diffuse bilateral WM signal abnormality of cerebral edema without infarction (3 points) (A and B). The DMVs are prominent bilaterally, seen on T2 (C) and SWI (D) (ovals). No WM lesions are visible. R indicates right; L, left.

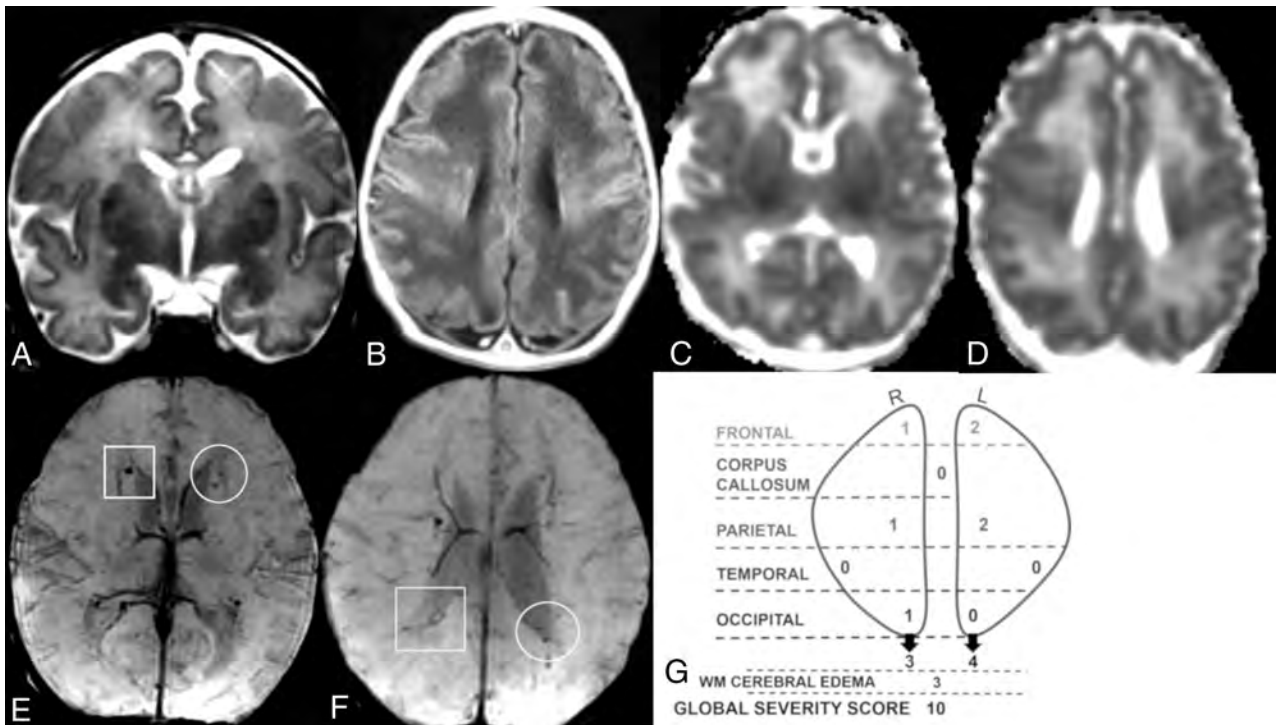


FIG 2. Coronal T2 (A), axial T1 (B), ADC (C and D), and SWI (E and F) MR images of a 7-day-old girl. Global severity score = 10 (second quartile) (G). There is diffuse bilateral WM cerebral edema (3 points) (A and B) and multiple acute bilateral, asymmetric (left > right) hemorrhagic WM lesions (T1 bright and T2 dark) without restricted diffusion (C–F). On the right, there are mild punctate lesions in the frontal (1 point), parietal (1 point), and occipital WM (1 point, not shown) (E and F, boxes), and on the left, there are moderate punctate lesions in the frontal (2 points) and parietal WM (2 points) (E and F, circles). No corpus callosum or temporal region WM lesions are visible. R indicates right; L, left.

infants demonstrated signs of fetal distress during the labor and delivery process (decelerations or a nonreassuring biophysical profile). Twenty percent were intubated, and 4% required chest compressions or epinephrine during the postdelivery resuscita-

tion. The average 5-minute Apgar score was 7.8 ± 1.7 . Neonatal comorbidities included encephalopathy (20%), neonatal infection (18%), hypoglycemia (35%), complex congenital heart disease (8%), and prothrombotic disorders (8%). Forty-three per-

cent of infants required mechanical ventilation, and 18% required inotropes in the first week of life. Infants presented on day of life 4.5 ± 5.3 with seizures (55%), apnea (53%), lethargy (49%), and poor feeding (35%). The average age at referral of these infants to our institution was 4.7 ± 4.8 days, and the average age at diagnosis via MR imaging was postnatal day 10.1 ± 6.1 .

The DMV WM injury global severity scores ranged from 1 to 53 and were divided into quartiles. The median score for the cohort was 11 (interquartile range [25th–75th percentile], 5–25). Seventy-six percent and 73% of patients had lesions in the frontal and parietal WM, respectively. Twelve percent and 41% of patients had lesions in the occipital and temporal WM, respectively. Acute parenchymal and corpus callosum lesions showed restricted diffusion. Representative MR images from a patient in each quartile with corresponding diagrammatic scoring are shown in

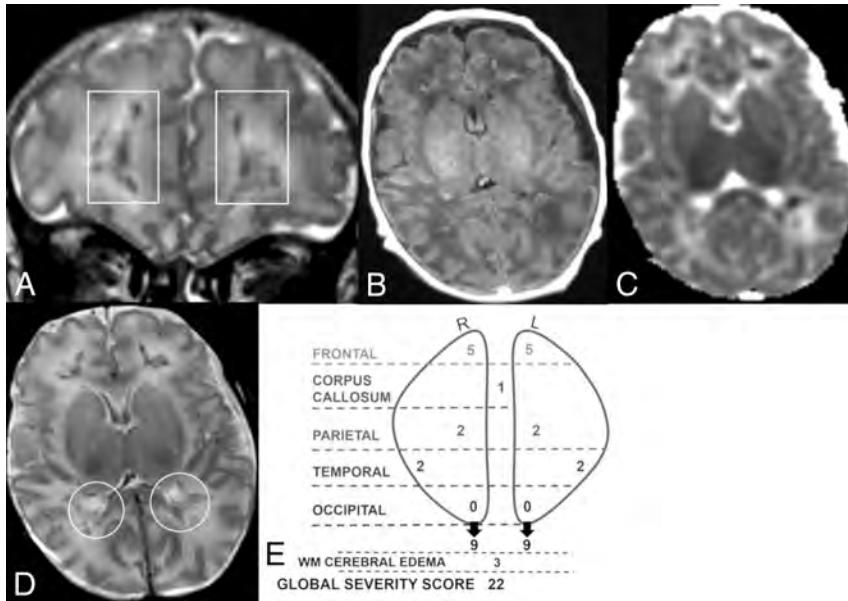


FIG 3. Coronal T2 (A) and axial T1 FLAIR (B), ADC (C), and T2 (D) MR images of a 21-day-old boy. Global severity score = 22 (third quartile) (E). There is diffuse bilateral WM cerebral edema (3 points) (A–D) and multiple acute bilateral symmetric hemorrhagic WM lesions (T1 bright and T2 dark): frontal (moderate punctate, 2 points, and severe linear, 3 points) (A, boxes), parietal (moderate punctate, 2 points) (D, circles), and temporal regions (moderate punctate, 2 points, not shown). There are no visible occipital WM lesions. R indicates right; L, left.

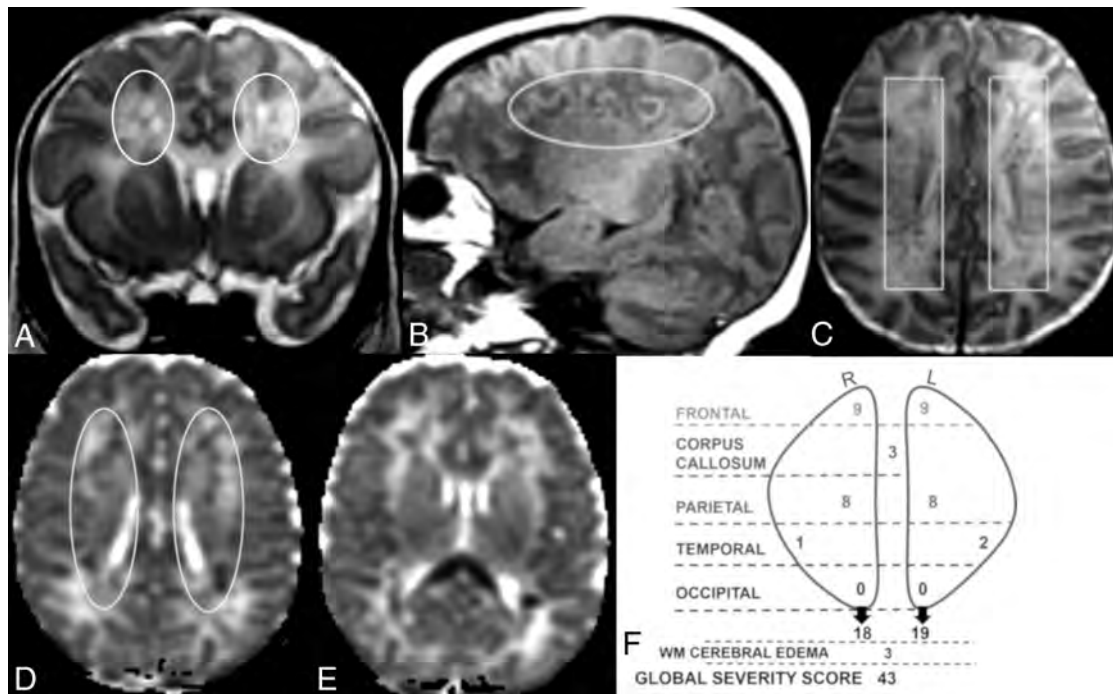


FIG 4. Coronal T2 (A) and sagittal T1 (B), axial T2 (C), and axial ADC (D and E) MR images of a 12-day-old boy. Global severity score = 43 (fourth quartile) (F). There is diffuse bilateral WM cerebral edema (3 points) and multiple bilateral hemorrhagic WM lesions with restricted diffusion (A–F). There are symmetric bilateral frontal and parietal lesions: severe linear lesions (3 points; C, boxes) and severe cavitory lesions with restricted diffusion (6 points; A, B, and D, ovals). There are bilateral temporal lesions: right (mild punctate, 1 point) and left (moderate punctate, 2 points, not shown). There is restricted diffusion throughout the corpus callosum (3 points, E). No occipital WM lesions are visible. R indicates right; L, left.

Figs 1–4, illustrating the range of severity and morphology of the various lesions. Tables 2 and 3 demonstrate the distribution of injury-severity scores by region. Only occipital regional severity scores and WM cerebral edema scores were not significantly different among quartiles.

Perinatal clinical variables were compared with global severity score quartiles (Table 4). Perinatal variables included factors associated with an increased risk of perinatal morbidity and mortality such as the 5-minute Apgar score, chorioamnionitis, small for gestational age, neonatal infection, ventilator requirement, inotrope use, and seizures. We observed no significant difference in perinatal risk factors among the severity score quartiles.

DISCUSSION

By leveraging the largest cohort to date with imaging for DMV thrombosis and infarction, we developed a neuroimaging scoring system, allowing a comprehensive and objective classification of WM injury in term and late preterm neonates. In our cohort of infants with DMV thrombosis and infarction, WM injury global severity scores were independent of gestational age at birth and other perinatal risk factors for morbidity and mortality. While the average age at referral of these infants to our institution was 4.7 days, the average age at MR imaging diagnosis was 10.1 days, suggesting that this entity is either under-recognized or that patients are not referred for immediate imaging. These factors may

be due a lack of MR imaging availability in most regional nurseries, necessitating transport to a neonatal intensive care unit with a higher level of care.

We compared regional WM injury scores with the global severity score and found that the occipital WM scores and WM cerebral edema scores were not significantly different among quartiles and therefore do not seem to impact the global severity score. Scores for all other regions were significantly different among quartiles. Thus, a modified, simpler score that excludes occipital and WM cerebral edema scores might be considered in future studies. This lesional distribution concentrated in the frontoparietal area has been described previously.^{5,10} It has been hypothesized that the higher frequency of transcerebral veins in the temporal and occipital regions and the thinner WM and shorter medullary veins in the temporal region are protective factors and thus contribute to the predominantly frontoparietal pattern seen in our patients and others studied.⁵

We noted a difference in gestational age at birth among global severity score quartiles with infants of a slightly younger gestational age (36–37 weeks) clustered around the median in the second and third quartiles, and infants born at an older gestational age (38 weeks), in the first and fourth quartiles. This U-shaped distribution of gestational age and global severity score quartiles is likely not clinically significant but may suggest that other unidentified factors affect severity.

We observed no difference between the global severity score quartile and selected perinatal variables (Table 4). We considered using a neonatal disease-severity scoring system (such as the Scores for Neonatal Acute Physiology) to stratify our patients by clinical disease severity at the time of presentation. However, most scoring systems are based on physiologic variables or treatment in the first 24 hours of life.¹³ Most of our patients appeared healthy at birth and did not come to medical attention until postnatal days 4–5, making use of these scoring systems inappropriate.

Table 2: Injury severity scores: WM cerebral edema and corpus callosum^a

Region	Score 0	Score 1	Score 2	Score 3	P Value
WM cerebral edema	4 (8)	2 (4)	9 (18)	36 (71)	.52
Corpus callosum	26 (51)	10 (20)	8 (16)	7 (14)	<.001

^a Data are number of patients (%).

Table 3: Injury severity scores by region^a

Region	Score 0–2	Score 3–5	Score 6–8	Score ≥9	P Value
Right frontal	24 (47)	14 (28)	8 (16)	5 (10)	<.001
Right parietal	33 (65)	8 (16)	9 (18)	1 (2)	<.001
Right occipital	50 (98)	1 (2)	0 (0)	0 (0)	.68
Right temporal	43 (84)	6 (12)	2 (4)	0 (0)	.006
Left frontal	31 (61)	10 (20)	7 (14)	3 (6)	<.001
Left parietal	37 (73)	5 (10)	7 (14)	2 (4)	<.001
Left occipital	49 (96)	0 (0)	2 (4)	0 (0)	.67
Left temporal	43 (84)	7 (14)	1 (2)	0 (0)	<.001

^a Data are number of patients (%).

Table 4: Global severity score and perinatal variables^a

	1st Quartile (Score = 1–5) (n = 14)	2nd Quartile (Score = 6–11) (n = 13)	3rd Quartile (Score = 12–25) (n = 12)	4th Quartile (Score ≥ 26) (n = 12)	P Value
Gestation at birth (wk)	38.2 ± 1.3	36.3 ± 2.4	36.7 ± 2.5	38 ± 1.9	.05 ^d
Birth weight (g)	3445.8 ± 618	3066 ± 989	2947 ± 619	3247 ± 570	.34 ^d
Male sex	8 (57)	8 (62)	9 (75)	7 (58)	.87 ^e
5-Minute Apgar	7.8 ± 1.6	7.9 ± 1.4	8 ± 1.5	7.4 ± 2.4	.92 ^d
Compressions/epinephrine ^b	1 (7)	0 (0)	0 (0)	1 (8)	.97 ^e
Chorioamnionitis	0 (0)	0 (0)	0 (0)	1 (8)	.98 ^e
Small for gestational age	0 (0)	2 (15)	3 (25)	2 (17)	.75 ^e
Neonatal infection ^c	1 (7)	2 (15)	3 (25)	3 (25)	.84 ^e
Ventilator requirement	2 (14)	7 (54)	6 (50)	7 (58)	.18 ^e
Inotrope use	0 (0)	3 (23)	2 (17)	4 (33)	.52 ^e
Seizures	7 (50)	5 (38)	6 (50)	10 (83)	.25 ^e

^a Data are mean or number (%).

^b Compressions or epinephrine or both were given in the delivery room during resuscitation.

^c Neonatal infection is defined as systemic/serious infection in the first week of life.

^d The ANOVA was used to measure variance in means among 4 quartiles in continuous variables.

^e The Kruskal-Wallis test was used for frequency distribution of categorical variables.

Limitations of this study included the retrospective, nonharmonized imaging data. However, the scoring system is relatively simple and can be applied to routine MR neuroimaging sequences. We also acknowledge the sample size, which may have contributed to the lack of significance of some perinatal risk factors. However, this remains the largest cohort examined to date.

There is no method to predict prognosis for term and late preterm infants with perinatal DMV thrombosis and infarction. This standardized scoring system allows us to stratify patients by severity of objective radiologic findings at the time of diagnosis. Further investigation is needed to compare severity scores at diagnosis with outcome data. Correlation of long-term effects of lesions on motor, cognitive, and behavioral performance may lead to a predictive model to help guide parental counseling and recommend therapies and early intervention.

No clinical outcome data related to DMV pathology in neonates or children exist beyond a few isolated case reports. In another cohort, follow-up MR imaging studies demonstrated evolution of the lesions across time with WM necrosis, development of cystic spaces, volume reduction, and hyperintense signal intensity of the periventricular WM on T2-weighted and FLAIR images, yielding a pattern of appearance similar to that of periventricular leukomalacia.⁵ It is likely that for DMV pathology, as for periventricular leukomalacia,^{14,15} a scoring system could be used to evaluate the long-term association of perinatal lesions with motor, cognitive, and behavioral performance in prospectively acquired datasets. However, unlike the published periventricular leukomalacia scoring system, the current DMV thrombosis and infarction classification can only be used in late preterm or term infants because this insult is not related in pathophysiology to encephalopathy of prematurity.

CONCLUSIONS

A 102-point MR imaging scoring system provides a comprehensive and objective classification of WM injury after DMV thrombosis and infarction in late preterm and term neonates. The DMV WM injury global severity score is independent of gestational age and other antenatal risk factors. This standardized scoring system can be used to stratify patients into severity groups for future work on the neurodevelopmental outcomes of patients after DMV thrombosis and infarction.

Disclosures: Kristen L. Benninger—RELATED: Grant: 1R01HD081120–01A1 from the Eunice Kennedy Shriver National Institute of Child Health and Human Development, Comments: R01 to Nathalie L. Maitre.* *Money paid to the institution.

REFERENCES

1. deVeber G, Andrew M, Adams C, et al; Canadian Pediatric Ischemic Stroke Study Group. **Cerebral sinovenous thrombosis in children.** *N Engl J Med* 2001;345:417–23 CrossRef Medline
2. Moharir MD, Shroff M, Pontigon AM, et al. **A prospective outcome study of neonatal cerebral sinovenous thrombosis.** *J Child Neurol* 2011;26:1137–44 CrossRef Medline
3. Yang JY, Chan AK, Callen DJ, et al. **Neonatal cerebral sinovenous thrombosis: sifting the evidence for a diagnostic plan and treatment strategy.** *Pediatrics* 2010;126:e693–700 CrossRef
4. Saxonhouse MA. **Thrombosis in the neonatal intensive care unit.** *Clin Perinatol* 2015;42:651–73 CrossRef Medline
5. Arrigoni F, Parazzini C, Righini A, et al. **Deep medullary vein involvement in neonates with brain damage: an MR imaging study.** *AJNR Am J Neuroradiol* 2011;32:2030–36 CrossRef Medline
6. Taoka T, Fukusumi A, Miyasaka T, et al. **Structure of the medullary veins of the cerebral hemisphere and related disorders.** *Radiographics* 2017;37:281–97 CrossRef Medline
7. Friedman DP. **Abnormalities of the deep medullary white matter veins: MR imaging findings.** *AJR Am J Roentgenol* 1997;168:1103–08 CrossRef Medline
8. Okudera T, Huang YP, Fukusumi A, et al. **Micro-angiographical studies of the medullary venous system of the cerebral hemisphere.** *Neuropathology* 1999;19:93–111 CrossRef Medline
9. Vilan A, Ribeiro JM, Reis C, et al. **Deep medullary veins and brain injury.** *J Pediatr* 2018;200:290–90.e1 CrossRef Medline
10. Doneda C, Righini A, Parazzini C, et al. **Prenatal MR imaging detection of deep medullary vein involvement in fetal brain damage.** *AJNR Am J Neuroradiol* 2011;32:E146–49 CrossRef Medline
11. Konanki R, Varma DR, Ratha C, et al. **Teaching NeuroImages: fetal deep medullary vein thrombosis presenting as progressive intracerebral hemorrhage.** *Neurology* 2015;85:e5–6 CrossRef Medline
12. Harris PA, Taylor R, Thielke R, et al. **Research Electronic Data Capture (REDCap): a metadata-driven methodology and workflow process for providing translational research informatics support.** *J Biomed Inform* 2009;42:377–81 CrossRef Medline
13. Dorling JS, Field DJ, Manktelow B. **Neonatal disease severity scoring systems.** *Arch Dis Child Fetal Neonatal Ed* 2005;90:F11–16 CrossRef Medline
14. Martinez-Biarge M, Groenendaal F, Kersbergen KJ, et al. **MRI based preterm white matter injury classification: the importance of sequential imaging in determining severity of injury.** *PLoS One* 2016; 11:e0156245 CrossRef Medline
15. De Vries LS, Van Haastert IL, Rademaker KJ, et al. **Ultrasound abnormalities preceding cerebral palsy in high-risk preterm infants.** *J Pediatr* 2004;144:815–20 CrossRef Medline

Volumetric MRI Study of the Brain in Fetuses with Intrauterine Cytomegalovirus Infection and Its Correlation to Neurodevelopmental Outcome

A. Grinberg, E. Katorza, D. Hoffman, R. Ber, A. Mayer, and S. Lipitz



ABSTRACT

BACKGROUND AND PURPOSE: In recent years, effort has been made to study 3D biometry as a method for fetal brain assessment. In this study, we aimed to compare brain volumes of fetuses with cytomegalovirus infection and noninfected controls. Also, we wanted to assess whether there is a correlation to their neurodevelopmental outcome as observed after several years.

MATERIALS AND METHODS: A retrospective cohort study examined MR imaging brain scans of 42 fetuses (at 30–34 weeks' gestational age) that were diagnosed with intrauterine cytomegalovirus infection. Volumetric measurements of 6 structures were assessed using a semiautomated designated program and were compared with a control group of 50 fetuses. Data collected included prenatal history and MR imaging and sonographic and neurodevelopmental follow-up.

RESULTS: We found that all brain volumes measured were smaller in the cytomegalovirus-infected group and that there was a correlation between smaller cerebellar volume and lower Vineland II Adaptive Behavior Scales questionnaire scores, especially in the fields of daily living and communication skills.

CONCLUSIONS: In this study, we found that brain volumes are affected by intrauterine cytomegalovirus infection and that it has a developmental prognostic meaning. Such information, which should be supported by further research, may help clinicians further analyze imaging data to treat and make a better assessment of these fetuses.

ABBREVIATIONS: CMV = cytomegalovirus; CV = cerebellum volume; ICC = intraclass correlation coefficient; LEBV = left eyeball volume; LHV = left hemisphere volume; REBV = right eyeball volume; RHV = right hemisphere volume; STV = supratentorial volume; VABS-II = Vineland II Adaptive Behavior Scale

Cytomegalovirus (CMV) infection is the most common intrauterine infection, affecting 0.3%–2% of live-born neonates.¹ Only 10%–20% of infected fetuses will show signs of infection at birth: intrauterine growth restriction, microcephaly, hepatosplenomegaly, thrombocytopenia, brain parenchymal calcifications, ventricle enlargement, cerebellar hypoplasia, and so forth. Different neurodevelopmental sequelae such as mental retardation and motor/hearing or visual impairment can manifest later in life, even in asymptomatic neonates.²

Because CMV is the most common environmental cause of

sensorineural hearing loss and a relatively common cause of mental retardation,³ it is important to improve the clinicians' ability to assess and predict the outcome of congenital CMV infection in order to provide the most accurate counseling to worried couples.

Today, the main assessment modalities of CMV-infected fetuses are sonography and 2D MR imaging.⁴ In recent years, the possibility of using 3D biometrics as a tool for fetal brain assessment has been investigated.^{5–8} This area is innovative with very limited information in the literature. There were only a few studies on quantitative MR imaging in CMV,⁹ but none had a follow-up or tried to examine a correlation to future outcomes. This type of quantitative information can lead to a better understanding of CMV infection effects on the developing brain, especially if correlated with the neurodevelopmental outcome.

In this study, we aimed to compare volumetric measurements of different structures in the fetal brain between CMV-infected fetuses and a control group of noninfected fetuses. In addition, we wanted to examine the correlation between brain volumes of the infected fetuses and their developmental outcome as observed after several years.

Received September 3, 2018; accepted after revision December 1.

From the Antenatal Diagnostic Unit (A.G., E.K., D.H., R.B., S.L.), Department of Obstetrics and Gynecology, and Department of Diagnostic Radiology (A.M.), Chaim Sheba Medical Center, Tel-Hashomer, Israel; and Sackler School of Medicine (A.G., E.K., D.H., R.B., A.M., S.L.), Tel Aviv University, Tel Aviv, Israel.

Anya Grinberg and Eldad Katorza contributed equally to this work.

Please address correspondence to Anya Grinberg, MD, Department of Obstetrics and Gynecology, Chaim Sheba Medical Center, Tel-Hashomer 52621, Ramat Gan, Israel; e-mail: Anya.grinberg@gmail.com

Indicates article with supplemental on-line tables.

<http://dx.doi.org/10.3174/ajnr.A5948>

MATERIALS AND METHODS

Subjects and Settings

This is a historic prospective cohort study that examined all cases (between January 2009 and June 2014) of women with CMV infection during pregnancy who underwent fetal MR imaging in our Chaim Sheba medical center (all CMV-infected women are indicated for clinical, MR imaging, and sonographic follow-up).

Forty-two fetuses were recruited according to the following criteria:

- 1) MR imaging was performed due to maternal primary CMV infection.
- 2) CMV infection occurred periconceptionally or during the first or second trimester of pregnancy.
- 3) Amniocentesis was performed and confirmed fetal CMV infection.
- 4) Fetal brain MR imaging was performed at 30–34 weeks' gestational age.
- 5) The developmental outcome was checkable (women who underwent termination of pregnancy were not included).
- 6) The data regarding pregnancy, follow-up, delivery, and outcome were available (women with a lack of information or who refused to answer the Vineland questionnaire were not included).
- 7) The MR imaging scans were of fair quality, enabling us to perform the necessary measurements.

The measurements were compared with those of a control group composed of 50 fetuses that underwent MR imaging for a non-neurologic reason as a part of a different cohort study performed in our institution, using the same semiautomated program.¹⁰ These scans were obtained at the same gestational ages and were found to contain no brain pathology according to a neuroradiologist's expert opinion. The scans Source, the measuring methods, and the volume calculations were identical.

To assess volume differences between the cases in the study and the control group that were measured in different gestational weeks, we created a *z* score for each brain volume of the case group using the means and SDs of each gestational week of the control group.

Data obtained from medical records included the following: pregnancy history, infection history, sonographic and MR imaging follow-up findings, perinatal history, and medical follow-up.

MR Imaging and the Semiautomated Algorithm

Fetal brain MR imaging was performed using a 1.5T system (Optima MR450w, 70 cm bore scanner; GE Healthcare, Milwaukee, Wisconsin). Single-shot fast spin-echo T2-weighted sequences in 3 orthogonal planes were performed using the half-Fourier technique (NEX = 0.53) with the following parameters: section thickness = 3 or 4 mm, no gap, flexible coil (8-channel cardiac coil), FOV determined by the size of the fetal head with a range of 24 × 24 cm to 30 × 30 cm, acquisition time between 40 and 45 seconds, matrix = 320 × 224, TE = 90 ms, TR = 1298 ms, pixel bandwidth = 122 Hz/pixel, specific absorption rate values = 1.1–1.7 W/kg.⁸

The algorithm is a recent development of our group.¹⁰ It is based on an initial contour manually drawn in the brain parenchyma of the midcoronal slice that defines the origin of interest. The initial contour is then automatically propagated by a level-

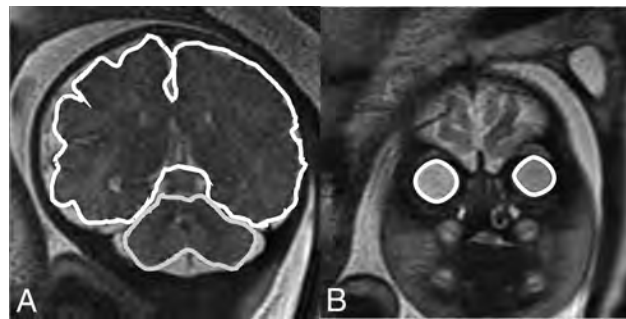


FIG 1. Representative slices of structure boundaries; A, STV and CV. B, REBV and LEBV.

set-based active contour algorithm until convergence into a new contour. The convergence is based on the representative pixels that are included in the initial contour. The next step is forward and backward propagation starting at the midcoronal slice, achieving contours automatically for every slice. Each new contour is based on the previous one, with a prefixed downsize volume for every slice. When it is completed, the user can adjust the resulting contour to achieve maximal accuracy. The volume is computed as the total number of voxels enclosed by the contours multiplied by the voxel size.

Measurements

All measurements were obtained in the coronal plane. For each fetus, we measured 8 structures: the supratentorial brain, right and left cerebral hemispheres, right and left lateral ventricles, right and left eyeballs, and the cerebellum. Measurements were used as follows (Fig 1). Of the volumes measured, 6 structures were assessed in the study:

Supratentorial Brain. We included the parenchyma of the frontal, parietal, occipital, and temporal lobes (including the third ventricle) and excluded the lateral ventricles (measured separately and subtracted), the brain stem, the cerebellum, and the fourth ventricle. Anterior, posterior, superior, and lateral boundaries were defined as the outer edge of the cerebral cortex. The inferior border matched the cortex and an imaginary line crossing the brain stem between the edges of the tentorium cerebelli.

Hemispheres (Right Hemisphere Volume [RHV] and Left Hemisphere Volume [LHV]). The volumes were measured separately using the same lateral boundaries, with the Sylvian fissure as a medial boundary and excluding the lateral ventricles.

Cerebellum. We included the cerebellar peduncles and vermis. The brain stem and the fourth ventricle were excluded.

Eyeballs (Right Eyeball Volume [REBV] and Left Eyeball Volume [LEBV]). Eyeballs were defined as the vitreous body and the lens, excluding the optic nerve.

The intraclass correlation coefficient (ICC) and limits of agreement were used to study the reliability of the measurements across measurers. Interobserver variability was tested comparing measurements of 15 fetuses made by 2 independent observers. Intraobserver variability was tested by repeating measures of 15 fetus samples. Results were defined as poor for ICC < 0.6, satis-

factory agreement for $0.6 < ICC < 0.8$, good for $0.8 < ICC < 0.9$, and excellent for $ICC > 0.9$.

Neurodevelopmental Outcome

Children were evaluated using the Vineland II Adaptive Behavior Scale (VABS-II) questionnaire,¹¹ which examines 4 areas of development from birth through adulthood:

- 1) Communication (receptive, expressive, written)
- 2) Daily living skills (personal, domestic, community)
- 3) Socialization (interpersonal relationships, play, leisure time, and coping skills)
- 4) Motor skills (gross, fine).

Because it is a norm-based instrument, the examinee's adaptive functioning is compared with that of others his or her age.

The standard score derived from this instrument has a mean of 100 ± 15 , and the adaptive level is derived from it. Scores of children were considered abnormal if the standard score was < 86 (below an adequate adaptive level).

The published Israeli version of the VABS-II questionnaire was administered, but no Israeli norms are available for the full age range. Because there was no reason to believe that children in Israel and the United States would develop mental and motor skills differently, we used the norms of the United States.¹²

Statistics

Categoric variables were expressed as number and percentages. Distribution of continuous variables was assessed using a histogram and Q-Q plot. Continuous variables were described using median and interquartile range or mean and SD as appropriate. The intraclass correlation coefficient was used to evaluate the inter- and intraobserver agreement.

Continuous variables were compared between the CMV-infected group and noninfected controls and also among individuals in the CMV-infected group, using an independent-samples *t* test or Mann-Whitney *U* test. The 1-sample Wilcoxon signed rank test was used to compare the calculated *z* scores of the CMV cohort to zero. The Spearman Correlation coefficient was used to evaluate the association among continuous variables.

A 2-tailed $P < .05$ was considered statistically significant. The false discovery rate method of Benjamini-Hochberg was used to conduct correction for multiple comparisons. Analyses were performed with SPSS Statistics for Windows (Version 24.0, 2016; IBM, Armonk, New York).

Ethics Approval

The study was approved by the Sheba Medical Center institutional review board (No. 0256-13-SMC).

RESULTS

Population

A total of 95 singleton pregnant women diagnosed with periconceptional and first- and second-trimester CMV infection were assessed in our clinic during the study period (between January 2009 and June 2014). Of these women, 36 did not undergo MR imaging in our institution, 2 underwent termination of pregnancy, and 4 fetuses tested negative for CMV infection with amniocentesis. Six other women were excluded because MR imaging

was performed in a gestational week not matching our criteria. Five more women were excluded for poor-quality MR imaging scans. Overall, 42 fetuses were eligible according to the study criteria.

Clinical Characteristics

From the main population of CMV-infected pregnant women, 2 (4.8%) women were infected around conception; 20 (47.6%), during first trimester; and 20 (47.6%), during the second trimester. Imaging follow-up during pregnancy found 15 women (35.7%) with abnormal findings on fetal sonography and 9 women (21.4%) with abnormal findings on fetal brain MR imaging. More clinical characteristics of pregnancies and fetuses of our study are described in On-line Table 1.

Delivery and outcome characteristics are described in On-line Table 2. Fourteen fetuses (33.3%) had abnormal perinatal outcomes, and 13 (31%) had abnormal findings on brain sonography at birth. Of those neonates, 18 (42.8%) were treated with ganciclovir, with a median time of 12 months (interquartile range, 12–12 months). Clinical retrospective follow-up of these children revealed that 2 (4.8%) had motor impairment, 6 (14.3%) had auditory impairment, and 4 (9.5%) had auditory impairment that resolved after treatment with ganciclovir.

Intra- and Interobserver Variability Assessment

The results of inter and intraobserver reliability of measurements are shown in On-line Table 3.

The volume measurements of the supratentorial volume (STV), right hemisphere volume, left hemisphere volume, cerebellum volume (CV), and Left Lateral Ventricle Volume (LLVV) showed excellent intra- and interobserver reliability: The lowest ICC for volume was 0.94. ICC measurements of right eyeball volume and Right Lateral Ventricle Volume (RLVV) showed good interobserver reliability, and left eyeball volume showed satisfactory interobserver reliability.

Volumetric MRI Results

Scatterplots of volumetric measurements according to gestational age of the CMV-infected group and the noninfected controls are presented in Fig 2. Table 1 presents the means or medians of the volumes found in the case group (fetuses with CMV infection) compared with the control group (noninfected fetuses). As shown, each volume of brain structures we examined was smaller in the case group; the cerebellum was the only structure that was smaller, but with a statistically insignificant difference. To overcome the volume differences resulting from measurement in different gestational weeks, we standardized the volumes of the CMV-infected group to the *z* score using the means of the volumes of the control group (healthy population) for each gestational week during MR imaging, as presented in Table 2. We showed, for all brain volumes measured, that *z* is always below zero, with a significance level of $< .05$; hence, we proved that when neutralizing gestational age as a confounder, all volumes (STV, RHV, LHV, CV, REBV, LEBV) of the case group (CMV-infected fetuses) are smaller and, specifically, < 1 SD from the volumes of the controls ($P \leq .001$).

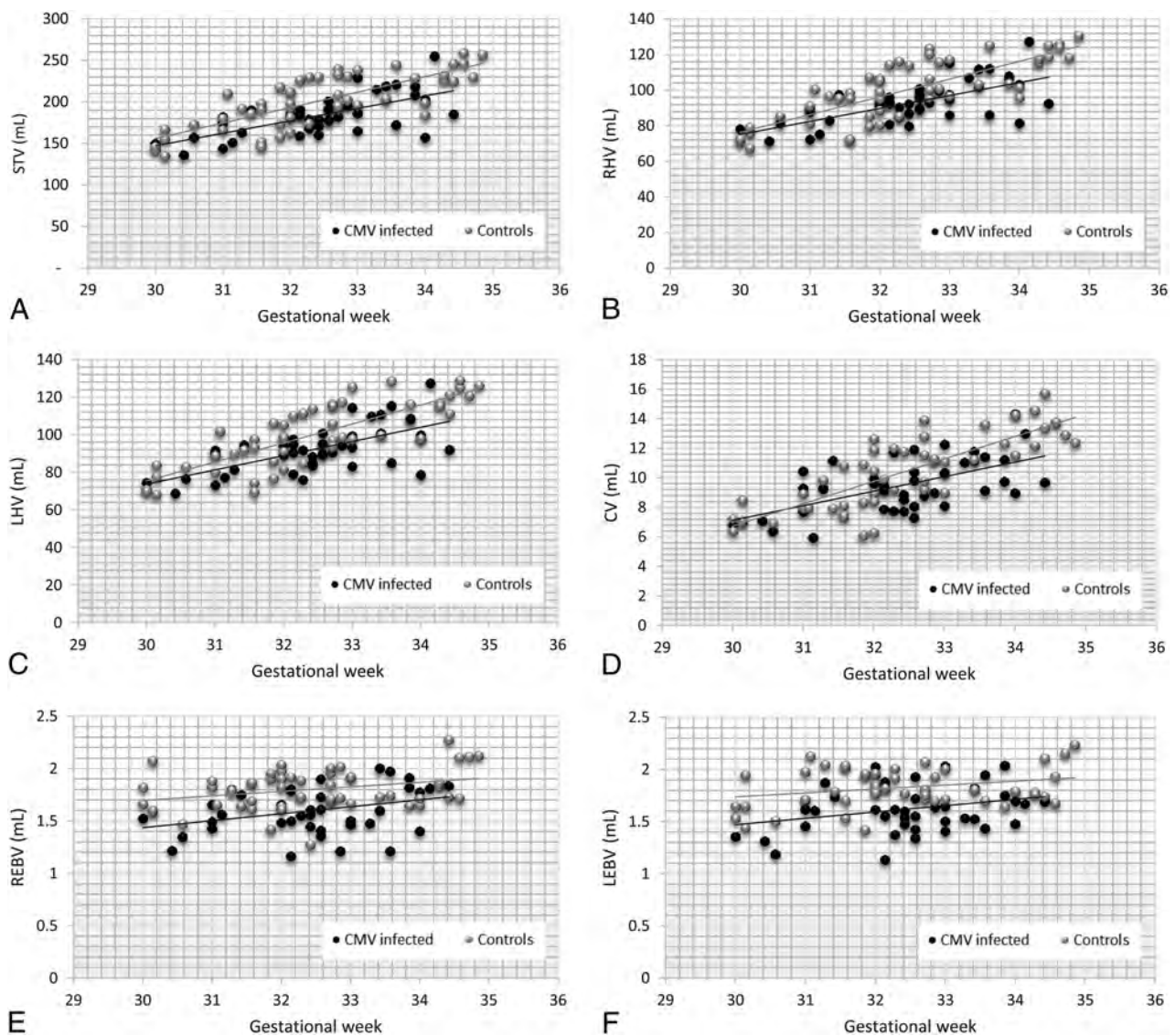


FIG 2. Scatterplots of volumetric measurements according to the gestational age of the CMV-infected group and the noninfected controls. Simple linear regression lines are shown for each set of data. A, STV. B, RHV. C, LHV. D, CV. E, REBV. F, LEBV.

Table 1: Means/medians of brain volume measurements for CMV-infected and control groups^a

Volume (mL)	CMV-Infected Fetuses (n = 42)	Control Fetuses (n = 50)	P
STV	184.7 (24.2)	200.9 (32.6)	.008 ^b
RHV	93.2 (11.8)	100.2 (17.1)	.022 ^b
LHV	92.4 (12.5)	99.5 (17.1)	.02 ^b
CV	9.5 (1.7)	10.3 (2.2)	.084
REBV	1.58 (1.46–1.79)	1.82 (1.66–1.92)	<.001 ^b
LEBV	1.61 (1.47–1.76)	1.79 (1.71–1.96)	<.001 ^b

^a STV, RHV, LHV, CV are presented as mean (SD); REBV and LEBV are presented as median (interquartile range).

^b Significant.

Table 2: Brain volumes of CMV-infected fetuses demonstrated as z scores^a

Volumes	Z Score	P ^b
STV	-1.26 (-1.71 to -0.31)	<.001
RHV	-1.06 (-1.65 to -0.15)	<.001
LHV	-1.08 (-1.6 to -0.14)	<.001
CV	-1.11 (-1.8 to -0.5)	<.001
REBV	-1.13 (-2.14 to -0.28)	.001
LEBV	-1.64 (-2.58 to -0.26)	<.001

^a Data are presented as median and interquartile range.

^b All P values are significant.

Neurologic and Developmental Outcome

Neurologic and developmental outcome was assessed using the Vineland II Adaptive Behavior Scales (characteristics of the Vineland adaptive level results are described in On-line Table 4). The mean age of children evaluated was 3.4 years (range, 2.2–4.2 years). Two children (4.8%) had moderately low communication

skills, 3 (7.1%) had moderately low daily living skills scores, 5 (11.9%) had moderately low social skills scores, 4 (9.5%) had moderately low motor skills scores, and 3 (7.1%) had moderately low complete adaptive behavior results. Abnormal outcome was established on the basis of the following: 1) VABS-II results of any category were below adequate, 2) motor impairment was seen in clinical follow-up, or 3) there was any hearing impairment (present or treated with ganciclovir). From our study population, 14 children were defined by the criteria mentioned above as having

abnormal neurologic and/or developmental outcomes (see their characteristics in On-line Table 5).

Volumetric Measurements and Neurodevelopmental Outcome

We used the Spearman rank correlation coefficient test to examine the correlation between brain volumes (represented by *z* scores) and the developmental outcome (represented by the Vineland II standard scores). We found a correlation between cerebellar volume and daily living skills: The smaller the cerebellum volumes were, the bigger the impairment in daily living skills was, with a significance of .041. When corrected for multiple comparisons, this correlation became insignificant ($P = .246$). We have not found any other significant correlation to VABS-II results (On-line Table 6).

Then we compared the VABS-II results obtained in very small brain volumes (<2 SDs of the *z* score) with the VABS-II results of all the rest (above -2 SDs of the *z* score). We found that a small fetal cerebellum was associated with a lower Vineland score of the child in the fields of communication (significance of .027), daily living skills (significance of .009), and overall adaptive level (significance of .043). After we corrected for multiple comparisons, only the association between a small fetal cerebellum and daily living skills stayed significant ($P = .045$). We have not found a significant correlation to motor skills or social skills, or with any other brain volume we measured (On-line Tables 7 and 8).

We have not found a significant correlation between brain volumes and any other clinical outcome in our study group such as hearing impairment (present or past) or findings on brain sonography at birth (small for gestational age). We have also not found a correlation between brain volumes and trimester of infection (On-line Table 9).

DISCUSSION

In this study, we compared brain volumes of fetuses with intrauterine CMV infection and noninfected controls. We also assessed their neurologic and developmental outcome as observed after several years. We found that all brain volumes measured were smaller in the CMV-infected group and that there is a correlation between cerebellar volume and developmental outcome.

Our study joins the growing amount of research in the new field of quantitative MR imaging. A 3D assessment provides information on the volume of different brain structures; thus, much can be learned and deduced about normal brain development and brain pathologies.^{7,13,14} A few studies have already shown some interesting results using quantitative MR imaging in the research of heart disease, idiopathic ventriculomegaly, and intrauterine growth restriction.^{5,6,8} There were only a few studies on quantitative MR imaging in CMV-infected fetuses, but none included a follow-up or tried to examine a correlation to future outcomes. Hoffmann et al⁹ examined the volume of hemispheres and temporal lobes in 27 fetuses with intrauterine CMV infection, and compared with a control group of healthy fetuses, temporal lobe volumes, normalized to whole, were smaller than the volumes in the noninfected control group. Our study contributes to and renews the knowledge of quantitative MR imaging in CMV-infected fetuses and demonstrates a statistically significant decrease (of >1

SD) in the supratentorial, both hemispheric, eyeball, and cerebellum volumes.

We assume that the fetal brain volume decrease is attributed to the brain damage caused by the viral infection. The damage is a combined result of some possible mechanisms: loss of neural stem cells and intermediate progenitors; interruption to stem cell migration and cell differentiation processes; astroglia insult, and therefore disruption of their supportive functions in the brain; neurotoxicity due to the inflammatory processes; and hypoxia due to severe placentitis.¹⁵

In this study, we also found a correlation between lower cerebellar volumes and lower VABS-II scores, specifically in the fields of communication and daily living skills. The cerebellum is considered particularly vulnerable to the negative effect of an insult due to its rapid growth during gestation.¹⁶ There is an association between cerebellar injury and neurodevelopmental sequelae, including cognitive, language, behavioral, social, and motor deficits.¹⁷ Children with congenital CMV infection exhibit a range of disabilities in these areas²; therefore, the findings of the effect on the cerebellar volume may be of great importance during follow-up and postinfection counseling.

The time of infection has a prognostic significance; most fetal and neonatal sequelae are associated with first- or second-trimester infections.^{18,19} Because the risk of an abnormal outcome of the fetus with third-trimester infection is minimal, we focused on patients who acquired primary CMV infection during the first and second trimesters. Hoffmann et al⁹ found, in their research, that infection during the first and second trimesters had a greater effect on volume differences than in the third trimester. In our research, we did not find a connection between the trimester of infection and brain volumes; perhaps a larger sample size is needed. Also, in this study, we did not find a correlation between brain volumes and hearing impairment; this may be due to several reasons: a small sample size or the pathogenesis of the sensorineural hearing loss possibly being different from the pathogenesis that causes decreased brain volumes.

The importance of this study is not only in its results, but we also demonstrate the use of a new tool, a semiautomated designated program that enables easy measurement of brain volumes that is less time-consuming and user-dependent. By applying this method in pathologic and healthy brain research, we believe that fetal brain volumetry can turn from a research tool into a practical clinical one.

We acknowledge some limitations of this study. First, we decided not to include pregnancies that underwent termination because one of our main goals was to find correlation to the outcome. However, there might be an importance in characterizing these fetuses because it might be reasonable to think that they might have had more severe findings. Also, we had a small sample size due to difficulty in finding women who met all the inclusion criteria. Nevertheless, this study was able to produce statistically significant statements and is relatively not small compared with other fetal volumetric studies.^{8,9} Also, the control group from which the normal volumes were derived was not composed of fetuses of volunteers but belonged to a cohort of patients with either a suspected brain pathology dismissed by MR imaging or a

family-related history. Lack of healthy pregnant women for reference is a common limitation in this research field.^{13,20}

CONCLUSIONS

Our study shows that in first- and second-trimester primary CMV intrauterine infection, brain volumes are affected, what bears a developmental prognostic meaning. There is a need to continue to explore this field of quantitative MR imaging and its ability to predict abnormal outcome in CMV-infected fetuses, with larger sample sizes and multi-institutional studies, to obtain significant results to characterize these volume differences, provide a deeper insight of the neurologic and developmental outcome, and influence important decision-making.

REFERENCES

1. Alford CA, Stagno S, Pass RF, et al. **Congenital and perinatal cytomegalovirus infections.** *Rev Infect Dis* 1990;12(Suppl 7):S745–53 Medline
2. Ornoy A, Diav-Citrin O. **Fetal effects of primary and secondary cytomegalovirus infection in pregnancy.** *Reprod Toxicol* 2006;21:399–409 CrossRef Medline
3. Pultoo A, Jankee H, Meetoo G, et al. **Detection of cytomegalovirus in urine of hearing-impaired and mentally retarded children by PCR and cell culture.** *J Commun Dis* 2000;32:101–08 Medline
4. Benoist G, Salomon LJ, Mohlo M, et al. **Cytomegalovirus-related fetal brain lesions: comparison between targeted ultrasound examination and magnetic resonance imaging.** *Ultrasound Obstet Gynecol* 2008;32:900–05 CrossRef Medline
5. Pier DB, Levine D, Kataoka ML, et al. **Magnetic resonance volumetric assessments of brains in fetuses with ventriculomegaly correlated to outcomes.** *J Ultrasound Med* 2011;30:595–603 CrossRef Medline
6. Limperopoulos C, Tworetzky W, McElhinney DB, et al. **Brain volume and metabolism in fetuses with congenital heart disease: evaluation with quantitative magnetic resonance imaging and spectroscopy.** *Circulation* 2010;121:26–33 CrossRef Medline
7. Grossman R, Hoffman C, Mardor Y, et al. **Quantitative MRI measurements of human fetal brain development in utero.** *Neuroimage* 2006;33:463–70 CrossRef Medline
8. Polat A, Barlow S, Ber R, et al. **Volumetric MRI study of the intrauterine growth restriction fetal brain.** *Eur Radiol* 2017;27:2110–18 CrossRef Medline
9. Hoffmann C, Grossman R, Bokov I, et al. **Effect of cytomegalovirus infection on temporal lobe development in utero: quantitative MRI studies.** *Eur Neuropsychopharmacol* 2010;20:848–54 CrossRef Medline
10. Ber R, Hoffman D, Hoffman C, et al. **Volume of structures in the fetal brain measured with a new semiautomated method.** *AJNR Am J Neuroradiol* 2017;38:2193–98 CrossRef Medline
11. Sparrow SS, Cicchetti DV, Balla AD. *Vineland Adaptive Behavior Scales.* 2nd ed. Circle Pines: American Guidance Service; 2005
12. Sparrow SS, Cicchetti DV. **Diagnostic uses of the Vineland Adaptive Behavior Scales.** *J Pediatr Psychol* 1985;10:215–25 CrossRef Medline
13. Hatab MR, Kamourieh SW, Twickler DM. **MR volume of the fetal cerebellum in relation to growth.** *J Magn Reson Imaging* 2008;27:840–45 CrossRef Medline
14. Clouchoux C, Guizard N, Evans AC, et al. **Normative fetal brain growth by quantitative in vivo magnetic resonance imaging.** *Am J Obstet Gynecol* 2012;206:173.e1–8 CrossRef Medline
15. Cheeran MC, Lokensgard JR, Schleiss MR. **Neuropathogenesis of congenital cytomegalovirus infection: disease mechanisms and prospects for intervention.** *Clin Microbiol Rev* 2009;22:99–126, Table of Contents CrossRef Medline
16. Volpe JJ. **Cerebellum of the premature infant: rapidly developing, vulnerable, clinically important.** *J Child Neurol* 2009;24:1085–104 CrossRef Medline
17. Limperopoulos C, Robertson RL, Sullivan NR, et al. **Cerebellar injury in term infants: clinical characteristics, magnetic resonance imaging findings, and outcome.** *Pediatr Neurol* 2009;41:1–8 CrossRef Medline
18. Pass RF, Fowler KB, Boppana SB, et al. **Congenital cytomegalovirus infection following first trimester maternal infection: symptoms at birth and outcome.** *J Clin Virol* 2006;35:216–20 CrossRef Medline
19. Gindes L, Teperberg-Oikawa M, Sherman D, et al. **Congenital cytomegalovirus infection following primary maternal infection in the third trimester.** *BJOG* 2008;115:830–35 CrossRef Medline
20. Clouchoux C1, Kudelski D, Gholipour A, et al. **Quantitative in vivo MRI measurement of cortical development in the fetus.** *Brain Struct Funct* 2012;217:127–39 CrossRef Medline

Brain DSC MR Perfusion in Children: A Clinical Feasibility Study Using Different Technical Standards of Contrast Administration

S. Gaudino, M. Martucci, A. Botto, E. Ruberto, E. Leone, A. Infante, A. Ramaglia, M. Caldarelli, P. Frassanito, F.M. Triulzi, and C. Colosimo

ABSTRACT

BACKGROUND AND PURPOSE: Dynamic susceptibility contrast MR perfusion imaging has limited results in children due to difficulties in reproducing technical standards derived from adults. This prospective, multicenter study aimed to determine DSC feasibility and quality in children using custom administration of a standard dose of gadolinium.

MATERIALS AND METHODS: Eighty-three consecutive children with brain tumors underwent DSC perfusion with a standard dose of gadobutrol administered by an automated power injector. The location and size of intravenous catheters and gadobutrol volume and flow rates were reported, and local and/or systemic adverse effects were recorded. DSC was qualitatively evaluated by CBV maps and signal intensity–time curves and quantitatively by the percentage of signal drop and full width at half-maximum, and the data were compared with the standards reported for adults. Quantitative data were grouped by flow rate, and differences among groups were assessed by analysis of covariance and tested for statistical significance with a *t* test.

RESULTS: No local or systemic adverse events were recorded independent of catheter location (63 arm, 14 hand, 6 foot), size (24–18 ga), and flow rates (1–5 mL/s). High-quality CBV maps and signal intensity–time curves were achieved in all patients, and quantitative evaluations were equal or superior to those reported for adults. No significant differences ($P \geq .05$) were identified among the higher-flow-rate groups in the quantitative data.

CONCLUSIONS: A custom administration of a standard dose of gadobutrol allows safe and high-quality DSC MR perfusion imaging in children.

ABBREVIATIONS: FWHM = full width at half maximum; GBCA = gadolinium-based contrast agent; PSD = percentage of signal drop

Dynamic susceptibility-weighted contrast-enhanced perfusion MR imaging provides hemodynamic information complementary to traditional structural MR imaging. Currently, DSC perfusion is routinely used in clinical practice to diagnose, man-

age, and investigate brain tumors in adult patients. DSC-derived cerebral blood volume maps can provide quantitative estimation of relative CBV that can be used to grade gliomas, differentiate brain tumor types, and distinguish tumors from non-neoplastic lesions.¹ The noninvasive character of DSC perfusion, susceptibility for microvascular hemodynamic alterations, short acquisition times, lack of ionizing radiation, and the current widespread availability of MR imaging scanners make DSC-PWI ideally suited for children.² However, performing DSC MR perfusion in pediatric patients can be challenging due to several technical issues: the need to use a power injector and difficulties in obtaining proper venous access (18–20 ga), reaching a high-flow injection rate (5 mL/s), and guaranteeing patient immobility. These limitations discourage the use of DSC-PWI in children, and most pediatric neuroradiologists still prefer manual injection of contrast medium. It is well-known that DSC imaging relies on the rapid acquisition of as many images as possible during the passage of the contrast media through the brain to measure the degree of T2/T2* signal changes with time and that it needs magnetic sus-

Received September 7, 2018; accepted after revision December 1.

From the Operative Unit Radiodiagnostica e Neuroradiologia (S.G., A.B., E.R., E.L., A.I., A.R., C.C.), Dipartimento di Diagnostica per Immagini, Radioterapia Oncologica e Ematologia, and Istituto di Radiologia (E.R., E.L., A.R., C.C.), Fondazione Policlinico Universitario A. Gemelli Istituto di Ricovero e Cura a Carattere Scientifico, Rome, Italy; Operative Unit of Neuroradiologia (M.M.), Azienda Ospedaliera, Università di Padova, Padova, Italy; Neurochirurgia infantile (M.C., P.F.), Fondazione Policlinico Universitario Agostino Gemelli Istituto di Ricovero e Cura a Carattere Scientifico, Rome, Italy; Neuroradiology Unit (F.M.T.), Fondazione Istituto di Ricovero e Cura a Carattere Scientifico, Cà Granda Ospedale Maggiore Policlinico, Milan, Italy; Department of Pathophysiology and Transplantation (F.M.T.), University of Milan, Milan, Italy; and Università Cattolica del Sacro Cuore (E.R., E.L., A.R., C.C.), Milan, Italy.

Please address correspondence to Simona Gaudino, MD, UOC Radiodiagnostica e Neuroradiologia, Institute of Radiology, Fondazione Policlinico Universitario A. Gemelli IRCCS, Largo A. Gemelli 1, 00168, Rome, Italy; e-mail: Simona.gaudino@gmail.com

Indicates article with supplemental on-line table.

<http://dx.doi.org/10.3174/ajnr.A5954>

ceptibility contrast agents to be injected as a narrow bolus by a power injector because high intravascular concentrations of gadolinium are required for T2-weighted magnetic susceptibility effects to dominate image contrast.

This prospective, bicenter study (Fondazione Policlinico Universitario A. Gemelli Istituto di Ricovero e Cura a Carattere Scientifico, Roma, Fondazione Istituto di Ricovero e Cura a Carattere Scientifico, Ca' Granda Ospedale Maggiore Policlinico, Milan) therefore aimed to determine the feasibility and safety of DSC MR perfusion imaging in children and to assess DSC perfusion quality using a "custom child" administration of a standard dose of gadolinium-based contrast agent (GBCA) (0.1 mmol/kg of gadobutrol, Gadovist; Bayer Schering Pharma, Berlin, Germany), defined as the use of a power injector at lower flow rates (1–5 mL/s) and by various venous accesses (18–24 ga) and locations (arm, foot, hand), with or without sedation. We compared the results obtained in children with the DSC quality standards reported in the literature for adults, considered the state of the art.

To our knowledge, this is the first study to evaluate the feasibility, safety, and quality of DSC-PWI in pediatric patients.

MATERIALS AND METHODS

Study Population

The local ethics committee approval was obtained at both sites for this prospective, bicenter study. A supplementary approval was obtained to extend the age of inclusion following the label extension in the European Union for diagnostic use of gadobutrol in pediatric patients younger than 2 years of age, including term neonates. Written informed consent was provided for each pediatric participant by the parent or legal guardian. Eighty-three consecutive pediatric patients (6 months to 16 years of age; mean age, 8.15 ± 4.7 years) from 2 centers were enrolled from February 2015 to October 2017. All patients had a diagnosis of previously untreated intra-axial brain tumor. Sedation was performed in patients younger than 6 years of age.

DSC Imaging Protocol

DSC perfusion MR images were obtained during the first pass of a gadobutrol bolus with 1.5T or 3T MR imaging scanners (Signa Excite and EchoSpeed; GE Healthcare, Milwaukee, Wisconsin; and Achieva, Philips Healthcare, Best, the Netherlands, respectively) using a gradient-echo EPI sequence (TR = 1500–2250, TE = 35–45 ms, flip angle = 35°–90°, NEX = 1, matrix size = 128×128 , section thickness = 4–5 mm, gap = 0.4–0.5 mm). A total of 60 image volumes were acquired, and the first 10 acquisitions were obtained to establish a precontrast baseline before starting the contrast agent injection. A standard contrast medium dose of 0.1 mmol/kg of body weight was injected followed by a 10–20 mL saline flush. Various peripheral intravenous catheters (18-, 20-, 22-, or 24-ga), locations (hand, arm, or foot), and flow-rates (1–5 mL/s) were used, depending on the age of the patient and the availability/site of venous access. Automated contrast agent and saline administration was performed using a power injector (Medrad® Spectris Solaris® EP; MedRad, Indianola, Pennsylvania) in all examinations. Choices of venous access, catheter size, and flow rate included the direct supervision of a physician (anesthesiologist and/or

neuroradiologist) to provide the safe administration of contrast and aiming to obtain a compact bolus. The catheter site was checked at the end of imaging and 24 hours after MR imaging, and adverse events were recorded.

DSC Image Processing

Perfusion and conventional MR imaging data were transferred from MR imagers to an independent personal computer for qualitative and quantitative perfusion analysis. Perfusion parametric maps were obtained using the dedicated software package nordICE (NordicNeuroLab, Bergen, Norway). Realignment was performed to minimize patient motion during dynamic scanning, and relative CBV maps were generated using an established tracer kinetic model applied to first-pass data.^{3,4}

To reduce recirculation effects, we fitted concentration-time course curves to a γ -variate function to approximate the first-pass response as it would appear in the absence of recirculation. The dynamic curves were corrected mathematically to reduce the effect of contrast agent leakage, as described previously,⁵ and the relative CBV was computed by numeric integration of the curve after eliminating recirculation and contrast agent leakage.

DSC Data Evaluation Part 1: Qualitative Analysis

Qualitative analysis was performed by 2 fully independent and blinded readers, a neuroradiologist with >10 years of experience in neuro-MR imaging and a third-year radiology resident. Each reader evaluated the relative CBV maps from each examination in a fully randomized order in terms of global image quality and the adequacy of differentiation between white and gray matter. As previously described,⁶ each reader evaluated CBV perfusion color maps by scoring the visibility of the insular ribbon, basal ganglia, and internal capsule on a scale of 1–5 according to the following criteria: 1, no, not visible or not distinguishable from surrounding tissue; 2, poor, barely distinguishable from surrounding tissue; 3, moderate, visible but unclear delineation from surrounding tissue; 4, good, visible with acceptable delineation from surrounding tissue; and 5, excellent, easily visible with sharp delineation from the surrounding tissue.

Arterial bolus quality was then evaluated using the 5-grade scale (no, poor, moderate, good, excellent) previously reported by Tombach et al⁶ on the basis of signal intensity–time curves derived from ROIs placed in the lenticular nucleus of the unaffected side. The scale enabled an integrated assessment of the shape of the curve, the steepness of the signal intensity decrease, the bolus width (wide or narrow), the signal intensity loss, the smoothness of the curve (smooth or jagged), and the presence of a second-pass enhancement peak. Interreader agreement was assessed for each qualitative evaluation.

DSC Data Evaluation Part 2: Quantitative Analysis

Quantitative analysis was performed using signal intensity–time curves derived from ROIs positioned on the lenticular nucleus and frontal white matter of the unaffected side.⁷ ROIs of at least 30 mm² were generally used and were placed by a third neuroradiologist with >10 years' experience in neuro-MR imaging and at least 5 years' experience in DSC-MR imaging. The percentage of signal drop (PSD) from pre- to

postcontrast and the full width at half maximum (FWHM) were determined from each signal intensity–time curve for each ROI, as reported in Essig et al.⁷

Statistical Analysis

The descriptive analysis included age, weight, quantity of contrast agent, flow rate, catheter gauge, and catheter site. The distribution of the continuous variables was assessed by the Shapiro-Wilk test, which showed a normal distribution of the considered variables.

Qualitative and quantitative data have been compared with the DSC quality standards reported in the literature for adults: approximately 30%–40% signal drop and 6–7 seconds of FWHM.⁷ Inter-reader agreement was assessed with the Cohen κ test for the qualitative evaluation. For the quantitative data, Pearson correlations were used to assess relationships between PSD and FWHM and parameters such as age, weight, quantity of contrast agent, flow rate, and catheter gauge and site; a 1-way ANOVA with logistic analysis was performed to compare the PSD and FWHM with these parameters.

Quantitative data were separated into 2 groups by flow rates for statistical analysis (low-flow group: flow rates from 1 to 3 mL/s; high-flow group: flow rates 4 and 5 mL/s), and differences between flow rate groups were evaluated by analysis of covariance and tested for statistical significance with a *t* test for paired samples.

Quantitative data were also divided into 3 groups by age (group 1: 0–6 years of age; group 2: 6–12 years of age; group 3: 13–16 years of age), and differences between male and female sex in each group were tested by a *t* test for paired samples. A *P* value < .05 was considered statistically significant.

RESULTS

Seventy-six patients were imaged on the 1.5T system, and 7, on the 3T system. The locations for the intravenous catheters were the arm (63/83), hand (14/83), and foot (6/83), and the gauges used were 18 ga (9/83), 20 ga (42/83), 22 ga (24/83), and 24 ga (8/83). The mean weight of the patients was 33.18 ± 17.26 kg, and gadobutrol volume ranged from 1 to 7 mL (mean, 3.36 ± 1.722 mL). Flow rates ranged from 1 to 5 mL/s: 5 mL/s in 8 patients, 4 mL/s in 46 patients, 3 mL/s in 18 patients, 2 mL/s in 8 patients, 1 mL/s in 3 patients. Thirty-three patients received sedation, and all were 6 years of age or younger. No access site–related or systemic complications were detected at the end of imaging or 24 hours later. High-quality CBV maps (minimum value, 4) and signal intensity–time curves (minimum value 3) were achieved in all examinations, with very good interobserver agreement for CBV maps ($\kappa = 0.756$) and good agreement for signal intensity–time curves ($\kappa = 0.724$) (On-line Table).

Most quantitative evaluations obtained in the lenticular nucleus were equal-to-superior compared with data for adults reported in the literature: The mean PSD was $41.42\% \pm 8.063\%$ (range, 29%–70%) and mean FWHM was $6.171 \text{ s} \pm 1.254 \text{ s}$ (range, 3.2–9.6) (On-line Table). The lowest flow rate was 1 mL/s in 3 patients and resulted in a mean PSD of 31.66%, 7.233-second mean FWHM, and a very high qualitative score for the CBV map and curve (On-line Table). The lenticular FWHM was above the threshold of 7 seconds in 20 patients (Fig 1). Quantitative evaluations obtained in the frontal white matter

showed a lower mean PSD ($22.12\% \pm 6.53\%$; range, 12%–37%) and a higher mean FWHM (6.833 ± 1.254 ; range, 3.8–9.5).

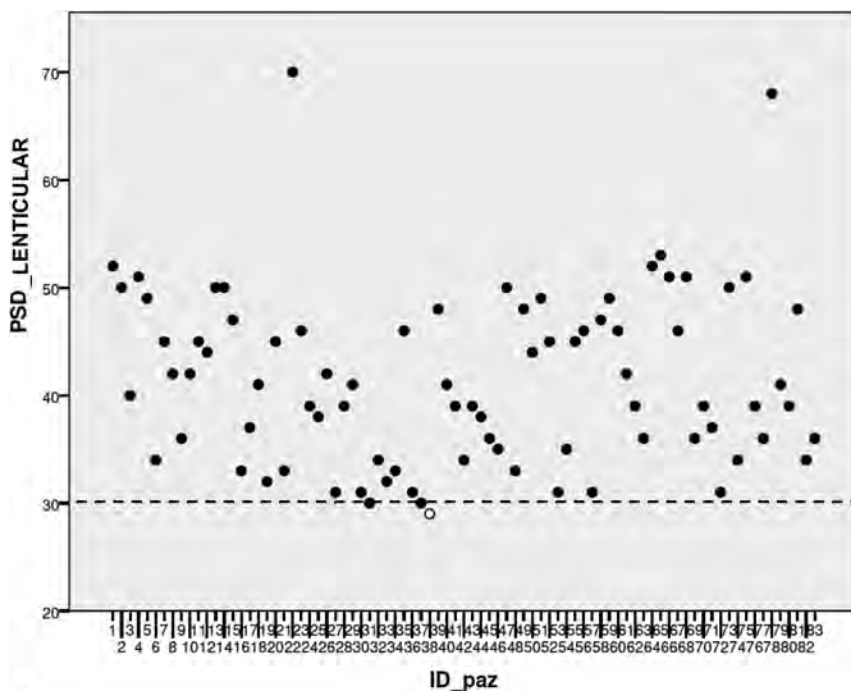
In both the lenticular nucleus and frontal white matter, no significant difference ($P \geq .05$) was found between quantitative FWHM and different flow-rate groups at 1–5 mL/s (Fig 2A). Among the different flow-rate groups, a significant difference ($P = .037$) in the PSD was found between 1 and 3 mL/s in the lenticular nucleus (Fig 2B). A difference in the PSD was also found in the frontal white matter between the 1- and 3-mL/s flow-rate groups, but the result was slightly above statistical significance ($P = .059$). No significant differences ($P \geq .05$) were found in the PSD and FWHM among the high (4–5 mL/s) and low (1–3 mL/s) flow-rate groups, and no significant relationships were found between the PSD and age, sex, weight, flow rate, catheter gauge, and quantity of contrast agent. Significant correlations were found between the lenticular FWHM and age ($P = .028$), weight ($P = .015$), and quantity of contrast agent ($P = .012$). In the 0- to 6-year-old group, boys showed a significantly higher lenticular FWHM ($P = .013$), while in the 13- to 16-year-old group, girls showed higher lenticular FWHM ($P = .017$) (Fig 3).

DISCUSSION

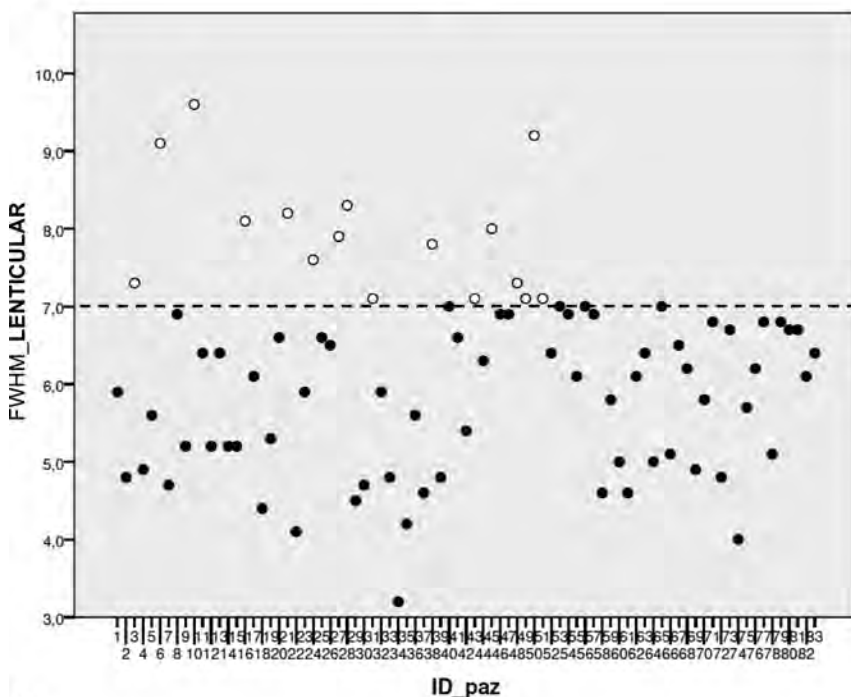
The diagnosis of pediatric brain tumors is almost always based on patient age, tumor location, and conventional neuroimaging findings. However, additional goals for brain MR imaging for pediatric brain tumors should include differentiating specific tumor types, grading tumors, distinguishing viable tumor from necrotic tissue, guiding stereotactic biopsy, and determining treatment responses. Perfusion MR imaging provides the degree of neovascularity/tumor angiogenesis and is extremely useful for tumor characterization, grading, and prognosis.

There are currently 3 available techniques for perfusion MR imaging: dynamic susceptibility contrast imaging, dynamic contrast-enhanced imaging, and arterial spin-labeling. Arterial spin-labeling is particularly easy, safe, and suitable for children due to the lack of exogenous contrast agent administration, but this technique is still gaining clinical acceptance. Both DSC and dynamic contrast-enhanced imaging need the same exogenous contrast agent (GBCA), with a universally accepted role in the characterization of brain tumors and mandatory administration in such clinicoradiologic scenarios, independent of patient age. A clear advantage of arterial spin-labeling is that CBF quantification is not affected by T1 and T2 leakage effects with blood-brain barrier disruption, but arterial spin-labeling can currently provide values of only CBF (relative and absolute), which showed a good correlation with DSC CBV. On the other hand, DSC imaging sets also contain information regarding the flow and permeability properties of the tumor microvascular system, and DSC provides several perfusion parameters, reported as useful in the assessment of pediatric brain tumors: percentage of signal recovery, pattern of contrast leakage, and time-to-maximum.^{8,9}

DSC imaging is currently considered the standard perfusion MR imaging method for brain tumors and is far more commonly used in the clinical setting because of its relatively short imaging time and the wider availability of image-processing tools. However, DSC imaging is technically more challenging in children compared with adult patients because it requires high-flow con-



A



B

FIG 1. Scatterplot of the PSD and FWHM distribution in the study population. *Dotted lines* indicate the threshold values of 30% for PSD (A) and 7 seconds for FWHM (B).

trast injection, a compact bolus, proper venous access (18–20 ga), and patient immobility according to the American Society of Functional Neuroradiology recommendations.¹⁰ Few studies report the use of DSC imaging in pediatric patients to date and often include confounding inclusion/exclusion criteria. Ho et al^{8,11} evaluated the utility of relative CBV data from DSC imaging for grading pediatric primary brain tumors but did not provide detailed information regarding injection rates or patient age. Our

study is the first to systematically determine the feasibility, safety, and quality of DSC MR perfusion imaging in children, using a custom child administration of a standard dose of gadolinium (0.1 mmol/kg dose of gadobutrol; Gadovist). We first demonstrated the technical feasibility of DSC-PWI in children and considered that the technique remains within the estimated cost, does not need additional or particular tools, and will be profitable in terms of clinical information. We carefully analyzed the safety of MR perfusion examinations in children, and all were well-tolerated and without adverse effects, notably with respect to the intravenous administration of contrast material performed with a power injector and various flow rates. We accurately customized the contrast medium administration for each patient, because we know from experience that the size of the child affects venous access and the ability to meet the standard adult requirements. Our safety standards required that 1 member of the MR imaging team (neuroradiologist, nurse, anesthesiologist) obtain peripheral venous access or check the pre-existing venous access site when patients and their parents arrive at the MR imaging unit. The key step was the accurate determination of the best venous access, which specified the appropriate needle gauge and the subsequent contrast medium flow rate. The peripheral IV catheters were always checked before examination by applying 5–10 mL of saline solution and were evaluated for blood return, and the connective tubing was attached to 1 of the power injectors. A new peripheral venous access site was inserted if the IV catheter could not be adequately flushed with saline or if the patient experienced pain at the injection site when not sedated. All aspects of the examination were explained to the parents of the children before the study, including the use of venous access to inject a small volume of contrast medium, and

this information was well-received by parents. We strongly believe that our safety standards, customized to each patient, allow DSC studies to be performed safely, with no extravasation or other local reactions/adverse effects recorded.

Finally, we analyzed and reported the DSC perfusion quality. We intentionally chose gadobutrol for its high relaxivity and high concentration. Values obtained for FWHM with gadobutrol were lower than those obtained with other less concentrated contrast

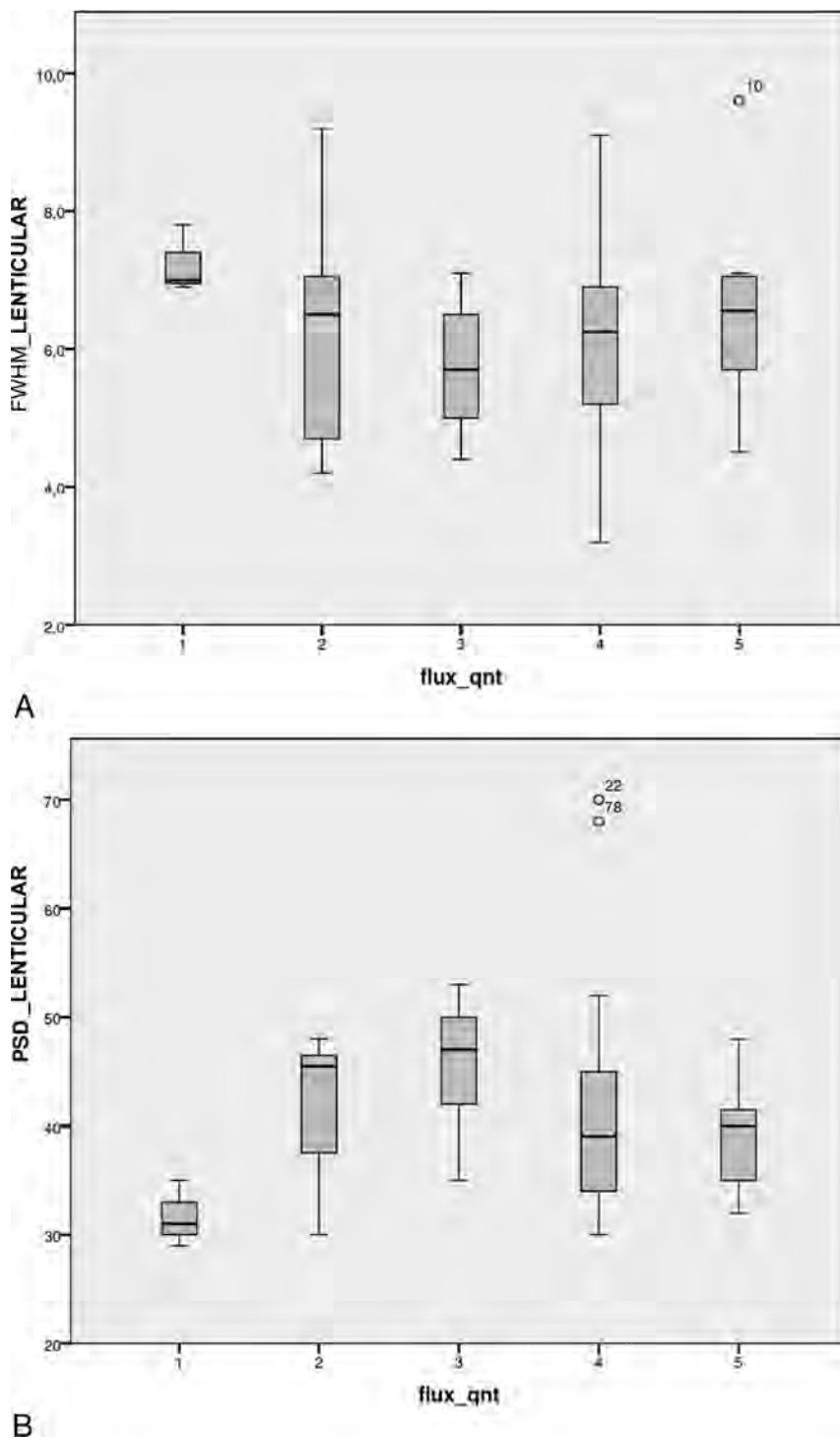


FIG 2. Boxplot of lenticular FWHM (A) shows no significant correlation with flow rate. Boxplot of lenticular PSD (B) shows a significant difference between the 1- and 3-mL/s groups.

agents,⁷ and although it has been reported that the reduced gadobutrol injection time did not show a positive effect on the bolus geometry in adults,¹² we speculated that a reduced bolus volume and consequently reduced injection rate may be advantageous for the bolus profile in our pediatric population. The comparison or enlargement of our data with those of future studies is now possible and in line with these suggestions.

We achieved high-quality CBV maps and signal intensity–

and smaller perfusion cross-sectional area in juvenile brains may reduce the general broadening of the bolus, leading to a bolus geometry similar to that obtained with the higher flow rates and volumes of contrast media in adults.² It is also well-accepted that cerebral blood flow tends to decrease throughout childhood, reaching adult levels by the late teens.¹³ It should be assumed that the width of the curve (FWHM) is more influenced by the increase in the bolus distribution in the vascular tree than the PSD,

time curves in all patients, even with very low-flow injection rates such as 1–2 mL/s. A flow rate of 1 mL/s was effective in achieving good-quality maps and curves (respectively evaluated with the maximum score and rated as good or excellent by the 2 readers) in 3 patients between 5 and 7 months of age, with a mean PSD value (31.6%) that is considered appropriate for routine clinical studies⁷ and a mean FWHM only slightly higher than 7 seconds, but similar to others obtained with faster flow rates in our population. In addition, neither the PSD nor FWHM showed statistically significant differences for gray and white matter between the groups' high- and low-flow rates. This means that even performing DSC-PWI at a lower flow rate we achieved good perfusion data. We demonstrated that a compact contrast bolus is achievable even using lower flow rates, particularly for young-age and low-weight children, resulting in a good or excellent quality of the curve and a high PSD. A univocal explanation for the FWHM of >7 seconds in 20 patients was not fully identified, but the relatively higher FWHM did not negatively affect the image quality in these 20 patients, and only 1 (a patient with a flow rate of 1 mL/s) had a PSD slightly lower than the accepted threshold of 30%.

As expected, the PSD was higher for gray matter than for white matter, whereas the FWHM was lower.⁷

Only the FWHM of the lenticular nuclei correlated with age, weight, and, consequently, the amount of contrast medium. The reasons for the similar PSDs obtained despite different injection rates and the higher FWHM obtained with increasing age, weight, and contrast amount remain to be clarified. Multiple factors may compete with the contrast flow velocity in children and exert a greater power to narrow the contrast bolus. Faster heart rates, faster circulation, shorter distance to reach the brain, a smaller capillary bed of the lung,

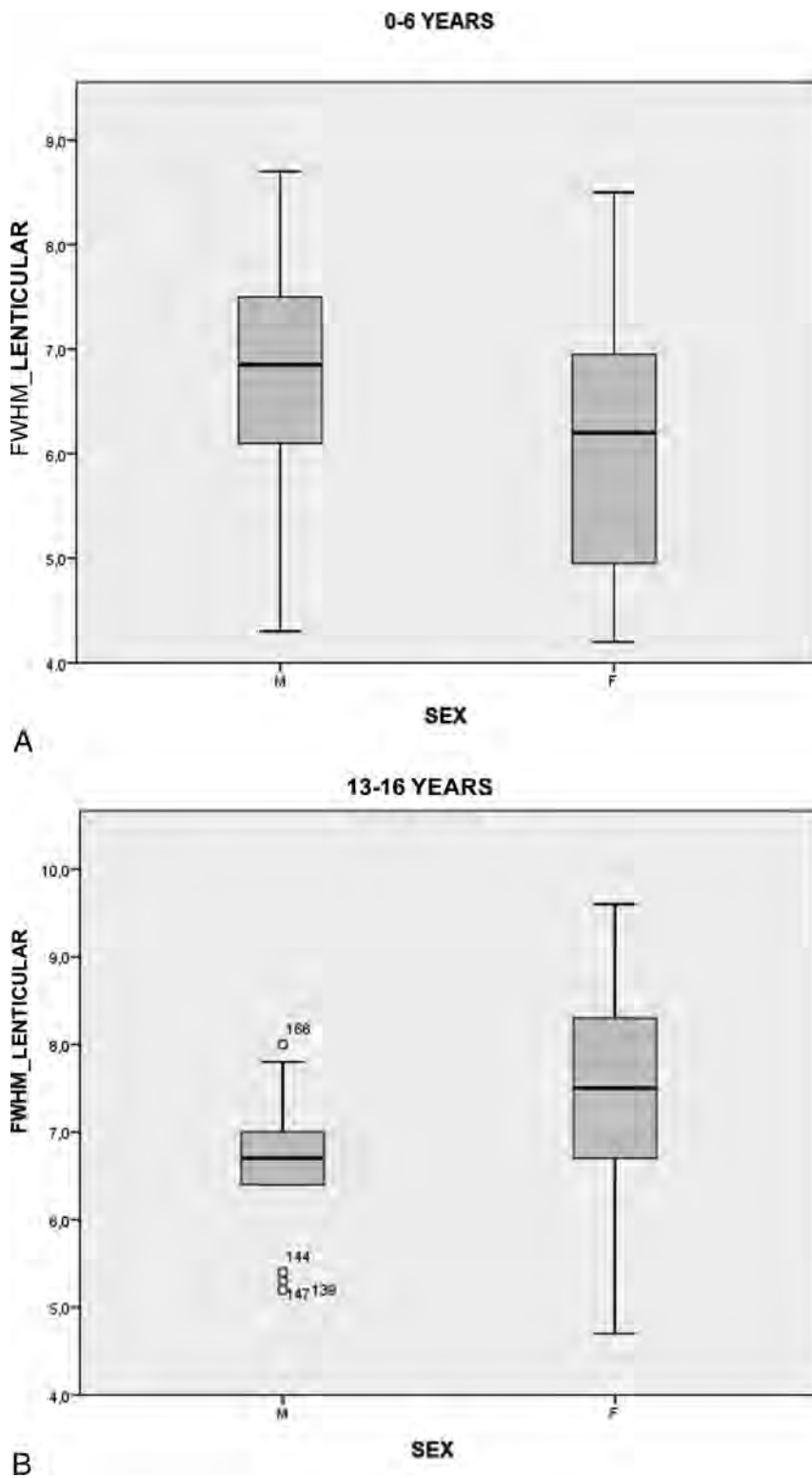


FIG 3. Boxplot of lenticular FWHM shows a significant correlation with sex the 0- to 6-year-old (A) and 13- to 16-year-old (B) groups.

with other parameters such as flow velocity being equal. In our population, the result of the highest PSD among the group with flow rates of 3 mL/s in gray matter (Fig 2B) is not completely clear; a larger population is needed to perform stronger statistical analyses among age-related groups. In adults, sex differences in cerebral perfusion have been reported, with women having higher

CBF values than men, but the factors modulating this sex difference in perfusion remain unclear. In our population, girls showed a lower FWHM of gray matter in the 0- to 6-year-old group, but it was higher in the 13- to 16-year-old group (Fig 3). Differences in hematocrit and steroid hormone levels have been brought into play to explain the sex difference in adult cerebral perfusion,^{14,15} but more studies on pediatric brain perfusion are warranted to define a sex difference in brain hemodynamics and to better understand the biologic causes.

Sedation was always used in children younger than 6 years of age, and while some anesthetic agents used in pediatric anesthesia decrease CBF indirectly,¹⁶ no cases of low-quality DSC perfusion studies were recorded in our population. Moreover, the use of DSC MR perfusion does not significantly extend the duration of sedation because it lasts approximately 1–1.30 minutes. Ultimately, our effort was to determine that DSC is feasible in pediatric patients; thus, when the use of gadolinium is deemed clinically necessary, the gadolinium bolus can be used to obtain DSC perfusion with administration parameters suitable for pediatric populations. Gadolinium deposition in the brain after the use of gadolinium-based contrast agents has been documented extensively in the literature.^{17–19} Brain deposition is most noticeable with linear agents in both adults and children, and at present, the GBCA gadobutrol seems less likely to deposit within the brain in comparison with other linear and macrocyclic GBCAs.¹⁸ Bjørnerud et al²⁰ reported, in an adult population, an increased T1 signal intensity in the dentate nucleus after a very high number (>30) of administrations of gadobutrol, but in pediatric patients, this agent was not associated with the MR imaging evidence of brain deposition.²¹ However, while gadobutrol may be less likely to deposit within the brain in comparison with other GBCAs, in our study, we chose this contrast agent due only to its characteristics of high relaxivity and high concentration.

because in early 2014, when we were planning this study, there was not yet scientific evidence of gadolinium deposition in the brain. Finally, to date, no detrimental impact of these depositions has been identified.

The primary limitation of the study is the small population, which does not allow the identification of factors that can influence

the quality of perfusion images more than others. Therefore, DSC should be performed in a larger pediatric population to clarify the mechanisms behind the similar bolus geometry despite the different injection flow rates in children with respect to adults. Another limitation is the low number of perfusion studies obtained at 3T, which does not allow comparisons of the quality of perfusion at 1.5T and 3T. However, considering the high quality of perfusion that we achieved at 1.5T and that, in general, 3T provides a greater SNR,²² we can speculate that pediatric brain DSC perfusion at low-flow rates may benefit from higher field strengths.

With such a wide age range of patients, to homogenize our data and have similar acquisitions, we decided not to use a preload because the precise administration of a quarter dose of 1 mol of contrast for children weighing less than 10 kg meant being able to administer less than 0.2 mL. In adult populations, to reduce the so called “leakage effect,” we usually use a preload of one-quarter of the total dose, about 5–10 minutes before the DSC acquisition as well as postprocessing leakage-correction algorithms. Benefits of the use of preload administration are particularly evident in the presence of BBB disruption, which may cause an underestimation of the relative CBV,²³ but in our population, quantitative data of DSC were measured in normal-appearing gray and white matter, where there was no evidence of alterations of the BBB. One of the limits of our study is the use of different flip angles, due to the different vendors and magnetic fields, while we used the same postprocessing leakage-correction algorithm.

CONCLUSIONS

This study provides support for the hypothesis that a custom child administration of a standard dose of gadobutrol allows safe and high-quality DSC perfusion MR imaging in a pediatric population. The feasibility and reliability of DSC-PWI in children argue for the inclusion of DSC in the routine clinical MR imaging protocol for pediatric brain tumors.

Disclosures: Cesare Colosimo—UNRELATED: Consultancy: Bracco.

REFERENCES

1. Cha S. **Dynamic susceptibility-weighted contrast-enhanced perfusion MR imaging in pediatric patients.** *Neuroimaging Clin N Am* 2006;16:137–47, ix CrossRef Medline
2. Huisman TA, Sorensen AG. **Perfusion-weighted magnetic resonance imaging of the brain: techniques and application in children.** *Eur Radiol* 2004;14:59–72 Medline
3. Rosen BR, Belliveau JW, Vevea JM, et al. **Perfusion imaging with NMR contrast agents.** *Magn Reson Med* 1990;14:249–65 CrossRef Medline
4. Østergaard L, Weisskoff RM, Chesler DA, et al. **High resolution measurement of cerebral blood flow using intravascular tracer bolus passages, Part I: mathematical approach and statistical analysis.** *Magn Reson Med* 1996;36:715–25 CrossRef Medline
5. Boxerman JL, Schmainda KM, Weisskoff RM. **Relative cerebral blood volume maps corrected for contrast agent extravasation significantly correlate with glioma tumor grade, whereas uncorrected maps do not.** *AJNR Am J Neuroradiol* 2006;27:859–67 Medline
6. Tombach B, Benner T, Reimer P, et al. **Do highly concentrated gadolinium chelates improve MR brain perfusion imaging? Intraindividually controlled randomized crossover concentration compar-**

7. Essig M, Lodemann KP, Le-Huu M, et al. **Intraindividual comparison of gadobenate dimeglumine and gadobutrol for cerebral magnetic resonance perfusion imaging at 1.5 T.** *Invest Radiol* 2006;41:256–63 CrossRef Medline
8. Ho CY, Cardinal JS, Kamer AP, et al. **Contrast leakage patterns from dynamic susceptibility contrast perfusion MRI in the grading of primary pediatric brain tumors.** *AJNR Am J Neuroradiol* 2016;37:544–51 CrossRef Medline
9. Koob M, Girard N, Ghattas B, et al. **The diagnostic accuracy of multiparametric MRI to determine pediatric brain tumor grades and types.** *J Neurooncol* 2016;127:345–53 CrossRef Medline
10. Welker K, Boxerman J, Kalnin A, et al; American Society of Functional Neuroradiology MR Perfusion Standards and Practice Subcommittee of the ASFNRClinical Practice Committee. **ASFNRC recommendations for clinical performance of MR dynamic susceptibility contrast perfusion imaging of the brain.** *AJNR Am J Neuroradiol* 2015;36:E41–51 CrossRef Medline
11. Ho CY, Cardinal JS, Kamer AP, et al. **Relative cerebral blood volume from dynamic susceptibility contrast perfusion in the grading of pediatric primary brain tumors.** *Neuroradiology* 2015;57:299–306 CrossRef Medline
12. Giesel FL, Mehndiratta A, Essig M. **High-relaxivity contrast-enhanced magnetic resonance neuroimaging: a review.** *Eur Radiol* 2010;20:2461–74 CrossRef Medline
13. Chiron C, Raynaud C, Mazière B, et al. **Changes in regional cerebral blood flow during brain maturation in children and adolescents.** *J Nucl Med* 1992;33:696–703 Medline
14. Liu Y, Zhu X, Feinberg D, et al. **Arterial spin labeling MRI study of age and gender effects on brain perfusion hemodynamics.** *Magn Reson Med* 2012;68:912–22
15. Ghisleni C, Bollmann S, Biason-Lauber A, et al. **Effects of steroid hormones on sex differences in cerebral perfusion.** *PLoS One* 2015;10:e0135827 CrossRef Medline
16. Harreld JH, Helton KJ, Kaddoum RN, et al. **The effects of propofol on cerebral perfusion MRI in children.** *Neuroradiology* 2013;55:1049–56 CrossRef Medline
17. Radbruch A, Weberling LD, Kieslich PJ, et al. **Gadolinium retention in the dentate nucleus and globus pallidus is dependent on the class of contrast agent.** *Radiology* 2015;275:783–91 CrossRef Medline
18. Kanda T, Osawa M, Oba H, et al. **High signal intensity in dentate nucleus on unenhanced T1-weighted MR images: association with linear versus macrocyclic gadolinium chelate administration.** *Radiology* 2015;275:803–09 CrossRef Medline
19. Robert P, Violas X, Grand S, et al. **Linear gadolinium-based contrast agents are associated with brain gadolinium retention in healthy rats.** *Invest Radiol* 2016;51:73–82 CrossRef Medline
20. Bjørnerud A, Vatnehol SA, Larsson C, et al. **Signal enhancement of the dentate nucleus at unenhanced MR imaging after very high cumulative doses of the macrocyclic gadolinium-based contrast agent gadobutrol: an observational study.** *Radiology* 2017;285:434–44 CrossRef Medline
21. Tibussek D, Rademacher C, Caspers J, et al. **Gadolinium brain deposition after macrocyclic gadolinium administration: a pediatric case-control study.** *Radiology* 2017;285:223–30 CrossRef Medline
22. Essig M, Shiroishi MS, Nguyen TB, et al. **Perfusion MRI: the five most frequently asked technical questions.** *AJR Am J Roentgenol* 2013;200:24–34 CrossRef Medline
23. Leu K, Boxerman JL, Ellingson BM. **Effects of MRI protocol parameters, preload injection dose, fractionation strategies, and leakage correction algorithms on the fidelity of dynamic-susceptibility contrast MRI estimates of relative cerebral blood volume in gliomas.** *AJNR Am J Neuroradiol* 2017;38:478–84 CrossRef Medline

High-Grade Gliomas in Children with Neurofibromatosis Type 1: Literature Review and Illustrative Cases

C.D. Spyris, R.C. Castellino, M.J. Schniederjan, and N. Kadom



ABSTRACT

SUMMARY: High-grade gliomas in patients with neurofibromatosis type 1 are rare and may therefore not be considered in the differential of brain lesions. Here, we describe 5 children with neurofibromatosis type 1; four of them developed various types of high-grade gliomas. The fifth patient had imaging features concerning for a high-grade lesion, but tissue diagnosis showed a low-grade glioma. The cases and literature summary provided here are to raise awareness for the occurrence of high-grade gliomas in children with neurofibromatosis type 1 and the limited ability of imaging features alone to predict a high-grade malignancy.

ABBREVIATIONS: HGG = high-grade glioma; LGG = low-grade glioma; NF1 = neurofibromatosis type 1

Brain tumors associated with neurofibromatosis type 1 (NF1) are typically low-grade gliomas (LGGs), such as pilocytic astrocytomas.¹ The mutation of neurofibromin, a protein that regulates growth and the proto-oncogene *Ras*, causes unregulated cell growth and can result in formation of either LGGs or high-grade gliomas (HGGs).² The incidence of HGG in children with NF1 is low and ranges from 0.28% to 5%.³⁻⁵

Using MR imaging for differentiating LGG from HGG can be problematic. While typical imaging features of LGG include lack of contrast enhancement, lack of restricted diffusion, and lack of hyperperfusion,⁶⁻⁹ the lack of MR imaging contrast enhancement in supratentorial brain tumors does not always equate with low-grade malignancy.¹⁰⁻¹² In addition, contrast enhancement is a typical imaging feature of pilocytic astrocytoma, a common low-grade tumor in NF1.^{10,13} Thus, tissue sampling may become necessary for some patients.¹⁴

Here, we present several pediatric patients with NF1 with suspicion for HGG based on imaging, along with clinical features and

neuropathology outcomes. Our goal was to raise awareness of HGG in children with NF1 and to facilitate appropriate management, including tissue sampling.

MATERIALS AND METHODS

The study received an exempt status by the institutional review board at Children's Healthcare of Atlanta and was Health Insurance Portability and Accountability Act-compliant. mPower™ (Nuance, Burlington, Massachusetts) was used to identify brain imaging studies performed during an 18-month period (January 1, 2015, to June 30, 2016) at our institution. Of 176 unique patients with NF1, five had concerning imaging findings.

Case Series

Patient 1. A 7-year-old boy with no known medical history presented to an outside institution with a 1-month history of roving eye movements with upgaze palsy, ataxia, and headaches. An outside MR imaging at baseline demonstrated a $2.6 \times 2.2 \times 2.5$ cm pineal region mass (Fig 1) with restricted diffusion (Fig 1C, -D), loss of the NAA peak, and elevated choline on MR spectroscopy. Tissue sampling at an outside facility showed a low-grade pineal parenchymal tumor. A 6-week MR imaging follow-up showed lesion growth to $2.9 \times 2.5 \times 2.9$ cm, which was localized to the tectal plate rather than the pineal gland, and interval development of an irregular and centrally necrotic-appearing area of contrast enhancement (Fig 1B). The patient was diagnosed with NF1 on admission in accordance with diagnostic criteria.¹⁵ Subtotal resection of the mass was performed, and pathology was now read as consistent with a midline, *H3 K27M*-mutant glioblastoma multiforme (On-line Table). When we compared it with the initial

Received August 8, 2018; accepted September 19.

From the Departments of Radiology and Imaging Sciences (C.D.S., N.K.), Pediatrics (R.C.C.), and Pathology and Laboratory Medicine (M.J.S.), Emory University School of Medicine, Atlanta, Georgia; Aflac Cancer & Blood Disorders Center (R.C.C.), Children's Healthcare of Atlanta, Atlanta, Georgia; and Department of Radiology (N.K.), Children's Healthcare of Atlanta, Egleston Campus, Atlanta, Georgia.

Paper previously presented as an oral Excerpta at: Annual Meeting of the American Society of Neuroradiology and the Foundation of the ASNR Symposium, April 22-27, 2017; Long Beach, California.

Please address correspondence to Nadja Kadom, MD, Emory University School of Medicine, Department of Radiology and Imaging Sciences, 1405 Clifton Rd NE, Atlanta, GA 30322; e-mail: nkadom@emory.edu; @nkpiano

Indicates article with supplemental on-line table.

<http://dx.doi.org/10.3174/ajnr.A5888>

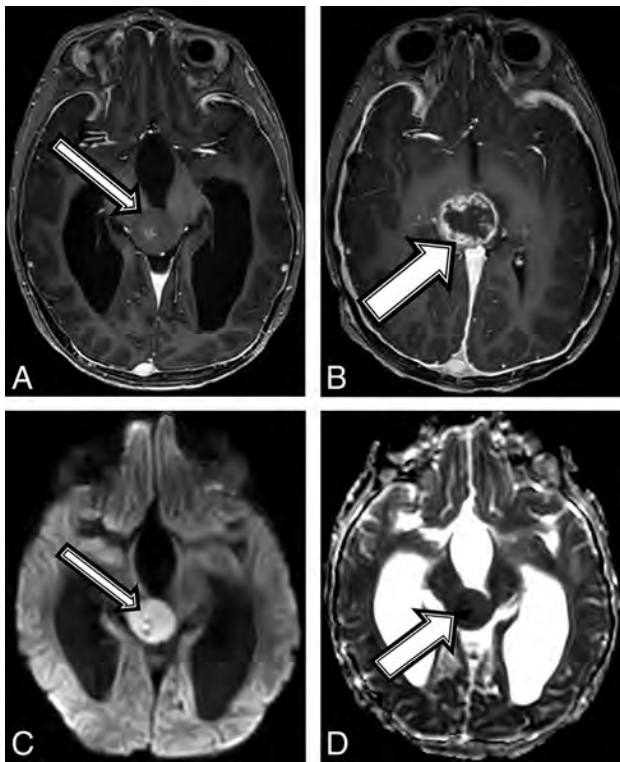


FIG 1. A 7-year-old boy with NF1 and a pathologic diagnosis of a midline, *H3 K27M*-mutant glioblastoma (patient 1). Axial T1 postcontrast at baseline (A) and after 6 weeks of follow-up (B). Baseline (A, arrow) smoothly margined T1 hypointense mass is shown centered within the midbrain and tectal plate with mild central enhancement; 6 weeks later, the mass increased in size (B, arrow) with new peripheral enhancement. Imaging at baseline shows a high diffusion signal on DWI (C) and a low signal on ADC (D), suggestive of high cellularity.

pathology, the current specimen displayed a different histomorphology with necrosis and vascular proliferation, which could have been related to intratumoral heterogeneity or possibly secondary to malignant transformation of the tumor. After a 6-week course of focal radiation therapy, the patient is currently stable clinically and by imaging surveillance.

Patient 2. An 11-year-old girl with no known medical history presented with a 1-month history of left upper extremity weakness, left foot drop, facial droop, mild dysarthria, headache, and intermittent nausea and vomiting. MR imaging demonstrated a peripherally enhancing heterogeneous mass containing blood products centered within the right thalamus (Fig 2A). The patient was diagnosed with NF1 on admission in accordance with diagnostic criteria.¹⁵ Tissue sampling showed histomorphology consistent with a grade II–III astrocytoma (On-line Table). However, the amount of Ki-67/MIB1 staining was elevated at 10%, and *H3 K27M* immunostaining was strongly positive, consistent with a diffuse midline, *H3 K27M*-mutated glioma (World Health Organization grade IV). After chemotherapy induction, follow-up MR imaging demonstrated tumor progression and aggressive features consistent with a high-grade malignancy (Fig 2B). Despite aggressive treatment, the patient's tumor progressed and the patient died 17 months after the initial diagnosis.

Patient 3. An asymptomatic 10-year-old boy with a diagnosis of NF1 in accordance with diagnostic criteria¹⁵ and previously

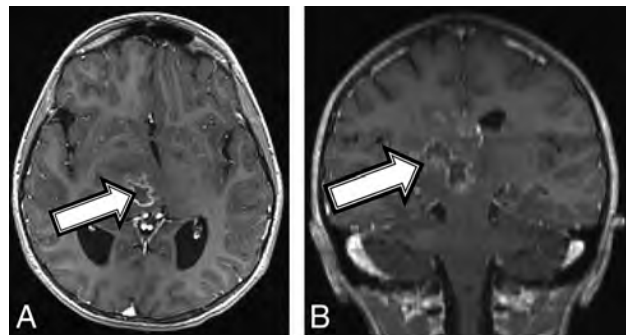


FIG 2. An 11-year-old girl with a final diagnosis of a grade II astrocytoma by histomorphology and a midline, diffuse HGG with *H3 K27M* mutation based on immunostaining (patient 2). Baseline axial T1 (A) and coronal (B) T1 postcontrast MR imaging shows a heterogeneous mass (A and B, arrows) centered in the right thalamus with a peripherally enhancing central cyst or area of necrosis.

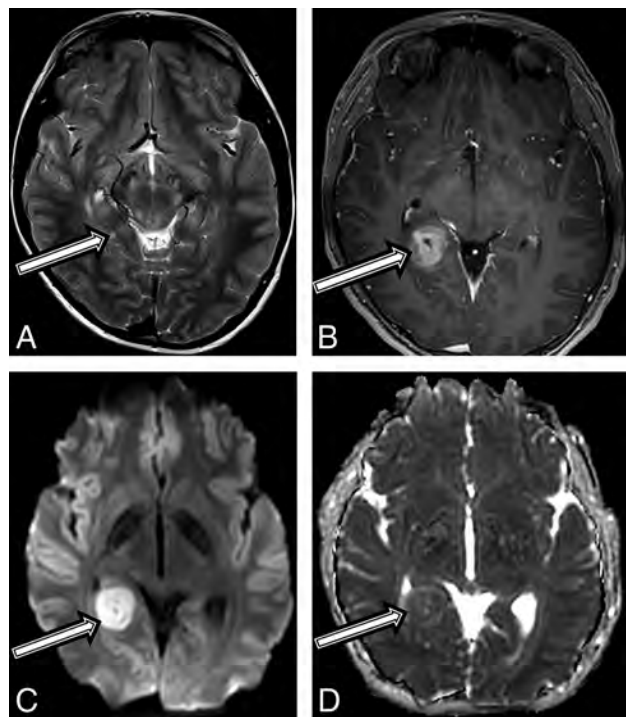


FIG 3. A 10-year-old boy with a final diagnosis of an anaplastic pleomorphic xanthoastrocytoma (patient 3). Axial T2-weighted images at baseline (A) and postcontrast axial T1 at 21 months (B) after diagnosis show a growing, well-defined mass in the right posterior mesial temporal lobe (A, arrow), which developed new inhomogeneous enhancement (B, arrow). MR imaging at 21 months shows new high-diffusion signal on DWI (C) and low signal on ADC (D), suggestive of high cellularity.

treated optic glioma underwent a routine brain MR imaging surveillance scan, and a tiny T2 hyperintense focus along the posterior aspect of the right hippocampus was found (Fig 3A). Follow-up MRIs performed 6 and 12 months later demonstrated a progressive increase in size, new heterogeneous contrast enhancement (Fig 3B), and new restricted diffusion (Fig 3C, -D). After gross total tumor resection, neuropathology revealed a high-grade pleomorphic glioma, with imaging and histologic features consistent with a pleomorphic xanthoastrocytoma (On-line Table). Due to the high-grade features of this tumor, he was treated with

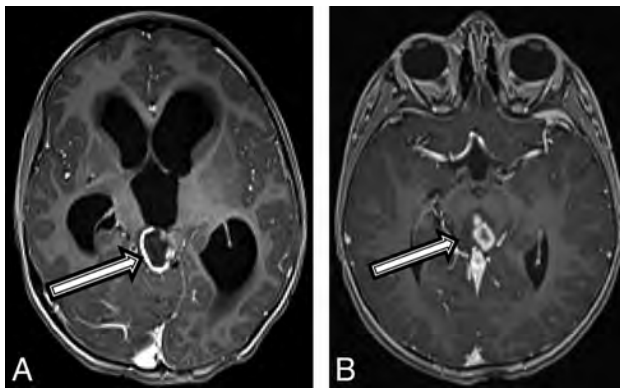


FIG 4. A 4-year-old boy with a diffuse HGG with *H3 K27M* mutation (patient 4). Axial T1 postcontrast MR imaging (A) at the initial presentation and on 6-month follow-up (B). There was initially a peripherally enhancing T2 hyperintense mass centered within the tectum (A, arrow) causing hydrocephalus. After 6 months, the lesion has increased in size, peripheral enhancement is no longer seen, but multiple centrally enhancing lesions are seen (B, arrow).

focal proton radiation therapy. The patient is currently active and asymptomatic 18 months after completion of proton radiation.

Patient 4. A 4-year-old boy with a history of “skin spots” presented to our institution with headache, nausea and vomiting, weight loss, fatigue, and forehead swelling for 1 month. A brain MR imaging revealed a heterogeneous and partially enhancing mass measuring $3.5 \times 2.3 \times 2.1$ cm in the midbrain tectum with compression of the cerebral aqueduct leading to severe obstructive hydrocephalus (Fig 4A). The patient was diagnosed with NF1 on admission in accordance with diagnostic criteria.¹⁵ Tissue biopsy revealed a diffuse, midline World Health Organization grade IV glioma with immunohistochemistry positive for nuclear *H3 K27M*-mutant protein, *α-thalassemia/mental retardation syndrome X-linked (ATRX)*, and wild type *p53*, with an MIB-1/Ki-67 index of 10%. However, OncoScan (<https://www.thermofisher.com/order/catalog/product/902695>) copy-number microarray only revealed a *PIK3CA p.H1047R* point mutation, but no copy number changes. Given that the molecular findings were inconsistent with a high-grade malignancy, the initial plan was to follow the patient clinically and by MR imaging. On follow-up MR imaging at 3 and 6 months, the lesion remained relatively stable in size but developed multiple peripherally enhancing components within the mass (Fig 4B). The patient experienced intratumoral hemorrhage, and MR imaging at that time showed evidence of tumor dissemination. The patient was started on chemotherapy with carboplatin and vincristine with a plan for re-evaluation for evidence of tumor progression by MR imaging after the induction phase of chemotherapy.

Patient 5. A 7-year-old boy with a medical history of migraines and slowed speech presented to an outside institution with a 2-month history of clumsiness, truncal ataxia, worsening headache, nausea and vomiting, somnolence, and worsened slowed/slurred speech. MR imaging demonstrated a robustly enhancing suprasellar mass and a peripherally enhancing mass centered within the left globus pallidus (Fig 5A), an infiltrating T2 hyperintense signal with punctuate foci of enhancement in the right basal ganglia, and enlargement of the optic nerves, chiasm, and

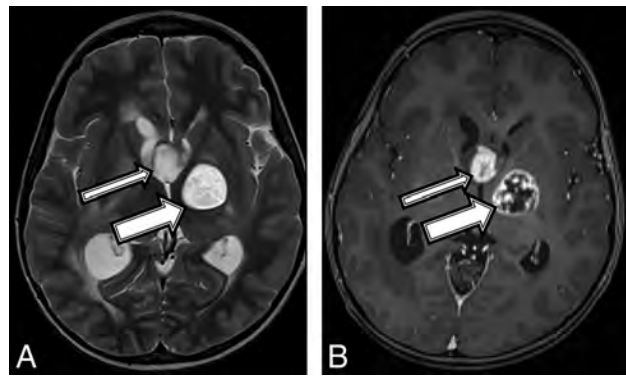


FIG 5. A 7-year-old boy with a final diagnosis of a pilocytic astrocytoma (patient 5). Axial T2 (A) and T1 postcontrast (B) MR images demonstrate a robustly enhancing T2 hyperintense suprasellar mass (thin arrows) and a T1 hypointense, T2 hyperintense mass centered within the left globus pallidus (thick arrows) with robust peripheral and patchy central enhancement.

optic radiations. The constellation of findings was most compatible with an infiltrating optic pathway/hypothalamic glioma. The patient was diagnosed with NF1 on admission in accordance with diagnostic criteria.¹⁵ Tissue sampling showed a high-grade infiltrating astrocytoma, but without morphologic criteria diagnostic for glioblastoma multiforme, with staining negative for *p53* and a mutation of the *BRAF* gene (*V600E*) mutant protein (On-line Table). A second biopsy of both the suprasellar mass and the left globus pallidus revealed findings more compatible with a pilocytic astrocytoma with low Ki-67/MIB-1 immunostaining. The patient was intolerant of initial chemotherapy with carboplatin and vincristine, so he was treated with vinblastine for 8 months. Follow-up MR imaging 2 months later showed an enlarging, enhancing mass lesion in the inferior right basal ganglia (Fig 5B). He began treatment with 5'-Inosinic acid, polymers, complex with 5'-cytidylic acid, polymers and L-lysine, homopolymer, compound with cellulose carboxymethyl ether (cancer drug) (Poly-ICLC) at that time and has experienced improvement of neurologic symptoms; his MRI findings have remained stable on immunotherapy with Poly-ICLC for 24 months.

DISCUSSION

In our case series, new enhancement on MR imaging or a change in the contrast-enhancement pattern in a pre-existing presumed low-grade lesion occurred in 3 of our patients (patients 1–3) and correctly indicated a higher grade malignancy.¹⁶ Only 2 patients (patients 1 and 4) had restricted diffusion on conventional DWI and also had a high-grade glioma.⁷ The use of kurtosis diffusion imaging may have demonstrated superiority to conventional diffusion metrics in distinguishing various cerebral glioma grades.¹⁷ Most interesting, patient 5 had concerning clinical and MR imaging signs but turned out to have a low-grade histopathology.

There are 2 scenarios by which an HGG may occur in patients with NF1: 1) Lesions presumed to be pilocytic astrocytoma convert to HGG at that site years later¹⁸; or 2) patients with presumed low-grade lesions subsequently develop a high-grade glioma at a different location.¹⁹ In our study, 1 patient (patient 3) developed a new lesion at a different site that grew slowly during a 16-month period; the other 4 patients did not have prior neuroimaging.

Recent retrospective analyses found that pediatric LGGs rarely transform to HGGs. In 1 retrospective analysis of 886 pediatric LGGs, only 2.9% of pediatric LGGs transformed into HGGs.²⁰

Approximately half of biopsied intracranial tumors in patients with NF1 are pilocytic or pilomyxoid astrocytomas, and the remainder are mostly diffuse/infiltrating gliomas, of which some are high-grade (anaplastic astrocytoma or glioblastoma).¹ Lesions of the 3 patients with HGGs in our series were diffuse and contained an *H3 K27M* point mutation. NF1 mutations have been demonstrated in a subset of *H3 K27M*-mutant HGGs.²¹ Another HGG in our series was an anaplastic pleomorphic xanthoastrocytoma, a rare tumor that has been reported several times in the literature in the context of NF1.²²⁻²⁵ Recently, the molecular genetic definition of HGG and apparent LGG has gained more importance, emphasizing the need to obtain tissue surgically.²⁶ The 2-year survival in patients with NF1 with HGG is higher than in patients without NF1.²⁷

Despite the small number of cases, we believe that raising awareness of an HGG in patients with NF1 among neuroradiologists is important. We were unable to evaluate the relative specificity of MR spectroscopy, perfusion, and kurtosis imaging, which may have prevented the tissue biopsy in the patient without HGG.

In conclusion, HGG in children with NF1 is rare, but concerning imaging signs should be taken seriously. We pursue tissue sampling when imaging findings are highly concerning for an HGG, though one of our patients in this series had a low-grade tumor on surgical pathology.

REFERENCES

- Rodríguez FJ, Perry A, Gutmann DH, et al. **Gliomas in neurofibromatosis type 1: a clinicopathologic study of 100 patients.** *J Neuro-pathol Exp Neurol* 2008;67:240–49 CrossRef Medline
- Fangusaro J. **Pediatric high grade glioma: a review and update on tumor clinical characteristics and biology.** *Front Oncol* 2012;2:105 CrossRef Medline
- Byrne S, Connor S, Lascelles K, et al. **Clinical presentation and prognostic indicators in 100 adults and children with neurofibromatosis 1 associated non-optic pathway brain gliomas.** *J Neurooncol* 2017;133:609–14 CrossRef Medline
- Blatt J, Jaffe R, Deutsch M, et al. **Neurofibromatosis and childhood tumors.** *Cancer* 1986;57:1225–29 CrossRef Medline
- Gutmann DH, Rasmussen SA, Wolkenstein P, et al. **Gliomas presenting after age 10 in individuals with neurofibromatosis type 1 (NF1).** *Neurology* 2002;59:759–61 CrossRef Medline
- Upadhyay N, Waldman AD. **Conventional MRI evaluation of gliomas.** *Br J Radiol* 2011;84(Spec No 2):S107–11 CrossRef Medline
- Hilario A, Ramos A, Perez-Nuñez A, et al. **The added value of apparent diffusion coefficient to cerebral blood volume in the preoperative grading of diffuse gliomas.** *AJNR Am J Neuroradiol* 2012;33:701–07 CrossRef Medline
- Kao HW, Chiang SW, Chung HW, et al. **Advanced MR imaging of gliomas: an update.** *Biomed Res Int* 2013;2013:970586 CrossRef Medline
- Sugahara T, Korogi Y, Kochi M, et al. **Usefulness of diffusion-weighted MRI with echo-planar technique in the evaluation of cellularity in gliomas.** *J Magn Reson Imaging* 1999;9:53–60 CrossRef Medline
- Panigrahy A, Blüml S. **Neuroimaging of pediatric brain tumors: from basic to advanced magnetic resonance imaging (MRI).** *J Child Neurol* 2009 24:1343–65 CrossRef Medline
- Muragaki Y, Chernov M, Maruyama T, et al. **Low-grade glioma on stereotactic biopsy: how often is the diagnosis accurate?** *Minim Invasive Neurosurg* 2008;51:275–79 CrossRef Medline
- Ginsberg LE, Fuller GN, Hashmi M, et al. **The significance of lack of MR contrast enhancement of supratentorial brain tumors in adults: histopathological evaluation of a series.** *Surg Neurol* 1998;49:436–40 CrossRef Medline
- Gold DR, Cohen BH. **Brain tumors in neurofibromatosis.** *Curr Treat Options Neurol* 2003;5:199–206 CrossRef Medline
- Kondziolka D, Lunsford LD, Martinez AJ. **Unreliability of contemporary neurodiagnostic imaging in evaluating suspected adult supratentorial (low-grade) astrocytoma.** *J Neurosurg* 1993;79:533–36 Medline
- Friedman JM. **Neurofibromatosis 1.** 1998 October 2, Updated 2018 May 17. In: Adam MP, Ardinger HH, Pagon RA, Wallace SE, Bean LJH, Stephens K, Amemiya A, eds. **GeneReviews.** Seattle, WA: University of Washington; 1993–2018. <https://www.ncbi.nlm.nih.gov/books/NBK1109/>. Accessed December 2, 2018
- Pierallini A, Bonamini M, Bozzao A, et al. **Supratentorial diffuse astrocytic tumours: proposal of an MRI classification.** *Eur Radiol* 1997;7:395–99 CrossRef Medline
- Qi C, Yang S, Meng L, et al. **Evaluation of cerebral glioma using 3T diffusion kurtosis tensor imaging and the relationship between diffusion kurtosis metrics and tumor cellularity.** *J Int Med Res* 2017;45:1347–58 CrossRef Medline
- Miaux Y, Guermazi A, Cornu P, et al. **High-intensity lesion on T1-weighted MR images in neurofibromatosis type 1: a case of pre-malignant lesion.** *Acta Neurochir (Wien)* 1997;139:1085–87 CrossRef Medline
- Distelmaier F, Fahsold R, Reifemberger G, et al. **Fatal glioblastoma multiforme in a patient with neurofibromatosis type 1: the dilemma of systematic medical follow-up.** *Childs Nerv Syst* 2007;23:343–37 CrossRef Medline
- Mistry M, Zhukova N, Merico D, et al. **BRAF mutation and CDKN2A deletion define a clinically distinct subgroup of childhood secondary high-grade glioma.** *J Clin Oncol* 2015;33:1015–22 CrossRef Medline
- Mukasa A, Aihara K, Gotoh K, et al. **Frequent H3F3A K27M mutations in thalamic gliomas from young adult patients.** *Neuro Oncol* 2014;16:140–46 CrossRef Medline
- Neal MT, Ellis TL, Stanton CA. **Pleomorphic xanthoastrocytoma in two siblings with neurofibromatosis type 1 (NF-1).** *Clin Neuro-pathol* 2012;31:54–56 CrossRef Medline
- Prayson RA. **Pleomorphic xanthoastrocytoma arising in neurofibromatosis type 1.** *Clin Neuropathol* 2012;31:152–54 CrossRef Medline
- Takei H, Rouah E, Bhattacharjee MB. **Cerebellar pleomorphic xanthoastrocytoma in a patient with neurofibromatosis type 1: a case report and literature review.** *Int J Clin Exp Pathol* 2015;8:7570–74 Medline
- Mackay A, Burford A, Molinari V, et al. **Molecular, pathological, radiological, and immune profiling of non-brainstem pediatric high-grade glioma from the HERBY Phase II randomized trial.** *Cancer Cell* 2018;33:829–42 CrossRef Medline
- Callovini GM. **Is it appropriate to redefine the indication for stereotactic brain biopsy in the MRI era? Correlation with final histological diagnosis in supratentorial gliomas.** *Minim Invasive Neurosurg* 2008;51:109–13 CrossRef Medline
- Huttner AJ, Kieran MW, Yao X, et al. **Clinicopathologic study of glioblastoma in children with neurofibromatosis type 1.** *Pediatr Blood Cancer* 2010;54:890–96 CrossRef Medline

A 3T Phase-Sensitive Inversion Recovery MRI Sequence Improves Detection of Cervical Spinal Cord Lesions and Shows Active Lesions in Patients with Multiple Sclerosis

A. Fechner, J. Savatovsky, J. El Methni, J.C. Sadik, O. Gout, R. Deschamps, A. Gueguen, and A. Lecler



ABSTRACT

BACKGROUND AND PURPOSE: Magnetic Resonance Imaging is the modality of choice to detect spinal cord lesions in patients with Multiple Sclerosis (MS). However, this imaging is challenging. New sequences such as phase-sensitive inversion recovery have been developed to improve detection. Our aim was to compare a 3D phase-sensitive inversion recovery and a conventional imaging dataset including postcontrast T2WI and T1WI to detect MS spinal cord lesions.

MATERIALS AND METHODS: This retrospective single-center study included 100 consecutive patients with MS (mean age, 41 years) from January 2015 to June 2016. One senior neuroradiologist and 1 junior radiologist blinded to clinical data checked for new spinal cord lesions, individually analyzing conventional and 3D phase-sensitive inversion recovery datasets separately, placing a 3-week delay between the 2 readings. A consensus reading was done with a third senior neuroradiologist. A Wilcoxon test was used to compare the 2 imaging datasets. Intra- and interobserver agreement was assessed by the κ coefficient.

RESULTS: 3D phase-sensitive inversion recovery detected significantly more lesions than conventional imaging (480 versus 168, $P < .001$). Eleven patients had no detected lesions on T2WI, whereas 3D phase-sensitive inversion recovery detected at least 1 lesion. All postcontrast T1WI enhancing lesions were also visible on 3D phase-sensitive inversion recovery. The signal-to-noise ratio was significantly higher using 3D phase-sensitive inversion recovery (0.63 versus 0.46, $P = .03$). Mean reading confidence was significantly higher using 3D phase-sensitive inversion recovery. Inter- and intraobserver agreement was good for both datasets.

CONCLUSIONS: Our study showed that 3D phase-sensitive inversion recovery significantly improved detection of cervical spinal cord lesions, including both enhancing and nonenhancing lesions in patients with MS.

ABBREVIATIONS: CNR = contrast-to-noise ratio; PSIR = phase-sensitive inversion recovery; MAGNIMS = Magnetic Resonance Imaging in Multiple Sclerosis; MERGE = Multi-Echo Recombined Gradient Echo; PST-IR = phase-sensitive T1-weighted inversion-recovery MR imaging

Multiple sclerosis is a neurodegenerative autoimmune demyelinating disease affecting the central nervous system, primarily involving the brain and the spinal cord. Imaging of the spinal cord is recommended because these results can detect silent lesions, described in 30%–40% of patients with radiologically or clinically isolated syndrome.¹ Spinal imaging defines lesion dissemination in spatial terms, thus increasing accurate MS diagnoses according to the Magnetic Resonance Imaging in MS

(MAGNIMS) and McDonald criteria,^{2,3} once differential diagnoses have been excluded. Imaging also helps predict management decisions because high spinal cord lesion load is linked to poorer prognosis.⁴

MR imaging is the technique of choice to fully visualize the spinal cord.⁵ This type of imaging proves challenging due to many visual artifacts generated from this area caused by cardiac pulsations, breathing, and CSF movement.^{6–9} Spinal cord lesions are classically studied with sagittal and axial T2-weighted sequences and postcontrast T1-weighted sequences, but these sequences were reported to lack sensitivity during the search of MS lesions.

To overcome challenges with spine imaging and increase both the sensitivity and specificity to detect inflammatory medullary lesions, the literature indicates a few other reliable MR imaging sequences, such as proton-density imaging,¹⁰ STIR,^{11,12} phase-sensitive T1-weighted inversion-recovery MR imaging (PST-IR),¹³ Multi-Echo Recombined Gradient Echo (MERGE; GE Healthcare, Milwaukee, Wisconsin),¹⁴ white matter-suppressed

Received September 17, 2018; accepted after revision November 29.

From the Departments of Neuroradiology (A.F., J.S., J.C.S., A.L.) and Neurology (O.G., R.D., A.G.), Fondation Ophtalmologique Adolphe de Rothschild, Paris, France; and Laboratoire MAP5, UMR CNRS 8145 (J.E.M.), Université Paris Descartes, Paris, France.

Please address correspondence to Augustin Lecler, MD, PhD, Department of Neuroradiology, Fondation Ophtalmologique Adolphe de Rothschild, 25 rue Manin, 75019 Paris, France; e-mail: alecler@for.paris

 Indicates article with supplemental on-line photos.

<http://dx.doi.org/10.3174/ajnr.A5941>

T1 inversion recovery,¹⁵ double inversion recovery,¹⁶ and MPRAGE.¹⁷ Recent studies have shown that the phase-sensitive inversion recovery (PSIR) sequence, consisting of a heavily T1-weighted inversion recovery combined with phase-sensitive reconstruction,^{13,18} had the highest lesion-to-cord contrast and lesion-limit definition.¹³ Therefore, this sequence seemed particularly promising for the detection of spinal cord lesions.

Our center developed a 3D-PSIR sequence at 3T for the spine. The aim of this study was to evaluate its sensitivity to detect spinal cord lesions in patients with MS compared with a conventional set including postcontrast T2WI and T1WI sequences.

MATERIALS AND METHODS

Study Design

We conducted a retrospective systematic chart review in a tertiary referral center specializing in neurologic diseases, the Rothschild Ophthalmological Foundation, Paris, France. This study was approved by our institutional research ethics board and adhered to the tenets of the Declaration of Helsinki. This study follows the Strengthening the Reporting of Observational Studies in Epidemiology guidelines.¹⁹

Patients

From January 2015 to June 2016, one hundred consecutive patients were included. Inclusion criteria were the following: 1) older than 18 years of age; 2) a confirmed diagnosis of multiple sclerosis using the 2010 criteria for MS³; 3) the presence of spinal cord MR imaging, including 1 conventional set of sagittal T2- and postcontrast T1-weighted imaging and one 3D-PSIR sequence.

Clinical Charts

All patients' medical charts were systematically reviewed to retrieve clinical data such as the type of MS, demographics, and the score from the Expanded Disability Status Scale.²⁰

MR Imaging

All MR imaging examinations were performed with the same 3T Ingenia scanner (Philips Healthcare, Best, the Netherlands) with a 16-channel head coil and a posterior spine coil. Two sets of images were acquired during the same examination. The first one was considered a conventional set, including sagittal T2 (TR, 2805 ms; TE, 100 ms; number of excitations, 2; slice thickness, 2 mm with no gap; FOV, 360 × 360 mm; bandwidth, 773 Hz; acquisition matrix, 376 × 297; acquisition duration, 3 minutes and 48 seconds) and sagittal T1WI (TR, 512 ms; TE, 16 ms; number of excitations, 1; slice thickness, 3 mm with no gap; FOV, 360 × 360 mm; bandwidth, 260 Hz; acquisition matrix, 328 × 272; acquisition duration, 2 minutes and 6 seconds), as recommended by the MAGNIMS consensus guidelines.² The second one, a 3D-PSIR set, included 2 magnitude images and 1 phase-corrected real image automatically provided from a unique optimized 3D-PSIR acquisition (scan mode 3D; sagittal native acquisition plane; technique, fast-field echo; TR, 5.8 ms; TE, 2.6 ms; number of excitations, 1; slice thickness, 1 mm with no gap; FOV, 320 × 220 mm; bandwidth, 362 Hz; acquisition matrix, 320 × 220; voxel size, 1.0 × 1.0 × 1.0 mm; turbo field echo factor, 69; turbo field echo prepulse inversion time, 350 ms; turbo field echo shots, 79; turbo

field echo shot duration, 400 ms; turbo field echo shot interval, 758 ms; flip angle, 15°; fat suppression with spectral presaturation with inversion recovery; acquisition duration, 4 minutes and 6 seconds) (On-line Figs 1 and 2). The first sequences were acquired 10 minutes after a single bolus (0.1 mmol/kg) of gadobutrol (Gadovist; Bayer Schering Pharma, Berlin, Germany). The conventional set sequences were always acquired before the 3D-PSIR.

Image Analysis

Two radiologists, blinded to clinical data, individually read the randomized results of the conventional set and those of the 3D-PSIR reformatted sequence in the sagittal plane; 3 weeks or more passed between the 2 readings. The first senior neuroradiologist was specialized in neuroimaging with 8 years of experience (A.L.), and the second was a junior radiologist with no experience in neuroimaging (A.F.). Six weeks later, a criterion standard consensus reading session was performed by the third reader, a second senior neuroradiologist with 20 years of experience (J.S.), also blinded to clinical data. At the end of this last consensus session, readers eventually looked at the entire imaging dataset, including all planes of the 3D-PSIR or axial T2WI if performed to determine whether the lesions observed in 3D-PSIR were false-positive. A final reading session was performed 6 weeks later to analyze intraobserver concordance. All reading sessions were performed on a dedicated workstation with the Carestream Vue PACS software.

The readers assessed the following characteristics of patients' MR imaging:

- The primary judgment criterion was the presence and number of spinal cord lesions, defined as hyperintense lesions on T2WI and hypo- or hyperintense lesions on the phase-corrected real image or magnitude images of the 3D-PSIR, respectively (On-line Fig 1). To avoid overestimation, readers were instructed not to count lesions in areas too full of artifacts and to report only evident and well-delineated lesions on the 3D-PSIR sequence.
- The precise level of the lesions in the sagittal plane, according to the related cervical level.
- The precise location of the lesions in the axial plane, defined as central or peripheral, and the length of the lesions in the sagittal plane.
- The confidence in detecting spinal cord lesions, was measured as follows: 1 corresponded to low confidence; 2, moderate-to-high confidence; and 3, very high confidence.
- The presence of active lesions defined as an enhancement on the postcontrast T1WI or a high signal intensity on both magnitude and phase-corrected real 3D-PSIR images.

Quantitative measurements of MR imaging signals were obtained by drawing 3 ROIs per patient: in the largest spinal cord lesion (lesion signal) and in the normal-appearing spinal cord (cord signal) and background (background signal).

The contrast-to-noise ratio (CNR) was calculated according to the following formula: $CNR = (\text{Lesion Signal} - \text{Cord Signal}) / \text{Noise SD}$.

The SNR was calculated according to the following formula: $SNR = (\text{Lesion Signal} - \text{Background Signal}) / \text{Noise SD}$.

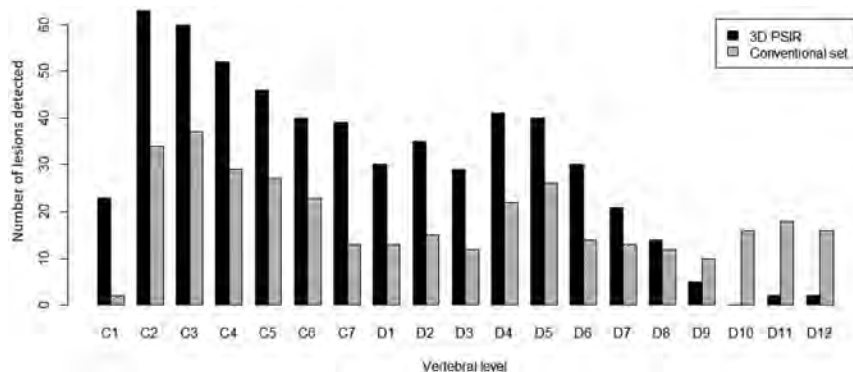


FIG 1. Comparison of the number and distribution of MS lesions detected in the spinal cord using the conventional set (gray) compared with 3D-PSIR (black) imaging.

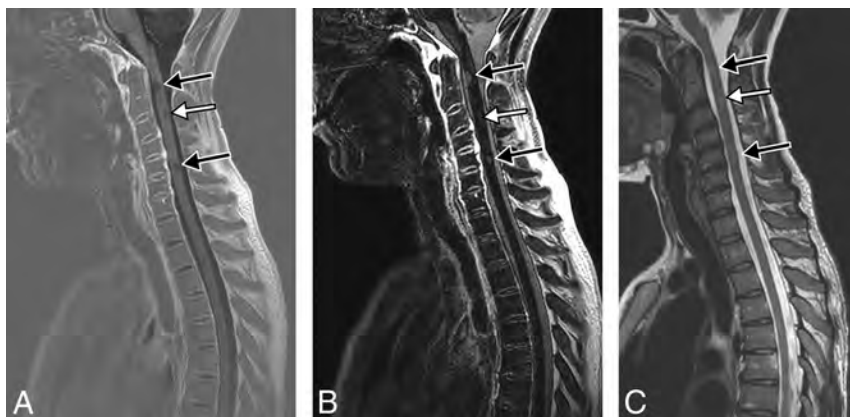


FIG 2. Follow-up MR imaging of a 32-year-old woman with relapsing-remitting MS. 3D-PSIR reformatted in the sagittal plane shows 2 conspicuous (black arrows) and 1 less obvious (white arrow) cervical spinal cord lesions seen as hypointense on the phase-corrected real image (A) and hyperintense on the magnitude image (B). The same lesions are all difficult to see on the sagittal T2WI (C).

Statistical Analysis

Quantitative variables were presented as mean (SD) and median (interquartile range); and categorical variables, as percentages. A Wilcoxon test was used to compare the number of lesions detected between both datasets as well as the readers' confidence and quantitative CNR and SNR values. Inter- and intraobserver agreement for the MR imaging reading was assessed using a nonweighted Cohen κ statistic and was interpreted as follows: 0.0–0.2, poor correlation; 0.21–0.4, fair correlation; 0.41–0.6, moderate correlation; 0.61–0.8, good correlation; and 0.81–1, almost perfect correlation.²¹ A P value $< .05$ was considered statistically significant. Data were analyzed using the R software package.²²

RESULTS

Demographic and Clinical Characteristics

One hundred consecutive patients with MS were included (55 women and 45 men; mean age, 41 years; 82 with relapsing-remitting MS, 12 with secondary-progressive MS, and 6 with primary-progressive MS). The mean Expanded Disability Status Scale score was 3.2 ± 2.1 . The mean disease duration was 13.6 ± 9.2 years.

Spinal Cord Lesions

Of 100 patients, 67 had at least 1 spinal cord lesion, and 10 had an active enhancing lesion, found using both MR imaging methods

under investigation. Lesions were more likely to be located on the periphery of the spinal cord than centrally: 379 (79%) versus 101 (21%). There was no statistical difference in the measurement of the mean length between the 2 imaging sets: 11.44 versus 10.23 mm using 3D-PSIR or the conventional set, respectively.

Detection of Lesions

3D-PSIR detected significantly more overall lesions than the conventional set (480 versus 168, respectively, $P = 6 \times 10^{-13}$). 3D-PSIR also detected significantly more lesions in both cervical (270 versus 83, $P = 9 \times 10^{-6}$) and dorsal regions (210 versus 85, $P = 2 \times 10^{-4}$) (Figs 1 and 2). Eleven patients had at least 1 lesion on 3D-PSIR images with no lesion detected on the conventional set (Fig 3). None of these lesions were considered false-positive. All lesions detected with the conventional set above T10 were also visible on 3D-PSIR. All enhancing lesions were visible on both 3D-PSIR and the conventional set (Fig 4).

Confidence in lesion detection was significantly higher with 3D-PSIR than with the conventional set (mean confidence, 2.6 versus 2.2; $P = 3 \times 10^{-11}$), with 95% of lesions detected with a moderate-to-very-high degree of confidence, and 67%, with a very high degree of confidence on 3D-PSIR versus 87% and 50% on the conventional set, respectively.

CNR and SNR Evaluation

Both CNR and SNR were significantly higher with 3D-PSIR than with the conventional set (mean, 0.48 versus 0.26; $P < 1 \times 10^{-5}$; and 0.63 versus 0.46, $P = .03$, respectively).

Interreader Concordance

Overall interreader concordance was good ($\kappa = 0.7$) without any differences between the 3D-PSIR and the conventional set ($\kappa = 0.7$ and 0.8, respectively).

Overall intrareader concordance was good ($\kappa = 0.7$ and 0.8 for readers 1 and 2, respectively), without any differences between the 3D-PSIR and the conventional set.

DISCUSSION

Our study showed that 3D-PSIR improved overall spinal cord lesion detection in patients with MS, with higher reader-reported confidence and SNR, showing a substantial number of lesions not seen with a conventional imaging set and active enhancing lesions.

Our results are consistent with those in previous studies evaluating new sequences that overcome the challenges of spine im-

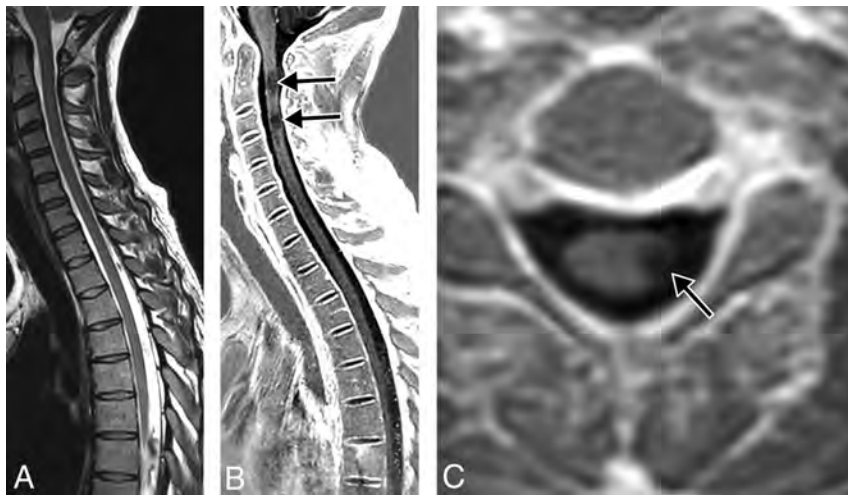


FIG 3. Follow-up MR imaging of a 40-year-old woman with secondary-progressive MS. Sagittal T2WI (A) shows no spinal cord lesions. 3D-PSIR reformatted in the sagittal plane (B) demonstrates 2 cervical spinal cord lesions (black arrows). 3D-PSIR reformatted in the axial plane (C) provides accurate localization of the lesions (black arrow).

aging in MS by increasing both the sensitivity and specificity of the MR imaging, such as proton-density imaging,¹⁰ STIR,^{11,12} PST1-IR,¹³ MERGE,¹⁴ double inversion recovery,¹⁶ and MPRAGE.¹⁷ We reported significantly higher detection of spinal cord lesions with 3D-PSIR, with 65% of overall lesions not visible on the conventional set, which is consistent with the 28%–72% increased detection rate using the optimized spinal cord sequences in the literature.^{10,12,14,16,23,24} Eleven (11%) patients without any lesions detected with the conventional set had at least 1 lesion captured using 3D-PSIR, which is similar to the 3%–24% previously reported.^{10,12,16}

One unreported-yet-major interest of 3D-PSIR was its ability to detect enhancement of active spinal cord lesions with similar detection rates compared with postcontrast T1 sequences. 3D-PSIR is derived from a T1WI sequence, thus making it sensitive to contrast injection.^{13,18} This finding means that a unique “all-in-one” 3D-PSIR sequence might be sufficient to provide data on both the spinal cord lesion burden and its activity at the same time, reflecting the dissemination in space and time of the McDonald criteria and supporting accurate monitoring of treatment efficacy.²⁵ However, only 10 patients had enhancing lesions; thus, our sample was too small to draw any firm conclusions regarding the detectability of enhancement with the 3D-PSIR.

Spinal cord imaging remains challenging because the targeted surface area on the body is small in a region prone to numerous imaging artifacts due to respiration, cardiac contractions, partial volumes, or CSF pulsations.^{6–9} Our study demonstrated that the use of a high-resolution 3D-PSIR sequence helped overcome some of these problems and that analyzing data in 3 different planes with 3D-PSIR enabled a higher lesion count, a better delineation and localization of the lesions, and exclusion of equivocal abnormalities, as reported by studies evaluating the clinical interest of biplanar or 3D MR imaging.^{16,17,24} We showed that the confidence in detection and lesion conspicuity was significantly higher with 3D-PSIR as opposed to the conventional set, which may be explained by the increased contrast of both CNR and SNR, as reported in the literature for 2D-PSIR sequences.^{12,13,18,26} On

visual inspection, 3D-PSIR sequences subjectively provided a markedly higher lesion-to-cord contrast and signal-to-noise ratio so that readers were more confident and comfortable making clinical judgements.

Improving detection of spinal cord lesions is crucial for patients facing a potential diagnosis of MS. Clearly identified lesions fulfill the McDonald criteria for early and definitive diagnosis,³ and they are highly predictive of conversion to MS in patients with clinically or radiologically isolated symptoms.^{1,27} Quantification of disease activity is important for monitoring treatment efficacy.²⁵ Therefore, recent US Consortium of Multiple Sclerosis Centers and MAGNIMS consensus guidelines modified their recommendations for performing the most sensitive spinal cord

MR imaging protocol, using at least 2 MR images such as T2 and short T1 inversion recovery, T2 and double inversion recovery, T2 and postcontrast T1 sequences,²⁸ or a combination of either T2 and short T1 inversion recovery, T2 and double inversion recovery, or T2 and postcontrast T1 sequences,² respectively. The advantages of 3D-PSIR related to the above suggest that a single 3D-PSIR sequence could be a potential replacement strategy and should at least be considered as a standard spinal cord sequence in patients with MS.

In our study, the duration of the 3D-PSIR was almost the same as that of the sagittal T2WI (15 seconds longer) and was almost 2 minutes faster than the conventional imaging set (4 minutes and 54 seconds faster). Reformatted images in the axial plane would serve as an advantageous replacement of an optional supplementary conventional axial T2WI by reducing the acquisition time (the duration of the axial T2WI was 3 minutes and 12 seconds in our center; thus, the overall saved time could reach 8 minutes and 6 seconds) and would provide greater spinal cord coverage. Moreover, the new guidelines suggest that performing brain and cervical cord MR imaging at the same time would be advantageous for the diagnostic evaluation of patients with or without transverse myelitis and would reduce the number of patients requiring subsequent MR imaging appointments.²⁸

Decreasing gadolinium injections by simultaneously performing brain and spinal cord MR imaging using a unique contrast injection of gadolinium could help with patient safety for the long term. We support this approach in these often young patients because they will have a high number of MRIs during their lifetimes and thus receive high doses of contrast injections, which can negatively affect their safety because the product might accumulate in their brains.^{29–31} However, combining the brain and spine MR imaging is time-consuming and difficult to establish in current practice. The addition of a single 3D-PSIR covering the spinal cord to the brain MR imaging would therefore be a good compromise between a reasonable MR imaging duration time (4 minutes longer) and the accurate evaluation of MS.

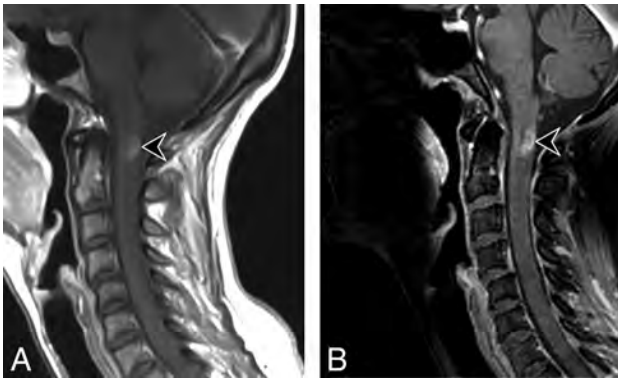


FIG 4. Follow-up of a 32-year-old woman with relapsing-remitting MS presenting with acute paresthesia of the upper arm. Sagittal post-contrast T1WI (A) shows an enhancing cervical spinal cord lesion (black arrowhead) corresponding to an active inflammatory lesion. 3D-PSIR reformatted in the sagittal plane shows the same enhancing lesion on the magnitude image (B).

Our study has several limitations. First, although this was a relatively large cohort in comparison with previous studies evaluating optimized spinal cord MR imaging sequences, the overall number of patients is low in a single center.

Second, our 3D-PSIR did not cover the entire spinal cord, but only the cervical region down to two-thirds of the dorsal region, whereas the conventional set analyzed the whole spinal cord. This coverage could have provided an underestimation of lesions detected with 3D-PSIR. The MR imaging signal decreased at the lower part of the spinal cord and levels under T9 were not correctly visualized. However, current recommendations indicate that coverage should include the cervical cord at a minimum because most spinal cord lesions in MS involve the cervical cord³² and that the routine examination of the thoracic cord is not necessary unless there are clinical symptoms at that level.²⁸

Third, we compared 3D-PSIR with 1-mm slices with a conventional set of postcontrast 2D T2WI and T1WI with 2- to 3-mm thickness; thus, the higher detection rate of the 3D-PSIR might be due, in part, to the higher resolution or the 3D acquisitions. We tried to minimize the 3D effect by reading only the 2D sagittal planes of the 3D-PSIR. We also did not compare the PSIR with a STIR sequence, which has a higher sensitivity compared with T2WI. However, this institutional practice was in accord with the last US Consortium of Multiple Sclerosis Centers and European MAGNIMS consensus guidelines,^{2,28} and conventional T1 and T2 sequences remain the most commonly used for spinal cord MS lesion detection in clinical institutions.³³

Fourth, we always performed the conventional set sequences before the 3D-PSIR, so the postgadolinium impregnation time was longer for 3D-PSIR, which could potentially have had an impact on the detection of spine lesions. However, the 10-minute delay before gadolinium injection and the image acquisitions is supposed to have minimized this effect.

Fifth, readers knew which method they were assessing, which could have led to a certain bias.

Finally, we did not correlate the results with pathology specimens and therefore cannot be sure that all lesions detected were, in fact, MS lesions. However, nonspecific white matter lesions are reported to be extremely uncommon in the spinal cord, in con-

trast to their frequent occurrence in the brain,³⁴ and it was impossible to have a real standard of reference because this would imply postmortem histologic examinations. Moreover, there are good histopathologic data to support the accuracy of optimized spinal cord sequences.³⁵

CONCLUSIONS

Our study showed that 3D-PSIR improved overall spinal cord lesion detection in patients with MS, with higher reader-reported confidence and SNR, showing a substantial number of lesions not seen with a conventional imaging set and active enhancing lesions. Further studies would be helpful to evaluate prospectively the value of the imaging method in comparison with other new MR images.

ACKNOWLEDGMENT

Laura McMaster provided professional English-language medical editing of this article.

Disclosures: Alix Fechner—UNRELATED: Employment: Fondation Ophtalmologique de Rothschild. Roman Deschamps—UNRELATED: Support for Travel to Meetings for the Study or Other Purposes: Biogen. Antoine Gueguen—UNRELATED: Board Membership: Roche, Merck, Mylan, Novartis; Consultancy: Mylan, Novartis; Payment for Lectures Including Service on Speakers Bureaus: Teva Pharmaceutical Industries, Roche; Travel/Accommodations/Meeting Expenses Unrelated to Activities Listed: Roche, Novartis, Teva Pharmaceutical Industries. Julien Savatovsky—UNRELATED: Payment for Lectures Including Service on Speakers Bureaus: Medtronic, Sanofi, Biogen; Travel/Accommodations/Meeting Expenses Unrelated to Activities Listed: Bayer HealthCare, Philips Healthcare.

REFERENCES

- Okuda DT, Mowry EM, Cree BA, et al. **Asymptomatic spinal cord lesions predict disease progression in radiologically isolated syndrome.** *Neurology* 2011;76:686–92 CrossRef Medline
- Filippi M, Rocca MA, Ciccarelli O, et al; MAGNIMS Study Group. **MRI criteria for the diagnosis of multiple sclerosis: MAGNIMS consensus guidelines.** *Lancet Neurol* 2016;15:292–303 CrossRef Medline
- Polman CH, Reingold SC, Banwell B, et al. **Diagnostic criteria for multiple sclerosis: 2010 revisions to the McDonald criteria.** *Ann Neurol* 2011;69:292–302 CrossRef Medline
- Coret F, Bosca I, Landete L et al. **Early diffuse demyelinating lesion in the cervical spinal cord predicts a worse prognosis in relapsing-remitting multiple sclerosis.** *Mult Scler* 2010;16, 935–41 CrossRef Medline
- Rovira À, Wattjes MP, Tintoré M, et al. **Evidence-based guidelines: MAGNIMS consensus guidelines on the use of MRI in multiple sclerosis—clinical implementation in the diagnostic process.** *Nat Rev Neurol* 2015;11:471–82 CrossRef Medline
- Vargas MI, Delavelle J, Kohler R, et al. **Brain and spine MRI artifacts at 3 Tesla.** *J Neuroradiol* 2009;36:74–81 CrossRef Medline
- Bot JC, Barkhof F, Lycklama à Nijeholt GJ, et al. **Comparison of a conventional cardiac-triggered dual spin-echo and a fast STIR sequence in detection of spinal cord lesions in multiple sclerosis.** *Eur Radiol* 2000;10:753–58 CrossRef Medline
- Taber KH, Herrick RC, Weathers SW, et al. **Pitfalls and artifacts encountered in clinical MR imaging of the spine.** *Radiographics* 1998;18:1499–1521 CrossRef Medline
- McGowan J C. **Technical issues for MRI examination of the spinal cord.** *J Neurol Sci* 2000;172(Suppl 1):S27–31 CrossRef Medline
- Chong AL, Chandra RV, Chuah KC, et al. **Proton density MRI increases detection of cervical spinal cord multiple sclerosis lesions compared with T2-weighted fast spin-echo.** *AJNR Am J Neuroradiol* 2016;37:180–84 CrossRef Medline
- Thorpe JW, MacManus DG, Kendall BE, et al. **Short tau inversion recovery fast spin-echo (fast STIR) imaging of the spinal cord in**

- multiple sclerosis. *Magn Reson Imaging* 1994;12:983–89 CrossRef Medline
12. Nayak NB, Salah R, Huang JC, et al. **A comparison of sagittal short T1 inversion recovery and T2-weighted FSE sequences for detection of multiple sclerosis spinal cord lesions.** *Acta Neurol Scand* 2014;129:198–203 CrossRef Medline
 13. Poonawalla AH, Hou P, Nelson FA, et al. **Cervical spinal cord lesions in multiple sclerosis: T1-weighted inversion-recovery MR imaging with phase-sensitive reconstruction.** *Radiology* 2008;246:258–64 CrossRef Medline
 14. White ML, Zhang Y, Healey K. **Cervical spinal cord multiple sclerosis: evaluation with 2D multi-echo recombined gradient echo MR imaging.** *J Spinal Cord Med* 2011;34:93–98 CrossRef Medline
 15. Sundarakumar DK, Smith CM, Hwang WD, et al. **Evaluation of focal cervical spinal cord lesions in multiple sclerosis: comparison of white matter-suppressed T1 inversion recovery sequence versus conventional STIR and proton density-weighted turbo spin-echo sequences.** *AJNR Am J Neuroradiol* 2016;37:1561–66 CrossRef Medline
 16. Riederer I, Karampinos DC, Settles M, et al. **Double inversion recovery sequence of the cervical spinal cord in multiple sclerosis and related inflammatory diseases.** *AJNR Am J Neuroradiol* 2015;36:219–25 CrossRef Medline
 17. Nair G, Absinta M, Reich DS. **Optimized T1-MPRAGE sequence for better visualization of spinal cord multiple sclerosis lesions at 3T.** *AJNR Am J Neuroradiol* 2013;34:2215–22 CrossRef Medline
 18. Hou P, Hasan KM, Sittton CW, et al. **Phase-sensitive T1 inversion recovery imaging: a time-efficient interleaved technique for improved tissue contrast in neuroimaging.** *AJNR Am J Neuroradiol* 2005;26:1432–38 Medline
 19. Vandenbroucke JP, von Elm E, Altman DG, et al; STROBE Initiative. **Strengthening the Reporting of Observational Studies in Epidemiology (STROBE): explanation and elaboration.** *Int J Surg* 2014;12:1500–24 CrossRef Medline
 20. Kurtzke JF. **Rating neurologic impairment in multiple sclerosis: an expanded disability status scale (EDSS).** *Neurology* 1983;33:1444–52 CrossRef Medline
 21. Landis JR, Koch GG. **An application of hierarchical kappa-type statistics in the assessment of majority agreement among multiple observers.** *Biometrics* 1977;33:363–74 Medline
 22. R Core Team. **R: A language and environment for statistical computing.** Vienna: R Foundation for Statistical Computing. 2014. <http://www.R-project.org/>. Accessed 2016
 23. Martin N, Malfair D, Zhao Y, et al. **Comparison of MERGE and axial T2-weighted fast spin-echo sequences for detection of multiple sclerosis lesions in the cervical spinal cord.** *AJR Am J Roentgenol* 2012;199:157–162 CrossRef Medline
 24. Weier KI, Mazraeh J, Naegelin Y, et al. **Biplanar MRI for the assessment of the spinal cord in multiple sclerosis.** *Mult Scler* 2012;18:1560–69 CrossRef Medline
 25. Gass A, Rocca MA, Agosta F, et al; MAGNIMS Study Group. **MRI monitoring of pathological changes in the spinal cord in patients with multiple sclerosis.** *Lancet Neurol* 2015;14:443–54 CrossRef Medline
 26. Alcaide-Leon P, Pauranik A, Alshafai L, et al. **Comparison of sagittal FSE T2, STIR, and T1-weighted phase-sensitive inversion recovery in the detection of spinal cord lesions in MS at 3T.** *AJNR Am J Neuroradiol* 2016;37:970–75 CrossRef Medline
 27. Sombekke MH, Wattjes MP, Balk LJ, et al. **Spinal cord lesions in patients with clinically isolated syndrome: a powerful tool in diagnosis and prognosis.** *Neurology* 2013;80:69–75 CrossRef Medline
 28. Traboulsee A, Simon JH, Stone L, et al. **Revised Recommendations of the Consortium of MS Centers Task Force for a Standardized MRI Protocol and Clinical Guidelines for the Diagnosis and Follow-Up of Multiple Sclerosis.** *AJNR Am J Neuroradiol* 2016;37:394–401 CrossRef Medline
 29. Ramalho J, Castillo M, AlObaidy M, et al. **High signal intensity in globus pallidus and dentate nucleus on unenhanced T1-weighted MR images: evaluation of two linear gadolinium-based contrast agents.** *Radiology* 2015;276:836–44 CrossRef Medline
 30. McDonald RJ, McDonald JS, Kallmes DF, et al. **Intracranial gadolinium deposition after contrast-enhanced MR imaging.** *Radiology* 2015;275:772–82 CrossRef Medline
 31. Kanda T, Osawa M, Oba H, et al. **High signal intensity in dentate nucleus on unenhanced T1-weighted MR images: association with linear versus macrocyclic gadolinium chelate administration.** *Radiology* 2015;275:803–09 CrossRef Medline
 32. Tartaglino LM, Friedman DP, Flanders AE, et al. **Multiple sclerosis in the spinal cord: MR appearance and correlation with clinical parameters.** *Radiology* 1995;195:725–32 CrossRef Medline
 33. Curley M, Josey L, Lucas R, et al; Ausimmune Investigator Group. **Adherence to MRI protocol consensus guidelines in multiple sclerosis: an Australian multi-centre study.** *J Med Imaging Radiat Oncol* 2012;56:594–98 CrossRef Medline
 34. Bot JC, Barkhof F, Polman CH, et al. **Spinal cord abnormalities in recently diagnosed patients with MS: added value of spinal MRI examination.** *Neurology* 2004;62:226–33 CrossRef Medline
 35. Nijeholt GJ, Bergers E, Kamphorst W, et al. **Post-mortem high-resolution MRI of the spinal cord in multiple sclerosis: a correlative study with conventional MRI, histopathology and clinical phenotype.** *Brain* 2001;124:154–66 CrossRef Medline

Renal Contrast on CT Myelography: Diagnostic Value in Patients with Spontaneous Intracranial Hypotension

K.A. Kinsman, J.T. Verdoorn, P.H. Luetmer, M.S. Clark, and F.E. Diehn

ABSTRACT

BACKGROUND AND PURPOSE: The significance of renal contrast on CT myelography is uncertain. This project examined different patient populations undergoing CT myelography for the presence of renal contrast to determine whether this finding is of diagnostic value in spontaneous intracranial hypotension.

MATERIALS AND METHODS: Four groups of patients were analyzed for renal contrast on CT myelography. The control group underwent CT myelography for reasons other than spontaneous intracranial hypotension ($n = 47$). Patients in study group 1 had spontaneous intracranial hypotension but CT myelography negative for dural CSF leak and CSF venous fistula ($n = 83$). Patients in study group 2 had spontaneous intracranial hypotension and CT myelography positive for dural CSF leak ($n = 44$). Patients in study group 3 had spontaneous intracranial hypotension and CT myelography suggestive of CSF venous fistula due to a hyperdense paraspinous vein ($n = 17$, eleven surgically confirmed).

RESULTS: Renal contrast was present on the initial CT myelography in 0/47 patients in the control group, 10/83 patients in group one, 1/44 patients in group 2, and 7/17 patients in group 3. Renal contrast on initial CT myelography in patients with suspected or surgically confirmed CSF venous fistula was significantly more likely than in patients with a dural CSF leak ($P = .0003$).

CONCLUSIONS: Renal contrast on initial CT myelography was seen only in patients with spontaneous intracranial hypotension. This was more common in confirmed/suspected CSF venous fistulas compared with dural leaks. Early renal contrast in patients with spontaneous intracranial hypotension should prompt scrutiny for a hyperdense paraspinous vein, and, if none is found, potentially advanced diagnostic studies.

ABBREVIATIONS: CTM = CT myelography; CVF = CSF venous fistula; SIH = spontaneous intracranial hypotension

Spontaneous intracranial hypotension (SIH) typically presents clinically with an orthostatic headache but can also have a plethora of additional associated symptoms such as nausea, visual difficulties, tinnitus, and, with time, development of gait disturbance, personality change, and decreased level of consciousness.¹ In most cases, SIH is caused by a spinal dural CSF leak. In some patients, the site of the CSF leak cannot be identified by current imaging techniques, including standard and dynamic CT myelography (CTM) and off-label intrathecal gadolinium MR myelography.

Recently, CSF venous fistula (CVF) has been described as a cause of SIH, in which there is a direct connection between the CSF and a draining vein.² Schievink et al² described 3 patients who had a direct fistula between the subarachnoid space and spinal epidural veins on digital subtraction myelography. Subsequently, a hyperdense paraspinous vein sign on CTM has been described as a similar indicator of a CVF.³ In this study, the 3 patients with the hyperdense paraspinous vein sign had surgically confirmed CVF. The prevalence of this standard CTM marker of CVF has subsequently been evaluated, occurring in 7% of patients with SIH who do not have evidence of a dural CSF leak.⁴

In nuclear medicine indium-111 (¹¹¹In) DTPA cisternography, early renal collecting system activity before 4 hours after injection is considered a sign of CSF leak.⁵ We have noticed the presence of renal collecting system contrast (referred to as “renal contrast” from this point forward) on CTM performed for SIH and have wondered whether it is of any clinical significance because it is presumably a CTM correlate to early radiotracer activity

Received August 15, 2018; accepted after revision November 29.

From the Department of Radiology, Mayo Clinic, Rochester, Minnesota.

Paper previously presented orally at: Annual Meeting of the American Society of Spine Radiology, February 23–26, 2017; San Diego, California.

Please address correspondence to Jared Verdoorn, MD, Department of Radiology, Mayo Clinic, 200 First St SW, Rochester MN 55905; e-mail: verdoorn.jared@mayo.edu

<http://dx.doi.org/10.3174/ajnr.A5934>

in the renal collecting system. We have questioned whether early renal contrast on CTM could be a secondary sign of CSF leak and/or CVF. The purpose of this project was to investigate different patient populations undergoing CTM for the presence of renal contrast to determine whether this finding is of diagnostic value in SIH.

MATERIALS AND METHODS

Institutional review board approval with waived consent was obtained for this Health Insurance Portability and Accountability Act–compliant retrospective research study. All included patients provided authorization for data to be used in research.

Patient Selection

Four groups of patients were identified, including a control group and 3 study groups: study group 1, study group 2, and study group 3.

The control group included patients who underwent CTM for reasons other than SIH. Patients in the control group were derived from a data base search of our single institution electronic medical record to identify approximately 50 patients who underwent CTM for a non-SIH indication in 2015.

Study group 1 included patients with SIH and CTM negative for a dural CSF leak or the hyperdense paraspinous vein sign. Patients in study group 1 were derived from a data base search to identify approximately 100 patients who underwent CTM for an indication of SIH from 2011 to 2015 without evidence of a dural CSF leak or the hyperdense paraspinous vein sign.

Study group 2 included patients with SIH and CTM positive for a dural CSF leak. Patients in study group 2 were derived from a data base search to identify approximately 50 consecutive patients with SIH and CTM positive for dural CSF leak from 2011 to 2014.

Study group 3 included patients with SIH and CTM suggestive of CVF due to the presence of a hyperdense paraspinous vein. Patients in study group 3 were derived in 2 ways: Some patients were found via an electronic medical record data base search for patients with SIH and CTM positive for a hyperdense paraspinous vein. The remaining patients in study group 3 were obtained from a prior retrospective review of data on CTMs performed for SIH at our institution, in which the hyperdense paraspinous vein sign was present convincingly but had been found retrospectively because at the time of their CTM, CVF was not a recognized entity. All patients in study group 3 were further evaluated by clinical chart review to note whether CVF had been surgically confirmed following CTM, and a subgroup analysis was performed.

Patients referred to CTM for SIH had been diagnosed clinically by neurologists at our institution who frequently see patients for the indications of SIH. Patients who received IV contrast before CTM the day of or day before the procedure were excluded. Note was made of whether the renal collecting systems were included in the field of imaging, and patients in whom the renal collecting systems could not be at least partially visualized were also excluded. Demographic information of the patients, including age and sex, was recorded. Type and volume of intrathecal contrast injected for each CTM were noted.

Imaging Review

Each CTM was retrospectively analyzed for renal contrast by a board-certified neuroradiologist from our institution, including initial CTM images and delayed images (if obtained). Although the renal contrast finding is subjective, reviewers were asked to only grade the CTMs as positive for this finding if they had the highest level of suspicion (ie, if they were convinced and would interpret the studies as positive for renal contrast clinically). The reviewing radiologists were blinded to the indication for the CTM and the CTM group assignment. Any case deemed positive for renal contrast was confirmed by a second neuroradiologist. If renal contrast was present on the initial CTM, the initial CTM was reviewed for contrast leakage at the lumbar puncture site because this has been suggested as a potential cause of false-positive early renal collecting system radiotracer activity on nuclear medicine ^{111}In DTPA cisternography.⁶

The presence of a hyperdense paraspinous vein was evaluated subjectively. In cases of a hyperdense paraspinous vein identified in prior retrospective review of CTMs initially interpreted as negative,⁴ reviewers had been asked to look for a linear/curvilinear opacified structure extending from the thecal sac or a nerve root sleeve suggesting a hyperdense paraspinous vein.³ Only cases with a high index of suspicion were graded as positive (ie, if the case would be or had been interpreted positive clinically), and any case deemed positive for a hyperdense paraspinous vein was confirmed by 2 additional neuroradiologists. In cases of a hyperdense paraspinous vein that was identified by an electronic medical record data base search (ie, cases that had prospectively been called clinically), a second neuroradiologist reviewed the case to confirm the finding.

Times from injection of myelographic contrast to initial and delayed (if performed) CTM were recorded. The patient groups were compared for rates of the presence of renal contrast, including on both initial and delayed CTM images. In cases positive for renal contrast on the initial CTM with concurrent MR myelography performed, the MR myelogram was also evaluated for the presence of renal contrast.

Statistical Analysis

Comparison between rates of the presence of renal contrast on initial and delayed CTM among the groups was performed using a 2-tailed Fisher exact test. Comparison of the time between intrathecal contrast injection and initial CTM imaging was performed using a 2-tailed Mann-Whitney *U* test. A *P* value < .05 was deemed statistically significant.

RESULTS

A summary of the results from the control group and the 3 study groups is provided in the Table. After we excluded patients with IV contrast before CTM ($n = 19$) and patients in whom the renal collecting systems could not be at least partially visualized ($n = 1$), the total study population was 191 patients.

Control Group (Non-SIH)

Forty-eight patients were identified. One (2%) was excluded due to IV contrast before CTM, leaving 47 patients in the control group. All patients received iohexol, either Omnipaque 180 (60%) or Om-

Summary of results from the control and 3 study groups

Group	Control Group: Non-SIH	Study Group 1: SIH+/CSF Leak-/ Hyperdense Vein-	Study Group 2: SIH+/CSF Leak+	Study Group 3: SIH+/ Hyperdense Vein+
Included patients (No.)	47	83	44	17
Mean age (range) (yr)	66 (35–91)	59 (31–87)	54 (28–71)	56 (37–84)
Male sex	62%	45%	36%	41%
Mean intrathecal contrast volume injected (range) (mL)	14 (10–20)	15 (12–20)	13 (6–20)	14 (12–18)
Initial CTM				
All patients: mean time from contrast injection to initial CTM (range) (min)	35 (19–101)	40 (2–113)	20 (2–87)	41 (4–83)
Patients with renal contrast (No.) (%)	0/47 (0%)	10/83 (12%)	1/44 (2%)	7/17 (41%)
Patients with renal contrast: mean time from contrast injection to initial CTM (range) (min)	NA	61 (17–96)	Contrast injection time not documented in this patient	37 (4–62)
Delayed imaging				
Patients with delayed imaging (No.) (%)	0/47 (0%)	73/83 (88%)	11/44 (25%)	15/17 (88%)
All patients: mean time from contrast injection to delayed CTM (range) (min)	NA	199 (79–364)	162 (93–325)	195 (100–386)
Patients with renal contrast (No.) (%)	NA	23/73 (32%)	3/11 (27%)	8/15 (53%)
Patients with renal contrast: mean time from contrast injection to delayed imaging (range) (min)	NA	220 (126–364)	211 (97–325)	184 (100–386)

Note:—NA indicates not applicable.

nipaque 240 (40%) iodinated contrast (GE Healthcare, Piscataway, New Jersey) intrathecally. Of the 47 patients, none (0%) had renal contrast on the initial CTM. No patients had delayed imaging performed, because the non-SIH indication did not necessitate it.

Study Group 1 (SIH, CTM Negative for Dural CSF Leak or Hyperdense Paraspinal Vein)

Ninety-four patients were identified in group 1. Eleven (12%) were excluded due to IV contrast before CTM, leaving 83 patients in study group 1. All patients received either Omnipaque 180 (35%) or Omnipaque 240 (65%). Of the 83 patients, 10 (12%) had renal contrast on the initial CTM (4 of whom had contrast leakage at the injection site) at a mean time of 61 minutes postinjection (range, 17–96 minutes). Seventy-three (88%) of these 83 patients had delayed imaging, with 23 (32%) of 73 having renal contrast at a mean time of 220 minutes postinjection (range, 126–364 minutes).

Study Group 2 (SIH, CTM Positive for Dural CSF Leak)

Fifty-one patients were identified in group 2. Seven (14%) were excluded, 6 (12%) due to IV contrast before CTM, and 1 (2%) due to only thoracic imaging being performed without inclusion of the kidneys, leaving 44 patients in study group 2. All patients received either Omnipaque 180 (70%) or Omnipaque 240 (30%). Of the 44 patients, 1 (2%) had renal contrast on initial CTM and did not have contrast leakage at the injection site. Unfortunately, the time of intrathecal contrast injection was not documented in this patient, so the postinjection time at which renal contrast was seen on the initial CTM could not be determined. Only 11 (25%) of these 44 patients had delayed imaging because a dural CSF leak was usually identified on the initial CTM, with 3 (27%) of 11 having renal contrast at a mean time of 211 minutes postinjection (range, 97–325 minutes).

Study Group 3 (SIH, CTM Positive for Hyperdense Paraspinal Vein)

Nineteen patients were identified in group 3, twelve (63%) through data base search and 7 (37%) who had previously been identified in a retrospective review after the hyperdense paraspinal vein sign had been described. Two (11%) were excluded due to

IV contrast before CTM, leaving 17 patients in study group 3. All patients received either Omnipaque 180 (29%) or Omnipaque 240 (71%). Of the 17 patients, seven (41%) had renal contrast on the initial CTM (Figure) at a mean time of 37 minutes postinjection (range, 4–62 minutes), and only 1 had contrast leakage at the injection site. Fifteen (88%) of these 17 patients had delayed imaging, with 8 (53%) of 15 having renal contrast at a mean time of 184 minutes postinjection (range, 100–386 minutes).

Of the 17 patients in study group 3, eight (47%) received an injection of intrathecal normal saline as part of their myelogram, and 5 (50%) of these 8 patients also received 0.5 mL of gadopentetate dimeglumine, Magnevist (Bayer HealthCare Pharmaceuticals, Wayne, New Jersey), as part of their myelogram. These were injected as part of advanced myelographic techniques (MR and positive pressure myelography) looking for CVF. The mean volume of saline injected in these patients was 43 mL (range, 16–70 mL). Of the 4 patients who underwent MR myelography, renal contrast findings on MR myelography were concordant with those on CT myelography when both were available at similar time points. One patient who underwent MR myelography had renal contrast on the initial CTM, which was also present on initial MR myelography. Of the 3 patients who underwent MR myelography without renal contrast on the initial CTM, 2 did not have early MR imaging and 1 did not have the renal collecting systems included in the MR imaging FOV. When we excluded the 8 patients who underwent positive pressure \pm MR myelography from the analysis due to the potential for false-positives resulting from increased intrathecal pressure, four (44%) of the 9 remaining patients had renal contrast on the initial CTM at a mean time of 28 minutes postinjection (range, 4–44 minutes). Seven (78%) of these 9 patients had delayed imaging, with 3 (43%) of 7 having renal contrast (mean time, 129 minutes; range, 100–147 minutes).

Study Group 3: Surgically Confirmed Subgroup

Subgroup analysis of the 11 patients with surgically confirmed CVF showed that 4 (36%) of 11 had renal contrast on initial imaging at a mean time of 49 minutes postinjection (range, 34–62 minutes). Nine (82%) of these 11 patients had delayed imaging,



FIGURE. Axial CT images from the initial CTM for a study group 3 patient with a hyperdense paraspinal vein sign (arrow, A) at T12–L1 on the right (better visualized while scrolling through consecutive images) and renal contrast (arrows, B).

with 5 (56%) of 9 having renal contrast at a mean time of 217 minutes postinjection (range, 150–386 minutes).

Study Group 3: Not Surgically Confirmed Subgroup

Subgroup analysis of the 6 patients with a hyperdense paraspinal vein who did not proceed to an operation showed that 3 (50%) of 6 had renal contrast on initial imaging at a mean time of 22 minutes postinjection (range, 4–40 minutes). Six (100%) of these 6 patients had delayed imaging, with 3 (50%) of 6 having renal contrast at a mean time of 129 minutes (range, 100–147 minutes).

RESULTS

Among the patients with SIH in whom CTM identified the etiology of the syndrome, renal contrast on the initial CTM with suspected or surgically confirmed CVF was significantly more likely than with a dural CSF leak ($P < .001$). This finding remained statistically significant even with exclusion of the 8 patients in study group 3 who received concurrent intrathecal normal saline \pm Magnevist ($P = .002$). Renal contrast on delayed CTM with suspected or surgically confirmed CVF was seen more commonly than with a dural CSF leak, but this difference was not statistically significant ($P = .25$).

In the setting of suspected CVF with surgical confirmation, renal contrast on the initial CTM was significantly more likely than with a dural CSF leak ($P < .004$). Renal contrast on delayed CTM was also seen more commonly, but this difference was not statistically significant ($P = .36$).

In those suspected of CVF on CTM who did not undergo surgical confirmation, renal contrast on the initial CTM was significantly more likely than with a dural CSF leak ($P < .004$). Renal contrast on delayed CTM was also seen more commonly, but this difference was not statistically significant ($P = .60$).

Renal contrast was seen only on initial CTM in patients with SIH; it was not seen in any of the patients in the control group. This finding was statistically significant when comparing all patients with SIH with the control group ($P = .008$) and when comparing the hyperdense paraspinal vein group with the control group ($P < .001$), and this difference remained statistically significant when excluding patients with SIH in whom renal contrast was seen on the initial CTM in the setting of contrast leakage from

the injection site in all patients with SIH ($P = .04$) and in the hyperdense paraspinal vein group ($P < .001$). There was also a significant difference between the SIH-positive, CTM-negative group and the control group with regard to renal contrast on initial CTM ($P = .010$), which was not statistically significant when excluding the patients with SIH in whom there was contrast leakage from the injection site ($P = .08$). There was no difference between the rates of renal contrast on the initial CTM in the control group versus the group positive for a dural leak.

There was a significant difference in the time between intrathecal contrast injection and the initial CTM imaging in

the dural CSF leak group compared with each of the other 3 groups ($P = .004$ when comparing the dural CSF leak with hyperdense paraspinal vein groups, and $P < .001$ when comparing the dural CSF leak group with the control and SIH-positive/leak-negative groups). There was no significant difference between the time to initial CTM imaging when comparing the control, SIH-positive/leak-negative, and hyperdense paraspinal vein groups.

DISCUSSION

The presence of renal contrast on the initial CTM was more likely in patients with a hyperdense paraspinal vein sign and in those with surgically confirmed CVF than in patients with a dural CSF leak. This increased prevalence was also seen on delayed imaging, but the difference was not statistically significant. None of the patients undergoing CTM for non-SIH indications ($n = 47$) had renal contrast on the initial CTM. Given that renal contrast on the initial CTM was seen only in patients with SIH, this finding is compatible with abnormal CSF physiology (a CSF-leak state). Furthermore, renal contrast on the initial CTM may be a predictor of CVF because it was frequently seen in these patients and was only present in 1 patient with a dural CSF leak. Intuitively, the presence of early renal contrast makes sense in the setting of CVF because myelographic contrast directly enters the venous system and would therefore be cleared sooner by the kidneys than in a dural CSF leak, in which contrast first enters the epidural space. This phenomenon seems similar to early renal uptake on nuclear medicine cisternography with a CSF leak.^{6,7}

The physiology and dynamics of absorption of iodinated contrast from the CSF following intrathecal injection have been previously described.⁸ The iodinated contrast absorption rate increases with an increased CSF absorption rate and more rapid mixing of contrast material with the CSF. More rapid mixing would be expected to occur in CT myelography because contrast is run throughout the spinal canal by tilting the table. Contrast absorption begins nearly immediately following injection through the spinal arachnoid villi and granulations, though this clearly does not result in renal collecting system opacification on the initial CTM in most patients. In patients with SIH, there may be increased CSF production in an attempt to compensate for a

low CSF pressure state, as well as decreased venous pressure/vein dilation as can sometimes be seen on imaging studies.⁹ These could potentially increase the rate of CSF absorption and therefore intrathecal contrast absorption in patients with SIH. Although this phenomenon could potentially contribute to early renal contrast in patients with SIH, it would not explain why early renal contrast is seen more commonly in CVF than in a dural CSF leak, and this seems more likely due to contrast directly entering a vein rather than the epidural space in a CVF.

In our study, 12% of patients with SIH but a CTM negative for leak (standard dural type or CVF) had renal contrast on the initial CTM. This may represent a patient population with undetected CVF. Given that CVF is a relatively new diagnosis, potentially many cases of CVF are currently not being recognized, particularly on conventional CTM. For example, a series of patients studied by Schievink et al¹⁰ showed that CVF was identified on digital subtraction myelography in 10 (19%) of 53 patients without evidence of CSF leak on CTM. Prior studies have shown that CVF can respond successfully to surgical treatment, thus making the diagnosis of the utmost importance because many of these patients have debilitating symptoms.^{2,3,10} Perhaps the 12% of patients in our study with SIH with CTM negative for leak but renal contrast present on initial CTM would be those most likely to benefit from more advanced myelographic techniques to search for CVF, particularly if their condition is debilitating. Such techniques include digital subtraction myelography and intrathecal gadolinium myelography, potentially using positive pressure for either technique.

The presence of renal contrast and a hyperdense paraspinous vein was subjectively evaluated, though only graded positive if there was a high index of suspicion. To our knowledge, there is no standard threshold Hounsfield unit value in the literature indicating that the renal collecting system are positive for renal contrast, hence the subjective evaluation. While possible Hounsfield unit threshold values have been suggested for identifying the presence of a hyperdense paraspinous vein,¹¹ in our practice, we have found that the presence of a hyperdense paraspinous vein sign on CTM can be quite subtle, sometimes only seen using dual-energy CT, thus limiting the practical utility of a specific Hounsfield unit threshold. Additionally, some CVFs are better visualized on MR myelography in cases of concurrently performed CTM and MR myelography as was also the case in our study.

Limitations of this study include the limited patient sample size, with most notably only 17 patients with a hyperdense paraspinous vein sign and only 11 of these proceeding to an operation with confirmatory surgical findings of CVF. The control group was also relatively small; this feature could potentially result in rare cases of missed renal contrast on initial CTM in patients without SIH, though the statistical analysis does demonstrate a significant difference in renal contrast on the initial CTM between all patients with SIH and the control group, and an even more significant difference between the hyperdense paraspinous vein group and the control group. While a few patients with SIH with an initial CTM positive for renal contrast had contrast leakage from the lumbar puncture site, this seems quite unlikely to be the cause of early renal contrast. If early renal contrast was due to contrast leakage from the puncture site rather than a CVF, it

would be expected that >1 patient in the dural CSF leak group would have had early renal contrast because a dural CSF leak results in extradural contrast analogous to contrast leakage from the puncture site. Also, some patients in the control group would likely have had renal contrast on the initial CTM because a small amount of contrast leakage from the puncture site is common. The retrospective nature of the study was also a limitation due to a lack of standardization of imaging times and a lack of delayed imaging in the control group. This particularly included shorter times between intrathecal contrast injection and initial CTM in the dural CSF leak group compared with the other groups. One reason is that many of the patients with dural CSF leaks had a high pretest probability of a fast CSF leak and therefore had intrathecal contrast injected while on the CT table (as opposed to under fluoroscopy in the other groups), leading to a decreased time to the initial CT imaging. Contrast type (including the 8 patients in Study Group 3 who received concurrent normal saline ± Magnavist) and volume were not standardized. Also, relatively few patients in the dural CSF leak group had delayed CTM because leaks were usually identified on the initial CTM.

CONCLUSIONS

Early renal contrast on CTM, if present, appears to be a secondary sign of CSF leak and suggests CVF rather than a dural tear as the cause of the CSF leak. If renal contrast is present on the initial CTM in a patient with SIH, the radiologist should carefully scrutinize the study for a hyperdense paraspinous vein, and if none is found, more advanced diagnostic studies should at least be considered. The presence of early renal contrast on CTM also appears to be limited to patients with SIH, compatible with the abnormal CSF physiology in these patients. Given the limited size and retrospective nature of our single-institution study, further prospective studies with larger groups of patients are needed to validate these findings.

ACKNOWLEDGMENTS

The authors acknowledge the assistance of Sonia Watson, PhD, in editing the manuscript.

REFERENCES

1. Mokri B. **Spontaneous low pressure, low CSF volume headaches: spontaneous CSF leaks.** *Headache* 2013;53:1034–53 CrossRef Medline
2. Schievink WI, Moser FG, Maya MM. **CSF-venous fistula in spontaneous intracranial hypotension.** *Neurology* 2014;83:472–73 CrossRef Medline
3. Kranz PG, Amrhein TJ, Schievink WI, et al. **The “hyperdense paraspinous vein” sign: a marker of CSF-venous fistula.** *AJNR Am J Neuroradiol* 2016;37:1379–81 CrossRef Medline
4. Clark MS, Diehn FE, Verdoorn JT, et al. **Prevalence of hyperdense paraspinous vein sign in patients with spontaneous intracranial hypotension without dural CSF leak on standard CT myelography.** *Diagn Interv Radiol* 2018;24:54–59 CrossRef Medline
5. Halkar R, Pettigrew R, Lipman C, et al. **Rapid transit of tracer to the kidneys and urinary bladder in radionuclide cisternography: a sign of CSF leak.** *Clin Nucl Med* 1997;22:121–23 CrossRef Medline
6. Mokri B. **Radioisotope cisternography in spontaneous CSF leaks: interpretations and misinterpretations.** *Headache* 2014;54:1358–68 CrossRef Medline

7. Kranz PG, Luetmer PH, Diehn FE, et al. **Myelographic techniques for the detection of spinal CSF leaks in spontaneous intracranial hypotension.** *AJR Am J Roentgenol* 2016;206:8–19 CrossRef Medline
8. Sage MR. **Kinetics of water-soluble contrast media in the central nervous system.** *AJR Am J Roentgenol* 1983;141:815–24 CrossRef Medline
9. Herwerth M, Prothmann S, Kreiser K, et al. **Spontaneous cerebrospinal fluid leak with venous engorgement mimicking a contrast-enhancing cervical mass.** *JAMA Neurol* 2016;73:886–87 CrossRef Medline
10. Schievink WI, Moser FG, Maya MM, et al. **Digital subtraction myelography for the identification of spontaneous spinal CSF-venous fistulas.** *J Neurosurg Spine* 2016;24:960–64 CrossRef Medline
11. Kranz PG, Amrhein TJ, Gray L. **CSF venous fistulas in spontaneous intracranial hypotension: imaging characteristics on dynamic and CT myelography.** *AJR Am J Roentgenol* 2017;209:1360–66 CrossRef Medline

Single-Needle Lateral Sacroplasty Technique

 P.J. Nicholson,  C.A. Hilditch,  W. Brinjikji,  A.C.O. Tsang, and  R. Smith

ABSTRACT

SUMMARY: Sacral insufficiency fractures result in significant morbidity, and percutaneous sacroplasty has emerged as a promising technique for their treatment. We present a technical note regarding our method of treating these fractures using a “single-needle” lateral technique with a combination of conebeam CT and biplane fluoroscopy. We treated 10 patients, in whom the median Visual Analog Scale pain score decreased from 7.0 to 0 ($P < .001$). We concluded that single-needle sacroplasty is feasible and safe using this technique.

Sacral fractures can be secondary to osteoporosis (sacral insufficiency fractures) or malignancy, are relatively common, and can cause severe pain. This pain can be especially debilitating in elderly patients, in whom pain-related mobility impairment can have a detrimental effect on quality of life as well as predispose patients to a range of conditions associated with long-term immobility such as deep venous thrombosis and respiratory problems. Traditionally, these lesions are treated with bed rest, anesthesia, and physiotherapy.¹ In the past decade, sacroplasty has emerged as an effective technique for the treatment of these painful lesions.² This primarily stemmed from vertebral augmentation techniques, with the injection of polymethylmethacrylate cement. Since it was first described, sacroplasty has been shown to be effective in decreasing pain and improving quality of life.³

Even during the first description of the procedure,⁴ it was recognized that combining the benefits of CT and fluoroscopy would allow accurate needle tip positioning as well as real-time monitoring of cement injection. To this end, we use a biplane fluoroscopy machine equipped with conebeam CT capabilities (Allura Xper FD20/10; Philips Healthcare, Best, the Netherlands) for all of our sacroplasty procedures. In conjunction with needle-trajectory-planning software (XperGuide; Philips Healthcare), this allows meticulous planning of the needle position and trajectory. Sacroplasty is commonly performed using multiple needles to cover

both the sacral ala and the central component of the bone. Each needle-placement site is associated with an individual risk of damage to nerves or vascular structures, along with a risk of infection and the inherent pain and soft-tissue swelling associated with each puncture. There is therefore an onus on the operator to deliver cement using as few delivery needles as possible. A percutaneous transiliac approach for stabilizing screw insertion has been used in orthopedic surgery. Thus, we began by using a long “single-needle” lateral technique, positioning the needle across the transverse axis of the sacrum (ie, from one sacral ala to the other). By beginning deposition of cement at this ala and then progressively withdrawing the needle and progressively injecting cement in continuity under real-time fluoroscopic guidance, the operator can successfully perform an excellent sacroplasty using a single needle, thereby avoiding the risk of complications outlined above. The transverse cement placement incorporates the support of the column of the central sacral body with the column of the ala.

MATERIALS AND METHODS

This study was performed with the approval of the research and ethics board of Toronto Western Hospital. A prospective data base was maintained, following all patients who underwent spinal and sacral augmentation procedures. From this, all patients who underwent sacroplasty using a single-needle technique were identified. All patients had undergone a pre-procedural clinical assessment, followed by a clinic visit at 30 days following the procedure. Continuous variables were reported as mean (95% confidence intervals), while Visual Analog Scale scores were reported as median (interquartile range). Pain Visual Analog Scale scores were also subjected to a paired *t* test using GraphPad Prism software, Version 6.04 for Windows, (GraphPad Software, San Diego, California).

Received July 30, 2018; accepted after revision September 28.

From the Division of Neuroradiology (P.J.N., C.A.H., W.B., A.C.O.T., R.S.), Joint Department of Medical Imaging, Toronto Western Hospital, University of Toronto, Toronto, Ontario, Canada; and Division of Neurosurgery (A.C.O.T.), Department of Surgery, Queen Mary Hospital, University of Hong Kong, Hong Kong.

Please address correspondence to Patrick J. Nicholson, MD, Division of Neuroradiology, Joint Department of Medical Imaging, Toronto Western Hospital, University of Toronto, 399 Bathurst St, Toronto, Ontario, M5T 2S8, Canada; e-mail: paddynicholson@gmail.com

<http://dx.doi.org/10.3174/ajnr.A5884>



FIG 1. Posteroanterior fluoroscopic image showing the Tl-ga needle inserted via the left sacral ala in a transiliac approach.



FIG 3. Posteroanterior fluoroscopic image showing the needle having been withdrawn in a transiliac fashion along its insertion path, injecting aliquots of cement as it is withdrawn.

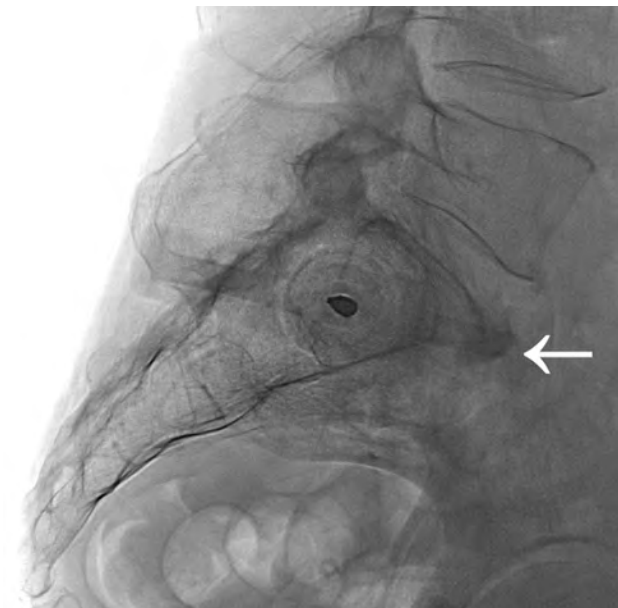


FIG 2. Lateral fluoroscopic image showing the same needle inserted into S1, positioned within the intramedullary cavity between the anterior and posterior cortices of the bone. Note an osteophyte anterior to the anterior margin of the sacrum (*white arrow*).

Technique and Illustrative Case

A 75-year-old woman had experienced painful sacral fractures (Fig 1). She had a history of multiple myeloma for which she had received radiation therapy to her spine and pelvis. Her mobility and quality of life were markedly impaired, to the extent that she required a walker and was using considerable amounts of opiate medication daily. She ranked her average daily pain as 7 on the Visual Analog Scale when assessed in the spinal clinic. The procedure was performed with the patient under conscious sedation provided by the anesthesiology service. The patient was positioned prone on the angiography table for the procedure, with straps used to minimize movement. Most important, a foam wedge was used to elevate the ipsilateral side of the patient (ie, the side of the entry point). The most common entry site is via the left sacral ala, which is the on the side of the operator when the patient is positioned prone. Conebeam CT was performed, and a needle



FIG 4. Lateral fluoroscopic image following needle withdrawal showing the polymethylmethacrylate cement confined to the sacral cortex.

trajectory was chosen on the planning software package (Fig 2) using XperGuide software. A 10-mL mix of 1% lidocaine and 0.25% marcaine was injected in the subcutaneous tissues down to

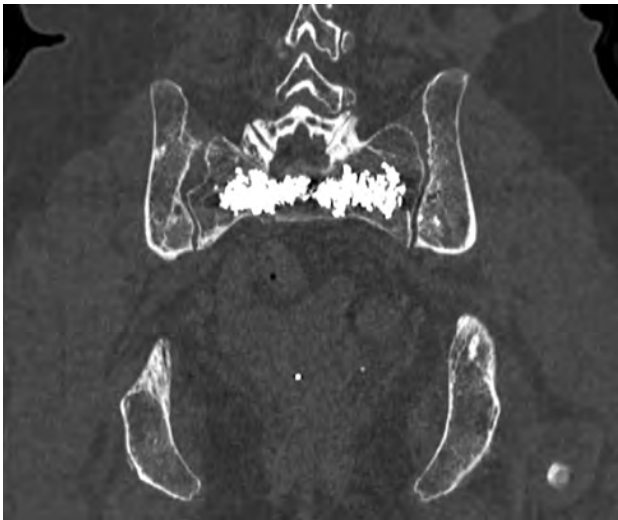


FIG 5. Axial reconstruction from a postoperative CT scan showing the cement well-positioned within the intramedullary cavity of the sacrum.

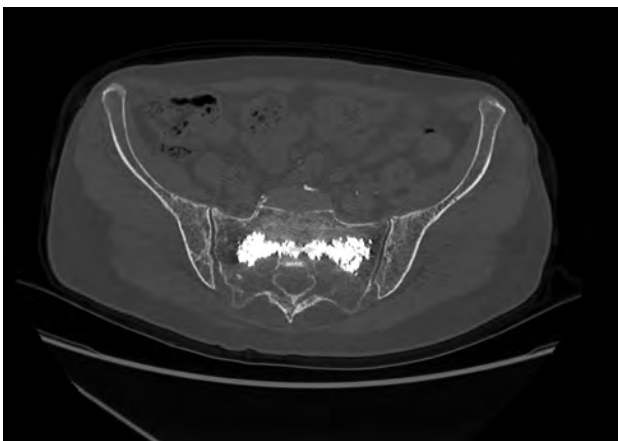


FIG 6. Coronal reconstruction from a postoperative CT scan showing the cement well-positioned within the intramedullary cavity of the sacrum.

the level of the periosteum. Following a skin incision, an 11-ga (15 cm) diamond-tipped needle was used to perform the sacroplasty, while accessing the sacrum from the left side. The needle crossed the midline to the contralateral sacral ala (Figs 3 and 4). We injected 11 mL of cement using real-time biplane fluoroscopic guidance, injecting slowly in discrete aliquots of cement as the needle was withdrawn to the ipsilateral sacral ala via the midline sacral body. Continuous fluoroscopic monitoring for extrusion of cement outside the sacral bone was performed. The patient tolerated the procedure well and was ambulating again 1 hour after returning to the day surgery ward. At her 1-month follow-up visit, she reported that she was pain-free and no longer required opiates for anesthesia (Figs 5 and 6).

RESULTS

During a 1-year period, 10 patients underwent single-needle lateral sacroplasty using this technique. Their clinical details and outcome data are summarized in the Table. The median patient mean age was 67.5, IQR 12.75 (95% CI, 57.8–77.2 years). Six of

Patient details and outcome data

Sex	Age (yr)	Cement Volume Injected (mL)	Primary Disease	Pain Preprocedure (VAS)	Pain 1 Month Postprocedure (VAS)
Female	36	14	Breast carcinoma	4	0
Male	59	11	Myeloma	7	2
Female	62	12	Non-small cell lung carcinoma	7	0
Male	66	25	Myeloma	5	0
Male	86	10	Osteoporosis	7	0
Female	69	10	Osteoporosis	10	6
Female	69	10	Breast carcinoma	8	4
Female	77	11	Osteoporosis	7	3
Female	75	11	Myeloma	7	0
Male	76	8	Non-small cell lung carcinoma	8	0

Note:—VAS indicates Visual Analog Scale.

the 10 patients were women. Fracture etiology was osteoporotic insufficiency in 3 patients (30%), while the remainder had cancer-related fractures (70%). The median Visual Analog Scale score before the procedure was 7.0 (interquartile range, 7–7.5), while the median Visual Analog Scale score measured at 30-day follow-up was 0 (interquartile range, 0–2.75; $P \leq 0.01$). One patient experienced severe right-leg pain in the S1 distribution the day after the procedure. This resolved following an epidural nerve root injection of steroid and local anesthesia, and she remained pain-free on follow-up.

DISCUSSION

Sacroplasty is emerging as a valuable tool for the treatment of sacral fractures, both insufficiency fractures and those related to cancer.⁵ While the technique shows great promise, there are many inherent challenges to overcome. These include the relatively complex anatomy of the sacral bone, as well as the need for accurate needle placement to avoid damage to either the surrounding pelvic organs or the neurovascular structures that course through the sacrum. Conventional radiographic views are therefore insufficient due to the relatively high associated rates of needle malposition.⁶ Angiography suites equipped with conebeam CT have allowed acquisition of volumetric CT images on the angiography table, thereby combining the advantages of traditional CT imaging guidance with those of real-time biplane fluoroscopy. These allow real-time high-resolution image reconstruction in any plane. When used with needle-tracking/planning software, this acquisition allows precise trajectory planning and real-time needle and cement-position monitoring. This biplane equipment or planning software or both are not strictly necessary; indeed, many groups perform this procedure using, for example, CT fluoroscopy. However, we think that if it is available with your equipment, the use of biplane \pm planning software does offer benefit and its use should be at least considered.

The classification of Denis et al⁷ of sacral insufficiency fractures organizes these fractures according to direction, location, and level. Most of these fractures occur in the craniocaudal direction, so the use of a lateral- or transverse-axis approach allows cement deposition across the fracture line, buttressing the fracture on either side.

The type of fracture and underlying pathology also guide our approach. A single-needle approach is possible in some but not all solid tumors; occasionally, a multiple-needle approach may be

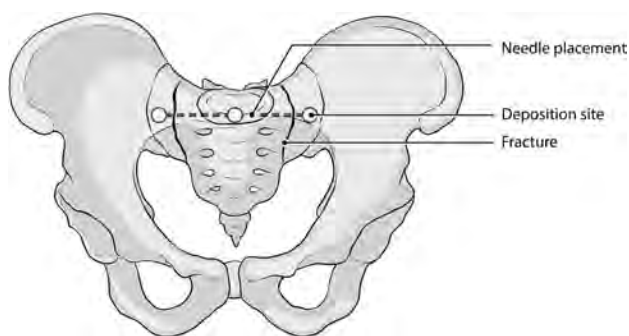


FIG 7. Illustration of the correct needle trajectory showing the needle path and method of cement deposition in the anteroposterior plane.

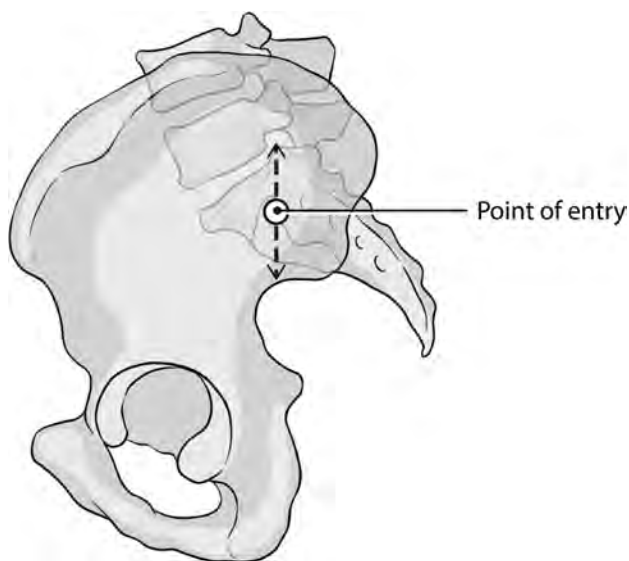


FIG 8. Illustration of the correct needle trajectory showing the needle path and method of cement deposition in the lateral plane.

necessary to target multiple solid lesions. A single-needle approach is more often feasible in patients with primary osteoporosis, secondary osteoporosis (eg, secondary to systemic treatment or pelvic irradiation), or diffuse disease (eg, multiple myeloma). We therefore carefully review the preoperative imaging and underlying etiology and tailor our treatment approach accordingly.

The curved structure of the sacral bone means that traditional anteroposterior and lateral radiographic views are often insufficient to provide safe working angles for needle placement.⁸ Percutaneous screws have been used for fixation for posterior sacral

fractures,⁹ and the technique has shown promise. Lateral sacroplasty emulates this approach, taking advantage of the lateral view to minimize needle and cement penetration through the anterior cortex of the bone (Figs 7 and 8). This transverse-axis approach usually means using 2 separate needles for both sacral alae, however. Our approach allows good cement filling of the intramedullary space of the sacrum using a single skin incision and bone puncture and, therefore, comes with inherently less risk of hematoma and infection. There is also less pain locally for the patient following the procedure.

CONCLUSIONS

Sacroplasty is emerging as a useful tool for the treatment of sacral fractures, either due to osteoporosis or cancer. We have presented our single-needle technique, which uses the advantages of on-table conebeam CT combined with real-time biplane fluoroscopic guidance. This allows a complete sacroplasty using only 1 needle, and in our series, it was associated with significant reduction in pain scores as measured by the Visual Analog Scale.

REFERENCES

1. Bydon M, Fredrickson M, De la Garza-Ramos R, et al. **Sacral fractures.** *Neurosurg Focus* 2014;37:E12 CrossRef
2. Pereira LP, Clarençon F, Cormier E, et al. **Safety and effectiveness of percutaneous sacroplasty: a single-centre experience in 58 consecutive patients with tumours or osteoporotic insufficient fractures treated under fluoroscopic guidance.** *Eur Radiol* 2013;23:2764–72 CrossRef Medline
3. Siggins K, Sabou S, Pasku D, et al. **Systematic review of sacroplasty for metastases to the sacrum.** *Spine J* 2016;16:S89
4. Pommersheim W, Huang-Hellinger F, Baker M, et al. **Sacroplasty: a treatment for sacral insufficiency fractures.** *AJNR Am J Neuroradiol* 2003;24:1003–07 Medline
5. Hirsch, JA, Barr JD, Zoarski GH. **Sacroplasty: beyond the beginning.** *J Neurointerv Surg* 2013;5:395 CrossRef Medline
6. Routt ML Jr, Simonian PT, Agnew SG, et al. **Radiographic recognition of the sacral alar slope for optimal placement of iliosacral screws: a cadaveric and clinical study.** *J Orthop Trauma* 1996;10:171–77 CrossRef Medline
7. Denis F, Davis S, Comfort T. **Sacral fractures: an important problem—retrospective analysis of 236 cases.** *Clin Orthop Relat Res* 1988; 227:67–81 Medline
8. Xu R, Ebraheim NA, Robke J, et al. **Radiologic evaluation of iliosacral screw placement.** *Spine (Phila Pa 1976)* 1996;21:582–88 CrossRef Medline
9. Suzuki T, Hak DJ, Ziran BH, et al. **Outcome and complications of posterior transiliac plating for vertically unstable sacral fractures.** *Injury* 2009;40:405–09 CrossRef Medline

Maternal-Fetal Medicine Specialists Should Manage Patients Requiring Fetal MRI of the Central Nervous System

It has been established that fetal MR imaging can provide increased sensitivity and specificity for fetal central nervous system abnormalities,¹ but whether a given diagnostic test will change management should also be considered when the value of the test is assessed.

Having worked with the first fetal MR imaging program in a rural region in the central United States some years ago, I recall that the requests for fetal MR imaging ramped up in the years following its initiation: Forty-six fetal MRIs in 44 patients were performed to interrogate possible CNS abnormalities during the first 58 months of the program. Our experience in this nonacademic community setting mirrored larger studies that have since confirmed the improved accuracy of MR imaging compared with sonography.² With fetal MR imaging as the criterion standard in this small sample, sonography was shown to be 61% accurate for ventriculomegaly, 80% accurate for callosal dysgenesis, 93% accurate for holoprosencephaly, and 100% accurate for encephalocele. However, only 14% of the MR imaging scans were performed in cases in which changing the sonography-based diagnosis would have affected counseling, and no management changes were observed during pregnancy in this community as a result of MR imaging findings. In contrast, a study performed at a larger American academic center reported that antenatal management changes were observed in 18.6% of cases in the early years of fetal MR imaging.³

An element of “Gizmo Idolatry”⁴ may be more likely to manifest at nonacademic medical centers. Most data on fetal MRIs have arisen from the academic setting as opposed to the nonacademic community setting, and it is likely that these epicenters of advanced pathology are more likely to see and treat advanced CNS disorders. My concern is that if fetal MR imaging use becomes more widespread without consultation with a maternal-fetal medicine specialist, the availability of the examination, rather than its potential to change medical management, will drive use.

Fetal MR imaging requires considerable resources. Technologist training, radiologists being present for supervision, and counseling by the interpreting physician all add considerable complexity to the study. Fetal MR imaging is considerably more expensive than sonography, though the actual reimbursement may not be commensurate with the amount of time and resources allocated.

In summary, the superior diagnostic quality that fetal MR imaging provides has been well-established. Increasing availability is almost always followed by increased use without necessarily adding value to the health care system, and more science may be needed to justify the cost of this examination if the result would not add management-changing information to the ultrasound result. Fetal MR imaging may be quite valuable in the hands of skilled specialists in large quaternary care centers when ultrasound suggests pathology, but a more liberal application of fetal MR imaging may not be advantageous on a cost-benefit basis. If ordering fetal MR imaging in a patient with normal findings on prenatal sonography becomes commonplace as has been suggested,¹ the potential for increased cost to the health care system is great, particularly if we drift away from emphasizing high-quality sonography as an acceptable standard in fetal imaging.

REFERENCES

1. Griffiths PD, Mooney C, Bradburn M, et al. **Should we perform in utero MRI on a fetus at increased risk of a brain abnormality if ultrasonography is normal or shows non-specific findings?** *Clin Radiol* 2018;73:123–34 CrossRef Medline
2. Griffiths PD, Bradburn M, Campbell MJ, et al; MERIDIAN collaborative group. **Use of MRI in the diagnosis of fetal brain abnormalities in utero (MERIDIAN): a multicentre, prospective cohort study.** *Lancet* 2017;389:538–46 CrossRef Medline
3. Levine D, Barnes PD, Robertson RR, et al. **Fast MR imaging of fetal central nervous system abnormalities.** *Radiology* 2003;229:51–61 CrossRef Medline
4. Leff B, Finucane TE. **Gizmo idolatry.** *JAMA* 2008;299:1930–32 Medline

 C.M. Pfeifer

Department of Radiology
University of Texas Southwestern Medical Center
Dallas, Texas

<http://dx.doi.org/10.3174/ajnr.A5894>

The “Bovine Aortic Arch”: Time to Rethink the True Origin of the Term?

We read with some bemusement the ongoing debate about the term “bovine aortic arch” and calls for a change in name. The most recent is the letter by Rajagopal and Sharma, who nicely describe the embryologic basis but fail to prove that “bovine” is a misnomer.¹

We recently reviewed the bovine aortic arch as part of a collection of animal signs in radiology.² The debate about the bovine arch in the literature focuses on the recognition that this is not the normal aortic branching pattern in bovines. This is insufficient evidence to describe “bovine” as a misnomer, particularly when this fact was known several decades before the first articles to use the term (one of which even cited this preceding literature).

The appropriate question then becomes why is this variation called a bovine arch when it is not found in bovines?

Many signs in clinical medicine represent analogies being made to something known: pattern finding being an important and fundamental process in the way humans think. Describing the pattern of the stars as being in the shape of animals or heroes is just one of the more ancient examples. The uptake of the analogy depends on whether others find the association useful.

There are many ways in which one may ascribe an animal term. Some are indeed named because they are the normal pattern in such animals: such as avian appendix and feline esophagus. Galen’s writing describes several anatomic features resembling an animal, including muscle (“musculus” being Latin for “little mouse”) and coracoid process (Greek for “like a crow”). A few are named after movements resembling an animal such as the bullfrog swallow and jellyfish sign in pleural effusions. The eating disorder “Pica” is even named after an animal’s behavior (Pica being Latin for crow, a bird considered to eat anything). Many signs are named after the radiologic appearance resembling an animal, including butterfly glioma and the hummingbird sign as well as anatomic variants such as butterfly vertebra and fish tail pancreas.

There are also examples in which the origin of a term has not been recognized and alternate associations have been made. Many fish terms have been used to describe osteoporotic vertebrae, including “fish-mouth” and “fish-tail” (both being analogies with the radiologic appearance). The correct terminology was debated in the literature until Murphy and DiVito determined that Albright initially likened the pathologic pattern in humans to the normal vertebrae in fish.³ The homonyms of “thrush,” the bird

(from old English “songbird”) and the disease (from Scandinavian “rotten”), represent another example in which some have tried to find a visual association because of not being aware of the different etymology of the terms.

Recognizing the many ways in which one can be ascribe an animal descriptor widens the options for the origin of the term “bovine.” We favor Jiri Vitek’s radiologic derivation.⁴ During the decades when angiography was the primary method of assessing the cerebral vessels, overlapping of structures limited clear delineation of the anatomy. When the left common carotid artery arises from the brachiocephalic artery, it has a more horizontal initial course than with an aortic origin. This resembles the horns of a bovine, which are characteristically horizontal at the top of the bovine head before they curve superiorly (Figure).

In conclusion, the term “bovine aortic arch” is a widely used and a simple description. We believe that it is time to drop the notion that the name derives from the anatomic pattern in bovines because we are not aware of any evidence to support this as the origin of the term. No one, for example, would describe butterfly vertebra as a misnomer, even though butterflies do not have vertebrae.

Disclosures: Lloyd J. Ridley—UNRELATED: Payment for Lectures Including Service on Speakers Bureaus: AstraZeneca, Comments: state speaker honorarium for AstraZeneca.

REFERENCES

1. Rajagopal R, Sharma S. **Comment on “Common Origin of Brachiocephalic and Left Common Carotid Arteries: Proposal of New Terminology.”** *AJNR Am J Neuroradiol* 2018;39:E105 CrossRef Medline
2. Han J, Xiang H, Ridley WE, et al. **Bovine aortic arch.** *J Med Imaging Radiat Oncol* 2018;62 (supplement 1): 20–21 Medline
3. Murphy WA Jr, DiVito DM. **Fuller Albright, postmenopausal osteoporosis, and fish vertebrae.** *Radiology* 2013;268:323–26 CrossRef Medline
4. Vitek JJ. **Comment on: Bovine aortic arch variant in humans: clarification of a common misnomer.** *AJNR Am J Neuroradiol* 2007;28:1205, author reply 1205 CrossRef Medline

 L.J. Ridley

Department of Radiology
Concord Repatriation General Hospital
Concord, New South Wales, Australia

 J. Han

Medical Imaging
University of Sydney
Sydney, New South Wales, Australia

 H. Xiang

Department of Radiology
Concord Repatriation General Hospital
Concord, New South Wales, Australia



FIGURE. A, Volume-rendered 3D image of a bovine arch derived from a CT angiogram. B, Graphic of a bovine head drawn onto the volume-rendered image shown in A.

REPLY:

We read with interest the comments by Ridley et al and have the following observations.

The term “bovine arch,” according to Vitek,¹ was coined to describe the angiographic appearance seen with a common origin of the innominate artery and the left common carotid artery, in which the left common carotid artery was seen to have a proximal horizontal course in the superior mediastinum before curving superiorly to enter the neck. Before the 1970s, this anatomic variant was called by its Latin name, “truncus communis with sinistra.” The term “bovine arch” was first used in the literature only in the 1970s. There is confusion in the current literature about the derivation of the name bovine arch as to whether it refers to the anatomic pattern or its angiographic appearance.

Viewed in the anatomic context, the course of the proximal left common carotid artery when arising from the innominate artery could vary from being horizontal to more vertical in the superior mediastinum before coursing superiorly to exit the thoracic outlet. In patients having a more horizontal course of the proximal left common carotid artery, the characteristic bull horn–like appearance is seen on angiography as described by Vitek.¹ This is usually seen in the elderly, in whom the tortuous course of the proximal carotid artery could be the result of vascular aging.

Etymologically, analogous names have followed, 2 of which are “avian” and “amphibian” arches. Whereas the avian arch refers to a common trunk for both carotid arteries and a common trunk for both subclavian arteries originating from the aortic arch

as is seen in birds, the amphibian arch refers to a double aortic arch as seen in amphibians.²

Thirdly anatomists and cardiovascular researchers have begun to replace Greek and Latin names with more anglicized names to reflect the anatomic/pathologic abnormality in an accurate manner and to facilitate a unified reporting system and communication across the world, for instance, “common arterial trunk” in place of “truncus arteriosus.” Even though animal names have been used to facilitate understanding by medical students, they are unscientific in a purist’s view and should not be used in scientific communication involving anatomic abnormalities. With the exceptional advancements in orthogonal imaging technologies, an anatomic abnormality can have a varied appearance.

Therefore, use of the term “bovine arch” for a common origin is not inclusive of all its patterns seen radiologically and does not reflect the true ‘bovine’ anatomy. Hence, it would be preferable to use a more anatomically appropriate term, brachio-bicarotid trunk, for the anatomic variation.

REFERENCES

1. Vitek JJ. **Bovine aortic arch.** *AJNR Am J Neuroradiol* 2007;28:1205 CrossRef Medline
2. Ergun O, Tatar IG, Durmaz HA, et al. **A case of a rare aortic arch variation: the avian form.** *JBR-BTR* 2014;97:349–50 Medline

 **R. Rajagopal**
 **S. Sharma**

Department of Cardiovascular Radiology and Endovascular Interventions
Cardiothoracic Neurosciences Center
All India Institute of Medical Sciences
Ansari Nagar, New Delhi, India

<http://dx.doi.org/10.3174/ajnr.A5965>

Is Delayed Speech Development a Long-Term Sequela of Birth-Related Subdural Hematoma?

In 2008, Rooks et al¹ published an interesting study on the incidence of subdural hematoma (SDH) in neonates.¹ Of 101 neonates examined by MR imaging, 46 developed SDH. The study also identified associations between the duration of delivery and the development of SDH and reported an increased risk of SDH associated with cases of cephalhematoma and delivery duration of >120 minutes. These are important findings with reference to the appearance and natural course of birth-related SDH.

The 43 (3 children dropped out in the follow up) children who developed birth-related SDH were followed for 2 years; 7 exhibited delayed speech by the end of follow-up. One of these children was also evaluated for an autism spectrum disorder.¹ This proportion (7/43) corresponds to a prevalence of 16.3% (exact 95% CI, 6.8%–30.7%).

Rooks et al¹ claimed that the findings regarding speech delay were similar to the known prevalence (not incidence) in the general population, citing a review that reported a 15% prevalence of speech delay in the preschool period.² Although it was not explicitly stated, we believe that this figure emanates from a well-cited review by Law et al.³ This review reported study estimates of the prevalence of speech delay among 6-year-olds (excluding children with autism) ranging from 12.6% to 16.5% cited by Rooks et al.¹ No studies on speech delay among 5-year-olds or younger were cited. In a more recent publication on speech and language delay in 5-year-olds or younger, the authors concluded that there is still a lack of information on the prevalence in this group.⁴

According to Rooks et al,¹ approximately 46% (3 dropped out in the follow up) (46/101) of neonates develop SDH after birth. Even if the true prevalence of delayed speech among those without SDH were 0%, there is a prevalence of 7.5% ($0.46 \times 16.3\%$) for speech delay in the general population, which includes children both with and without SDH. Given the lack of information on the prevalence for 5-year-olds and younger, this possibility cannot be excluded.

Hence, the question is why the authors chose to compare the prevalence at 2 years of age in the group with birth-related SDH with the prevalence of historical controls from a general popula-

tion of 6-year-olds. We believe it would have been more rewarding to compare the proportion of children with SDH with delayed speech with the proportion among the 55 without SDH. A follow-up of the 55 children without birth-related SDH as a control group could have shed light on the question of whether there are any sequelae to birth-related SDH. Unfortunately, the authors seem to have missed this opportunity. It is known that traumatic deliveries might result in large hemorrhages with poor prognosis.⁵ However, it remains unclear whether delivery-associated SDH in some instances might result in subclinical symptoms or whether it is truly asymptomatic.

REFERENCES

1. Rooks VJ, Eaton JP, Ruess L, et al. **Prevalence and evolution of intracranial hemorrhage in asymptomatic term infants.** *AJNR Am J Neuroradiol* 2008;29:1082–89 CrossRef Medline
2. Feldman HM. **Evaluation and management of language and speech disorders in preschool children.** *Pediatr Rev* 2005;26:131–42 CrossRef Medline
3. Law J, Boyle J, Harris F, et al. **Prevalence and natural history of primary speech and language delay: findings from a systematic review of the literature.** *Int J Lang Commun Disord* 2000;35:165–88 CrossRef Medline
4. Siu AL; US Preventive Services Task Force. **Screening for speech and language delay and disorders in children aged 5 years or younger: US Preventive Services Task Force Recommendation Statement.** *Pediatrics* 2015;136:474–81 CrossRef Medline
5. Tan AP, Svrckova P, Cowan F, et al. **Intracranial hemorrhages in neonates: a review of etiologies, patterns and predicted clinical outcome.** *Eur J Paediatr Neurol* 2018;22:690–717 CrossRef Medline

 **N. Lynøe**

Learning, Informatics, Management and Ethics (LIME)
Stockholm Centre for Healthcare Ethics
Karolinska Institutet
Stockholm, Sweden

 **D. Olsson**

Learning, Informatics, Management and Ethics (LIME)
Medical Statistic Unit
Karolinska Institutet
Stockholm, Sweden

 **A. Eriksson**

Department of Community Medicine and Rehabilitation, Forensic Medicine
Umeå University
Umeå, Sweden

<http://dx.doi.org/10.3174/ajnr.A5890>

REPLY:

We appreciate the comments of Dr Lynøe and colleagues.

The objective of our study was to determine the prevalence, size, location, and appearance of subdural hemorrhage (SDH) in asymptomatic term infants and the natural history of the hemorrhage until imaging resolution. Determining the developmental outcome of neonatal SDH was not a primary or secondary outcome objective of our study. We did review the development of those children with birth-related SDH seen at their 2-year well-child visit and reported that 6/43 (14%) were found to have early speech and language delays and 1 patient (2%) was suspected of having an autism spectrum disorder, given early language and social delays.¹

Dr Lynøe and colleagues raised concern about a paucity of literature on the prevalence of speech delay in children younger than 5–6 years of age, so comparison between our groups at 2 years with historical controls is problematic. We would suggest that the prevalence of early speech and language delays might be even higher than that reported in older children because some early delays resolve with long-term follow-up and early intervention. This is certainly true of a subset of children who are “late talkers.” The prevalence of speech delay in our study is thought to be consistent with that found in the literature, including a recent publication by Mondal et al,² who report a speech and language delay prevalence of 27% in children younger than 3 years of age seen in an “Under Five” clinic. These children were screened using a language-evaluation scale as well as a developmental screening tool. Mondal et al report that the developmental screening device used may not suffice as a screening tool for speech and language delay because it had a sensitivity of only 33% in detecting speech delay, likely because the tool had few language items for groups younger than 24 months of age.

Suggesting any association of neonatal SDH with subsequent developmental delay, to include isolated speech delay, on the basis

of our study results is not recommended because we did not investigate other risk factors for developmental delay, which may include male sex, family history of speech and language delay, low parental educational level, low birth weight, lower socioeconomic status, environmental exposure, prenatal complications, impaired hearing, and so forth.^{2,3}

As mentioned by Lynøe and colleagues, we did not review the records of those neonates with normal imaging findings at birth because developmental outcome was not the objective of our study. A long-term, prospective study would be helpful in addressing this question of long-term sequelae related to birth SDH.

REFERENCES

1. Rooks VJ, Eaton JP, Ruess L, et al. **Prevalence and evolution of intracranial hemorrhage in asymptomatic term infants.** *AJNR Am J Neuroradiol* 2008;29:1082–89 CrossRef Medline
2. Mondal N, Bhat B, Plakkal N, et al. **Prevalence and risk factors of speech and language delay in children less than three years of age.** *Journal of Comprehensive Pediatrics* 2016;7:1–7 CrossRef
3. Wallace IF, Berkman ND, Watson LR, et al. **Screening for speech and language delay in children 5 years old and younger: a systematic review.** *Pediatrics* 2015;136:e448–62 CrossRef Medline

V.J. Rooks

Department of Radiology
Tripler Army Medical Center
Honolulu, Hawaii

Department of Radiology and Radiological Sciences
F. Edward Hebert School of Medicine
Uniform Services University of the Health Sciences
Bethesda, Maryland

L. Ruess

Nationwide Children's Hospital
Columbus, Ohio

G.W. Peterman

Marshfield Clinic
Marshfield, Wisconsin

R.C. Pedersen

Clinical Professor of Pediatrics and Psychiatry
John A. Burns School of Medicine
University of Hawaii
Hawaii Permanente Medical Group
Honolulu, Hawaii

<http://dx.doi.org/10.3174/ajnr.A5969>